

**Structural Investigations on Organometallic Complexes and
Nanomaterials by X-ray Absorption Fine Structure and
Raman Spectroscopy**

Von der Fakultät Chemie der Universität Stuttgart
zur Erlangung der Würde eines Doktors der
Naturwissenschaften (Dr. rer. nat.)
genehmigte Abhandlung

Vorgelegt von

Venkata Krishnan

aus Gobichetipalayam T.N., Indien

Hauptberichter	:	Prof. Dr. Helmut Bertagnolli
Mitberichter	:	Prof. Dr. Klaus Müller
Mitprüfer	:	Prof. Dr. Dietrich Gudat
Tag der mündlichen Prüfung	:	13. Juli 2006

Institut für Physikalische Chemie
der Universität Stuttgart

2006

Eidesstattliche Erklärung

Die vorliegende Arbeit entstand von Juli 2002 bis Juni 2006 am Institut für Physikalische Chemie der Universität Stuttgart unter der Anleitung von Prof. Dr. Helmut Bertagnolli. Hiermit versichere ich, dass die vorliegende Arbeit selbständig verfasst und nur die angegebenen Quellen und Hilfsmittel verwendet wurden.

Stuttgart, den 20. Juni 2006

Venkata Krishnan

Hauptberichter : Prof. Dr. Helmut Bertagnolli
Mitberichter : Prof. Dr. Klaus Müller
Mitprüfer : Prof. Dr. Dietrich Gudat
Tag der mündlichen Prüfung : 13. Juli 2006



Wilhelm Conrad Roentgen (1845 - 1923)

Nobel Laureate in Physics (1901)

Discoverer of X-rays

“The scientist must consider the possibility, which usually amounts to a certainty, that his work will be superseded by others within a relatively short time, that his methods will be improved upon and that the new results will be more accurate and the memory of his life and work will gradually disappear”

W. C. Roentgen during his address on assuming the rectorship of the University of Würzburg (Germany) in 1894, a year before the discovery of X-rays



Chandrasekhara Venkata Raman (1888 - 1970)

Nobel Laureate in Physics (1930)

Discoverer of Raman effect

“In the history of science, we often find that the study of some natural phenomenon has been the starting point in the development of a new branch of knowledge”

C. V. Raman in his lecture to the assembly upon receiving the Nobel Prize in Physics in 1930, two years after the discovery of Raman effect.

Dedicated to my beloved teacher



Prof. O. P. Vidyakar

Former Head

Department of Chemistry

PSG College of Technology

Coimbatore, Tamil Nadu, India

Acknowledgement

I sincerely express my deep sense of gratitude to **Prof. Dr. Helmut Bertagnolli** for his inspiring guidance, constant encouragement and support throughout the work. I thank him very much for providing me the freedom to explore the realms of science and for sharing his wide knowledge and expertise. I very much appreciate the pressure-free working environment he provides to the group members, thereby leading to a highly productive atmosphere, where everyone understands their responsibilities and acts accordingly. I am highly grateful to him for standing by my side in times of difficulties, solving the problems and motivating me to progress ahead. In spite of his busy schedule, he made himself always available whenever I approached him. I sincerely thank him for being open and positive to all my suggestions, especially with regard to establishing new collaborations. I am very much grateful that he let me present our research activities at numerous conferences, workshops, seminars and meetings.

I would like to thank **Dr. Dieter Leicht** for his immense help in administrative procedures and for contributing a lively atmosphere in the work group. I thank him very much for the mail correspondences we had, even before I landed in Stuttgart. I also thank him for the understanding and adjustments in the practical courses, which I handled, during my tenure, under his direction.

I specially thank **Mrs. Gisela Hoppe** for her secretarial assistance and support in bureaucratic formalities. I also thank her for the untiring efforts she had taken to prepare my work contracts and helping me in understanding the German rules and regulations.

I am highly indebted and grateful to **Martin** for his guidance and help at each and every step of my initial period in Stuttgart. I thank him very much for introducing me to the field of XAFS and Raman spectroscopy. I will forever be thankful for the support and care he had vested on me throughout the period of my doctoral work.

My hearty thanks to **Eric** for his friendly support and understanding, and for contributing a pleasant environment in the office. I sincerely thank him for his assistance during the beamtimes and valuable suggestions during the data analysis. I will remember forever all the interesting scientific and non-scientific discussions we had together. I wish to have a colleague like him in future too.

Many thanks to **Ulrich** for making me feel at ease during my initial period. Even though the overlap phase was short, the pleasant impressions will remain forever. It will be ever in my memory the first German words, which he taught me.

I am very much grateful to **Prof. Dr. M. S. Vijaya, Dr. S. Sentilnathan** and my **M.Sc. classmates** for their motivation, encouragement and persistent support during my search for a Ph.D. position.

I express my unbound gratefulness to **Gokul** for his great support throughout my doctoral tenure. I will ever remember and remain thankful for all the great help he did to me even before I came to Stuttgart. I very much appreciate his helping nature, especially for accepting me in his room without even seeing me.

Many thanks to **Sankaran** for reading and correcting my thesis in detail. I very much appreciate his comments, discussions and valuable suggestions during the final phase of my work. I am grateful to him for the trust he vested on me in deciding his career.

I am especially grateful to my research students **Sandra** and **Sonja** for their immense help in performing and interpreting Raman measurements. I am pleased to thank the beginners' practical's **students** for their contribution in improving my teaching abilities.

My hearty thanks to my colleagues, in particular **Tanja, Matthias, Gerhard, Jutta, Markus, Rivo, Irene, Maren** and **Fabio** for their support in one way or the other in successful completion of this work. I also thank the then beamline scientists **Dr. Julia Wienold** and **Dr. Stefan Mangold** for their assistance handling the beamlines.

I am thankful to **Dr. Isabella Waldner** for her help in translating the summary into German and for support in DAAD and other administrative formalities. I am grateful to **Mrs. Diana Zauser** for drawing figures for my dissertation and publications. Without her works my very first publication would not have come out in the form as it is now.

I thank **Mrs. Gabriele Bräuning** and **Mrs. Annette Hirtler** for their help in the laboratory, **Mr. Jochen Graf, Mr. Walter Ottmüller** and **Mr. Thomas Weigend** for mechanical workshop support, **Mr. Jürgen Hußke** for electrical workshop support and **Mr. Werner Hopf** for the glass blower support.

I am glad to thank **Mrs. Inge Knechtel** for teaching me German language in an excellent way. I appreciate her well-structured and enjoyable method of instruction.

I am very grateful to my **family members** and **well-wishers** for everything that they have done for me. I am very glad to thank my friends, especially **Samir, Mahendra, Nitin, Tushar, Kailash, Nachi** and **Kamal** for their support and understanding, and for contributing a pleasant living environment in Stuttgart. I owe my deep sense of gratitude to my friends **Arun** and **Saravana** for their consistent motivation, encouragement and moral support rendered to me, which made me to progress persistently.

I would like to express my sincere gratitude to **Prof. Dr. Ekkehard Lindner** for establishing the Graduiertenkolleg ‘Chemie in Interphasen’, thereby paving way for me to perform doctoral studies in Germany. I greatly admire his lecturing skills and his personality as a professor. I would also like to thank **Mrs. Heidrun Lindner** for her kindness and care towards me.

Special thanks to **Prof. Dr. Christian Ochsenfeld** for providing me the opportunity to perform my first practical course in his work group. I admire his piercing insights, enthusiasm and cheerful attitude towards work. I also thank **Prof. Dr. Klaus Müller** for allowing me to carry out the second practical course in his work group.

I express my sincere thanks to all my collaborators listed below, for their support, comments, suggestions and discussions. The entire edifice of this work is built on the foundation of their fruitful collaborations.

(1) Faculty of Chemistry, University of Tübingen, Tübingen, Germany

- **Prof. Dr. Ekkehard Lindner** and his colleagues
- **Prof. Dr. Michael Hanack** and his colleagues
- **Prof. Dr. Hermann Mayer** and his colleagues

(2) Department of Chemical Sciences, University of Padua, Padua, Italy

- **Prof. Dr. Eugenio Tondello** and his colleagues
- **Dr. Lidia Armelao** and her colleagues
- **Dr. Silvia Gross** and her colleagues
- **Dr. Davide Barreca** and his colleagues
- **Dr. Antonella Glisenti** and her colleagues

(3) Department of Chemistry, Bharathiar University, Coimbatore, India

- **Prof. Dr. K. Natarajan** and **Mr. R. Prabhakaran**

(4) Central Electrochemical Research Institute (CECRI), Karaikudi, India

- **Dr. C. O. Augustin** and **Mr. R. Kalai Selvan**

Last but not the least I would like to express my whole hearted gratitude to **DFG** for the financial support of this project, **Graduiertenkolleg ‘Chemie in Interphasen’** for my doctoral fellowship and **DAAD** for funding my stay and travel to Padua, Italy. I also thank **HASYLAB** at DESY, Hamburg and **ANKA** at FZK, Karlsruhe for their kind support for the synchrotron radiation experiments.

Above all I am highly grateful to the **God Almighty** for his abundant blessings. I am ever thankful to him for being with me all the time and leading me in the right direction.

Publications in journals

- (1) **V. Krishnan**, M. P. Feth, E. Wendel, Y. Chen, M. Hanack, H. Bertagnolli
EXAFS Spectroscopy - Fundamentals, Measurement techniques, Data evaluation and Applications in the field of Phthalocyanines
Z. Phys. Chem. **2004**, *218* (1), 1-15.
- (2) R. Prabhakaran, A. Geetha, M. Thilagavathi, R. Karvembu, **V. Krishnan**, H. Bertagnolli, K. Natarajan
Synthesis, characterization, EXAFS investigation and antibacterial activities of new ruthenium(III) complexes containing tetradentate Schiff base
J. Inorg. Biochem. **2004**, *98* (12), 2131-2140.
- (3) D. Barreca, A. Gasparotoo, C. Maragno, R. Seraglia, E. Tondello, A. Venzo, **V. Krishnan**, H. Bertagnolli
Cadmium *O*-alkylxanthates as CVD precursors of CdS: a chemical characterization
Appl. Organomet. Chem. **2005**, *19* (1), 59-67.
- (4) H. Bertagnolli, W. J. Blau, Y. Chen, D. Dini, M. P. Feth, S. M. O'Flaherty, M. Hanack, **V. Krishnan**
Synthesis, characterization and optical limiting properties of a gallium phthalocyanine dimer
J. Mater. Chem. **2005**, *15* (6), 683-689.
- (5) **V. Krishnan**, S. Heislbetz, M. M. Natile, A. Glisenti, H. Bertagnolli
Influence of preparation technique and iron doping on the structure and reactivity of mixed Fe-Ti-O nanocomposites
Mater. Chem. Phys. **2005**, *92* (2-3), 394-402.
- (6) L. Armelao, H. Bertagnolli, S. Gross, **V. Krishnan**, U. Lavrencic-Stangar, K. Müller, B. Orel, G. Srinivasan, E. Tondello, A. Zattin
Zr and Hf oxoclusters as building blocks for the preparation of nanostructured hybrid materials and binary oxides MO₂-SiO₂ (M = Hf, Zr)
J. Mater. Chem. **2005**, *15* (19), 1954-1965.
- (7) **V. Krishnan**, G. Bottaro, S. Gross, L. Armelao, E. Tondello, H. Bertagnolli
Structural evolution and effects of calcium doping on nanophasic LaCoO₃ powders prepared by non-alkoxidic sol-gel technique
J. Mater. Chem. **2005**, *15* (20), 2020-2027.
- (8) D. -Y. Wu, E. Lindner, H. A. Mayer, Z. -J. Jiang, **V. Krishnan**, H. Bertagnolli
Sol-gel processed diaminediphosphineruthenium(II) complexes for the catalytic hydrogenation of α,β -unsaturated ketones
Chem. Mater. **2005**, *17*, 3951-3959.

- (9) D. Barreca, A. Gasparotto, C. Maragno, R. Seraglia, E. Tondello, A. Venzo, **V. Krishnan**, H. Bertagnolli
Synthesis and characterization of zinc bis(*O*-isopropylxanthate) as a single-source chemical vapor deposition precursor for ZnS
Appl. Organomet. Chem. **2005**, *19* (9), 1002-1009.
- (10) R. Prabhakaran, **V. Krishnan**, A. Geetha, H. Bertagnolli, K. Natarajan
Synthesis, EPR, electrochemistry and EXAFS studies of ruthenium(III) complexes with a symmetrical tetradentate N₂O₂ Schiff base
Inorg. Chim. Acta **2006**, *359* (4), 1114-1120.
- (11) R. Prabhakaran, **V. Krishnan**, K. Pasumpon, D. Sukanya, E. Wendel, C. Jayabalakrishnan, H. Bertagnolli, K. Natarajan
Preparation, spectral characterization, electrochemistry, EXAFS, antibacterial and catalytic activity of new ruthenium(III) complexes containing ONS donor ligands with triphenylphosphine/arsine
Appl. Organomet. Chem. **2006**, *20* (3), 203-213.

Publications in annual reports

- (1) **V. Krishnan**, M. Seiler, M. P. Feth, I. Warad, S. Al-Garabli, E. Lindner, H. Bertagnolli
EXAFS investigations on diamine(diphosphine) and diamine(ether-phosphine) ruthenium(II) complexes
HASYLAB Annual report **2002**, 267-268.
- (2) M. P. Feth, G. Kickelbick, **V. Krishnan**, D. Holzinger, S. Gross, V. Torma, H. Bertagnolli
Structural investigation of the formation of organically surface-modified metal oxo clusters by EXAFS spectroscopy
HASYLAB Annual report **2002**, 397-398.
- (3) M. P. Feth, M. Kreitmair, **V. Krishnan**, H. Bertagnolli, A. Erko, M. Fieber-Erdmann, A. Klein
Structural investigations of square-planar Ni(II)-complexes by XANES and EXAFS spectroscopy
BESSY Annual report **2002**, 46-48.
- (4) **V. Krishnan**, A. Glisenti, M. P. Feth, E. Wendel, M. Bauer, M. M. Natile, H. Bertagnolli
Structural studies on mixed oxide nanocomposites of Ti_xFe_yO_z by EXAFS spectroscopy
ANKA Annual report **2003**, 42-43.
- (5) M. P. Feth, G. Kickelbick, S. Gross, M. Bauer, **V. Krishnan**, E. Wendel, U. Schubert, H. Bertagnolli
EXAFS investigations on nanocomposites composed of surface-modified hafnium oxo clusters and organic polymers
HASYLAB Annual report **2003**, 291-292.

- (6) **V. Krishnan**, Y. Chen, M. P. Feth, E. Wendel, M. Bauer, M. Hanack, H. Bertagnolli
EXAFS spectroscopic studies on μ -oxo-bridged gallium phthalocyanine dimer
HASYLAB Annual report 2003, 293-294.
- (7) M. Bauer, T. Kauf, E. Wendel, **V. Krishnan**, J. Christoffers, H. Bertagnolli
EXAFS investigations on the Fe(III)-catalyzed Michael reaction
ANKA Annual report 2004, 33-34.
- (8) **V. Krishnan**, A. Zattin, S. Gross, L. Armelao, E. Tondello, H. Bertagnolli
EXAFS spectroscopic investigations on nanostructured Hf_xO_y embedded in silica matrix
ANKA Annual report 2004, 35-36.
- (9) E. Wendel, T. Schurr, M. Bauer, **V. Krishnan**, A. Klein, H. Bertagnolli
Structural studies on *cis* and *trans* platinum(II) dmsO complexes
ANKA Annual report 2004, 37-38.
- (10) E. Wendel, M. Schmidt, **V. Krishnan**, M. Bauer, R. Gläser, H. Bertagnolli
EXAFS investigations on platinum particles supported on mesoporous MCM-41
HASYLAB Annual report 2004, 223-224.
- (11) **V. Krishnan**, D. -Y. Wu, I. Warad, E. Wendel, M. Bauer, E. Lindner, H. Bertagnolli
EXAFS studies on polysiloxane supported interphase catalysts based on ruthenium (II) complexes
HASYLAB Annual report 2004, 225-226.
- (12) M. Bauer, G. Kickelbick, E. Wendel, **V. Krishnan**, H. Bertagnolli
Structural investigations on titanium alkoxides in solution with EXAFS/XANES- spectroscopy
HASYLAB Annual report 2004, 375-376.
- (13) **V. Krishnan**, S. Gross, E. Wendel, M. Bauer, L. Armelao, E. Tondello, H. Bertagnolli
X-ray absorption fine structure studies on NiO clusters embedded in porous silica
ANKA Annual report 2005, 40-41.
- (14) E. Wendel, M. Schmidt, G. Upper, **V. Krishnan**, M. Bauer, M. Türk, R. Gläser, H. Bertagnolli
EXAFS investigations on platinum compounds supported on mesoporous MCM-41
ANKA Annual report 2005, 42-43.

- (15) E. Wendel, F. Meneghetti, **V. Krishnan**, S. Gross, E. Tondello, H. Bertagnolli
Influence of calcination temperature and composition on the formation of
ZrO₂-SiO₂ mixed oxides
HASYLAB Annual report 2005, 377-378.
- (16) **V. Krishnan**, M. M. Natile, E. Wendel, M. Bauer, A. Glisenti, H. Bertagnolli
Structural studies on mixed W–Ce–O nanocomposites by means of EXAFS
spectroscopy
HASYLAB Annual report 2005, 513-514.

Poster presentations

- (1) **V. Krishnan**, I. Warad, M. P. Feth, E. Wendel, M. Bauer, Z. -L. Lu,
M. Sunjuk, H.A. Mayer, E. Lindner, H. Bertagnolli
EXAFS spectroscopic investigations on the structure of ruthenium(II)
complexes in asymmetric transfer hydrogenation catalysis
*Presented at the workshop on XAS at third generation sources: highlights and
future perspectives, Grenoble, France (Jun 19 to 20, 2003).*
- (2) **V. Krishnan**, G. Bottaro, M. P. Feth, E. Wendel, M. Bauer, S. Gross,
L. Armelao, H. Bertagnolli
Structural investigations on nanophasic pure and Ca²⁺-doped LaCoO₃ by X-ray
absorption spectroscopy
*Presented at the ninth European conference on solid state chemistry, Stuttgart,
Germany (Sep 03 to 06, 2003).*
- (3) **V. Krishnan**, A. Glisenti, M. P. Feth, E. Wendel, M. Bauer, M. M. Natile,
H. Bertagnolli
Structural studies on mixed oxide nanocomposites of Ti_xFe_yO_z by X-ray
absorption spectroscopy
*Presented at the second ANKA users meeting, Karlsruhe, Germany (Sep 15
to 16, 2003).*
- (4) **V. Krishnan**, Y. Chen, M. P. Feth, E. Wendel, M. Bauer, M. Hanack,
H. Bertagnolli
EXAFS spectroscopic studies on μ-oxo-bridged metallophthalocyanine dimers
*Presented at the HASYLAB users meeting, Hamburg, Germany (Jan 29 to 30,
2004).*
- (5) T. Asthalter, **V. Krishnan**, O. Leupold, H. -C. Wille, L. Pasquinia, E. Bauer,
P. Mueller-Buschbaum
The vibrational properties of Eu₂O₃ nanoparticles as studied by nuclear
inelastic absorption
*Presented at the fourteenth ESRF users meeting, Grenoble, France (Feb 10 to
11, 2004).*
- (6) T. Asthalter, V. Olszowka, **V. Krishnan**, H. Bertagnolli
Vibrational and structural properties of europium-rich nanoparticles
Presented at Bunsen meeting 2004, Dresden, Germany (May 20 to 22, 2004).

- (7) **V. Krishnan**, S. Gross, L. Armelao, H. Bertagnolli
EXAFS investigations on hydrolysis and condensation mechanisms of metal alkoxides under sol-gel conditions
Presented at the seventh international conference on reaction mechanisms, Dublin, Ireland (Jul 04 to 08, 2004).
- (8) T. Asthalter, V. Olszowka, **V. Krishnan**, H. Bertagnolli, H. -C. Wille, O. Leupold
Confined phonons and chemical structure of europium hydroxide nanoparticle
Presented at the eleventh international conference on phonon scattering in condensed matter, St. Petersburg, Russia (Jul 25 to 30, 2004).
- (9) G. Bandoli, H. Bertagnolli, S. Gross, **V. Krishnan**, M. Montolli, G. Pace, A. Ravazzolo, R. Seraglia, E. Tondello, A. Venzo
Vinyl-functionalised cyclophosphazenes as molecular building blocks for the development of inorganic-organic hybrid materials
Presented at the fourth international conference on inorganic materials, Antwerp, Belgium (Sep 19 to 21, 2004).
- (10) **V. Krishnan**, A. Zattin, S. Gross, L. Armelao, E. Tondello, H. Bertagnolli
EXAFS spectroscopic investigations on nanostructured Hf_xO_y embedded in silica matrix
Presented at the third ANKA users meeting, Karlsruhe, Germany (Sep 23 to 24, 2004).
- (11) L. Armelao, H. Bertagnolli, S. Gross, **V. Krishnan**, U. Lavrencic-Stangar, K. Müller, B. Orel, G. Srinivasan, E. Tondello, A. Zattin
 $\text{MO}_2\text{-SiO}_2$ (M=Hf, Zr) binary oxide systems from inorganic-organic hybrid materials: synthesis, characterisation and thermal behaviour under heating
Presented at the thirteenth meeting on synthesis and methodologies in inorganic chemistry, Brixen, Italy (Dec 05 to 07, 2004).
- (12) **V. Krishnan**, S. Gross, L. Armelao, H. Bertagnolli, E. Tondello
EXAFS spectroscopy as a tool to investigate the hydrolysis and condensation reaction mechanisms of metal alkoxides as precursors in sol-gel process
Presented at the thirteenth meeting on synthesis and methodologies in inorganic chemistry, Brixen, Italy (Dec 05 to 07, 2004).
- (13) L. Armelao, H. Bertagnolli, D. Camozzo, S. Gross, **V. Krishnan**, E. Tondello
Carboxylic acids as solvent for the preparation of metal sulphide nanoparticles
Presented at the thirteenth meeting on synthesis and methodologies in inorganic chemistry, Brixen, Italy (Dec 05 to 07, 2004).
- (14) D. Barreca, C. Maragno, A. Gasparotto, R. Seraglia, E. Tondello, A. Venzo, **V. Krishnan**, H. Bertagnolli
Investigation of Cd-, Zn xanthates as single source CVD precursors for CdS and ZnS
Presented at the twenty third informal meeting on mass spectrometry, Fiera di Primiero, Italy (May 15 to 19, 2005).

- (15) S. Gross, L. Armelao, H. Bertagnolli, **V. Krishnan**, K. Müller, G. Srinivasan, A. Zattin
 Physikalisch-chemische Untersuchungen zur Umwandlung von Hybridmaterialien in nanostrukturierte gemischte Oxide
Presented at the thirteenth meeting on solid state analytics, Chemnitz, Germany (Jun 26 to 29, 2005).
- (16) **V. Krishnan**, R. Prabhakaran, A. Geetha, K. Natarajan, H. Bertagnolli
 EXAFS studies on ruthenium(III) complexes containing tetradentate N₂O₂ Schiff base ligand
Presented at the thirteenth IUPAC symposium on organometallic chemistry directed towards organic synthesis, Geneva, Switzerland (Jul 17 to 21, 2005).
- (17) S. Gross, L. Armelao, H. Bertagnolli, **V. Krishnan**, S. Mascotto, K. Müller, G. Srinivasan, E. Tondello, A. Zattin
 Spectroscopic investigations of the conversion of inorganic-organic hybrid materials into nanostructured mixed oxides
Presented at the fifth national conference on science and technology of materials (INSTM), Cagliari, Italy (Sep 26 to 29, 2005).
- (18) **V. Krishnan**, E. Wendel, M. Bauer, H. Bertagnolli
 Investigations on the structure of NiO and Pt nanoclusters embedded in porous materials by EXAFS spectroscopy
Presented at the fourth ANKA users meeting, Karlsruhe, Germany (Oct 06 to 07, 2005).

Oral presentations

- (1) EXAFS spectroscopy – A powerful tool in the structural investigations of disordered systems
Presented at fourth workshop of graduate college on chemistry in interphases, Blaubeuren, Germany (Nov 14, 2002).
- (2) EXAFS spectroscopic investigations on catalytically active metal complexes
Presented at fifth workshop of graduate college on chemistry in interphases, Blaubeuren, Germany (Nov 11, 2003).
- (3) X-ray absorption spectroscopic studies on ruthenium complexes
Presented at sixth workshop of graduate college on chemistry in interphases, Blaubeuren, Germany (Nov 16, 2004).
- (4) Structural investigations on nanomaterials by XAFS and Raman spectroscopy
Presented at the department of chemical sciences, University of Padua, Padua, Italy (Jun 10, 2005).
- (5) Investigations on the local structure of catalytically active metal complexes by means of XAFS spectroscopy
Presented at seventh workshop of graduate college on chemistry in interphases, Lauterbad, Germany (Nov 16, 2005).

Participation in conferences, workshops, seminars and meetings

- (1) Fourth workshop of graduate college on chemistry in interphases at Blaubeuren, Germany (Nov 12 to 14, 2002).
- (2) Workshop on scientific communication at Eberhard Karls University, Tübingen, Germany (Jan 20 to 22, 2003).
- (3) Summer school on theoretical and computational materials science organised by International Max Planck Research School for Advanced Materials (IMPRS-AM) at Max Planck institute of metals research, Stuttgart, Germany (Jun 02 to 06, 2003).
- (4) Workshop on XAS at third generation sources: highlights and future perspectives at ESRF, Grenoble, France (Jun 19 to 20, 2003).
- (5) Ninth European conference on solid state chemistry at University of Stuttgart, Stuttgart, Germany (Sep 03 to 06, 2003).
- (6) Second ANKA users meeting for synchrotron radiation users at FZK, Karlsruhe, Germany (Sep 15 to 16, 2003).
- (7) Workshop on rhetoric and communication at Eberhard Karls University, Tübingen, Germany (Oct 01 to 02, 2003).
- (8) Fifth workshop of graduate college chemistry in interphases at Blaubeuren, Germany (Nov 11 to 13, 2003).
- (9) HASYLAB users meeting for synchrotron radiation users at DESY, Hamburg, Germany (Jan 29 to 30, 2004).
- (10) Workshop on nanomaterials part I: organic and inorganic materials organised by International Max Planck Research School for Advanced Materials (IMPRS-AM) at Max Planck institute of metals research, Stuttgart, Germany (Apr 26 to 28, 2004).
- (11) Seventh international conference on reaction mechanisms at University College Dublin, Dublin, Ireland (Jul 04 to 08, 2004).
- (12) Workshop on website designing at Eberhard Karls University, Tübingen, Germany (Aug 16 to 17, 2004).
- (13) Third ANKA users meeting for synchrotron radiation users at FZK, Karlsruhe, Germany (Sep 23 to 24, 2004).
- (14) Workshop on nanomaterials part II: metals and semiconductors organised by International Max Planck Research School for Advanced Materials (IMPRS-AM) at Max Planck institute of metals research, Stuttgart, Germany (Sep 27 to 29, 2004).

- (15) Sixth workshop of graduate college on chemistry in interphases at Blaubeuren, Germany (Nov 16 to 18, 2004).
- (16) Twenty sixth HMI tutorial session on neutron scattering at Hahn-Meitner-Institute, Berlin, Germany (Feb 21 to 25, 2005).
- (17) Fifty fifth meeting of Nobel laureates at Lindau, Germany (Jun 26 to Jul 01, 2005).
- (18) Thirteenth IUPAC symposium on organometallic chemistry directed towards organic synthesis at Geneva, Switzerland (Jul 17 to 21, 2005).
- (19) Fourth ANKA users meeting for synchrotron radiation users at FZK, Karlsruhe, Germany (Oct 06 to 07, 2005).
- (20) Seventh workshop of graduate college on chemistry in interphases at Lauterbad, Germany (Nov 16 to 18, 2004).

Research visits

- (1) Group of Prof. Dr. C. Ochsenfeld, Institute of Physical and Theoretical Chemistry, University of Tuebingen, Germany, worked on “Quantum mechanical modelling of large molecules using DFT” (Jan 23 to Feb 05, 2003).
- (2) Group of Prof. Dr. K. Müller, Institute of Physical Chemistry, University of Stuttgart, Germany, worked on “Variable temperature FT-IR studies on the conformational order of C₁₈ stationary phase supported on different metal oxide substrates” (Apr 25 to May 06, 2005).
- (3) Group of Prof. Dr. E. Tondello, Department of Chemical Sciences, University of Padua, Padua, Italy, worked on “Synthesis and characterization of nanomaterials using XRD and XPS techniques” (Jun 06 to 19, 2005).

Beamtimes

- (1) Beamline X1 at HASYLAB, Hamburg, Germany – Sep 08 to 12, 2002.
- (2) Beamline X1 at HASYLAB, Hamburg, Germany – Feb 21 to 25, 2003.
- (3) XAS beamline at ANKA, Karlsruhe, Germany – Apr 07 to 11, 2003.
- (4) Beamline X1 at HASYLAB, Hamburg, Germany – Jul 25 to 30, 2003.
- (5) Beamline X1 at HASYLAB, Hamburg, Germany – Jul 30 to Aug 04, 2003.
- (6) XAS beamline at ANKA, Karlsruhe, Germany – Sep 22 to 27, 2003.
- (7) Beamline ID22N, ESRF, Grenoble, France – Dec 03 to 09, 2003.

- (8) Beamline X1 at HASYLAB, Hamburg, Germany – Jan 29 to Feb 03, 2004.
- (9) XAS beamline at ANKA, Karlsruhe, Germany – Feb 16 to 21, 2004.
- (10) XAS beamline at ANKA, Karlsruhe, Germany – May 03 to 08, 2004.
- (11) Beamline E4 at HASYLAB, Hamburg, Germany – Jun 01 to 06, 2004.
- (12) XAS beamline at ANKA, Karlsruhe, Germany – Oct 25 to 30, 2004.
- (13) XAS beamline at ANKA, Karlsruhe, Germany – Apr 12 to 16, 2005.
- (14) Beamline X1 at HASYLAB, Hamburg, Germany – Jun 15 to 19, 2006.

Contents

List of symbols and abbreviations	5
Chapter 1 Introduction	9
1.1. Importance of the work	9
1.2. Aim of the work	10
Chapter 2 Theory of XAFS and Raman spectroscopy	13
2.1. Theory of XAFS	13
2.1.1. XAFS phenomenon	13
2.1.2. XAFS formalism	16
2.1.3. Multiple scattering	20
2.1.4. AXAFS spectroscopy	22
2.2. Theory of Raman spectroscopy	25
2.2.1. Raman scattering	25
2.2.2. Raman selection rules	27
2.2.3. Theory of Raman effect	28
Chapter 3 Experimental methods and data analysis	30
3.1. XAFS measurements	30
3.1.1. Principle	30
3.1.2. Measurement modes	31
3.1.3. Sample preparation	34
3.2. XAFS data analysis	35
3.2.1. Data conversion	35
3.2.2. Pre-edge subtraction and normalisation	35
3.2.3. Absorption edge determination and energy correction	36
3.2.4. Background subtraction and data reduction	37
3.2.5. Interpretation of EXAFS function	39
3.2.6. AXAFS evaluation	42
3.3. Raman and infrared spectroscopic measurements	44
3.3.1. Raman measurements	44
3.3.2. Infrared measurements	44

Chapter 4 Investigations on organometallic complexes	45
4.1. Studies on optically active metallophthalocyanines	45
4.1.1. Introduction	45
4.1.2. Dimeric phthalocyanines	45
4.1.3. μ -oxo-bridged phthalocyanines	51
4.1.4. Bisaxially substituted phthalocyanines	57
4.1.5. Conclusion	62
4.2. Studies on catalytically active ruthenium(II) complexes	63
4.2.1. Introduction	63
4.2.2. Monomeric and embedded complexes	64
4.2.3. Supported complexes	68
4.2.4. AXAFS investigations on complexes with different ligands	70
4.2.5. Role of co-catalyst in asymmetric hydrogenation reaction	74
4.2.6. Conclusion	78
4.3. Studies on bio-active ruthenium(III) complexes	79
4.3.1. Introduction	79
4.3.2. Ligand I complexes	80
4.3.3. Ligand II complexes	86
4.3.4. Effects of multiple scattering	91
4.3.5. AXAFS investigations on complexes with different substituents	93
4.3.6. Conclusion	95
4.4. Studies on catalytically active iridium complexes	96
4.4.1. Introduction	96
4.4.2. Reference complexes	97
4.4.3. Hydrogenation reaction	101
4.4.4. Conclusion	105
4.5. Studies on xanthates	106
4.5.1. Introduction	106
4.5.2. Cadmium bis(<i>O</i> -isopropylxanthate)	106
4.5.3. Zinc bis(<i>O</i> -isopropylxanthate)	109
4.5.4. Conclusion	113

Chapter 5 Investigations on nanomaterials	114
5.1. Studies on nanostructured mixed oxide materials	114
5.1.1. Introduction	114
5.1.2. Nanophasic undoped and Ca-doped lanthanum cobaltite	115
5.1.3. Mixed La–Sr–Co–Fe–O nanocomposites	125
5.1.4. Mixed Fe–Ti–O nanocomposites	132
5.1.5. Mixed W–Ce–O nanocomposites	136
5.1.6. Mixed Ce–Y–Zr–O nanocomposites	139
5.1.7. Conclusion	147
5.2. Studies on ferrite based nanomaterials	149
5.2.1. Introduction	149
5.2.2. Copper ferrite nanoparticles	150
5.2.3. Copper ferrite–tin oxide nanocomposites	156
5.2.4. Copper ferrite–cerium oxide nanocomposites	159
5.2.5. Copper ferrite–nickel oxide nanocomposites	162
5.2.6. Conclusion	166
5.3. Studies on inorganic-organic hybrid materials	167
5.3.1. Introduction	167
5.3.2. Zirconium oxo cluster materials	169
5.3.3. Hafnium oxo cluster materials	173
5.3.4. Mixed zirconium and hafnium oxo cluster materials	178
5.3.5. Conclusion	182
5.4. Mechanistic studies on nucleation of ZnS nanoparticles	183
5.4.1. Introduction	183
5.4.2. Reactions with zinc acetate	184
5.4.3. Reactions with zinc oxide	189
5.4.4. Conclusion	192
5.5. Time resolved <i>in situ</i> studies on key steps of sol-gel process	193
5.5.1. Introduction	193
5.5.2. Structure of pure alkoxides	194
5.5.3. Hydrolysis and condensation of pure alkoxides	201
5.5.4. Influence of chemical modification by acetyl acetone	208
5.5.5. Hydrolysis and condensation of chemically modified alkoxides	216

5.5.6. Structure of mixture of alkoxides	223
5.5.7. Hydrolysis and condensation of mixture of alkoxides	229
5.5.8. Conclusion	235
Chapter 6 Summary and outlook	236
Zusammenfassung und Ausblick	241
References	247
Appendix	261
Curriculum vitae	273

List of symbols and abbreviations

Symbols (arranged according to the order of first occurrence)

μ	X-ray absorption coefficient
E	Photon energy
$\mu(E)$	X-ray absorption coefficient as a function of photon energy
$\mu_0(E)$	Background absorption
$\chi(E)$	Modulation of the X-ray absorption coefficient
k	Photoelectron wave vector
E_0	Position of the absorption edge
$\chi(k)$	EXAFS function
m_e	Mass of the electron ($9.109 \cdot 10^{-31}$ kg)
h	Planck's constant ($6.626 \cdot 10^{-34}$ J s ⁻¹)
ε	Polarisation vector of the electric field
γ	Electron coordinate
N_j	Atoms of j^{th} type
$F_j(k)$	Backscattering amplitude
σ_j	Debye-Waller factor
r_j	Interatomic distance
$\phi_{ij}(k)$	Phase shift
$\lambda_j(k)$	Mean free path of the photoelectron
$S_i(k)$	Amplitude reduction factor
σ_{stat}	Static disorder
σ_{vib}	Vibrational disorder
$F(r)$	Radial distribution function
$\text{Mod}(r)$	Modulus function
$w(k)$	Window function
$2r_{\text{eff}}$	Total scattering path length
R_a	Effective radius of the atom
V_a	Atomic potential relative to the interstitial zero potential
μ_a	Atomic absorption
μ_{free}	Atomic background of the free atom
χ_{atomic}	AXAFS signal

Symbols and abbreviations

R_{mt}	Muffin-tin radius
V_{int}	Interstitial potential
δ_l^a	Central atom phase shift
Φ_e	Phase shift function
f_e	Effective curved wave scattering amplitude
P	Dipole moment
E	Electric field
α	Polarisability of the molecule
Q	Normal mode of vibration
ν_0	Frequency of laser light
I_0	X-ray intensity incident on the sample
I	X-ray intensity transmitted through the sample
t	Thickness of the sample
ρ	Density
Z	Atomic number
A	Atomic mass
λ	Wave length of the incident X-rays
2θ	Scattering angle
n	Order of diffraction
I_F	Fluorescence intensity
A_{Total}	Total absorption
A_{True}	True absorption
R-factor	Agreement of the fitted function to the experimental spectrum
ΔE_0	Shift of the threshold energy
E_F	Fermi energy

Abbreviations (arranged according to the alphabetical order)

<i>acac</i>	Acetylacetone
AFAC	Amplitude reduction factor
ANKA	Angstromquelle Karlsruhe
AXAFS	Atomic X-ray absorption fine structure
CFSE	Crystal field stabilisation energy

Symbols and abbreviations

Cp*	Pentamethylcyclopentadiene
CVD	Chemical vapour deposition
DESY	Deutsches electron synchrotron
DEXAFS	Dispersive X-ray absorption fine structure
EN	Electronegativity
Et	Ethyl
EXAFS	Extended X-ray absorption fine structure
FG	Functional group
FT	Fourier transform
FZK	Forschungszentrum Karlsruhe
HASYLAB	Hamburger Synchrotron radiation laboratory
HRTEM	High resolution transmission electron microscopy
O ⁱ Pr	iso-propoxide
IR	Infrared
M	Metal/Metalloid
MAMTES	Methacryloxy methyl triethoxy silane
MAPTMS	Methacryloxy propyl trimethoxy silane
Me	Methyl
NMR	Nuclear magnetic resonance
O ⁿ Bu	n-butoxide
OMc	Methacrylate
OR	Alkoxy group
Pc	Phthalocyanine
PCP	Phosphorus carbon phosphorus
Py	Pyridine
QXAFS	Quick X-ray absorption fine structure
R	Alkyl group
SEXAFS	Surface X-ray absorption fine structure
SOFC	Solid oxide fuel cells
^t Bu	tertiary butyl
OTf	Triflate (trifluoromethanesulfonate)
THF	Tetrahydrofuran
TMOS	Tetramethoxysilane

Symbols and abbreviations

TWC	Three way catalysts
UV	Ultraviolet
XAFS	X-ray absorption fine structure
XANES	X-ray absorption near edge structure
Xan	Xanthates
XAS	X-ray absorption spectroscopy
XRD	X-ray diffraction
YSZ	Yttria stabilised zirconia

Chapter 1 Introduction

1.1. Importance of the work

Organometallic complexes and nanomaterials are getting increasingly important in recent times in several fields of science and technology. An insight into the structure of the materials is of vital concern as the functional properties are strongly dependent on the chemical structure. In many cases, it is difficult to obtain single crystals suitable for X-ray structural determination; therefore other techniques have to be employed to probe the structure of these materials. In this context, spectroscopic techniques such as X-ray absorption fine structure (XAFS), Raman and infrared spectroscopy are suitable to structurally characterise disordered systems regardless of the state of the samples.

The XAFS spectroscopy using a synchrotron radiation source is a powerful tool to determine the local structure around a specific element. The extended X-ray absorption fine structure (EXAFS) spectroscopy provides information on the coordination number, the nature of the scattering atoms surrounding the absorbing atom, the interatomic distance between absorbing and backscattering atoms and the Debye-Waller factor, which accounts for the static disorders and thermal vibrations [1.1.1, 1.1.2]. The X-ray absorption near edge structure (XANES) region provides information on oxidation states, vacant orbitals, electronic configuration and site symmetry of the absorbing atom [1.1.3]. The XANES spectra may have pre-edge peaks related to the electronic transitions taking place between the different shells of the excited atom. The strength of such pre-edge peaks strongly depends on the coordination geometry around the absorbing atom, and can therefore be used as an indicator of geometric changes [1.1.4]. The atomic X-ray absorption fine structure (AXAFS) spectroscopy provides information on the charge densities (responsible for bonding), anisotropy of the local embedded atom, charge distribution among the atoms, chemical effects, metal-support interactions, electron self-energy and core-hole effects.

Vibrational spectroscopic methods such as Raman and infrared spectroscopy provide information on molecular vibrations, yielding complementary structural insights [1.1.5]. In particular, Raman spectroscopy has the advantage of obtaining spectra from 10 to 4000 cm^{-1} , which is not accessible with the conventional infrared spectroscopy. The low wave number region is sensitive for the metal containing vibrations and is the region of interest for organometallic complexes and nanomaterials, having active metal centers.

1.2. Aim of the work

Organometallic complexes such as metallophthalocyanines are optically active materials and have been studied in detail for many years, especially with regard to their physical properties. Their highly conjugated aromatic π -electron system can give rise to large nonlinear optical response, and can be readily modified by physical or chemical methods. Moreover, axial substituents in phthalocyanines favourably influence nonlinear optical absorption due to the presence of a dipole moment perpendicular to the macrocycle. A part of the aim of this work is to study the molecular structure of phthalocyanine compounds as the structure has direct implications on the properties. For most of the phthalocyanines, it is very difficult to obtain suitable single crystals required for X-ray structural determination, therefore EXAFS spectroscopy is employed to probe the neighbourhood environment of the metal atom.

Transition metal complexes are increasingly used for different industrially important catalytic reactions such as asymmetric hydrogenation catalysis, stereo selective catalysis etc. Interphase catalysis is gaining great importance in recent years due to its ability to combine the advantages of homogeneous and heterogeneous catalysis with a remarkable decrease in the drawbacks like leaching and reduced catalytic activity of the reactive center. An important condition for the optimisation of the interphases is the exact knowledge of the structural correlation between each component in such systems. Here the local environment around the metal atom, which represents the active center in the interphase systems, plays a decisive role. Due to the amorphous nature of the interphases, it is not possible to obtain structural information using conventional X-ray diffraction methods. Hence, the local structure and the coordination geometry around the central metal atom are determined by EXAFS spectroscopy in order to verify whether the complexes retain its structure in the interphase system.

Metal complexes containing Schiff base ligands have been employed as biological models in understanding the structure of biomolecules and biological processes. In this framework, ruthenium complexes are of particular interest as they exhibit anticancer and antibiotic behaviour besides, exhibiting antibacterial activities. Due to the interrelationship between the structure and the biological activity, it is important to have some knowledge about the structure of the complexes. As single crystals suitable for X-ray structure determination could not be obtained, the local structure and the coordination geometry of the complexes are determined by EXAFS spectroscopy.

Homogeneous catalytic dehydrogenation of saturated hydrocarbons by transition metal complexes has gained significant importance in the recent years and the chemistry of iridium has played a central role in the expansion of this challenging field. There is considerable interest in determining the mechanistic pathways in this reaction and other C-H interactions so that more efficient complexes can be designed to facilitate the reaction. Theoretical calculations suggest a more prominent role for an oxidative addition pathway from Ir(III) to Ir(V) in catalytic C-H activation reactions. As XAFS spectroscopy is a viable tool to determine the changes in the structure and oxidation state occurring during the course of a reaction, time-resolved XAFS measurements were performed on hydrogenation reaction of catalytically active PCP pincer ligand iridium complexes, in *in operando* conditions to detect the different catalytic intermediates, in particular to structurally characterise the theoretically postulated Ir(V) species.

Organometallic complexes like cadmium- and zinc bis(*O*-alkylxanthates) have technological importance as they are potential single-source molecular precursors for the generation of metal sulphide thin films by chemical vapour deposition. The focus of the work is a detailed chemical characterisation of $\text{Cd}(\text{O-}^i\text{PrXan})_2$ and $\text{Zn}(\text{O-}^i\text{PrXan})_2$, aimed at obtaining valuable information on their physico-chemical characteristics.

Nanostructured mixed oxides play a vital role in numerous fields of materials technology, especially applied catalysis and energy conversion. Mixed oxides offer great possibilities for allowing the tuning of the properties of the materials, as the properties of these multi-component system are strongly influenced by the composition and the preparation method. The primary aim of the work is to study the influence of various parameter, namely, preparation method, annealing temperature, composition and doping on the structure of the mixed oxide by means of XAFS and Raman spectroscopy.

Ferrite based nanomaterials have been increasingly investigated for nanomagnetism and have shown great potential for many important technological applications, ranging from information storage and electronic devices to medical diagnostics and drug delivery. By adjusting the chemical identity of the metal cations, the magnetic configurations of the ferrite materials can be engineered on a molecular level to provide a wide range of magnetic properties. The main aim of the work is to investigate the local structure and cation distribution in CuFe_2O_4 nanoparticles and to study the influence of SnO_2 , CeO_2 or NiO on the structure of CuFe_2O_4 based nanocomposites.

Hybrid materials prepared by combining inorganic and organic units at a molecular level have enhanced physical properties and are suitable for a variety of applications ranging from catalysis to biomedical devices. The primary aim of the work is to study the structure of inorganic-organic hybrid materials formed by incorporating zirconium and hafnium oxo clusters in different polysiloxane matrices, especially to verify whether the cluster core is retained in the materials formed. Another focus of the work is to investigate the local structure of the mixed metal oxides obtained by the calcination of the hybrid materials.

Metal sulphide nanoparticles are intensively investigated particularly due to their interesting physico-chemical properties attributable to quantum confinement effects. Synthetic routes for the preparation of sulphide nanoparticles are of fundamental importance for the study of the properties at the nanoscale level. As an example, the reactions leading to the formation of zinc sulphide nanoparticles from thioacetic acid and different zinc precursors in different media, are studied by means of time resolved *in situ* XAFS spectroscopy.

The sol-gel process is a very powerful method for the preparation of nanostructured ceramics, glasses, coatings, fibres and new mixed organic-inorganic materials of technical importance. The primary aim of the work is to investigate the key steps of the sol-gel process in order to study the structural evolution of the system from the metal alkoxide stage to the polycondensate stage. In this framework, time resolved *in situ* XAFS and Raman spectroscopic measurements are performed on germanium, hafnium and tantalum alkoxides to investigate the hydrolysis and condensation reactions in pure state and as a mixture with pre-hydrolysed silicon alkoxide. In addition, complexation of the bidentate ligand, acetylacetonate and the influence of this chemical modification on the kinetics of the hydrolysis and condensation reactions are also studied.

Chapter 2 Theory of XAFS and Raman spectroscopy

2.1. Theory of XAFS

2.1.1. XAFS phenomenon

Electrons of an atom jump from one energy level to another or to the continuum by absorbing energy from an incident photon. The absorption edge energy is characteristic of a particular element. The excitation of electrons due to the incident photon energy is also characteristic of a particular shell. The X-ray photon energy tuned to the binding energy of some core level of an atom in the material corresponds to the absorption edge. The XAFS spectroscopy refers to the measurement of the X-ray absorption coefficient μ as a function of photon energy E above the threshold of an absorption edge [2.1.1, 2.1.2]. A schematic illustration of the XAFS phenomenon is presented in Figure 2.1.1.

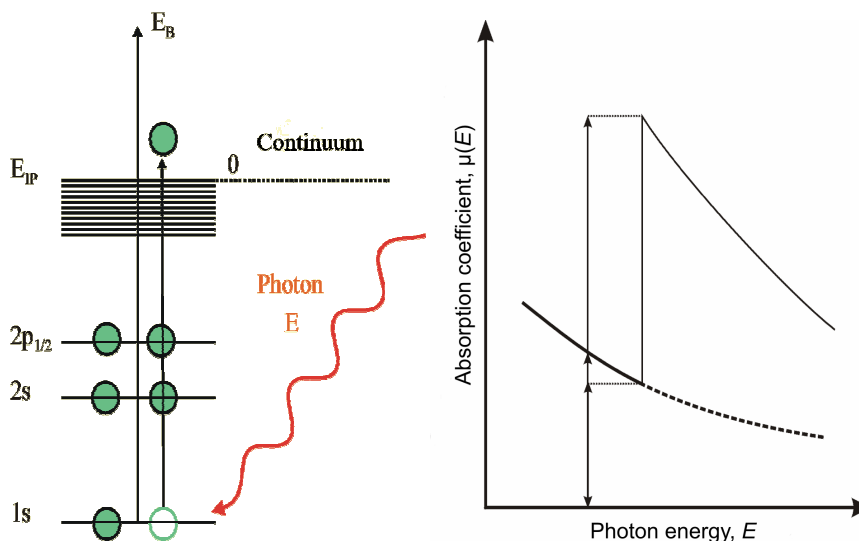


Figure 2.1.1. Schematic representation of the XAFS phenomenon.

The absorption, in terms of absorption coefficient μ can be determined from the measurement of the attenuation of X-rays upon their passage through a material. The absorption decreases with increasing energy of the incident X-rays until a threshold is reached, where the energy is sufficient to remove an electron from an inner shell [2.1.3]. At this threshold, $\mu(E)$ increases steeply and beyond this point, $\mu(E)$ resumes a steady decrease, as portrayed in Figure 2.1.1 (right). The core state is eventually filled, by the emission of fluorescent X-rays or Auger electron as shown in Figure 2.1.2. In X-ray fluorescence, radiation having energy equal to the difference of the core levels is emitted. X-ray fluorescence occurs at discrete energies that are characteristic of the absorbing atom, and can be used to identify the absorbing atom. In Auger effect, an

electron is promoted into the continuum from another core level. In both cases, the emission probability is directly proportional to the absorption probability.

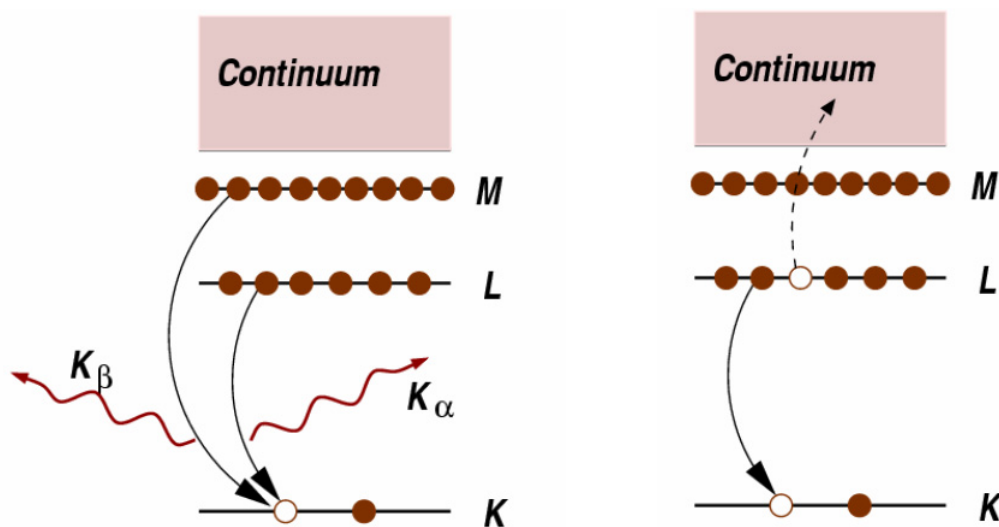


Figure 2.1.2. Schematic depiction of X-ray fluorescence (left) and Auger effect (right).

The probability for absorption of an X-ray photon by an electron of an inner shell is dependent on the initial and final states of the excited electron. The absorption of X-ray radiation generates a photoelectron that can be considered as a spherical wave originating from the absorbing atom and getting backscattered by the neighbouring atoms as shown in Figure 2.1.3. The outgoing and incoming photoelectron waves interfere with each other. The resulting constructive and destructive interferences vary with wavelength causing oscillation in the absorption coefficient above the absorption edge. The absorption probability is higher in the case of constructive interference and lower in the case of destructive interference [2.1.4].

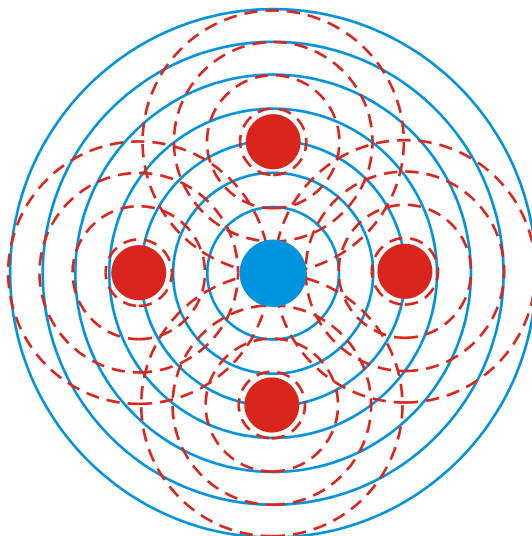


Figure 2.1.3. Schematic illustration of outgoing and backscattered waves.

For an isolated atom, $\mu(E)$ has a sharp step at the core-level binding energy and is a smooth function of energy above the edge as there are no other atoms in the vicinity. Here there is only the outgoing photoelectron wave and there is no incoming electron wave due to the absence of neighbouring atoms. This condition is schematically represented in Figure 2.1.4. On the other hand, when other atoms are in the vicinity of the absorbing atom, $\mu(E)$ shows small oscillations up to about 1000 eV above the absorption edge. Here the outgoing photoelectron wave is backscattered by the neighbouring atoms, thereby causing interference between the outgoing and the incoming waves. This condition is schematically presented in Figure 2.1.5.

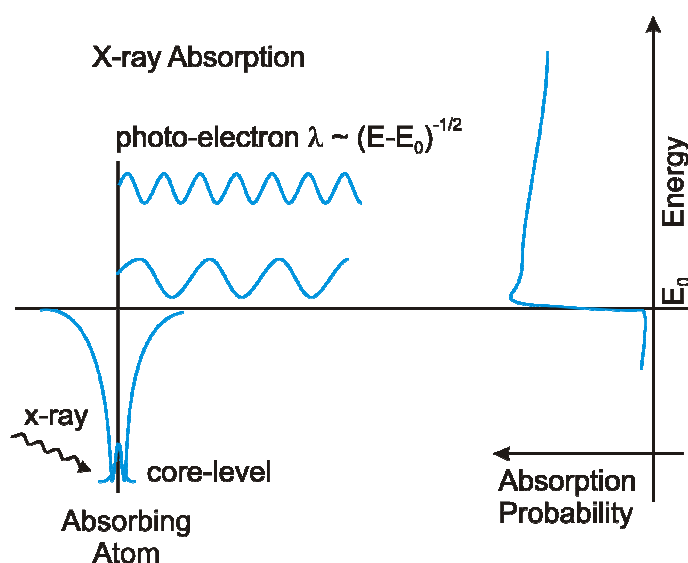


Figure 2.1.4. Schematic representation of XAFS of an isolated atom.

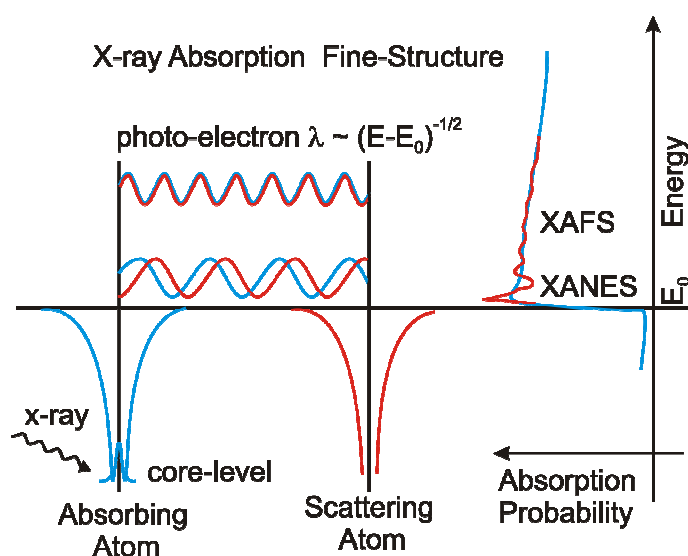


Figure 2.1.5. Schematic representation of XAFS of atom surrounded by backscattering atoms.

The XAFS spectrum can be divided into three parts, viz., pre-edge, edge and post-edge regions and each region contains valuable structural information. About 30 eV before the edge to about 40 eV after the edge, comprising the pre-edge and edge regions is termed as XANES and the post-edge region above 40 eV is known as EXAFS. A typical XAFS spectrum is shown in Figure 2.1.6.

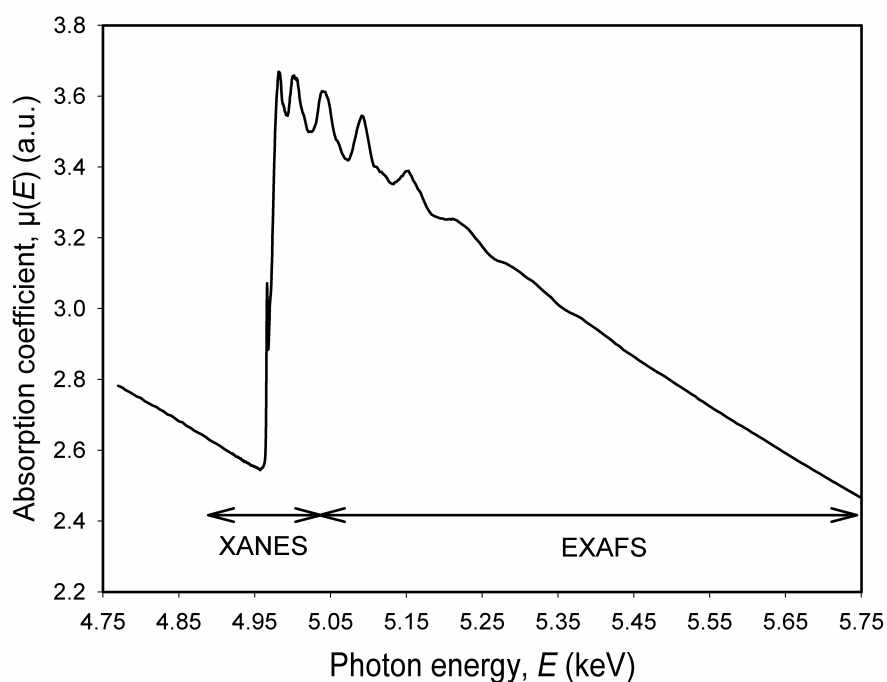


Figure 2.1.6. Typical XAFS spectrum (with a pre-edge peak). [XAFS spectrum of titanium foil measured in transmission mode at Ti K-edge at 4966 eV at the XAS beamline at ANKA, Karlsruhe].

The measurement of the energy dependence of the X-ray absorption coefficient can be used to determine the local environment around the element, which absorbs the X-rays. Since the positions of the K and L edges are dependent on the element under investigation, a suitable choice of incident X-ray energies makes it possible to excite a particular element and probe its environment.

2.1.2. XAFS formalism

The absorption process occurs when the X-ray photon energy matches with the binding energy of the electron in a core shell. The electron gains the energy and gets transferred to the continuum. In addition, electronic transitions within the inner shells, i.e., from a core atomic orbital to a higher unoccupied atomic orbital, gives rise in special cases to pre-edge peaks in the XANES region of the XAFS spectrum [2.1.5].

Such pre-edge signals are predominantly observed in transition elements due to the presence of unoccupied d-orbitals. The XANES features arise from effects such as many body interactions, multiple scattering, distortion of the excited state wave function by the coulomb field, band structures etc. [2.1.6 - 2.1.8]. The theory of XANES has not yet been completely developed; therefore, mostly only qualitative comparisons are employed. A detailed description of existing theories on XANES can be found in literature [2.1.9].

The EXAFS region of the XAFS spectrum can be theoretically described by considering the wave property of the photoelectron [2.1.10]. In order to determine the relationship between the quantities characterising the neighbourhood environment around the absorbing atom, it is necessary to correct and normalise the modulation of $\mu(E)$ for the background absorption $\mu_0(E)$ using equation 2.1.1.

$$\chi(E) = \frac{\mu(E) - \mu_0(E)}{\mu_0(E)} \quad (2.1.1)$$

The next step is to convert $\chi(E)$ into the function $\chi(k)$, where k is the magnitude of the photoelectron wave vector and is calculated according to equation 2.1.2 from the energy E of the incident X-ray photon and the position of the absorption edge E_0 .

$$k = \left[\frac{8\pi^2 m_e}{h^2} (E - E_0) \right]^{1/2} \quad (2.1.2)$$

Here m_e is the mass of the electron ($9.109 \cdot 10^{-31}$ kg) and h is the Plank's constant ($6.626 \cdot 10^{-34}$ J s).

Since the X-ray absorption is a transition between two quantised levels, one can describe the X-ray absorption coefficient $\mu(E)$ using Fermi's golden rule within the dipole approximation for the photon induced transition of an electron from an initial state to a final state,

$$\mu(E) \propto \left| \langle f | \varepsilon \cdot \gamma | i \rangle \right|^2 \quad (2.1.3)$$

In this expression, ε is the polarisation vector of the electric field, γ is the electron coordinate, $|i\rangle$ is the initial state (X-ray photon, core electron and no photoelectron) and $\langle f|$ is the final state (no X-ray photon, electron hole and photoelectron). The condition for the validity of the dipole approximation is that the wavelength of the photons must be much greater than the size of the initial state. Generally this criterion is well satisfied for light atoms and less tightly bound states.

The EXAFS formalism as a function of photoelectron wave vector k , obtained using single scattering theory is presented in equation 2.1.4.

$$\chi(k) = \sum_j N_j \cdot S_i(k) \cdot F_j(k) \cdot \exp[-2 \cdot \sigma_j^2 \cdot k^2] \cdot \exp\left[\frac{-2 \cdot r_j}{\lambda_j(k)}\right] \cdot \frac{\sin(2 \cdot k \cdot r_j + \phi_{ij}(k))}{kr_j^2} \quad (2.1.4)$$

Here $F_j(k)$ is the backscattering amplitude from each of the N_j neighbouring atoms of the j^{th} type with a Debye-Waller factor σ_j , to account for thermal vibrations (assuming harmonic vibration) and static disorder (assuming Gaussian pair distribution) and at a distance r_j from the absorbing atom. The term $\phi_{ij}(k)$ is the total phase shift experienced by the photoelectron. The term $\exp(-2r_j/\lambda_j(k))$ is due to inelastic losses in the scattering process (due to neighbouring atoms and the medium in between) with λ_j being the electron mean free path. The term $S_i(k)$ is the amplitude reduction factor due to many body effects such as shake up/off processes at the central atom (denoted by i).

The amplitude function $F_j(k)$ depends only on the type of the backscatterers (except, the reduction factor $S_i(k)$ which is mainly a function of the absorber) and the phase function $\phi_{ij}(k)$ contains the contributions from both the absorber and the backscatterer,

$$\phi_{ij}^l(k) = \phi_i^l(k) + \phi_j(k) - l\theta \quad (2.1.5)$$

Here $l = 1$ for K and L_{I} edges and $l = 2$ or 0 for $L_{\text{II,III}}$ edges. The terms $\phi_i(k)$ and $\phi_j(k)$ correspond to the phase shift experienced by the absorber and backscatterer, respectively and θ denotes the phase of the backscattering amplitude. Qualitatively, the physical origin of this dependence is that the photoelectron experiences the central atom phase shift twice, once going out and once coming back, but experiences the neighbouring atom phase shift once by propagating from the absorber to the neighbouring atoms and back to the absorber. The phase shifts are unique only if the energy threshold E_0 is specified. Changing E_0 will change the momentum k and hence the phase function $\phi(k)$.

The Debye-Waller factor σ plays an important role in EXAFS spectroscopy. It contains important structural and chemical information about the disorders found in a system. The Debye-Waller factor σ has two components σ_{stat} and σ_{vib} due to static disorder and thermal vibrations, respectively. In principle, these two factors can be separated by a temperature dependent study. However, if σ_{vib} can be estimated from vibrational spectroscopy or if σ_{stat} is known from other studies, the other term can be calculated from the experimentally determined Debye-Waller factor.

There are two categories of inelastic scattering processes which tend to decrease the EXAFS amplitude. The first is caused by multiple excitations at the central atom whereas the second is associated with excitation of the neighbouring environment, including the neighbouring atoms and the intervening medium, by the photoelectron. In equation (2.1.4), the inelastic losses due to multiple excitations (many body effects such as shake up/off processes) at the absorber are approximated by the amplitude reduction factor $S_i(k) \leq 1$, while the inelastic losses due to excitation of the neighbouring environment is approximated by $\exp(-2r_j/\lambda_j(k))$.

The EXAFS function in k -space contains all necessary information, however, it is not readily visualised. In this case, Fourier transformation of the EXAFS function yields a radial distribution function $F(r)$, as depicted in equation (2.1.6), and therefore indicates the distribution of the backscatterers in real space.

$$F(r) = \frac{1}{\sqrt{2\pi}} \int_{k_{\min}}^{k_{\max}} \chi(k) \cdot k^n \cdot w(k) \cdot \exp(2 \cdot i \cdot k \cdot r) dk \quad (2.1.6)$$

The modulus function $Mod(r)$, comprising of the real and imaginary parts of the radial distribution function $F(r)$, is presented in equation (2.1.7),

$$Mod(r) = \sqrt{\text{Re}^2[F(r)] + \text{Im}^2[F(r)]} \quad (2.1.7)$$

Here k_{\min} and k_{\max} denote the starting and the ending values of the specified k -range and $w(k)$ represents the window function. It should be mentioned that the modulus function yields signal maxima with space shifts of 0.2 - 0.3 Å in comparison to the real values. Nevertheless, this shift is compensated by the modern analysis programs, wherein a space corrected modulus function is obtained.

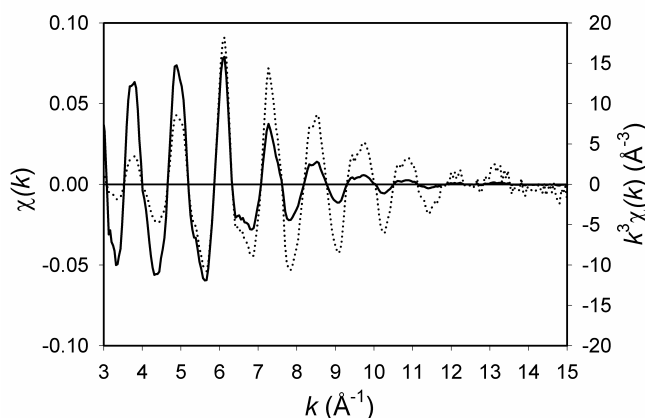


Figure 2.1.7. Unweighed (solid line) and k^3 weighed (dotted line) $\chi(k)$ function of titanium foil measured in transmission mode at Ti K-edge at 4966 eV.

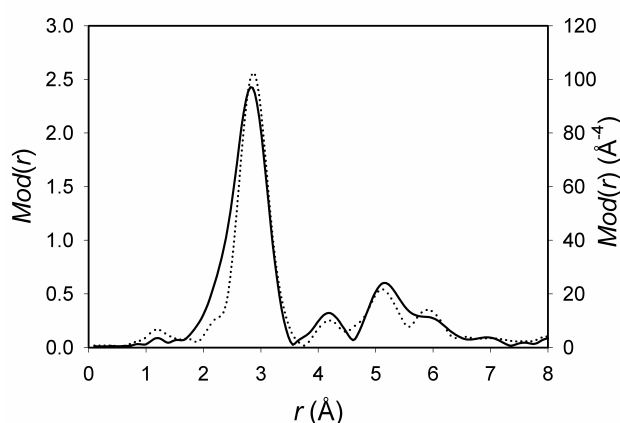


Figure 2.1.8. $Mod(r)$ function of unweighed (solid line) and k^3 weighed (dotted line) $\chi(k)$ function for titanium foil measured in transmission mode at Ti K-edge at 4966 eV.

A typical EXAFS spectrum and its corresponding Fourier transform plot are shown in Figures 2.1.7 and 2.1.8, respectively. The EXAFS function $\chi(k)$ is often weighed by k^n in order to amplify the oscillations at high k -range. The higher weighing also leads to a better resolution of signals in the modulus function, if the absorption spectrum possesses a good signal to noise ratio. In the EXAFS function, many parameters of interest are highly correlated. These include, energy shifts and interatomic distances on one hand and coordination number and Debye-Waller factor on the other. The different correlated parameters can be decoupled by measuring model systems alongside with the real systems. Energy shifts and amplitude reduction factor are invariant parameters, which do not change with temperature, pressure and other external conditions.

2.1.3. Multiple scattering

The single electron single scattering theory of EXAFS makes use of the fact that in most cases multiple scattering is not important. This assumption is generally valid if one considers that multiple scattering processes can be accounted for by adding all scattering paths that originate and terminate at the central atom (absorber). Each of these processes then behaves like $\sin(2kr_{\text{eff}})$ where $2r_{\text{eff}}$ is the total scattering path length which is much larger than that of the direct backscattering from the nearest neighbours. Thus, multiple scattering will give rise to rapidly oscillating waves in k space, which tend to cancel out. The amplitude of these waves is also significantly attenuated by the large scattering path lengths, making it relatively unimportant in comparison with the direct backscattering.

On the other hand, multiple scattering in EXAFS can become important when atoms are arranged in an approximately collinear array. In such case, the outgoing photoelectron is strongly forward scattered by the intervening atoms, resulting in a significant amplitude enhancement. A general schematic of multiple scattering in a simple lattice of atoms is shown in Figure 2.1.9 and the different types of scattering paths are depicted in Figure 2.1.10. The red circle represents the absorber atom, the blue circles represent the scattering atoms and the coloured lines represent the scattering paths.

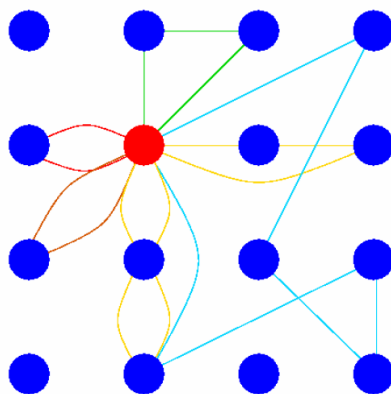


Figure 2.1.9. Schematic representation of multiple scattering in a lattice of atoms.

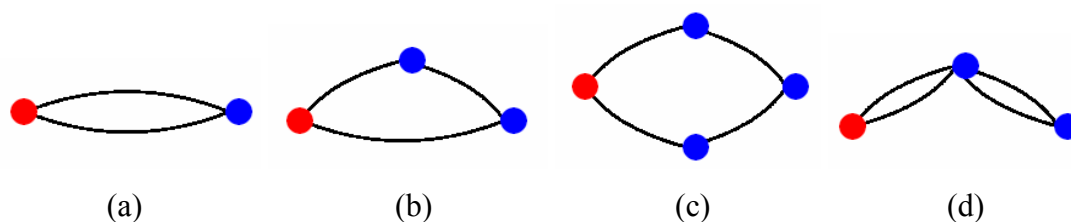


Figure 2.1.10. Several types of multiple scattering paths. [(a) single scattering, (b) double scattering, (c) quadrilateral triple scattering and (d) triangular triple scattering].

The single scattering paths illustrate the direct backscattering of the photoelectron wave by the neighbouring atoms. The simplistic EXAFS function mentioned in equation (2.1.4) accounts only for these scattering paths. The double scattering paths are important when the forward scattering angle is close to 180° . The quadrilateral triple scattering paths are rarely important if one or more scattering angle is far from 0° or 180° . The triangular triple scattering paths are important when the scattering angle at the middle atom is $\sim 180^\circ$. In addition, both the amplitude and the phase are modified by the intervening atoms for bond angles ranging from 180° to $\sim 75^\circ$. The effect, however, drops off very rapidly for bond angles below 150° . For these systems, it is necessary to rewrite equation (2.1.4) to take into account multiple scattering involving the intervening atoms. The scattering angle, order of scattering, number of intervening

atoms in a path and path length are the most important parameters, which influence the multiple scattering phenomenon. A detailed theoretical description of the multiple scattering formalism can be found in literature [2.1.11, 2.1.12].

2.1.4. AXAFS spectroscopy

AXAFS arises from scattering within an embedded atom due to the backscattering of the photoelectron at interstitial charge densities. This extra fine structure originates from resonant scattering in the periphery of the absorbing atom [2.1.13]. The effect is like an internal Ramsauer-Townsend resonance, where the photoelectron is a spherical wave created at the center of the atom, rather than a wave scattered by an atom [2.1.14]. While the regular EXAFS stems from the backscattering of the photoelectron at neighbouring atoms and concerned with the geometric structure, the AXAFS contribution is assigned to the scattering at the charge densities between the atoms and is concerned with the electronic structure [2.1.15]. A qualitative picture illustrating the atomic potentials of the absorber (A) and a nearby backscatterer (S) (not necessarily bound to one another) is shown in Figure 2.1.11. The atomic potential is characterised by the effective radius of the atom R_a , and the potential relative to the interstitial zero potential V_a [2.1.16].

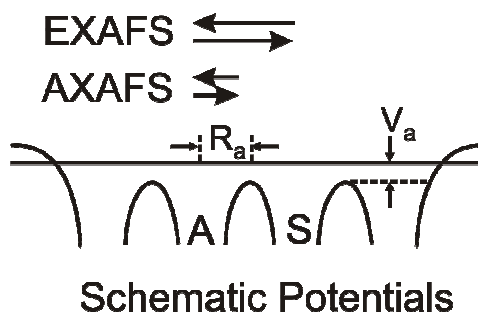


Figure 2.1.11. Illustration of schematic potentials in a solid showing the EXAFS and AXAFS scattering, adapted from literature [2.1.16].

AXAFS occurs especially nearer to the edge than XANES and the oscillatory structure is analogous to that occurring from neighbouring atoms. AXAFS is the dominant background fine structure even though it has features in the same energy range as multielectron excitations [2.1.14]. AXAFS occurs as low frequency oscillation in EXAFS spectrum. In k -space AXAFS oscillations show themselves as slowly varying sine wave, as illustrated in Figure 2.1.12. In Fourier transform plot of the EXAFS function, AXAFS yields peaks at low r values, as shown in Figure 2.1.13. These short

distance peaks can not be attributed to meaningful bond lengths of neighbouring atoms, as these distances point to a location inside the periphery of the absorber atom itself. The AXAFS intensity depends on the embedded atom potential, the interstitial potential and the distribution of the absorber atom electron density [2.1.17].

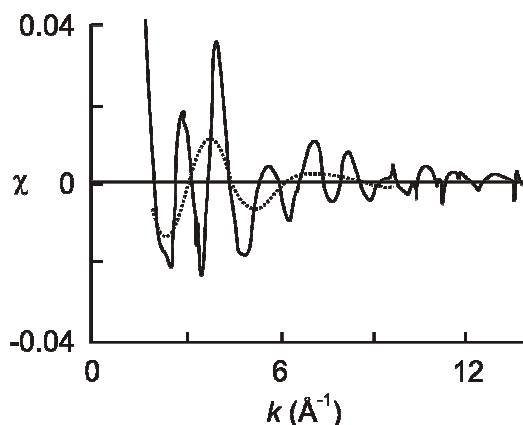


Figure 2.1.12. Schematic illustration of EXAFS (solid line) and AXAFS (dotted line) contributions in k -space, adapted from literature [2.1.17].

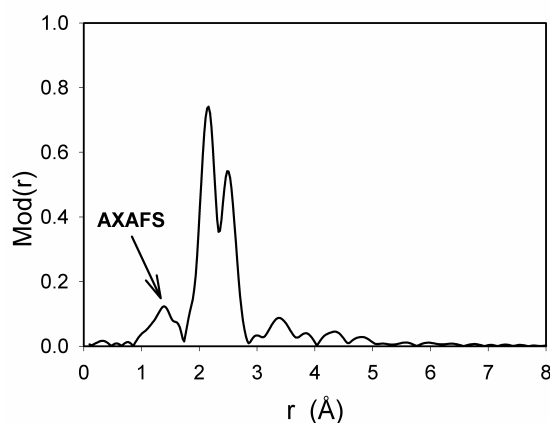


Figure 2.1.13. Schematic illustration of AXAFS contributions in the Fourier transform plot of the EXAFS spectra.

The AXAFS features arise from the difference between a free atom potential and an embedded atom potential. The embedded atom has an atomic absorption μ_a , which can be viewed as a combination of the atomic background of the free atom μ_{free} and the AXAFS signal χ_{atomic} , which results from alteration of the potential by a chemical environment other than vacuum,

$$\mu_a = \mu_{free}(1 + \chi_{atomic}) \quad (2.1.8)$$

The atomic absorption μ_a is related to the total X-ray absorption spectrum μ_{total} according to equation (2.1.9), which isolates $\chi_{neighbours}$ attributable to EXAFS scattering,

$$\chi_{neighbours} = \frac{\mu_{total} - \mu_a}{\mu_a} \quad (2.1.9)$$

Combining equations (2.1.8) and (2.1.9), one arrives at the expression for the total absorption coefficient μ_{total} given by (2.1.10),

$$\mu_{total} = \mu_{free}(1 + \chi_{atomic})(1 + \chi_{neighbours}) = \mu_{free}(1 + \chi_{total}) \quad (2.1.10)$$

The AXAFS function is derived using the muffin-tin approximation illustrated in Figure 2.1.14. The muffin-tin approximation ‘clips’ the exact potential at the muffin-tin radius R_{mt} and sets it equal to the interstitial potential V_{int} [2.1.13, 2.1.14]. Inside the muffin-tin radius, the potential is assumed to be spherical and outside, it is assumed to be flat and zero, i.e., no forces are exerted on the particle in the interstitial region. The effect of this approximation is negligible for EXAFS, but significant for AXAFS [2.1.16].

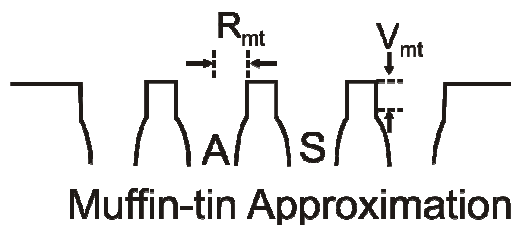


Figure 2.1.14. Schematic view of muffin-tin approximation.

The AXAFS formalism is presented in equation 2.1.11,

$$\chi_{atomic} = -\frac{1}{kR_{mt}^2} |f_e| (\sin(2kR_{mt} + 2\delta_i^a + \Phi_e)) \quad (2.1.11)$$

Here R_{mt} corresponds to muffin-tin radius, δ_i^a denotes the central atom phase shift, Φ_e refers to the phase shift function and f_e corresponds to the effective curved wave scattering amplitude given by the equation (2.1.12),

$$f_e = |f_e| \exp(i\Phi_e) \quad (2.1.12)$$

Each free atom potential overlaps with the potential of neighbouring atoms in a solid, so the embedded atom potential is significantly altered, particularly in the bonding region. Therefore, AXAFS depends on the nature of the neighbouring atoms and how they are bonded to the absorber atom.

AXAFS is interesting in its own right, as it depends critically on the scattering potential in the outer part of the absorbing atom. Thus, it provides a new and useful probe of chemical effects, the electron self-energy, core-hole effects and other contributions to the embedded atom potentials.

2.2. Theory of Raman spectroscopy

2.2.1. Raman scattering

When light is scattered from a molecule most photons are elastically scattered. The scattered photons have the same energy and, therefore, wavelength (frequency), as the incident photons. However, a small fraction of light (approximately 1 in 10^7 photons) is scattered at optical frequencies different from, and usually lower than, the frequency of the incident photons. This process leading to inelastic scattering is termed as the Raman scattering, while the process leading to elastic scattering is called as Rayleigh scattering. Most of the Raman scattered photons are shifted to longer wavelengths (Stokes lines), but a small portion are shifted to shorter wavelengths (anti-Stokes lines). Raman scattering can occur with a change in vibrational, rotational or electronic energy of a molecule. The primary concern is on the vibrational Raman effect [2.2.1].

The Raman effect arises when a photon is incident on a molecule and interacts with the polarisability of the molecule. It is a form of vibronic spectroscopy, although the spectrum contains vibrational frequencies. In classical terms, the interaction can be viewed as a perturbation of the molecule's electric field. In quantum mechanical terms, the scattering is described as a molecular excitation to a virtual state lower in energy than a real electronic transition with nearly coincident de-excitation and a change in vibrational energy. The scattering event occurs in femtoseconds. The virtual state description of scattering is shown in Figure 2.2.1.

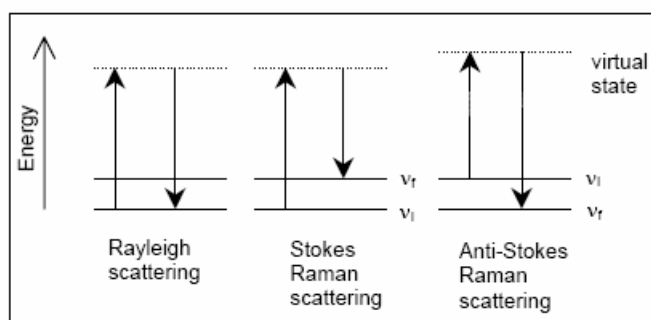


Figure 2.2.1. Energy level diagram of Rayleigh scattering, Stokes Raman scattering and anti-Stokes Raman scattering.

In all the cases, the incident photon excites an electron into a higher virtual energy level and then the electron decays back to a lower level, emitting a scattered photon. The difference in energy between the incident photon and the Raman scattered photon is equal to the energy of a vibration of the scattering molecule [2.2.2]. The vibrational

energy is ultimately dissipated as heat and due to the low intensity of Raman scattering, the heat dissipation does not cause a measurable temperature rise in the material. A plot of intensity of scattered light (Raman intensity) versus energy difference (expressed in wave number) is Raman spectrum. A typical Raman spectrum is shown in Figure 2.2.2.

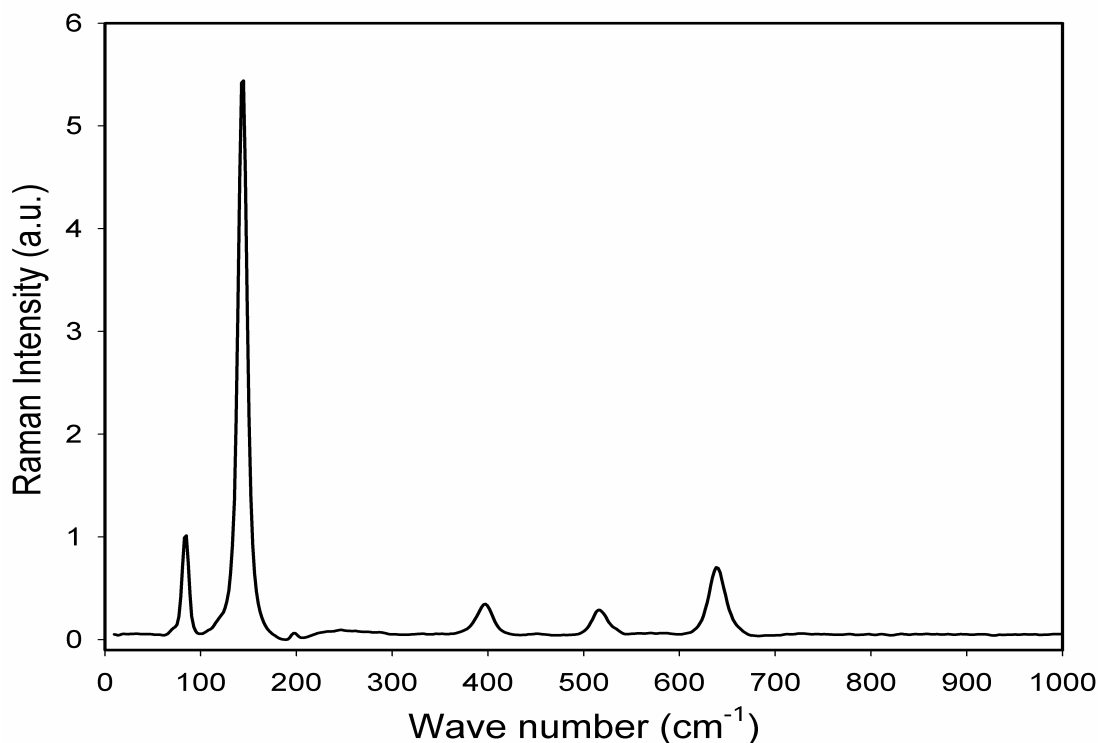


Figure 2.2.2. Typical Raman spectrum. [Raman spectrum of TiO₂ in anatase form].

At room temperature the thermal population of vibrationally excited states is low, although not zero. Therefore, the initial state is the ground state, and the scattered photon will have lower energy (longer wavelength) than the exciting photon. Thus giving rise to Stokes scattering. A small fraction of the molecules are in vibrationally excited states. Raman scattering from vibrationally excited molecules leaves the molecule in the ground state. This gives rise to anti-Stokes scattering. The anti-Stokes shifted Raman spectrum is always weaker than the Stokes shifted spectrum, but at room temperature it is strong enough to be useful for vibrational frequencies less than about 1500 cm⁻¹. The Stokes and anti-Stokes spectra contain the same frequency information [2.2.3]. The ratio of anti-Stokes to Stokes intensity at any vibrational frequency is a measure of temperature.

The energy of a vibrational mode depends on molecular structure and environment. Atomic mass, bond order, molecular substituents, molecular geometry and bonding influence the vibrational force constant which, in turn dictates the vibrational energy.

Vibrational Raman spectroscopy is not limited to intramolecular vibrations. Crystal lattice vibrations and other motions of extended solids are also Raman active.

2.2.2. Raman selection rules

A simple classical electromagnetic field description of Raman spectroscopy can be used to explain many of the important features of Raman band intensities [2.2.4]. The dipole moment P , induced in a molecule by an external electric field E , is proportional to the field as shown in equation (2.2.1).

$$P = \alpha E \quad (2.2.1)$$

Here the proportionality constant α refers to the polarisability of the molecule. The polarisability measures the ease with which the electron cloud around a molecule can be distorted. The induced dipole emits or scatters light at the optical frequency of the incident light wave.

Raman scattering occurs because a molecular vibration can change the polarisability. The change is described by the polarisability derivative with respect to the corresponding normal mode of vibration. The selection rule for a Raman active vibration, that there is a change in polarisability during the vibration is given in equation (2.2.2),

$$\frac{\partial \alpha}{\partial Q} \neq 0 \quad (2.2.2)$$

Here the term Q denotes the corresponding normal mode of the vibration. The Raman selection rule is analogous to the selection rule for an infrared active vibration, which states that there must be a net change in permanent dipole moment during the vibration. From group theory it is straightforward to show that if a molecule has a center of symmetry, vibrations which are Raman active will be infrared inactive, and vice versa [2.2.1].

If a vibration does not greatly change the polarisability, then the polarisability derivative will be nearly zero, and the intensity of the Raman band will be low. The vibrations of a highly polar moiety, such as O-H bond, are usually weak. An external electric field cannot induce a large change in the dipole moment and stretching or bending the bond does not lead to substantial changes. Typical strong Raman scatterers are moieties with anisotropic electron clouds, such as C=C bonds. The π electron cloud of the double bond is easily distorted in an external electric field. Bending or stretching

the bond changes the distribution of electron density substantially, and causes a large change in induced dipole moment.

Raman scattering is partially polarised, even for molecules in a gas or liquid state, where the individual molecules are randomly oriented. The effect is most easily seen with an exciting source which is plane polarised. In isotropic media polarisation arises because the induced electric dipole has components which vary spatially with respect to the coordinates of the molecule. Raman scattering from totally symmetric vibrations will be strongly polarised parallel to the plane of polarisation of the incident light. The scattered intensity from non-totally symmetric vibrations is 75% as strong in the plane perpendicular to the plane of polarisation of the incident light as in the plane parallel to it. The situation is more complicated in crystalline materials as the polarisation components depend on the orientation of the crystal axes with respect to the plane of polarisation of the incident light [2.2.5].

2.2.3. Theory of Raman effect

The classical description of Raman effect explains the polarisation induced in the molecule by the oscillating electric field of the incoming light. This induced dipole then radiates scattered light, with or without exchanging energy with vibrations in the molecule. Both classical and quantum theories of Raman scattering are based on equation (2.2.1) and play a vital role in understanding the effect and interpreting spectra. A schematic illustration of Raman scattering is shown in Figure 2.2.3.

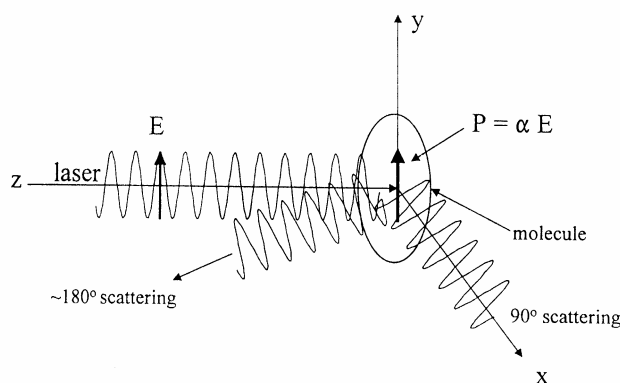


Figure 2.2.3. Schematic representation of Raman scattering.

The classical treatment of Raman scattering is based on the effects of molecular vibrations on the polarisability. Consider the incident optical field to be governed by equation (2.2.3),

$$E = E_0 \cos 2\pi\nu_0 t \quad (2.2.3)$$

Here ν_0 is the frequency of the laser light. The molecular vibrations are usually considered to be composed of normal modes Q_j , of which there are $3N-6$ (or $3N-5$ for a linear molecule) in a molecule with N atoms,

$$Q_j = Q_j^o \cos 2\pi\nu_j t \quad (2.2.4)$$

Here ν_j denotes the characteristic harmonic frequency of the j^{th} normal mode. The polarisability of electrons in the molecule will be modulated by the molecular vibration so that,

$$\alpha = \alpha_0 + \left(\frac{\partial \alpha}{\partial Q_j} \right) Q_j + \dots \quad (2.2.5)$$

From equation (2.2.1), the polarisation is the product of equations (2.2.3) and (2.2.5), which yields equation (2.2.6) after noting that $\cos \alpha \cos \beta = [\cos (\alpha+\beta) + \cos (\alpha-\beta)]/2$, and neglecting higher order terms in equation (2.2.5),

$$P = \alpha_0 E_0 \cos 2\pi\nu_0 t + E_0 Q_j^o \left(\frac{\partial \alpha}{\partial Q_j} \right) \frac{\cos 2\pi(\nu_0 + \nu_j)t + \cos 2\pi(\nu_0 - \nu_j)t}{2} \quad (2.2.6)$$

According to the hypothesis that the polarised electrons will radiate light at the frequency of their oscillations, equation (2.2.6) demonstrates that light will be scattered at three frequencies. The first term is Rayleigh scattering, which is at the same frequency as the laser, and has a magnitude proportional to α_0 , the inherent polarisability of the molecule. The second term is anti-Stokes Raman scattering, which occurs at $\nu_0 + \nu_j$, and the third term is Stokes Raman scattering at $\nu_0 - \nu_j$ [2.2.6].

Although equation (2.2.6) was derived classically and is incomplete, it does provide some useful insights. The quantum mechanical approach to Raman scattering relates scattering frequencies and intensities to vibrational and electronic energy states of the molecule. The standard perturbation theory hypothesises that the frequency of the incident light is low compared to the frequency of the first electronic excited state. The small changes in the ground state wave function are described in terms of the sum of all possible excited vibronic states of the molecule. A detailed description of the quantum theory of Raman effect can be found in literature [2.2.3].

Chapter 3 Experimental methods and data analysis

3.1. XAFS measurements

3.1.1. Principle

The X-ray absorption spectroscopy measures the X-ray absorption coefficient μ as a function of the photon energy E . The most common technique involves the direct measurement of $\mu(E)$. The absorption coefficient μ is determined by measuring the intensity of the X-rays passing through the sample, using Lambert-Beer law [3.1.1], given by the equation (3.1.1),

$$I = I_0 \exp(-\mu t) \quad (3.1.1)$$

Here, the term I_0 represents to the X-ray intensity incident on the sample, I denotes the X-ray intensity transmitted through the sample and t refers to the thickness of the sample. The X-ray absorption process is pictorially depicted in Figure 3.1.1.

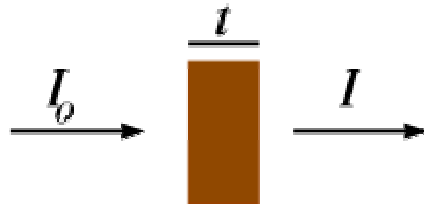


Figure 3.1.1. Schematic representation of X-ray absorption process.

At most X-ray energies, the absorption coefficient μ is a smooth function of energy with a value that depends on the sample density ρ , the atomic number Z , the atomic mass A and the X-ray energy E , roughly as given in the expression (3.1.2),

$$\mu \approx \frac{\rho Z^4}{AE^3} \quad (3.1.2)$$

Due to the Z^4 dependence, the absorption coefficient for different elements is unique and a good contrast between different elements can be achieved for nearly any sample thickness and concentrations by adjusting the X-ray energy.

In order to measure μ as a function of E , a continuous spectrum is used and X-rays of a particular wavelength are filtered out using appropriate monochromator crystals. The energy of the incident radiation is adjusted by a stepwise change of the incident angle of the monochromator, which reflects radiation of wavelength λ according to the Bragg's law [3.1.2] given in equation (3.1.3),

$$n\lambda = 2d \sin \theta \quad (3.1.3)$$

Here, λ refers to the wavelength of the incident X-rays, d is the spacing between the lattice planes of the crystal, 2θ is the scattering angle and n is the order of diffraction ($n = 1, 2, 3, \dots$). According to this law a double crystal monochromator, with the second crystal at a slightly detuned angle to the first one, selects a beam of wavelength λ , while simultaneously suppressing beams with wavelengths $\lambda/2$, $\lambda/3$, etc. Generally, Si(111) double crystal monochromators are used for elements having absorption energies from 3 keV to 15 keV, Si(311) for energies from 15 keV to 30 keV and Si(511) for energies from 30 keV to 80 keV. For a typical XAFS measurement, the scan range is from ~ 300 eV before the edge to ~ 1300 eV after the edge. The details of energy scanning summarised in Table 3.1.1 were predominantly used for the XAFS measurements in the present work.

Table 3.1.1. Details of the parameters used for energy scanning

Region	Starting energy (eV)	Ending energy (eV)	Step size (eV)
Pre-edge	-300	-30	5.0
XANES	-30	+40	0.3
EXAFS	+40	+1300	0.5

All values are relative to the nominal value of edge energy.

The XAFS is a fairly small signal. Hence, in order to obtain good statistics the photon flux should be at least 10^6 photons s^{-1} . Synchrotron radiation sources, which provide high energy X-rays, have photon flux greater than 10^8 photons s^{-1} and are best suited for XAFS measurements. In the present work, XAFS measurements were performed at the beamlines X1, E4 and A1 at HASYLAB, Hamburg and at the XAS beamline at ANKA, Karlsruhe. The main parameters of interest for HASYLAB and ANKA synchrotron radiation sources and the instrument specification for the different beamlines are presented in Appendix.

3.1.2. Measurement modes

The principal XAFS measurement modes are transmission and fluorescence. For concentrated samples, XAFS spectrum is best measured in transmission mode. Here the absorption is measured directly by measuring the transmission through the sample, as given in equation (3.1.4), which corresponds to equation (3.1.1) mentioned earlier,

$$\mu(E)t = \ln\left(\frac{I_0}{I}\right) \quad (3.1.4)$$

The experimental setup for transmission mode measurements is schematically shown in Figure 3.1.2. The transmission mode uses ionisation chambers, filled with inert gases, for the detection of the incident and transmitted X-ray intensities. A picture of the ion chambers is presented in Figure 3.1.3.

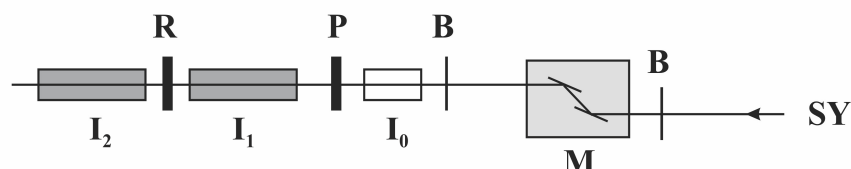


Figure 3.1.2. Schematic of experimental setup for transmission mode measurements. [SY – synchrotron radiation, B – slit, M – monochromator, P – sample, R – reference material and I_0 , I_1 , I_2 – ionisation chambers].



Figure 3.1.3. Picture of ionisation chamber. [Photograph from the XAS beamline at ANKA, Karlsruhe].

The sample to be measured, the reference material and the ion chambers are arranged in a line. The reference material is used for energy calibration purpose and is generally a material (metal foil or compound) whose edge energy value lies close to the absorption edge of the sample. The sample is located between the first and the second ion chambers, and the reference material is located between the second and the third ion chambers. The detection limit is determined by the element of interest and the other elements present in the sample. For transmission mode measurements, the sample has to be uniform and free of pin holes. For powder samples, the grain size should not be larger than the absorption length. The transmission mode of measurement is simple and gives excellent data in a short time interval.

Since the absorption of X-rays is linked to the creation of an electron vacancy, it is possible to use all subsequent decay processes to determine the absorption coefficient. An electron from an outer shell can fill the vacancy, accompanied by the emission of fluorescence radiation. The absorption coefficient μ can be related to the intensity of the fluorescence I_F , associated with the absorption process, using the expression (3.1.5),

$$\mu(E) \sim \frac{I_F}{I_0} \quad (3.1.5)$$

The fluorescence yield increases with increasing atomic number and this process has the advantage that the background radiation can be removed by using suitable filters, which increases the sensitivity of the method. For thick samples or samples with low concentration of the element of interest (down to the ppm level), monitoring the X-ray fluorescence is the preferred mode of measurement. The experimental setup for fluorescence mode measurements is schematically shown in Figure 3.1.4.

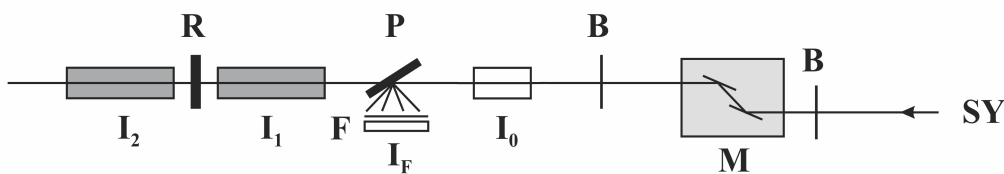


Figure 3.1.4. Schematic of experimental setup for fluorescence mode measurements. [SY – synchrotron radiation, B – slit, M – monochromator, P – sample, R – reference material, F – filter, I_F – fluorescence detector and I_0 , I_1 , I_2 – ionisation chambers].

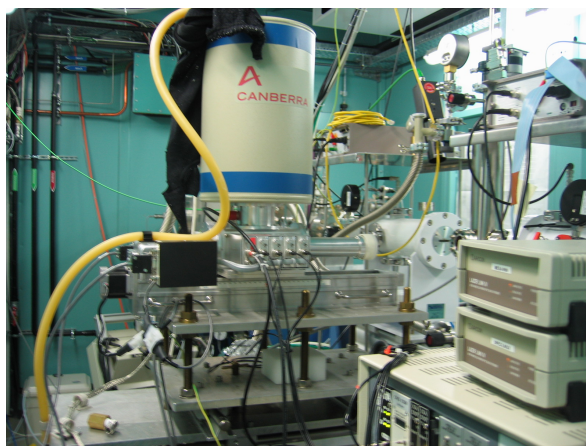


Figure 3.1.5. Picture of solid state X-ray fluorescence detector. [Photograph from the XAS beamline at ANKA, Karlsruhe].

The emitted fluorescence is measured at right angle to the incident beam; the sample is therefore rotated by 45° for optimal fluorescence counts. In general, solid state detectors with Si or Ge as X-ray absorber are used for the detection of fluorescence.

This uses electronic energy discrimination and hence, a characteristic fluorescence line could be measured, thereby avoiding the influence from the scatterer and other fluorescence lines. A typical solid state fluorescence detector is shown in Figure 3.1.5. For fluorescence mode measurements, the sample has to have a larger area, so that the fluorescence counts are high. In order to obtain a good statistics in fluorescence mode, several spectra need to be accumulated and averaged.

In transmission and fluorescence modes, the typical measurement times range between 20 and 60 minutes per spectra, when synchrotron radiation is used. Rapid rotation of the monochromator crystals can reduce these times to a few seconds, however, the experimental effort is increased drastically [3.1.3]. This technique is used to monitor fast reactions and is known as QXAFS (Q - quick). The continuous X-ray spectrum can be split up by Bragg reflection when incident on a special type of a curved crystal and, after passage through the sample, can be measured by using an array detector [3.1.4, 3.1.5]. This technique is suitable for measuring highly dilute samples and is known as DEXAFS (D - dispersive). The detection of the emitted Auger electrons during the absorption process also yields structural information. This method can be employed where the other methods fail. Due to the small mean free wavelength of the emitted electrons ($\sim 100 \text{ \AA}$), the Auger method is especially suited for the study of surfaces, SEXAFS (S - surfaces).

3.1.3. Sample preparation

In the present work, XAFS investigations were performed on both solid and liquid samples. In the case of solid samples, the mass of the substance required for XAFS measurement was calculated using the sum formula of the sample employing the program XMAS [3.1.6], where the concentration of the sample was adjusted to yield an extinction of 1.5. The powder samples were grounded to obtain fine grains. The samples in solid state were embedded in polymer matrices and pressed into pellets having diameters between 0.8 cm and 1.3 cm. The polymer matrices were used to give stability to the pellets. Polyethylene or cellulose was chosen for this purpose, as they are composed of low Z elements. Care was taken to obtain uniform, homogeneous pellets devoid of pin holes. The pellets were encapsulated by Kapton[®] tape and mounted on to the sample holders. In the case of liquid samples, the required quantity was filled into the specially designed liquid sample cell [3.1.7] comprising of Kapton[®] foil windows.

3.2. XAFS data analysis

3.2.1. Data conversion

The raw XAFS data obtained from the different beamlines need to be converted to a suitable format, which can be processed further. The data conversion involves the conversion of the measured intensities to the absorption coefficient $\mu(E)$. In the present work, this was performed using the program WINXAS 2.0 [3.2.1, 3.2.2]. This program calculates the dark current corrected absorption intensities of the sample and automatically multiplies it with the thickness of the sample to arrive at the total absorption A_{Total} , given by the equation (3.2.1),

$$A_{\text{Total}} = \mu(E) \cdot t = \ln \left(\frac{I_0(E)}{I_1(E)} \right) \quad (3.2.1)$$

The raw data obtained from the HASYLAB beamlines (X1, E4 and A1) can be directly uploaded in WINXAS 2.0 and the XAFS spectrum can be visualised. However, the raw data obtained from the ANKA beamline (XAS) has to be reformatted using Microsoft[®] EXCEL, before uploading in WINXAS 2.0.

3.2.2. Pre-edge subtraction and normalisation

The total absorption A_{Total} mentioned in equation (3.2.1) consists of the absorption from the absorber and the basic absorption caused by Compton scattering. This basic absorption is subtracted from the total absorption, by fitting a Victoreen polynomial, as mentioned in equation 3.2.2, to the pre-edge region and extrapolating it over the entire energy range [3.2.3-3.2.5].

$$A_V = \mu_V(E) \cdot t = \frac{a}{E^3} + \frac{b}{E^4} \quad (3.2.2)$$

Here, a and b are constants, which are determined during the fitting of the polynomial using least square method. By subtracting the Victoreen function from the total absorption, one arrives at the real (true) absorption A_{True} , given by the equation (3.2.3),

$$A_{\text{True}} = A_{\text{Total}} - A_V \quad (3.2.3)$$

Normalisation is performed by fitting a polynomial of zeroth order (a constant) to the post-edge region of the spectrum. By dividing the true absorption A_{True} by a constant, the normalised spectrum with an edge jump of 1.0 is obtained. The pre-edge subtraction and normalisation are schematically shown in Figures 3.2.1 and 3.2.2, respectively.

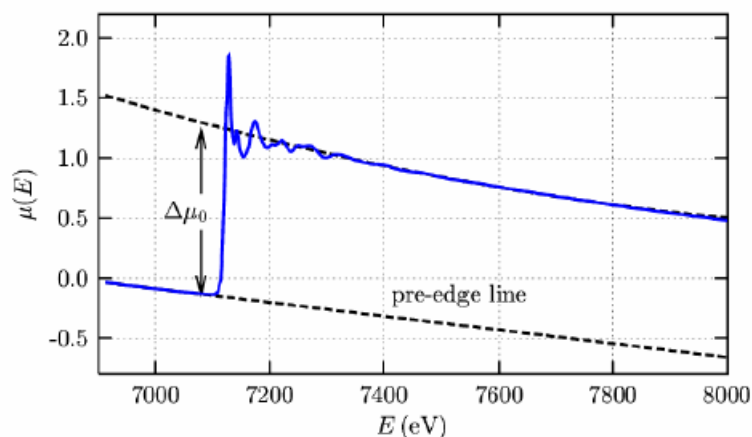


Figure 3.2.1. Schematic representation of pre-edge subtraction (Fe_2O_3), adapted from literature [3.2.6].

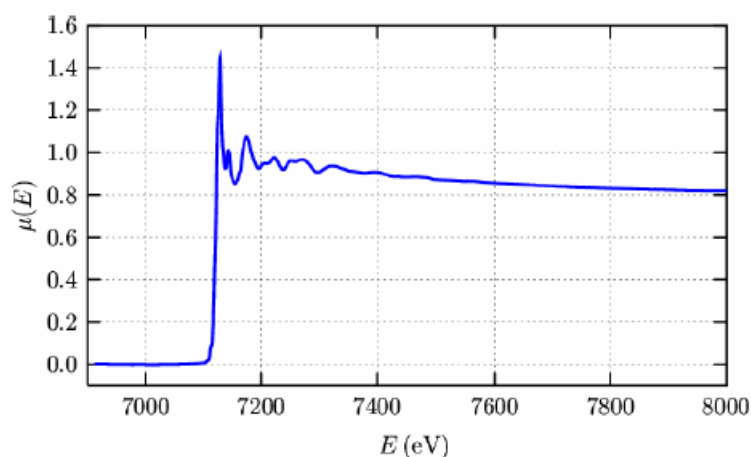


Figure 3.2.2. Schematic representation of normalisation (Fe_2O_3), adapted from literature [3.2.6].

In the present work, the pre-edge subtraction and normalisation were performed using the program WINXAS 2.0 and the normalised spectrum was saved in ASCII format for further analysis.

3.2.3. Absorption edge determination and energy correction

For EXAFS evaluation, conversion of energy space to k -space is required and for the transformation into k -space, it is necessary to know the relative position of the absorption edge E_0 . This can be determined either with the program WINXAS 2.0 or with the program EXRD [3.2.7]. The program EXRD employs two different methods, viz., inflection method and intersection method, for the calculation of the absorption edge. In inflection method, E_0 is determined from the position of the first inflection point within the absorption edge. In intersection method, E_0 is determined from the

position of the intersection of the experimental spectrum and a set of functions, which result from the multiplication of the experimental spectrum with standardised Gaussian distribution functions of different half widths [3.2.8]. The absorption edge values determined by these two methods deviate only by about 5 eV.

The absorption edge can be approximately equated to the energy with the maximum derivative. A typical XAFS spectrum and its derivative are depicted in Figure 3.2.3.

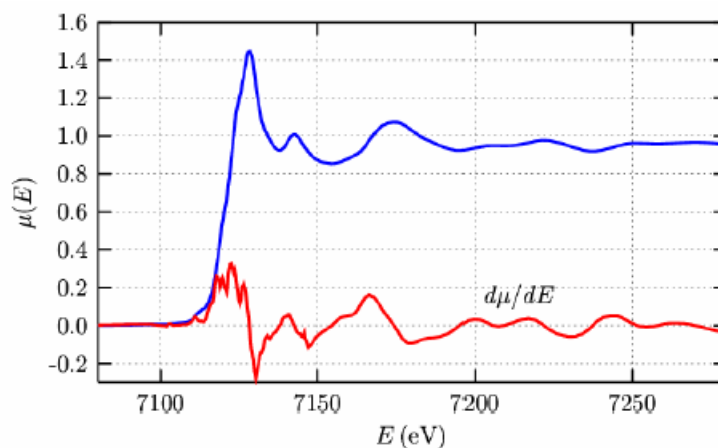


Figure 3.2.3. Typical XAFS spectrum (Fe_2O_3) and its derivative, adapted from literature [3.2.6].

During the EXAFS analysis only the energy difference relative to the absorption edge is considered; hence, an exact energy calibration is not necessary. However, for the comparison of the XANES spectra of different samples an exact determination of the edge position is essential. The energy correction is performed using the well known edge positions of the reference materials, which are measured along with the samples.

3.2.4. Background subtraction and data reduction

The background function can be defined as the part of the measured spectrum that does not contain any structural information. Background subtraction is the most critical step in the analysis procedure. The process starts with the modulation of the X-ray absorption coefficient $\mu(E)$ for the background absorption $\mu_0(E)$, where $\mu_0(E)$ refers to the absorption coefficient without neighbouring atoms. Since, there exists no exact theoretical expression for $\mu_0(E)$, it must therefore be determined empirically. Even though there are different criteria for the choice of background, the determination of $\mu_0(E)$ is a critical aspect. The EXAFS oscillations can be dampened too much if $\mu_0(E)$ matches the experimental data too closely. In the present work, the program AUTOBK

[3.2.9] was used for background removal. The method employed subtracts a spline that best eliminates the non-structural portion from the measured spectrum. The spline used to approximate the background is a third order polynomial spline with knots that are equally spaced in k -space [3.2.10]. Since each knot is associated with one degree of freedom, the maximum number of knots allowed in a spline is given by the equation (3.2.4),

$$N_{knots} = \frac{2 \cdot R_{bkg} \cdot \Delta k}{\pi} \quad (3.2.4)$$

Here, the term Δk denotes the k -range of useful data and R_{bkg} refers to the upper limit of the low- R region over which the background is to be fit. Typically, R_{bkg} will be about half the distance of the first shell peak. To minimise R components higher than R_{bkg} in the background, the knots are set to be equally spaced in k -space, so that R_{bkg} can be thought of as the Nyquist frequency, above which no signal can be measured. The value of R_{bkg} is chosen in such a way that, on one hand the artefacts are eliminated and on the other the signals from the real backscatterers are not suppressed. The fitting of the spline function to the experimental spectrum is performed using Levenberg-Marquardt algorithm [3.2.11] according to least squares method. This approach to background removal can be applied to nearly all systems to give reasonable results. The background subtraction process is schematically shown in Figure 3.2.4.

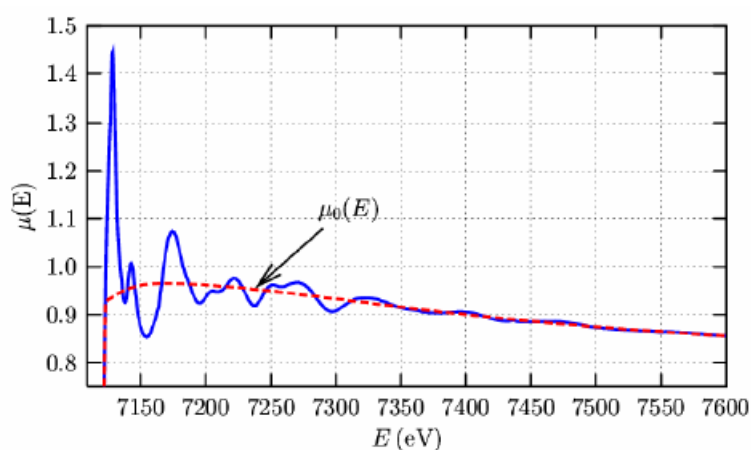


Figure 3.2.4. Schematic representation of background subtraction (Fe_2O_3), adapted from literature [3.2.6].

The normalised EXAFS function $\chi(E)$ is obtained from the X-ray absorption coefficient $\mu(E)$ and the background absorption $\mu_0(E)$ using the equation (3.2.5),

$$\chi(E) = \frac{\mu(E) - \mu_0(E)}{\Delta\mu_0(E_0)} \quad (3.2.5)$$

Here, the term $\Delta\mu_0(E_0)$ is a constant and it refers to the absorption jump. It can be mathematically expressed using the equation (3.2.6),

$$\Delta\mu_0(E_0) = \mu_0^{\text{post-edge}}(E_0) - \mu_0^{\text{pre-edge}}(E_0) \quad (3.2.6)$$

The absorption jump is generally experimentally determined by comparing the values of the two extrapolated functions at the absorption energy E_0 , which were fitted to the pre- and post-edge regions. In the data reduction step the program AUTOBK automatically converts the $\chi(E)$ function to $\chi(k)$ function using the relationship between the energy E and the wave vector k , as earlier mentioned in Chapter 2. The $\chi(k)$ function is schematically shown in Figure 3.2.5.

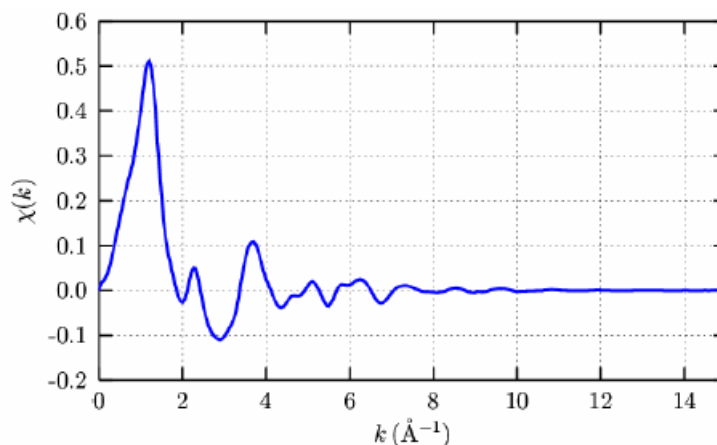


Figure 3.2.5. Schematic representation of the $\chi(k)$ function (Fe_2O_3), adapted from literature [3.2.6].

The obtained data is in ASCII format and can be directly used for data evaluation in many cases. However, certain data evaluation programs require $\chi(E)$ function as input file, and in such cases the obtained $\chi(k)$ function has to be converted back to $\chi(E)$ function.

3.2.5. Interpretation of the EXAFS function

The interpretation of the EXAFS function is performed based on a Curve-Fitting algorithm, where a complex theoretical function is fitted to the experimental spectrum, by variation of the different structural parameters. In practice, the experimental $\chi(k)$ function is weighed appropriately in powers of k and multiplied by a window function

during the evaluation. Generally, a window function [3.2.12], as depicted in Figure 3.2.6, is used for this purpose.

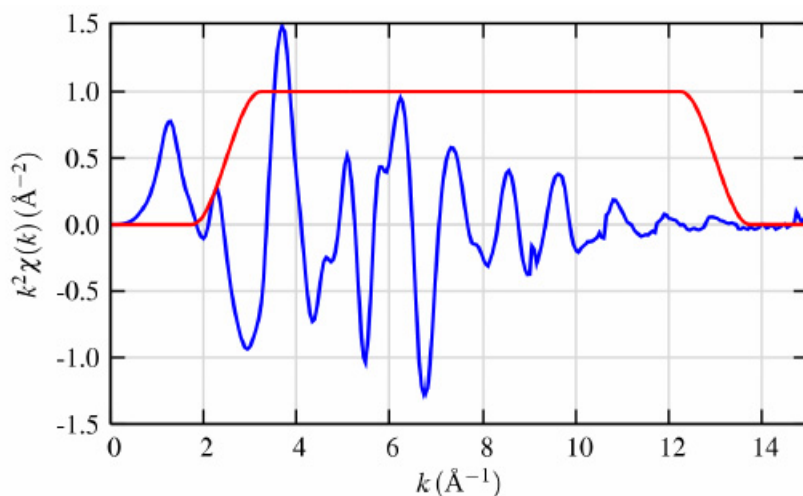


Figure 3.2.6. Schematic representation of a Hanning window function multiplied to $k^2\chi(E)$ function (Fe_2O_3), adapted from literature [3.2.6].

Subsequently, the obtained k -weighted $\chi(k)$ function, composed of sine waves, is Fourier transformed from k -space to R -space. The Fourier transformation makes $\chi(R)$ complex, with both real and imaginary parts as depicted in Figure 3.2.7. Usually only the amplitude is shown, but in reality there are oscillations in $\chi(R)$ function. Both real and imaginary components are used in data evaluation.

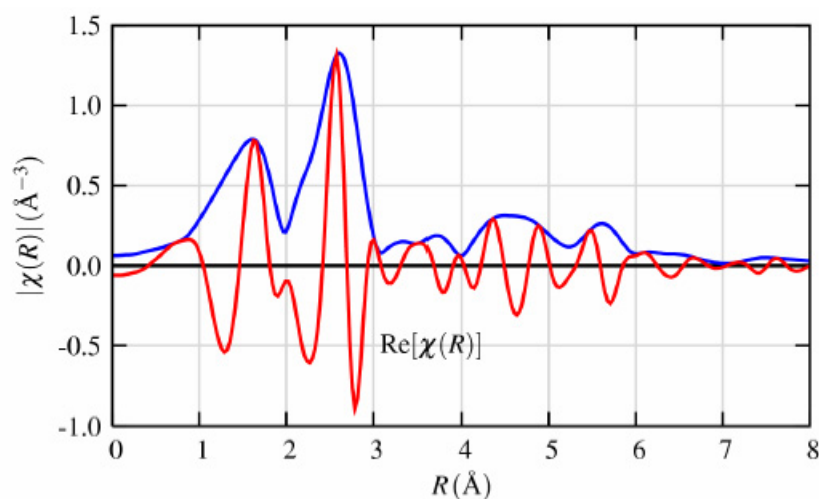


Figure 3.2.7. Schematic representation of the $\chi(R)$ function (Fe_2O_3), adapted from literature [3.2.6].

In the present work, the data evaluation in k -space is performed using the programs EXCURV92 and EXCURV98 [3.2.13], which require $\chi(E)$ function as input file. This

program uses a special formalism based on the electron scattering theory [3.2.14] to calculate the theoretical backscattering amplitudes and phases, as well as the lifetime of the photoelectron. This program employs the formalism of curved wave theory [3.2.15, 3.2.16] to model the theoretical function, which will later be fitted to the experimental spectrum. The curved wave theory describes the electron wave incident on the backscattering atom as a curved wave and not as a plane wave. The optimisation of fitting is performed by an iterative least squares method. The agreement of the fitted function to the experimental spectrum is denoted by means of R-factor given by the equation (3.2.7),

$$R - factor = \sum_{i=1}^N \frac{1}{S_i} (|\chi_i^{\text{exp}}(k) - \chi_i^{\text{theo}}(k)|) \cdot 100 \% \quad (3.2.7)$$

Here, the term S_i refers to the weighing factor computed by the analysis program. The lower the value of R-factor, the better is the fit.

In the analysis of the EXAFS function, it should be noted that the EXAFS spectrum is a one dimensional representation of a three dimensional object. Therefore, there could be more than one structural model, which can describe the experimental spectrum adequately. For this reason, it is necessary to consider additional information such as crystallographic data during the data evaluation. With exact knowledge of the coordination geometry, the coordination numbers can be fixed to the known values, while iterating the other parameters. Another possibility is to set limits for the parameters, within which they may be varied. It should also be noted that some of the fit parameters are related to one another (coordination number and Debye-Waller factor, and interatomic distance and energy zero) and cannot be decoupled easily. Hence, care should be taken when these parameters are iterated against each other. Furthermore, the backscattering amplitudes of the neighbouring elements in the periodic table are only slightly different; hence, an unambiguous differentiation between near neighbours is nearly infeasible. Moreover, for different types of backscatterers with almost identical interatomic distances, the backscatterer with higher atomic number shadows the one with lower atomic number.

The fitting of a theoretical function to the experimental data is in most case the only way to interpret EXAFS spectra. Appropriate care should be taken to obtain reliable results. The distances can be determined with an accuracy of up to 1%, the coordination numbers can be ascertained to within 10 – 30% for the different shells. When model

compounds, optimised measurement conditions and accurate data analysis are employed, the error boundary could be significantly reduced.

In the present work, the $\chi(k)$ functions were weighed with k^3 and single scattering theory was predominantly employed for evaluation. The potentials and phase shifts were calculated based on XALPHA approximations. The EXAFS analysis performed using the program EXCUR92 yielded the shift of the threshold energy (ΔE_0), whereas the analysis performed using the program EXCURV98 provided the Fermi energy (E_F) value. For clarity reasons, the EXAFS spectrum and the Fourier transform plot are shifted along the ordinate axis in many cases. The exact zero position of the EXAFS spectrum and that of the corresponding Fourier transform can be obtained by observing the value on the ordinate axis at the intersection point.

3.2.6. AXAFS evaluation

As already mentioned in Chapter 2, the AXAFS features arise from the difference between the free atom potential and the embedded atom potential. The objective is to remove the contributions due to free atom and consider only those from the embedded atom. The AXAFS contributions may overlap with the multiple electron excitations (MEE) and Ramsauer-Townsend resonances (RTR) at the low R -ranges, and with EXAFS oscillations at the high R -ranges. Hence, both these features need to be separated from the AXAFS signals. The criteria used for background removal, outlined in literature [3.2.17], is given below,

- (1) In the Fourier transform diminish the contribution at $R < 0.5 \text{ \AA}$, i.e., MEE and RTR, as much as possible. Verify whether the MEE and RTR fully remain in the background by examining the background.
- (2) Confirm that the EXAFS intensity at $R > 1.5 \text{ \AA}$ is unchanged (unreduced).
- (3) Examine both k^1 and k^3 weighed spectra, for different k -ranges, including low k -values.

These criteria can be applied generally. Nevertheless, they are constructed for XAFS data of samples in which the AXAFS and the EXAFS peaks in the Fourier transform of the XAFS data have less or no overlap. In the present work, the program AUTOBK was used for the AXAFS background removal as well. Calculations were performed with different sets of R_{bkg} values on a specific sample, viz., diphenyl(ether-phosphine) ruthenium (II) complex and the best R_{bkg} value was selected. The chosen value was used

in the isolation of background from the AXAFS signal for all the other samples. It is always possible that the choice of the R_{bkg} value does not lead to an optimal separation between MEE, AXAFS and EXAFS. However, it should be noted that even without an optimal background subtraction, identical trends in the final AXAFS data could still be found as long as the background subtraction is performed consistently. The final trend in the AXAFS areas will be same even though the absolute areas may be different.

3.3. Raman and infrared spectroscopic measurements

3.3.1. Raman measurements

The Raman spectra were recorded on Bruker RFS 100/S Fourier transform Raman spectrometer with an air cooled near infrared Nd:YAG laser with a wavelength of 1064 nm. The intensity of the laser can be varied from 0 to 1.5 W in steps of 1 mW. The scattered light was collected at an angle of 180° with a high sensitivity Ge diode detector, cooled with liquid nitrogen. For the exact positioning of the sample, a He-Ne precision laser was used. The spectral resolution of the instrument is 4 cm⁻¹. In the present work, the liquid samples were measured with a power level of 1250 mW and the solid samples were measured with power levels ranging from 30 to 500 mW. For an average measurement, minimum of 1024 scans were collected. The details of the instrumental parameters involved in the Raman measurements are presented in Appendix. The measured spectra were analysed using the finger-print method, where they are compared with the spectra of other known compounds.

3.3.2. Infrared measurements

The infrared spectra were recorded on Bruker IFS 66v/S Fourier transform infrared spectrometer with a Globar light source and KBr beam splitter. The spectra were accumulated with a DLATGS detector in absorption mode. The spectral resolution of the instrument is 2 cm⁻¹. In the present work the samples in solid state were prepared as KBr pellets and measured under ambient conditions. For an average measurement, minimum of 512 scans were collected. The details of the instrumental parameters involved in the infrared measurements are presented in Appendix. Similar to the analysis of the Raman spectra, the infrared spectra were also analysed using the finger-print method.

Chapter 4 Investigations on organometallic complexes

4.1. Studies on optically active metallophthalocyanines

4.1.1. Introduction

Metallophthalocyanine complexes have been studied in detail for many years, especially with regard to their physical properties. The systematic development of synthetic methodologies for the functionalisation of phthalocyanine and its related compounds has paved the way for the preparation of novel organic or polymeric compounds of interest in the search of new materials with excellent photophysical, optoelectronic properties as well as biological activities [4.1.1 - 4.1.3]. Phthalocyanines are extremely stable pigments and from an application point of view are especially important as they belong to a group of few compounds, which have high optical sensitivity and can be excited with laser diodes. Their highly conjugated aromatic π -electron system can give rise to large nonlinear optical response, and can be readily modified by physical or chemical methods [4.1.4].

Axial substitution on phthalocyanines generally increases their solubility and, therefore, reduces molecular aggregation [4.1.5, 4.1.6]. In terms of optical limiting effectiveness in the visible range, axial substitution can improve the efficiency of nonlinear optical materials [4.1.7, 4.1.8]. Moreover, axial substituents in phthalocyanines favourably influence nonlinear optical absorption for the presence of a dipole moment perpendicular to the macrocycle [4.1.9]. These compounds show higher nonlinear absorption coefficients, lower limiting thresholds, and an earlier onset of the optical limiting behaviour [4.1.10]. It is thus undoubtedly very interesting to study the molecular structure of phthalocyanine compounds as the structure has direct implications on the properties. For most of the phthalocyanines, it is very difficult to obtain suitable single crystals required for X-ray structural determination, therefore EXAFS spectroscopy could be employed to probe the neighbourhood environment of the metal atom.

4.1.2. Dimeric phthalocyanines

4.1.2.1. Peripherally substituted gallium phthalocyanine dimer

The gallium phthalocyanine dimer, $[\text{Bu}_4\text{PcGa}]_2 \cdot 2\text{dioxane}$, was prepared by the work group of Prof. Dr. M. Hanack, Institute of Organic Chemistry, University of Tuebingen,

by Wurtz coupling reaction of ${}^t\text{Bu}_4\text{PcGaCl}$ in the presence of 1,4-dioxane using magnesium as catalyst and iodine as co-catalyst, and was found to exhibit significantly enhanced optical limiting response relative to the starting material [4.1.11]. The EXAFS measurement of the compound was performed at the Ga K-edge at 10367 eV at the beamline X1 at HASYLAB, Hamburg, using Si(111) double crystal monochromator at ambient conditions. Energy calibration was monitored using 20 μm thick iridium metal foil having L_{III} -edge at 11215 eV. The experimentally determined and theoretically calculated EXAFS functions of $[\text{}^t\text{Bu}_4\text{PcGa}]_2 \cdot 2\text{dioxane}$ are shown in k space as well as by Fourier transforms in real space in Figure 4.1.1. The structural parameters are summarised in Table 4.1.1 and the molecular structure is depicted in Figure 4.1.2. In the fitting procedure, the intramolecular coordination numbers were fixed to the known values for the ligands around the gallium atom in the compound. The other parameters including intermolecular coordination number, interatomic distance, Debye-Waller factor and energy zero value were determined by iterations.

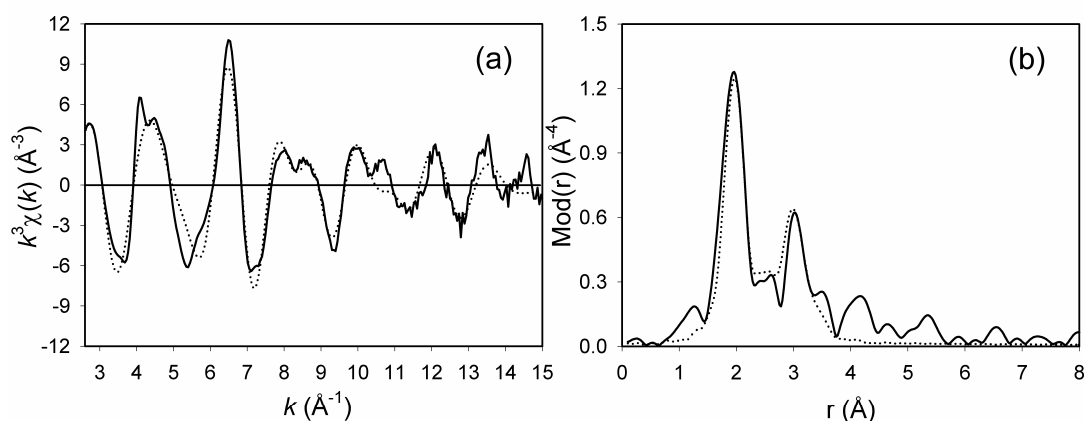


Figure 4.1.1. Experimental (solid line) and calculated (dotted line) EXAFS functions (a) and their corresponding Fourier transform plots (b) of $[\text{}^t\text{Bu}_4\text{PcGa}]_2 \cdot 2\text{dioxane}$ measured at the Ga K-edge.

Table 4.1.1. EXAFS determined structural parameters of $[\text{}^t\text{Bu}_4\text{PcGa}]_2 \cdot 2\text{dioxane}$

Compound	A-Bs ^a	N ^b	r ^c [Å]	σ ^d [Å]	ΔE_0 ^e [eV]	k-range [Å ⁻¹]	R-factor
$[\text{}^t\text{Bu}_4\text{PcGa}]_2 \cdot 2\text{dioxane}$	Ga-N _{Pyrrrole} /O _{Dioxane}	5	2.00 ± 0.02	0.067 ± 0.007	13.83	2.6 - 15.0	32.66
	Ga-C	8	3.00 ± 0.03	0.071 ± 0.016			
	Ga-N _{Aza}	4	3.33 ± 0.04	0.081 ± 0.026			
	Ga-Ga	1	2.46 ± 0.03	0.095 ± 0.016			

^a absorber (A) - backscatterers (Bs), ^b coordination number N, ^c interatomic distance r, ^d Debye-Waller factor σ with its calculated deviation and ^e shift of the threshold energy ΔE_0 .

The analysis of the data shows the contribution of phthalocyanine macrocycle in the spectra. Due to the similar backscattering behaviour of nitrogen and oxygen, occurring at nearly the same distance from the metal atom, a combined shell with a coordination number of five is determined at a distance of about 2.00 Å. This includes the four backscattering nitrogen atoms from pyrrole and one backscattering oxygen atom from the dioxane ligand. Another four backscattering nitrogen atoms from the aza nitrogen atoms are found at 3.33 Å distance. An additional shell consisting of eight carbon atoms, having gallium-carbon distances at 3.00 Å was observed. The fit improved significantly by having a gallium backscatterer at a distance of 2.46 Å. For comparison, the reported gallium-gallium bond lengths in some organo-gallium compounds are 2.38 Å for $\text{Ga}_2(\text{CH}(\text{SiMe}_3)_2)_2(\mu\text{-O}_2\text{CCH}_3\text{-O, O}')_2$ [4.1.12], 2.38 Å for $[\text{Ga}_2\text{Cl}_4(\text{dioxane})_2]_x$ [4.1.13], 2.45 Å for $[(\text{Me}_3\text{Si})_2\text{C}(\text{Ph})\text{C}(\text{Me}_3\text{Si})\text{NGaCl}]_2$ [4.1.14] and 2.56 Å for $[(\text{Me}_3\text{Si})_2\text{HC}]_4\text{Ga}_2$ [4.1.15]. When the coordination number for gallium was iterated, it resulted in a value of 0.7; therefore the coordination number was fixed to one. This result is consistent with an arrangement of the complex as a dimer. In addition, it should be noted that the backscattering behaviour of Ga ($Z = 32$), Cl ($Z = 17$) and I ($Z = 53$) are different, thus these elements can be well distinguished by EXAFS spectroscopy, especially when these backscatterers occur in a distance range of 2-3 Å. Hence, no evidence was found that this compound is ${}^t\text{Bu}_4\text{PcGaI}$, a possible by-product.

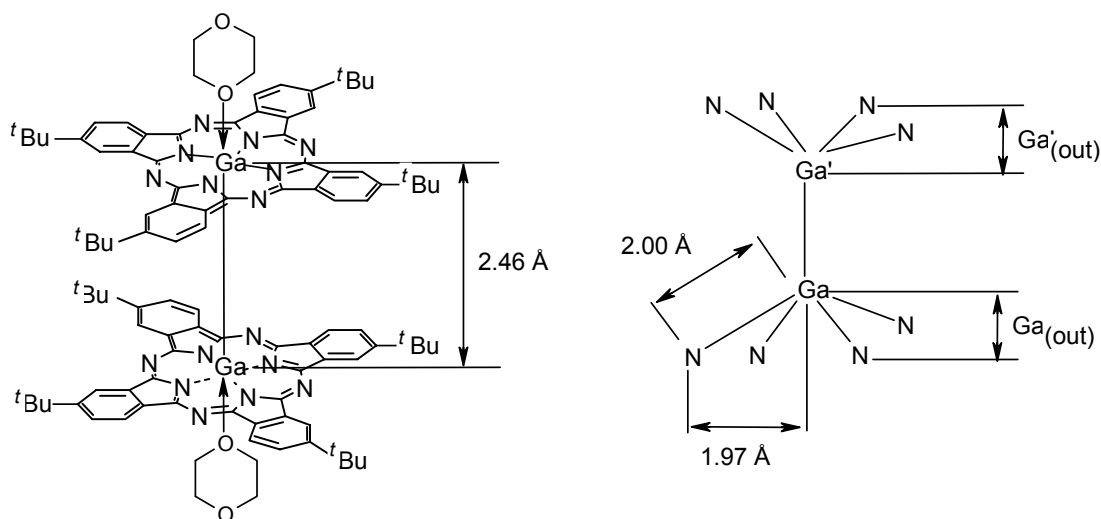


Figure 4.1.2. Molecular structure of $[\text{}^t\text{Bu}_4\text{PcGa}]_2 \cdot 2\text{dioxane}$.

The effect of the metal ions on the phthalocyanine ring had been widely studied and four structural effects on the phthalocyanine ring, viz. ring contraction occurring in nickel phthalocyanine, equilibrium ring geometry in the case of cobalt, iron, copper and

manganese phthalocyanines, ring expansion in zinc and platinum phthalocyanines and metal non-planarity and ring doming in the case of tin and lead phthalocyanines [4.1.16]. The shortest interplanar ring spacing in gallium phthalocyanines was found to be 3.34 Å in the case of PcGaCl for parallel stacking arrangement [4.1.17]. When such a short interplanar ring spacing is assumed in the present case, the intermolecular metal-metal distance should be about 3.35 Å, but the EXAFS results indicate gallium-gallium distance to be 2.46 Å, which suggests that the two gallium atoms in the molecule are projected inwards of the phthalocyanine ring and the gallium center is located 0.45 Å out of the plane formed by the four coordinated nitrogen atoms. In addition, when a rigid phthalocyanine molecule with an average cavity diameter of about 3.85 Å, which is not deformed by the metal atom is assumed, the shortest metal-nitrogen distance occurs at 1.97 Å [4.1.18, 4.1.19]. But the present results indicate gallium-nitrogen and gallium-oxygen distance of 2.00 Å, which also suggests that the gallium center is located 0.45 Å out of the plane. This value is in good agreement with the reported out of plane value of 0.439 Å in crystalline PcGaCl [4.1.17]. Further, in a rigid phthalocyanine molecule, the shortest distance between the metal center and the nearest carbon occurs at 2.96 Å, while in the present case it results a gallium-carbon distance of 3.00 Å. From these values an out-of-plane location of gallium equal to 0.54 Å was found, which is in agreement with the value determined from the shortest gallium-nitrogen separation values. Since the compound was found to be a dimer, it is believed that the *t*-butyl groups in the periphery of the macrocycles have no sterical hindrance with each other and the two phthalocyanine macrocycles are arranged in a staggered conformation. In any case, the exact geometry of these groups cannot be determined by EXAFS spectroscopy and the existence of a mixture of regioisomers could not be ruled out. Furthermore, the sterically less crowded staggered conformation is preferred when interplanar spacing is less than 3.5 Å, while the eclipsed conformation occurs at larger spacings [4.1.20].

4.1.2.2. Peripherally substituted ruthenium phthalocyanine dimer

The hexadecafluoro ruthenium phthalocyanine dimer, (F₁₆PcRu)₂, was prepared by the work group of Prof. Dr. M. Hanack, Institute of Organic Chemistry, University of Tuebingen, by refluxing tetrafluorophthalonitrile with RuCl₃·3H₂O in 2-ethoxyethanol [4.1.21]. The EXAFS measurements of the compound was performed at the Ru K-edge

at 22117 eV at the beamline X1 at HASYLAB, Hamburg, using Si(311) double crystal monochromator under ambient conditions. Energy calibration was monitored with a 20 μm thick ruthenium metal foil. The experimentally determined and fitted EXAFS functions of $(\text{F}_{16}\text{PcRu})_2$ are shown in k space as well as by Fourier transforms in real space in Figure 4.1.3 and the structural parameters are summarised in Table 4.1.2. The molecular structure of $(\text{F}_{16}\text{PcRu})_2$ is given in Figure 4.1.4.

In the fitting procedure, the coordination numbers were fixed to the known values of the phthalocyanine molecule and the other parameters including interatomic distances, Debye-Waller factor and energy zero value were determined by iterations. The analysis of the data shows the contribution of phthalocyanine macrocycle in the spectra. In agreement with the well-known structure of phthalocyanines [4.1.18], four nitrogen backscatterers at 2.04 \AA , arising from the pyrrole nitrogen atoms, and another four nitrogen backscatterers at 3.32 \AA , stemming from the aza nitrogen atoms, were found. In addition, another shell consisting of eight carbon backscatterers at 3.02 \AA was observed. All these distances can be assigned to intramolecular contributions.

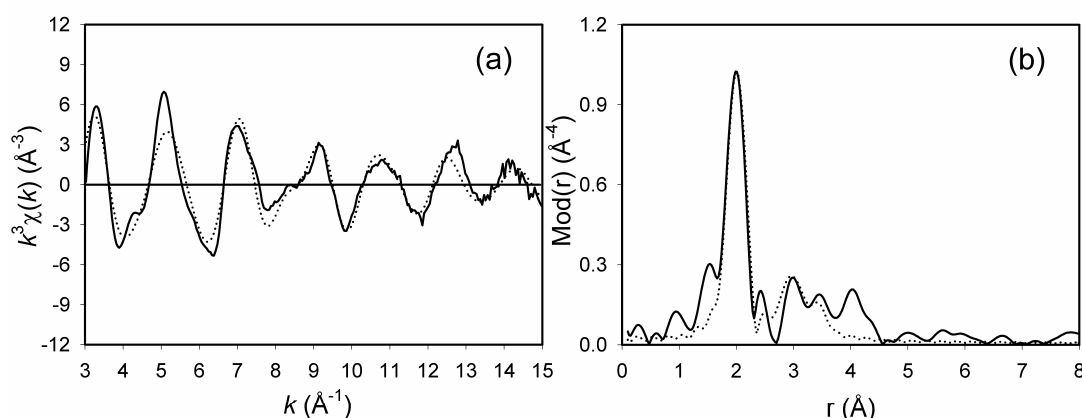


Figure 4.1.3. Experimental (solid line) and calculated (dotted line) EXAFS functions (a) and their corresponding Fourier transform plots (b) of $(\text{F}_{16}\text{PcRu})_2$ measured at the Ru K-edge.

Table 4.1.2. EXAFS determined structural parameters of $(\text{F}_{16}\text{PcRu})_2$

Compound	A-Bs ^a	N ^b	r ^c [\AA]	σ ^d [\AA]	ΔE_0 ^e [eV]	k -range [\AA^{-1}]	R-factor
$(\text{F}_{16}\text{PcRu})_2$	Ru-N _{pyrrole}	4	2.04 ± 0.02	0.059 ± 0.006	22.50	3.0 - 15.0	33.90
	Ru-C	8	3.02 ± 0.03	0.122 ± 0.015			
	Ru-N _{Aza}	4	3.32 ± 0.04	0.081 ± 0.009			
	Ru-Ru	1	2.43 ± 0.03	0.122 ± 0.015			

^a absorber (A) - backscatterers (Bs), ^b coordination number N, ^c interatomic distance r, ^d Debye-Waller factor σ with its calculated deviation and ^e shift of the threshold energy ΔE_0 .

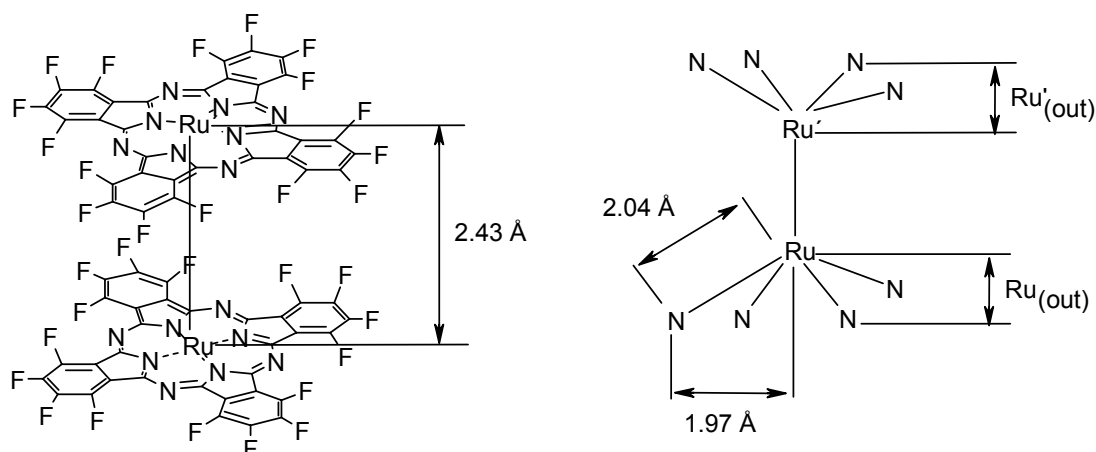


Figure 4.1.4. Molecular structure of $(F_{16}PcRu)_2$.

Besides the expected three shells of the phthalocyanine macrocycle, a significant improvement in the fit index was obtained by considering a ruthenium backscatterer at a distance of 2.43 Å. This distance is in good agreement with the reported Ru-Ru bond distances in other organo-ruthenium complexes, for example 2.40 Å in $(PcRu)_2$ [4.1.22], 2.41 Å in $[Ru(OEP)]_2$ [4.1.23], 2.38 Å in $Ru_2(C_{22}H_{22}N_4)$ [4.1.24] and 2.42 Å in tBu_4PcRu [4.1.25]. This result is consistent with a dimeric structure for $(F_{16}PcRu)_2$. Furthermore, in the Fourier transform plot, a peak at about 4 Å could be noticed. This is supposed to be due to eight carbon backscatterers in the phthalocyanine macrocycle [4.1.26, 4.1.27]. A fitting with these backscatterers in this distance range does not increase the agreement of the experimental EXAFS function with the fitted function, hence this shell was not considered for evaluation. For $(F_{16}PcRu)_2$, when a short interplanar ring spacing of about 3.35 Å, as like in many phthalocyanines [4.1.20, 4.1.28] or graphite [4.1.29] is assumed, the inter-macrocycle metal-metal distance should be about 3.35 Å, but the results indicate Ru-Ru distance of 2.43 Å, which suggests that the two ruthenium atoms in the molecule are projected inwards of the phthalocyanine ring and the ruthenium center is located 0.46 Å out of the plane formed by the four coordinated nitrogen atoms. Moreover, when a rigid phthalocyanine molecule with an average cavity diameter of about 3.85 Å, which is not deformed by the metal atom is assumed, the shortest metal-nitrogen distance occurs at 1.97 Å [4.1.18, 4.1.19]. But the results show Ru-N distance of 2.04 Å, which also suggests that the ruthenium center is located 0.53 Å out of the plane. This value is in good agreement with the reported out of plane values of 0.49 Å in $(PcRu)_2$ [4.1.22], 0.4 Å in tBu_4PcRu [4.1.25] and 0.41 Å in $(PcRu)_2$ [4.1.26].

4.1.3. μ -oxo-bridged phthalocyanines

4.1.3.1. μ -oxo-bridged gallium phthalocyanine dimer

The compound, $({}^t\text{Bu}_4\text{PcGa})_2\text{O}$ was prepared by the work group of Prof. Dr. M. Hanack, Institute of Organic Chemistry, University of Tuebingen, by the reaction of ${}^t\text{Bu}_4\text{PcGaCl}$ with excess of concentrated H_2SO_4 at 253 K and was shown to exhibit good optical limiting properties [4.1.30]. The EXAFS measurement of the compound was performed at the Ga K-edge at 10367 eV at the beamline X1 at HASYLAB, Hamburg using Si(111) double crystal monochromator at ambient conditions. Energy calibration was monitored using an iridium metal foil having L_{III} -edge at 11215 eV. The experimentally determined and theoretically calculated EXAFS functions of $({}^t\text{Bu}_4\text{PcGa})_2\text{O}$ are shown in k space as well as by Fourier transforms in real space in Figure 4.1.5. The structural parameters are summarised in Table 4.1.3 and the molecular structure is depicted in Figure 4.1.6.

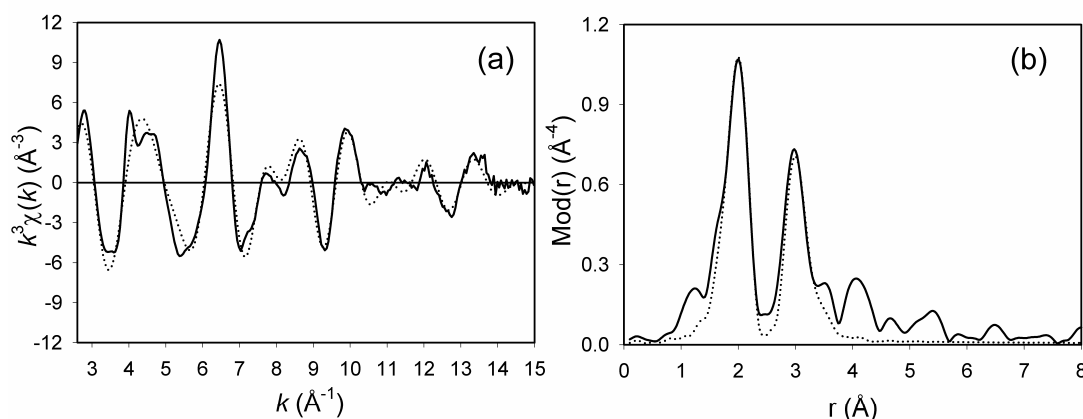


Figure 4.1.5. Experimental (solid line) and calculated (dotted line) EXAFS functions (a) and their corresponding Fourier transform plots (b) of $({}^t\text{Bu}_4\text{PcGa})_2\text{O}$ measured at the Ga K-edge.

Table 4.1.3. EXAFS determined structural parameters of $({}^t\text{Bu}_4\text{PcGa})_2\text{O}$

Compound	A-Bs ^a	N ^b	r ^c [Å]	σ ^d [Å]	ΔE_0 ^e [eV]	k-range [Å ⁻¹]	R-factor
$({}^t\text{Bu}_4\text{PcGa})_2\text{O}$	Ga-O	1	1.87 ± 0.02	0.052 ± 0.005	14.69	2.6 - 15.0	33.57
	Ga-N _{Pyrrrole}	4	2.02 ± 0.02	0.057 ± 0.006			
	Ga-C	8	3.01 ± 0.03	0.062 ± 0.013			
	Ga-N _{Aza}	4	3.33 ± 0.04	0.088 ± 0.026			

^a absorber (A) - backscatterers (Bs), ^b coordination number N, ^c interatomic distance r, ^d Debye-Waller factor σ with its calculated deviation and ^e shift of the threshold energy ΔE_0 .

The influence of the phthalocyanine macrocycle in the spectra is evident from the data analysis. The central gallium atom has two clearly distinguishable nitrogen shells,

one stemming from the pyrrole nitrogen atoms, at a distance of 2.02 Å with a coordination number of four and another arising from the aza nitrogen atoms, at a distance of 3.33 Å also with the same coordination number of four, were determined. Another shell, consisting of eight equivalent gallium-carbon backscatterers at 3.01 Å was found. An oxygen shell with a coordination number of one, arising from the bridging oxygen atom at a distance of 1.87 Å improves the fit index to a considerable value. When a rigid phthalocyanine molecule, which is not deformed by the metal atom is assumed, the shortest metal atom and nitrogen distance corresponds to 1.97 Å [4.1.18, 4.1.19]. The results indicate gallium-nitrogen separations at a distance of 2.02 Å, which leads to the conclusion that the gallium center is located 0.45 Å out of the plane described by the four nitrogen atoms directly bonded to it.

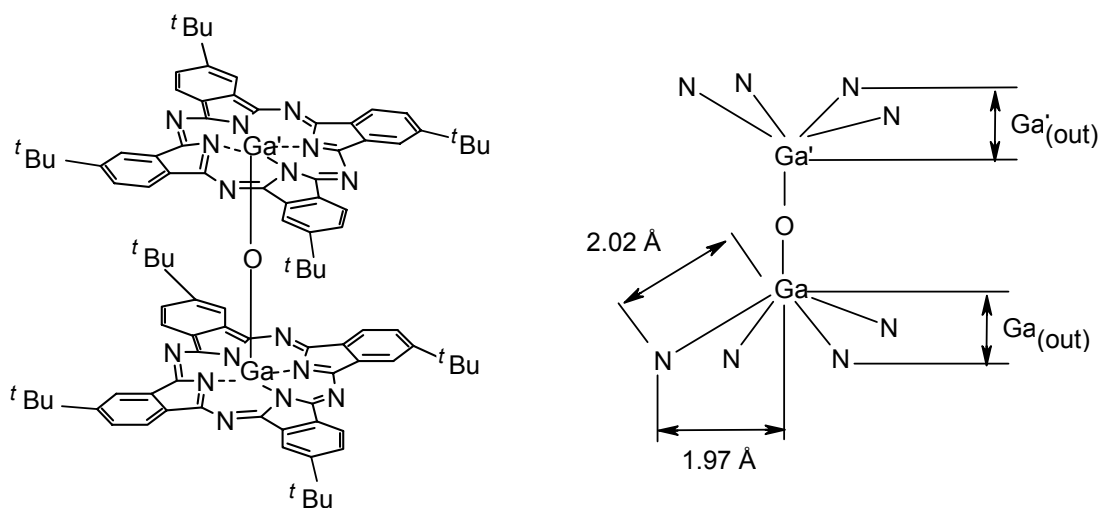


Figure 4.1.6. Molecular structure of $(t\text{Bu}_4\text{PcGa})_2\text{O}$.

In the peripherally unsubstituted aluminium phthalocyanine $(\text{PcAl})_2\text{O}$ [4.1.20], the oxygen atom is located in the center of symmetry of the molecule, to which the two macrocycle units are bound through aluminium on opposite sites. Each of the PcAl units form a square pyramid with the four inner nitrogen atoms at the base and the pentacoordinate aluminium atom located in the apical position, 0.459 Å above the center of the four nitrogen atoms bonded to it. The oxygen bridge between the two metallophthalocyanine macrocycles is supposed to be linear, which predicts, the distance between the two gallium atoms would be 3.74 Å. Single gallium backscatterer at this distance, contributes only to a very weak signal and could not be determined with EXAFS spectroscopy.

4.1.3.2. μ -oxo-bridged gallium-indium phthalocyanine dimer

The compound, ${}^t\text{Bu}_4\text{PcGa-O-InPc}{}^t\text{Bu}_4$ was prepared by the work group of Prof. Dr. M. Hanack, Institute of Organic Chemistry, University of Tuebingen, from ${}^t\text{Bu}_4\text{PcGaCl}$ and ${}^t\text{Bu}_4\text{PcInCl}$ as starting materials. The compound possess no advantages over $[({}^t\text{Bu}_4\text{PcGa})_2\text{O}]$ and $[({}^t\text{Bu}_4\text{PcIn})_2\text{O}]$ from the point of view of optical limiting as it does not increase the ratio of the excited to ground state absorption cross sections nor does it reduce the saturation energy density [4.1.31]. EXAFS measurement of the compound was performed at the Ga K-edge at 10367 eV and at the In K-edge at 27940 eV using Si(111) and Si(311) double crystal monochromators, respectively, at the beamline X1 at HASYLAB, Hamburg at ambient conditions. Energy calibration was monitored using an iridium metal foil for the Ga K-edge measurement and an indium metal foil for the In K-edge measurement. The experimentally determined and theoretically calculated EXAFS functions of ${}^t\text{Bu}_4\text{PcGa-O-InPc}{}^t\text{Bu}_4$ measured at the Ga K-edge are shown in k space as well as by Fourier transforms in real space in Figure 4.1.7. The structural parameters are given in Table 4.1.4 and molecular structure is depicted in Figure 4.1.8.

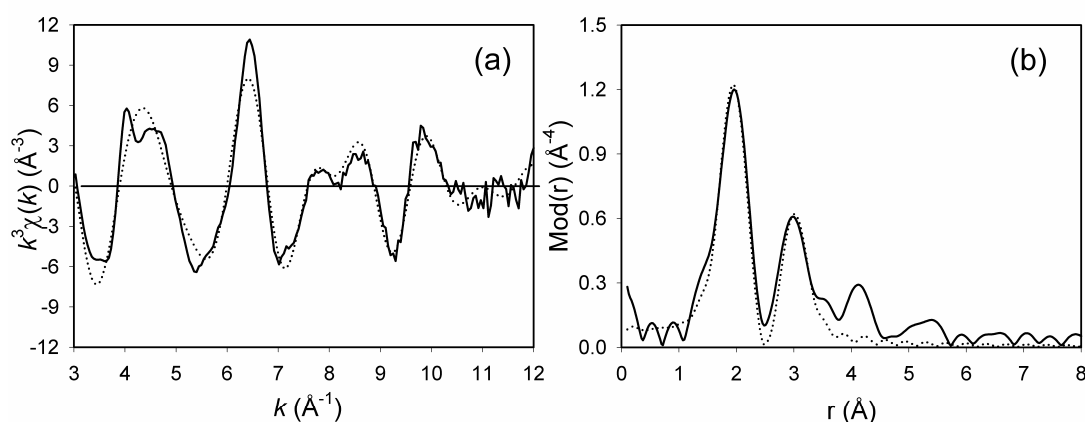


Figure 4.1.7. Experimental (solid line) and calculated (dotted line) EXAFS functions (a) and their corresponding Fourier transform plots (b) of ${}^t\text{Bu}_4\text{PcGa-O-InPc}{}^t\text{Bu}_4$ measured at the Ga K-edge.

Table 4.1.4. EXAFS determined parameters of ${}^t\text{Bu}_4\text{PcGa-O-InPc}{}^t\text{Bu}_4$ at Ga K-edge

Compound	A-Bs ^a	N ^b	r ^c [Å]	σ ^d [Å]	ΔE_0 ^e [eV]	k -range [Å ⁻¹]	R-factor
${}^t\text{Bu}_4\text{PcGa-O-InPc}{}^t\text{Bu}_4$	Ga-O	1	1.88 ± 0.02	0.050 ± 0.005	13.92	3.0 - 12.0	31.35
	Ga-N _{pyrrole}	4	2.02 ± 0.02	0.066 ± 0.007			
	Ga-C	8	3.02 ± 0.03	0.066 ± 0.014			
	Ga-N _{Aza}	4	3.35 ± 0.04	0.086 ± 0.026			

^a absorber (A) - backscattersers (Bs), ^b coordination number N, ^c interatomic distance r, ^d Debye-Waller factor σ with its calculated deviation and ^e shift of the threshold energy ΔE_0 .

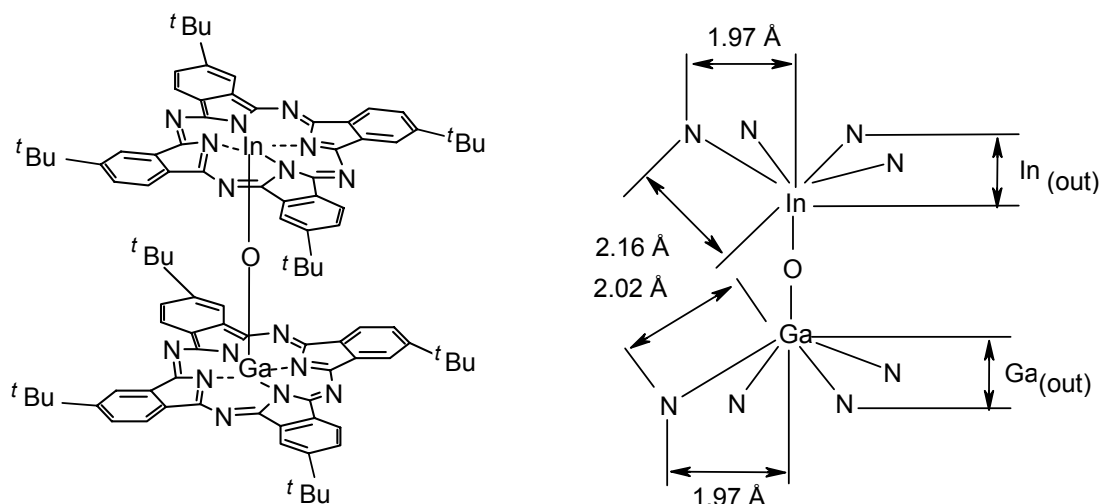


Figure 4.1.8. Molecular structure of $t\text{Bu}_4\text{PcGa-O-InPc}t\text{Bu}_4$.

The phthalocyanine macrocycle has strong influence on the near edge structure of the complex. The central gallium shows two distinct nitrogen shells, one from the pyrrole nitrogen atoms, at a distance of 2.02 Å with a coordination number of four and another from the aza nitrogen atoms, at a distance of 3.35 Å again with a coordination number of four. Another shell consisting of eight carbon backscatterers at 3.02 Å was found. An oxygen shell with a coordination number of one, arising from the bridging oxygen atom was determined at a distance of 1.88 Å. The out of plane distance of the gallium atom from the plane formed by the four bonding nitrogen atoms was found to be 0.45 Å. This is in very good agreement with the value of 0.439 Å reported for PcGaCl [4.1.20].

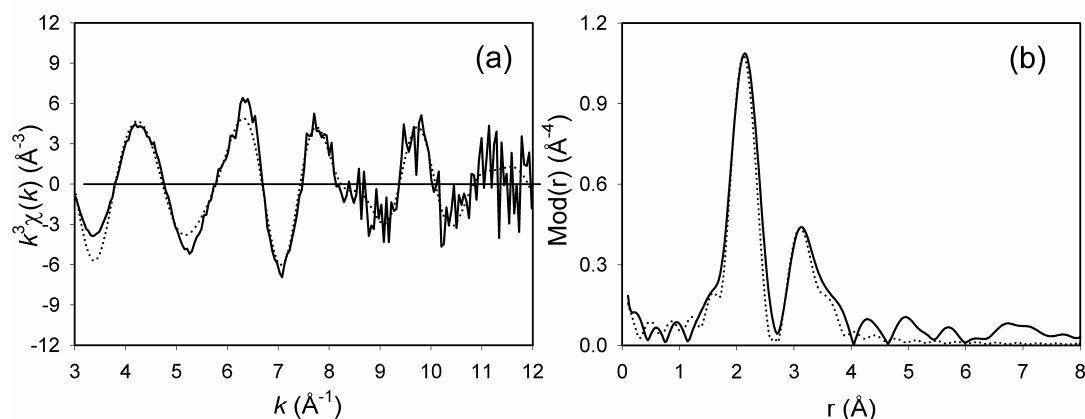


Figure 4.1.9. Experimental (solid line) and calculated (dotted line) EXAFS functions (a) and their corresponding Fourier transform plots (b) of $t\text{Bu}_4\text{PcGa-O-InPc}t\text{Bu}_4$ measured at the In K-edge.

Table 4.1.5. EXAFS determined parameters of ${}^t\text{Bu}_4\text{PcGa-O-InPc}{}^t\text{Bu}_4$ at In K-edge

Compound	A-Bs ^a	N ^b	r ^c [Å]	σ ^d [Å]	ΔE_0 ^e [eV]	k-range [Å ⁻¹]	R-factor
${}^t\text{Bu}_4\text{PcGa-O-InPc}{}^t\text{Bu}_4$	In-O/N _{pyrrole}	5	2.16 ± 0.02	0.064 ± 0.006	11.89	3.0 - 12.0	35.58
	In-C	8	3.13 ± 0.03	0.087 ± 0.009			
	In-N _{Aza}	4	3.44 ± 0.04	0.065 ± 0.014			

^a absorber (A) - backscatterers (Bs), ^b coordination number N, ^c interatomic distance r, ^d Debye-Waller factor σ with its calculated deviation and ^e shift of the threshold energy ΔE_0 .

The experimentally determined and theoretically calculated EXAFS functions of ${}^t\text{Bu}_4\text{PcGa-O-InPc}{}^t\text{Bu}_4$ measured at the In K-edge are shown in *k* space as well as by Fourier transforms in real space in Figure 4.1.9 and the structural parameters are given in Table 4.1.5. In the fitting procedure a combined shell was fitted for the bridging oxygen and the pyrrole nitrogen atoms, with a coordination number of five at a distance of 2.16 Å, as it was difficult to separate the individual contributions of each due to the similar backscattering behaviour of the two near neighbour elements occurring at almost the same distance. Further eight carbon backscatterers were found at a distance of 3.13 Å. Four nitrogen backscatterers arising from the aza nitrogen atoms at 3.44 Å was also determined. The out of plane distance of indium described by the plane formed by the four bonding nitrogen atoms was found to be 0.89 Å. This value is in agreement with the value of 0.78 Å reported for axially bridged indium phthalocyanine dimer [4.1.32].

4.1.3.3. μ -oxo-bridged indium phthalocyanine dimer

The compound $({}^t\text{Bu}_4\text{PcIn})_2\text{O}$ was prepared by the work group of Prof. Dr. M. Hanack, Institute of Organic Chemistry, University of Tuebingen, using a similar procedure as described for $({}^t\text{Bu}_4\text{PcGa})_2\text{O}$ [4.1.30]. The EXAFS measurement of the compound was performed at the In K-edge at 27940 eV at the beamline X1 at HASYLAB, Hamburg using Si(311) double crystal monochromator at ambient conditions. Energy calibration was monitored using an indium metal foil. The experimentally determined and theoretically calculated EXAFS functions of $({}^t\text{Bu}_4\text{PcIn})_2\text{O}$ are shown in *k* space as well as by Fourier transforms in real space in Figure 4.1.10. The structural parameters are tabulated in Table 4.1.6 and the molecular structure is depicted in Figure 4.1.11.

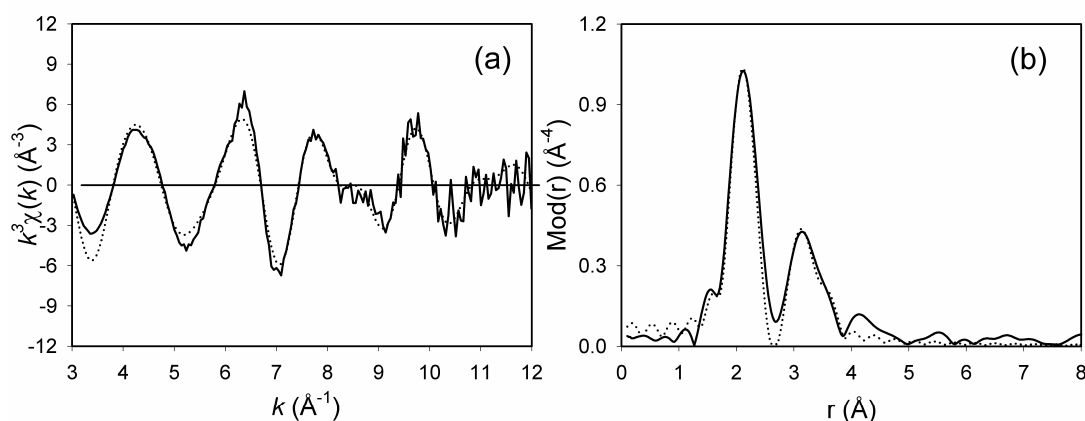


Figure 4.1.10. Experimental (solid line) and calculated (dotted line) EXAFS functions (a) and their corresponding Fourier transform plots (b) of $(t\text{Bu}_4\text{PcIn})_2\text{O}$ measured at the In K-edge.

Table 4.1.6. EXAFS determined structural parameters of $(t\text{Bu}_4\text{PcIn})_2\text{O}$

Compound	A-Bs ^a	N ^b	r ^c [Å]	σ ^d [Å]	ΔE_0 ^e [eV]	k-range [Å ⁻¹]	R-factor
$(t\text{Bu}_4\text{PcIn})_2\text{O}$	In-O/N _{pyrrole}	5	2.16 ± 0.02	0.068 ± 0.007	12.99	3.0 - 12.0	28.99
	In-C	8	3.13 ± 0.03	0.088 ± 0.009			
	In-N _{Aza}	4	3.44 ± 0.04	0.057 ± 0.012			

^aabsorber (A) - backscatterers (Bs), ^bcoordination number N, ^cinteratomic distance r, ^dDebye-Waller factor σ with its calculated deviation and ^eshift of the threshold energy ΔE_0 .

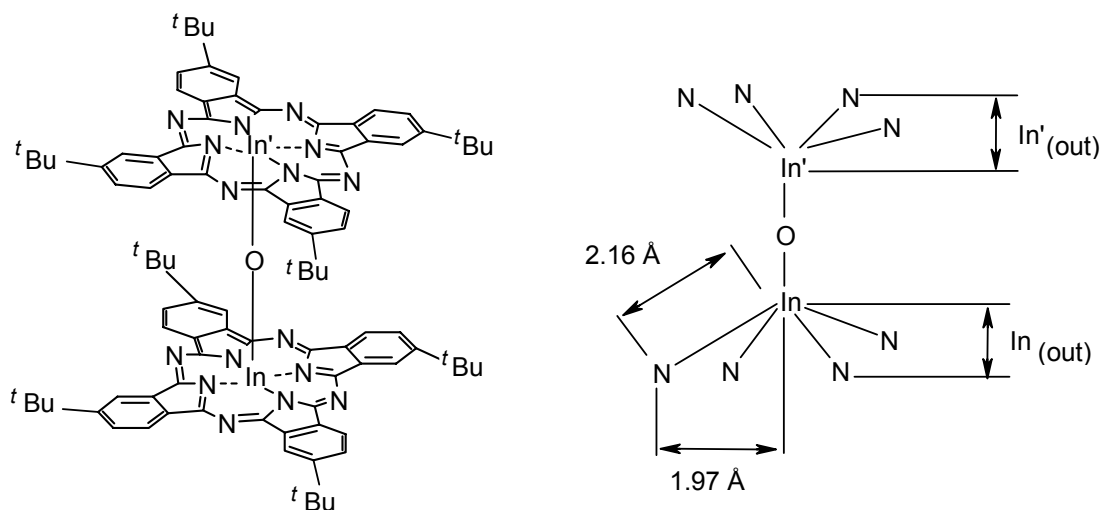


Figure 4.1.11. Molecular structure of $(t\text{Bu}_4\text{PcIn})_2\text{O}$.

The contribution of the phthalocyanine macrocycle in the spectra is evident in this complex as well. In the fitting procedure a combined shell was fitted for the bridging oxygen and the pyrrole nitrogen atoms, with a coordination number of five at a distance of 2.16 Å, due to the same reason stated earlier in the case of $t\text{Bu}_4\text{PcGa-O-InPc}t\text{Bu}_4$.

Eight carbon backscatterers at 3.13 Å and four nitrogen backscatterers arising from the aza nitrogen atoms at 3.44 Å were fitted, as they significantly improve the fit index value. In this complex also, the indium center was found to be located 0.89 Å out of plane described by the four nitrogen atoms directly bonded to it.

4.1.4. Bisaxially substituted phthalocyanines

4.1.4.1. Bis(tetrahydrofuran)hexadecafluoro(phthalocyaninato)ruthenium

The compound, $F_{16}PcRu(THF)_2$, was prepared by the work group of Prof. Dr. M. Hanack, Institute of Organic Chemistry, University of Tuebingen, by the reaction of $(F_{16}PcRu)_2$ in excess of dry tetrahydrofuran under an inert atmosphere [4.1.21]. EXAFS measurement of the compound was performed at the Ru K-edge at 22117 eV at the beamline X1 at HASYLAB, Hamburg using Si(311) double crystal monochromator at ambient conditions. Energy calibration was monitored using a ruthenium metal foil. The experimentally determined and theoretically calculated EXAFS functions in k space and their Fourier transforms in real space for $F_{16}PcRu(THF)_2$ are shown in Figure 4.1.12.

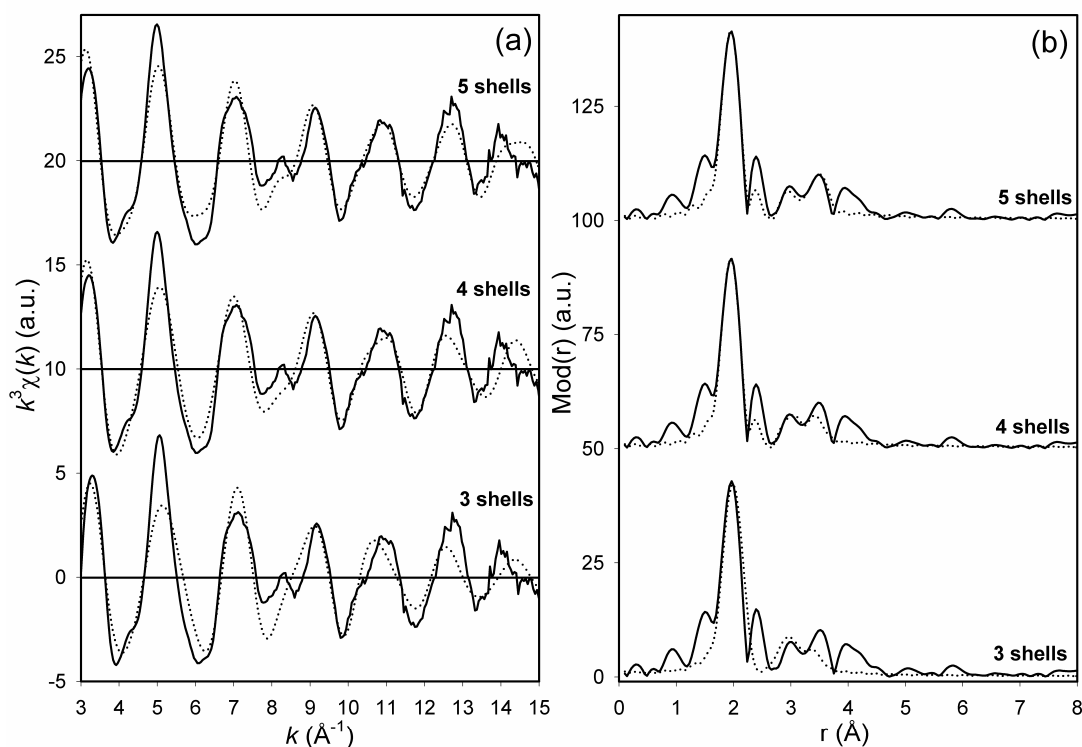
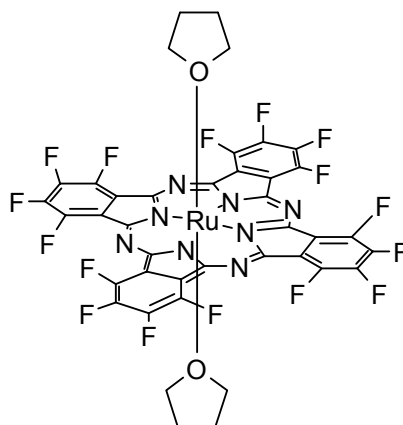


Figure 4.1.12. Experimental (solid line) and calculated (dotted line) EXAFS functions (a) and their corresponding Fourier transform plots (b) of $F_{16}PcRu(THF)_2$ measured at Ru K-edge; simulation with three, four and five shells.

Table 4.1.7. EXAFS determined structural parameters of $F_{16}PcRu(THF)_2$

Case	A-Bs ^a	N ^b	r ^c [Å]	σ ^d [Å]	E_F ^e [eV]	k-range [Å ⁻¹]	R-factor
3 shells	Ru-N _{Pyrrrole}	4	2.03 ± 0.02	0.067 ± 0.007	6.300	2.97 - 15.04	44.80
	Ru-C	8	3.02 ± 0.03	0.122 ± 0.018			
	Ru-N _{Aza}	4	3.31 ± 0.04	0.087 ± 0.013			
4 shells	Ru-N _{Pyrrrole}	4	2.03 ± 0.02	0.059 ± 0.006	4.077	3.00 - 15.02	36.31
	Ru-C	8	3.10 ± 0.03	0.122 ± 0.018			
	Ru-N _{Aza}	4	3.34 ± 0.04	0.077 ± 0.012			
	Ru-O _{THF}	2	2.18 ± 0.02	0.084 ± 0.008			
5 shells	Ru-N _{Pyrrrole}	4	2.03 ± 0.02	0.059 ± 0.006	3.701	2.98 - 15.02	34.31
	Ru-C	8	3.08 ± 0.03	0.122 ± 0.018			
	Ru-N _{Aza}	4	3.28 ± 0.04	0.067 ± 0.010			
	Ru-O _{THF}	2	2.18 ± 0.02	0.081 ± 0.008			
	Ru-C _{THF}	4	3.44 ± 0.04	0.050 ± 0.010			

^a absorber (A) - backscatterers (Bs), ^b coordination number N, ^c interatomic distance r, ^d Debye-Waller factor σ with its calculated deviation and ^e Fermi energy E_F .

**Figure 4.1.13.** Molecular structure of $F_{16}PcRu(THF)_2$.

Simulations were performed with three, four and five shells separately in order to elucidate the contributions from different backscatterers. The obtained structural parameters are summarised in Table 4.1.7 and the molecular structure is depicted in Figure 4.1.13. In the Fourier transform plots, several coordination shells are visible and the analysis of the data shows the contribution of phthalocyanine macrocycle in the spectra. The three shells could be fitted independently in such a way that the determined distances led to meaningful interatomic distances in the phthalocyanine macrocycle itself, such that the number of parameters are much less than the number of independent data points [4.1.33, 4.1.34]. Furthermore, two additional shells stemming from the tetrahydrofuran ligand could also be fitted, as no ring atoms are located within this distance [4.1.18]. The results reveal the coordination of two tetrahydrofuran molecules

to ruthenium metal center, where the two proximal carbon atoms surrounding the oxygen atom in each of the tetrahydrofuran molecules contributes to the signal. Further, in the Fourier transform plots one could observe a peak at about 4 Å and is supposed to be due to eight carbon backscatterers in the phthalocyanine macrocycle [4.1.25, 4.1.27]. This shell was not considered in the EXAFS evaluation as the contribution from this shell was insignificant.

When the contribution from the carbon backscatterers of the tetrahydrofuran ligand was omitted, the R-factor, which is a measure of the fit index, worsens by about 6%. When the contributions from both the oxygen and carbon shells of the tetrahydrofuran ligand are ignored, the R-factor worsens significantly to about 23%. It could be inferred that by including the fifth shell having the carbon backscatterers of the tetrahydrofuran ligand, the ruthenium-nitrogen (aza) distance get shortened by about 0.03 Å and the ruthenium-carbon distance gets elongated by about 0.05 Å when compared with the intramolecular contributions alone. Even though these differences are nearly within the error limit, one could notice the slight variations in the determined parameters by the inclusion of an additional shell.

4.1.4.2. Bis(pyridine)hexadecafluoro(phthalocyaninato)ruthenium

The compound, $F_{16}PcRu(Py)_2$, was prepared by the work group of Prof. Dr. M. Hanack, Institute of Organic Chemistry, University of Tuebingen, by the reaction of $(F_{16}PcRu)_2$ in excess of dry pyridine under an inert atmosphere [4.1.21]. The EXAFS measurement of the compound was performed at the Ru K-edge at 22117 eV at the beamline X1 at HASYLAB, Hamburg using Si(311) double crystal monochromator at ambient conditions. Energy calibration was monitored using a ruthenium metal foil. The experimentally determined and theoretically calculated EXAFS functions in k space and their Fourier transforms in real space for $F_{16}PcRu(Py)_2$ are shown in Figure 4.1.14.

Simulations were performed with three, four and five shells separately in order to elucidate the contributions from different backscatterers. The structural parameters are tabulated in Table 4.1.8 and the molecular structure is depicted in Figure 4.1.15. For a good simulation of the EXAFS function for $F_{16}PcRu(Py)_2$ also, five shells are required, as like $F_{16}PcRu(THF)_2$. These are the three shells from the phthalocyanine macrocycle and the remaining two shells from the pyridine ligand. The three shells arising from the intramolecular contributions have similar structural parameters as determined earlier for

the $F_{16}PcRu(THF)_2$. In addition, the nitrogen shell determined at 2.22 Å can only be assigned to the ligand pyridine as there are no ring atoms located in this distance range [4.1.18]. The iteration of the coordination number resulted in a value of 1.8 and was fixed to the nearest integer value of two. This result indicates that there are two pyridine molecules coordinated to the ruthenium metal center. Further, a carbon shell could be fitted at a distance of about 3.44 Å, which also belongs to pyridine ligand. Iteration of the coordination number in this case provided a value of 3.4 and was then fixed to four, considering the contributions from the two proximal carbon atoms surrounding the nitrogen atom in each of the pyridine molecules.

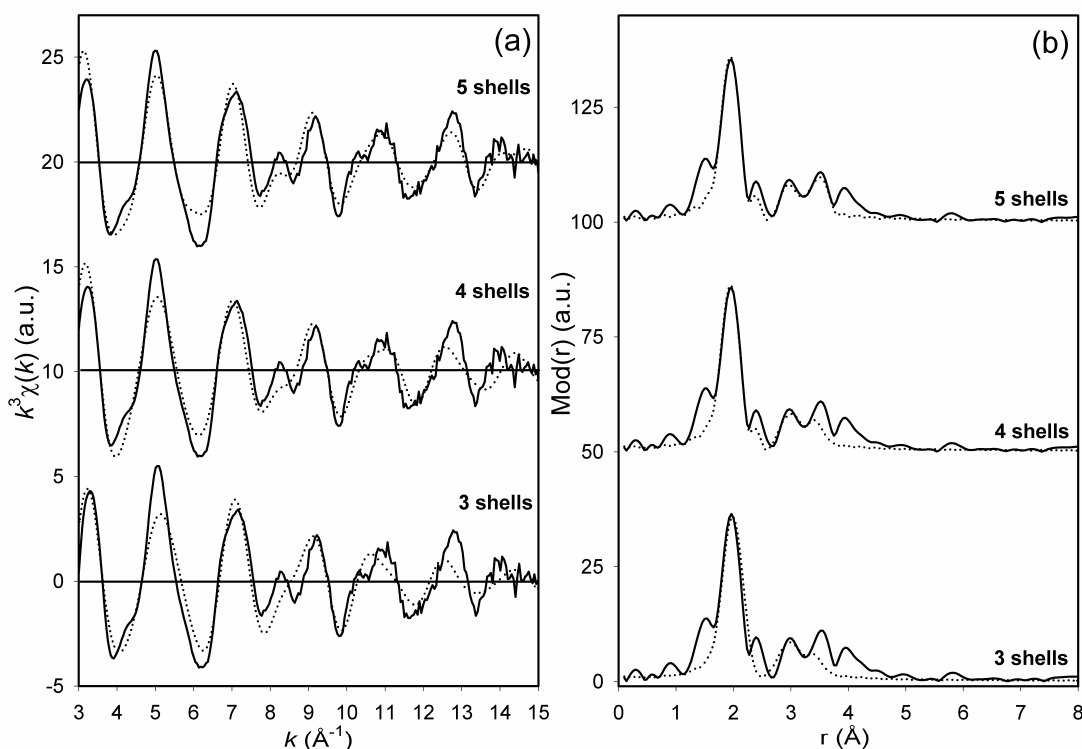


Figure 4.1.14. Experimental (solid line) and calculated (dotted line) EXAFS functions (a) and their corresponding Fourier transform plots (b) of $F_{16}PcRu(Py)_2$ measured at Ru K-edge; simulation with three, four and five shells.

When the contribution from the pyridine carbon shell was not considered, the R-factor worsens by about 13%. When the contributions from both the nitrogen and carbon shells of the pyridine ligand were discarded, the R-factor worsens by about 21%. Similar to $F_{16}PcRu(THF)_2$, in $F_{16}PcRu(Py)_2$ also, the influence of the inclusion of an additional shell on the determined intramolecular parameters could be noted. In this case as well, the peak at about 4 Å evident from the Fourier transform plot was not

considered in the EXAFS calculations due to its insignificant contribution to the improvement of the R-factor.

Table 4.1.8. EXAFS determined structural parameters of $F_{16}PcRu(Py)_2$

Case	A-Bs ^a	N ^b	r ^c [Å]	σ ^d [Å]	E_F ^e [eV]	k-range [Å ⁻¹]	R-factor
3 shells	Ru-N _{pyrrole}	4	2.04 ± 0.02	0.074 ± 0.007	6.145	2.97 - 15.04	43.93
	Ru-C	8	3.04 ± 0.03	0.122 ± 0.018			
	Ru-N _{Aza}	4	3.31 ± 0.04	0.087 ± 0.013			
4 shells	Ru-N _{pyrrole}	4	2.03 ± 0.02	0.067 ± 0.007	4.506	2.96 - 15.03	39.72
	Ru-C	8	3.07 ± 0.03	0.122 ± 0.018			
	Ru-N _{Aza}	4	3.34 ± 0.04	0.081 ± 0.012			
	Ru-N _{py}	2	2.21 ± 0.02	0.087 ± 0.009			
5 shells	Ru-N _{pyrrole}	4	2.04 ± 0.02	0.067 ± 0.007	3.850	2.96 - 15.02	34.72
	Ru-C	8	3.07 ± 0.03	0.116 ± 0.017			
	Ru-N _{Aza}	4	3.28 ± 0.04	0.063 ± 0.009			
	Ru-N _{py}	2	2.22 ± 0.02	0.081 ± 0.008			
	Ru-C _{py}	4	3.44 ± 0.04	0.050 ± 0.010			

^a absorber (A) - backscatterers (Bs), ^b coordination number N, ^c interatomic distance r, ^d Debye-Waller factor σ with its calculated deviation and ^e Fermi energy E_F .

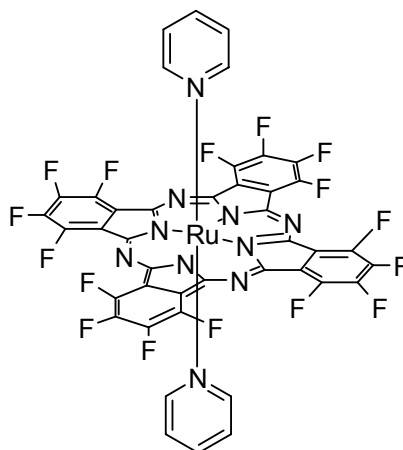


Figure 4.1.15. Molecular structure of $F_{16}PcRu(Py)_2$.

In one of the previous works from our group [4.1.26], the Ru-Ru distance was determined at 4.14 Å in $PcRu(nBuNH_2)_2$, where both the ligands are on the same side. But in the present case, in both $F_{16}PcRu(THF)_2$ and $F_{16}PcRu(Py)_2$, no Ru-Ru distance in this range could be detected. Even though there exists a peak at about 4 Å, it could not be fitted with a ruthenium backscatterer. These results show that the ligands are vertically located below and above the phthalocyanine ring and form an octahedral arrangement around the ruthenium center together with the four nitrogen (pyrrole) atoms of the phthalocyanine macrocycle. The axial coordination of the ligands prevents

the formation of a dimeric phthalocyanine unit coupled over a Ru-Ru double bond. Since the corresponding backscatterers from both top and bottom ligands were determined at the same distances, the out of plane displacement of the metal center is very unlikely, as this displacement would lead to a distorted octahedral geometry. Further, from the determined structural parameters, it is not possible to make any comments concerning the non-planarity of the macrocycle.

4.1.5. Conclusion

Optically active metallophthalocyanines were investigated by EXAFS spectroscopy for the local structure around the metal center. In the case of dimeric gallium and ruthenium phthalocyanines, the metal–metal distances were found to be 2.46 Å and 2.43 Å respectively, and the metal centers were located about 0.5 Å out of plane from the macrocycle, projecting inwards. The results obtained from the gallium and indium μ -oxo-bridged phthalocyanine dimers were in agreement with the general structure of the phthalocyanine complexes. The peripherally fluorinated ruthenium phthalocyanines with tetrahydrofuran or pyridine ligands indicated a six-fold coordination of the ruthenium atom and the substituted ligands were located axially in an octahedral arrangement on both sides of the phthalocyanine macrocycle. In all the cases, the influence of the phthalocyanine macrocycle in the spectra was evident from the data analysis.

4.2. Studies on catalytically active ruthenium(II) complexes

4.2.1. Introduction

Interphase catalysis is gaining great importance in recent years due to its ability to combine the advantages of homogeneous and heterogeneous catalysis with a remarkable decrease of drawbacks like leaching and reduced catalytic activity of the reactive center [4.2.1, 4.2.2]. Interphases are systems in which a stationary phase (comprised of active centers, polymer and spacer) and a mobile component (gas, liquid or dissolved reactants) penetrate each other on a molecular scale without forming a homogeneous phase. When such interphases are provided with a swellable polymer, they will be able to imitate homogeneous conditions as the active centers become highly mobile simulating the properties of a solution [4.2.3]. In such systems, the catalysts are easily separable from the reaction products and can be used for several cycles [4.2.4]. The density of the active centers can be influenced by co-condensates, which are applied in the form of multi-functionalised siloxanes. These co-condensates enlarge the space between the active metal center and the carrier matrix, thereby improving the accessibility of the catalytically active reaction center. The schematic of an interphase system comprising of stationary and mobile phases is shown in Figure 4.2.1.

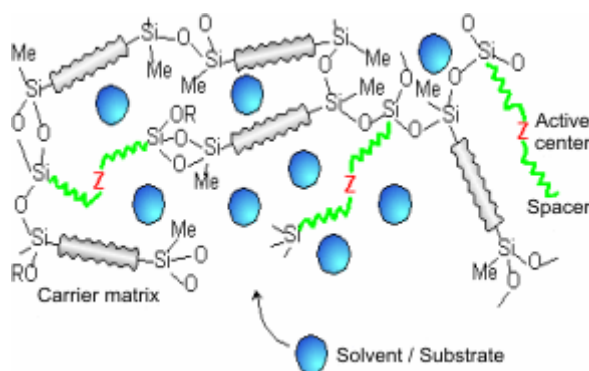


Figure 4.2.1. Schematic representation of an interphase system comprising of stationary phase and mobile phase (reproduced from www.interphasen.de).

Transition metal complexes are increasingly used for different industrially important catalytic reactions such as asymmetric hydrogenation catalysis, stereo selective catalysis etc. [4.2.5, 4.2.6]. Ruthenium(II) complex system containing diphosphine and 1,2-diamine ligands proved to be excellent catalysts for the hydrogenation of ketones, in the presence of a base and 2-propanol, under mild conditions [4.2.7, 4.2.8]. Subsequently, several chiral ruthenium(II) complexes were developed for asymmetric hydrogenation of functionalised ketones [4.2.9, 4.2.10]. Supporting these complexes in polymer

matrices avoids leaching, while the activity and enantioselectivity remains unaltered [4.2.11]. The catalytic activity is traced back to the electronic properties of the coordination center and the stereo selectivity is controlled by the chiral ligand [4.2.12].

An important condition for the optimisation of the interphases is the exact knowledge of the structural correlation between each component in such systems. Here the local environment around the metal atom, which represents the active center in the interphase systems, plays a decisive role. Due to the amorphous nature of the interphases, it is not possible to obtain structural information using conventional X-ray diffraction methods. Hence, the local structure and the coordination geometry around the central metal atom in the interphase system are determined by EXAFS spectroscopy. In the present work, the transmission mode EXAFS measurements were performed at the ruthenium K-edge at 22117 eV, at the beamline X1 at HASYLAB, Hamburg. The complexes were measured with Si(311) double crystal monochromator at ambient conditions. In the fitting procedure, the coordination numbers were fixed to known values for different backscatterers surrounding the excited atom, and the other parameters including interatomic distances, Debye-Waller factor and Fermi energy value were varied by iterations.

4.2.2. Monomeric and embedded complexes

The different monomeric ruthenium(II) complexes containing diamine(diphosphine) and diamine(ether-phosphine) ligands were synthesised by the work group of Prof. Dr. E. Lindner, Institute of Inorganic Chemistry, University of Tuebingen, using the procedure described in literature and were found to be highly catalytically active in the hydrogenation of α,β -unsaturated ketones [4.2.13, 4.2.14]. The embedded complexes were prepared by sol-gel process with the monomer complex and tetramethoxysilane (TMOS) in the ratio 1:10. As a representative example, three embedded complexes studied by means of EXAFS spectroscopy are presented here along with their corresponding monomeric counterparts. The structure of the different complexes investigated in the present work is depicted in Figure 4.2.2. The experimentally determined and theoretically calculated EXAFS functions in k -space and their Fourier transforms in real space for the different monomeric and embedded complexes, measured at Ru K-edge, are shown in Figures 4.2.3 to 4.2.8. The obtained structural parameters are tabulated in Table 4.2.1.

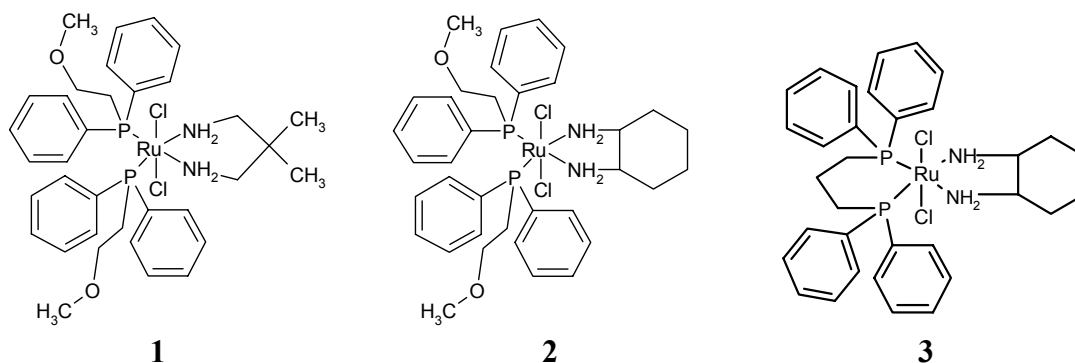


Figure 4.2.2. Structure of ruthenium(II) complexes **1**, **2** and **3**.

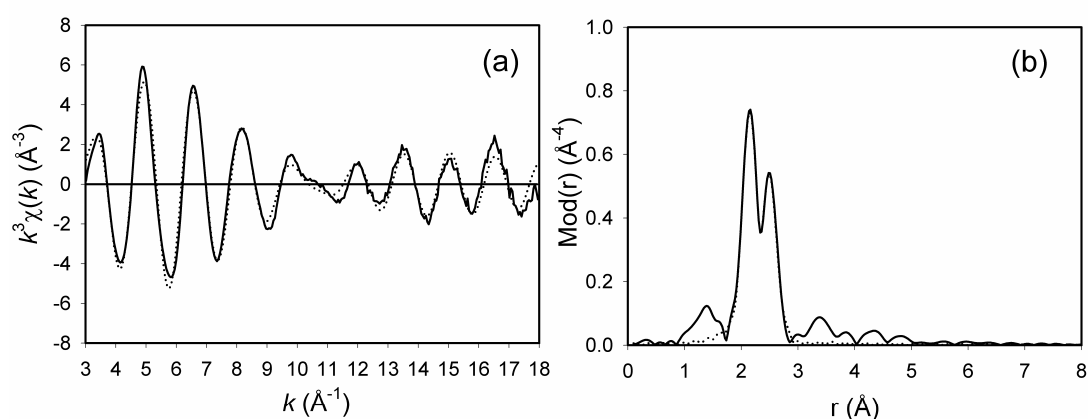


Figure 4.2.3. Experimental (solid line) and calculated (dotted line) EXAFS functions (a) and their Fourier transforms (b) for monomeric complex **1**.

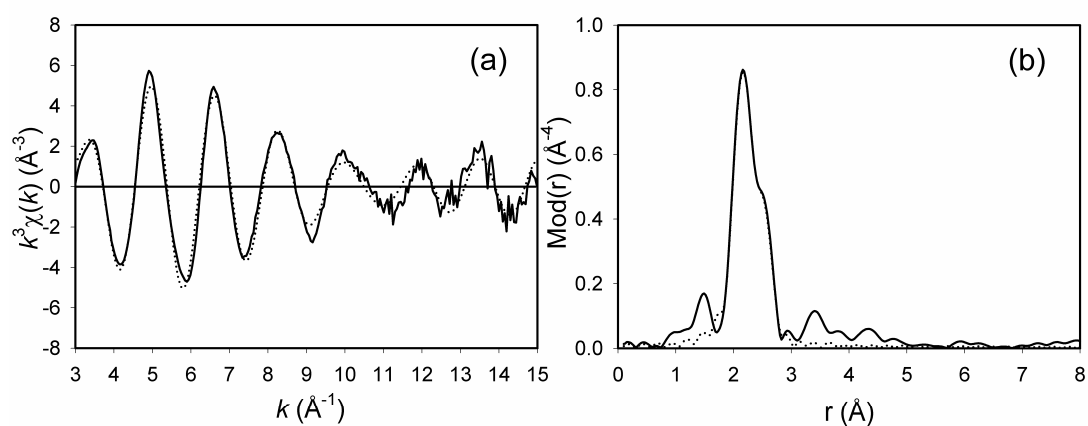


Figure 4.2.4. Experimental (solid line) and calculated (dotted line) EXAFS functions (a) and their Fourier transforms (b) for complex **1** embedded in TMOS.

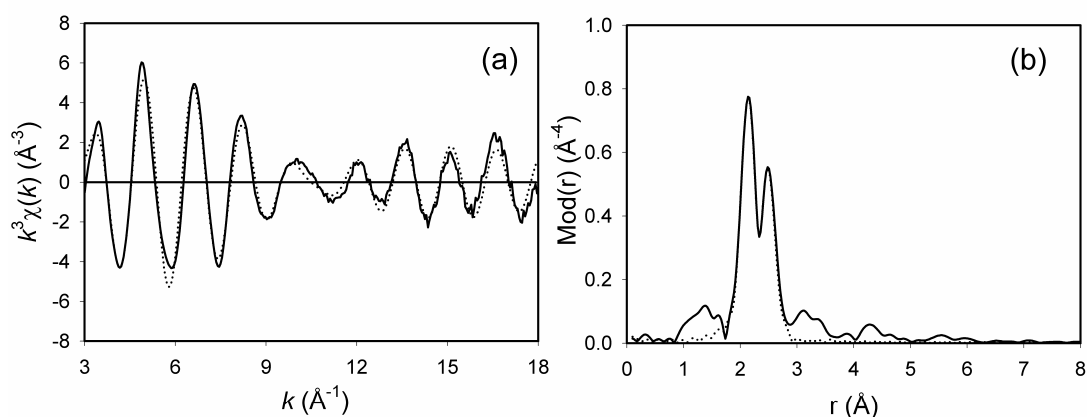


Figure 4.2.5. Experimental (solid line) and calculated (dotted line) EXAFS functions (a) and their Fourier transforms (b) for monomeric complex **2**.

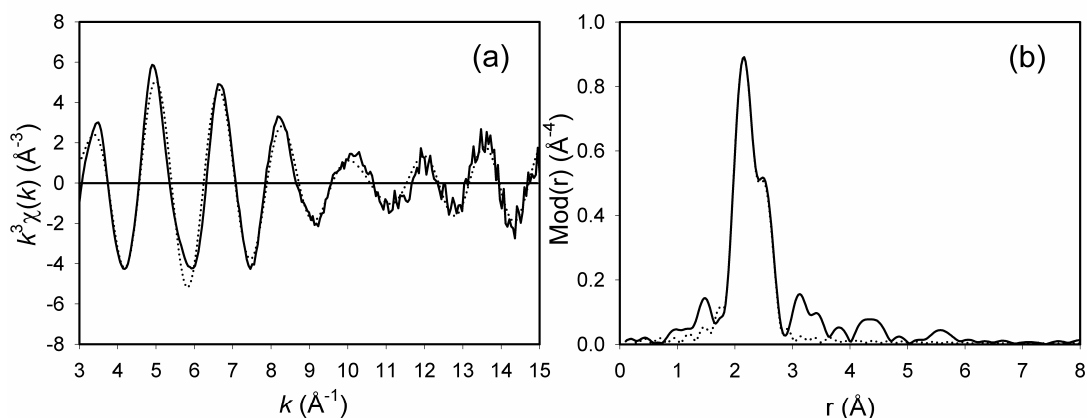


Figure 4.2.6. Experimental (solid line) and calculated (dotted line) EXAFS functions (a) and their Fourier transforms (b) for complex **2** embedded in TMOS.

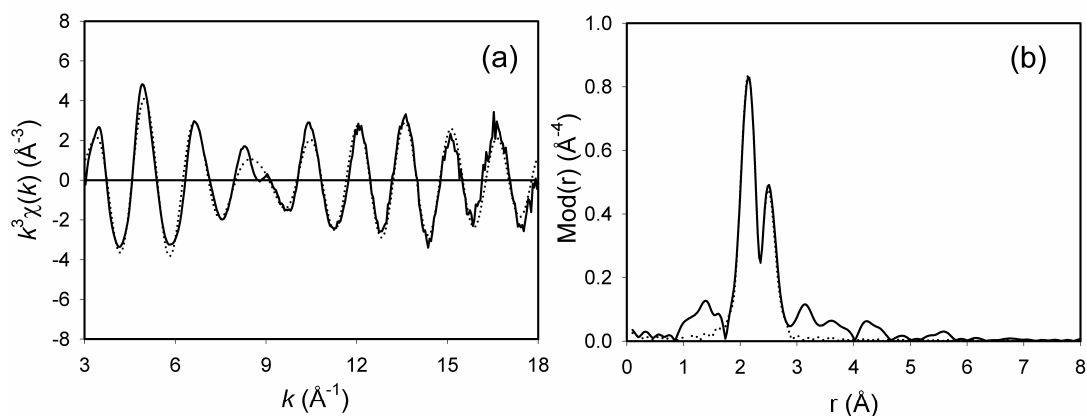


Figure 4.2.7. Experimental (solid line) and calculated (dotted line) EXAFS functions (a) and their Fourier transforms (b) for monomeric complex **3**.

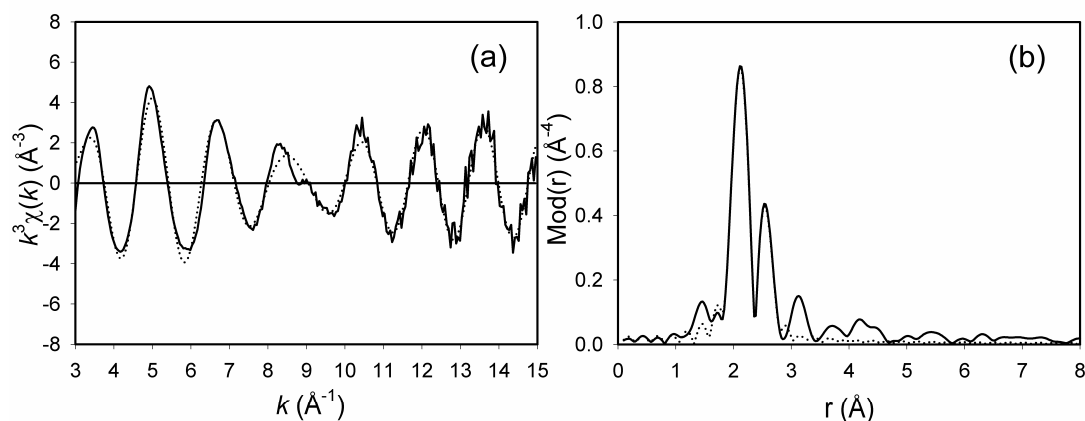


Figure 4.2.8. Experimental (solid line) and calculated (dotted line) EXAFS functions (a) and their Fourier transforms (b) for complex **3** embedded in TMOS.

Table 4.2.1. EXAFS determined structural parameters for monomeric and embedded ruthenium(II) complexes

Complex	Case	A-Bs ^a	N ^b	r ^c [Å]	σ ^d [Å]	ΔE ₀ ^e [eV]	k-range [Å ⁻¹]	R-factor
1	Monomer	Ru-N Ru-P Ru-Cl	2 2 2	2.18 ± 0.02 2.29 ± 0.02 2.42 ± 0.02	0.050 ± 0.005 0.069 ± 0.007 0.061 ± 0.006	21.57	3.0 - 18.0	21.88
	Embedded	Ru-N Ru-P Ru-Cl	2 2 2	2.18 ± 0.02 2.28 ± 0.02 2.40 ± 0.03	0.059 ± 0.006 0.059 ± 0.006 0.067 ± 0.008	21.28	3.0 - 15.0	23.05
2	Monomer	Ru-N Ru-P Ru-Cl	2 2 2	2.18 ± 0.02 2.28 ± 0.02 2.41 ± 0.02	0.050 ± 0.005 0.062 ± 0.006 0.058 ± 0.006	22.07	3.0 - 18.0	25.03
	Embedded	Ru-N Ru-P Ru-Cl	2 2 2	2.18 ± 0.02 2.28 ± 0.02 2.40 ± 0.03	0.067 ± 0.007 0.050 ± 0.005 0.059 ± 0.007	22.65	3.0 - 15.0	25.41
3	Monomer	Ru-N Ru-P Ru-Cl	2 2 2	2.19 ± 0.02 2.26 ± 0.02 2.41 ± 0.02	0.064 ± 0.006 0.048 ± 0.005 0.065 ± 0.007	22.66	3.0 - 18.0	23.07
	Embedded	Ru-N Ru-P Ru-Cl	2 2 2	2.18 ± 0.02 2.25 ± 0.02 2.41 ± 0.03	0.050 ± 0.005 0.050 ± 0.005 0.067 ± 0.008	23.27	3.0 - 15.0	23.61

^a absorber (A) - backscatterers (Bs), ^b coordination number N, ^c interatomic distance r, ^d Debye-Waller factor σ with its calculated deviation and ^e shift of the threshold energy ΔE₀.

In all the cases, the k^3 -weighted EXAFS function could be best described by a three shell model. The first shell consisting of two nitrogen backscatterers arising from the diamine ligand is found at 2.18 Å distance, the second shell having two phosphorous

backscatterers stemming from the phosphine ligand is determined at 2.29 Å distance in ether-phosphine complexes (**1** and **2**) and 2.26 Å distance in diphosphine complex (**3**). The only difference in the diamine(ether-phosphine) ruthenium(II) complex (**2**) in comparison to the diamine(diphosphine) ruthenium(II) complex (**3**) is that the two phosphorus atoms are not rigidly bonded through the carbon atom, but bonded freely to the oxygen atom through carbon atoms. As a consequence, a slight lengthening of the ruthenium-phosphorus bond could be observed in the case of diamine(ether-phosphine) ruthenium(II) complex (**2**). In addition, the third shell comprising of two chlorine backscatterers is fitted at 2.41 Å distance in all the complexes. The results obtained for the monomeric complexes are in good agreement with that determined using single crystal X-ray diffraction [4.2.13, 4.2.14]. The EXAFS results reveal that the complexes retain their structure even when they are embedded in TMOS.

4.2.3. Supported complexes

The different monomeric ruthenium(II) complexes containing diamine(diphosphine) and diamine(ether-phosphine) ligands were supported on polysiloxane matrices using the procedure mentioned in literature [4.2.5, 4.2.15]. The catalytic studies performed on these stationary phase materials revealed that the materials are highly suitable for the hydrogenation of α,β -unsaturated ketones [4.2.15]. The preparation and catalytic studies were performed by the work group of Prof. Dr. E. Lindner, Institute of Inorganic Chemistry, University of Tuebingen. EXAFS spectroscopic studies were carried out to determine the local environment around the active center in the materials, especially to answer the question of structural integrity in the supported complexes. As a representative example, two supported complexes (one supported from phosphine side and the other from amine side) shown in Figure 4.2.9, studied by EXAFS are presented here.

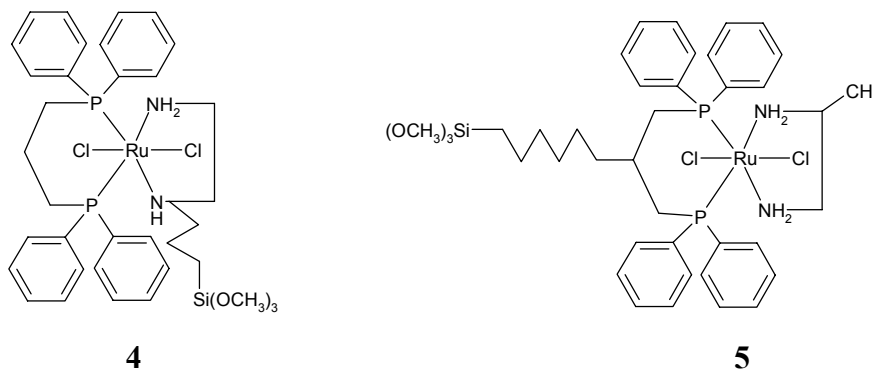


Figure 4.2.9. Structure of supported ruthenium(II) complex (**4** and **5**).

The experimentally determined and theoretically calculated EXAFS functions in k -space and their Fourier transforms in real space for the two supported complexes, measured at Ru K-edge, are shown in Figures 4.2.10 and 4.2.11. The obtained structural parameters are given in Table 4.2.2.

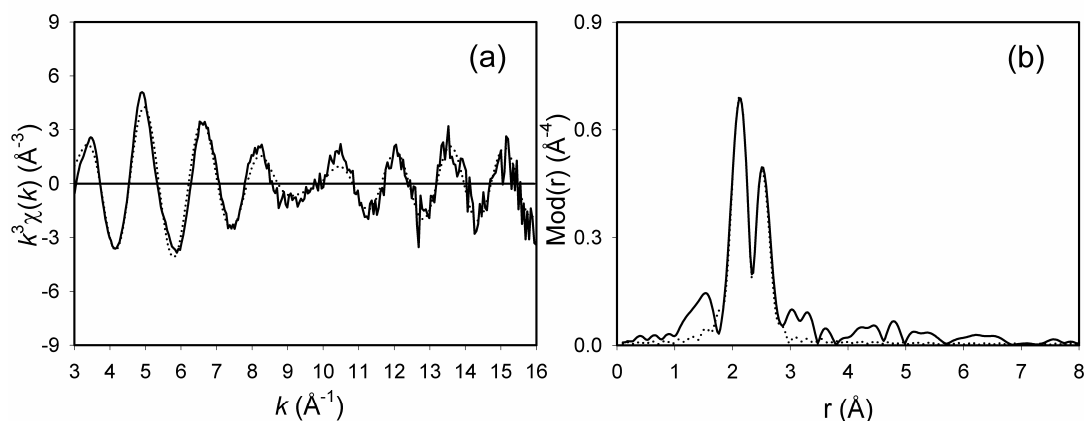


Figure 4.2.10. Experimental (solid line) and calculated (dotted line) EXAFS functions (a) and their Fourier transforms (b) for complex **4** (supported from amine side).

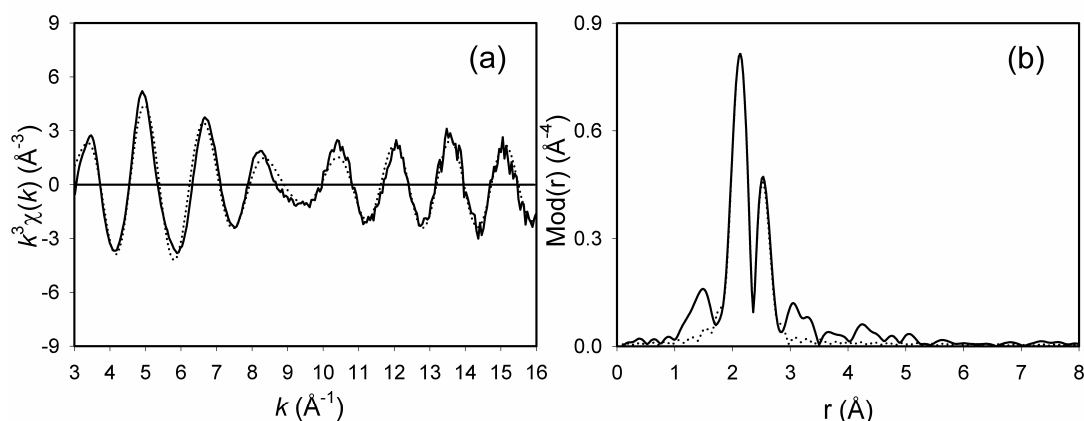


Figure 4.2.11. Experimental (solid line) and calculated (dotted line) EXAFS functions (a) and their Fourier transforms (b) for complex **5** (supported from phosphine side).

Table 4.2.2. EXAFS determined structural parameters for supported complexes

Complex	A-Bs ^a	N ^b	r ^c [Å]	σ ^d [Å]	ΔE ₀ ^e [eV]	k-range [Å ⁻¹]	R-factor
4	Ru-N	2	2.17 ± 0.02	0.050 ± 0.005	22.92	3.0 - 16.0	24.40
	Ru-P	2	2.26 ± 0.02	0.055 ± 0.006			
	Ru-Cl	2	2.41 ± 0.03	0.067 ± 0.008			
5	Ru-N	2	2.19 ± 0.02	0.050 ± 0.005	22.72	3.0 - 16.0	32.24
	Ru-P	2	2.26 ± 0.02	0.055 ± 0.006			
	Ru-Cl	2	2.41 ± 0.03	0.063 ± 0.007			

^aabsorber (A) - backscatterers (Bs), ^bcoordination number N, ^cinteratomic distance r, ^dDebye-Waller factor σ with its calculated deviation and ^eshift of the threshold energy ΔE₀.

function was weighed with k^1 . The AXAFS signal was isolated from total XAFS, by subtracting the fitted EXAFS contribution from the experimental spectrum using the procedure mentioned in literature [4.2.17]. The experimentally determined and theoretically calculated EXAFS functions in k -space and their Fourier transforms in real space for the complexes **6**, **7** and **8**, measured at Ru K-edge, are shown in Figures 4.2.13, 4.2.14 and 4.2.15, respectively. The EXAFS determined structural parameters are summarised in Table 4.2.3. In addition, the experimentally determined Fourier transforms illustrating the AXAFS features are shown in Figure 4.2.16. Since the polarisation of the absorbing atom can be correlated with electronegativity (EN) of the neighbouring atoms, the AXAFS determined parameters are compared with the sum of the electronegativity values of the near neighbours in Table 4.2.4.

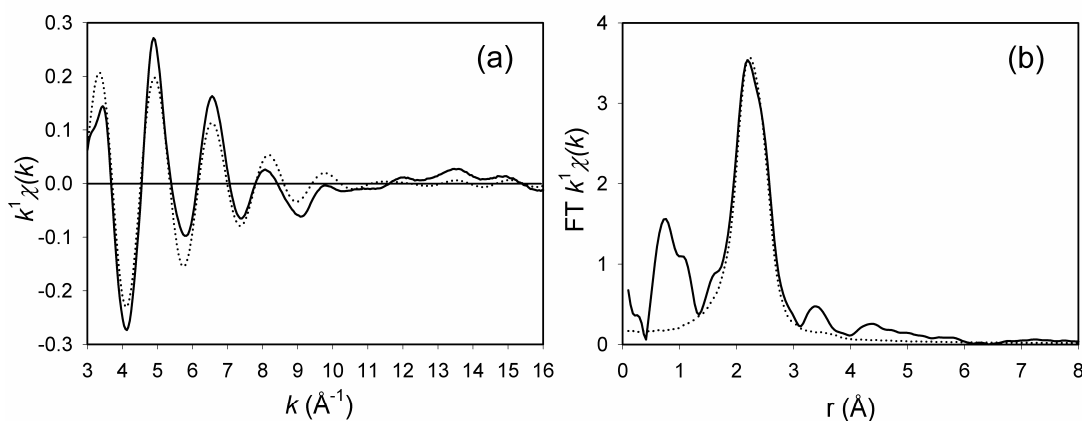


Figure 4.2.13. Experimental (solid line) and calculated (dotted line) EXAFS functions (a) and their Fourier transforms (b) for complex **6**.

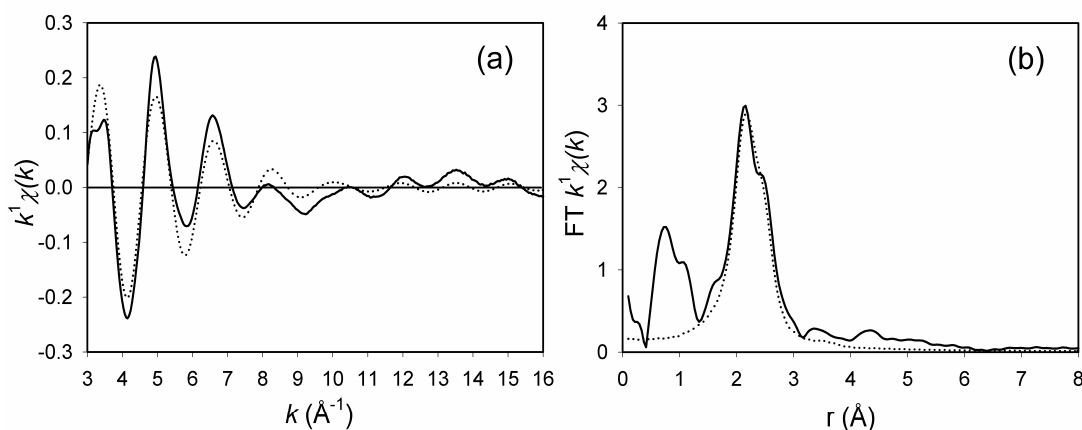


Figure 4.2.14. Experimental (solid line) and calculated (dotted line) EXAFS functions (a) and their Fourier transforms (b) for complex **7**.

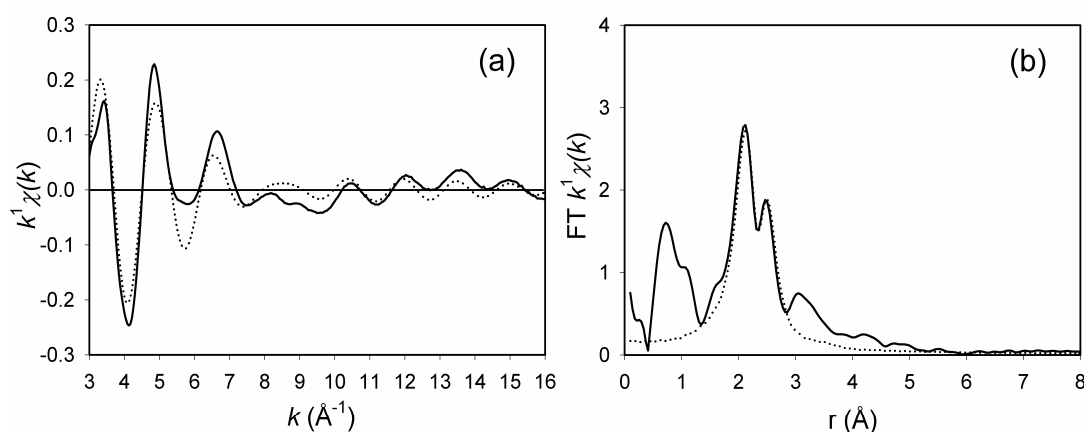


Figure 4.2.15. Experimental (solid line) and calculated (dotted line) EXAFS functions (a) and their Fourier transforms (b) for complex **8**.

Table 4.2.3. EXAFS determined structural parameters for complexes **6**, **7** and **8**

Complex	A-Bs ^a	N ^b	r ^c [Å]	σ ^d [Å]	E _F ^e [eV]	k-range [Å ⁻¹]	R-factor
6	Ru-N	2	2.21 ± 0.02	0.059 ± 0.006	6.354	2.98 - 16.03	43.20
	Ru-P	2	2.29 ± 0.02	0.050 ± 0.005			
	Ru-Cl	2	2.40 ± 0.03	0.055 ± 0.007			
7	Ru-N	2	2.23 ± 0.02	0.084 ± 0.008	7.020	2.98 - 16.04	48.21
	Ru-P	2	2.28 ± 0.02	0.050 ± 0.005			
	Ru-Cl	2	2.40 ± 0.03	0.063 ± 0.008			
8	Ru-N	2	2.19 ± 0.02	0.077 ± 0.008	5.051	2.98 - 16.02	50.11
	Ru-P	2	2.28 ± 0.02	0.050 ± 0.005			
	Ru-Cl	2	2.44 ± 0.03	0.063 ± 0.008			

^a absorber (A) - backscatterers (Bs), ^b coordination number N, ^c interatomic distance r, ^d Debye-Waller factor σ with its calculated deviation and ^e Fermi energy E_F.

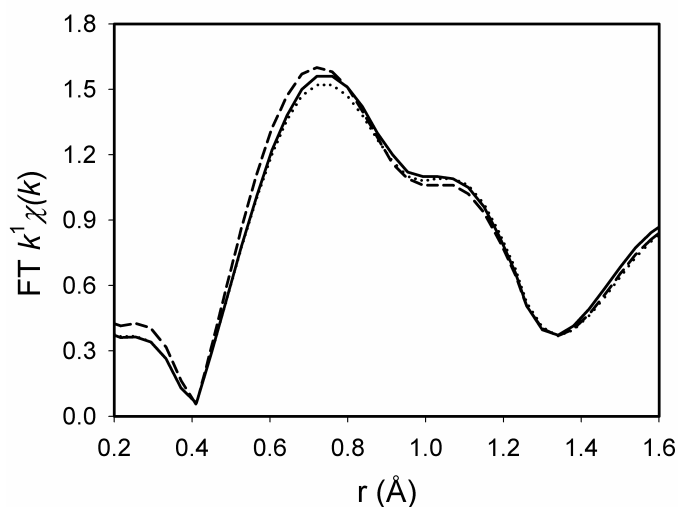


Figure 4.2.16. Experimentally determined Fourier transforms of the AXAFS spectra of complexes **6** (solid line), **7** (dotted line) and **8** (dashed line), measured at Ru K-edge.

Table 4.2.4. AXAFS determined parameters compared with the electronegativity values

Complex	r-range [Å]	Peak position [Å]	Intensity	Overall area [Å ²]	Neigh- bours	EN	N	Overall EN	Sum EN
6	0.41 - 1.34	0.74	1.57	0.9434	N	3.0	2	6.0	16.2
		1.07	1.09		P	2.1	2	4.2	
					Cl	3.0	2	6.0	
7	0.41 - 1.34	0.74	1.52	0.9313	N	3.0	2	6.0	16.2
		1.07	1.09		P	2.1	2	4.2	
					Cl	3.0	2	6.0	
8	0.41 - 1.34	0.72	1.61	0.9541	N	3.0	2	6.0	16.2
		1.07	1.06		P	2.1	2	4.2	
					Cl	3.0	2	6.0	

The EXAFS determined structural parameters are in accordance with the values determined using single crystal X-ray diffraction for the respective complexes [4.2.13, 4.2.14]. In the AXAFS spectra, no remarkable changes could be observed in the peak shapes and positions, emphasising that the local structure around the ruthenium nucleus is the same in all the three cases. However, changes could be observed in the AXAFS features (quantified by FT area) between the complexes with different ligands, which could be attributed to the changes in the electron density on the metal atom.

The complexes **6** and **7** have nearly the same structure; the only difference is that the complex **6** has ether-phosphine ligand, whereas the complex **7** has diphosphine ligand. As a result, these two complexes have different electronic structure around the central ruthenium atom, as revealed by AXAFS. The observed differences in the electronic properties could be correlated with the catalytic activity of these two complexes (**6** and **7**). In the selective hydrogenation of *trans*-4-phenyl-3-butene-2-one, complex **6** yields 80% of *trans*-4-phenyl-3-butene-2-ol and 20% of 4-phenyl-2-butanol, whereas complex **7** yields 100% of *trans*-4-phenyl-3-butene-2-ol [4.2.13, 4.2.14]. The AXAFS studies indicate that the polarisation of the absorbing atom by neighbours (including far atoms) is due to space field effects, where the transmission of charge takes place through space due to the intramolecular columbic interaction between the active metal center and a remote unipole or dipole.

4.2.5. Role of co-catalyst in asymmetric hydrogenation reaction

As mentioned earlier, ruthenium(II) complexes containing ether-phosphine and diphosphine ligands, proved to be excellent catalysts for the hydrogenation of ketones. The addition of a co-catalyst like alkali metal hydroxides/alkoxides to the complex dissolved in a secondary alcohol has emerged as a vital issue in the hydrogenation process. The role of the co-catalyst in determining the catalytic activity of this hydrogenation reaction has been reported in literature [4.2.18], where the researchers have shown the importance of an alkali metal cation in the metal alkoxide co-catalysts. Furthermore, they demonstrated that the alkali metal cations affect the activity in the order $K > Na \sim Rb > Li$ and an increase in the alkali metal cation concentration with a constant amount of base enhances the catalytic activity. Due to these reasons, the co-catalyst $t\text{BuOK}$ was chosen for the present investigations. Herein the influence of this co-catalyst on the structure of catalytic intermediate species in the asymmetric hydrogenation reaction by ruthenium(II) complexes is presented. The structure of the investigated diamine(ether-phosphine) (**9**) and diamine(diphosphine) (**10**) ruthenium(II) complexes are depicted in the Figure 4.2.17.

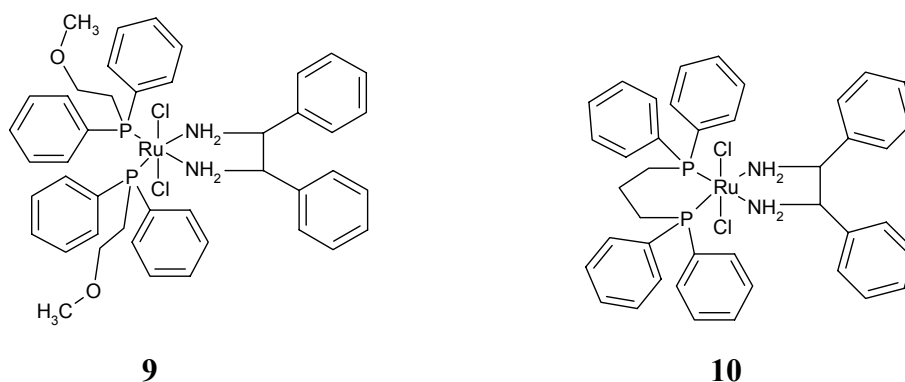


Figure 4.2.17. Structure of ruthenium(II) complexes **9** and **10**.

The reaction of these complexes with $t\text{BuOK}$ was performed by dissolving the complex in 2-propanol, which serves as the conventional hydrogen source. EXAFS spectroscopic measurements were performed on the complexes prior to the reaction, after dissolution in 2-propanol and after the addition of the co-catalyst, $t\text{BuOK}$ to the dissolved complex. The experimentally determined and theoretically calculated EXAFS functions in k -space and the corresponding Fourier transforms in real space for complex **9** before the reaction, after dissolution in 2-propanol and after addition of $t\text{BuOK}$ to the dissolved complex, measured at Ru K-edge are shown in Figures 4.2.18, 4.2.19 and 4.2.20, respectively. The obtained structural parameters are summarised in Table 4.2.5.

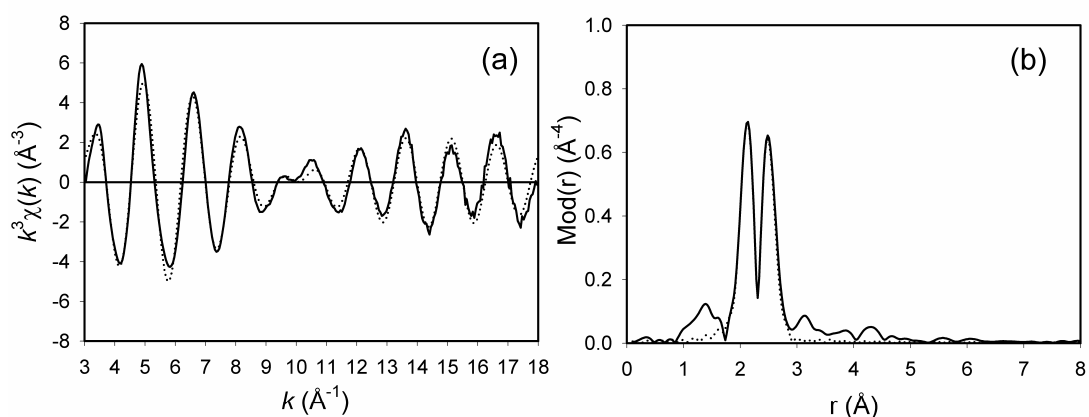


Figure 4.2.18. Experimental (solid line) and calculated (dotted line) EXAFS functions (a) and their Fourier transforms (b) of complex **9** before reaction.

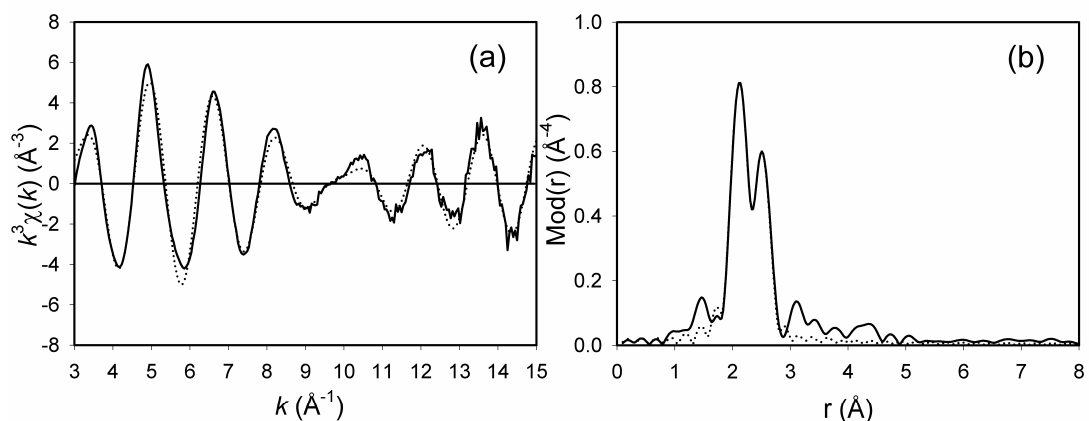


Figure 4.2.19. Experimental (solid line) and calculated (dotted line) EXAFS functions (a) and their Fourier transforms (b) of complex **9** after dissolution in 2-propanol.

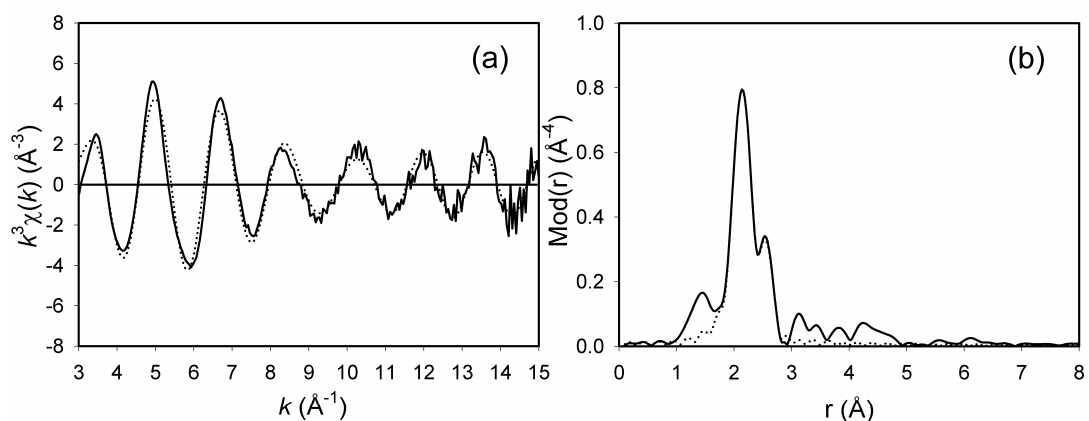


Figure 4.2.20. Experimental (solid line) and calculated (dotted line) EXAFS functions (a) and their Fourier transforms (b) of complex **9** after addition of $t\text{BuOK}$ to the dissolved complex.

Table 4.2.5. EXAFS determined structural parameters for complex **9**

Case	A-Bs ^a	N ^b	r ^c [Å]	σ^d [Å]	ΔE_0^e [eV]	k-range [Å ⁻¹]	R-factor
Before reaction	Ru-N	2	2.17 ± 0.02	0.050 ± 0.005	22.26	3.0 - 18.0	22.06
	Ru-P	2	2.27 ± 0.02	0.067 ± 0.007			
	Ru-Cl	2	2.42 ± 0.03	0.054 ± 0.006			
After dissolution in 2-propanol	Ru-N	2	2.17 ± 0.02	0.050 ± 0.005	22.49	3.0 - 15.0	20.68
	Ru-P	2	2.27 ± 0.02	0.059 ± 0.006			
	Ru-Cl	2	2.41 ± 0.03	0.055 ± 0.006			
After addition of ^t BuOK	Ru-N	2	2.15 ± 0.02	0.067 ± 0.007	22.73	3.0 - 15.0	29.47
	Ru-P	2	2.30 ± 0.02	0.074 ± 0.007			
	Ru-Cl	1	2.43 ± 0.03	0.050 ± 0.006			

^a absorber (A) - backscatterers (Bs), ^b coordination number N, ^c interatomic distance r, ^d Debye-Waller factor σ with its calculated deviation and ^e shift of the threshold energy ΔE_0 .

The analysis of the data shows the influence of the co-catalyst on the coordination geometry around the ruthenium center. The k^3 -weighted EXAFS function was described best by three different shells similar to the earlier cases. As it can be derived from the Fourier transforms, the nitrogen and phosphorous shells give rise to only one intense peak, but their contribution to the EXAFS function is significant. The other peak attributable to the chlorine shell is more sensitive to the co-catalyst. For complex **9** before reaction, two nitrogen backscatterers at 2.17 Å, two phosphorous backscatterers at 2.27 Å, and two chlorine backscatterers at 2.42 Å could be determined, which is in good agreement with those obtained from single crystal X-ray diffraction [4.2.13]. The structure remained almost unaltered after dissolution in 2-propanol even when the solution was left to stay for several days. However, when the co-catalyst ^tBuOK was added to the solution of **9** in 2-propanol, structural changes could be noticed. It is interesting to observe the abstraction of only one of the two chlorine atoms bonded to the metal. Furthermore, the formation of Ru-O species could not be evidenced from the EXAFS analysis. These results suggest the formation of a monochlorinated ruthenium(II) complex as an intermediate species.

In order to further validate the proposed results, the same reaction was studied with diamine(diphosphine) ruthenium(II) complex **10**. The experimentally determined and theoretically calculated EXAFS functions in k -space and the corresponding Fourier transforms in real space for complex **10**, before reaction and after the addition of ^tBuOK to the complex dissolved in 2-propanol, measured at Ru K-edge are shown in Figures 4.2.21 and 4.2.22, respectively. The structural parameters are tabulated in Table 4.2.6.

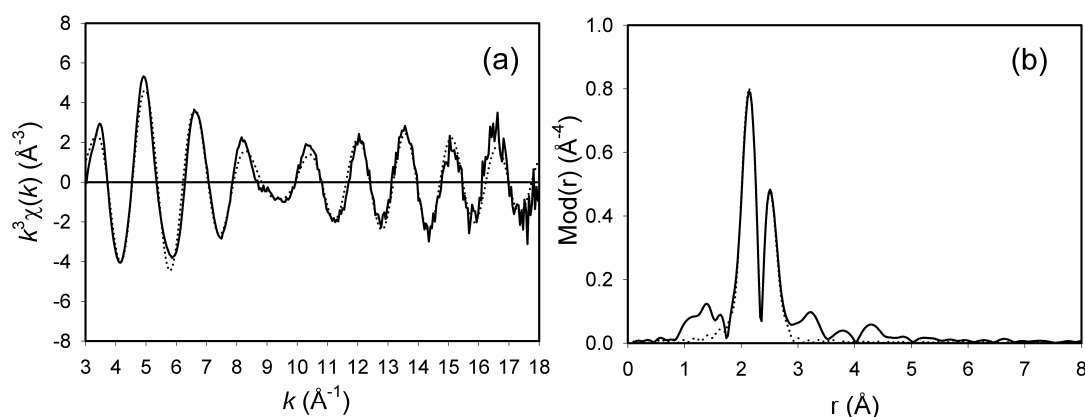


Figure 4.221. Experimental (solid line) and calculated (dotted line) EXAFS functions (a) and their Fourier transforms (b) of complex **10** before reaction.

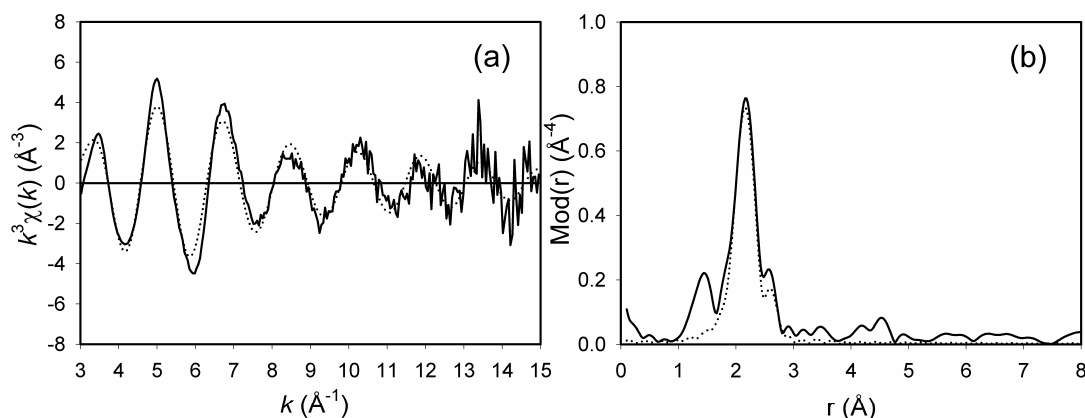


Figure 4.222. Experimental (solid line) and calculated (dotted line) EXAFS functions (a) and their Fourier transforms (b) of complex **10** after addition of ^tBuOK to the dissolved complex.

Table 4.2.6. EXAFS determined structural parameters for complex **10**

Case	A-Bs ^a	N ^b	r ^c [Å]	σ ^d [Å]	ΔE ₀ ^e [eV]	k-range [Å ⁻¹]	R-factor
Before reaction	Ru-N	2	2.17 ± 0.02	0.050 ± 0.005	21.78	3.0 - 18.0	25.04
	Ru-P	2	2.26 ± 0.02	0.060 ± 0.006			
	Ru-Cl	2	2.42 ± 0.03	0.063 ± 0.006			
After addition of ^t BuOK	Ru-N	2	2.15 ± 0.02	0.077 ± 0.008	23.16	3.0 - 15.0	38.74
	Ru-P	2	2.30 ± 0.02	0.077 ± 0.008			
	Ru-Cl	1	2.44 ± 0.03	0.071 ± 0.008			

^a absorber (A) - backscatterers (Bs), ^b coordination number N, ^c interatomic distance r, ^d Debye-Waller factor σ with its calculated deviation and ^e shift of the threshold energy ΔE₀.

Similar to the results obtained for complex **9**, complex **10** also reveals the abstraction of a single chlorine in the course of the reaction when ^tBuOK was added to the complex dissolved in 2-propanol. In addition, the formation of Ru-O species could not be

evidenced in this complex as well. These results illustrate the formation of a monochlorinated complex as an intermediate species in the asymmetric hydrogenation reaction and also demonstrate the leading role played by the co-catalyst in influencing the structure of this intermediate species.

4.2.6. Conclusion

The EXAFS investigations indicate that the catalytically active ruthenium(II) complexes retain their structural integrity when they are embedded or supported on polysiloxane matrices to form stationary phase materials. The variations in the catalytic activity of the complexes with different ligands can be correlated to the differences observed in the electronic structure around the active ruthenium center, probed by means of AXAFS studies. In addition, the investigations reveal that the co-catalyst plays a crucial role not only in enhancing the catalytic activity but also in determining the structure of the intermediate species. It is significant to note that out of the two chlorine atoms bonded to the ruthenium metal center, only one is abstracted during the reaction of the complex with the co-catalyst.

4.3. Studies on bio-active ruthenium(III) complexes

4.3.1. Introduction

Organometallic complexes containing Schiff bases play an important role in the coordination chemistry of transition metals, mainly due to their stability, ease of preparation, structural variability and variety of applications [4.3.1]. Ligands containing two bidentate components separated by a spacer group have been extensively studied [4.3.2, 4.3.3]. Schiff base ligands are being widely investigated with regard to their numerous applications in organic synthesis as well as in pharmacology. Several Schiff base ligands containing nitrogen, sulphur and oxygen have been synthesised and used as chelating agents [4.3.4, 4.3.5]. The planarity of the Schiff base ligand provides a means of creating a large vacant site, where coordination of a transition metal could be carried out [4.3.6, 4.3.7]. Transition metal complexes containing Schiff base ligands have been employed as biological models in understanding the structure of biomolecules and biological processes [4.3.8, 4.3.9]. The crucial role of Schiff bases in the biological function of bacteriorhodopsin has also been proven [4.3.10]. Moreover, it is well known that some drugs have increased activity when administered as metal complexes [4.3.11] and their interactions with DNA have been reported [4.3.12]. Ruthenium complexes have been shown to exhibit anticancer and antibiotic behaviours besides, exhibiting antibacterial activities [4.3.13, 4.3.14]. The ruthenium based anticancer drug, such as ImH[*trans*-RuCl₄(DMSO)Im] (NAMI-A), shows remarkably low general toxicity [4.3.15]. The pH-dependent cytotoxicity of [Ru(η^6 -*p*-cymene)Cl₂(PTA)] has been studied and reported in literature [4.3.16].

In view of the diverse chemistry possessed by Schiff base ligands and transition metal like ruthenium, a series of novel N, S and N, O chromophore containing ruthenium(III) complexes have been synthesised and their suitability for biological applications have been studied. Due to the interrelationship between the structure and the biological activity, it is important to have the knowledge about the structure of the complexes. In spite of several attempts, single crystals suitable for X-ray structure determination could not be obtained. Hence, the local structure and the coordination geometry of the complexes are determined by EXAFS spectroscopy. The transmission mode EXAFS measurements were performed at Ru K-edge at 22117 eV, As K-edge at 11867 eV and Br K-edge at 13474 eV, at the beamline X1 at HASYLAB, Hamburg and

at the XAS beamline at ANKA, Karlsruhe. The complexes were measured with Si(311) double crystal monochromator at Ru K-edge and with Si(111) double crystal monochromator at As and Br K-edges, at ambient conditions. For Ru K-edge measurements, ruthenium metal foil was used as the energy calibration reference. A 20 μm thick gold metal foil having L_{III} -edge at 11919 eV was used as reference for As K-edge measurements and the same foil having L_{II} -edge at 13734 eV was used as reference for Br K-edge measurements. In the fitting procedure, the coordination numbers were fixed to known values for different backscatterers surrounding the excited atom, and the other parameters including interatomic distances, Debye-Waller factor and Fermi energy value were varied by iterations.

4.3.2. Ligand I complexes

The different ruthenium(III) complexes containing Schiff base with N,S chromophore were prepared by the work group of Prof. Dr. K. Natarajan, Department of Chemistry, Bharathiar University, using $\text{RuX}_3(\text{EPh}_3)_3$ ($\text{E} = \text{P}$ or As ; $\text{X} = \text{Cl}$ or Br) or $\text{RuBr}_3(\text{PPh}_3)_2(\text{MeOH})$ as precursors and were found to exhibit antibacterial properties [4.3.17]. The structure of Schiff base ligand (ligand I) used in the present work and the structure of the obtained complexes are shown in Figures 4.3.1 and 4.3.2, respectively.

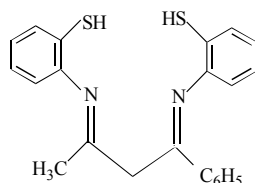


Figure 4.3.1. Structure of Schiff base ligand with N,S chromophore (ligand I).

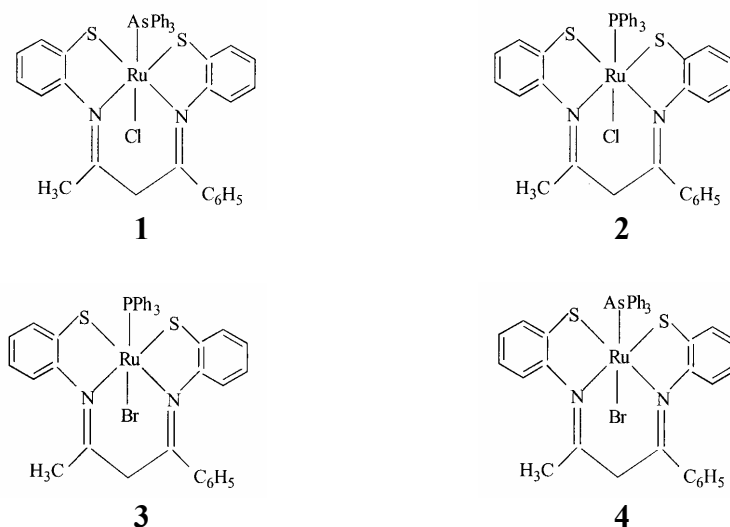


Figure 4.3.2. Structure of the different ruthenium(III) ligand I complexes.

Ru K-edge investigations

The experimentally determined and theoretically calculated EXAFS functions in k space and their Fourier transforms in real space for the different ruthenium(III) ligand I complexes measured at Ru K-edge are shown in Figure 4.3.3. The obtained structural parameters are summarised in Table 4.3.1.

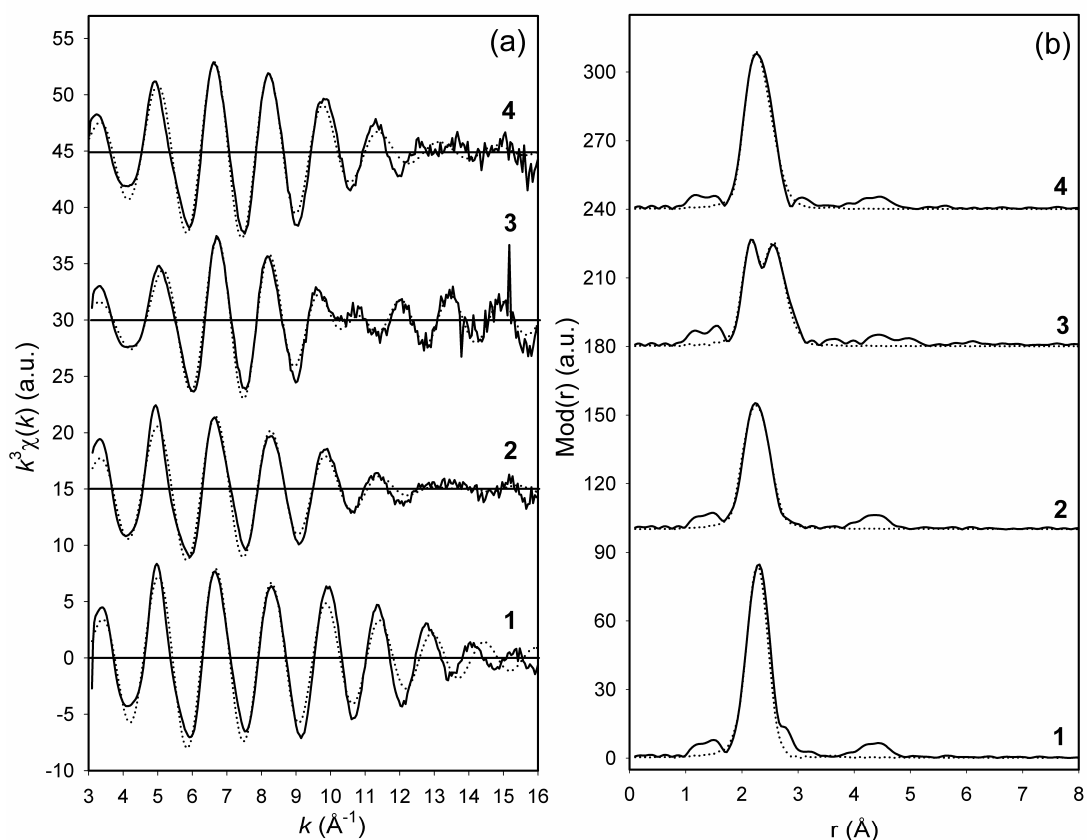


Figure 4.3.3. Experimental (solid line) and calculated (dotted line) EXAFS functions (a) and their corresponding Fourier transform plots (b) for the different ruthenium(III) ligand I complexes measured at the Ru K-edge.

In the analysis of the complexes **1** - **4**, the first shell is determined at about 2.16 \AA with two-nitrogen backscatterers arising from the coordinating ligand. This value is in agreement with the value of 2.17 \AA determined in $\text{C}_9\text{H}_{21}\text{N}_3\text{Ru}_2(\mu\text{-OH})_3(\text{PF}_6)_2\cdot\text{H}_2\text{O}$ [4.3.18] and 2.18 \AA reported for $\text{Cl}_2\text{Ru}(\eta^1\text{-Ph}_2\text{PCH}_2\text{-CH}_2\text{OCH}_3)_2(\text{diamine})_2\text{C}_6\text{H}_{10}(\text{NH}_2)_2$ [4.3.19]. In complexes **1**, **2** and **4**, the near neighbour atoms (phosphorus, sulphur or chlorine) could not be determined separately as they occur at similar distances and thus were fitted as a single shell with sulphur amplitude- and phase- functions at about 2.35 \AA distance. The determined distances are in good agreement with those reported in literature for analogous complexes for the respective backscatterers [4.3.20 - 4.3.22].

Table 4.3.1. Structural parameters for ruthenium(III) ligand I complexes

Complex	A-Bs ^a	N ^b	r ^c [Å]	σ ^d [Å]	E_F ^e [eV]	k-range [Å ⁻¹]	R-factor
1	Ru-N	2	2.15 ± 0.02	0.089 ± 0.009	4.73	3.09 - 16.02	30.63
	Ru-S/P/Cl	4	2.34 ± 0.03	0.071 ± 0.008			
2	Ru-N	2	2.14 ± 0.02	0.055 ± 0.006	3.56	3.11 - 16.01	26.04
	Ru-S/Cl	3	2.35 ± 0.03	0.084 ± 0.010			
	Ru-As	1	2.51 ± 0.03	0.116 ± 0.014			
3	Ru-N	2	2.17 ± 0.02	0.050 ± 0.005	4.00	3.10 - 16.01	26.60
	Ru-S	2	2.29 ± 0.03	0.084 ± 0.010			
	Ru-As/Br	2	2.55 ± 0.03	0.081 ± 0.010			
4	Ru-N	2	2.16 ± 0.02	0.050 ± 0.005	2.14	3.02 - 16.05	27.78
	Ru-S/P	3	2.35 ± 0.03	0.074 ± 0.008			
	Ru-Br	1	2.53 ± 0.03	0.089 ± 0.011			
2^f	As-C	3	1.92 ± 0.02	0.067 ± 0.007	-7.26	2.96 - 16.00	56.85
	As-Ru	1	2.51 ± 0.03	0.089 ± 0.010			
	As-C	6	2.91 ± 0.03	0.081 ± 0.009			
3^f	As-C	3	1.93 ± 0.02	0.063 ± 0.006	-6.51	3.00 - 16.00	49.83
	As-Ru	1	2.50 ± 0.03	0.074 ± 0.008			
	As-C	6	2.90 ± 0.03	0.081 ± 0.009			
2^g	As-C	3	1.91 ± 0.02	0.067 ± 0.007	-5.56	3.07 - 16.02	39.23
	As-Ru	1	2.51 ± 0.03	0.089 ± 0.010			
	As-C	6	2.92 ± 0.03	0.084 ± 0.009			
3^g	As-C	3	1.92 ± 0.02	0.063 ± 0.006	-3.75	3.10 - 16.00	37.11
	As-Ru	1	2.49 ± 0.03	0.074 ± 0.008			
	As-C	6	2.91 ± 0.03	0.081 ± 0.009			
3	Br-Ru	1	2.56 ± 0.03	0.077 ± 0.008	-0.51	2.94 - 14.04	30.71
4	Br-Ru	1	2.54 ± 0.03	0.089 ± 0.009	0.67	2.92 - 14.01	37.89

^a absorber (A) - backscatterers (Bs), ^b coordination number N, ^c interatomic distance r, ^d Debye-Waller factor σ with its calculated deviation, ^e Fermi energy E_F , ^f evaluated using multiple scattering formalism and ^g evaluated using Fourier filter analysis (1.0 - 3.0 Å range).

In the case of complex **3**, a well-defined sulphur shell with coordination number of two could be fitted at about 2.29 Å distance, as this complex does not have phosphorus or chlorine backscatterers. Such short ruthenium-sulphur distances are also reported in related organo-ruthenium complexes [4.3.23]. Due to the similar backscattering behaviour of arsenic and bromine backscatterers, they are fitted together with arsenic amplitude- and phase- functions at a distance of about 2.55 Å in complex **3**, whereas in the case of complex **2**, ruthenium-arsenic backscatterer with coordination number of one is found at about 2.51 Å distance and in the case of complex **4**, the ruthenium-bromine backscatterer again with a coordination number of one is determined at about 3.53 Å

distance. The determined ruthenium-arsenic and ruthenium-bromine distances are in agreement with those reported for *mer*-[RuBr₃(AsMe₂Ph)₃] [4.3.21]. The EXAFS results indicate a six-fold coordination geometry for the ruthenium atom.

As K-edge investigations

The EXAFS evaluation at As K-edge was performed using the multiple scattering formalism, as there could be considerable interference effects due to the neighbouring backscatterers. The multiple scattering calculations were performed considering all the different pathways surrounding the central arsenic atom. The maximum order of scattering and the maximum atoms in one path were set to three and the maximum path length was set to ten during the calculations. The experimentally determined and theoretically calculated EXAFS functions in k space and their Fourier transforms in real space for the different ruthenium(III) ligand I complexes measured at As K-edge are shown in Figure 4.3.4. The obtained structural parameters are given in Table 4.3.1.

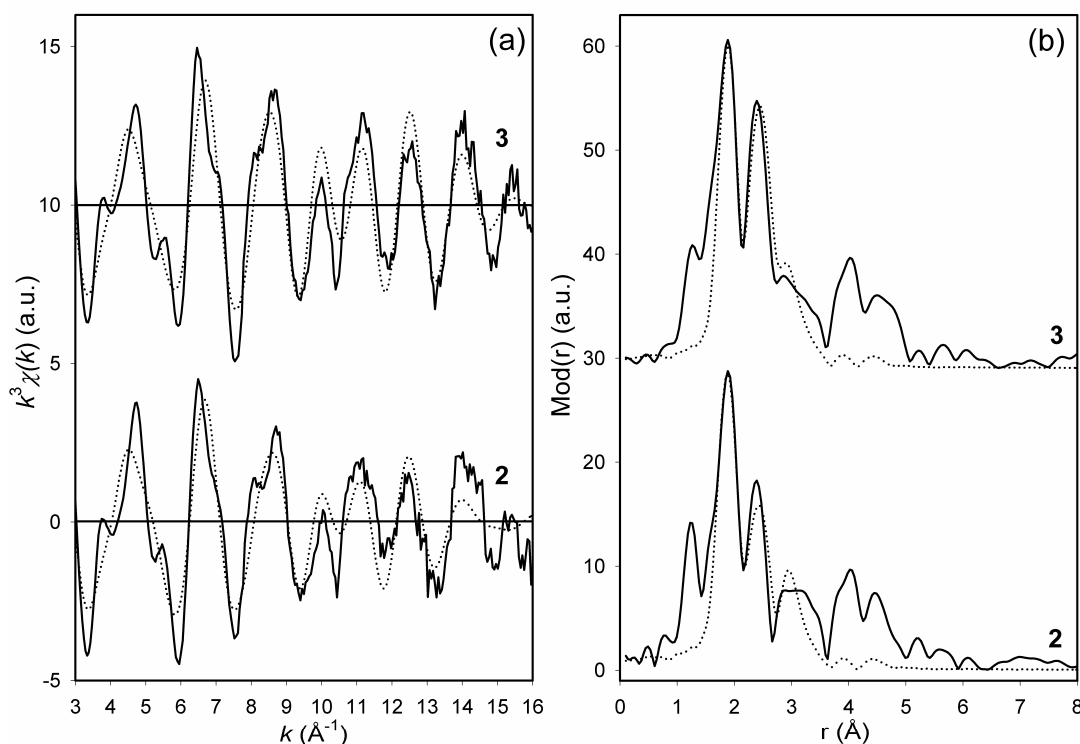


Figure 4.3.4. Experimental (solid line) and calculated (dotted line) EXAFS functions (a) and their corresponding Fourier transform plots (b) for the different ruthenium(III) ligand I complexes measured at the As K-edge evaluated using multiple scattering formalism.

In both the complexes **2** and **3**, the k^3 -weighted EXAFS function is best described by a three-shell model. The first shell at about 1.92 Å could be fitted with three carbon backscatterers originating from the three proximal carbon atoms of the coordinating triphenyl group. The reported arsenic-carbon distances ranges from 1.90 Å to 1.97 Å in *mer*-[RuCl₃(AsMe₂Ph)₃] and *mer*-[RuBr₃(AsMe₂Ph)₃] [4.3.21], the second shell consisting of a single ruthenium backscatterer is determined at about 2.51 Å and the third shell comprising of six carbon backscatterers stemming from the second near-neighbour carbon atoms of the phenyl ring is determined at about 2.91 Å distance. In both the complexes **2** and **3**, the arsenic-ruthenium interatomic distances determined at the As K-edge are in good agreement with those determined at the Ru K-edge.

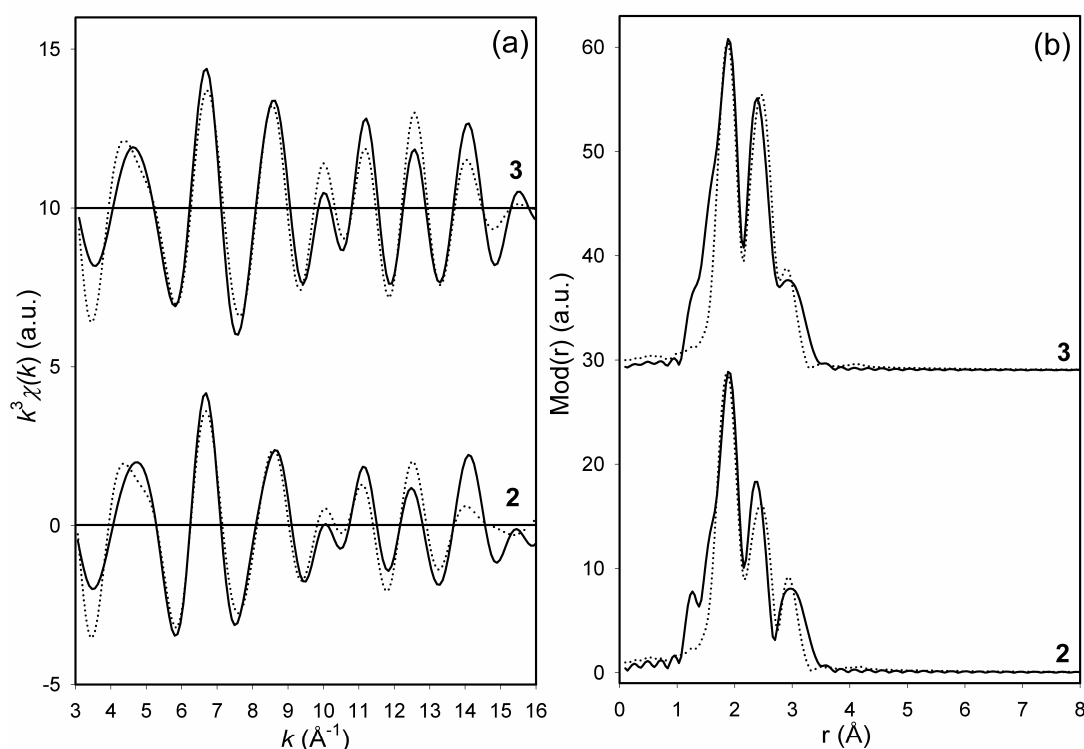


Figure 4.3.5. Experimental (solid line) and calculated (dotted line) EXAFS functions (a) and their corresponding Fourier transform plots (b) for the different ruthenium(III) ligand I complexes measured at the As K-edge evaluated using Fourier filter analysis (1.0 - 3.0 Å range).

In both the cases, the fitting of the EXAFS function to the experimental spectra resulted in very high R-factor values. This could be attributed to the ambiguous coordination geometry around the arsenic atom and apart from the first three shells; the other shells could not be fitted unequivocally. Furthermore, to confirm this supposition,

Fourier filter analysis was performed in the range 1.0 - 3.0 Å, in order that the contributions from only the first three shells are considered. The experimentally determined and theoretically calculated EXAFS functions in k space and their Fourier transforms in real space for the above mentioned complexes are shown in Figure 4.3.5 and the results of the Fourier filter analysis are summarised in Table 4.3.1. It could be noted that the R-factor value improves considerably by about 31% in the case of complex **2** and about 28% in the case of complex **3**.

Br K-edge investigations

The experimentally determined and theoretically calculated EXAFS functions in k space and their Fourier transforms in real space for the different ruthenium(III) ligand I complexes measured at Br K-edge are shown in Figure 4.3.6. The obtained structural parameters are tabulated in Table 4.3.1.

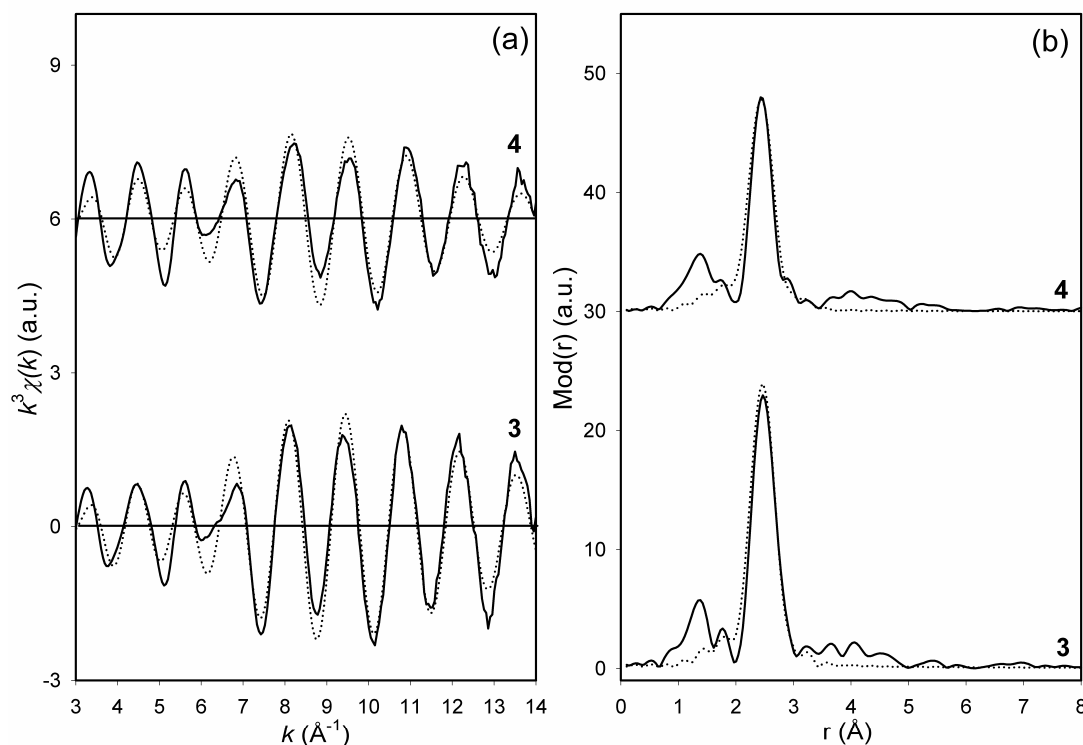


Figure 4.3.6. Experimental (solid line) and calculated (dotted line) EXAFS functions (a) and their corresponding Fourier transform plots (b) for the different ruthenium(III) ligand I complexes measured at the Br K-edge.

The Br K-edge EXAFS spectra of the complexes **3** and **4** are nearly similar to each other. Both of them show a single huge peak at about 2.55 Å, which could be

unequivocally fitted with a single ruthenium backscatterer. The determined bromine-ruthenium distances are in agreement with those reported for similar bromo-ruthenium complexes [4.3.21]. Moreover, the distances are also in accordance with those determined from the Ru K-edge measurements.

4.3.3. Ligand II complexes

The different ruthenium(III) complexes containing Schiff base with N,O chromophore were prepared by the work group of Prof. Dr. K. Natarajan, Department of Chemistry, Bharathiar University, using $\text{RuX}_3(\text{EPh}_3)_3$ ($\text{E} = \text{P}$ or As ; $\text{X} = \text{Cl}$ or Br) or $\text{RuBr}_3(\text{PPh}_3)_2(\text{MeOH})$ as precursors [4.3.24]. The structure of Schiff base ligand (ligand II) used in the present work and the structure of the obtained complexes are shown in Figures 4.3.7 and 4.3.8, respectively.

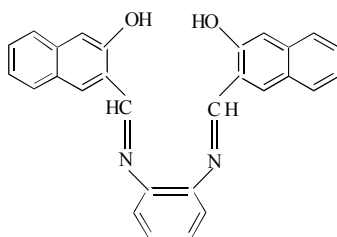


Figure 4.3.7. Structure of Schiff base ligand with N,O chromophore (ligand II).

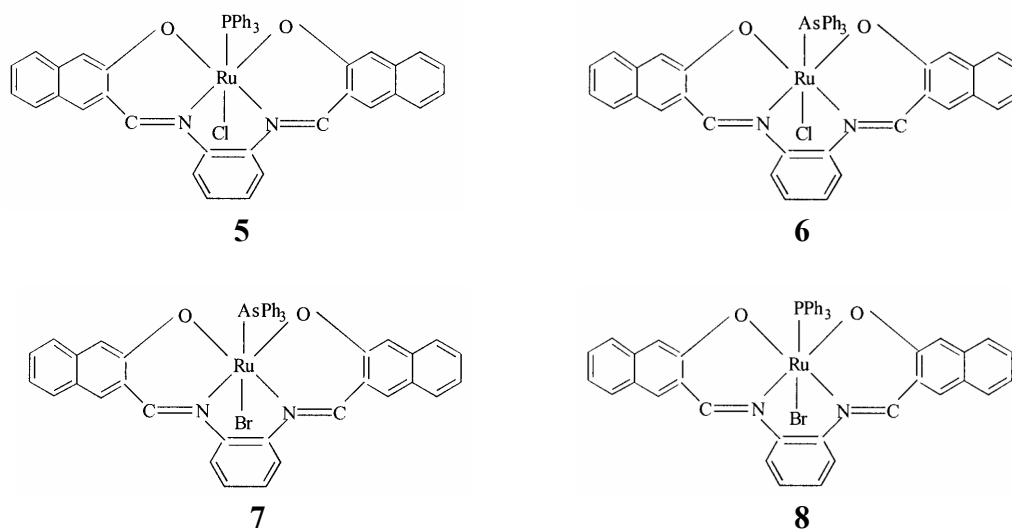


Figure 4.3.8. Structure of the different ruthenium(III) ligand II complexes.

Ru K-edge investigations

The experimentally determined and theoretically calculated EXAFS functions in k space and their Fourier transforms in real space for the different ruthenium(III) ligand II

complexes measured at Ru K-edge are shown in Figure 4.3.9. The obtained structural parameters are summarised in Table 4.3.2.

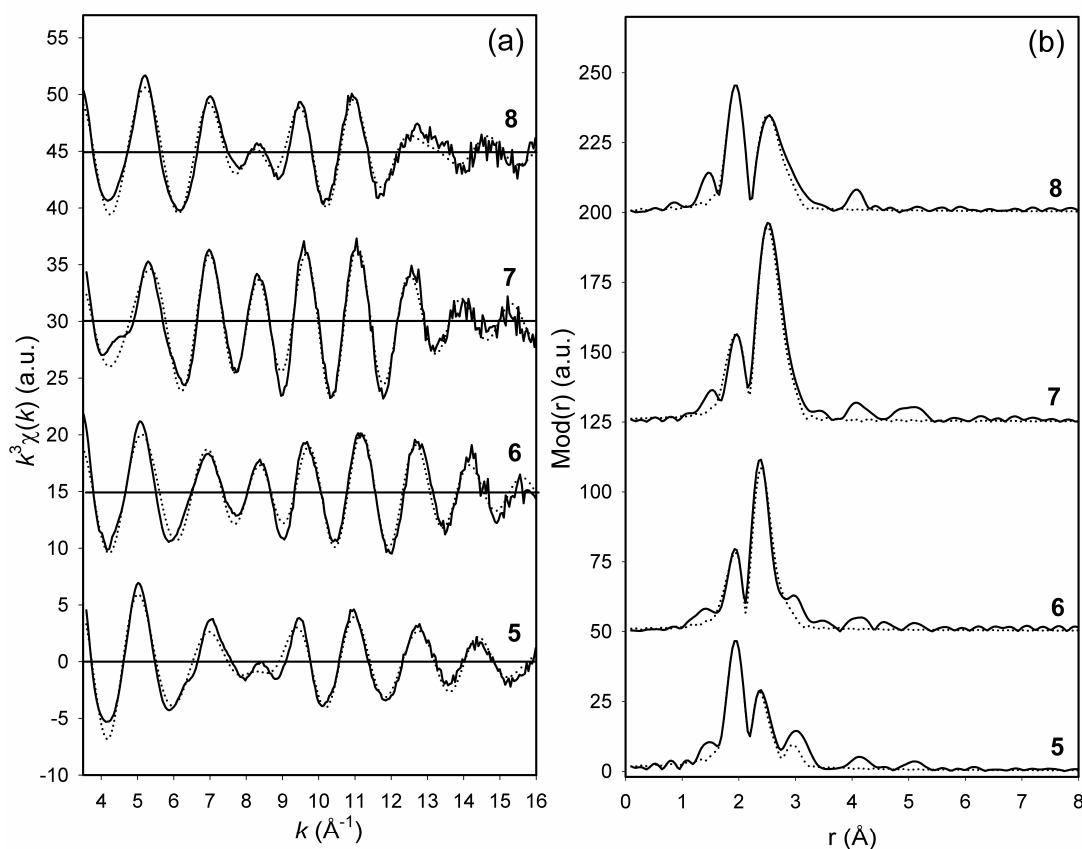


Figure 4.3.9. Experimental (solid line) and calculated (dotted line) EXAFS functions (a) and their corresponding Fourier transform plots (b) for the different ruthenium(III) ligand II complexes measured at Ru K-edge.

In the analysis of the complexes **5** - **8**, the first shell is found at about 2.01 Å consisting of two nitrogen and two oxygen backscatterers arising from the coordinating ligand. Due to the similar backscattering behaviour of the near neighbours, i.e., nitrogen and oxygen, occurring nearly at the same distance, they could not be fitted separately and thus were fitted as one shell with coordination number of four, with nitrogen amplitude- and phase- functions. The obtained Ru-N and Ru-O distances are in agreement with those found for similar organo-ruthenium complexes [4.3.25]. In complex **5**, the second shell is determined at 2.36 Å having one phosphorus and one chlorine backscatterer. For the same reason stated earlier, a single shell was fitted with a combined coordination number of two with chlorine amplitude- and phase- functions. The determined Ru-P and Ru-Cl distances found for the new complexes match well with the parameters reported in *cis*-[Ru(dppm)₂(MeCN)₂](BF₄)₂ (Ru-P distance ranges

from 2.34 Å to 2.37 Å) [4.3.20] and *mer*-[RuCl₃(AsMe₂Ph)₃] (Ru-Cl distance ranges from 2.35 Å to 2.39 Å) [4.3.21].

Table 4.3.2. Structural parameters for ruthenium(III) ligand II complexes

Complex	A-Bs ^a	N ^b	r ^c [Å]	σ ^d [Å]	E _F ^e [eV]	k-range [Å ⁻¹]	R-factor
5	Ru-N/O	4	2.01 ± 0.02	0.050 ± 0.005	6.514	3.59 - 16.08	25.00
	Ru-Cl/P	2	2.36 ± 0.03	0.077 ± 0.009			
	Ru-C	2	2.92 ± 0.03	0.050 ± 0.006			
6	Ru-N/O	4	2.01 ± 0.02	0.077 ± 0.008	8.064	3.46 - 16.05	26.57
	Ru-Cl	1	2.35 ± 0.03	0.050 ± 0.006			
	Ru-As	1	2.48 ± 0.03	0.063 ± 0.008			
	Ru-C	2	2.82 ± 0.03	0.081 ± 0.010			
7	Ru-N/O	4	2.01 ± 0.02	0.074 ± 0.007	8.619	3.59 - 16.00	24.67
	Ru-As/Br	2	2.50 ± 0.03	0.063 ± 0.007			
	Ru-C	2	2.90 ± 0.03	0.050 ± 0.007			
8	Ru-N/O	4	2.00 ± 0.02	0.059 ± 0.006	5.586	3.44 - 16.03	28.85
	Ru-P	1	2.34 ± 0.03	0.067 ± 0.008			
	Ru-Br	1	2.52 ± 0.03	0.071 ± 0.008			
	Ru-C	2	2.91 ± 0.03	0.050 ± 0.008			
6^f	As-C	3	1.93 ± 0.02	0.055 ± 0.006	-4.516	3.05 - 16.03	47.62
	As-Ru	1	2.49 ± 0.03	0.071 ± 0.008			
	As-C	6	2.90 ± 0.03	0.077 ± 0.009			
7^f	As-C	3	1.94 ± 0.02	0.055 ± 0.006	-7.526	2.82 - 16.00	40.80
	As-Ru	1	2.49 ± 0.03	0.077 ± 0.008			
	As-C	6	2.91 ± 0.03	0.077 ± 0.009			
6^g	As-C	3	1.92 ± 0.02	0.055 ± 0.006	-1.668	3.15 - 16.05	34.05
	As-Ru	1	2.48 ± 0.03	0.071 ± 0.008			
	As-C	6	2.91 ± 0.03	0.077 ± 0.009			
7^g	As-C	3	1.93 ± 0.02	0.055 ± 0.006	-5.238	3.00 - 16.00	29.52
	As-Ru	1	2.48 ± 0.03	0.077 ± 0.008			
	As-C	6	2.91 ± 0.03	0.077 ± 0.009			
7	Br-Ru	1	2.52 ± 0.03	0.074 ± 0.008	-0.665	2.93 - 14.04	29.75
8	Br-Ru	1	2.54 ± 0.03	0.087 ± 0.009	-2.375	2.93 - 13.53	28.23

^a absorber (A) - backscatterers (Bs), ^b coordination number N, ^c interatomic distance r, ^d Debye-Waller factor σ with its calculated deviation, ^e Fermi energy E_F, ^f evaluated using multiple scattering formalism and ^g evaluated using Fourier filter analysis (1.0 - 3.0 Å range).

In the case of complexes **6** and **8**, a well-defined second shell with either chlorine or phosphorus backscatterer with a coordination number of one is fitted at about 2.35 Å distance. Furthermore, in complex **6** a single arsenic backscatterer could be determined at about 2.48 Å distance. Due to the similar backscattering behaviour of arsenic and bromine atoms, they are fitted together with a combined coordination number of two,

with arsenic amplitude- and phase- functions at a distance of about 2.50 Å in complex **7**, whereas in the case of complex **8**, the single bromine backscatterer is determined at about 2.52 Å distance. The determined Ru-As and Ru-Br distances are in good agreement with those reported for *mer*-[RuBr₃(AsMe₂Ph)₃] [4.3.21]. In addition, in all the complexes an additional shell consisting of two carbon backscatterers, possibly originating from the proximal carbon atoms of the ligand, could be determined at about 2.90 Å distance (slightly shortened in the case of complex **6**). The EXAFS results indicate a six-fold coordination geometry for the ruthenium atom.

As K-edge investigations

The EXAFS evaluation at As K-edge was performed using the multiple scattering formalism, employing the same set of parameters as mentioned in the earlier case.

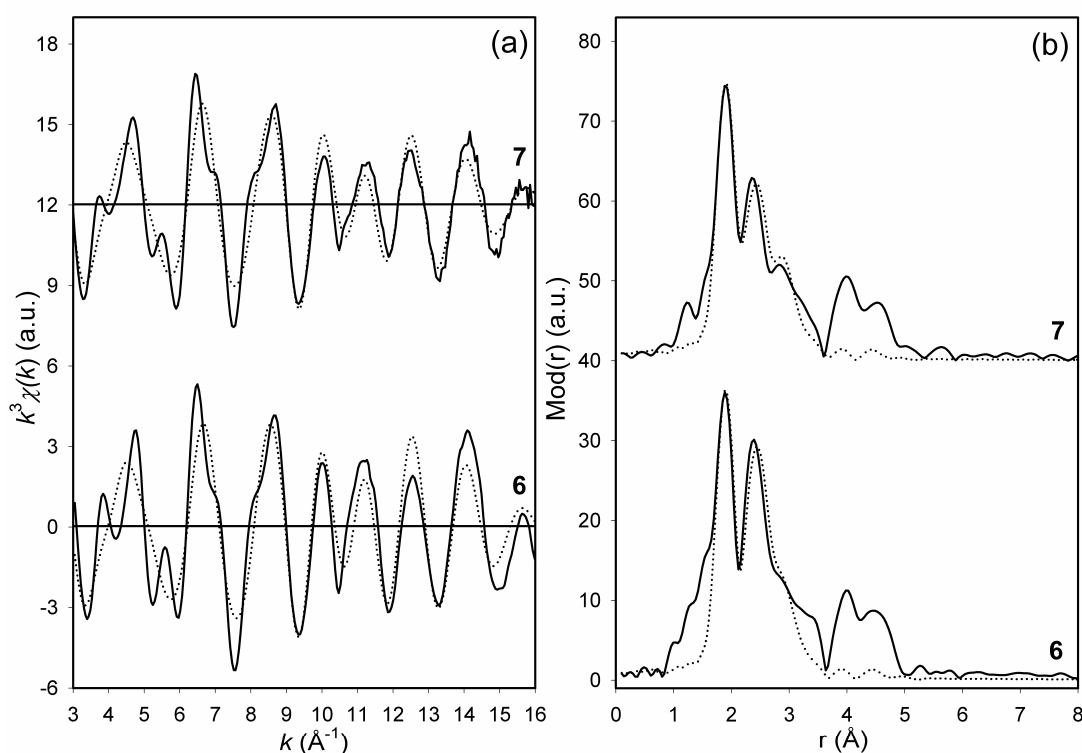


Figure 4.3.10. Experimental (solid line) and calculated (dotted line) EXAFS functions (a) and their corresponding Fourier transform plots (b) for the different ruthenium(III) ligand II complexes measured at the As K-edge evaluated using multiple scattering formalism.

The experimentally determined and theoretically calculated EXAFS functions in k space and their Fourier transforms in real space for the different ruthenium(III) ligand II

complexes measured at As K-edge are shown in Figure 4.3.10. The obtained structural parameters are given in Table 4.3.2. The EXAFS spectra of complexes **6** and **7** resembled the spectra obtained for the complexes **2** and **3** containing the ligand I. Hence, a similar three shell model is fitted in these cases as well. As observed for the ligand I complexes, the fitting of the EXAFS function to the experimental spectra of the ligand II complexes also resulted in very high R-factor values. Therefore, Fourier filter analysis was performed in the range 1.0 - 3.0 Å, so that the contributions from only the first three shells are considered. The experimentally determined and theoretically calculated EXAFS functions in k space and their Fourier transforms in real space for the above mentioned complexes are shown in Figure 4.3.11 and the results of the Fourier filter analysis are summarised in Table 4.3.2. It could be noted that the R-factor value improved considerably by about 29% in the case of complex **6** and about 28% in the case of complex **7**.

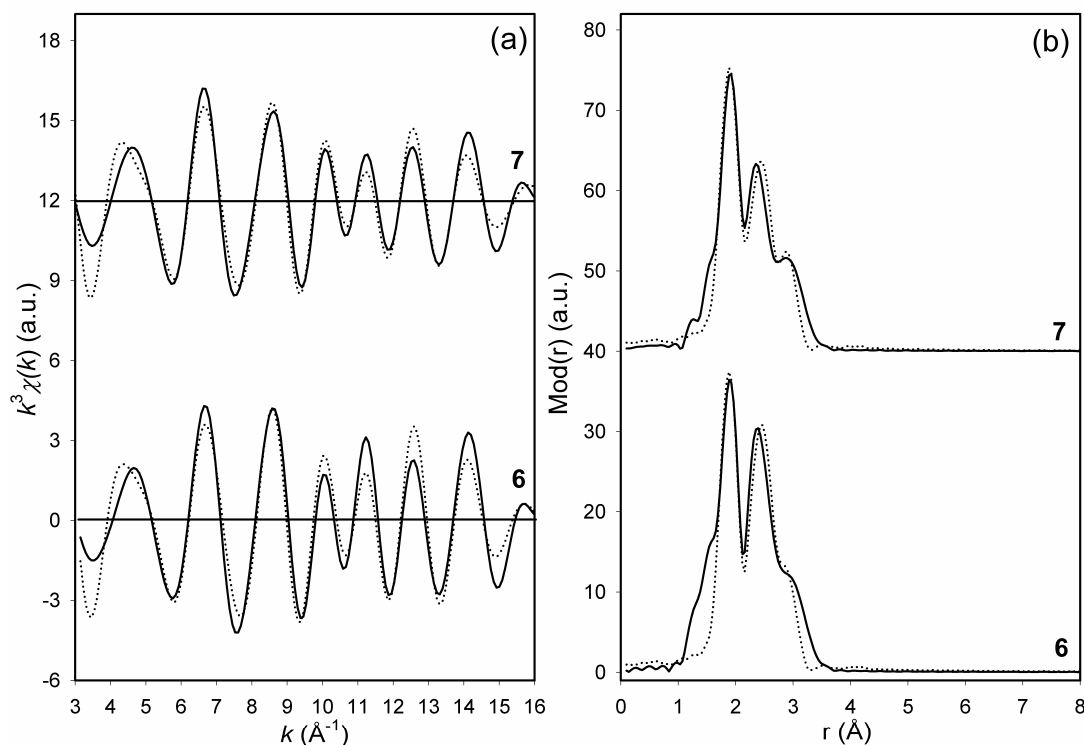


Figure 4.3.11. Experimental (solid line) and calculated (dotted line) EXAFS functions (a) and their corresponding Fourier transform plots (b) for the different ruthenium(III) ligand II complexes measured at As K-edge evaluated using Fourier filter analysis (1.0 - 3.0 Å range).

Br K-edge investigations

The experimentally determined and theoretically calculated EXAFS functions in k space and their Fourier transforms in real space for the different ruthenium(III) ligand II complexes measured at Br K-edge are shown in Figure 4.3.12. The obtained structural parameters are tabulated in Table 4.3.2.

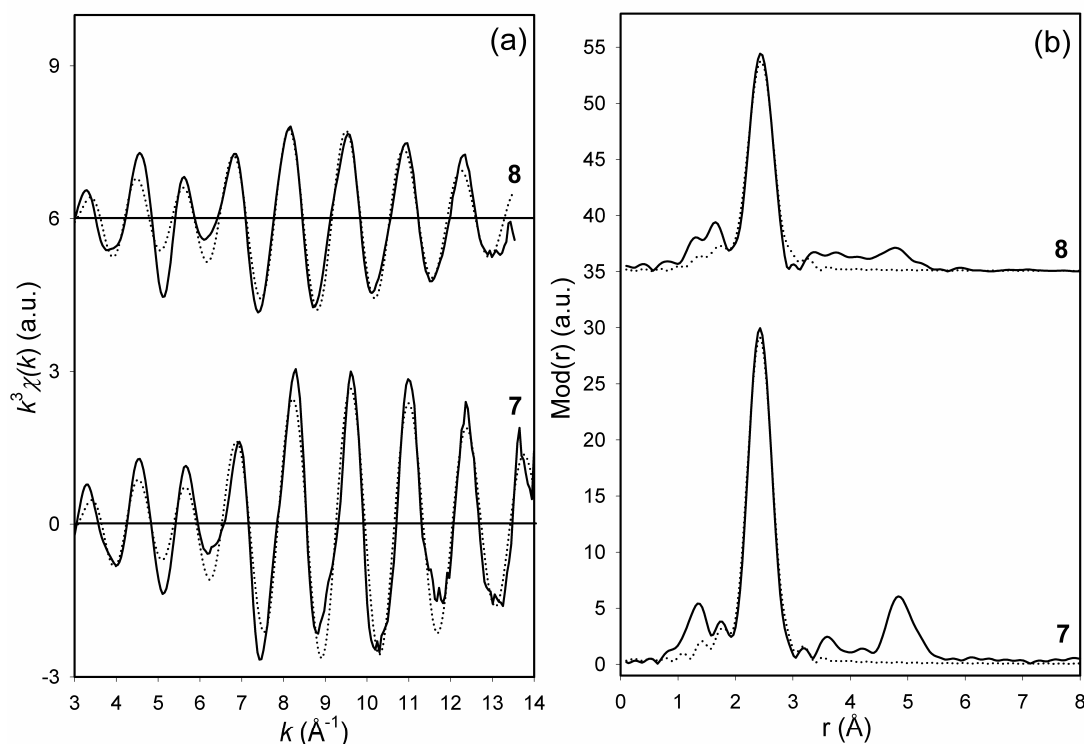


Figure 4.3.12. Experimental (solid line) and calculated (dotted line) EXAFS functions (a) and their corresponding Fourier transform plots (b) for the different ruthenium(III) ligand II complexes measured at Br K-edge.

The EXAFS spectra of the complexes **7** and **8** are almost similar. Both of them show a single huge peak in Fourier transform plot at about 2.52 \AA (for **7**) or 2.54 \AA (for **8**), which could be unambiguously fitted with a ruthenium backscatterer. The determined Br-Ru distances are in agreement with those in similar bromo-ruthenium complexes [4.3.21]. Furthermore, the values are in accordance with distances determined from the Ru K-edge measurements.

4.3.4. Effects of multiple scattering

In order to determine the influence of the different parameters, viz., order of scattering (o_{max}), number of atoms in one path (a_{max}) and path length (pl_{max}),

multiple scattering calculations were performed on a sub-structure of complex **3** (as the sub-structure is similar for all the complexes) as shown in Figure 4.3.13, with different combinations of the above mentioned parameters. The EXAFS obtained interatomic distance and Debye-Waller factor values for the different sets were similar; however differences in the Fermi energy and R-factor values could be observed. The determined values for the different parameter combinations are tabulated in Table 4.3.3.

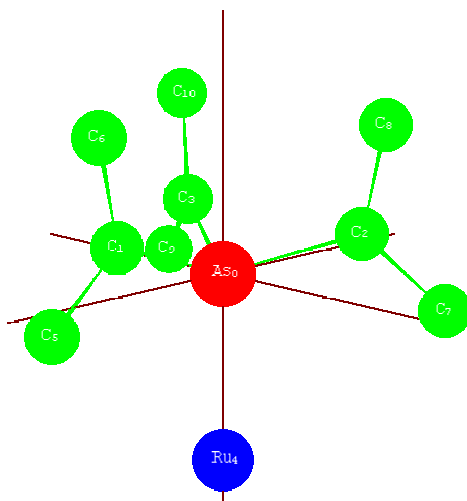


Figure 4.3.13. Sub-structure of complex **3** used for multiple scattering calculations.

Table 4.3.3. Different parameter combinations and the obtained values

Effect	Omax	Atmax	Plmax	E_F [eV]	R-factor
E1	3	3	10	-6.510	49.83
E2	4	3	10	-5.615	49.62
E3	5	3	10	-5.493	49.59
E4	3	4	10	-5.496	49.53
E5	3	5	10	-5.496	49.53
E6	3	3	12	-6.179	49.07
E7	3	3	15	-5.444	48.98
E8	5	5	15	-	-

The investigations reveal that the different set of parameters involved in the multiple scattering calculations does not play a critical role in obtaining a better fit for the system under consideration, as in all the cases the improvement in the R-factor value is insignificant. Furthermore, the obtained Fermi energy values for the different parameter

combinations are also within the error limits. The studies prove that the minimum set of values used for o_{max} , a_{max} and p_{lmax} , in the analysis of the As K-edge spectrum of the ligand I and ligand II complexes is already sufficient to obtain a reasonable fit.

4.3.5. AXAFS investigations on complexes with different substituents

As outlined in chapters 2, AXAFS can be used to study the charge densities that are responsible for bonding and to determine the electronic structure of the metal under investigation. AXAFS represents the change in scattering by the absorber atom itself relative to the free atom. This change is due to the bonding of the absorbing atom with its environment. Consequently, any change in the environment that alters the electronic structure of the absorbing atom should be reflected in the AXAFS [4.3.26]. The AXAFS investigations were performed on ruthenium(III) ligand I complexes, in order to study the influence of the different substituents atoms on the ruthenium metal center. The AXAFS signal was isolated from total XAFS by subtracting the fitted EXAFS contribution from the experimental spectrum.

In the present work, for all the cases, the data analysis in k space was performed using curved wave theory with XALPHA phase and amplitude functions and the resulting $\chi(k)$ function was weighed with k^1 . It should be noted that even without an optimal background subtraction, identical trends in the final AXAFS data could still be found as long as the background correction is performed consistently.

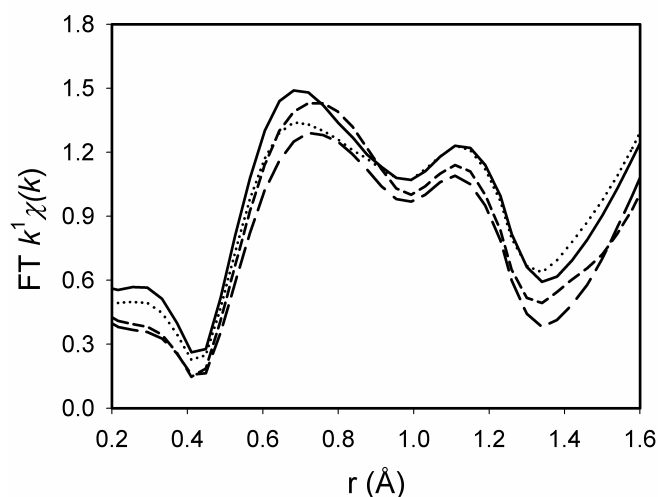


Figure 4.3.14. Experimentally determined Fourier transforms ($\Delta k = 3 - 16 \text{ \AA}^{-1}$) of the AXAFS spectra of complexes **1** - **4**, measured at Ru K-edge. [**1** (solid line), **2** (dotted line), **3** (long dashed line) and **4** (short dashed line)].

Table 4.3.4. AXAFS determined parameters compared with the electronegativity values

Complex	r-range [Å]	Peak position [Å]	Intensity	Overall area [Å ²]	Neigh- bours	EN	N	Overall EN	Sum EN
1	0.41 - 1.34	0.69	1.49	0.9949	N	3.0	2	6.0	16.1
		1.13	1.23		S	2.5	2	5.0	
					P	2.1	1	2.1	
					Cl	3.0	1	3.0	
2	0.41 - 1.34	0.68	1.35	0.9490	N	3.0	2	6.0	16.0
		1.13	1.22		S	2.5	2	5.0	
					As	2.0	1	2.0	
					Cl	3.0	1	3.0	
3	0.41 - 1.34	0.72	1.29	0.8428	N	3.0	2	6.0	15.8
		1.11	1.09		S	2.5	2	5.0	
					As	2.0	1	2.0	
					Br	2.8	1	2.8	
4	0.41 - 1.34	0.74	1.43	0.9185	N	3.0	2	6.0	15.9
		1.13	1.13		S	2.5	2	5.0	
					P	2.1	1	2.1	
					Br	2.8	1	2.8	

The experimentally determined Fourier transforms illustrating the AXAFS features, for the complexes **1** - **4**, measured at Ru K-edge are shown in Figure 4.3.14. As the polarisation of the absorbing atom can be correlated with electronegativity (EN) of the substituents, the AXAFS determined parameters are compared with the sum of the electronegativity values of the neighbouring atoms surrounding the excited atom in Table 4.3.4. The shape of the AXAFS peaks reflects the electronic structure and the position and intensity of the peaks correspond to the nature of chemical bonds. In the present work, the changes observed in the peak shapes and intensities illustrate that the local environment around the ruthenium nucleus is different in the different complexes. From the obtained results, a linear correlation could be established between the AXAFS (quantified by FT area) and the sum of the electronegativity of the substituents atoms. The investigations reveal that the polarisation of the absorbing atom by neighbours is due to bond inductive effects, where the transmission of charge takes place through a chain of atoms by electrostatic induction.

4.3.6. Conclusion

Based on the EXAFS studies, an octahedral structure has been proposed for both ligand I and ligand II ruthenium(III) complexes. However, the exact geometry of the coordinated ligands could not be verified by means of EXAFS. The effect of various parameters involved in the multiple scattering calculations has been elucidated and the studies reveal that a minimum set of values are already sufficient to yield a reasonable fit. AXAFS has been utilised as a tool to probe the influence of the different substituent atoms on the electronic properties of the central ruthenium atom.

4.4. Studies on catalytically active iridium complexes

4.4.1. Introduction

Homogeneous catalytic dehydrogenation of saturated hydrocarbons by transition metal complexes has gained significant importance in the recent years [4.4.1, 4.4.2] and the chemistry of iridium has played a central role in the expansion of this challenging field [4.4.3]. For example, the multifaceted complex $\text{Cp}^*(\text{PMe}_3)\text{IrMeOTf}$ can activate alkanes by σ -bond metathesis pathway, by oxidative addition-reductive elimination mechanism or by electrophilic activation [4.4.4, 4.4.5]. Similar pathways can be expected for the interaction of $(\text{PCP})\text{IrH}_2$ pincer complexes with alkanes. Consequently, there is considerable interest in determining which of these mechanistic pathways are important in catalytic dehydrogenation and other C-H interactions so that more efficient complexes can be designed to facilitate the reaction. Experimental observations in some instances seem to support reductive elimination of H_2 from Ir(III)H_2 to generate a reactive Ir(I) species [4.4.6]. This unsaturated fragment oxidatively adds RH to give an Ir(III)R(H) complex, which results in an olefin complex by β -H transfer. The release of olefin is the last step to re-form the starting material [4.4.7, 4.4.8]. Theoretical calculations suggest a more prominent role for an oxidative addition pathway from Ir(III) to Ir(V) in catalytic C-H activation reactions [4.4.9, 4.4.10]. Experimental reports on the verification of this pathway are scarce and predominantly use indirect methods for the detection of the catalytic intermediates [4.4.11].

The XAFS spectroscopy is a viable tool to determine the changes in the structure and oxidation state occurring during the course of a reaction. Due to this reason, time-resolved XAFS measurements were performed on hydrogenation reaction of PCP pincer ligand iridium complexes, in *in operando* conditions to detect the different catalytic intermediates, in particular to structurally characterise the theoretically postulated Ir(V) species. Additionally, few iridium complexes were also measured as references. The transmission mode XAFS measurements were performed at Ir L_{III} -edge at 11215 eV, at the beamline X1 at HASYLAB, Hamburg and at the XAS beamline at ANKA, Karlsruhe. The complexes were measured with Si(111) double crystal monochromator at ambient conditions and an iridium foil was used for energy calibration. In the fitting procedure, the coordination numbers were fixed to known values for different atoms surrounding the excited atom, and the other parameters were varied by iterations.

4.4.2. Reference complexes

In order to characterise the different iridium species with diverse oxidation states, involved in the hydrogenation reaction, it is necessary to have suitable references. For this reason, two iridium complexes depicted in Figure 4.4.1, in known oxidation states of +3 (complex **1**) and +5 (complex **2**), were investigated. The XANES region of the complexes **1** and **2**, measured at Ir L_{III}-edge are shown along with the iridium foil in Figure 4.4.2. The oxidation states and edge energy are tabulated in Table 4.4.1.



Figure 4.4.1. Structure of iridium complexes **1** and **2**.

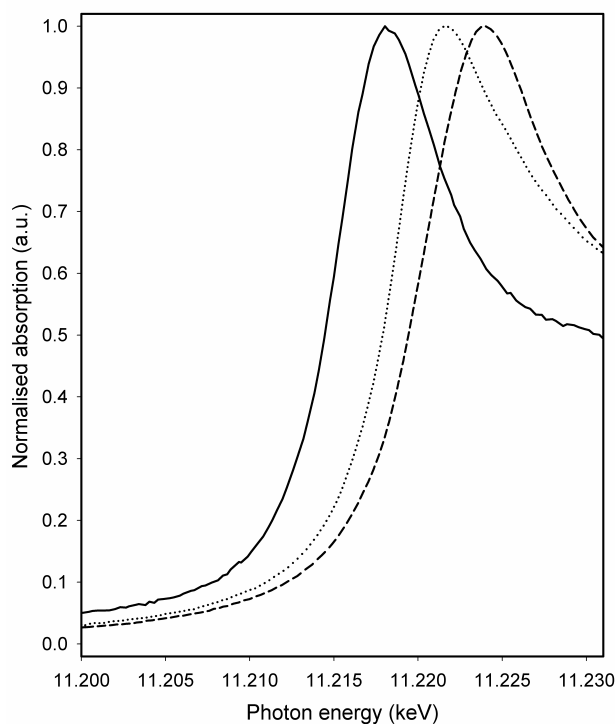


Figure 4.4.2. XANES region of complexes **1** and **2** along with the iridium foil measured at Ir L_{III}-edge. [Complex **1** (dotted line), complex **2** (dashed line) and iridium foil (solid line)].

Table 4.4.1. Edge energy and oxidation states of complexes **1** and **2**

Sample	Oxidation state	Absorption edge [eV]
Iridium foil	0	11215.0
Complex 1	+3	11218.5
Complex 2	+5	11220.3

In addition to the XANES investigations, EXAFS investigations were also performed on the complexes **1** and **2**, in order to determine the local structure around the iridium atom. The experimentally determined and the theoretically calculated EXAFS functions in k -space and their Fourier transforms in real space for complexes **1** and **2**, measured at Ir L_{III}-edge are shown in Figures 4.4.3 and 4.4.4, respectively. The corresponding structural parameters are summarised in Table 4.4.2.

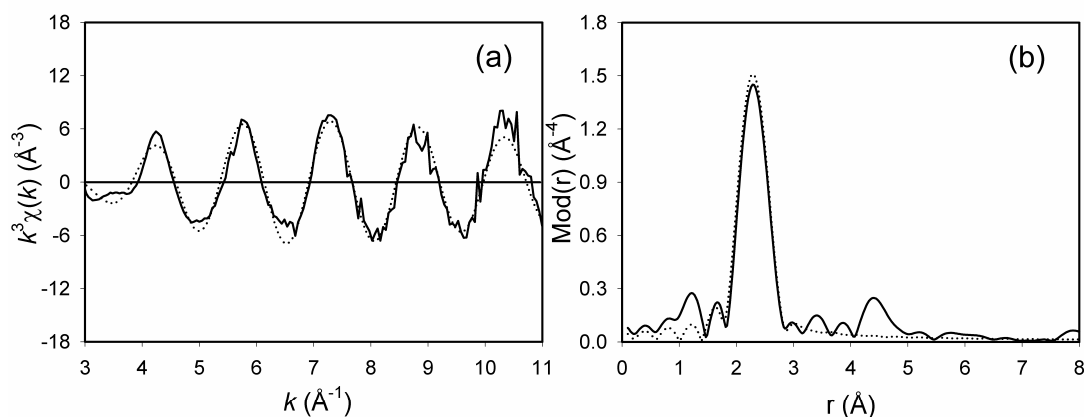
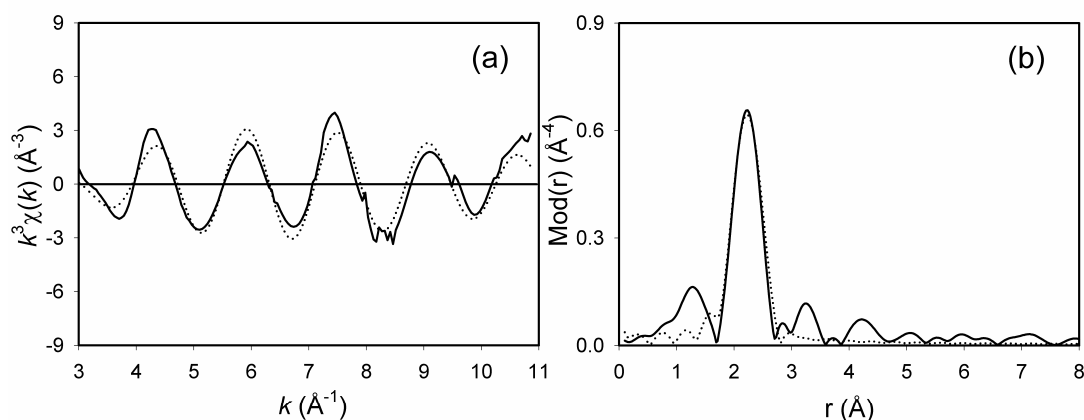
**Figure 4.4.3.** Experimental (solid line) and calculated (dotted line) EXAFS functions (a) and their Fourier transforms (b) of complex **1**, measured at Ir L_{III}-edge.**Figure 4.4.4.** Experimental (solid line) and calculated (dotted line) EXAFS functions (a) and their Fourier transforms (b) of complex **2**, measured at Ir L_{III}-edge.

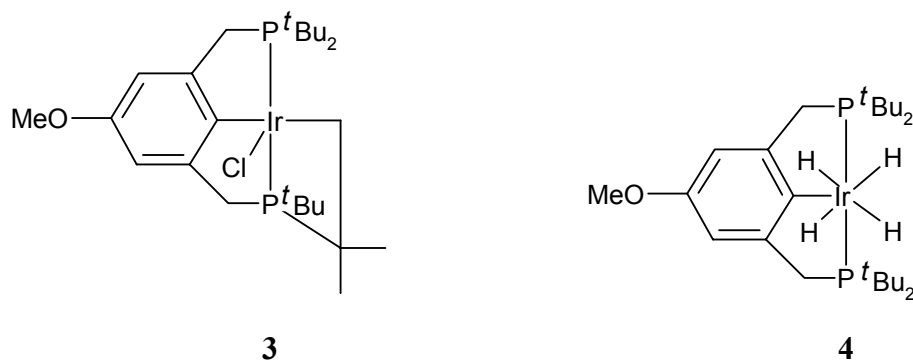
Table 4.4.2. EXAFS obtained structural parameters for reference iridium complexes

Complex	A-Bs ^a	N ^b	r ^c [Å]	σ ^d [Å]	ΔE_0 ^e [eV]	k-range [Å ⁻¹]	R-factor
1	Ir-P/Cl	4	2.36 ± 0.02	0.059 ± 0.006	16.34	3.0 - 11.0	27.83
2	Ir-P	2	2.30 ± 0.02	0.074 ± 0.007	16.79	3.0 - 11.0	35.81

^a absorber (A) - backscatterers (Bs), ^b coordination number N, ^c interatomic distance r, ^d Debye-Waller factor σ with its calculated deviation and ^e shift of the threshold energy ΔE_0 .

In the evaluation of the EXAFS function, a single shell could be fitted for both the complexes with phosphorus backscatterers, at a distance of 2.36 Å in the case of complex **1** and 2.30 Å in the case of complex **2**. Due to the similar backscattering behaviour of phosphorus and chlorine backscatterers occurring at nearly the same distance, they are fitted together with phosphorus amplitude- and phase- functions in complex **1**. The EXAFS analysis reveals the local structure around the iridium atom in complexes **1** and **2**.

In addition to complexes **1** and **2**, two iridium complexes with PCP pincer ligand (complexes **3** and **4**), depicted in Figure 4.4.5, in known oxidation states of +3 (complex **3**) and +5 (complex **4**), were also investigated. The XANES region of the complexes **3** and **4**, measured at Ir L_{III}-edge are shown along with the iridium foil in Figure 4.4.6. The oxidation states and edge energy are tabulated in Table 4.4.3.

**Figure 4.4.5.** Structure of iridium complexes **3** and **4**.**Table 4.4.3.** Edge energy and oxidation states of complexes **3** and **4**

Sample	Oxidation state	Absorption edge [eV]
Iridium foil	0	11215.0
Complex 3	+3	11218.2
Complex 4	+5	11220.0

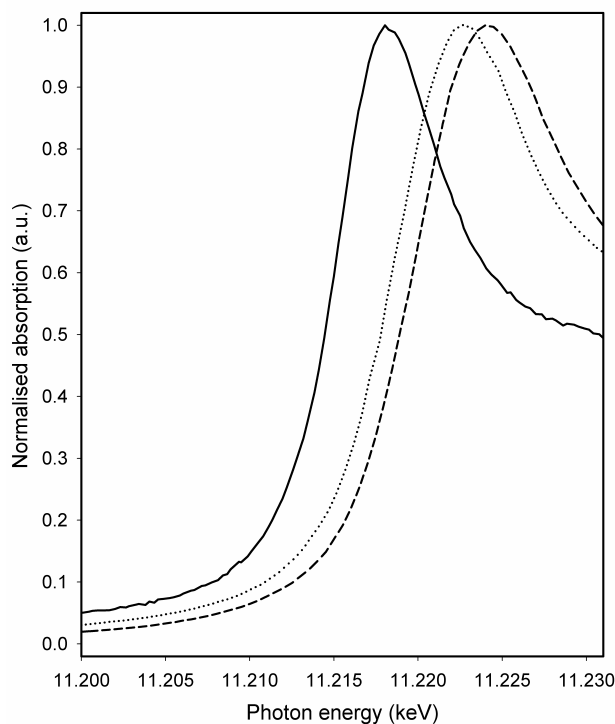


Figure 4.4.6. XANES region of complexes **3** and **4** along with the iridium foil measured at Ir L_{III}-edge. [Complex **3** (dotted line), complex **4** (dashed line) and iridium foil (solid line)].

In addition to the XANES investigations, EXAFS investigations were also performed on the complexes **3** and **4**. The experimentally determined and the theoretically calculated EXAFS functions in k -space and their Fourier transforms in real space for complexes **3** and **4**, measured at Ir L_{III}-edge are shown in Figures 4.4.7 and 4.4.8, respectively. The corresponding structural parameters are summarised in Table 4.4.4.

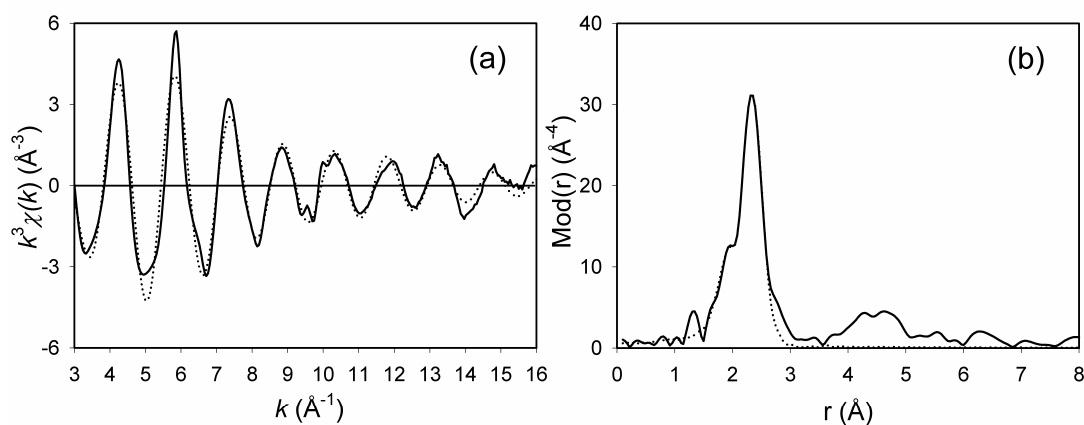


Figure 4.4.7. Experimental (solid line) and calculated (dotted line) EXAFS functions (a) and their Fourier transforms (b) of complex **3**, measured at Ir L_{III}-edge.

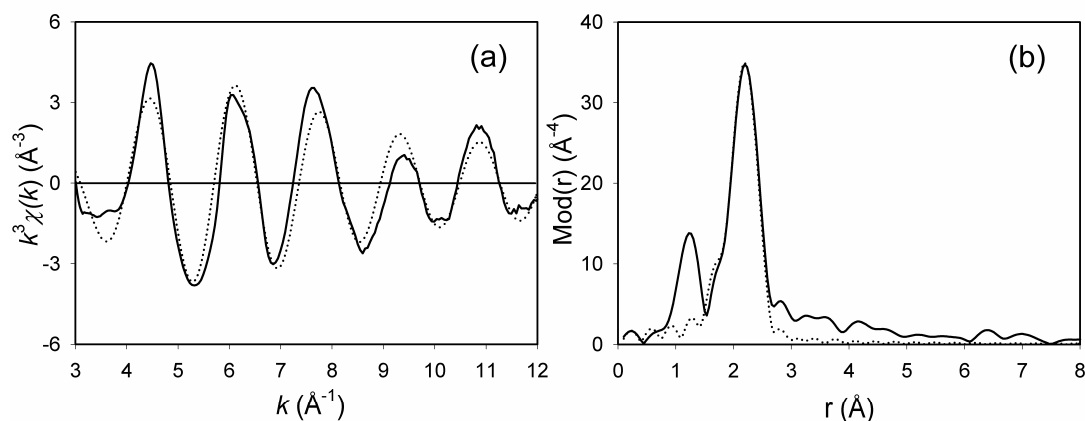


Figure 4.4.8. Experimental (solid line) and calculated (dotted line) EXAFS functions (a) and their Fourier transforms (b) of complex **4**, measured at Ir L_{III}-edge.

Table 4.4.4. EXAFS obtained structural parameters for reference iridium complexes

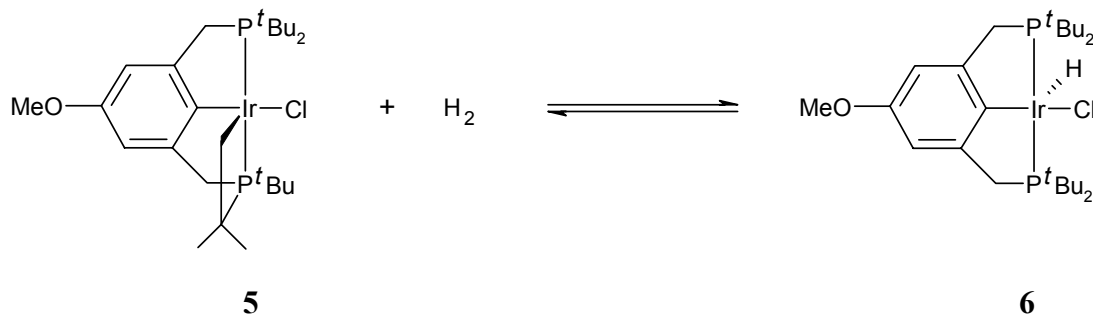
Complex	A-Bs ^a	N ^b	r ^c [Å]	σ ^d [Å]	E _F ^e [eV]	k-range [Å ⁻¹]	R-factor
3	Ir-C	2	2.03 ± 0.02	0.089 ± 0.009	3.009	2.95 - 16.05	28.00
	Ir-P	2	2.30 ± 0.03	0.084 ± 0.012			
	Ir-Cl	1	2.36 ± 0.03	0.059 ± 0.008			
4	Ir-C	1	1.94 ± 0.02	0.067 ± 0.007	10.35	3.01 - 12.03	33.06
	Ir-P	2	2.25 ± 0.03	0.071 ± 0.011			

^a absorber (A) - backscatters (Bs), ^b coordination number N, ^c interatomic distance r, ^d Debye-Waller factor σ with its calculated deviation and ^e Fermi energy E_F.

In the evaluation of the EXAFS function, a three shell model could be fitted for complex **3** and a two shell model could be fitted for complex **4**. The EXAFS analysis reveals the local structure around the iridium atom in complexes **3** and **4**.

4.4.3. Hydrogenation reaction

The hydrogenation reaction depicted in Scheme 4.4.1, was performed in *in operando* conditions in toluene medium, to determine the catalytically active intermediate species.



Scheme 4.4.1. Hydrogenation reaction of PCP pincer ligand iridium complex.

Before performing the hydrogenation reaction, the adduct and product complexes (**5** and **6**) were studied in solid state and dissolved in toluene, in order to investigate whether the complexes retain their structure when they are dissolved in toluene. The experimentally determined and the theoretically calculated EXAFS functions in k -space and their Fourier transforms in real space for complex **5** in solid state and as solution in toluene, measured at Ir L_{III}-edge are shown in Figures 4.4.9 and 4.4.10, respectively. The corresponding structural parameters are given in Table 4.4.5.

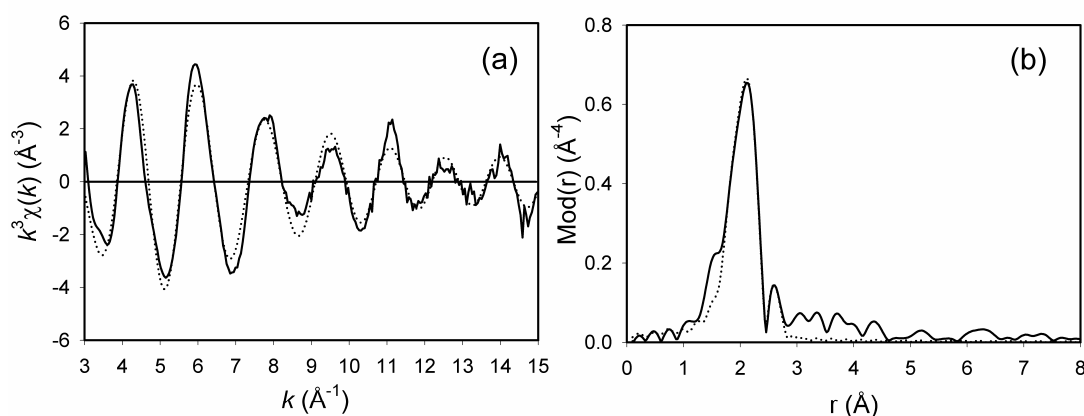


Figure 4.4.9. Experimental (solid line) and calculated (dotted line) EXAFS functions (a) and their Fourier transforms (b) of complex **5** in solid state, measured at Ir L_{III}-edge.

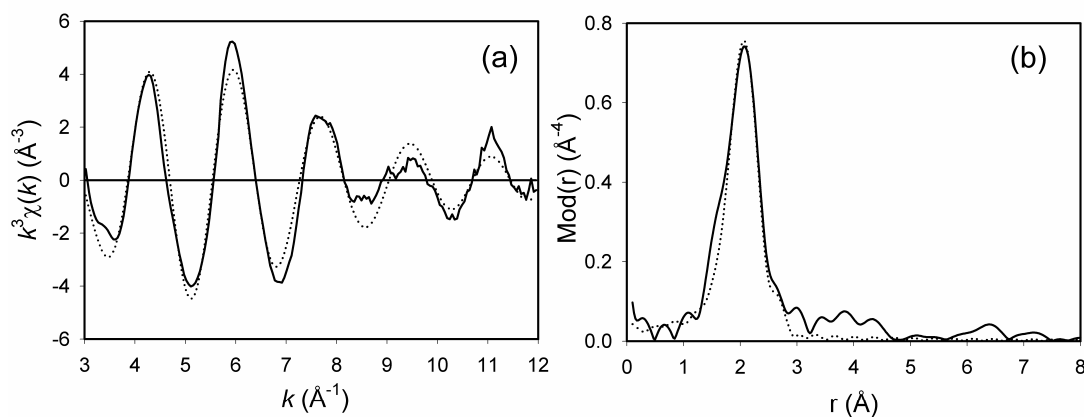


Figure 4.4.10. Experimental (solid line) and calculated (dotted line) EXAFS functions (a) and their Fourier transforms (b) of complex **5** in toluene, measured at Ir L_{III}-edge.

The experimentally determined and the theoretically calculated EXAFS functions in k -space and their Fourier transforms in real space for complex **6** in solid state and as solution in toluene, measured at Ir L_{III}-edge are shown in Figures 4.4.11 and 4.4.12, respectively. The corresponding structural parameters are summarised in Table 4.4.5.

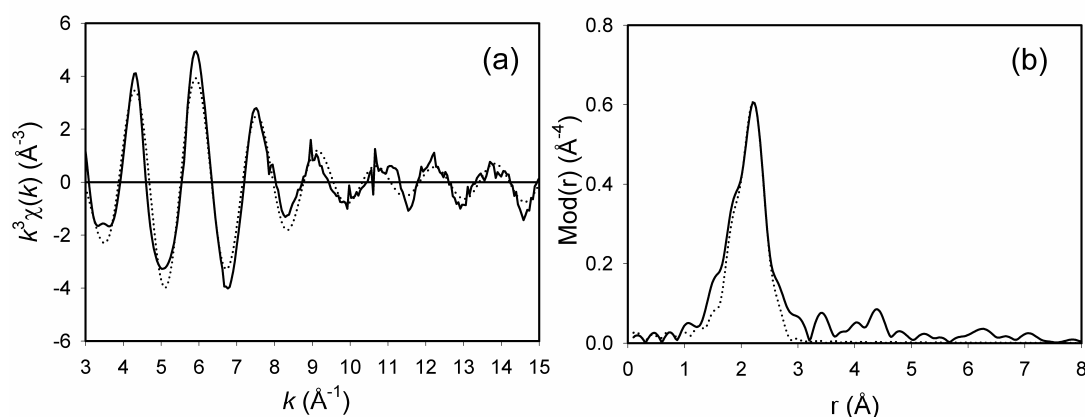


Figure 4.4.11. Experimental (solid line) and calculated (dotted line) EXAFS functions (a) and their Fourier transforms (b) of complex **6** in solid state, measured at Ir L_{III}-edge.

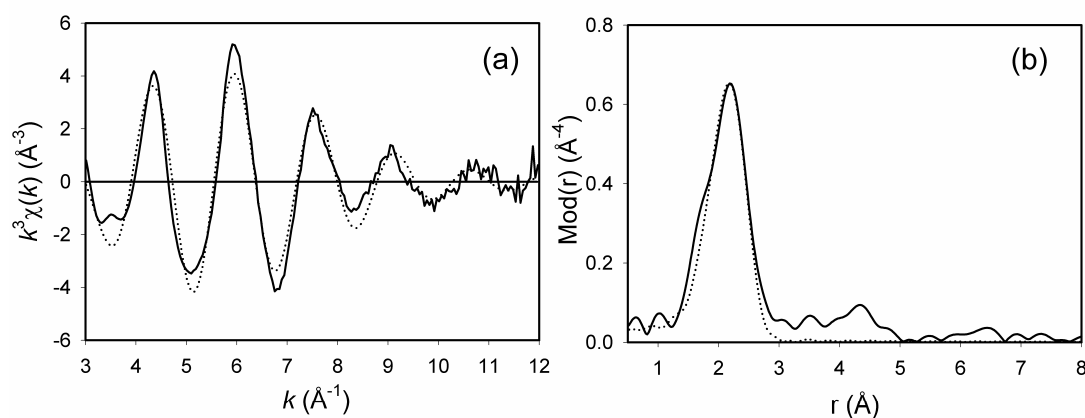


Figure 4.4.12. Experimental (solid line) and calculated (dotted line) EXAFS functions (a) and their Fourier transforms (b) of complex **6** in toluene, measured at Ir L_{III}-edge.

Table 4.4.5. EXAFS obtained structural parameters for complexes **5** and **6**

Complex	A-Bs ^a	N ^b	r ^c [Å]	σ ^d [Å]	ΔE ₀ ^e [eV]	k-range [Å ⁻¹]	R-factor
5 (solid)	Ir-C	2	2.02±0.02	0.064±0.006	20.32	3.0 - 15.0	27.74
	Ir-P	2	2.27±0.02	0.067±0.007			
	Ir-Cl	1	2.43±0.03	0.063±0.008			
5 (in toluene)	Ir-C	2	2.02±0.02	0.059±0.006	18.79	3.0 - 12.0	27.84
	Ir-P	2	2.27±0.02	0.060±0.006			
	Ir-Cl	1	2.41±0.03	0.058±0.007			
6 (solid)	Ir-C	1	2.01±0.02	0.050±0.005	20.58	3.0 - 15.0	30.95
	Ir-P	2	2.28±0.02	0.064±0.006			
	Ir-Cl	1	2.38±0.03	0.066±0.008			
6 (in toluene)	Ir-C	1	1.99±0.02	0.050±0.005	20.07	3.0 - 12.0	30.66
	Ir-P	2	2.26±0.02	0.059±0.006			
	Ir-Cl	1	2.37±0.03	0.050±0.006			

^a absorber (A) - backscatters (Bs), ^b coordination number N, ^c interatomic distance r, ^d Debye-Waller factor σ with its calculated deviation and ^e shift of the threshold energy ΔE₀.

In the evaluation of the EXAFS function, a three shell model could be fitted for complexes **5** and **6**. The EXAFS obtained values were in agreement with those reported in literature for the complexes [4.4.12]. The structural parameters are similar for the complexes in solid state and dissolved in toluene. The EXAFS analysis reveals that the complexes retain their structural integrity even after dissolution in toluene.

The hydrogenation reaction of the PCP pincer ligand iridium complex was monitored for about 7 hours. All the spectra measured at Ir L_{III}-edge during this time period were similar and hence the XANES spectrum obtained at the start of the reaction and the one recorded after 7 hours are shown along with the reference iridium complexes **1** (+3) and **2** (+5) in Figure 4.4.13.

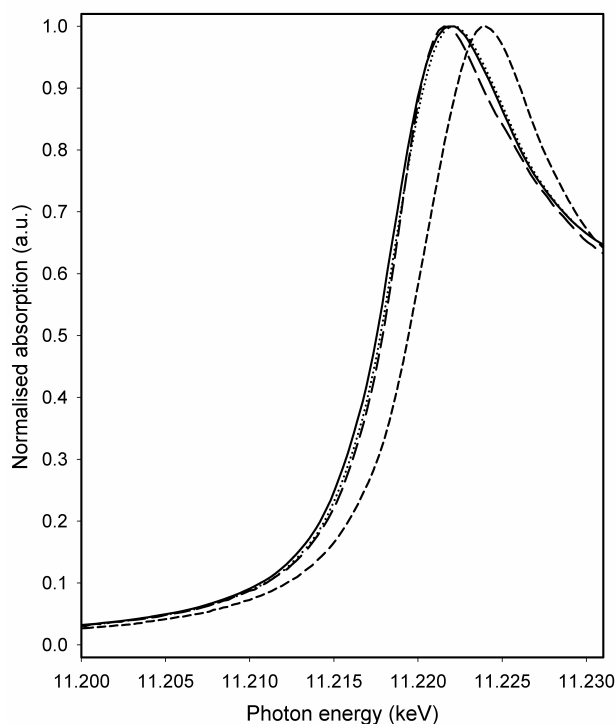


Figure 4.4.13. XANES spectrum collected at the start of the reaction and after 7 hours, along with those of the reference iridium complexes, measured at Ir L_{III}-edge. [Start of the reaction (solid line), after 7 hours (dotted line), complex **1** (long dashed line) and complex **2** (short dashed line)].

As the XAFS measurements revealed no changes in the obtained spectra during the monitored period, it was presumed that complex **5** did not undergo the hydrogenation reaction. The failure of the reaction was tentatively attributed to the inactivity of the reactant complex and insufficient hydrogen pressure for the reaction. These drawbacks were surmounted and the reaction was repeated again in a subsequent beamtime.

However, no remarkable variations in the oxidation state could be observed during the process of the reaction, in this case as well. The NMR investigations performed on the hydrogenation reaction reveals that after 7 hours reaction time, the ratio between complexes **5** and **6** is 3:1 [4.4.13]. Furthermore, it should be noted that the local structural difference between the reactant complex **5** and the product complex **6** is only a single carbon atom at 2.01 Å distance. Hence, when there is a mixture of complexes **5** and **6** in the reaction medium, it is infeasible to observe their individual contributions by means of XAFS spectroscopy. From the observed results, three possibilities could be suggested pertaining to the existence of the transient species,

- (1) The theoretically postulated Ir(V) intermediate species is not formed during the course of the reaction
- (2) The formed Ir(V) species is short lived and could not be detected by means of XAFS spectroscopy
- (3) The Ir(V) species is formed in inadequate quantity and its co-existence with the Ir(III) species (present in large quantity) prevents its clear determination.

4.4.4. Conclusion

The time-resolved XAFS measurements performed on the hydrogenation reaction of PCP pincer ligand iridium complexes, in *in operando* conditions propose several vague possibilities concerning the existence of the theoretically postulated Ir(V) intermediate species and an unequivocal conclusion could not be reached. Many questions such as, the time window of the reaction, the directional shift in the equilibrium of the reaction, the activity of the complexes, the optimal hydrogen pressure, the quantity of the Ir(V) intermediate species and its life time, remain unanswered. Optimisation of the reaction parameters using conventional techniques would provide deeper insights into the reaction mechanism.

4.5. Studies on xanthates

4.5.1. Introduction

Cadmium and zinc bis(*O*-alkylxanthates) are potential single-source molecular precursors for the generation of metal sulphide thin films by chemical vapour deposition (CVD) [4.5.1, 4.5.2]. A major role in tailoring material properties resides in a proper choice of the molecular precursors, whose nature strongly affects the composition, the microstructure and the morphology of the final product. In particular, single-source precursors containing all the elements to be deposited in a unique molecule can be used conveniently as building-blocks for single-step transformation of molecules into materials [4.5.3, 4.5.4]. The advantages of using metal xanthate as precursors are the preformed metal-sulphide bonds and their appreciable volatility and stability to air. These properties enable their clean conversion into metal sulphide in an inert atmosphere. Moreover, they allow toxic multiple-source systems to be avoided and provide better control over the composition and microstructure of the final product to be achieved [4.5.5].

The main focus of the work was a through chemical characterisation of Cd(*O*-^{*i*}PrXan)₂ and Zn(*O*-^{*i*}PrXan)₂, aimed at obtaining valuable information on their physico-chemical characteristics. In particular, the coordination geometry and local structure were investigated by EXAFS and their chemical structure in solid state was analysed by the combined use of Raman and FT-IR spectroscopic techniques.

4.5.2. Cadmium bis(*O*-isopropylxanthate)

The EXAFS measurement of the compound was performed at the Cd K-edge at 26711 eV at the beamline X1 at HASYLAB, Hamburg using Si(311) double crystal monochromator at ambient conditions. Energy calibration was monitored using cadmium metal foil. The experimentally determined and theoretically calculated EXAFS functions of Cd(*O*-^{*i*}PrXan)₂ are shown in *k* space as well as by Fourier transforms in real space in Figure 4.5.1. The structural parameters are summarised in Table 4.5.1 and the molecular structure is depicted in Figure 4.5.2. In the analysis of the experimental *k*³-weighted $\chi(k)$ function, only the first shell consisting of about four sulphur backscatterers could be fitted at a distance of about 2.54 Å. The other shells could not be determined as their contribution to the EXAFS function was insignificant.

The Debye-Waller factor was found to be 0.063 \AA . The obtained Cd-S distance and the coordination number are in good agreement with those of crystalline cadmium sulfide [4.5.6], suggesting that the compound is potentially very promising as a single-source CVD precursor for CdS thin films.

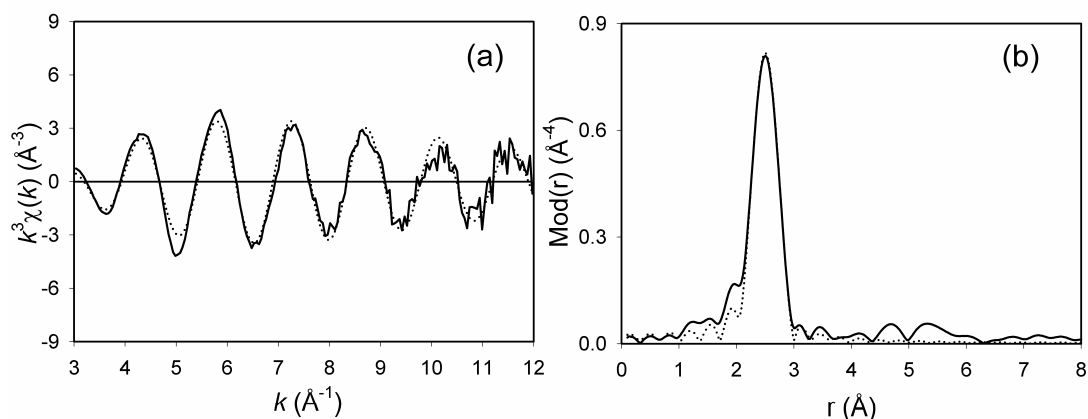


Figure 4.5.1. Experimental (solid line) and calculated (dotted line) EXAFS functions (a) and their corresponding Fourier transform plots (b) of $\text{Cd}(\text{O}^i\text{PrXan})_2$ measured at the Cd K-edge.

Table 4.5.1. EXAFS determined structural parameters of $\text{Cd}(\text{O}^i\text{PrXan})_2$

Compound	A-Bs ^a	N ^b	r ^c [Å]	σ ^d [Å]	ΔE_0 ^e [eV]	k-range [Å ⁻¹]	R-factor
$\text{Cd}(\text{O}^i\text{PrXan})_2$	Cd-S	4.3 ± 0.4	2.54 ± 0.03	0.063 ± 0.006	15.79	3.0 - 12.0	24.95

^a absorber (A) - backscatterers (Bs), ^b coordination number N, ^c interatomic distance r, ^d Debye-Waller factor σ with its calculated deviation and ^e shift of the threshold energy ΔE_0 .

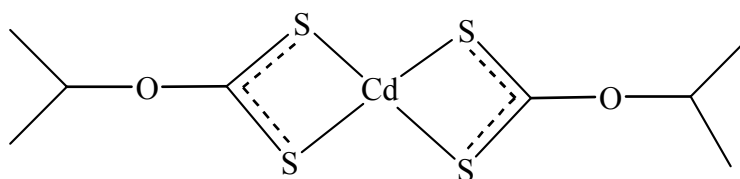


Figure 4.5.2. Molecular structure of $\text{Cd}(\text{O}^i\text{PrXan})_2$.

The Raman spectrum of $\text{Cd}(\text{O}^i\text{PrXan})_2$ (Figure 4.5.3) shows a variety of interesting signals and the results are in good agreement with those obtained from FTIR measurements (Figure 4.5.4). Both Raman and FT-IR assignments, based on the literature data [4.5.7-4.5.12], are summarised in Table 4.5.2. In the FT-IR spectrum, the most intense bands were observed at 1030 , 1094 and 1208 cm^{-1} and attributed to CS_2 , CCC and COC out-of-phase stretching vibrations, respectively. The CS_2 in-phase stretching is well evident in the Raman spectrum around 650 cm^{-1} . Other prominent

signals in the Raman spectrum are attributed as follows: 75 and 87 cm^{-1} , lattice vibrations; 473 cm^{-1} , COC and CCC in-phase bending vibrations; 1030 cm^{-1} , CS_2 out-of-phase stretching vibrations.

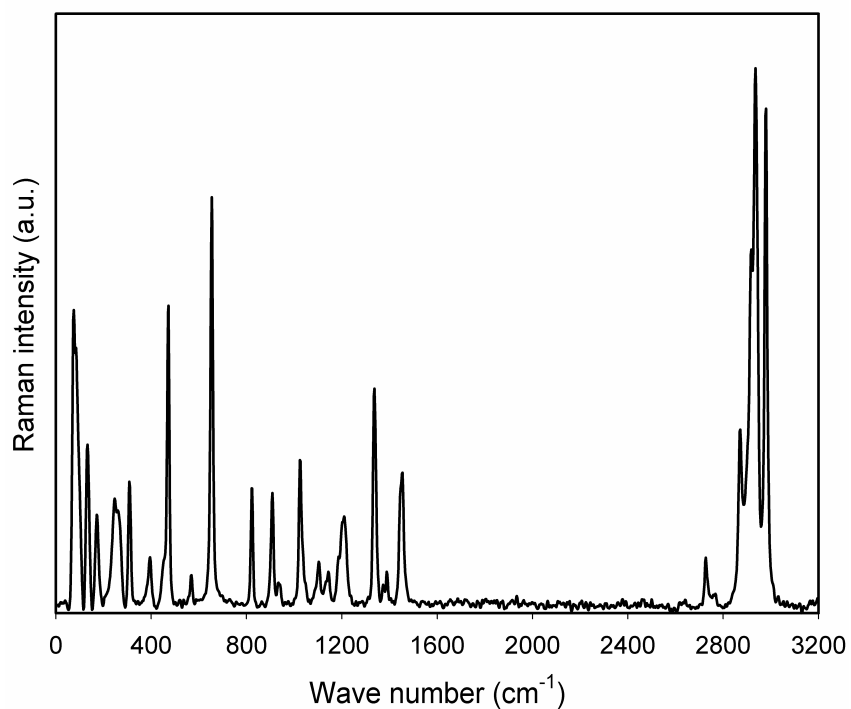


Figure 4.5.3. Raman spectrum of $\text{Cd}(\text{O-}^i\text{PrXan})_2$.

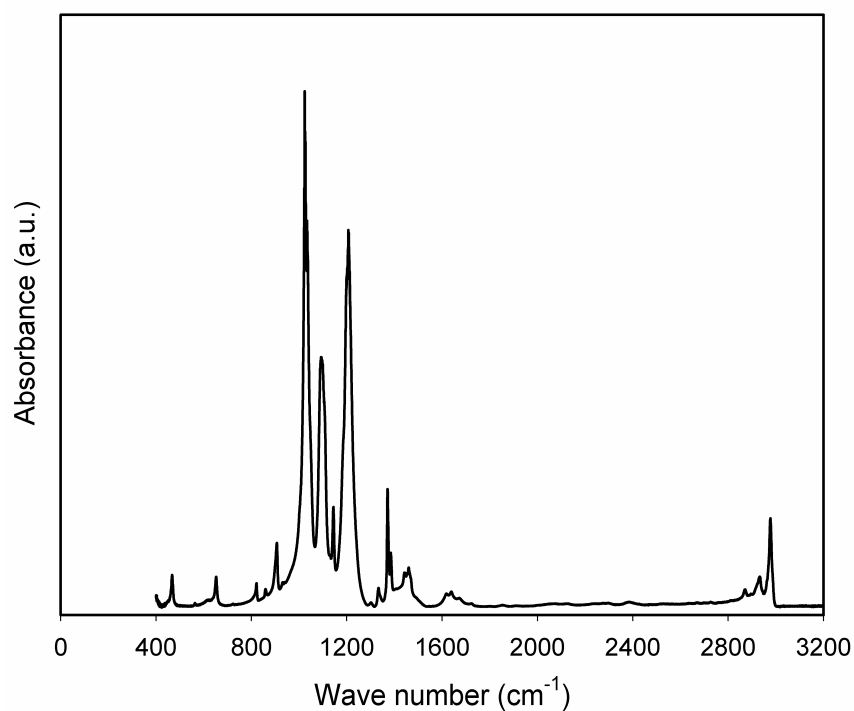


Figure 4.5.4. FT-IR spectrum of $\text{Cd}(\text{O-}^i\text{PrXan})_2$.

Table 4.5.2. Selected features and corresponding assignments in the vibrational spectra of Cd(*O*-^{*i*}PrXan)₂

Raman frequency [cm ⁻¹]	Infrared frequency [cm ⁻¹]	Assignment
75, 87		Lattice vibrations
132		Cd-S vibrations
173		CS ₂ rocking Cd-S vibrations
246, 262		Cd-S stretching vibrations
309		SCS, CCC in-phase bending
397		CCC, SCS out-of-phase bending Cd-S vibrations
473	468	COC, CCC in-phase bending
569	572	OCS ₂ wagging
655	652	CS ₂ in-phase stretching
825	821	OCC ₂ in-phase stretching
909	907	CH ₃ out-of-phase rocking perpendicular to OC(H)
1030	1025, 1034	CS ₂ out-of-phase stretching
1110	1094	CCC out-of-phase stretching
1150	1144	CH ₃ rocking, (S)CO stretching
1208	1208	COC out-of-phase stretching
1338	1333	CH wagging
1390	1372, 1385	CH ₃ in-phase deformation
1455	1460	CH ₃ out-of-phase deformation
2878	2871	CH ₃ in-phase stretching
2940	2932	CH ₃ out-of-phase stretching
2980	2977	CH ₃ out-of-phase stretching

The vibrational disorder, calculated basing on the Cd-S vibration at 246 cm⁻¹, using standard statistical mechanics equations [4.5.13], was 0.064 Å, in close agreement with the Debye-Waller factor found from EXAFS measurements. This result suggests that the major component of disorder in the system is due to vibrations rather than static displacements.

4.5.3. Zinc bis(*O*-isopropylxanthate)

The EXAFS measurement of the compound was performed at the Zn K-edge at 9659 eV at the beamline X1 at HASYLAB, Hamburg using Si(111) double crystal monochromator at ambient conditions. Energy calibration was monitored using zinc metal foil. The experimentally determined and theoretically calculated EXAFS

functions of $\text{Zn}(\text{O}^i\text{PrXan})_2$ are shown in k space as well as by Fourier transforms in real space in Figure 4.5.5. The structural parameters are summarised in Table 4.5.3 and the molecular structure is depicted in Figure 4.5.6. The EXAFS function indicate the presence of four sulphur backscatterers at a distance of about 2.34 Å, with no appreciable contribution from other shells and the Debye-Waller factor was found to be 0.081 Å. The obtained Zn-S distance and the coordination number are in good agreement with those of crystalline zinc sulfide [4.5.14], indicating that $\text{Zn}(\text{O}^i\text{PrXan})_2$ possesses a core structure very similar to that of ZnS.

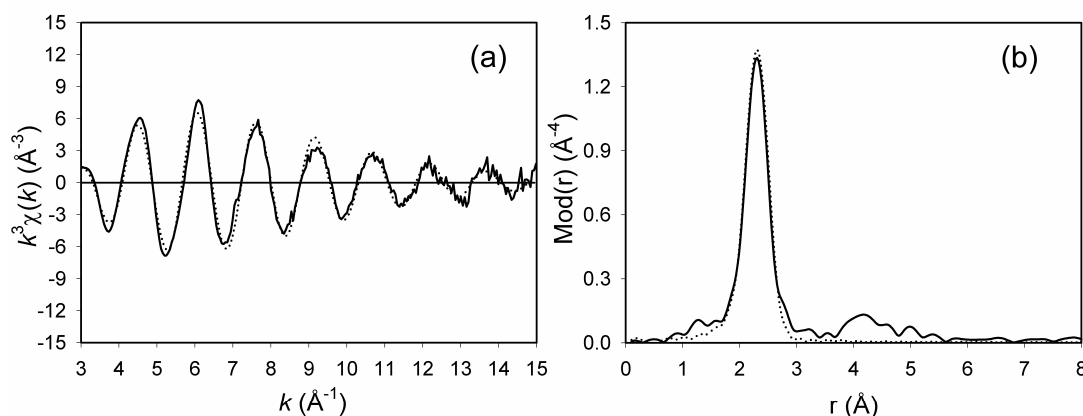


Figure 4.5.5. Experimental (solid line) and calculated (dotted line) EXAFS functions (a) and their corresponding Fourier transform plots (b) of $\text{Zn}(\text{O}^i\text{PrXan})_2$ measured at the Zn K-edge.

Table 4.5.3. EXAFS determined structural parameters of $\text{Zn}(\text{O}^i\text{PrXan})_2$

Compound	A-Bs ^a	N ^b	r ^c [Å]	σ ^d [Å]	ΔE ₀ ^e [eV]	k-range [Å ⁻¹]	R-factor
$\text{Zn}(\text{O}^i\text{PrXan})_2$	Zn-S	4.2 ± 0.4	2.34 ± 0.03	0.081 ± 0.006	15.30	3.0 - 15.0	21.92

^a absorber (A) - backscatterers (Bs), ^b coordination number N, ^c interatomic distance r, ^d Debye-Waller factor σ with its calculated deviation and ^e shift of the threshold energy ΔE₀.

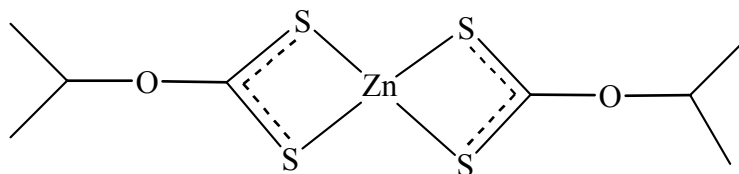


Figure 4.5.6. Molecular structure of $\text{Zn}(\text{O}^i\text{PrXan})_2$.

Raman and FTIR spectra of $\text{Zn}(\text{O}^i\text{PrXan})_2$ are shown in Figures 4.5.7 and 4.5.8, respectively. The band assignments, based on literature data [4.5.7 - 4.5.12], are summarised in Table 4.5.4.

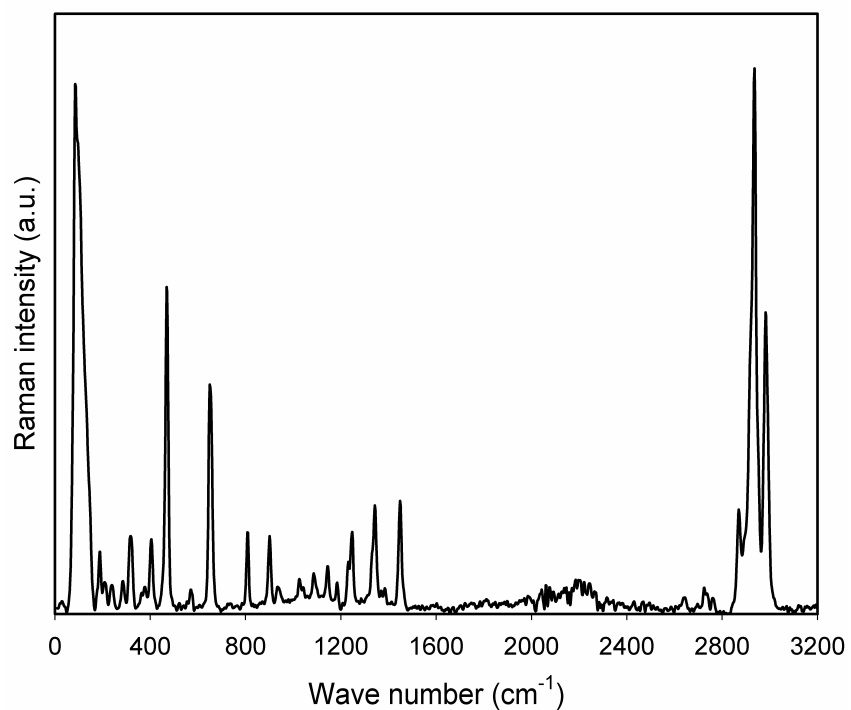


Figure 4.5.7. Raman spectrum of $\text{Zn}(\text{O}^i\text{PrXan})_2$.

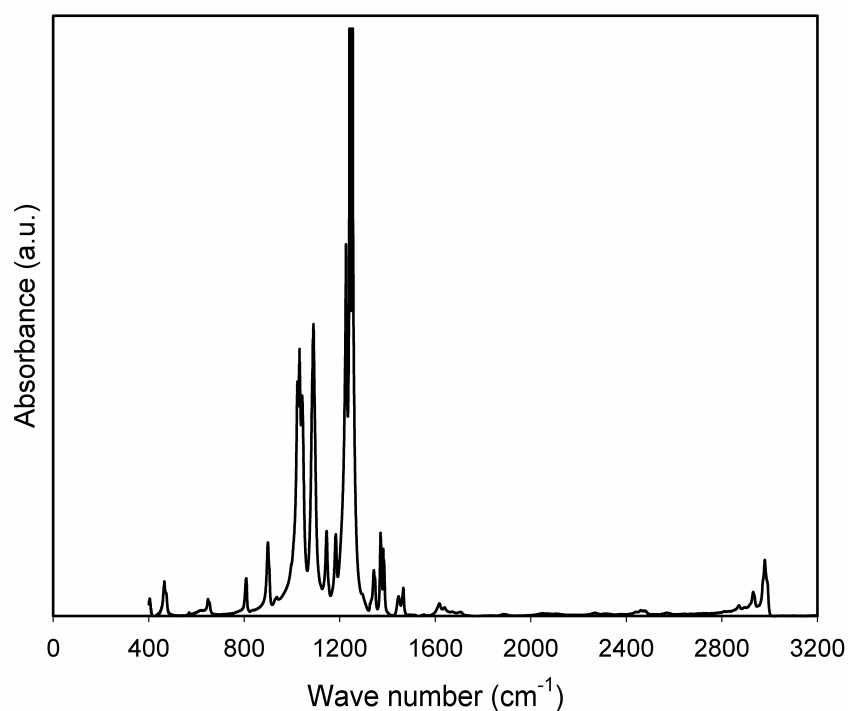


Figure 4.5.8. FT-IR spectrum of $\text{Zn}(\text{O}^i\text{PrXan})_2$.

The Zn-S stretching vibrations were determined at 319 and 405 cm^{-1} . The CS_2 in-phase stretching at 650 cm^{-1} is clearly evident in the Raman spectrum. In the FT-IR spectrum, the prominent signals at 1030 and 1090 cm^{-1} are attributed to CS_2 and CCC

out-of-phase stretching, in good agreement with Raman results. The intense absorptions in the range 1190-1250 cm^{-1} are assigned to COC out-of-phase stretching vibrations. Other significant Raman bands are assigned as follows: 87 cm^{-1} , lattice vibrations; 470 cm^{-1} , COC and CCC in-phase bending modes; 2940 and 2990 cm^{-1} , CH_3 out-of-phase stretching vibrations.

Table 4.5.4. Selected features and corresponding assignments in the vibrational spectra of $\text{Zn}(\text{O-}^i\text{PrXan})_2$

Raman frequency [cm^{-1}]	Infrared frequency [cm^{-1}]	Assignment
87		Lattice vibrations
188		CS_2 rocking
319		Zn-S stretching vibrations SCS, CCC in-phase bending
405		Zn-S stretching vibrations CCC, SCS out-of-phase bending
469	466	COC, CCC in-phase bending
572	-	OCS_2 wagging
652	648	CS_2 in-phase stretching
809	809	OCC_2 in-phase stretching
901	899	CH_3 out-of-phase rocking perpendicular to O-C(H)
935	-	CH_3 out-of-phase rocking parallel to O-C(H)
1030	1022, 1031	CS_2 out-of-phase stretching
1090	1090	CCC out-of-phase stretching
1150	1145	C-C, (S)C-O stretching
1191,1235, 1250	1183, 1245, 1255	COC out-of-phase stretching
1350	1343	CH wagging parallel to O-C(H)
1390	1371, 1382	CH_3 in-phase deformation
1450	1466	CH_3 out-of-phase deformation
2870	2872	CH_3 in-phase stretching
2940	2931	CH_3 out-of-phase stretching
2988	2979	CH_3 out-of-phase stretching

The vibrational disorder, calculated basing on the Zn-S vibration at 319 cm^{-1} , using standard statistical mechanics equations [4.5.13], was 0.052 Å, which is significantly lower than the Debye-Waller factor determined from EXAFS measurements. This result suggests that the disorder in the system is due to both vibrations and static displacements.

4.5.4. Conclusion

The chemical characterisation of $\text{Cd}(\text{O-}^i\text{PrXan})_2$ and $\text{Zn}(\text{O-}^i\text{PrXan})_2$ by EXAFS revealed that the compounds have metal–sulphur distances and coordination numbers similar to those of the corresponding metal sulphides, suggesting their suitability as single-source CVD precursors for the preparation of metal sulphide thin films. Furthermore, Raman and FT-IR spectroscopic techniques provided additional structural information about the investigated compounds.

Chapter 5 Investigations on nanomaterials

5.1. Studies on nanostructured mixed oxide materials

5.1.1. Introduction

Nanostructured mixed oxides are getting increasingly important in several fields of materials technology, especially applied catalysis and energy conversion. The novel physical properties of the nanostructured materials are mainly due to size effects and surface effects [5.1.1]. Mixed oxides offer great possibilities for allowing tuning of the properties of the materials, as the properties of the multi-component system are strongly influenced by the composition and the preparation procedure [5.1.2].

Lanthanum cobaltite based materials are attractive candidates for environmental catalysts, oxygen sensing devices, solid oxide fuel cells and magnetic media [5.1.3, 5.1.4]. Nanostructured systems with high defect content (oxygen vacancies and local lattice disorder) are expected to show superior properties to the conventional ones [5.1.5, 5.1.6]. Lanthanum cobaltite materials are particularly promising for the above mentioned applications due to the accessibility of cobalt in +2 and +3 oxidation states [5.1.6]. LaCoO_3 has been shown to have intrinsic p-type conductivity, which can be enhanced by substituting a lower valence ion on the La(III) sites [5.1.7].

The catalytic activity in oxidation reactions makes the mixed oxides materials suitable for fuel cell applications [5.1.8]. New active sites, and thus a different reactivity can be obtained by mixing different components and employing an appropriate preparation procedure. The significant differences in the activity of iron oxide and titanium oxide make the investigations on Fe–Ti–O mixed oxides interesting and significant insights could be obtained by studying the interplay of different parameters on the reactivity of these mixed oxides.

Cerium oxide based nanocomposite systems play an important role in oxidation reactions and could be used as advanced anodes for intermediate temperature solid oxide fuel cells (SOFC). Cerium oxide is a major component in the three-way catalysts (TWC) used for the treatment of automotive exhaust gases [5.1.9]. The oxygen storage capacity associated with a fast Ce(IV)/Ce(III) redox process, is one of the key properties of this material [5.1.7]. Appropriate preparation procedures allows the deposition of nanometer sized oxide particles on an active metal support, thus taking advantage of the reactivity of deposited nanoclusters and also the active metal support [5.1.10].

Yttria stabilised zirconia (YSZ) is an important ceramic material with useful mechanical, thermal, optical and electrical properties and these outstanding properties have been put to use in many applications such as catalysis, fuel cells, sensors etc. In these materials yttria is added to zirconia to obtain tetragonal and cubic phases at room temperature [5.1.11]. Zirconia doped with ceria enhances the oxygen storage capacity and the interactions between the different oxides play a critical role in developing novel and highly active materials for a number of processes [5.1.12].

5.1.2. Nanophasic undoped and Ca-doped lanthanum cobaltite

The nanophasic undoped and Ca-doped LaCoO_3 powders were prepared by the work group of Dr. L. Armelao, Department of Chemical Sciences, University of Padua, by employing the non-alkoxidic sol-gel technique [5.1.13]. The samples were prepared starting from methanolic solutions of $\text{La}(\text{NO}_3)_3 \cdot 6\text{H}_2\text{O}$, $\text{Co}(\text{CH}_3\text{COO})_2 \cdot 4\text{H}_2\text{O}$ and $\text{Ca}(\text{CH}_3\text{COO})_2 \cdot \text{H}_2\text{O}$. The molar concentration of the metals in solution were $[\text{Co}] = [\text{La}] = 0.15 \text{ M}$, whereas in the case of the doped samples $[\text{Ca}] = [\text{La}] = 0.075 \text{ M}$. The wet powders were first dried under vacuum and then annealed in air for one hour between 400 and 1000°C. The structural evolution and the effects of calcium doping on LaCoO_3 powders as a function of thermal annealing were investigated by means of XAFS spectroscopy.

The transmission mode XAFS measurements of the samples were performed at Co K-edge at 7709 eV and La K-edge at 38925 eV, at the beamline X1 at HASYLAB, Hamburg. The samples were measured at ambient conditions with Si(111) double crystal monochromator at the Co K-edge and with Si(511) double crystal monochromator at the La K-edge. For Co K-edge measurements a 20 μm thick cobalt metal foil and for La K-edge measurements LaCoO_3 in pellet form were used as the energy calibration references. Measurements at the Ca K-edge were attempted but were not successful owing to the presence of other strong absorbing atoms (lanthanum and cobalt). In the EXAFS analysis, the value of the amplitude factor (AFAC) was determined to be 0.8 from the fitting of the data of crystalline CoO and this value was fixed for all the other fittings at the Co K-edge. At the La K-edge, the value of the AFAC was determined to be 0.4 resulting from the fitting of the crystalline La_2O_3 and this value was fixed for all the other fittings at this edge. In the fitting procedure for

both cases, coordination number, interatomic distance, Debye-Waller factor and energy zero value were determined by iterations.

5.1.2.1. EXAFS investigations at the Co K-edge

The experimental EXAFS functions in k space and their Fourier transforms in real space were first determined for xerogels and are shown in Figure 5.1.1. The corresponding structural parameters are given in Table 5.1.1. In the EXAFS spectra of both undoped and Ca-doped xerogels, only the first shell with about six oxygen backscatterers at about 2.09 Å distance was fitted. The other shells could not be fitted since their contribution to the EXAFS signal was insignificant. The influence of calcium doping could not be unequivocally ascertained as only the contribution from the first shell could be determined, which did not show any local structural changes. These results indicate that in these xerogels the local structure typical of lanthanum cobaltite has not yet been formed. As a matter of fact, *as-prepared* sol-gel materials are usually amorphous and crystallization occurs after suitable thermal annealing.

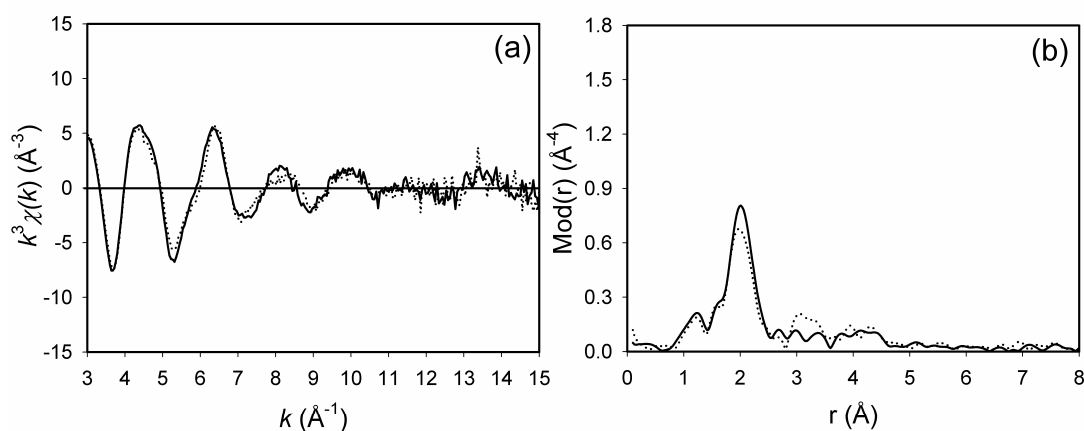


Figure 5.1.1. Experimental EXAFS functions (a) and their Fourier transform plots (b) of undoped (solid line) and Ca-doped (dotted line) LaCoO₃ xerogels measured at Co K-edge.

The comparison plots of the EXAFS functions in k space and their Fourier transforms for the undoped and Ca-doped LaCoO₃ powders annealed at 700 and 800°C are shown in Figures 5.1.2 and 5.1.3, respectively. The structural parameters are reported in Table 5.1.1.

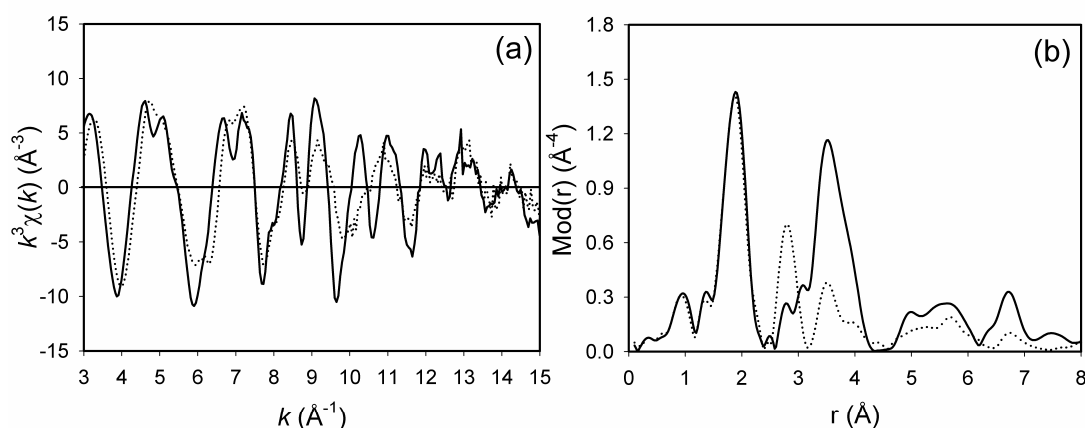


Figure 5.1.2. Experimental EXAFS functions (a) and their Fourier transform plots (b) of undoped (solid line) and Ca-doped (dotted line) LaCoO_3 annealed at 700°C measured at Co K-edge.

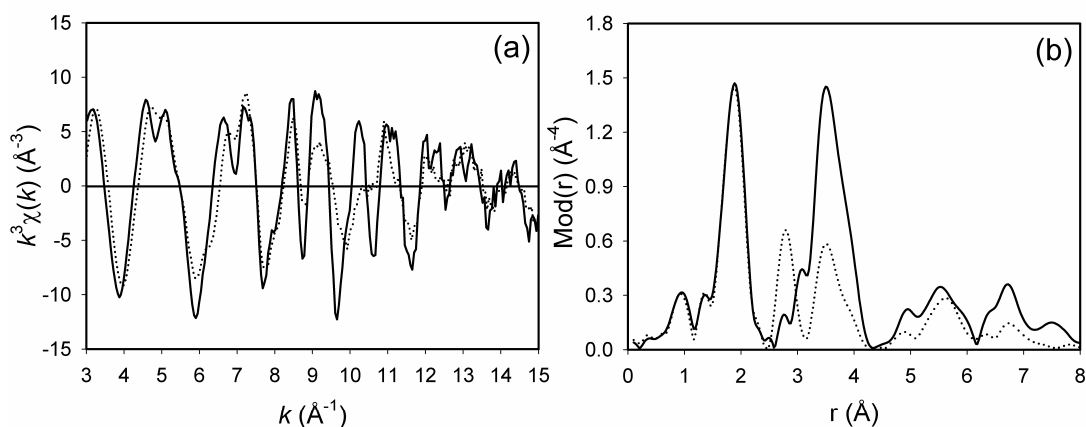


Figure 5.1.3. Experimental EXAFS functions (a) and their Fourier transform plots (b) of undoped (solid line) and Ca-doped (dotted line) LaCoO_3 annealed at 800°C measured at Co K-edge.

In both the undoped specimens, the experimental k^3 weighed $\chi(k)$ function could be fitted using a three-shell model. The first shell having about six oxygen backscatterers was found at 1.93\AA , the second shell consisting of about six lanthanum backscatterers was determined at 3.32\AA and the third shell with about six cobalt backscatterers was fitted at 3.54\AA . Data analysis shows that the structural parameters of the LaCoO_3 samples annealed at 700 and 800°C were similar and in agreement with those of crystalline bulk LaCoO_3 [5.1.14]. It is known that, at the nanometer level, the coordination numbers strongly depend on the crystallite size. But in the present case, substantial changes in the coordination numbers between the investigated samples and bulk LaCoO_3 could not be observed. This could be attributed to the fact that the

crystallites are considerably large, as evident from the XRD analysis [5.1.13] and the decrease in the coordination numbers could not be detected.

Concerning the Ca-doped samples, EXAFS spectra shows similar features for annealing at 700 and 800°C, but different from the corresponding undoped specimens. In the Ca-doped samples, a significant decrease in the coordination number of the second shell lanthanum backscatterers (at 3.32 Å) can be observed, suggesting the partial substitution of the La(III) species by Ca(II) ions. It can also be noted that the coordination number of the third shell cobalt backscatterers at 3.54 Å, is reduced from six to about three. These changes in the coordination numbers could not be associated with the changes in the crystallite size, as the size variation between the undoped and Ca-doped samples is within the same order of magnitude. Moreover, a new shell with cobalt backscatterers originates at about 2.81 Å. This shell was not observed in the undoped samples and is in agreement with the Co-Co distance of 2.85 Å, in Co₃O₄ [5.1.15], which suggests that Co₃O₄ is also formed during the process of annealing when calcium is incorporated in the LaCoO₃ network.

The experimental EXAFS functions in k space and their Fourier transforms in real space for the undoped and Ca-doped LaCoO₃ powders annealed at 1000°C are shown in Figure 5.1.4 and the obtained structural parameters are given in Table 5.1.1.

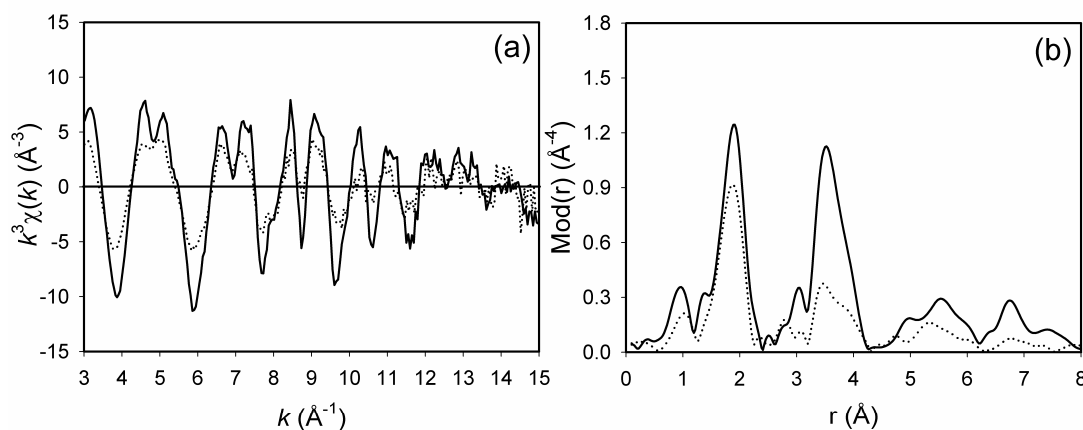


Figure 5.1.4. Experimental EXAFS functions (a) and their Fourier transform plots (b) of undoped (solid line) and Ca-doped (dotted line) LaCoO₃ annealed at 1000°C measured at Co K-edge.

Table 5.1.1. EXAFS determined structural parameters of undoped and Ca-doped LaCoO₃ powders measured at the Co K-edge.

Sample	A-Bs ^a	N ^b	r ^c [Å]	σ ^d [Å]	ΔE ₀ ^e [eV]	k-range [Å ⁻¹]	R-factor
Undoped LaCoO ₃ - xerogel	Co-O	6.4 ± 0.6	2.09 ± 0.02	0.098 ± 0.010	21.89	3.0 - 15.0	44.73
Ca-doped LaCoO ₃ - xerogel	Co-O	6.3 ± 0.6	2.08 ± 0.02	0.107 ± 0.011	22.38	3.0 - 15.0	52.96
Undoped LaCoO ₃ - annealed at 700°C	Co-O Co-La Co-Co	6.3 ± 0.6 6.4 ± 1.0 6.1 ± 1.2	1.93 ± 0.02 3.32 ± 0.03 3.54 ± 0.04	0.078 ± 0.008 0.102 ± 0.010 0.098 ± 0.015	22.07	3.0 - 15.0	37.05
Ca-doped LaCoO ₃ - annealed at 700°C	Co-O Co-Co Co-La Co-Co	5.9 ± 0.6 1.7 ± 0.2 3.6 ± 0.5 3.0 ± 0.6	1.91 ± 0.02 2.82 ± 0.03 3.32 ± 0.03 3.49 ± 0.04	0.078 ± 0.008 0.071 ± 0.007 0.102 ± 0.016 0.098 ± 0.020	24.03	3.0 - 15.0	34.63
Undoped LaCoO ₃ - annealed at 800°C	Co-O Co-La Co-Co	6.3 ± 0.6 6.7 ± 1.0 6.7 ± 1.3	1.93 ± 0.02 3.32 ± 0.03 3.54 ± 0.04	0.077 ± 0.008 0.099 ± 0.010 0.092 ± 0.014	22.26	3.0 - 15.0	37.34
Ca-doped LaCoO ₃ - annealed at 800°C	Co-O Co-Co Co-La Co-Co	6.2 ± 0.6 1.5 ± 0.5 4.0 ± 0.4 3.5 ± 0.7	1.92 ± 0.02 2.81 ± 0.03 3.32 ± 0.03 3.52 ± 0.04	0.077 ± 0.008 0.071 ± 0.007 0.099 ± 0.015 0.092 ± 0.018	24.23	3.0 - 15.0	34.65
Undoped LaCoO ₃ - annealed at 1000°C	Co-O Co-La Co-Co	6.3 ± 0.6 7.0 ± 1.0 6.1 ± 1.2	1.94 ± 0.02 3.33 ± 0.03 3.54 ± 0.04	0.083 ± 0.008 0.107 ± 0.011 0.094 ± 0.014	21.62	3.0 - 15.0	37.51
Ca-doped LaCoO ₃ - annealed at 1000°C	Co-O Co-La Co-Co	3.9 ± 0.4 1.3 ± 0.2 2.2 ± 0.4	1.93 ± 0.02 3.34 ± 0.03 3.54 ± 0.04	0.087 ± 0.009 0.084 ± 0.008 0.092 ± 0.012	18.54	3.0 - 15.0	45.09

^a absorber (A) - backscatters (Bs), ^b coordination number N, ^c interatomic distance r, ^d Debye-Waller factor σ with its calculated deviation and ^e shift of the threshold energy ΔE₀.

Annealing at 1000°C did not result in the modification of the local structure for the undoped LaCoO₃ powders, whereas calcium incorporation showed a completely different influence with respect to the effects observed at lower temperatures. The coordination number of the first oxygen shell was considerably reduced, thus suggesting either the formation of some calcium compounds (*i.e.* CaO, CaCO₃) or the formation of oxygen-defective LaCoO₃ with a distorted structure. In addition, the coordination numbers of the second shell lanthanum backscatters and the third shell cobalt backscatters were also significantly reduced. Such a decrease can be ascribed either to substitution of calcium at some of the lanthanum sites, like in the previous cases, or also

to the formation of other compounds such as, La_2O_3 , Co_3O_4 , rather than to the crystallite size effects. Upon a closer examination of Figure 5.1.4, one could observe a very small peak in the Fourier transform plot at about 2.81 \AA , which could possibly arise from Co_3O_4 [5.1.15]. Since its contribution to the EXAFS function was negligible it was not considered during the data evaluation. The obtained results suppose the formation of a distorted oxygen-defective LaCoO_3 along with other oxide-based compounds.

In all the cases, the Co-Ca distance could not be determined from the EXAFS analysis due to low calcium content [5.1.16] in the samples and signals from oxygen, cobalt and lanthanum backscatterers dominate the spectra. Since the EXAFS measurements at the Ca K-edge were not successful, it was not possible to unequivocally verify the presence of the calcium compounds.

5.1.2.2. EXAFS investigations at the La K-edge

The comparison of the experimental EXAFS functions in k space and their Fourier transforms in real space for the undoped and Ca-doped LaCoO_3 xerogels are shown in Figure 5.1.5 and the corresponding structural parameters are summarised in Table 5.1.2.

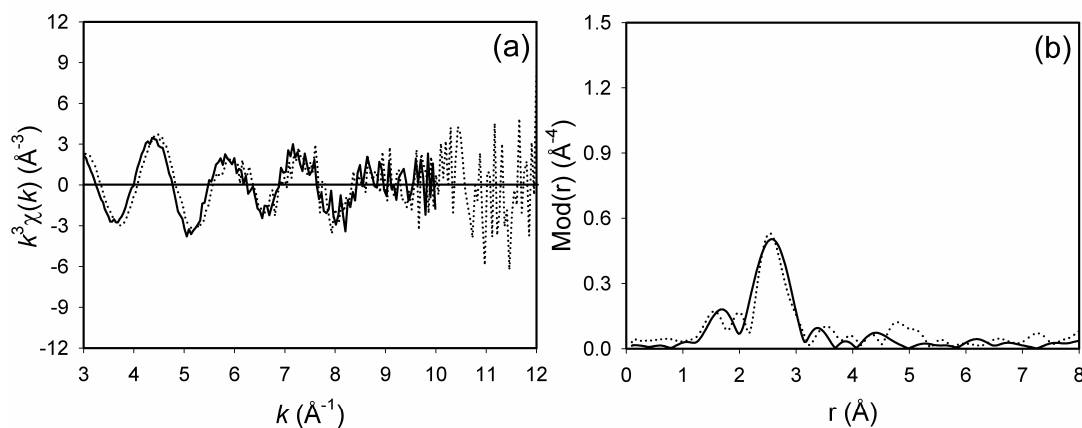


Figure 5.1.5. Experimental EXAFS functions (a) and their Fourier transform plots (b) of undoped (solid line) and Ca-doped (dotted line) LaCoO_3 xerogels measured at La K-edge.

Similar EXAFS spectra have been obtained for the undoped and Ca-doped xerogels. The contributions from only the first shell, consisting of about twelve oxygen backscatterers at about 2.56 \AA distance, could be determined in both the cases. As already observed for the Co K-edge, the analysis could not unambiguously ascertain the

effect of calcium doping as the formation of perovskite structure corresponding to LaCoO_3 could not be evidenced.

The experimental EXAFS functions in k space and their Fourier transforms in real space for the undoped and Ca-doped LaCoO_3 powders annealed at 700°C are shown in Figure 5.1.6 and the obtained structural parameters are given in Table 5.1.2.

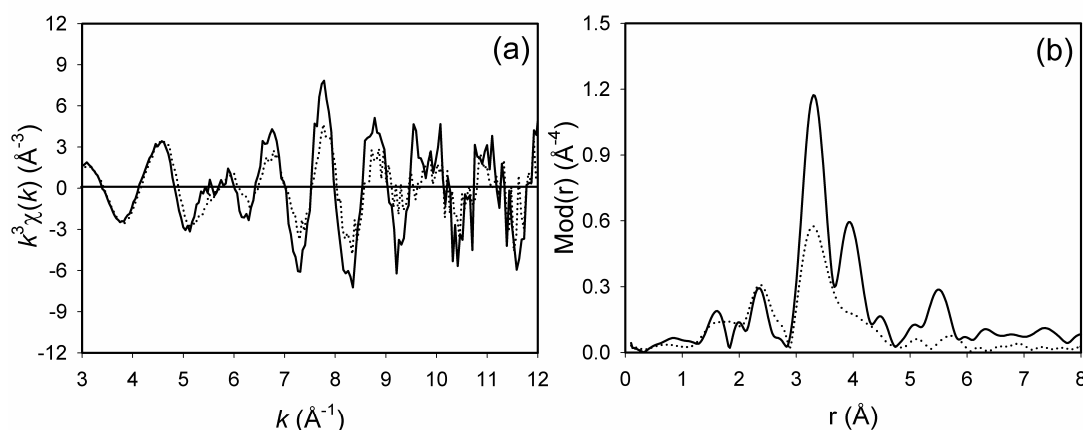


Figure 5.1.6. Experimental EXAFS functions (a) and their Fourier transform plots (b) of undoped (solid line) and Ca-doped (dotted line) LaCoO_3 annealed at 700°C measured at La K-edge.

For the specimen annealed at 700°C , a four-shell model could be fitted in the analysis of the experimental k^3 weighed $\chi(k)$ function. The first shell consisting of about three oxygen backscatterers is found at 2.42 Å , the second shell having about six oxygen backscatterers is determined at 2.60 Å , the third shell consisting of about eight cobalt backscatterers is detected at 3.31 Å and, finally, the fourth shell with about six lanthanum backscatterers is fitted at 3.80 Å . These distances and coordination numbers are in good agreement with the structural parameters of crystalline LaCoO_3 [5.1.14]. A further shell consisting of three oxygen backscatterers should be observed at about 3.00 Å [5.1.14]. Nevertheless, oxygen is a weak backscatterer and three oxygen backscatterers occurring at this distance contribute only to a weak signal; moreover, this could be probably shadowed by the contributions from the cobalt backscatterers at a closer distance. Concerning the EXAFS spectrum of Ca-doped sample, the coordination number of oxygen backscatterers decreased in the first shell and increased in the second shell; moreover, in the latter, the La–O distances resulted shorter. These results suggest that calcium incorporation induces a distortion in the perovskite structure. Furthermore, the coordination numbers of cobalt and lanthanum backscatterers are significantly

reduced, thus suggesting the formation of cobalt compounds (Co_3O_4) and the partial substitution of La(III) species by calcium.

The EXAFS functions in k space and the corresponding Fourier transforms for the undoped and Ca-doped samples annealed at 800 and 1000°C are shown in Figures 5.1.7 and 5.1.8, respectively. The corresponding structural parameters are compared in Table 5.1.2.

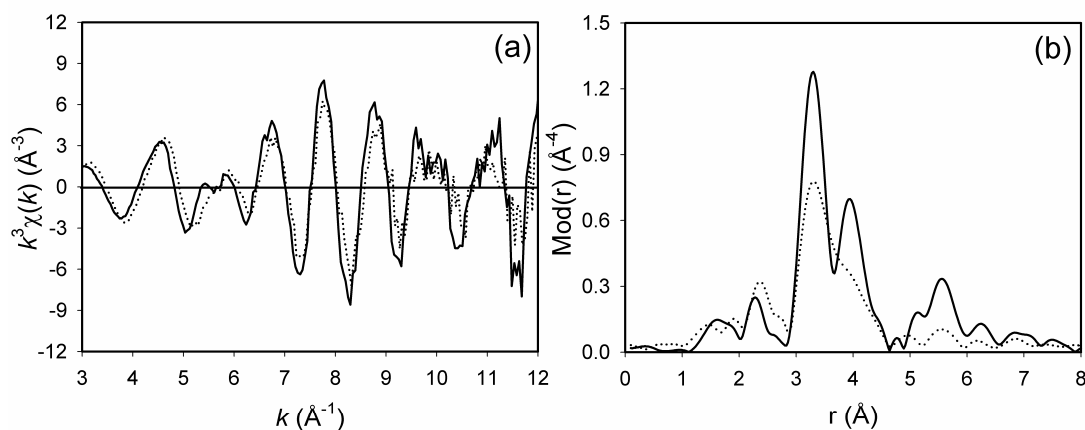


Figure 5.1.7. Experimental EXAFS functions (a) and their Fourier transform plots (b) of undoped (solid line) and Ca-doped (dotted line) LaCoO_3 annealed at 800°C measured at La K-edge.

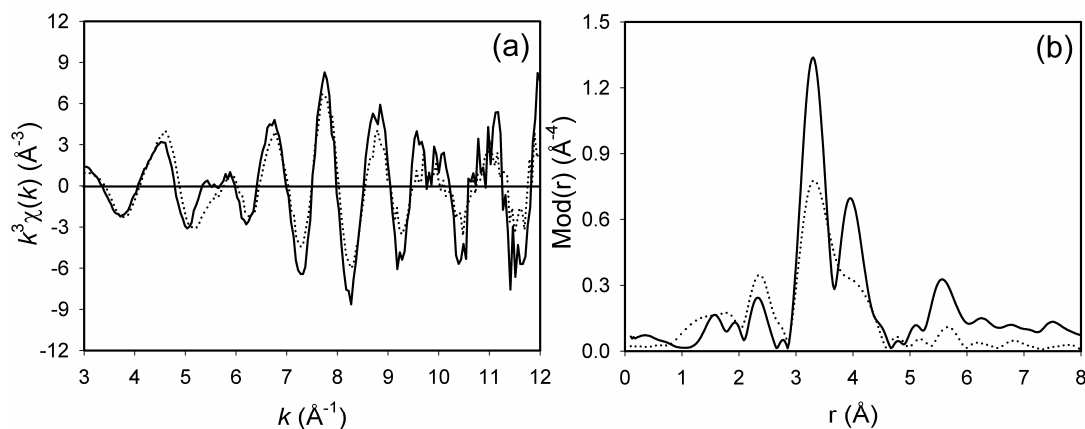


Figure 5.1.8. Experimental EXAFS functions (a) and their Fourier transform plots (b) of undoped (solid line) and Ca-doped (dotted line) LaCoO_3 annealed at 1000°C measured at La K-edge.

Table 5.1.2. EXAFS determined structural parameters of undoped and Ca-doped LaCoO₃ powders measured at the La K-edge.

Sample	A-Bs ^a	N ^b	r ^c [Å]	σ ^d [Å]	ΔE ₀ ^e [eV]	k-range [Å ⁻¹]	R-factor
Undoped LaCoO ₃ - xerogel	La-O	12.1 ± 1.2	2.58 ± 0.03	0.109 ± 0.011	21.76	3.0 - 10.0	38.09
Ca-doped LaCoO ₃ - xerogels	La-O	11.1 ± 1.1	2.55 ± 0.03	0.109 ± 0.011	22.65	3.0 - 12.0	59.17
Undoped LaCoO ₃ - annealed at 700°C	La-O	3.0 ± 0.3	2.42 ± 0.02	0.050 ± 0.005	24.75	3.0 - 12.0	43.50
	La-O	5.8 ± 0.6	2.60 ± 0.03	0.112 ± 0.011			
	La-Co	7.7 ± 1.2	3.31 ± 0.03	0.066 ± 0.010			
	La-La	5.7 ± 1.1	3.80 ± 0.04	0.080 ± 0.016			
Ca-doped LaCoO ₃ - annealed at 700°C	La-O	1.1 ± 0.8	2.39 ± 0.02	0.050 ± 0.005	23.83	3.0 - 12.0	42.77
	La-O	6.9 ± 0.4	2.51 ± 0.03	0.112 ± 0.012			
	La-Co	4.1 ± 0.6	3.30 ± 0.03	0.066 ± 0.010			
	La-La	1.9 ± 0.4	3.78 ± 0.04	0.080 ± 0.016			
Undoped LaCoO ₃ - annealed at 800°C	La-O	3.0 ± 0.3	2.42 ± 0.02	0.061 ± 0.006	23.97	3.0 - 12.0	38.73
	La-O	5.7 ± 0.6	2.60 ± 0.03	0.116 ± 0.012			
	La-Co	7.9 ± 1.2	3.31 ± 0.03	0.064 ± 0.010			
	La-La	5.9 ± 1.2	3.80 ± 0.04	0.078 ± 0.016			
Ca-doped LaCoO ₃ - annealed at 800°C	La-O	0.0 ± 0.0	-	-	25.28	3.0 - 12.0	33.19
	La-O	7.5 ± 1.2	2.47 ± 0.03	0.116 ± 0.012			
	La-Co	5.2 ± 0.8	3.30 ± 0.03	0.064 ± 0.009			
	La-La	3.8 ± 0.7	3.77 ± 0.04	0.078 ± 0.016			
Undoped LaCoO ₃ - annealed at 1000°C	La-O	3.1 ± 0.3	2.43 ± 0.02	0.060 ± 0.006	22.76	3.0 - 12.0	38.27
	La-O	5.1 ± 0.5	2.63 ± 0.03	0.112 ± 0.011			
	La-Co	7.9 ± 1.2	3.31 ± 0.03	0.061 ± 0.010			
	La-La	5.9 ± 1.2	3.80 ± 0.04	0.077 ± 0.016			
Ca-doped LaCoO ₃ - annealed at 1000°C	La-O	0.0 ± 0.0	-	-	25.90	3.0 - 12.0	33.58
	La-O	7.1 ± 0.7	2.48 ± 0.03	0.112 ± 0.011			
	La-Co	6.7 ± 1.0	3.30 ± 0.03	0.071 ± 0.010			
	La-La	4.4 ± 0.9	3.79 ± 0.04	0.084 ± 0.018			

^a absorber (A) - backscatterers (Bs), ^b coordination number N, ^c interatomic distance r, ^d Debye-Waller factor σ with its calculated deviation and ^e shift of the threshold energy ΔE₀.

In the case of undoped specimen, no significant changes in the local structure could be observed between the samples annealed at 800 and 1000°C and the structural parameters were in agreement with those of crystalline LaCoO₃ [5.1.14]. On the other hand, calcium doping had a strong influence on the local structure of both samples. In particular, the oxygen backscatterers were no longer observed as two different shells but as one shell, with a coordination number of about seven and at a distance of 2.48 Å, corresponding approximately to the average value of the first and second shell oxygen

distances in the undoped samples. These results also suppose a distortion in the perovskite structure due to calcium doping. Moreover, a reduction in the coordination number of cobalt and lanthanum backscatterers is observed in the case of both 800 and 1000°C treated Ca-doped samples with respect to LaCoO_3 powders, thus suggesting the formation of oxide-based cobalt compounds (Co_3O_4) and the La(III) substitution by Ca(II) ions in LaCoO_3 network.

The decrease in the coordination number was dependent on the annealing temperature and the variations could not be correlated with the crystallite size effects due to the same reasons mentioned earlier for the Co K-edge investigations. In general, the EXAFS studies at the La K-edge are in agreement with the observations at the Co K-edge.

5.1.2.3. XANES investigations

The XANES spectra measured at the Co K-edge are shown in Figure 5.1.9.

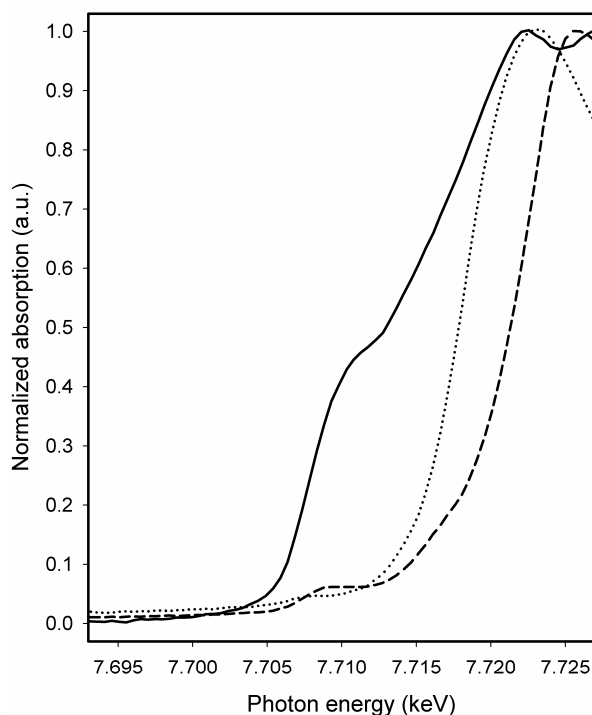


Figure 5.1.9. Comparison of the XANES regions of Ca-doped LaCoO_3 xerogel (dotted line) and Ca-doped LaCoO_3 annealed at 800°C (dashed line) along with cobalt metal foil (solid line).

The XANES region of both undoped and Ca-doped LaCoO_3 xerogels are alike and that of all the annealed samples are similar. Therefore, for clarity reasons, only

representative near edge regions of the Ca-doped LaCoO_3 xerogel and 800°C annealed sample are shown along with the cobalt metal foil, which was used as the energy calibration reference. In the annealed samples a small pre-peak could be observed, which could be attributed to $1s \rightarrow 3d$ electronic transition. This pre-peak is not evident in the case of the xerogels indicating differences in the coordination geometry around the cobalt atom when compared with that of the annealed samples. Moreover, the difference in the edge energy of the xerogels with respect to that of the annealed samples is unequivocally assigned to the expected changes in the oxidation states of cobalt between the xerogels (+2) and the annealed samples (+3). At the La K-edge, the XANES region does not show any remarkable features.

5.1.3. Mixed La–Sr–Co–Fe–O nanocomposites

The mixed La–Sr–Co–Fe–O nanocomposites were prepared by the work group of Dr. A. Glisenti, Department of Chemical Sciences, University of Padua [5.1.17]. The EXAFS measurements were performed on the samples **1** (La–Sr–Co–Fe–O – support) and **2** (Fe_2O_3 / La–Sr–Co–Fe–O – supported/support) at La L_{III} -edge at 5483 eV, Sr K-edge at 16105 eV, Co K-edge at 7709 eV and Fe K-edge at 7112 eV, in order to determine the local structure around each of the absorbing atoms and also to deduce the effect of Fe_2O_3 doping on La–Sr–Co–Fe–O mixed oxide. The La L_{III} -edge and Sr K-edge measurements were performed at the XAS beamline at ANKA, Karlsruhe and the Co and Fe K-edge measurements were performed at the beamline E4 at HASYLAB, Hamburg. The samples were measured at ambient conditions with Si(111) double crystal monochromator at the La, Co and Fe edges and with Si(311) double crystal monochromator at the Sr edge.

In the fitting procedure, the different parameters were determined by iterations for all the samples. Due to the similar backscattering behaviour of near neighbouring atoms (cobalt and iron), it was not possible to unequivocally identify the nature of the backscatterer, therefore in most of the cases, their contributions are mentioned together. Further, the crystal structure data of several pentary oxides containing lanthanum, strontium, cobalt and iron [5.1.18 - 5.1.20] revealed that lanthanum and strontium occupy same positions in the crystal lattice and have similar distances from the other atoms in the compound. Due to this reason, the heavier backscatterer (lanthanum) is

used in the evaluation, as the signals from the lighter backscatterer (strontium) could possibly be shadowed by the contributions from lanthanum.

5.1.3.1. EXAFS investigations at Co K-edge

The experimentally determined and theoretically simulated EXAFS functions in k space and their Fourier transforms in real space for samples **1** and **2** measured at Co K-edge are shown in Figures 5.1.10 and 5.1.11, respectively. The EXAFS determined structural parameters are tabulated in Table 5.1.3.

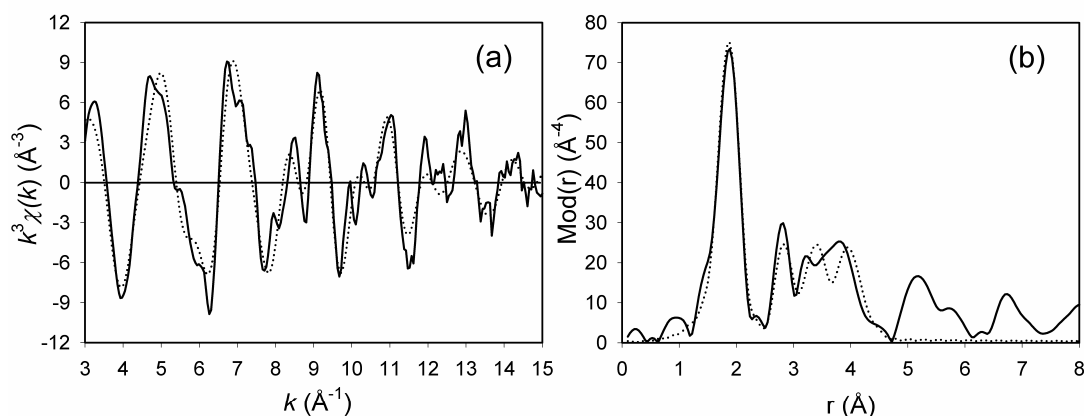


Figure 5.1.10. Experimental (solid line) and simulated (dotted line) EXAFS functions (a) and their corresponding Fourier transform plots (b) of sample **1** measured at the Co K-edge.

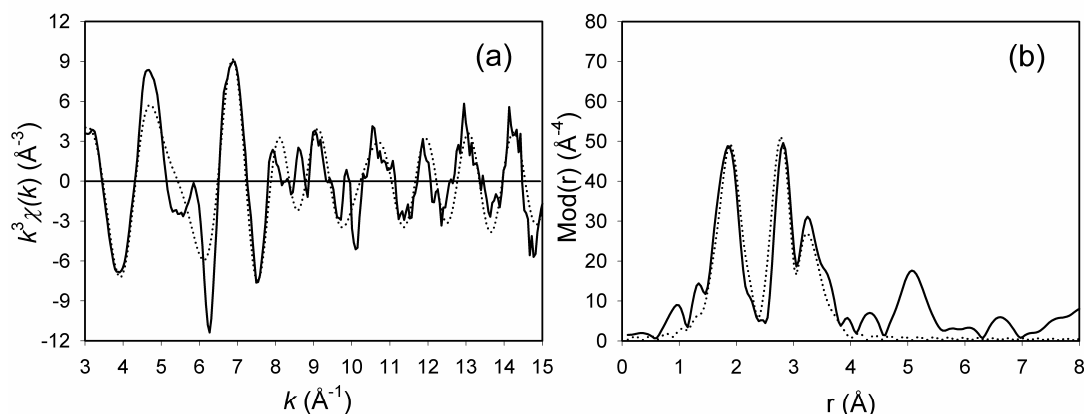


Figure 5.1.11. Experimental (solid line) and simulated (dotted line) EXAFS functions (a) and their corresponding Fourier transform plots (b) of sample **2** measured at the Co K-edge.

Table 5.1.3. Structural parameters of samples **1** and **2** measured at the Co K-edge.

Sample	A-Bs ^a	N ^b	r ^c [Å]	σ ^d [Å]	E_F ^e [eV]	k-range [Å ⁻¹]	R-factor
1	Co-O	6.2 ± 0.6	1.92 ± 0.02	0.074 ± 0.007	7.990	2.95 - 15.01	38.18
	Co-Co/Fe	2.1 ± 0.3	2.87 ± 0.03	0.089 ± 0.013			
	Co-La	1.6 ± 0.3	3.33 ± 0.04	0.077 ± 0.015			
	Co-Co/Fe	4.1 ± 0.8	3.92 ± 0.05	0.087 ± 0.017			
2	Co-O	6.2 ± 0.6	1.95 ± 0.02	0.097 ± 0.010	3.851	2.94 - 15.02	46.60
	Co-Co/Fe	2.5 ± 0.4	2.85 ± 0.03	0.050 ± 0.008			
	Co-Co/Fe	2.9 ± 0.4	3.00 ± 0.03	0.071 ± 0.011			
	Co-La	2.0 ± 0.3	3.34 ± 0.04	0.100 ± 0.015			

^a absorber (A) - backscatterers (Bs), ^b coordination number N, ^c interatomic distance r, ^d Debye-Waller factor σ with its calculated deviation and ^e Fermi energy E_F .

In the analysis of the EXAFS function, four-shell model could be fitted for sample **1**. The obtained structural parameters are in agreement with those of $\text{La}_{0.6}\text{Sr}_{0.4}\text{Co}_{0.9}\text{Fe}_{0.1}\text{O}_3$ [5.1.18]. Furthermore, the second shell cobalt distance of 2.87 Å corresponds to the Co–Co distance in Co_3O_4 [5.1.15] suggesting its formation as a possible by-product. Furthermore, the determined structural parameters are also in agreement with those of La_2CoO_4 [5.1.21] and hence its formation could also be supposed.

In sample **2**, the oxygen shell at 1.95 Å, the cobalt (iron) shell at 2.85 Å and the lanthanum shell at 3.34 Å could be fitted as like in the case of the sample **1**. In contrast to sample **1**, the cobalt (iron) shell occurring at 3.92 Å could not be detected as its contribution to the EXAFS function was insignificant. But, a new shell with cobalt (iron) backscatterers originated at about 3.00 Å distance, in agreement with the Co–Co distance of 3.01 Å, in CoO [5.1.22], suggesting that CoO could be formed during the process of Fe_2O_3 incorporation.

5.1.3.2. EXAFS investigations at Fe K-edge

The experimentally determined and theoretically simulated EXAFS functions in k space and their Fourier transforms in real space for samples **1** and **2** measured at Fe K-edge are shown in Figures 5.1.12 and 5.1.13, respectively and the resulting structural parameters are listed in Table 5.1.4. Due to the very low content of iron in the samples, the absorption jump was small and the obtained spectra could be evaluated only till 11 Å⁻¹ k -range.

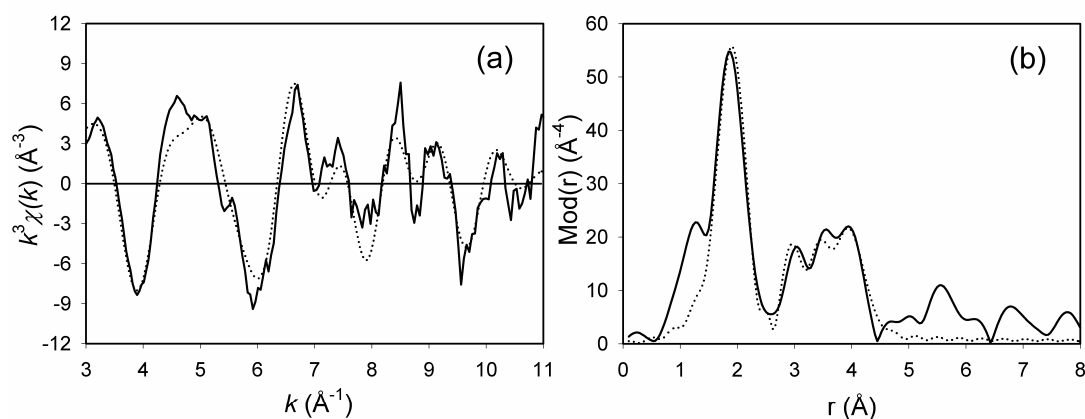


Figure 5.1.12. Experimental (solid line) and simulated (dotted line) EXAFS functions (a) and their corresponding Fourier transform plots (b) of sample **1** measured at the Fe K-edge.

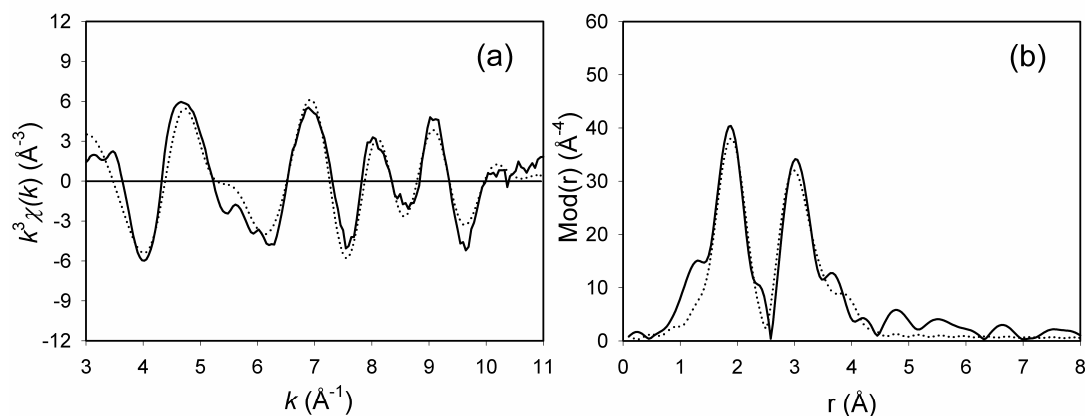


Figure 5.1.13. Experimental (solid line) and simulated (dotted line) EXAFS functions (a) and their corresponding Fourier transform plots (b) of sample **2** measured at the Fe K-edge.

Table 5.1.4. Structural parameters of samples **1** and **2** measured at the Fe K-edge.

Sample	A-Bs ^a	N ^b	r ^c [Å]	σ ^d [Å]	E _F ^e [eV]	k-range [Å ⁻¹]	R-factor
1	Fe-O	6.3 ± 0.6	1.96 ± 0.02	0.095 ± 0.010	6.687	2.96 - 11.02	37.43
	Fe-Co/Fe	1.8 ± 0.3	3.04 ± 0.03	0.092 ± 0.014			
	Fe-La	4.0 ± 0.8	3.26 ± 0.03	0.110 ± 0.022			
	Fe-Co/Fe	5.4 ± 1.4	3.94 ± 0.05	0.102 ± 0.026			
2	Fe-O	5.1 ± 0.5	1.96 ± 0.02	0.105 ± 0.011	9.261	2.96 - 11.00	34.04
	Fe-Fe	3.6 ± 0.5	2.92 ± 0.03	0.107 ± 0.016			
	Fe-Fe	1.6 ± 0.3	3.35 ± 0.03	0.084 ± 0.017			
	Fe-Fe	4.2 ± 1.1	3.64 ± 0.05	0.122 ± 0.031			

^a absorber (A) - backscatters (Bs), ^b coordination number N, ^c interatomic distance r, ^d Debye-Waller factor σ with its calculated deviation and ^e Fermi energy E_F.

The analysis of sample **1** shows the contributions from four shells and most of obtained values are in accordance with the structural parameters of $\text{La}_{0.6}\text{Sr}_{0.4}\text{Co}_{0.9}\text{Fe}_{0.1}\text{O}_3$ [5.1.18]. In the case of sample **2**, the structural parameters can be matched with those of Fe_2O_3 [5.1.22], in agreement with the XRD investigations [5.1.17]. The analysis reveals that the local environment around iron in sample **2** is similar to that of iron in Fe_2O_3 .

5.1.3.3. EXAFS investigations at La L_{III} -edge

The experimentally determined and theoretically simulated EXAFS functions in k space and their Fourier transforms in real space for samples **1** and **2** measured at La L_{III} -edge are shown in Figures 5.1.14 and 5.1.15, respectively and the obtained structural parameters are summarised in Table 5.1.5.

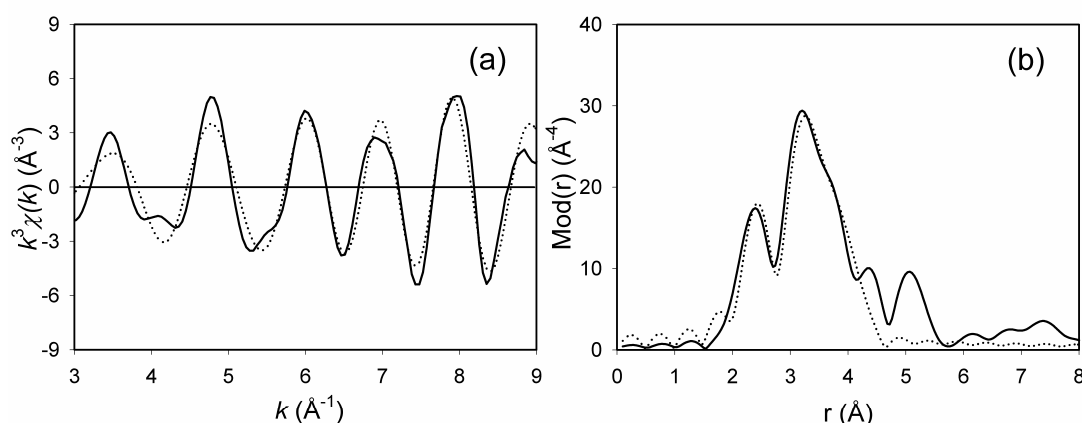


Figure 5.1.14. Experimental (solid line) and simulated (dotted line) EXAFS functions (a) and their corresponding Fourier transform plots (b) of sample **1** measured at La L_{III} -edge.

Table 5.1.5. Structural parameters of samples **1** and **2** measured at the La L_{III} -edge.

Sample	A-Bs ^a	N ^b	r ^c [Å]	σ ^d [Å]	E _F ^e [eV]	k-range [Å ⁻¹]	R-factor
1	La-O	11.4 ± 1.1	2.61 ± 0.02	0.118 ± 0.012	0.469	2.94 - 9.04	32.02
	La-Co/Fe	8.2 ± 1.2	3.32 ± 0.04	0.077 ± 0.012			
	La-La	5.1 ± 1.0	3.86 ± 0.05	0.084 ± 0.013			
2	La-O	10.2 ± 1.1	2.51 ± 0.02	0.122 ± 0.012	1.597	2.95 - 9.00	35.49
	La-Co/Fe	8.3 ± 1.2	3.34 ± 0.04	0.110 ± 0.017			
	La-La	3.6 ± 0.5	3.92 ± 0.05	0.095 ± 0.014			

^a absorber (A) - backscatterers (Bs), ^b coordination number N, ^c interatomic distance r, ^d Debye-Waller factor σ with its calculated deviation and ^e Fermi energy E_F.

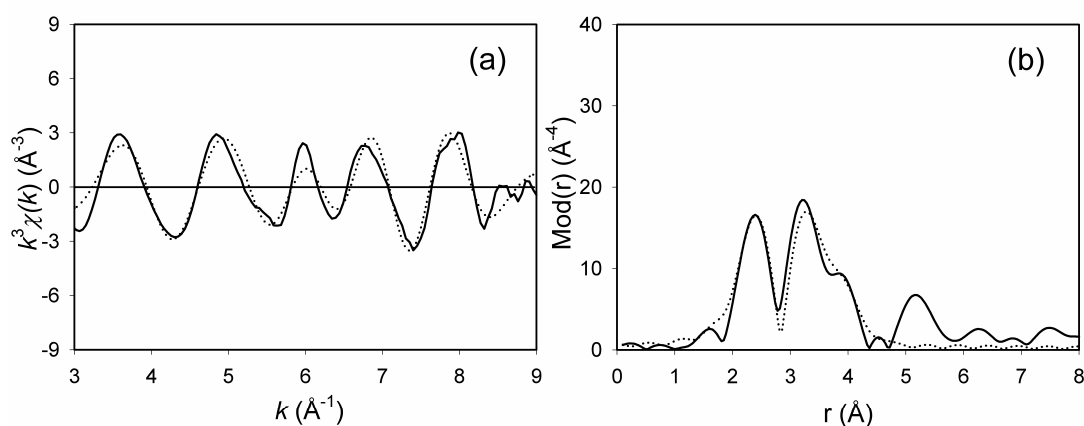


Figure 5.1.15. Experimental (solid line) and simulated (dotted line) EXAFS functions (a) and their corresponding Fourier transform plots (b) of sample **2** measured at La L_{III} -edge.

The EXAFS analysis at the La L_{III} -edge could be performed only till a k -range of 9 \AA^{-1} because of the interference from La L_{II} -edge at higher k -ranges. The first shell consisting of oxygen backscatterers could be determined at 2.61 \AA distance in sample **1** and at 2.51 \AA distance in sample **2**. The structural parameters of lanthanum cobaltite compounds [5.1.18 - 5.1.21] show the existence of three different La-O shells at distances of about 2.51 \AA , 2.72 \AA and 2.94 \AA . In the analysis, due to the short k -range, the oxygen backscatterers were no longer observed as different shells but as a single shell with a high Debye-Waller factor value. In accordance with the structural parameters of $\text{La}_{0.6}\text{Sr}_{0.4}\text{Co}_{0.9}\text{Fe}_{0.1}\text{O}_3$ [5.1.18] cobalt backscatterers are found at about 3.33 \AA distance in both the samples. Lanthanum backscatterers are observed at a distance of 3.86 \AA in the case of sample **1** and at 3.92 \AA in the case of sample **2**. The distance of 3.86 \AA is in accordance with the La-La distance in $\text{La}_{0.6}\text{Sr}_{0.4}\text{Co}_{0.9}\text{Fe}_{0.1}\text{O}_3$ [5.1.18] and the deviation observed in the sample **2** supposes a possible distortion in the perovskite structure due to Fe_2O_3 incorporation. The reduction in the coordination number of the backscatterers in sample **2** could probably be attributed to the formation of other lanthanum oxide-based compounds.

5.1.3.4. EXAFS investigations at Sr K-edge

The experimentally determined and theoretically simulated EXAFS functions in k space and their Fourier transforms in real space for samples **1** and **2** measured at Sr K-edge are shown in Figures 5.1.16 and 5.1.17, respectively.

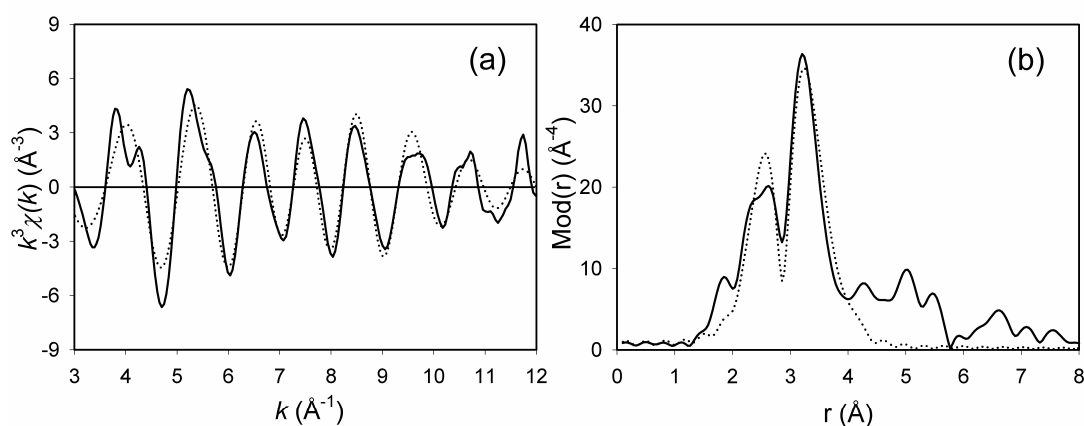


Figure 5.1.16. Experimental (solid line) and simulated (dotted line) EXAFS functions (a) and their corresponding Fourier transform plots (b) of sample **1** measured at the Sr K-edge.

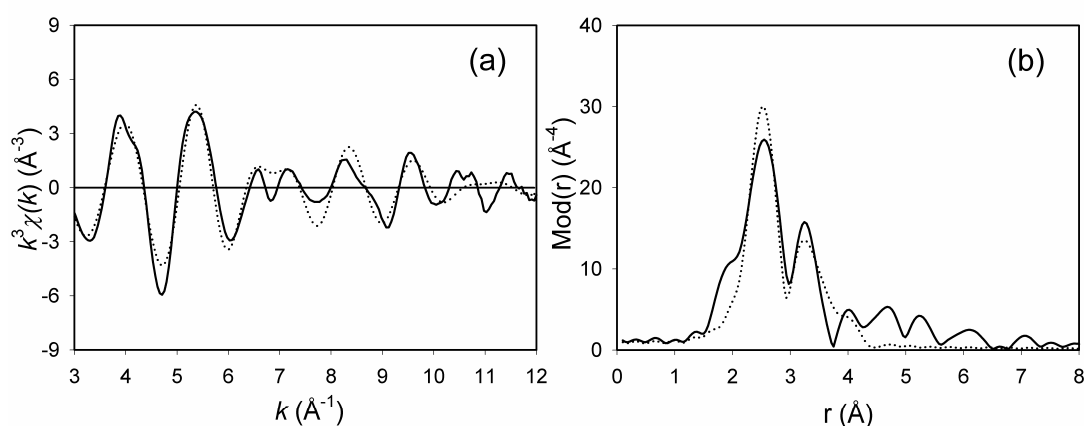


Figure 5.1.17. Experimental (solid line) and simulated (dotted line) EXAFS functions (a) and their corresponding Fourier transform plots (b) of sample **2** measured at the Sr K-edge.

Table 5.1.6. Structural parameters of samples **1** and **2** measured at the Sr K-edge.

Sample	A-Bs ^a	N ^b	r ^c [Å]	σ ^d [Å]	E _F ^e [eV]	k-range [Å ⁻¹]	R-factor
1	Sr-O	14.0 ± 1.4	2.60 ± 0.02	0.112 ± 0.011	8.484	2.95 - 12.04	38.55
	Sr-Co/Fe	8.0 ± 1.2	3.28 ± 0.04	0.089 ± 0.013			
	Sr-La	5.4 ± 0.8	3.74 ± 0.05	0.122 ± 0.018			
2	Sr-O	14.1 ± 1.4	2.59 ± 0.02	0.100 ± 0.010	10.21	2.95 - 12.01	37.52
	Sr-Co/Fe	6.8 ± 1.0	3.32 ± 0.04	0.122 ± 0.018			
	Sr-La	1.8 ± 0.3	3.92 ± 0.05	0.122 ± 0.018			

^a absorber (A) - backscatters (Bs), ^b coordination number N, ^c interatomic distance r, ^d Debye-Waller factor σ with its calculated deviation and ^e Fermi energy E_F.

The obtained structural parameters are given in Table 5.1.6. In the EXAFS analysis of samples **1** and **2** a three-shell model could be fitted. The first shell with about fourteen oxygen backscatterers is found at about 2.60 Å distance in both the samples in agreement with the average Sr–O distance in several strontium oxide based compounds [5.1.18, 5.1.20, 5.1.21]. The second shell is determined at about 3.30 Å in both the samples with cobalt (iron) backscatterers, in accordance with the distances of the corresponding backscatterers in $\text{La}_{0.6}\text{Sr}_{0.4}\text{Co}_{0.9}\text{Fe}_{0.1}\text{O}_3$ [5.1.18]. The third shell comprising of lanthanum backscatterers is determined at 3.74 Å in sample **1** and at 3.92 Å in sample **2**. This difference in the La–Sr distances suggests a possible distortion in the perovskite structure in sample **2** due to the incorporation of Fe_2O_3 . In comparison to sample **1**, the coordination number of the cobalt (iron) and lanthanum backscatterers is considerably decreased in sample **2**, suggesting the formation of other strontium oxide-based compounds. In general, it is observed that the EXAFS studies at the different edges complement each other.

5.1.4. Mixed Fe–Ti–O nanocomposites

The mixed Fe–Ti–O nanocomposites in different compositions were prepared by wet impregnation technique and the bulk mixed oxide of the same composition was obtained using the co-precipitation technique [5.1.23]. The samples were prepared by the work group of Dr. A. Glisenti, Department of Chemical Sciences, University of Padua. The influence of the preparation method and the iron doping on the structure of the mixed oxide were studied by means of XANES, EXAFS and Raman spectroscopic techniques. The XANES and EXAFS measurements at the Ti K-edge at 4966 eV were performed at the XAS beamline at ANKA, Karlsruhe. The samples were measured at ambient conditions with Si (111) double crystal monochromator and the energy calibration was performed using a titanium metal foil. Fluorescence mode EXAFS measurements were attempted at the Fe K-edge at 7112 eV at the beamline X1 at HASYLAB, Hamburg using a five-element germanium detector. These measurements did not yield reliable results due to the less fluorescence radiation emitted from the samples. This could be attributed to the very low iron content in the samples and also due to the high self-absorption of titanium in this energy range.

5.1.4.1. XANES investigations

The XANES spectra of two supported oxides ($[\text{Fe}/\text{Ti}]_{\text{nominal}} = 0.01$ and 0.09) and the bulk mixed oxide along with the reference TiO_2 polymorphs measured at the Ti K-edge are shown in Figure 5.1.18. For clarity reasons, the spectra are arranged one above the other. The XANES region of the supported and bulk mixed oxide samples are all similar and resembled that of rutile TiO_2 . All the spectra show two clearly distinct pre-peaks, which could be assigned to $1s \rightarrow 3d$ electronic transition.

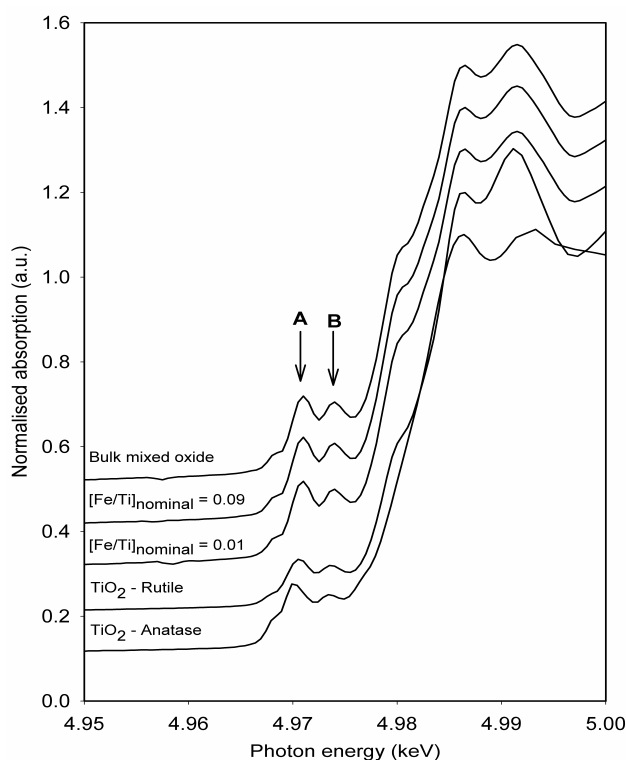


Figure 5.1.18. XANES region of two supported oxides ($[\text{Fe}/\text{Ti}]_{\text{nom}} = 0.01$ and 0.09) and the bulk mixed oxide along with the reference TiO_2 polymorphs measured at the Ti K-edge.

The rutile structure has the point group D_{2h} (mmm) and the octahedral coordination around the titanium is distorted. There exists a symmetry scheme correlation between O_h ($m\bar{3}m$) and D_{2h} (mmm) and the symmetry lowering ($O_h \rightarrow D_{2h}$) gives rise to the splitting on t_{2g} and e_g levels. This splitting is the crystal-field splitting, shown as A and B in Figure 5.1.18. Hence the pre-peak A could be assigned to $1s \rightarrow t_{2g}$ electronic transition and the pre-peak B could be assigned to $1s \rightarrow e_g$ electronic transition [5.1.24].

5.1.4.2. EXAFS investigations

The experimentally determined and theoretically simulated EXAFS functions in k space and their Fourier transforms in real space for the two supported oxides and the bulk mixed oxide measured at the Ti K-edge are shown in Figure 5.1.19.

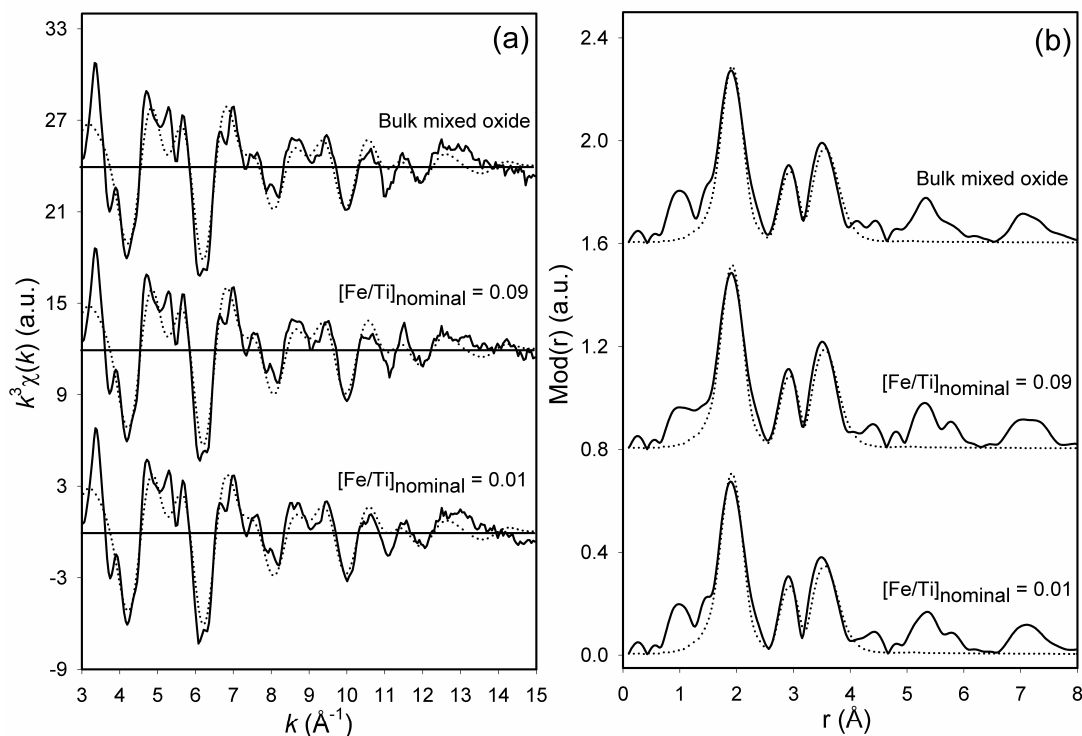


Figure 5.1.19. Experimental (solid line) and calculated (dotted line) EXAFS functions (a) and their corresponding Fourier transform plots (a) of the two supported oxides and the bulk mixed oxide measured at the Ti K-edge.

In the EXAFS data analysis, the amplitude factor was set to a value of 0.4 and the other parameters were determined by iterations. The EXAFS spectra of the two supported oxides and the bulk mixed oxide are similar to each other and in the analysis of the experimental k^3 weighed $\chi(k)$ function, a three-shell model could be fitted for all the three samples. The structural parameters are summarised in Table 5.1.7. The first shell consisting of about six oxygen backscatterers is found at about 1.95 \AA distance, the second shell having about two titanium backscatterers is determined at a distance of about 2.96 \AA and the third shell with about eight titanium backscatterers was fitted at about 3.56 \AA distance. These parameters are in good agreement with structural parameters of rutile TiO_2 [5.1.25].

Table 5.1.7. Structural parameters of Fe–Ti–O mixed oxides measured at the Ti K-edge.

Sample	A-Bs ^a	N ^b	r ^c [Å]	σ ^d [Å]	ΔE ₀ ^e [eV]	k-range [Å ⁻¹]	R-factor
[Fe/Ti] _{nom} = 0.01	Ti-O	6.3 ± 0.6	1.94 ± 0.02	0.084 ± 0.008	19.13	3.0 - 15.0	47.22
	Ti-Ti	1.9 ± 0.2	2.96 ± 0.03	0.084 ± 0.008			
	Ti-Ti	7.1 ± 0.8	3.55 ± 0.04	0.102 ± 0.011			
[Fe/Ti] _{nom} = 0.09	Ti-O	6.2 ± 0.6	1.95 ± 0.02	0.081 ± 0.008	18.74	3.0 - 15.0	44.81
	Ti-Ti	2.0 ± 0.2	2.96 ± 0.03	0.084 ± 0.008			
	Ti-Ti	7.3 ± 0.8	3.56 ± 0.04	0.100 ± 0.011			
Bulk mixed oxide	Ti-O	6.1 ± 0.6	1.95 ± 0.02	0.084 ± 0.008	18.64	3.0 - 15.0	47.51
	Ti-Ti	2.0 ± 0.2	2.97 ± 0.03	0.084 ± 0.008			
	Ti-Ti	7.5 ± 0.8	3.56 ± 0.04	0.102 ± 0.011			
TiO ₂ [5.1.25]	Ti-O	6	1.96	-	-	-	-
	Ti-Ti	2	2.96	-			
	Ti-Ti	8	3.57	-			

^a absorber (A) - backscatterers (Bs), ^b coordination number N, ^c interatomic distance r, ^d Debye-Waller factor σ with its calculated deviation and ^e shift of the threshold energy ΔE₀.

The results reveal that iron doping does not lead to significant local structural changes in the mixed oxides at the Ti K-edge. The Ti-Fe distance could not be determined from the EXAFS analysis due to the very low iron content in the mixed oxides and the signals from oxygen and titanium dominate the spectra.

5.1.4.3. Raman spectroscopic investigations

Raman studies on rutile TiO₂ were performed by many researchers and reported in the literature [5.1.26, 5.1.27]. The Raman spectra of two supported oxides and the bulk mixed oxide are shown in Figure 5.1.20. All the spectra were normalized to the reference peak at 84 cm⁻¹. The spectra from all of the three mixed oxides are in agreement with the well-known structure of rutile TiO₂. The peak at 143 cm⁻¹ could be ascribed to the B_{1g} mode of symmetry, the broad peak at about 235 cm⁻¹ could be attributed to the presence of two phonon bands, the peak at 450 cm⁻¹ is due to E_g symmetry mode and the peak at 612 cm⁻¹ is due to A_{1g} mode of symmetry [5.1.28]. The other peak due to B_{2g} mode of symmetry at 826 cm⁻¹ could not be clearly observed from the spectra in all the three mixed oxides [5.1.26]. The iron doping does not significantly influence the spectra and only the modes of symmetry of rutile TiO₂ could be observed in all the samples.

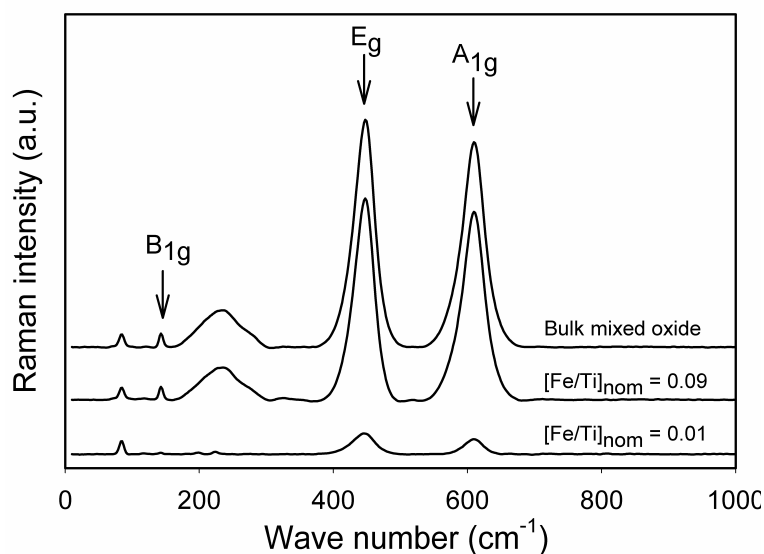


Figure 5.1.20. Raman spectra of two supported oxides and the bulk mixed oxide.

The intensity variation of the peaks in the different mixed oxide samples could be due to various factors like particle size variations, difference in elemental compositions, crystallization effects, phonon confinement effects, non-stoichiometry due to oxygen deficiencies and disorder induced by minor phases [5.1.29].

5.1.5. Mixed W–Ce–O nanocomposites

The mixed W–Ce–O nanocomposites in different compositions with varying mass percentages of different elements, were prepared by wet impregnation of CeO_2 powder with an aqueous solution containing increasing quantity of $(\text{NH}_4)_6(\text{W}_{12}\text{O}_{39})\cdot\text{H}_2\text{O}$ and calcined at 500°C in air [5.1.30], by the work group of Dr. A. Glisenti, Department of Chemical Sciences, University of Padua. The EXAFS measurements were performed on the samples at Ce K-edge at 40443 eV at the beamline X1 at HASYLAB, Hamburg. The samples were measured at ambient conditions with Si(511) double crystal monochromator and energy calibration was monitored by using crystalline ceria. In the EXAFS analysis, the amplitude factor was set to a value of 0.4 and the other parameters were determined by iterations.

5.1.5.1. EXAFS investigations

The experimentally determined and theoretically simulated EXAFS functions in k space and their Fourier transforms in real space for the different WO_3/CeO_2 samples measured at the Ce K-edge are shown in Figure 5.1.21. The corresponding structural parameters are summarised in Table 5.1.8.

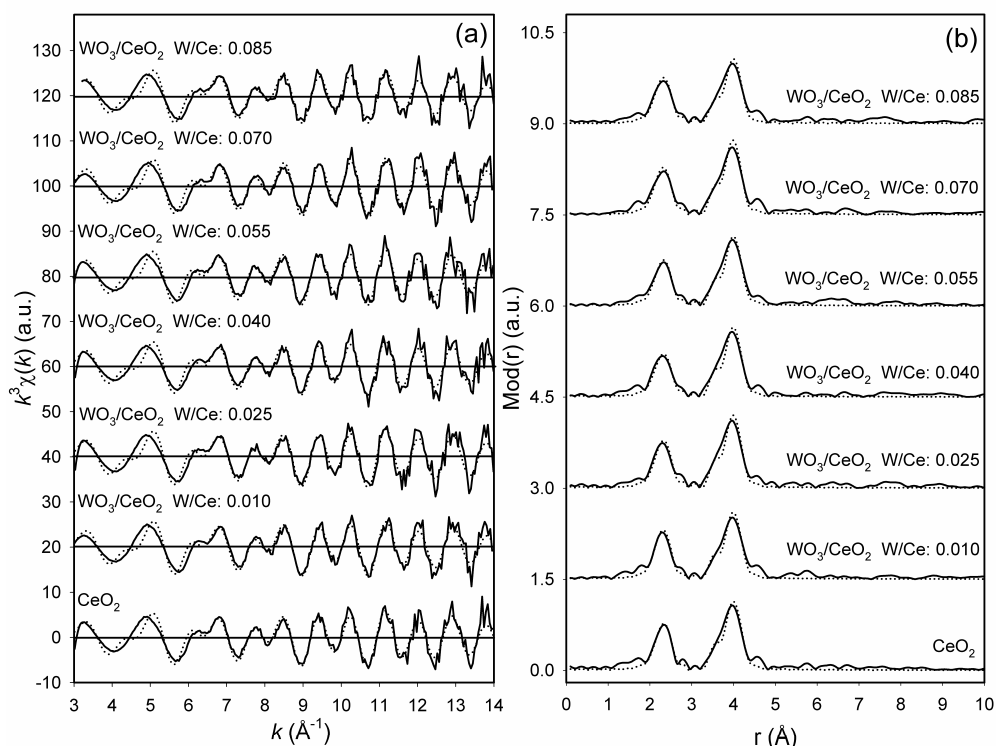


Figure 5.1.21. Experimental (solid line) and calculated (dotted line) EXAFS functions (a) and their corresponding Fourier transform plots (b) of WO_3/CeO_2 samples measured at Ce K-edge.

Table 5.1.8. Structural parameters of WO_3/CeO_2 samples measured at the Ce K-edge.

Sample	A-Bs ^a	N ^b	r ^c [Å]	σ ^d [Å]	ΔE_0 ^e [eV]	k-range [Å ⁻¹]	R-factor
CeO ₂	Ce-O	8.2 ± 0.8	2.35 ± 0.02	0.074 ± 0.007	24.93	3.0 - 14.0	34.35
	Ce-Ce	10.6 ± 1.5	3.84 ± 0.04	0.074 ± 0.010			
WO ₃ /CeO ₂ W/Ce:0.010	Ce-O	8.4 ± 0.8	2.33 ± 0.02	0.074 ± 0.007	21.41	3.0 - 14.0	35.71
	Ce-Ce	10.7 ± 1.5	3.83 ± 0.04	0.077 ± 0.011			
WO ₃ /CeO ₂ W/Ce:0.025	Ce-O	8.7 ± 0.9	2.34 ± 0.02	0.077 ± 0.008	25.22	3.0 - 14.0	34.38
	Ce-Ce	10.8 ± 1.5	3.83 ± 0.04	0.074 ± 0.010			
WO ₃ /CeO ₂ W/Ce:0.040	Ce-O	8.5 ± 0.9	2.34 ± 0.02	0.081 ± 0.008	25.18	3.0 - 14.0	36.60
	Ce-Ce	10.7 ± 1.5	3.84 ± 0.04	0.074 ± 0.010			
WO ₃ /CeO ₂ W/Ce:0.055	Ce-O	8.5 ± 0.9	2.34 ± 0.02	0.077 ± 0.008	24.24	3.0 - 14.0	37.12
	Ce-Ce	10.8 ± 1.5	3.84 ± 0.04	0.074 ± 0.010			
WO ₃ /CeO ₂ W/Ce:0.070	Ce-O	8.8 ± 0.9	2.33 ± 0.02	0.077 ± 0.008	21.14	3.0 - 14.0	34.25
	Ce-Ce	10.7 ± 1.5	3.83 ± 0.04	0.074 ± 0.010			
WO ₃ /CeO ₂ W/Ce:0.085	Ce-O	8.7 ± 0.9	2.33 ± 0.02	0.077 ± 0.008	25.66	3.0 - 14.0	35.61
	Ce-Ce	10.5 ± 1.5	3.83 ± 0.04	0.077 ± 0.011			

^a absorber (A) - backscatters (Bs), ^b coordination number N, ^c interatomic distance r, ^d Debye-Waller factor σ with its calculated deviation and ^e shift of the threshold energy ΔE_0 .

The EXAFS spectra of the different WO_3/CeO_2 samples having different doping compositions of WO_3 are similar to each other and are in good agreement with the structure of crystalline CeO_2 [5.1.31]. In the analysis of the EXAFS function, a two-shell model could be fitted for all the WO_3/CeO_2 samples. The first shell consisting of about eight oxygen backscatterers at a distance of about 2.34 Å and the second shell having about twelve cerium backscatterers at a distance of about 3.83 Å are determined. Moreover, the Ce–W distance could not be determined from the EXAFS analysis owing to the very low content of the dopant. It is interesting to note that the WO_3 doping does not modify the local structure of CeO_2 . Thus it can be deduced that the structure of CeO_2 remains stable even after doping with WO_3 .

5.1.5.2. Raman spectroscopic investigations

Raman spectroscopic studies on pure and doped CeO_2 materials were performed by various researchers and reported in literature [5.1.32-5.1.34]. The Raman spectra of different WO_3/CeO_2 samples are shown in Figure 5.1.22.

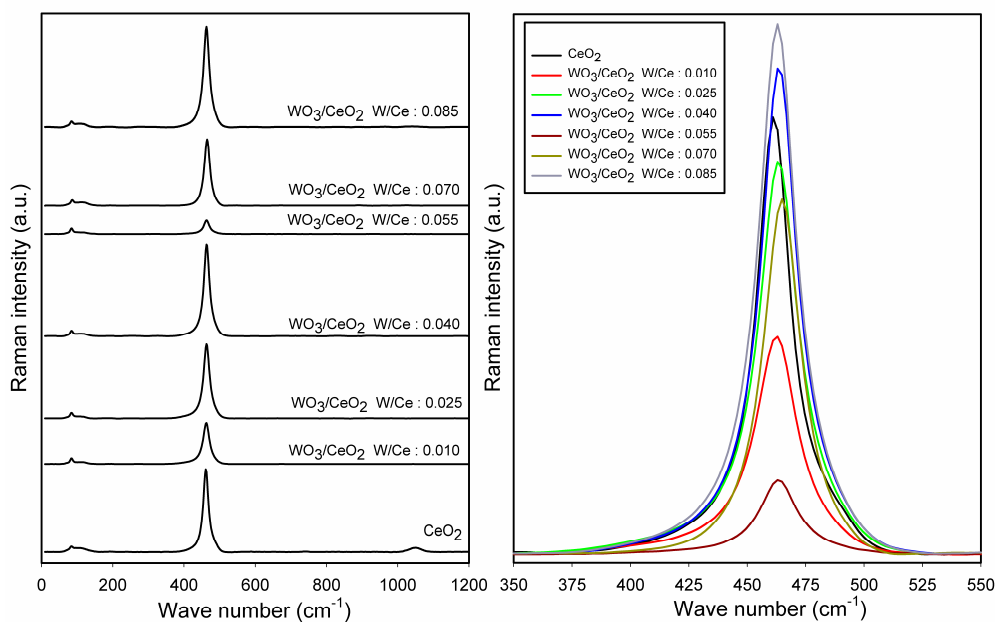


Figure 5.1.22. Raman spectra of different WO_3/CeO_2 samples.

All the spectra were normalized to the reference peak at 83 cm^{-1} . The spectra of all the different WO_3/CeO_2 samples are in agreement with that of crystalline CeO_2 . The characteristic peaks corresponding to the Raman allowed modes of WO_3 could not be observed due to the very low concentration of the dopant. The main band around $462\text{--}468\text{ cm}^{-1}$ is due to the first-order peak of F_{2g} symmetry of the fluorite type lattice and

can be viewed as a symmetric breathing mode of the oxygen atoms around cerium ions [5.1.34 - 5.1.36]. It can be observed that the different WO_3/CeO_2 samples do not exhibit any linear trend based on the concentration of the dopant. The Raman shift observed between the different WO_3/CeO_2 samples can be attributed to differences in the lattice constant due to particle size variations [5.1.34].

The change in the line width and intensity observed in the main band can be primarily attributed to the presence of oxygen vacancies [5.1.34,5.1.35], although effects of phonon confinement and inhomogeneous strain, which are associated with compositional or redox heterogeneities, can also contribute to a small extent to this observation [5.1.34]. The main factors that affect the frequency of the F_{2g} mode are the lattice strain and the presence of vacancies while phonon confinement only plays a limited role.

5.1.6. Mixed Ce–Y–Zr–O nanocomposites

The mixed Ce–Y–Zr–O nanocomposites in different compositions with varying mass percentages of different elements, were prepared by wet impregnation of yttria stabilised zirconia (YSZ) powder with an aqueous solution containing increasing quantity of $\text{Ce}(\text{NO}_3)_3 \cdot 6\text{H}_2\text{O}$ and calcined at 250°C in air [5.1.37], by the work group of Dr. A. Glisenti, Department of Chemical Sciences, University of Padua.

The EXAFS measurements were performed on the samples at Y and Zr K-edges at 17038 eV and 17998 eV, respectively, at the beamline X1 at HASYLAB, Hamburg. The samples were measured with Si(311) double crystal monochromator at ambient conditions and energy calibration was performed using zirconium metal foil at both Y and Zr edges. In the EXAFS data analysis, the amplitude factor was set to a value of 0.8 and the other parameters were determined by iterations. Due to the similar backscattering behaviour of near neighbouring atoms (yttrium and zirconium), it was not possible to unambiguously identify the nature of the backscatterer, therefore in all the cases, their contributions are mentioned together.

5.1.6.1. EXAFS investigations at Y K-edge

The experimentally determined and theoretically simulated EXAFS functions in k space and their Fourier transforms in real space for the different CeO_2/YSZ samples with low and high concentration of CeO_2 , measured at the Y K-edge are shown in

Figures 5.1.22 and 5.1.23, respectively. The corresponding structural parameters are listed in Table 5.1.9.

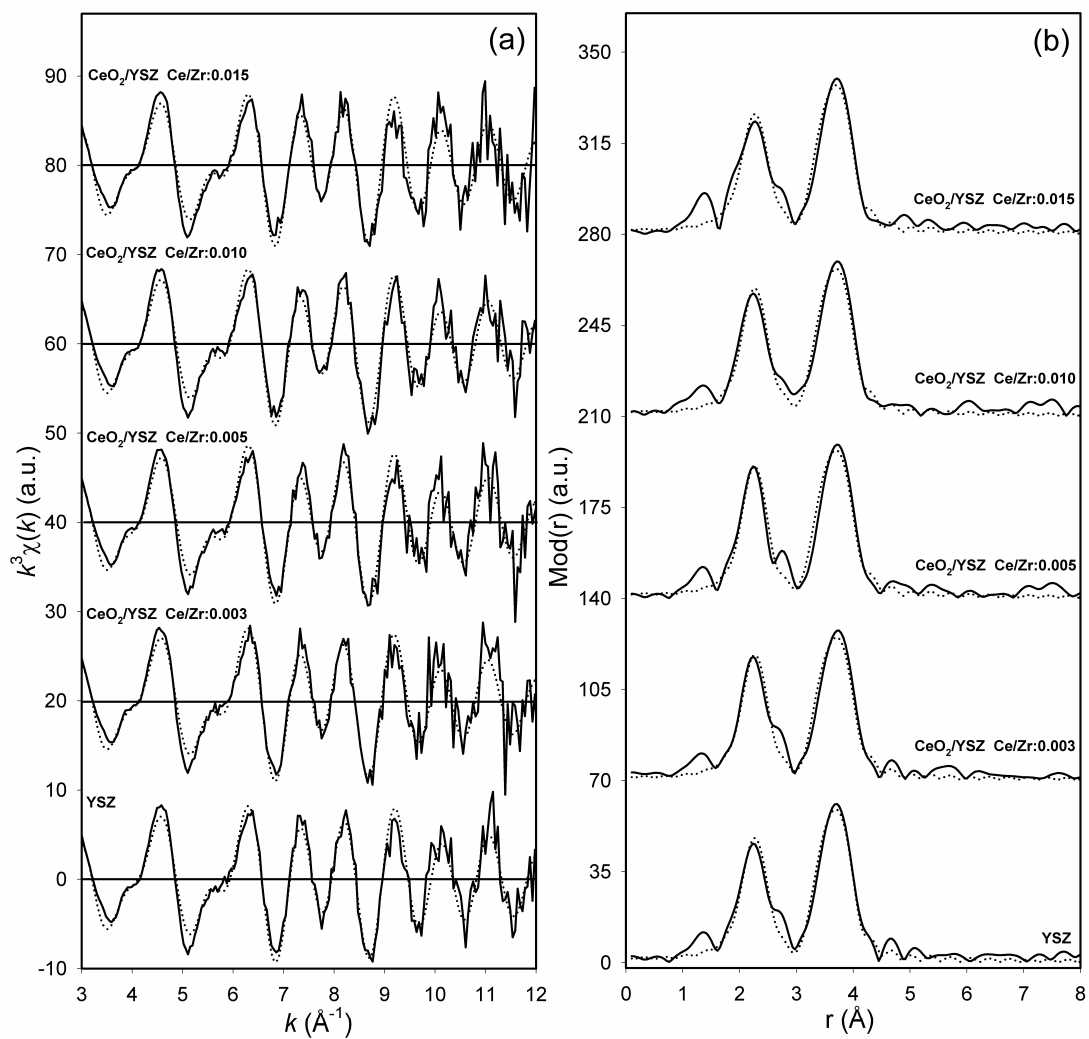


Figure 5.1.22. Experimental (solid line) and calculated (dotted line) EXAFS functions (a) and their Fourier transform plots (b) of YSZ samples with low CeO_2 doping.

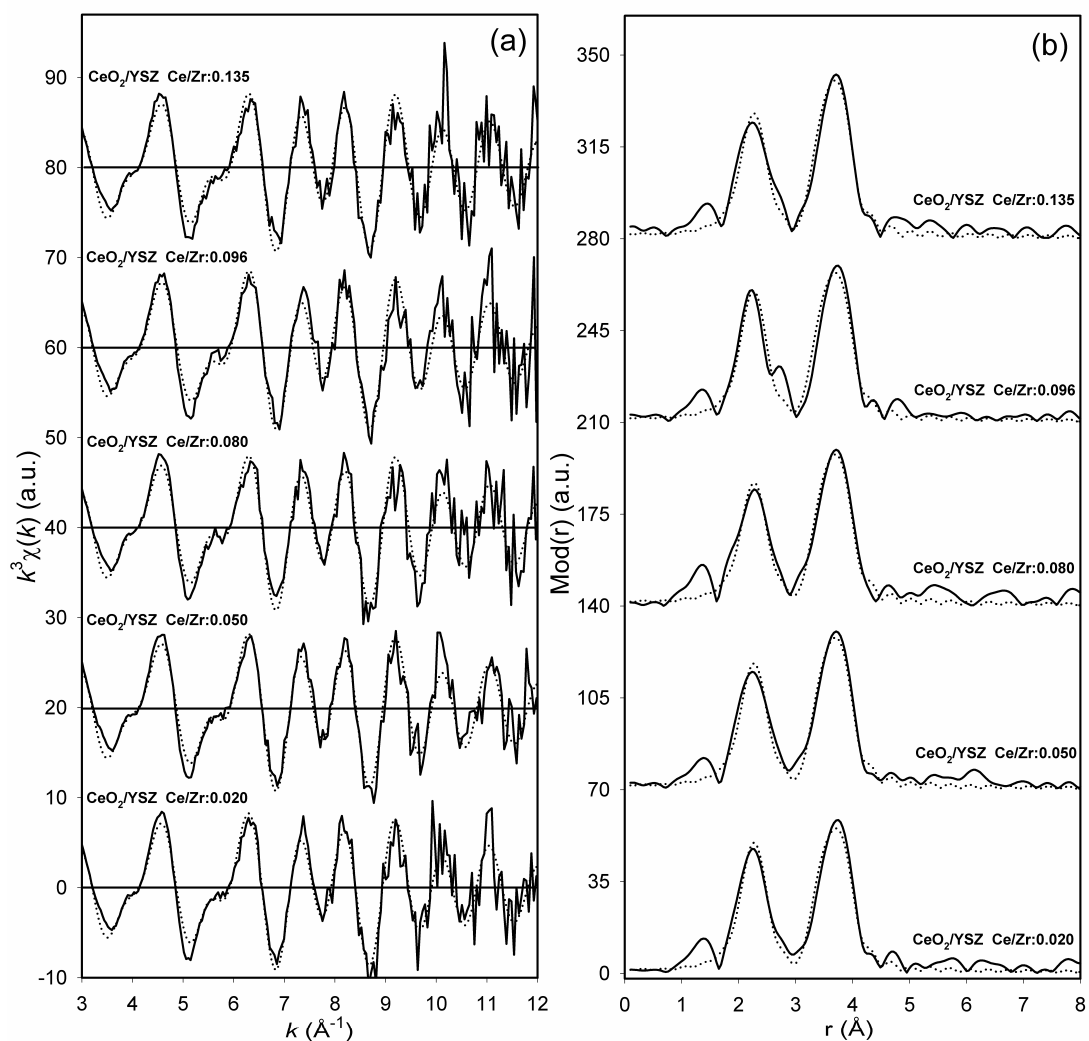


Figure 5.1.23. Experimental (solid line) and calculated (dotted line) EXAFS functions (a) and their Fourier transform plots (b) of YSZ samples with high CeO₂ doping.

EXAFS studies were performed on YSZ by several researchers and reported in literature [5.1.38 - 5.1.42]. The EXAFS spectra of the different CeO₂/YSZ samples having different doping compositions of CeO₂ are similar to each other and the obtained parameters are in good agreement with the structural parameters reported for YSZ in literature, wherein Y being an oversized cation prefers eightfold oxygen coordination, leaving the oxygen vacancies to the Zr cations [5.1.39, 5.1.41].

Table 5.1.9. Structural parameters of CeO₂/YSZ samples measured at the Y K-edge.

Sample	A-Bs ^a	N ^b	r ^c [Å]	σ ^d [Å]	E _F ^e [eV]	k-range [Å ⁻¹]	R-factor
YSZ	Y-O	8.5 ± 0.9	2.32 ± 0.02	0.097 ± 0.010	9.197	2.97 - 12.03	27.47
	Y-Y/Zr	11.9 ± 1.8	3.61 ± 0.05	0.097 ± 0.015			
CeO ₂ /YSZ Ce/Zr:0.003	Y-O	8.4 ± 0.8	2.32 ± 0.02	0.097 ± 0.010	9.094	2.96 - 12.02	32.34
	Y-Y/Zr	12.0 ± 1.8	3.61 ± 0.05	0.100 ± 0.015			
CeO ₂ /YSZ Ce/Zr:0.005	Y-O	8.1 ± 0.8	2.31 ± 0.02	0.092 ± 0.009	9.301	2.97 - 12.03	31.60
	Y-Y/Zr	12.0 ± 1.8	3.61 ± 0.05	0.097 ± 0.015			
CeO ₂ /YSZ Ce/Zr:0.010	Y-O	8.5 ± 0.9	2.32 ± 0.02	0.095 ± 0.010	9.164	2.97 - 12.03	28.99
	Y-Y/Zr	12.1 ± 1.8	3.61 ± 0.05	0.100 ± 0.015			
CeO ₂ /YSZ Ce/Zr:0.015	Y-O	8.6 ± 0.9	2.33 ± 0.02	0.100 ± 0.010	8.578	2.97 - 12.02	32.04
	Y-Y/Zr	11.8 ± 1.8	3.61 ± 0.05	0.097 ± 0.015			
CeO ₂ /YSZ Ce/Zr:0.020	Y-O	8.5 ± 0.9	2.32 ± 0.02	0.095 ± 0.010	9.100	2.96 - 12.02	33.87
	Y-Y/Zr	12.0 ± 1.8	3.62 ± 0.05	0.100 ± 0.015			
CeO ₂ /YSZ Ce/Zr:0.050	Y-O	8.6 ± 0.9	2.32 ± 0.02	0.097 ± 0.010	9.417	2.98 - 12.03	29.63
	Y-Y/Zr	12.1 ± 1.8	3.61 ± 0.05	0.097 ± 0.015			
CeO ₂ /YSZ Ce/Zr:0.080	Y-O	8.5 ± 0.9	2.33 ± 0.02	0.097 ± 0.010	8.553	2.97 - 12.02	34.93
	Y-Y/Zr	11.9 ± 1.8	3.61 ± 0.05	0.097 ± 0.015			
CeO ₂ /YSZ Ce/Zr:0.096	Y-O	8.2 ± 0.9	2.31 ± 0.02	0.095 ± 0.010	9.317	2.97 - 12.03	36.52
	Y-Y/Zr	11.9 ± 1.8	3.61 ± 0.05	0.097 ± 0.015			
CeO ₂ /YSZ Ce/Zr:0.135	Y-O	8.6 ± 0.9	2.32 ± 0.02	0.100 ± 0.010	8.703	2.98 - 12.02	34.26
	Y-Y/Zr	11.8 ± 1.8	3.61 ± 0.05	0.095 ± 0.014			

^a absorber (A) - backscatterers (Bs), ^b coordination number N, ^c interatomic distance r, ^d Debye-Waller factor σ with its calculated deviation and ^e Fermi energy E_F.

In the analysis of the EXAFS function, a two-shell model could be fitted for all the samples measured at the Y K-edge. The first shell consisting of about eight oxygen backscatterers at a distance of about 2.32 Å and the second shell having about twelve yttrium (zirconium) backscatterers at a distance of about 3.61 Å are determined. In addition, the Y-Ce distance could not be determined from the EXAFS analysis owing to the very low content of the dopant. The EXAFS analysis reveals that CeO₂ doping does not significantly alter the local environment around yttrium atoms.

5.1.6.2. EXAFS investigations at Zr K-edge

The experimentally determined and theoretically simulated EXAFS functions in *k* space and their Fourier transforms in real space for the different CeO₂/YSZ samples

with low and high concentration of CeO_2 , measured at the Zr K-edge are shown in Figures 5.1.24 and 5.1.25, respectively. The obtained structural parameters are tabulated in Table 5.1.10.

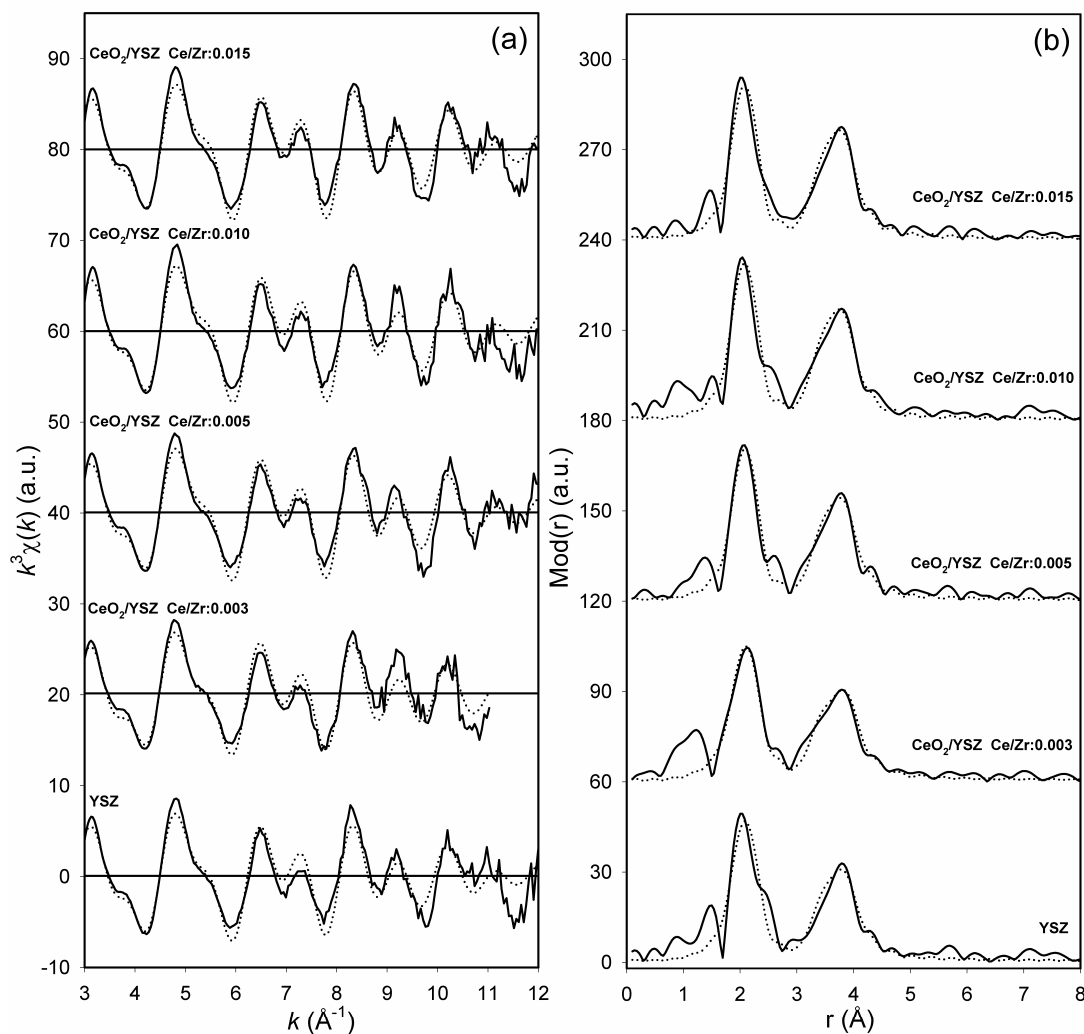


Figure 5.1.24. Experimental (solid line) and calculated (dotted line) EXAFS functions (a) and their Fourier transform plots (b) of YSZ samples with low CeO_2 doping.

Similar to the results obtained from the Y K-edge analysis, the EXAFS spectra of the different CeO_2/YSZ samples are alike and the structural parameters are in accordance with those reported in literature, wherein Zr has sevenfold coordination causing a distortion of the cubic fluorite structure [5.1.39, 5.1.41].

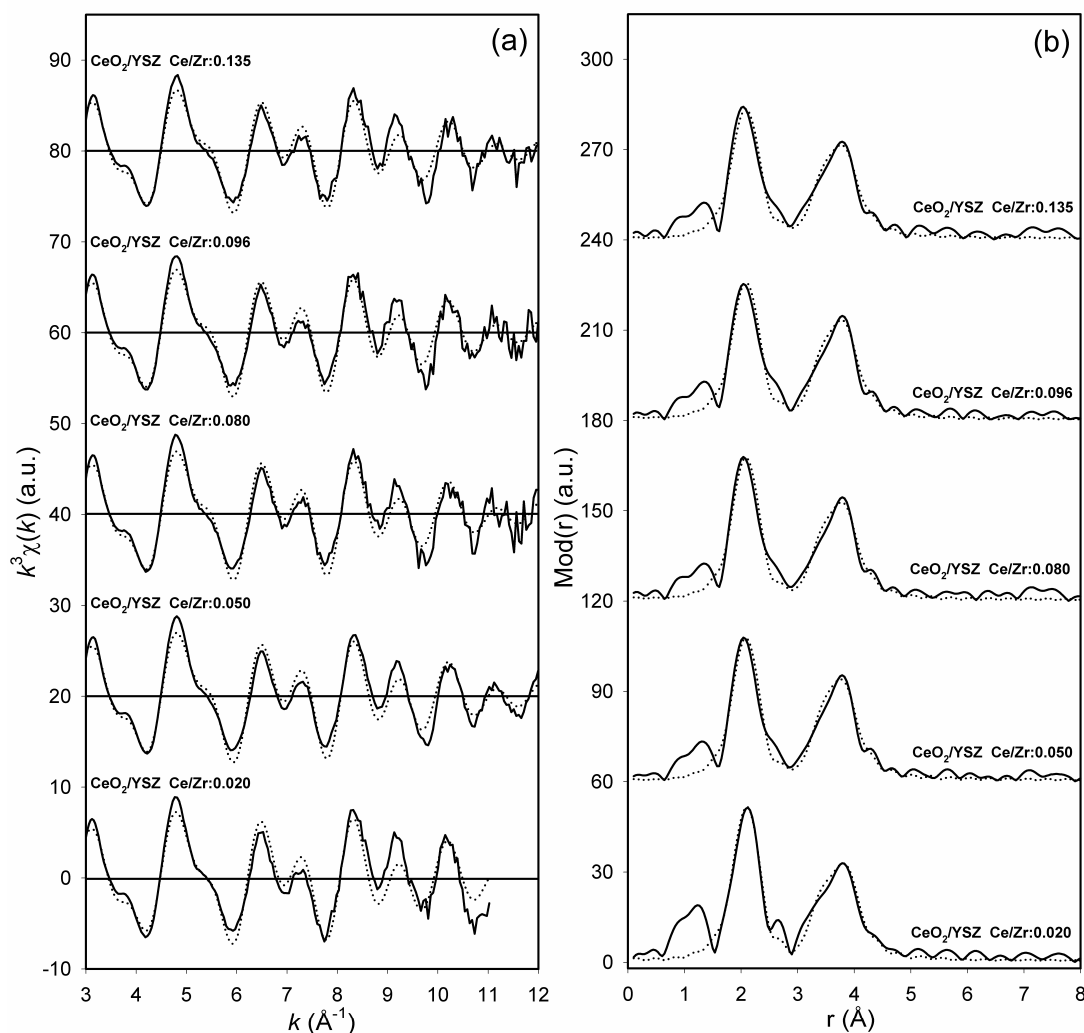


Figure 5.1.25. Experimental (solid line) and calculated (dotted line) EXAFS functions (a) and their Fourier transform plots (b) of YSZ samples with high CeO₂ doping.

In the analysis, a two-shell model can be used for all the samples, in this case as well. The first shell could be fitted at about 2.15 \AA with seven oxygen backscatters and the second shell could be found at about 3.58 \AA with twelve zirconium (yttrium) backscatters. Furthermore, the Zr-Ce distance could not be determined from the EXAFS analysis owing to the very low content of the dopant. The results show that CeO₂ doping does not significantly modify the local structure around the zirconium atoms.

Table 5.1.10. Structural parameters of CeO₂/YSZ samples measured at the Zr K-edge.

Sample	A-Bs ^a	N ^b	r ^c [Å]	σ ^d [Å]	E _F ^e [eV]	k-range [Å ⁻¹]	R-factor
YSZ	Zr-O Zr-Zr/Y	7.3 ± 0.7 11.8 ± 1.8	2.15 ± 0.02 3.58 ± 0.05	0.100 ± 0.010 0.118 ± 0.017	10.51	2.98 - 12.00	37.43
CeO ₂ /YSZ Ce/Zr:0.003	Zr-O Zr-Zr/Y	7.2 ± 0.7 11.5 ± 1.7	2.16 ± 0.02 3.58 ± 0.05	0.102 ± 0.010 0.116 ± 0.017	10.45	2.98 - 11.02	31.72
CeO ₂ /YSZ Ce/Zr:0.005	Zr-O Zr-Zr/Y	7.0 ± 0.7 11.4 ± 1.7	2.15 ± 0.02 3.58 ± 0.05	0.092 ± 0.009 0.114 ± 0.017	10.90	2.97 - 12.01	30.24
CeO ₂ /YSZ Ce/Zr:0.010	Zr-O Zr-Zr/Y	7.2 ± 0.7 11.8 ± 1.8	2.14 ± 0.02 3.57 ± 0.05	0.092 ± 0.009 0.112 ± 0.017	11.29	2.99 - 12.01	33.21
CeO ₂ /YSZ Ce/Zr:0.015	Zr-O Zr-Zr/Y	7.1 ± 0.7 11.7 ± 1.7	2.14 ± 0.02 3.58 ± 0.05	0.095 ± 0.009 0.112 ± 0.017	11.40	2.99 - 12.01	29.59
CeO ₂ /YSZ Ce/Zr:0.020	Zr-O Zr-Zr/Y	7.1 ± 0.7 11.6 ± 1.7	2.15 ± 0.02 3.58 ± 0.05	0.095 ± 0.009 0.114 ± 0.017	10.41	2.95 - 11.02	31.93
CeO ₂ /YSZ Ce/Zr:0.050	Zr-O Zr-Zr/Y	7.2 ± 0.7 11.6 ± 1.7	2.14 ± 0.02 3.58 ± 0.05	0.100 ± 0.010 0.114 ± 0.017	10.28	2.97 - 12.05	26.68
CeO ₂ /YSZ Ce/Zr:0.080	Zr-O Zr-Zr/Y	7.2 ± 0.7 11.6 ± 1.7	2.15 ± 0.02 3.58 ± 0.05	0.100 ± 0.010 0.116 ± 0.017	10.62	2.96 - 12.00	30.38
CeO ₂ /YSZ Ce/Zr:0.096	Zr-O Zr-Zr/Y	7.3 ± 0.7 11.6 ± 1.7	2.15 ± 0.02 3.58 ± 0.05	0.102 ± 0.010 0.114 ± 0.017	10.42	2.95 - 12.00	29.81
CeO ₂ /YSZ Ce/Zr:0.135	Zr-O Zr-Zr/Y	7.1 ± 0.7 11.6 ± 1.7	2.15 ± 0.02 3.58 ± 0.05	0.105 ± 0.011 0.116 ± 0.017	10.82	2.96 - 12.00	29.08

^a absorber (A) - backscatters (Bs), ^b coordination number N, ^c interatomic distance r, ^d Debye-Waller factor σ with its calculated deviation and ^e Fermi energy E_F.

5.1.6.3. Raman spectroscopic investigations

Raman spectroscopic studies on the different ZrO₂ polymorphs and YSZ are reported in literature [5.1.43-5.1.46]. The Raman spectra of different CeO₂/YSZ samples with low and high concentration of CeO₂ are shown in Figures 5.1.26 and 5.1.27, respectively. All the spectra were normalized to the reference peak at 85 cm⁻¹. Due to the amorphous nature of the analysed materials, the Raman spectra of the different CeO₂/YSZ samples did not show much features. Nevertheless, in most of the samples a broad band could be noticed around 530-670 cm⁻¹ and could be attributed to the F_{2g} zone centre optic mode of cubic ZrO₂ [5.1.43, 5.1.44], which is the only Raman active mode of cubic fluorite structure [5.1.45].

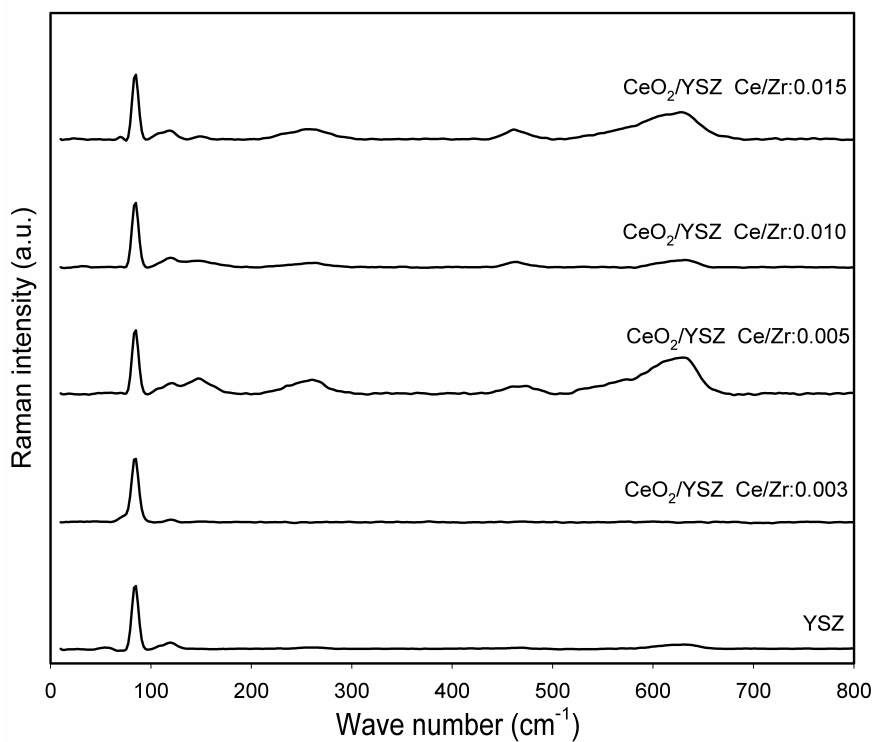


Figure 5.1.26. Raman spectra of the different CeO₂/YSZ samples with low CeO₂ doping.

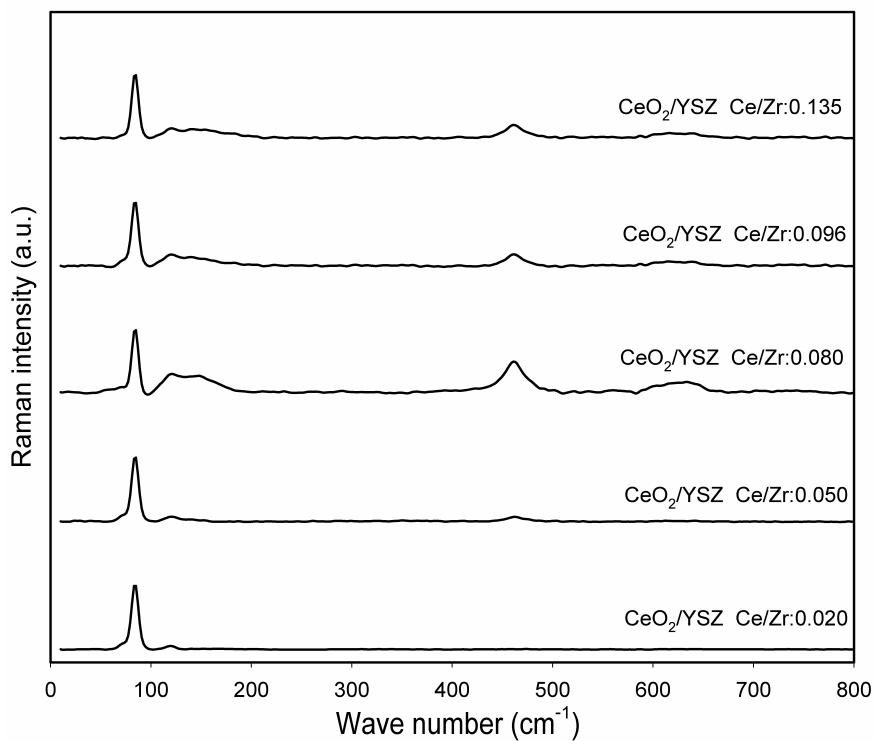


Figure 5.1.27. Raman spectra of the different CeO₂/YSZ samples with high CeO₂ doping.

The broadness and asymmetry of the observed Raman band could be attributed to the structural disorders associated within the oxygen sublattice [5.1.46]. Due to presence of oxygen vacancies Raman scattering occurs from points within the Brillouin zone [5.1.47]. The other prominent band is observed around 460-470 cm^{-1} , which could either be attributed to F_{2g} symmetry mode of the dopant CeO_2 [5.1.33] or to E_g symmetry mode of tetragonal ZrO_2 [5.1.48]. Unambiguous assignment was not possible for this particular band, as both the possibilities had equal probabilities. The peak intensity variations does not show any linear trend based on the concentration of the dopant, which could be attributed to various factors like particle size variations, difference in elemental compositions, crystallization effects, phonon confinement effects, non-stoichiometry due to oxygen deficiencies and disorder induced by minor phases [5.1.29].

5.1.7. Conclusion

The investigations on the nanophasic undoped and Ca-doped LaCoO_3 powders indicate that the perovskite network is not formed in the xerogels and the effects of calcium doping on the local structure could not be unequivocally inferred. Undoped LaCoO_3 powders evolved towards a nanocrystalline structure during thermal treatment but no significant local structural changes ascribable to the annealing temperatures were evidenced for the samples annealed between 700 and 1000°C. Conversely, calcium doping had a substantial influence on the local structure, which are dependant on the annealing temperatures. These changes could be attributed to the formation of cobalt and calcium oxide-based compounds, the distortion of the perovskite structure and the substitution of some of the La(III) species by Ca(II) ions. The expected change in the oxidation states of cobalt between the xerogels and the annealed samples could also be evidenced from the edge energy shift in the XANES region. The investigations on the La–Sr–Co–Fe–O nanocomposites revealed the formation of $\text{La}_{0.6}\text{Sr}_{0.4}\text{Co}_{0.9}\text{Fe}_{0.1}\text{O}_3$ along with Co_3O_4 and perhaps La_2CoO_4 in La–Sr–Co–Fe–O mixed oxide (support). The effect of Fe_2O_3 doping on La–Sr–Co–Fe–O mixed oxide is significant and changes in the local structure can be observed at all the different measured edges. Apart from the distortion in the perovskite structure, the formation of other oxide-based compounds such as CoO and Fe_2O_3 could be evidenced as a result of Fe_2O_3 doping. The investigations on mixed Fe–Ti–O nanocomposites reveal that the structure of the supported and bulk mixed

oxides prepared by wet impregnation and co-precipitation methods are similar to each other and resemble that of rutile TiO_2 . Furthermore, the iron doping does not significantly alter the local structure around the titanium atoms. The studies on mixed W–Ce–O nanocomposites show that the structure of the different WO_3/CeO_2 samples is similar to that of crystalline CeO_2 and WO_3 doping does not modify the local environment around the cerium atoms. Similarly the studies on mixed Ce–Y–Zr–O nanocomposites reveal that the YSZ retains its structural integrity even after doping with CeO_2 .

5.2. Studies on ferrite based nanomaterials

5.2.1. Introduction

Magnetic nanomaterials have long been of scientific and technological interest and among the magnetic materials; the cubic spinel structured ferrites having general formula MFe_2O_4 has been used in many industrial applications. By adjusting the chemical identity of M^{2+} cation, the magnetic configurations of MFe_2O_4 can be molecularly engineered to provide a wide range of magnetic properties [5.2.1]. Due to this versatility, MFe_2O_4 nanomaterials have been increasingly investigated for nanomagnetism and have shown great potential for many important technological applications, ranging from information storage and electronic devices to medical diagnostics and drug delivery [5.2.2].

The spinel ferrite unit cell is based on a close-packed oxygen lattice where metal cations reside on 8 of the 64 tetrahedral sites (A sites) and 16 of the 32 octahedral sites (B sites). The arrangement and packing of atoms in spinel unit cell is shown in Figure 5.2.1. If there is only one kind of cation in the octahedral sites, the spinel is called normal. If there is equal number of both kinds of cations in the octahedral sites, the spinel is inverse. If there is an unequal number of each kind of cation in the octahedral sites, the spinel is mixed.

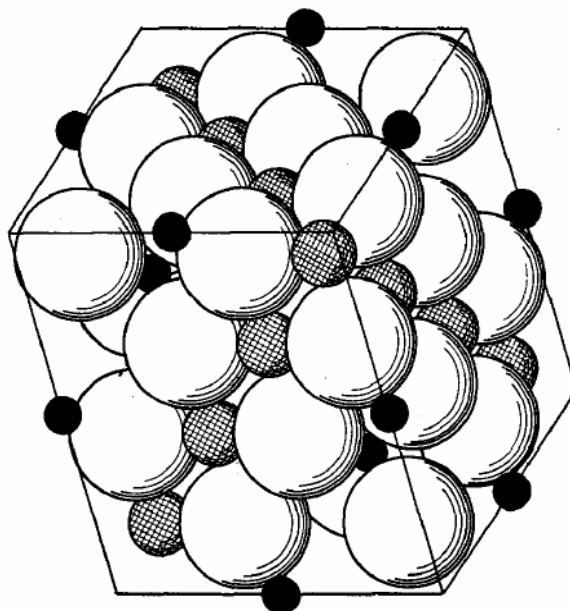


Figure 5.2.1. Arrangement and packing of atoms in spinel unit cell. [Large white spheres represent oxygen, small black spheres represent tetrahedral cations and cross-hatched spheres represent octahedral cations].

The copper ferrite nanoparticles and SnO₂, CeO₂ or NiO containing CuFe₂O₄ nanocomposites prepared by urea-nitrate combustion method [5.2.3] were obtained from Central Electrochemical Research Institute (CECRI), Karaikudi, India. The main aim of the work was to investigate the local structure and cation distribution in CuFe₂O₄ nanoparticles and to study the influence of SnO₂, CeO₂ or NiO on the structure of CuFe₂O₄ based nanocomposites. The transmission mode XAFS measurements were performed on the samples at Cu K-edge at 8979 eV Fe K-edge at 7112 eV, Ce L_{III}-edge at 5723 eV and Ni K-edge at 8333 eV at the beamline A1 at HASYLAB, Hamburg. The samples were measured at ambient conditions with Si(111) double crystal monochromator. In the fitting procedure, the various parameters, i.e., coordination number, interatomic distance, Debye-Waller factor and Fermi energy value, were determined by iterations.

5.2.2. Copper ferrite nanoparticles

In CuFe₂O₄ bulk materials, generally the copper ions occupy the octahedral sites and the iron ions occupy both the tetrahedral and octahedral sites. Among the octahedral sites, the copper ions are randomly distributed. The copper ion undergoes dsp^2 hybridisation to form four square, covalent bonds in an octahedral interstice of the spinel lattice. Thus, it is bound to the six near-neighbour anions by four coplanar covalent bonds and two linear ionic bonds. Due to the orbital overlap, the four coplanar covalent bonds are shorter than the two ionic bonds and the elementary octahedron becomes distorted from cubic to tetragonal symmetry [5.2.4]. Bulk CuFe₂O₄ is tetragonal below 760°C and the axial ratio c/a decreases monotonically from room temperature to 700°C. Above 760°C the copper ions are distributed in the anion interstices, and the lattice is cubic [5.2.5]. It is reported that, at room temperature 88% of copper ions are in octahedral sites and at 700°C the concentration of copper ions decrease to 74%. The fact that copper ions migrate from octahedral to tetrahedral sites indicates that they can be readily accommodated in tetrahedral sites although, because of square-bond formation, it is more stable in octahedral sites [5.2.5]. In ferrites, the divalent and trivalent metal ions occupy the site for which they have higher crystal field stability energy (CFSE) [5.2.6, 5.2.7]. For example, the Fe²⁺ cation has higher octahedral CFSE and occupies the octahedral sites, but Fe³⁺ cations have zero CFSE and therefore, can occupy either tetrahedral or octahedral sites depending on the preference

energy of the second cation in the structure [5.2.8]. In bulk CuFe_2O_4 , the iron ions are arbitrarily distributed between the tetrahedral and octahedral sites. The distribution and valence of the metal ions on the octahedral and tetrahedral sites determines the materials' magnetic and electronic properties. It is noteworthy to study whether the CuFe_2O_4 nanoparticles have a structure similar to that of bulk CuFe_2O_4 and to also investigate the cation distribution in the nanoparticles.

The experimentally determined and the theoretically calculated EXAFS functions in k -space and their Fourier transforms in real space for CuFe_2O_4 nanoparticles, measured at the Cu and Fe K-edges are shown in Figures 5.2.2 and 5.2.3, respectively. The corresponding structural parameters are tabulated in Table 5.2.1.

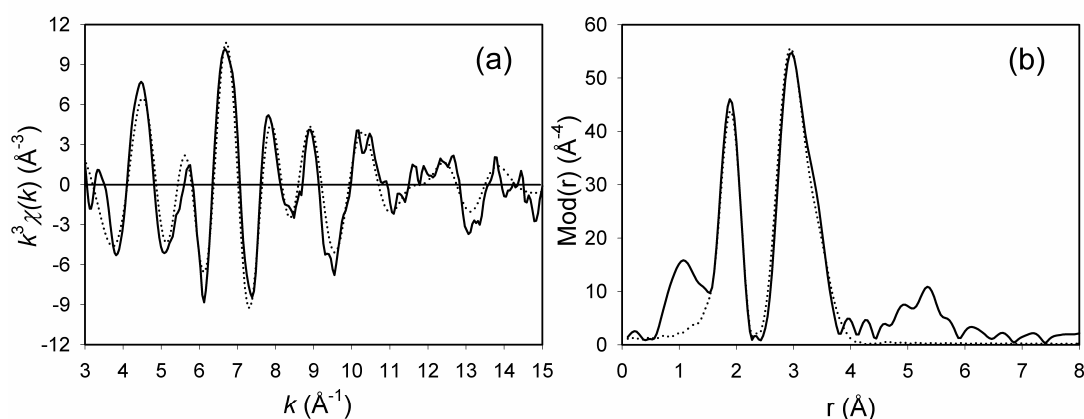


Figure 5.2.2. Experimental (solid line) and calculated (dotted line) EXAFS functions (a) and their Fourier transforms (b) for CuFe_2O_4 nanoparticles measured at the Cu K-edge.

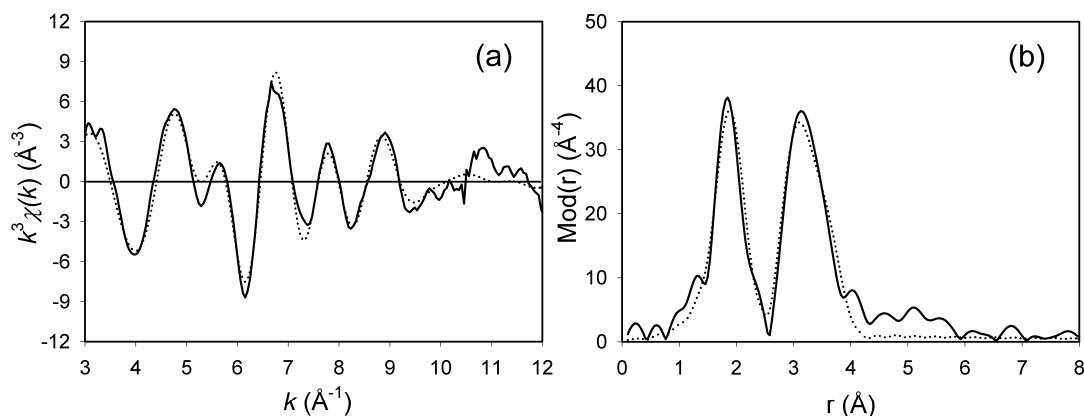


Figure 5.2.3. Experimental (solid line) and calculated (dotted line) EXAFS functions (a) and their Fourier transforms (b) for CuFe_2O_4 nanoparticles measured at the Fe K-edge.

Table 5.2.1. EXAFS obtained structural parameters for CuFe₂O₄ nanoparticles

Sample	A-Bs ^a	N ^b	r ^c [Å]	σ ^d [Å]	E _F ^e [eV]	k-range [Å ⁻¹]	R-factor
CuFe ₂ O ₄	Cu-O	3.7 ± 0.4	1.97 ± 0.02	0.067 ± 0.007	7.111	2.97 - 15.04	39.31
	Cu-O	1.7 ± 0.2	2.21 ± 0.02	0.095 ± 0.010			
	Cu-M _B	6.4 ± 1.0	2.94 ± 0.03	0.102 ± 0.015			
	Cu-M _A	3.1 ± 0.6	3.40 ± 0.04	0.110 ± 0.022			
	Fe-O	5.1 ± 0.5	1.95 ± 0.02	0.107 ± 0.011	4.850	2.97 - 12.03	28.39
	Fe-M _B	5.7 ± 0.9	2.99 ± 0.03	0.122 ± 0.018			
	Fe-M _{A/B}	5.6 ± 1.1	3.45 ± 0.04	0.122 ± 0.024			

^aabsorber (A) - backscatterers (Bs), ^b coordination number N, ^c interatomic distance r, ^d Debye-Waller factor σ with its calculated deviation and ^e Fermi energy E_F.

In the evaluation of the EXAFS function, it should be considered that depending on the site occupancy by the cation, the cation-oxygen and the cation-cation distances differ very much. For the analysis at the Cu K-edge, a four shell model is fitted. The analysis indicates two distinct oxygen shells at 1.97 Å and 2.21 Å distance with four and two backscatterers, respectively. This result clearly reveals that the copper ions occupy the octahedral interstices in the spinel lattice, wherein each copper atom forms four short coplanar covalent bonds and two long linear ionic bonds with the six near neighbouring oxygen atoms. The third shell was determined at 2.94 Å distance with about six metal backscatterers. This distance is typical of the cations occupying the octahedral sites (B sites), when the absorber is in an octahedral site [5.2.9] and is mentioned as M_B in the tables. In the case of CuFe₂O₄, both copper and iron atoms occupy the B sites and it was not possible to discriminate their individual contributions by means of EXAFS spectroscopy, therefore they were fitted together as a single metal shell with iron amplitude- and phase-functions. The fourth shell was found at 3.40 Å, a distance typical for the cations occupying the tetrahedral sites (A sites) [5.2.9] and is cited as M_A in the tables. This shell could be fitted with about three metal backscatterers using iron amplitude- and phase-functions. The obtained structural parameters are in agreement with the values reported for bulk CuFe₂O₄ in the space group *I4₁/amd* [5.2.10]. The results reveal that all the copper atoms occupy the octahedral sites and the occupancy of tetrahedral sites could not be validated.

For the analysis at the Fe K-edge, a three shell model is fitted. The first shell is centred at 1.95 Å distance and could be fitted with about five oxygen backscatterers. The asymmetric shape of this first peak in the Fourier transform plot corresponds to the two different Fe-O bond distances attributable to the presence of iron atoms in the

tetrahedral and octahedral sites. Similar observation has also been reported for NiZn-ferrite films [5.2.11]. In the Fourier transform plot, the second peak is broad and spreads over a wider range indicating the presence of both the second and the third shells in it. This also suggests that iron atoms occupy both tetrahedral and octahedral sites. The second shell could be fitted at a distance of 2.99 Å with about six metal backscatterers occupying the B sites, as this distance is typical of a cation present at the octahedral sites. The third shell found at 3.45 Å distance could be fitted with about six metal backscatterers. This distance is typical for metal backscatterers occupying tetrahedral sites, when the absorber is in an octahedral site. But, this distance is also characteristic for metal backscatterers occupying octahedral sites, when the absorber is in a tetrahedral site. Since the results illustrate the presence of iron in both tetrahedral and octahedral sites, the contributions for the third shell comes from the cations occupying both A and B sites, and is mentioned as $M_{A/B}$ in the tables. In the evaluation of the second and third shells, iron amplitude- and phase-functions were used. For all the three shells, the determined Debye-Waller factor values were high, indicating high disorder in the distribution of iron atoms between the tetrahedral and octahedral sites. The first shell Fe-O bond distance of 1.95 Å determined from EXAFS analysis is an average of the tetrahedrally and octahedrally coordinated iron atoms. In bulk CuFe_2O_4 in the space group $I4_1/amd$, the Fe-O distance is 1.74 Å for the iron atoms on the A sites and 2.14 Å for the iron atoms on the B sites [5.2.10]. Using these values, the percentage distribution of iron ions between the tetrahedral and octahedral interstices can be calculated employing the procedure reported in literature [5.2.12]. The calculations indicate that $58 \pm 5\%$ of iron ions are in A sites and $42 \pm 5\%$ are in B sites. Furthermore, the average coordination number calculated based on the same literature [5.2.12] resulted in a value of 4.8 ± 0.5 , which is in agreement with the value of 5.1 ± 0.5 determined from EXAFS analysis.

The XANES investigations were performed in order to complement the results obtained from EXAFS studies. The edge energy and oxidation states determined from the XANES analysis for CuFe_2O_4 nanoparticles at the Cu and Fe K-edges are tabulated in Table 5.2.2. The XANES region of CuFe_2O_4 nanoparticles measured at the Cu K-edge is shown along with the reference CuO in Figure 5.2.4.

Table 5.2.2. Edge energy and oxidation states for the different ferrite nanocomposites along with the reference compounds

Sample	Element	Oxidation state	Absorption edge [eV]
CuFe ₂ O ₄	Cu	+2	8991.0
	Fe	+3	7124.0
CuFe ₂ O ₄ -5% SnO ₂	Cu	+2	8991.0
	Fe	+3	7124.0
CuFe ₂ O ₄ -20% SnO ₂	Cu	+2	8991.0
	Fe	+3	7124.5
CuFe ₂ O ₄ -5% CeO ₂	Cu	+2	8991.0
	Fe	+3	7124.0
	Ce	+4	5717.0
CuFe ₂ O ₄ -20% CeO ₂	Cu	+2	8991.0
	Fe	+3	7124.0
	Ce	+4	5717.0
CuFe ₂ O ₄ -5% NiO	Cu	+2	8991.0
	Fe	+3	7123.5
	Ni	+2	8344.0
CuFe ₂ O ₄ -20% NiO	Cu	+2	8992.0
	Fe	+3	7124.0
	Ni	+2	8344.0
CuO	Cu	+2	8991.5
Fe ₂ O ₃	Fe	+3	7124.0
FeO	Fe	+2	7119.5
CeO ₂	Ce	+4	5716.5
NiO	Ni	+2	8343.5

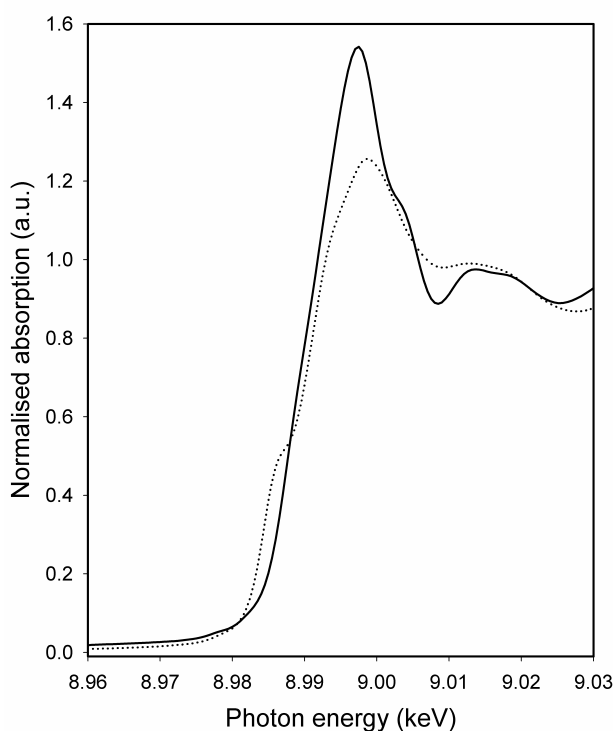


Figure 5.2.4. XANES region of CuFe₂O₄ (solid line) along with the reference CuO (dotted line) measured at the Cu K-edge.

In bulk CuFe₂O₄, the X-ray diffraction measurements at room temperature reported by Ohnishi et al. [5.2.13] indicate that approximately 10% of the copper atoms occupy the tetrahedral sites, and theory [5.2.14] suggests that the tetrahedrally coordinated copper ions should have +1 valence. It follows that, for such a sample, in the XANES region, one would expect to observe the contributions from a mixture of 90% Cu²⁺ and 10% Cu¹⁺ cations. In such a case there would be a small pre-edge peak signifying the contributions from Cu¹⁺ cations [5.2.15]. However, in the CuFe₂O₄ nanoparticles the pre-edge peak could not be evidenced, indicating the absence of Cu¹⁺ cations. This in turn reveals that there are no tetrahedrally coordinated copper ions, which is in agreement with the EXAFS studies. In addition, the similarity in the values for the absorption edge of CuFe₂O₄ nanoparticles and CuO reveals that copper is in +2 oxidation state in the nanoparticles.

The XANES region of CuFe₂O₄ nanoparticles measured at the Fe K-edge is shown along with the references Fe₂O₃ and FeO in Figure 5.2.5. The comparison of the absorption edge values of CuFe₂O₄ nanoparticles with those of Fe₂O₃ and FeO indicates that iron is in +3 oxidation state in the nanoparticles.

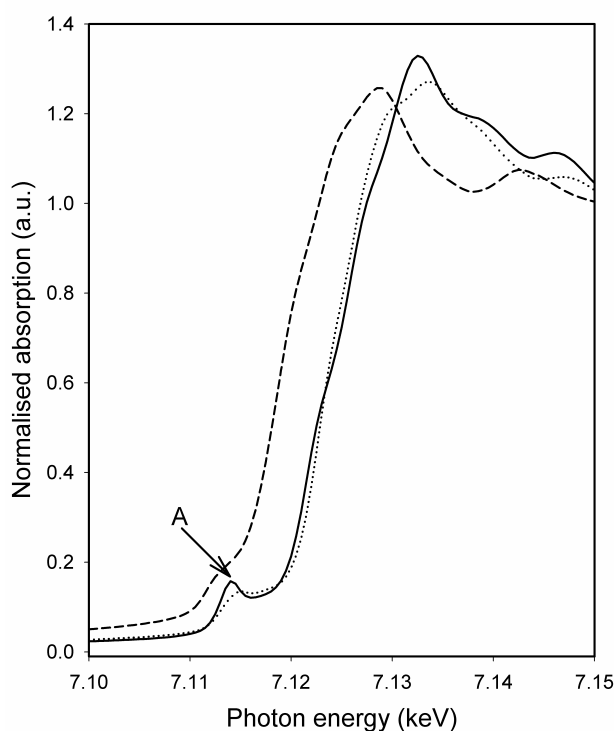


Figure 5.2.5. XANES region of CuFe_2O_4 (solid line) along with the references Fe_2O_3 (dotted line) and FeO (dashed line) measured at the Fe K-edge.

The XANES region of CuFe_2O_4 nanoparticles show an intense pre-edge peak (marked as A), which is characteristic of Fe^{3+} cations in tetrahedral sites. This pre-edge peak is attributed to $1s \rightarrow 3d$ electronic transition. Since $1s$ and $3d$ states are centrosymmetric, the transition probability should be small. When the ion is in a centrosymmetric octahedral site, quadrupole interactions are allowed. But when the ion is in a non-centrosymmetric tetrahedral site, dipole interactions are allowed, wherein the mixing of $4p$ and $3d$ orbitals intensifies the absorption [5.2.16]. In CuFe_2O_4 nanoparticles, the pre-edge peak is more pronounced due to the non-centrosymmetric tetrahedral crystal field. The XANES studies suggest that iron ions occupy more of A than B sites.

5.2.3. Copper ferrite-tin oxide nanocomposites

The experimentally determined and the theoretically calculated EXAFS functions in k -space and their Fourier transforms in real space for 5% and 20% (percentage by weight) SnO_2 containing CuFe_2O_4 nanocomposites, measured at the Cu and Fe K-edges are shown in Figures 5.2.6 and 5.2.7, respectively. The fitted parameters are given in Table 5.2.3.

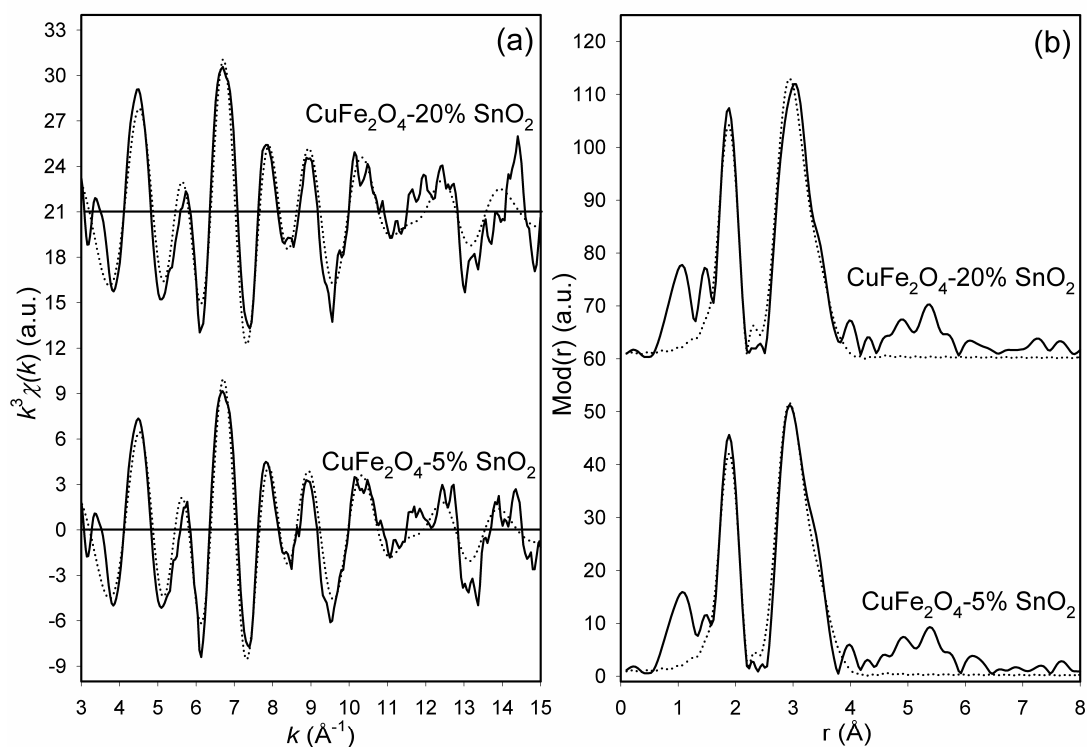


Figure 5.2.6. Experimental (solid line) and calculated (dotted line) EXAFS functions (a) and their Fourier transforms (b) for CuFe₂O₄-SnO₂ samples measured at Cu K-edge.

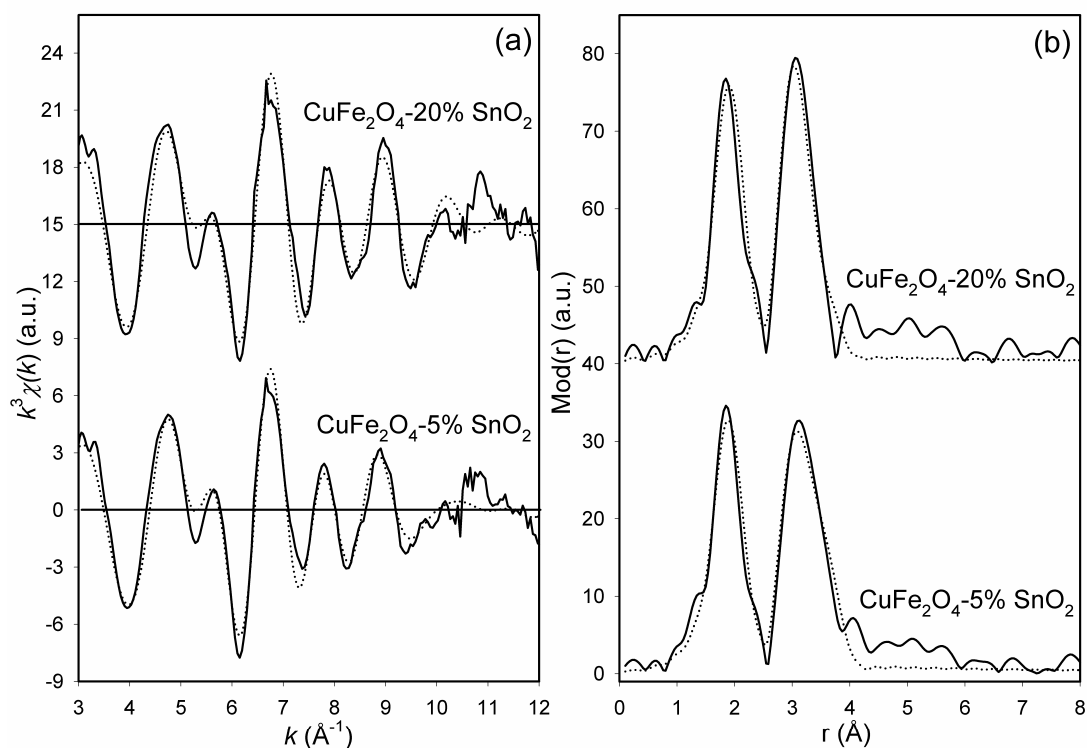


Figure 5.2.7. Experimental (solid line) and calculated (dotted line) EXAFS functions (a) and their Fourier transforms (b) for CuFe₂O₄-SnO₂ samples measured at Fe K-edge.

Table 5.2.3. EXAFS obtained structural parameters for CuFe₂O₄-SnO₂ nanocomposites

Sample	A-Bs ^a	N ^b	r ^c [Å]	σ ^d [Å]	E _F ^e [eV]	k-range [Å ⁻¹]	R-factor
CuFe ₂ O ₄ - 5% SnO ₂	Cu-O	3.5 ± 0.4	1.96 ± 0.02	0.067 ± 0.007	7.668	2.96 - 15.04	39.59
	Cu-O	1.5 ± 0.2	2.18 ± 0.02	0.077 ± 0.008			
	Cu- M _B	6.3 ± 1.0	2.93 ± 0.03	0.105 ± 0.016			
	Cu- M _A	3.2 ± 0.6	3.40 ± 0.04	0.114 ± 0.023			
	Fe-O	5.1 ± 0.5	1.96 ± 0.02	0.112 ± 0.011	4.678	2.99 - 12.02	27.72
	Fe- M _B	5.3 ± 0.8	2.99 ± 0.03	0.122 ± 0.018			
Fe- M _{A/B}	4.6 ± 0.9	3.45 ± 0.04	0.122 ± 0.024				
CuFe ₂ O ₄ - 20% SnO ₂	Cu-O	3.6 ± 0.4	1.96 ± 0.02	0.063 ± 0.006	7.957	2.95 - 15.04	43.64
	Cu-O	1.8 ± 0.2	2.17 ± 0.02	0.077 ± 0.008			
	Cu- M _B	6.6 ± 1.0	2.93 ± 0.03	0.105 ± 0.016			
	Cu- M _A	3.2 ± 0.6	3.39 ± 0.04	0.114 ± 0.023			
	Fe-O	5.2 ± 0.5	1.97 ± 0.02	0.107 ± 0.011	4.887	2.97 - 12.03	32.47
	Fe- M _B	6.5 ± 1.0	2.99 ± 0.03	0.118 ± 0.018			
Fe- M _{A/B}	4.7 ± 0.9	3.39 ± 0.04	0.145 ± 0.029				

^aabsorber (A) - backscatterers (Bs), ^b coordination number N, ^c interatomic distance r, ^d Debye-Waller factor σ with its calculated deviation and ^e Fermi energy E_F.

The EXAFS determined parameters for the CuFe₂O₄-SnO₂ (both 5% and 20%) nanocomposites at Cu and Fe K-edges resembled the structural parameters of their corresponding counterparts without SnO₂, indicating that the incorporation of SnO₂ does not lead to significant local structural changes in CuFe₂O₄ nanoparticles. The results are in agreement with the XRD investigations, which revealed the presence of Bragg peaks representative of SnO₂ and CuFe₂O₄ phases [5.2.17]. The HRTEM studies showed that SnO₂ forms a coating over CuFe₂O₄ nanoparticles [5.2.17]. The Cu-Sn or Fe-Sn distances could not be determined from EXAFS analysis as the contributions from the surface bound tin atoms are lower than the contributions from the core CuFe₂O₄ nanoparticles.

The XANES region of CuFe₂O₄-SnO₂ nanocomposites at the Cu and Fe K-edge are similar to those in CuFe₂O₄ nanoparticles. The edge energy and oxidation states determined from the XANES analysis at the Cu and Fe K-edges are summarised in Table 5.2.2. The comparison of the absorption edge values of CuFe₂O₄-SnO₂ nanocomposites with the corresponding reference compounds indicate that copper is in +2 and iron is in +3 oxidation state in the nanocomposites.

5.2.4. Copper ferrite-cerium oxide nanocomposites

The experimentally determined and the theoretically calculated EXAFS functions in k -space and their Fourier transforms in real space for 5% and 20% (percentage by weight) CeO_2 containing CuFe_2O_4 nanocomposites, measured at the Cu and Fe K-edges are shown in Figures 5.2.8 and 5.2.9, respectively. The determined structural parameters are given in Table 5.2.4.

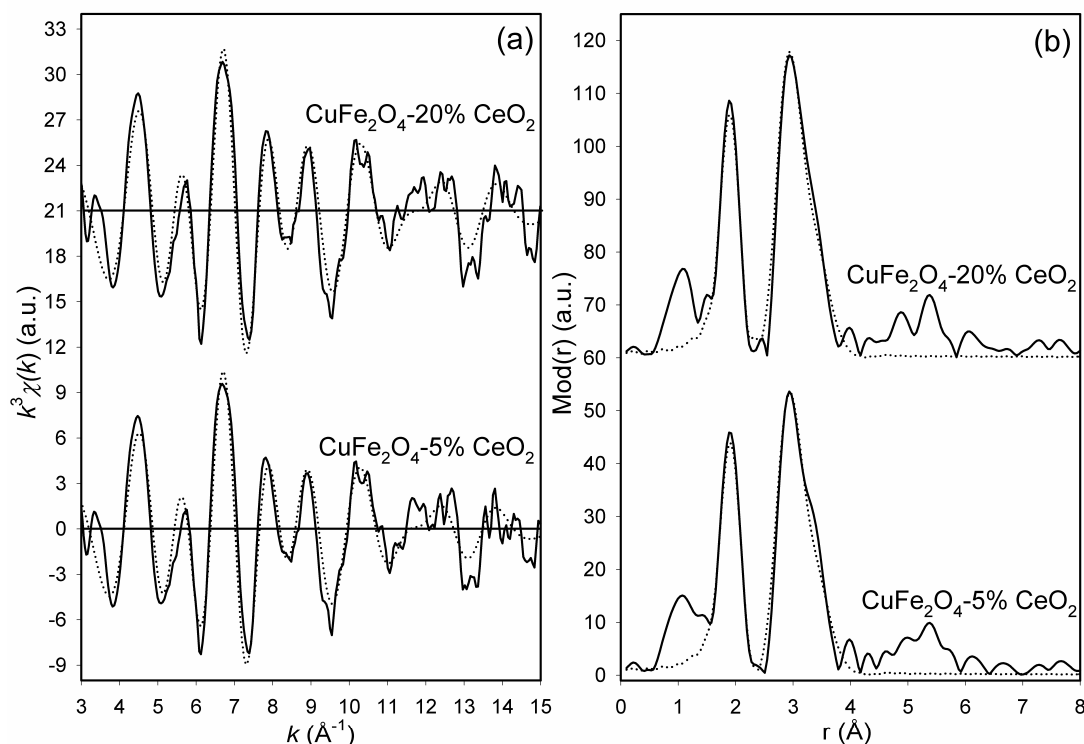


Figure 5.2.8. Experimental (solid line) and calculated (dotted line) EXAFS functions (a) and their Fourier transforms (b) for CuFe_2O_4 - CeO_2 nanocomposites measured at the Cu K-edge.

In this case as well, the structural parameters obtained from both Cu and Fe K-edge analyses are similar to those of CuFe_2O_4 nanoparticles. There are also no variations for the parameters obtained for the 5% and 20% CeO_2 containing samples, revealing that the addition of CeO_2 does not alter the local structure of CuFe_2O_4 nanoparticles. In agreement with the EXAFS studies, the XRD investigations also revealed the existence of CeO_2 and CuFe_2O_4 phases in these nanocomposites [5.2.18]. Furthermore, distances corresponding to Cu-Ce and Fe-Ce could not be determined from EXAFS analysis due to the same reasons mentioned earlier.

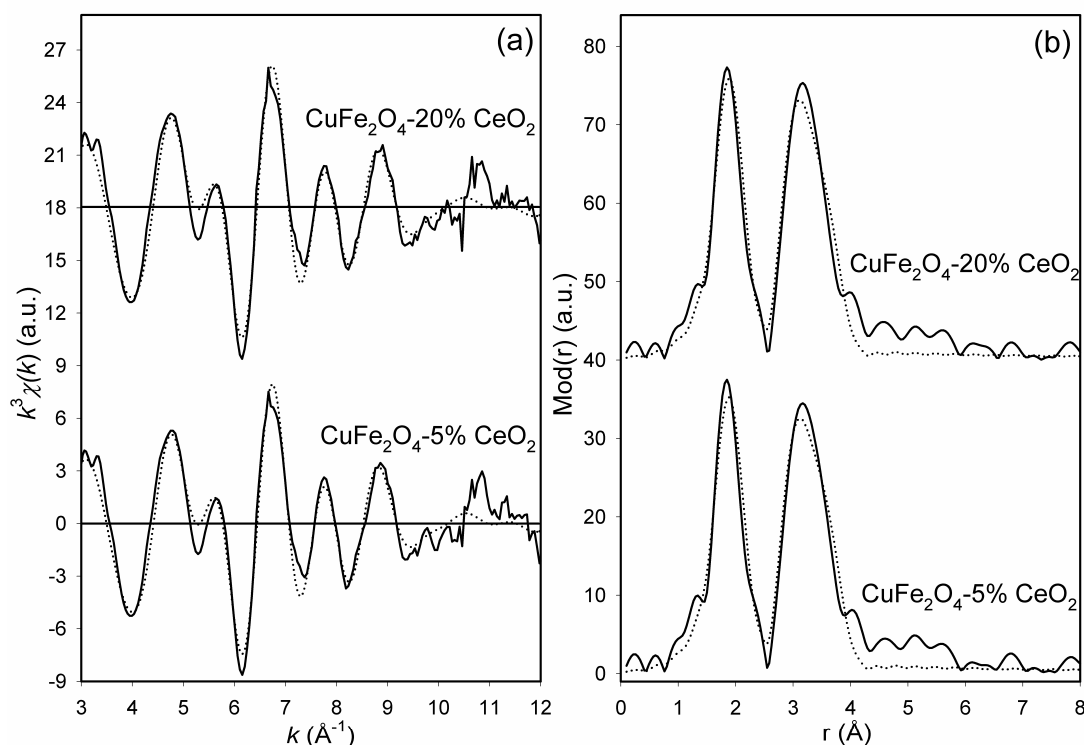


Figure 5.2.9. Experimental (solid line) and calculated (dotted line) EXAFS functions (a) and their Fourier transforms (b) for $\text{CuFe}_2\text{O}_4\text{-CeO}_2$ nanocomposites measured at the Fe K-edge.

Table 5.2.4. EXAFS obtained structural parameters for $\text{CuFe}_2\text{O}_4\text{-CeO}_2$ nanocomposites

Sample	A-Bs ^a	N ^b	r ^c [Å]	σ ^d [Å]	E_F ^e [eV]	k-range [Å ⁻¹]	R-factor
$\text{CuFe}_2\text{O}_4\text{-5% CeO}_2$	Cu-O	3.7 ± 0.4	1.97 ± 0.02	0.067 ± 0.007	7.144	2.97 - 15.04	41.33
	Cu-O	1.6 ± 0.2	2.22 ± 0.02	0.095 ± 0.010			
	Cu- M_B	6.3 ± 1.0	2.94 ± 0.03	0.102 ± 0.015			
	Cu- M_A	3.0 ± 0.6	3.40 ± 0.04	0.112 ± 0.022			
$\text{CuFe}_2\text{O}_4\text{-5% CeO}_2$	Fe-O	5.1 ± 0.5	1.95 ± 0.02	0.110 ± 0.011	4.802	2.96 - 12.03	28.06
	Fe- M_B	5.3 ± 0.8	2.99 ± 0.03	0.122 ± 0.018			
	Fe- $M_{A/B}$	6.0 ± 1.2	3.45 ± 0.04	0.122 ± 0.024			
$\text{CuFe}_2\text{O}_4\text{-20% CeO}_2$	Cu-O	3.6 ± 0.4	1.97 ± 0.02	0.063 ± 0.006	7.516	2.96 - 15.04	40.02
	Cu-O	1.7 ± 0.2	2.20 ± 0.02	0.084 ± 0.008			
	Cu- M_B	6.3 ± 1.0	2.93 ± 0.03	0.100 ± 0.015			
	Cu- M_A	3.2 ± 0.6	3.40 ± 0.04	0.112 ± 0.022			
$\text{CuFe}_2\text{O}_4\text{-20% CeO}_2$	Fe-O	5.1 ± 0.5	1.95 ± 0.02	0.107 ± 0.011	4.750	2.99 - 12.02	27.25
	Fe- M_B	5.4 ± 0.8	2.99 ± 0.03	0.122 ± 0.018			
	Fe- $M_{A/B}$	5.8 ± 1.2	3.45 ± 0.04	0.122 ± 0.024			

^a absorber (A) - backscatterers (Bs), ^b coordination number N, ^c interatomic distance r, ^d Debye-Waller factor σ with its calculated deviation and ^e Fermi energy E_F .

The XANES region of $\text{CuFe}_2\text{O}_4\text{-CeO}_2$ nanocomposites at the Cu and Fe K-edge are similar to those in CuFe_2O_4 nanoparticles. The edge energy and oxidation states determined from the XANES analysis at the Cu and Fe K-edges are given in Table 5.2.2. The analysis indicates that copper is in +2 and iron is in +3 oxidation state in the nanocomposites. The XANES region of the nanocomposites measured at the Ce L_{III}-edge is shown along with CeO_2 in Figure 5.2.10. For clarity reasons, the spectra are shifted along the ordinate.

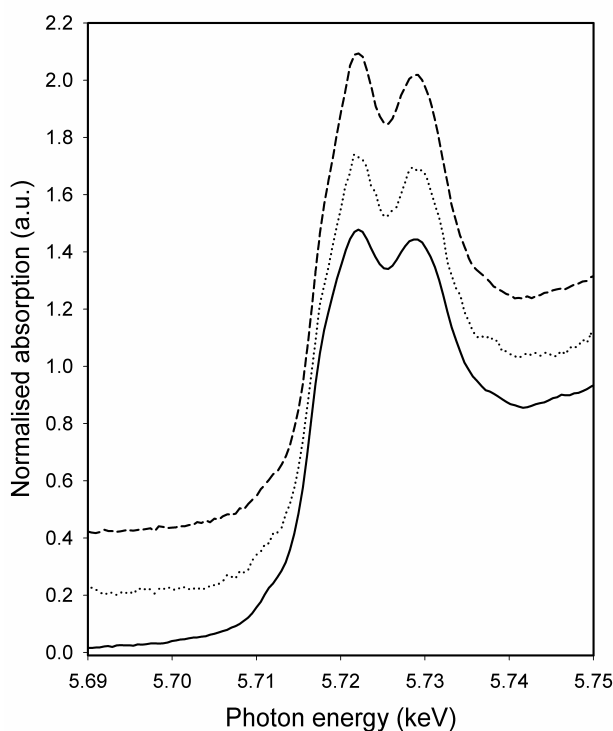


Figure 5.2.10. XANES region of $\text{CuFe}_2\text{O}_4\text{-5% CeO}_2$ (dotted line) and $\text{CuFe}_2\text{O}_4\text{-20% CeO}_2$ (dashed line) along with the reference CeO_2 (solid line) measured at the Ce L_{III}-edge.

The XANES region of the 5% and 20% $\text{CeO}_2\text{-CuFe}_2\text{O}_4$ nanocomposites are similar to each other and resembles that of crystalline CeO_2 and the similarity in the values for the absorption edge of the $\text{CeO}_2\text{-CuFe}_2\text{O}_4$ nanocomposites and CeO_2 reveals that cerium is in +4 oxidation state in the nanocomposites. All the spectra show two clearly distinct absorption peaks, which are characteristic of CeO_2 . These peaks are due to the resonance in the $2p \rightarrow 5d$ cross section modified by the local density of the unoccupied states, resulting in the $5, \epsilon d$ final state [5.2.19]. The peaks arise from many-body final state effects due to the mixing of multielectron configurations [5.2.20].

5.2.5. Copper ferrite-nickel oxide nanocomposites

The experimentally determined and the theoretically calculated EXAFS functions in k -space and their Fourier transforms in real space for 5% and 20% (percentage by weight) NiO containing CuFe_2O_4 nanocomposites, measured at the Cu K-edge are shown in Figure 5.2.11 and the determined structural parameters are tabulated in Table 5.2.5.

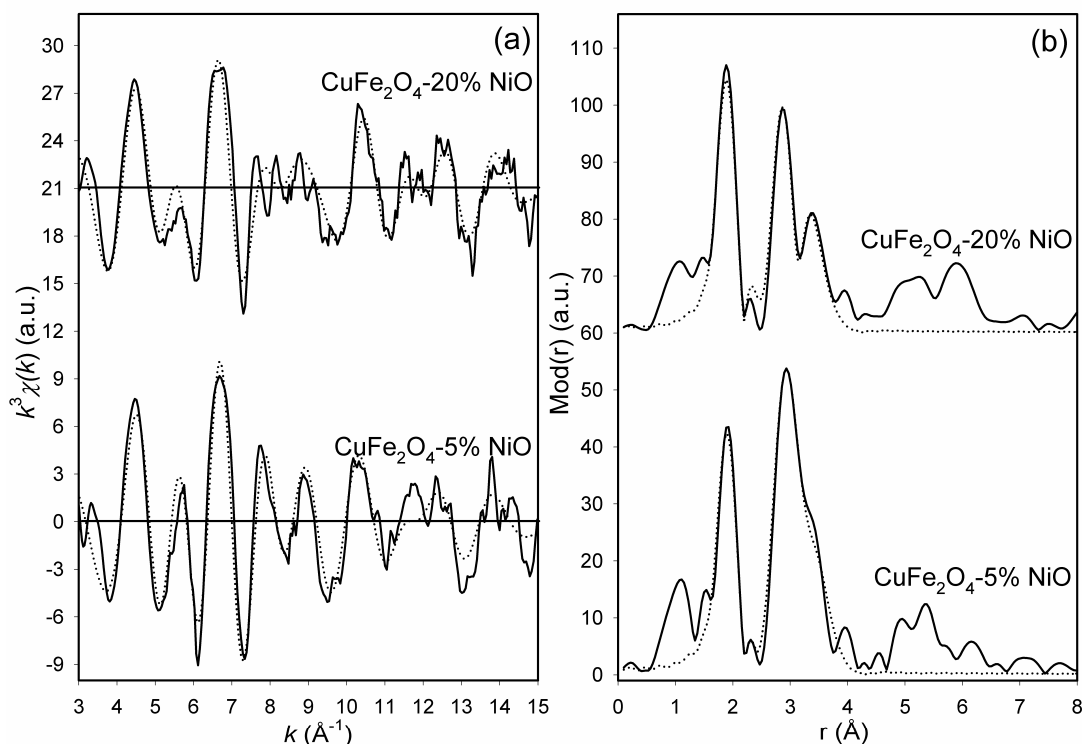


Figure 5.2.11. Experimental (solid line) and calculated (dotted line) EXAFS functions (a) and their Fourier transforms (b) for CuFe_2O_4 -NiO nanocomposites measured at the Cu K-edge.

The EXAFS spectra obtained for 5% and 20% CuFe_2O_4 -NiO nanocomposites are different from each other. The structural parameters obtained for 5% NiO containing CuFe_2O_4 nanocomposites are in agreement with those of CuFe_2O_4 nanoparticles. But in the case of 20% NiO containing CuFe_2O_4 nanocomposites, a significant decrease in the coordination number of the metal backscatterers occupying the octahedral site (at 2.93 \AA) and tetrahedral site (at 3.41 \AA) could be observed, suggesting the partial substitution of the metal ions in these sites by nickel ions. Even though nickel ions preferentially occupy the octahedral sites, recent studies on NiFe_2O_4 nanoparticles reveal that about 10% of nickel ions occupy the tetrahedral sites [5.2.21]. It is known that, at the

nanometer level, the coordination numbers strongly depend on the crystallite size. However, in the present case, the changes observed in the coordination numbers could not be associated with the changes in the crystallite size, as the crystallites are very large and the size variation between the different nanocomposites is within the same order of magnitude. Furthermore, a new shell with copper backscatterers originates at 3.12 Å distance. This shell was observed in the other CuFe_2O_4 based composites and was in agreement with Cu-Cu distance of 3.10 Å in CuO [5.2.22]. This result suggests the formation of CuO during the preparation of 20% CuFe_2O_4 -NiO nanocomposites.

The experimentally determined and the theoretically calculated EXAFS functions in k -space and their Fourier transforms in real space for 5% and 20% (percentage by weight) NiO containing CuFe_2O_4 nanocomposites, measured at the Fe K-edge are shown in Figure 5.2.12 and the obtained structural parameters are listed in Table 5.2.5.

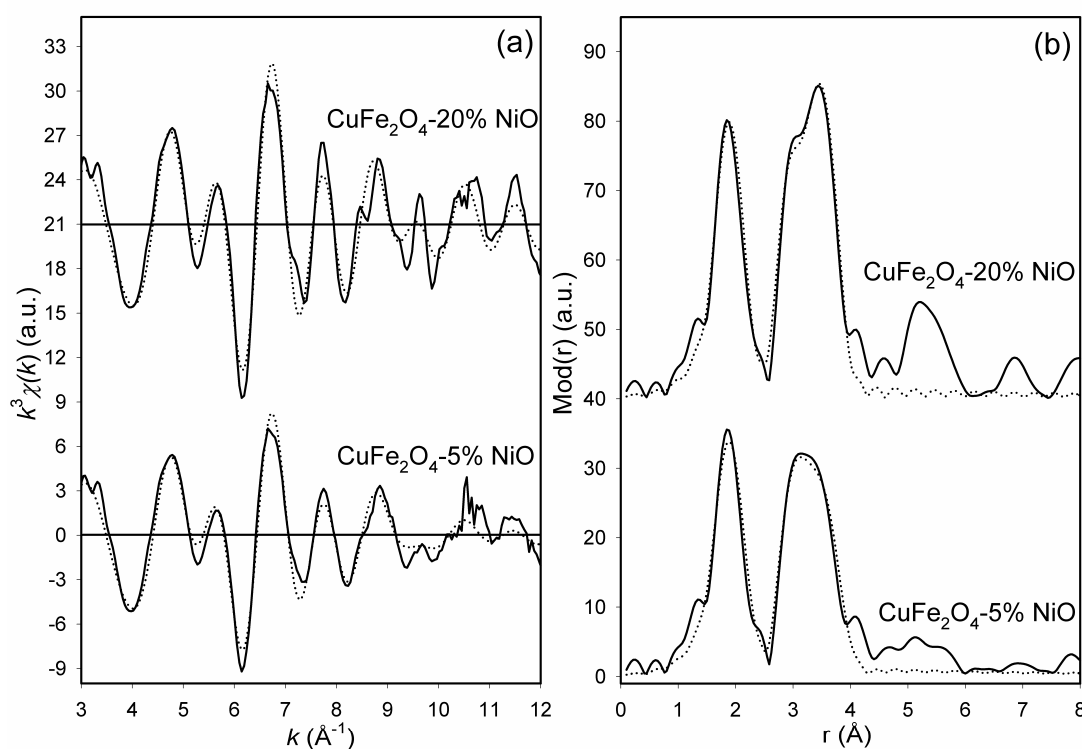


Figure 5.2.12. Experimental (solid line) and calculated (dotted line) EXAFS functions (a) and their Fourier transforms (b) for CuFe_2O_4 -NiO nanocomposites measured at the Fe K-edge.

The structural parameters determined from the Fe K-edge measurements for 5% and 20% CuFe_2O_4 -NiO nanocomposites are nearly similar to each other and resembles those of CuFe_2O_4 nanoparticles. However, the comparison of the Fourier transform plots of

the two nanocomposites shows significant differences in the shape of the second peak. In 5% $\text{CuFe}_2\text{O}_4\text{-NiO}$ nanocomposites, the second peak is broad whereas in the case of 20% $\text{CuFe}_2\text{O}_4\text{-NiO}$ nanocomposites a distinct shoulder like feature could be noticed. These variations could be attributed to the possible upsets in the ferric balance due to the displacement of metal cations. Similar observations have also been reported for NiZn ferrites [5.2.9].

The experimentally determined and the theoretically calculated EXAFS functions in k -space and their Fourier transforms in real space for 5% and 20% (percentage by weight) NiO containing CuFe_2O_4 nanocomposites, measured at the Ni K-edge are shown in Figure 5.2.13 and the resulting structural parameters are given in Table 5.2.5.

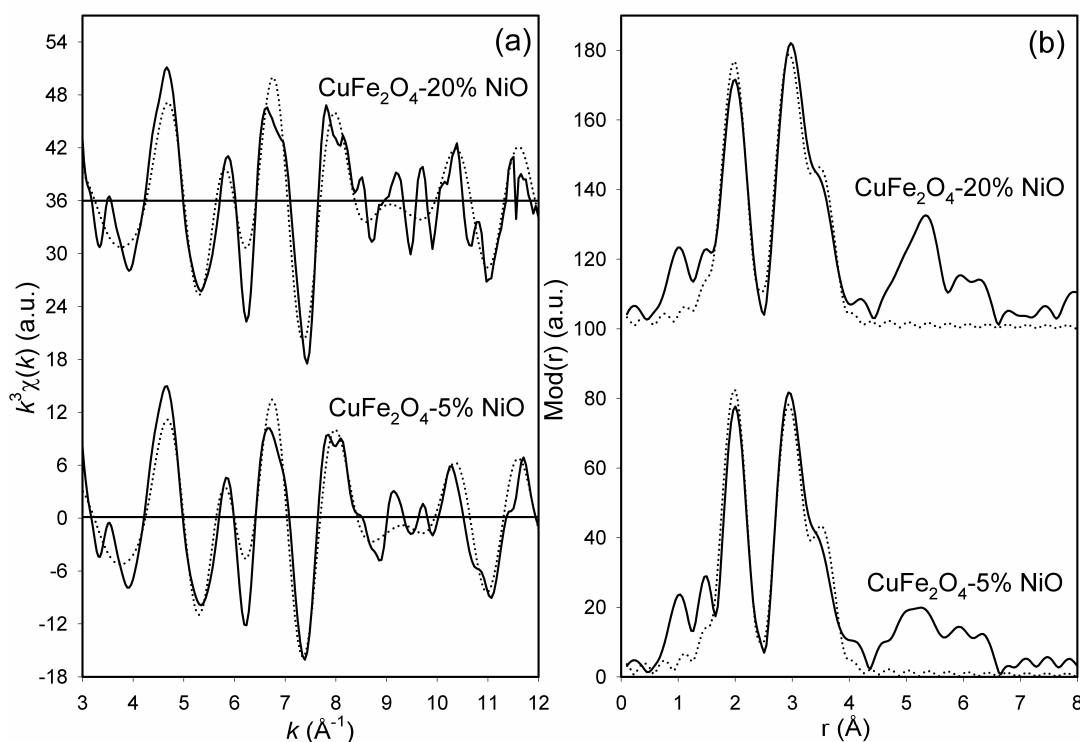


Figure 5.2.13. Experimental (solid line) and calculated (dotted line) EXAFS functions (a) and their Fourier transforms (b) for $\text{CuFe}_2\text{O}_4\text{-NiO}$ nanocomposites measured at the Ni K-edge.

The EXAFS spectra of 5% and 20% $\text{CuFe}_2\text{O}_4\text{-NiO}$ nanocomposites are similar to each other and in the analysis of the EXAFS function; a three shell model could be fitted for both the nanocomposites. The first shell with six oxygen backscatterers at about 2.03 \AA , the second shell with six metal backscatterers at about 2.92 \AA and third shell at about 3.43 \AA could be determined. The EXAFS obtained parameters could not be matched with those of NiO [5.2.23], but were in agreement with the structural

parameters of NiFe₂O₄ [5.2.24]. The results indicate the formation of NiFe₂O₄ during the preparation of CuFe₂O₄-NiO nanocomposites. The XRD studies also indicated the absence of the peaks characteristic of NiO and the presence of the peaks representative of NiFe₂O₄ and CuO [5.2.25].

Table 5.2.5. EXAFS obtained structural parameters for CuFe₂O₄-NiO nanocomposites

Sample	A-Bs ^a	N ^b	r ^c [Å]	σ ^d [Å]	E _F ^e [eV]	k-range [Å ⁻¹]	R-factor
CuFe ₂ O ₄ -5% NiO	Cu-O	3.6 ± 0.4	1.98 ± 0.02	0.067 ± 0.007	6.888	2.96 - 15.03	41.03
	Cu-O	1.6 ± 0.2	2.20 ± 0.02	0.071 ± 0.007			
	Cu- M _B	6.2 ± 1.0	2.93 ± 0.03	0.102 ± 0.015			
	Cu- M _A	3.5 ± 0.7	3.43 ± 0.04	0.112 ± 0.022			
	Fe-O	5.0 ± 0.5	1.95 ± 0.02	0.110 ± 0.011	4.374	2.98 - 12.02	27.85
	Fe- M _B	5.2 ± 0.8	2.98 ± 0.03	0.122 ± 0.018			
	Fe- M _{A/B}	6.1 ± 1.2	3.47 ± 0.04	0.116 ± 0.023			
	Ni-O	6.6 ± 0.7	2.04 ± 0.02	0.067 ± 0.007	12.36	2.97 - 12.04	38.25
	Ni- M _B	6.4 ± 1.0	2.92 ± 0.03	0.087 ± 0.013			
Ni- M _A	6.4 ± 1.3	3.43 ± 0.04	0.095 ± 0.019				
CuFe ₂ O ₄ -20% NiO	Cu-O	3.9 ± 0.4	1.97 ± 0.02	0.071 ± 0.007	4.944	2.97 - 15.02	42.79
	Cu-O	1.1 ± 0.1	2.18 ± 0.02	0.050 ± 0.005			
	Cu- M _B	4.7 ± 0.7	2.93 ± 0.03	0.092 ± 0.014			
	Cu-Cu	3.4 ± 0.5	3.12 ± 0.03	0.095 ± 0.014			
	Cu- M _A	2.0 ± 0.4	3.41 ± 0.04	0.105 ± 0.021			
	Fe-O	5.1 ± 0.5	1.95 ± 0.02	0.102 ± 0.010	4.412	2.98 - 12.02	32.33
	Fe- M _B	6.0 ± 0.9	2.98 ± 0.03	0.118 ± 0.018			
	Fe- M _{A/B}	6.0 ± 1.2	3.47 ± 0.04	0.092 ± 0.018			
	Ni-O	6.7 ± 0.7	2.03 ± 0.02	0.074 ± 0.007	12.22	2.98 - 12.04	44.85
Ni- M _B	6.4 ± 1.0	2.92 ± 0.03	0.087 ± 0.013				
Ni- M _A	6.4 ± 1.3	3.42 ± 0.04	0.095 ± 0.019				

^a absorber (A) - backscatterers (Bs), ^b coordination number N, ^c interatomic distance r, ^d Debye-Waller factor σ with its calculated deviation and ^e Fermi energy E_F.

The XANES spectra of 5% and 20% CuFe₂O₄-NiO nanocomposites measured at the Cu K-edge is shown along with spectra of CuFe₂O₄ nanoparticles and CuO in Figure 5.2.14. The XANES region of 5% CuFe₂O₄-NiO nanocomposites coincides with that of CuFe₂O₄ nanoparticles. But in the near-edge region of the 20% CuFe₂O₄-NiO nanocomposites the pre-edge feature (marked as A) characteristic of CuO could be evidenced. This feature corresponds to 1s→4p transition combined with the simultaneous 'shake down' transition of a high energy electron into the Cu 3d hole [5.2.15]. The XANES investigations further strengthen the results obtained from the EXAFS analysis.

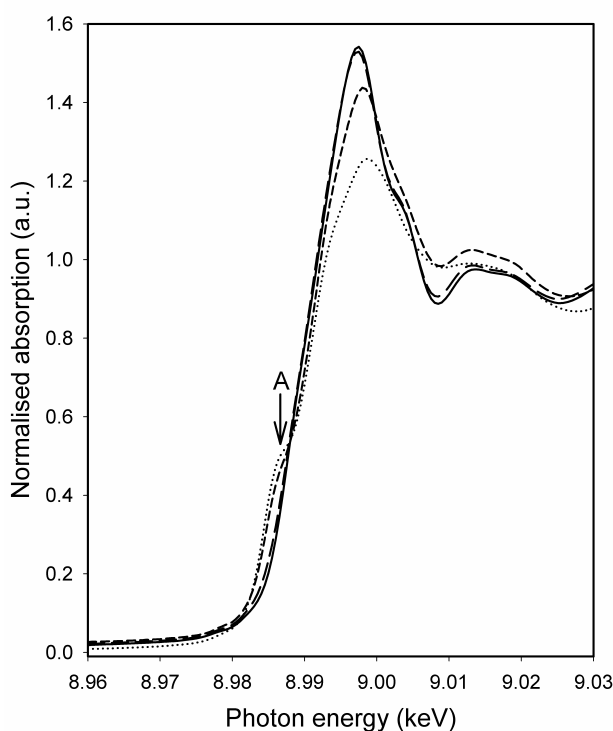


Figure 5.2.14. XANES region of CuFe₂O₄-5% NiO (long dashed line) and CuFe₂O₄-20% NiO (short dashed line) along with the references CuFe₂O₄ (solid line) and CuO (dotted line) measured at the Cu K-edge.

The XANES regions at the Fe and Ni K-edges show no remarkable features. The edge energy and oxidation states determined from the XANES analysis for CuFe₂O₄-NiO nanocomposites at the Cu, Fe and Ni K-edges are tabulated in Table 5.2.2. The comparison of the absorption edge values of CuFe₂O₄-NiO nanocomposites with the corresponding reference compounds indicate that copper, iron and nickel are in +2, +3 and +2 oxidation states, respectively in the nanocomposites.

5.2.6. Conclusion

The EXAFS and XANES investigations reveal that CuFe₂O₄ nanoparticles have a structure analogous to that of the bulk material. The studies indicate that all the copper ions occupy the octahedral sites and the iron ions are distributed between the tetrahedral and octahedral sites. The studies on CuFe₂O₄-SnO₂ and CuFe₂O₄-CeO₂ nanocomposites show that the incorporation of the tetravalent metal oxides does not alter the local structure of CuFe₂O₄ nanoparticles. However, the studies on CuFe₂O₄-NiO samples reveal the formation of NiFe₂O₄ and CuO, in addition to the existence of CuFe₂O₄ nanoparticles. A partial substitution of copper ions by nickel could also be evidenced.

5.3. Studies on inorganic-organic hybrid materials

5.3.1. Introduction

Novel materials endowed with enhanced mechanical, electrical, magnetic, electronic, optical and thermal properties suitable for a variety of applications ranging from catalysis to biomedical devices, can be prepared by combining inorganic and organic units at a molecular level [5.3.1]. To ensure the attainment of these properties, an even distribution of the guest building blocks in the host matrix and the absence of grain agglomeration are necessary requirements. The major problem of phase separation that often occurs in these kinds of materials can be avoided by having a covalent bond between the inorganic block and the organic polymer. The attachment of organic groups with crosslinking capability onto the surface of inorganic species allows incorporating the inorganic component by polymerisation reactions [5.3.2]. The hybrid materials, having interesting structural and physical properties, can be prepared by copolymerising unsaturated organic monomers with the transition metal oxo clusters substituted by polymerisable organic ligands [5.3.3, 5.3.4]. It has been shown that the properties of the hybrid materials not only depend on the cluster to monomer ratio, but also on the kind of incorporated cluster [5.3.5]. These hybrid materials, in which metal oxo clusters are homogeneously grafted onto a polysiloxane matrix, can also be conveniently used for the preparation of mixed metal oxide systems [5.3.6]. The schematic of the preparation of the inorganic-organic hybrid materials and the mixed metal oxides is portrayed in Figure 5.3.1.

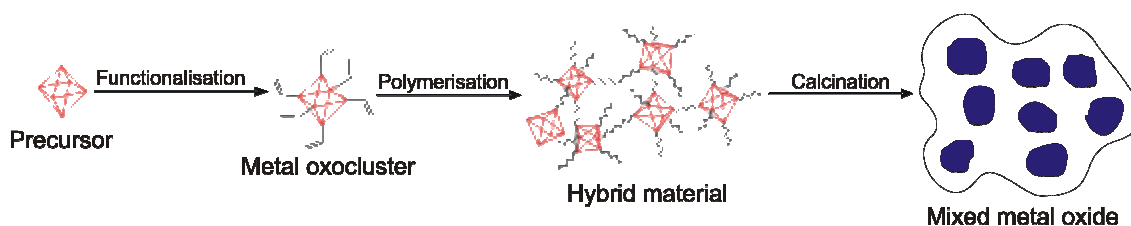


Figure 5.3.1. Preparation of inorganic-organic hybrid materials and mixed metal oxides

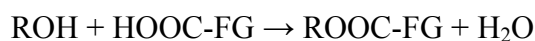
In order to control the composition and performance of the product material and the mutual arrangements of the building blocks, a route yielding a strong chemical bond among the components is highly desirable [5.3.1]. For the formation of these materials, the sol-gel process is often used due to its mild conditions. The addition of carboxylic acids to metal alkoxides produce well defined surface modified crystalline metal oxo clusters of the general formula $M_wO_x(OR)_y(OOC-FG)_z$ (M: metal, R: alkyl group, FG:

functional group). A series of different clusters of this type have already been prepared and characterised [5.3.7]. The composition and the structures of the oxo clusters depend on the metal alkoxide, carboxylic acid and the ratio between them [5.3.8-5.3.10]. A three step mechanism, as depicted in the scheme below, involving substitution, esterification and condensation has been proposed for the formation of metal oxo clusters and verified by a variety of different analytical methods [5.3.7].

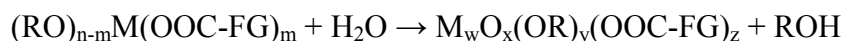
- (1) Partial substitution of alkoxide groups at the metal by carboxylic acids,



- (2) Formation of an ester by the reaction of free carboxylic acid and the released alcohol, and hence the controlled production of water,



- (3) Condensation of partially substituted building blocks in the solution,



The last equation is unbalanced as the number of metal atoms present in each type of oxo cluster is different depending on the degree of condensation. These metal oxo clusters can be supported on a polymer matrix in order to obtain inorganic-organic hybrid materials. Upon calcination these hybrid materials yield mixed metal oxides, where the guest particles are homogeneously distributed onto the host matrix.

The main aim of the work is to investigate the structure of inorganic-organic hybrid materials formed by incorporating zirconium and hafnium oxo clusters in different polysiloxane matrices, especially to verify whether the cluster core is retained in the materials formed. In addition, studies were also performed to determine the local structure of the mixed metal oxides obtained by the calcination of the hybrid materials. The metal oxo clusters, hybrid materials and the mixed metal oxides were prepared by the work group of Dr. S. Gross, Department of Chemical Sciences, University of Padua. The transmission mode XAFS measurements on the samples were performed at ambient conditions at the beamline X1 at HASYLAB, Hamburg and at the XAS beamline at ANKA, Karlsruhe. The zirconium samples were measured at the Zr K-edge at 17998 eV with Si (311) double crystal monochromator, while the hafnium samples were measured at the Hf L_{III}-edge at 9561 eV with Si(111) double crystal monochromator. In the fitting procedure, the various parameters, i.e., coordination number, interatomic distance, Debye-Waller factor and Fermi energy value, were determined by iterations.

5.3.2. Zirconium oxo cluster materials

Zirconium is particularly suitable for the preparation of polynuclear oxo bridged clusters, as Zr(IV) is a highly charged cation. The formation of zirconium oxo clusters is quite favoured over a large range of experimental conditions. In the present work Zr₄ cluster having the formula Zr₄O₂(OMc)₁₂ (OMc: OOC-HC(CH₃)=CH₂) was prepared from 80% (percentage by weight) Zr(O^{*n*}Bu)₄ in n-butanol and 7 molar equivalents of methacrylic acid. After the addition of the reactants the solution was mixed and allowed to stand. Three hours later nucleation of the crystals could be noticed and crystalline cluster was formed from the reaction mixture in one day. The excess solvent was decanted and the obtained crystals were dried at moderate vacuum. All procedures were carried out under argon atmosphere. The crystal structure of the Zr₄ cluster, known from literature [5.3.11] is shown in Figure 5.3.2.

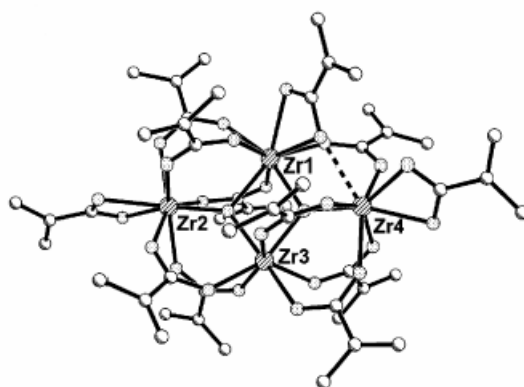


Figure 5.3.2. Molecular structure of Zr₄O₂(OMc)₁₂ adapted from literature [5.3.11].

The obtained Zr₄ cluster was incorporated into two different polysiloxanes, namely methacryloxymethyltriethoxysilane (MAMTES, CH₂=C(CH₃)COO(CH₂)₃Si(OCH₃)₃), methacryloxypropyltrimethoxysilane (MAPTMS, CH₂=C(CH₃)COO(CH₂)₃Si(OC₂H₅)₃) using the procedure mentioned in the literature [5.3.6]. As an example, two hybrid materials with MAMTES in different ratios (**HZ1** and **HZ2**) and one with MAPTMS (**HZ3**), investigated by means of EXAFS spectroscopy, are presented along with the pure Zr₄ cluster. The experimentally determined and theoretically calculated EXAFS functions in *k*-space and their Fourier transforms in real space for the pure Zr₄ cluster and the three hybrid materials, measured at the Zr K-edge, are shown in Figures 5.3.3 to 5.3.6, respectively. The obtained structural parameters are tabulated in Table 5.3.1.

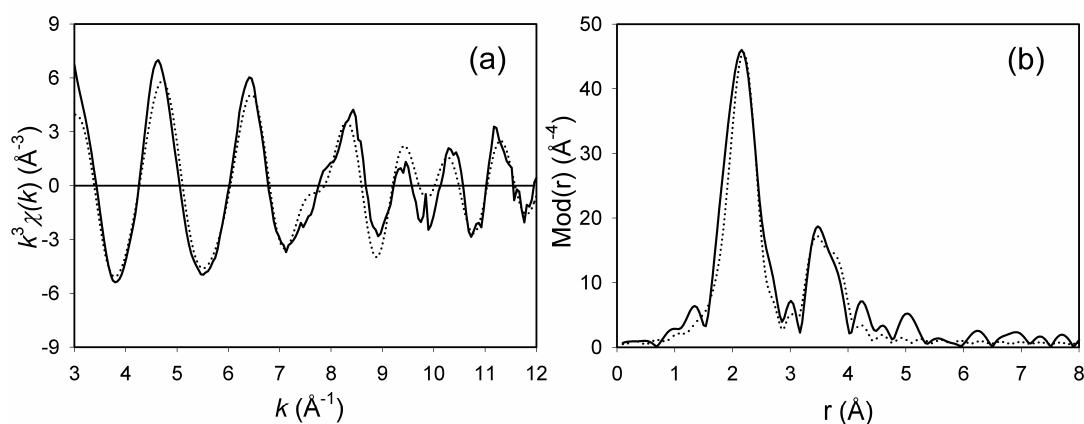


Figure 5.3.3. Experimental (solid line) and calculated (dotted line) EXAFS functions (a) and their Fourier transforms (b) for pure Zr4 cluster.

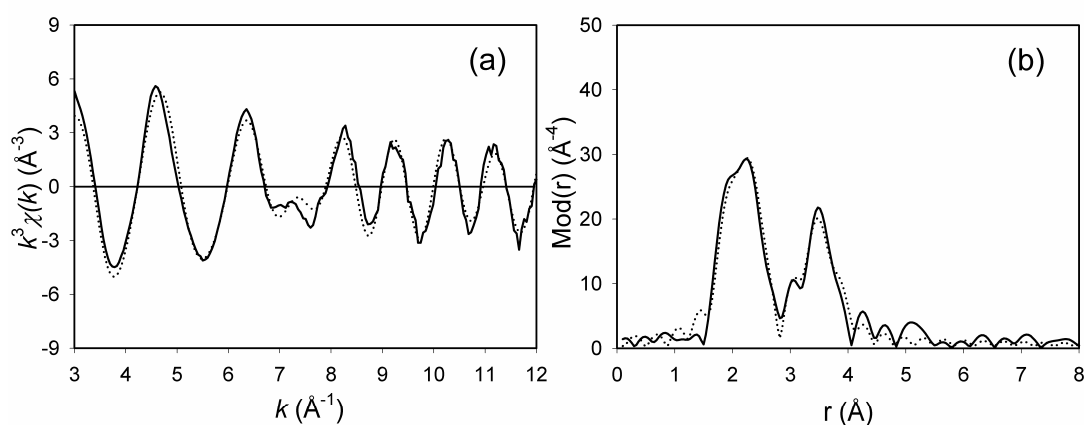


Figure 5.3.4. Experimental (solid line) and calculated (dotted line) EXAFS functions (a) and their Fourier transforms (b) for **HZ1** (MAMTES:Zr4 = 41:1).

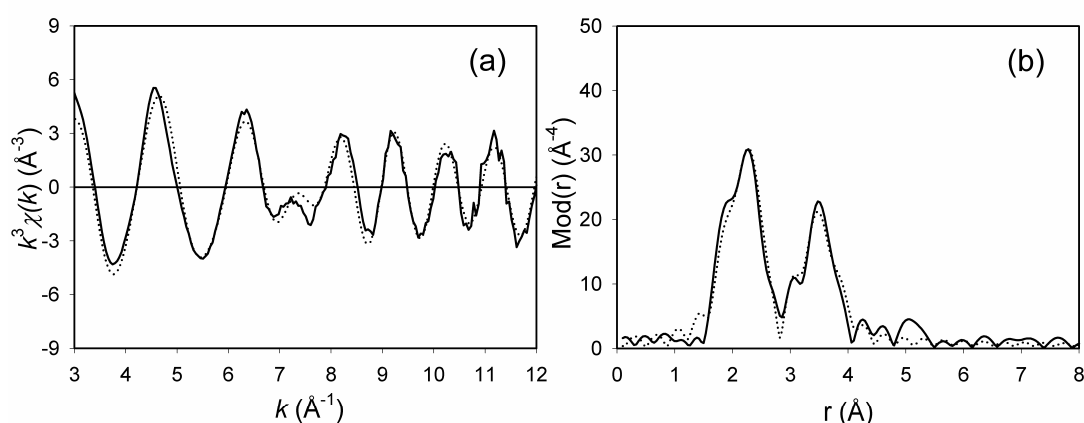


Figure 5.3.5. Experimental (solid line) and calculated (dotted line) EXAFS functions (a) and their Fourier transforms (b) for **HZ2** (MAMTES:Zr4 = 70:1).

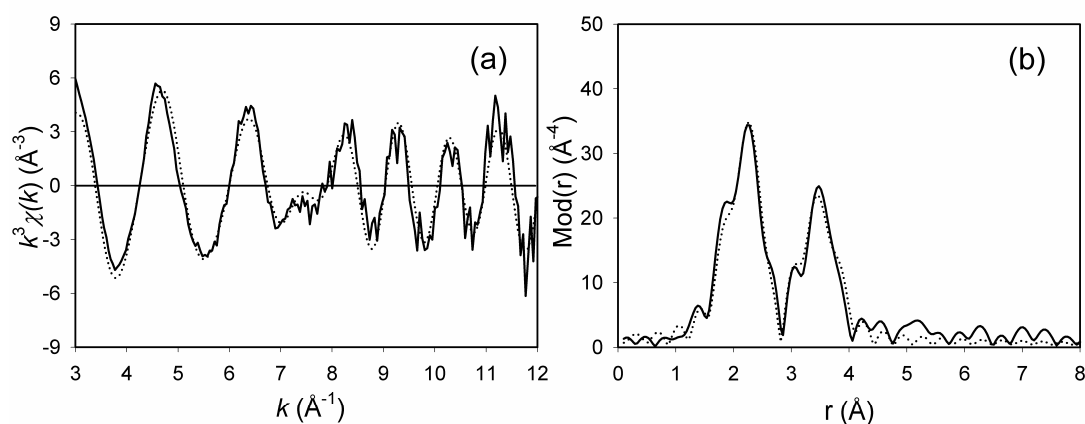


Figure 5.3.6. Experimental (solid line) and calculated (dotted line) EXAFS functions (a) and their Fourier transforms (b) for **HZ3** (MAPTMS:Zr4 = 44:1).

Table 5.3.1. EXAFS obtained structural parameters for the pure Zr4 cluster and the three hybrid materials

Sample	A-Bs ^a	N ^b	r ^c [Å]	σ ^d [Å]	E _F ^e [eV]	k-range [Å ⁻¹]	R-factor
Zr4 cluster	Zr-O	7.5 ± 0.8	2.23 ± 0.02	0.100 ± 0.010	2.237	2.98 - 12.01	29.41
	Zr-Zr	0.5 ± 0.1	3.30 ± 0.03	0.114 ± 0.017			
	Zr-Zr	2.0 ± 0.4	3.53 ± 0.04	0.077 ± 0.015			
HZ1	Zr-O	2.0 ± 0.2	2.12 ± 0.02	0.055 ± 0.006	1.922	2.97 - 12.01	22.26
	Zr-O	6.1 ± 0.6	2.29 ± 0.02	0.089 ± 0.009			
	Zr-Zr	0.6 ± 0.1	3.26 ± 0.03	0.050 ± 0.008			
	Zr-Zr	1.8 ± 0.4	3.57 ± 0.04	0.084 ± 0.017			
HZ2	Zr-O	2.0 ± 0.2	2.12 ± 0.02	0.055 ± 0.006	2.135	2.97 - 12.01	22.22
	Zr-O	6.0 ± 0.6	2.30 ± 0.02	0.089 ± 0.009			
	Zr-Zr	0.6 ± 0.1	3.26 ± 0.03	0.050 ± 0.008			
	Zr-Zr	1.8 ± 0.4	3.58 ± 0.04	0.084 ± 0.017			
HZ3	Zr-O	2.1 ± 0.2	2.11 ± 0.02	0.071 ± 0.007	2.847	2.97 - 12.02	29.34
	Zr-O	6.1 ± 0.6	2.28 ± 0.02	0.087 ± 0.009			
	Zr-Zr	0.6 ± 0.1	3.26 ± 0.03	0.050 ± 0.008			
	Zr-Zr	1.8 ± 0.4	3.55 ± 0.04	0.077 ± 0.015			

^a absorber (A) - backscatterers (Bs), ^b coordination number N, ^c interatomic distance r, ^d Debye-Waller factor σ with its calculated deviation and ^e Fermi energy E_F.

In the analysis of the EXAFS function, a three shell model can be fitted for the pure Zr4 cluster, wherein the coordination numbers were set to known averaged crystallographic values [5.3.11]. The obtained structural parameters are in agreement with the values reported in literature for the crystalline Zr4 cluster [5.3.7]. The EXAFS spectra and the Fourier transform plot of the three hybrid materials are similar, but are different from those of the pure Zr4 cluster. Furthermore, the analysis of the spectra of the hybrid materials reveals considerable changes in the obtained structural parameters

in comparison to the pure Zr₄ cluster. These observed variations could possibly be attributed to a distortion in the geometry of incorporated cluster or to a partial degradation of the cluster into higher aggregates. Cleavage of the cluster by interaction with the monomers is already reported in literature [5.3.12]. The EXAFS results reveal that Zr₄ cluster does not retain its structural integrity upon incorporation in the polysiloxane matrix, irrespective of the nature of the polysiloxane used and the ratio between the polysiloxane and the cluster.

The binary oxide sample (**CZ1**, ZrO_x-SiO_z) was prepared by the calcination of the hybrid material (MAPTMS:Zr₄ = 36:1) at 800°C for 3 hours in air. The experimentally determined and theoretically calculated EXAFS functions in *k*-space and their Fourier transforms in real space for **CZ1**, measured at the Zr K-edge, are shown in Figure 5.3.7 and the obtained structural parameters are summarised in Table 5.3.2.

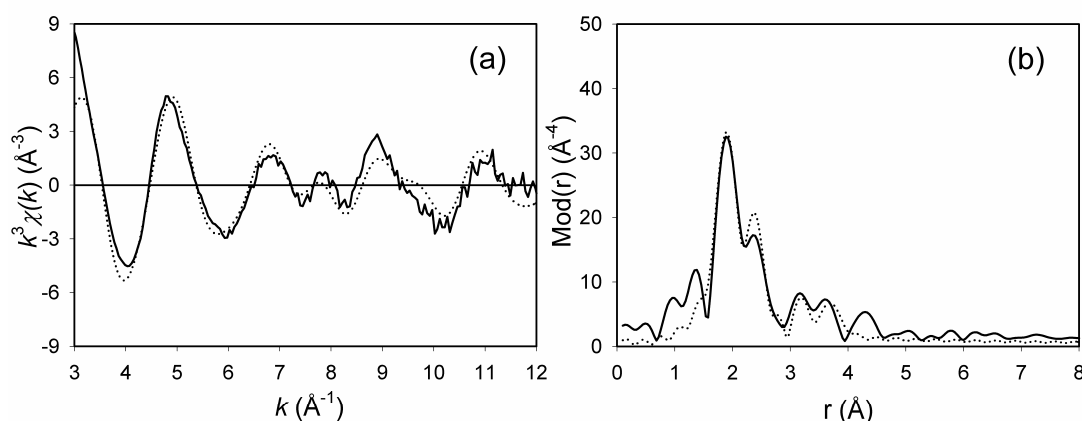


Figure 5.3.7. Experimental (solid line) and calculated (dotted line) EXAFS functions (a) and their Fourier transforms (b) for **CZ1**.

Table 5.3.2. EXAFS obtained structural parameters for ZrO_x-SiO_z binary oxide

Sample	A-Bs ^a	N ^b	r ^c [Å]	σ ^d [Å]	E _F ^e [eV]	<i>k</i> -range [Å ⁻¹]	R-factor
CZ1	Zr-O	3.3 ± 0.3	2.04 ± 0.02	0.067 ± 0.007	4.248	2.99 - 12.03	36.79
	Zr-O	5.7 ± 0.6	2.24 ± 0.02	0.100 ± 0.010			
	Zr-Zr	1.4 ± 0.3	3.38 ± 0.03	0.105 ± 0.016			

^a absorber (A) - backscatterers (Bs), ^b coordination number N, ^c interatomic distance r, ^d Debye-Waller factor σ with its calculated deviation and ^e Fermi energy E_F.

In the analysis of the EXAFS function, a three shell model comprising two oxygen shells and one zirconium shell could be fitted for the binary oxide. Distances corresponding to Zr-O-Si mixed bonds could not be evidenced from EXAFS evaluation, in agreement with the infrared spectroscopic studies [5.3.6]. The EXAFS determined

structural parameters could not be matched with any of the well known polymorphs of crystalline ZrO_2 . In this regard, further information was obtained from the XANES spectra. The comparison of the XANES region of **CZ1** with those of the tetragonal and monoclinic modifications of ZrO_2 is shown in Figure 5.3.8.

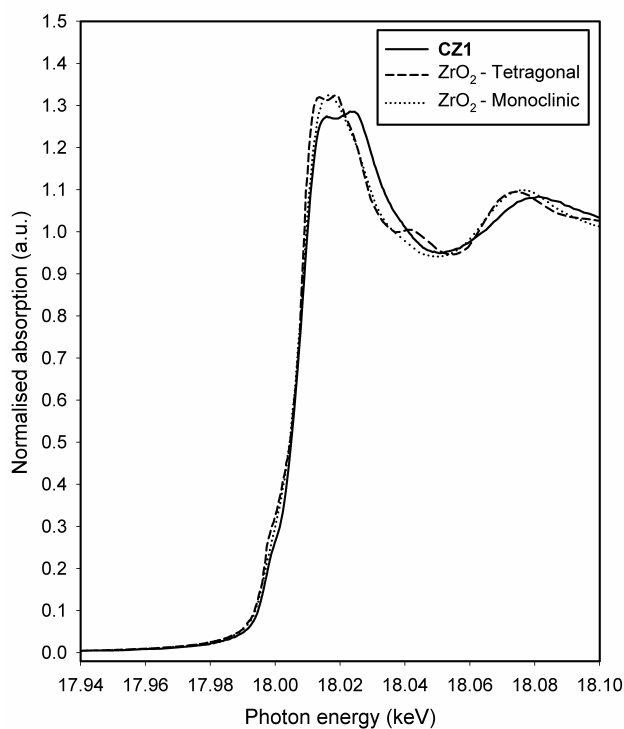


Figure 5.3.8. XANES region of **CZ1** and ZrO_2 polymorphs measured at Zr K-edge.

It could be observed that the XANES spectrum of **CZ1** is similar to that of the tetragonal polymorph, characterised by the presence of a twin peak over the absorption edge. Based on this evidence, the tendency towards the formation of tetragonal zirconia could be inferred. This information was further strengthened by the XRD studies on the sample calcined at $1000^{\circ}C$, which indicated the presence of tetragonal zirconia [5.3.6]. Moreover, EXAFS and XANES investigations on several zirconium containing binary oxide systems prepared using different thermal treatment methods indicated that the concentration of zirconium, the annealing temperature and the preparation technique have strong influences on the structure of the formed oxides [5.3.13].

5.3.3. Hafnium oxo cluster materials

The Hf₄ cluster having the formula $Hf_4O_2(OMc)_{12}$ was prepared from 95% (percentage by weight) $Hf(O^tBu)_4$ in n-butanol and 4 molar equivalents of methacrylic acid employing the procedure given in the literature [5.3.14]. The Hf₄ cluster is

isostructural, but not isomorphous with the Zr₄ cluster. The crystal structure of the Hf₄ cluster, known from literature [5.3.14] is shown in Figure 5.3.9.

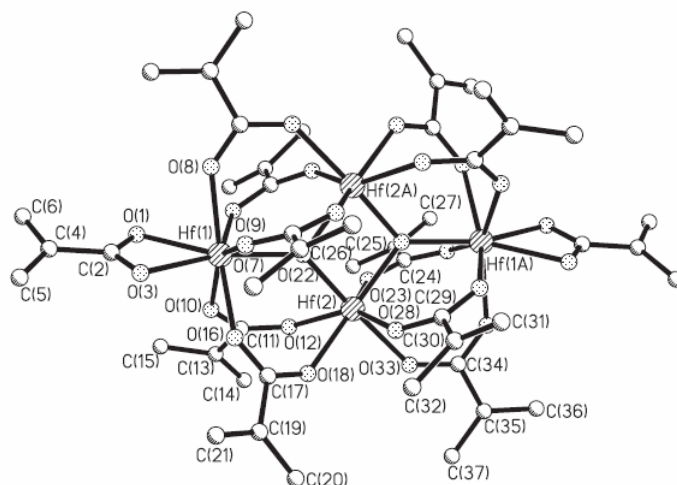


Figure 5.3.9. Molecular structure of Hf₄O₂(OMc)₁₂ adapted from literature [5.3.14].

Similar to the previous case, the obtained Hf₄ cluster was incorporated into the two different polysiloxanes, MAMTES and MAPTMS using the literature procedure [5.3.6]. As a representative example, two samples with MAMTES in different ratios (**HH1** and **HH2**) and one sample with MAPTMS (**HH3**) studied by means of EXAFS spectroscopy are presented here along with the pure Hf₄ cluster. The experimentally determined and theoretically calculated EXAFS functions in *k*-space and their Fourier transforms in real space for the pure Hf₄ cluster and the three hybrid materials, measured at the Hf L_{III}-edge, are shown in Figures 5.3.10 to 5.3.13, respectively. The structural parameters are summarised in Table 5.3.3.

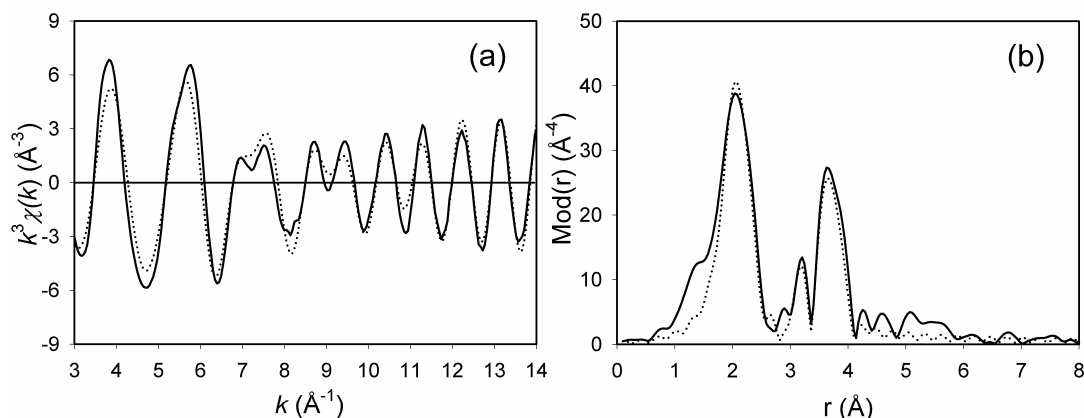


Figure 5.3.10. Experimental (solid line) and calculated (dotted line) EXAFS functions (a) and their Fourier transforms (b) for pure Hf₄ cluster.

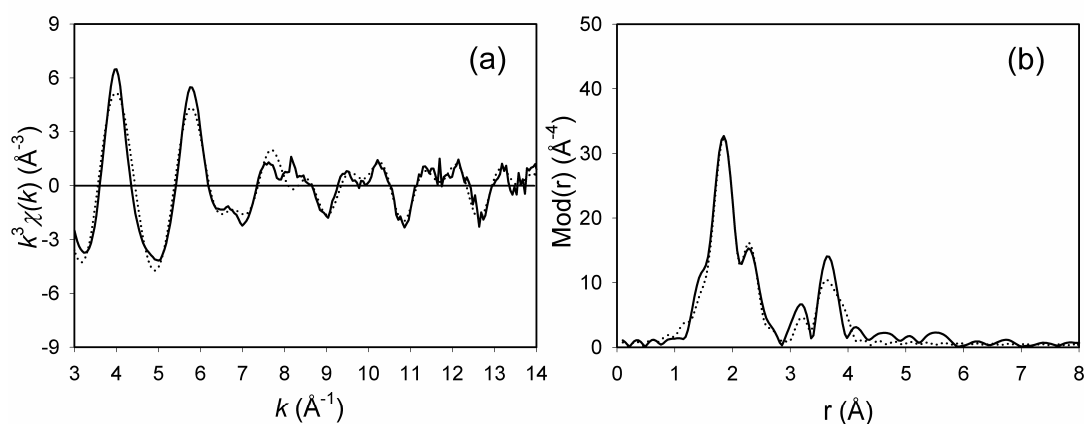


Figure 5.3.11. Experimental (solid line) and calculated (dotted line) EXAFS functions (a) and their Fourier transforms (b) for **HH1** (MAMTES:Hf4 = 19:1).

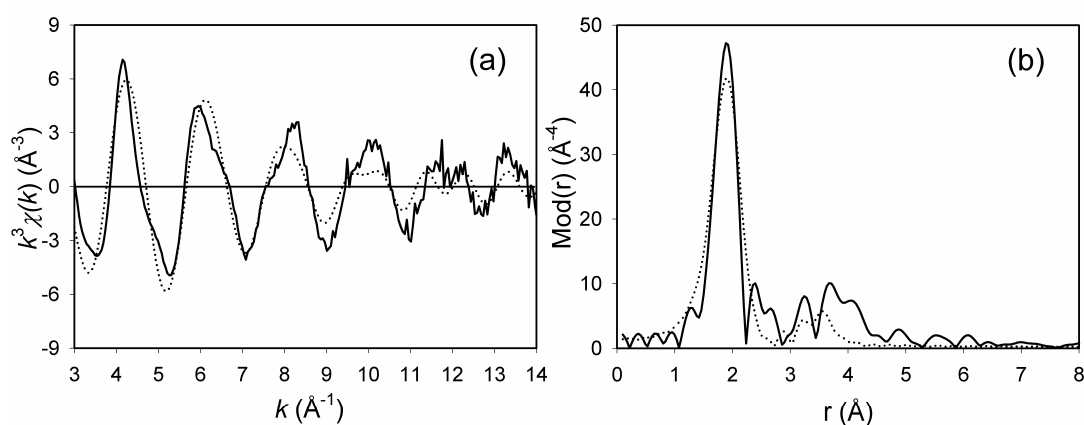


Figure 5.3.12. Experimental (solid line) and calculated (dotted line) EXAFS functions (a) and their Fourier transforms (b) for **HH2** (MAMTES:Hf4 = 118:1).

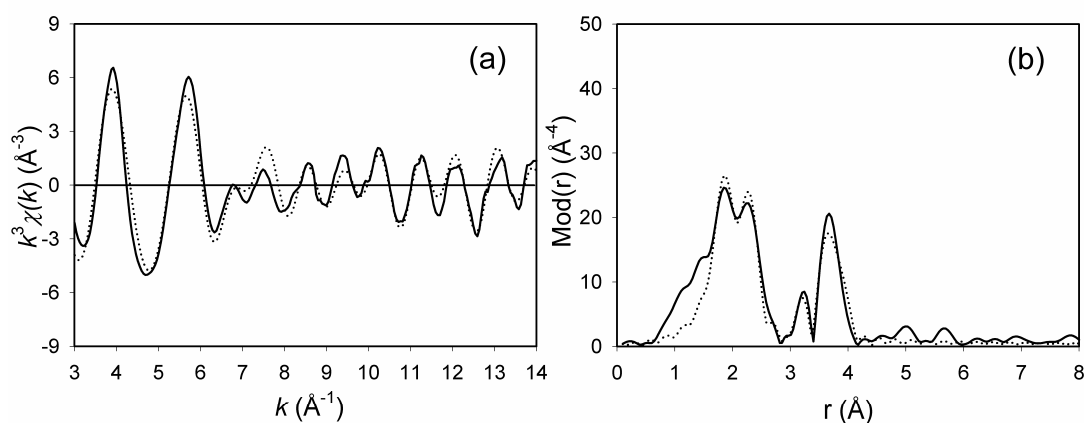


Figure 5.3.13. Experimental (solid line) and calculated (dotted line) EXAFS functions (a) and their Fourier transforms (b) for **HH3** (MAPTMS:Hf4 = 55:1).

Table 5.3.3. EXAFS obtained structural parameters for the pure Hf4 cluster and the three hybrid materials

Sample	A-Bs ^a	N ^b	r ^c [Å]	σ ^d [Å]	E _F ^e [eV]	k-range [Å ⁻¹]	R-factor
Hf4 cluster	Hf-O	7.5 ± 0.8	2.15 ± 0.02	0.102 ± 0.010	-0.009	2.97 - 14.01	27.23
	Hf-Hf	0.5 ± 0.1	3.35 ± 0.03	0.055 ± 0.008			
	Hf-Hf	2.0 ± 0.4	3.47 ± 0.04	0.050 ± 0.010			
HH1	Hf-O	4.2 ± 0.4	2.00 ± 0.02	0.081 ± 0.008	1.254	2.99 - 14.02	27.69
	Hf-O	4.3 ± 0.4	2.19 ± 0.02	0.089 ± 0.009			
	Hf-Hf	0.6 ± 0.1	3.39 ± 0.03	0.055 ± 0.008			
	Hf-Hf	1.1 ± 0.2	3.51 ± 0.04	0.059 ± 0.012			
HH2	Hf-O	7.5 ± 0.8	1.99 ± 0.02	0.112 ± 0.011	5.838	2.97 - 14.02	47.93
	Hf-Hf	0.5 ± 0.1	3.19 ± 0.03	0.077 ± 0.012			
	Hf-Hf	0.8 ± 0.2	3.45 ± 0.04	0.089 ± 0.018			
HH3	Hf-O	4.3 ± 0.4	2.05 ± 0.02	0.081 ± 0.008	1.685	2.97 - 14.03	32.26
	Hf-O	4.4 ± 0.4	2.23 ± 0.02	0.077 ± 0.008			
	Hf-Hf	0.8 ± 0.1	3.42 ± 0.03	0.050 ± 0.008			
	Hf-Hf	1.4 ± 0.3	3.53 ± 0.04	0.050 ± 0.010			

^a absorber (A) - backscatters (Bs), ^b coordination number N, ^c interatomic distance r, ^d Debye-Waller factor σ with its calculated deviation and ^e Fermi energy E_F.

In the analysis of the EXAFS function, a three shell model can be fitted for the pure Hf4 cluster similar to Zr4 cluster, wherein the coordination numbers were set to known averaged crystallographic values [5.3.14]. The obtained structural parameters are in agreement with the values reported in literature for the crystalline Hf4 cluster [5.3.15]. The structural parameters obtained for the three hybrid materials are different from each other and could not be matched with those of the pure Hf4 cluster, indicating the degradation of the cluster core in the hybrid materials. Such a degradation phenomenon has also been evidenced for Hf4 cluster incorporated in polymethylmethacrylate matrix [5.3.15]. The EXAFS results indicate that Hf4 cluster loses its structural integrity upon incorporation in the polysiloxane matrix, irrespective of the nature of the polysiloxane used and the ratio between the polysiloxane and the cluster.

Furthermore, EXAFS investigations were performed on the binary oxides (HfO_y-SiO_z) prepared by the calcination of the hybrid materials, in order to verify whether the nature of the polysiloxane and the ratio between the polysiloxane and the cluster has an influence on the local structure of the formed binary oxides. As a representative case, investigations performed on three selected samples, viz. **CH1** (MAMTES:Hf4 = 19:1), **CH2** (MAMTES:Hf4 = 69:1) and **CH3** (MAPTMS:Hf4 = 55:1), all annealed at 800°C for 3 hours in air, is presented.

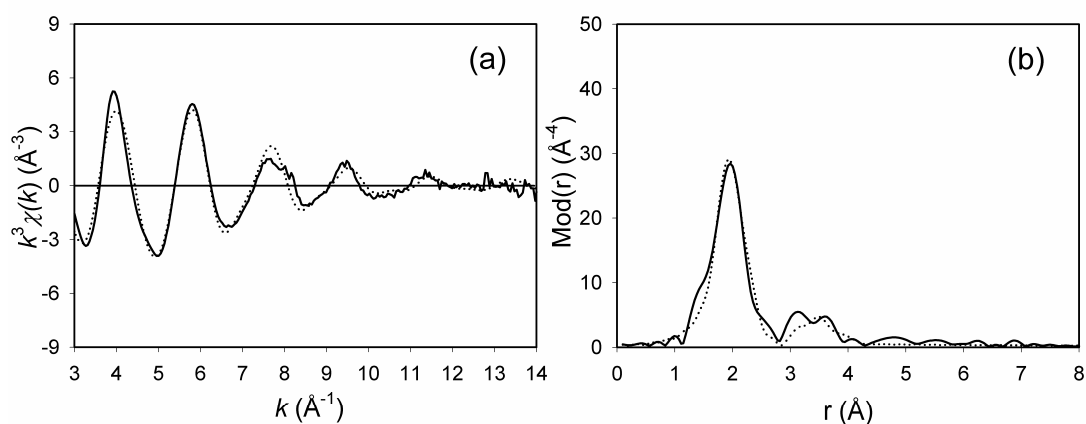


Figure 5.3.14. Experimental (solid line) and calculated (dotted line) EXAFS functions (a) and their Fourier transforms (b) for **CH1** (MAMTES:Hf4 = 19:1).

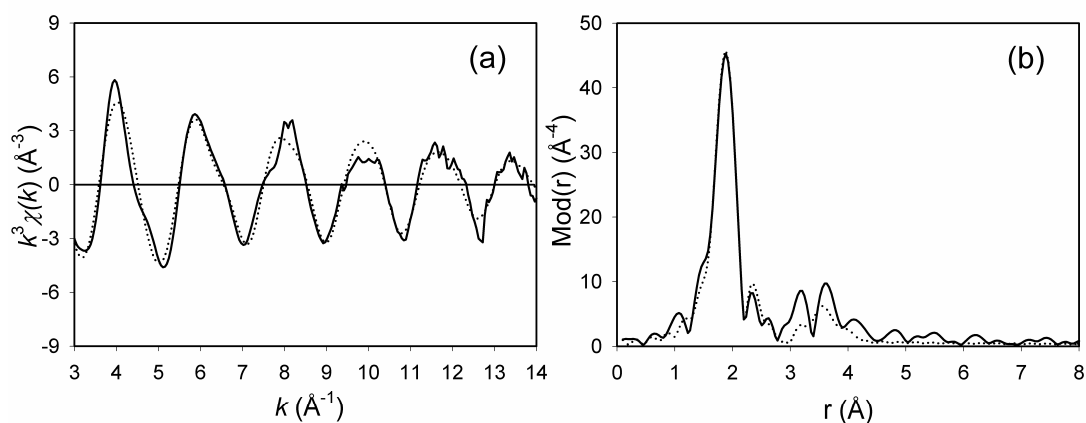


Figure 5.3.15. Experimental (solid line) and calculated (dotted line) EXAFS functions (a) and their Fourier transforms (b) for **CH2** (MAMTES:Hf4 = 69:1).

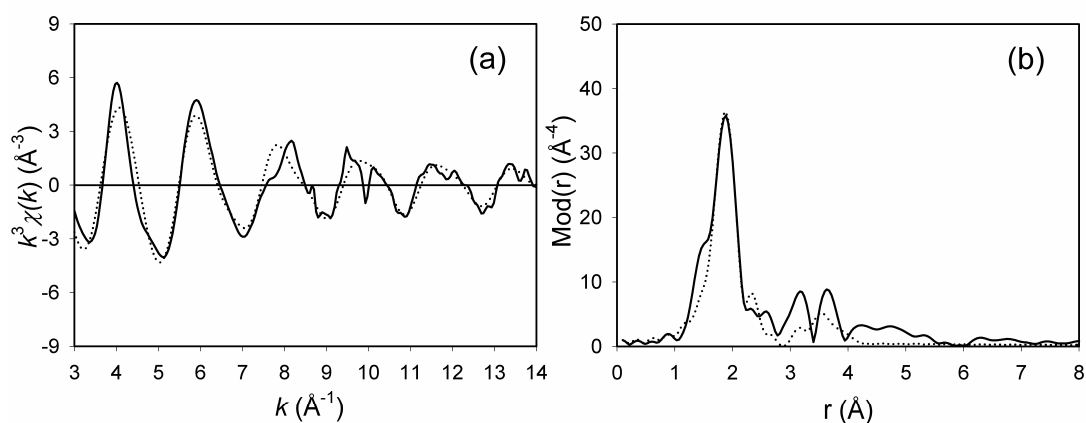


Figure 5.3.16. Experimental (solid line) and calculated (dotted line) EXAFS functions (a) and their Fourier transforms (b) for **CH3** (MAPTMS:Hf4 = 55:1).

Table 5.3.4. EXAFS obtained structural parameters for HfO_y-SiO_z binary oxides

Sample	A-Bs ^a	N ^b	r ^c [Å]	σ ^d [Å]	E _F ^e [eV]	k-range [Å ⁻¹]	R-factor
CH1	Hf-O	2.9 ± 0.3	2.02 ± 0.02	0.081 ± 0.008	1.347	2.99 - 14.02	27.14
	Hf-O	2.9 ± 0.3	2.16 ± 0.02	0.089 ± 0.009			
	Hf-Hf	2.3 ± 0.4	3.43 ± 0.03	0.122 ± 0.018			
CH2	Hf-O	4.4 ± 0.4	1.99 ± 0.02	0.067 ± 0.007	-0.091	2.97 - 14.01	25.49
	Hf-O	3.8 ± 0.4	2.22 ± 0.02	0.107 ± 0.011			
	Hf-Hf	2.2 ± 0.4	3.48 ± 0.03	0.112 ± 0.017			
CH3	Hf-O	4.1 ± 0.4	2.00 ± 0.02	0.077 ± 0.008	1.574	2.96 - 14.02	33.44
	Hf-O	2.3 ± 0.2	2.19 ± 0.02	0.084 ± 0.008			
	Hf-Hf	1.6 ± 0.2	3.45 ± 0.03	0.107 ± 0.016			

^a absorber (A) - backscatterers (Bs), ^b coordination number N, ^c interatomic distance r, ^d Debye-Waller factor σ with its calculated deviation and ^e Fermi energy E_F.

The experimentally determined and theoretically calculated EXAFS functions in *k*-space and their Fourier transforms in real space for **CH1**, **CH2** and **CH3**, measured at Hf L_{III}-edge, are shown in Figures 5.3.14, 5.3.15 and 5.3.16, respectively. The obtained structural parameters are tabulated in Table 5.3.4. In the analysis of the EXAFS function, a three shell model comprising two oxygen shells and one hafnium shell could be fitted for all the three binary oxides. However, the determined structural parameters were different for the three binary oxides, which could be attributed to the different polysiloxane to hafnium compositions in the samples. In addition, distances corresponding to Hf-O-Si mixed bonds could not be evidenced, in agreement with the infrared spectroscopic studies [5.3.6]. It was not possible to match the structural parameters determined by EXAFS with any of the well known crystalline polymorphs of HfO₂. The XANES region at the Hf L_{III}-edge also did not show any remarkable features.

5.3.4. Mixed zirconium and hafnium oxo cluster materials

Hybrid materials incorporating both Zr⁴ and Hf⁴ clusters in polysiloxane matrix were prepared using the procedure outlined in literature [5.3.16]. As an example, the results of the EXAFS measurements on one of the hybrid materials, **HZH1** (MAPTMS:(Zr⁴+Hf⁴) = 48:1, where Zr:Hf = 1.23) is presented. The experimentally determined EXAFS functions in *k*-space and their Fourier transforms in real space for **HZH1**, measured at Zr K-edge and Hf L_{III}-edge, are shown in Figures 5.3.17 and 5.3.18, respectively. Owing to the low absorption jump at the Zr K-edge, the signal to

noise ratio was low in the measured spectrum. In both the cases, the obtained spectra look unusual and could not be evaluated despite several attempts. Due to the existence of the numerous possibilities for the presence of different backscatterers at different distances, an unambiguous assignment of structural parameters using a theoretical model could not be performed. A visual comparison of the EXAFS spectrum and the Fourier transform plot of the hybrid material measured at Hf L_{III}-edge with those of pure Hf₄ cluster reveals that the cluster loses its structural identity upon incorporation in the polysiloxane matrix. However, no inferences could be derived from Zr K-edge measurements, as the obtained spectrum was of poor quality. Similar results were also observed for the other hybrid materials prepared in different compositions.

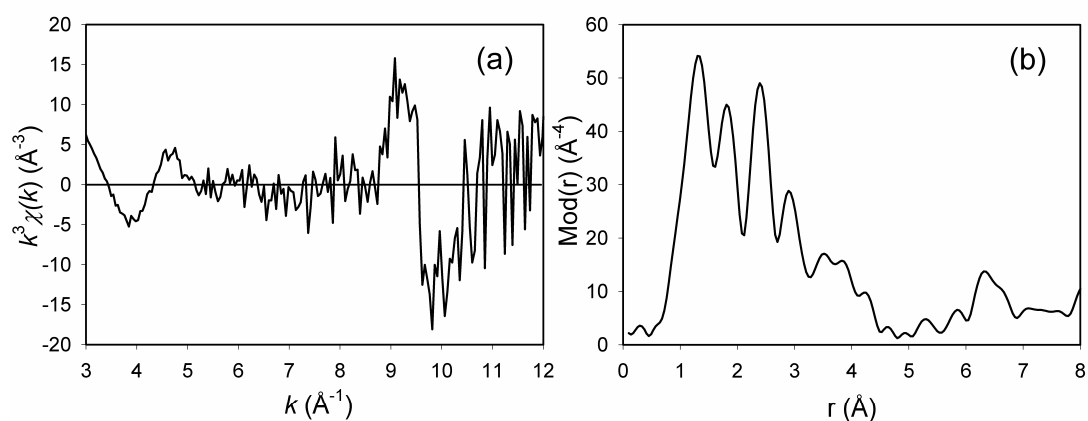


Figure 5.3.17. Experimental EXAFS functions (a) and their Fourier transforms (b) for **HZH1** (MAPTMS:(Zr₄+Hf₄) = 48:1, where Zr:Hf = 1.23) measured at Zr K-edge.

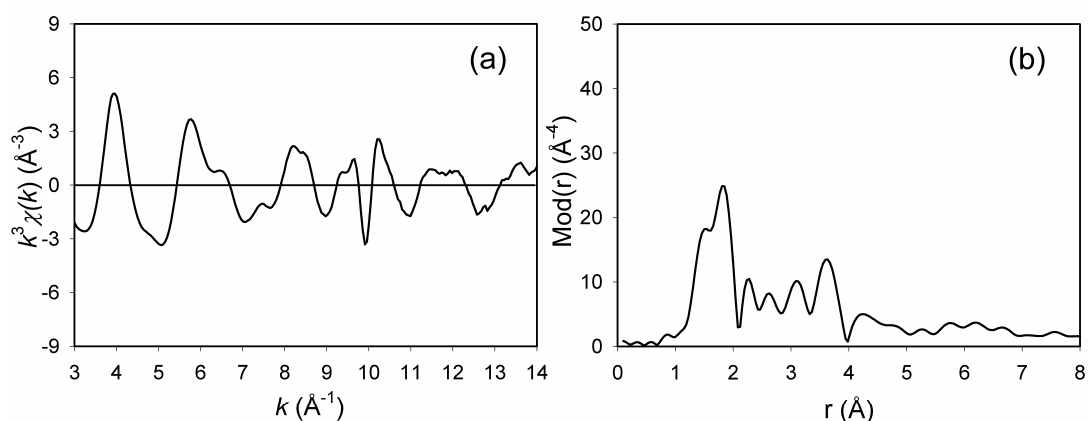


Figure 5.3.18. Experimental EXAFS functions (a) and their Fourier transforms (b) for **HZH1** (MAPTMS:(Zr₄+Hf₄) = 48:1, where Zr:Hf = 1.23) measured at Hf L_{III}-edge.

The mixed metal oxide sample (**CZH1**, ZrO_x-HfO_y-SiO_z) was prepared by the calcination of the hybrid material **HZH1** at 800°C for 3 hours in air. The experimentally

determined and theoretically calculated EXAFS functions in k -space and their Fourier transforms in real space for **CZH1**, measured at the Zr K-edge and Hf L_{III}-edge, are shown in Figures 5.3.19 and 5.3.20, respectively. The obtained structural parameters are given in Table 5.3.5.

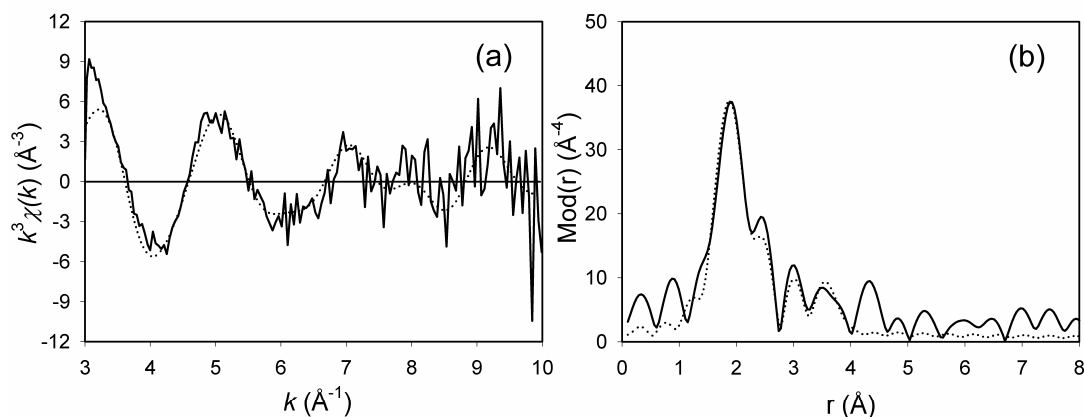


Figure 5.3.19. Experimental (solid line) and calculated (dotted line) EXAFS functions (a) and their Fourier transforms (b) for **CZH1** measured at Zr K-edge.

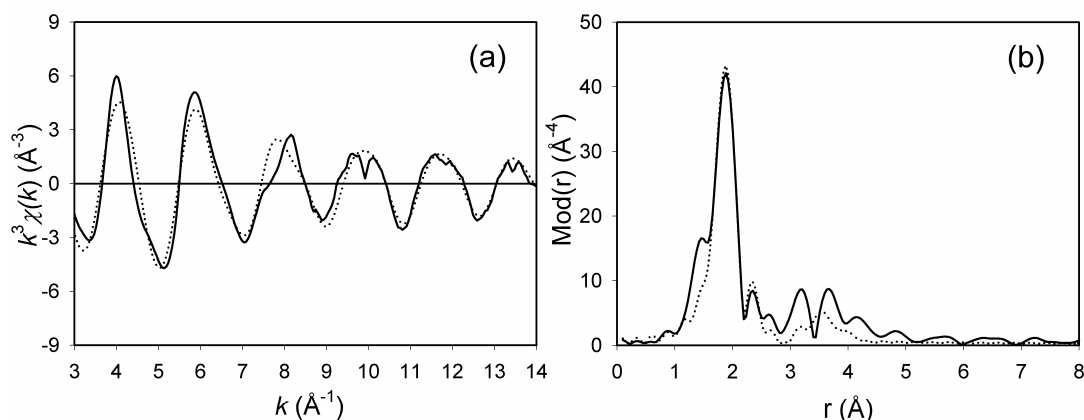


Figure 5.3.20. Experimental (solid line) and calculated (dotted line) EXAFS functions (a) and their Fourier transforms (b) for **CZH1** measured at Hf L_{III}-edge.

Table 5.3.5. EXAFS obtained structural parameters for ZrO_x-HfO_y-SiO_z binary oxide

Edge	A-Bs ^a	N ^b	r ^c [Å]	σ ^d [Å]	E _F ^e [eV]	k-range [Å ⁻¹]	R-factor
Zr K-edge	Zr-O	3.8 ± 0.4	2.01 ± 0.02	0.067 ± 0.007	5.867	2.99 - 9.99	47.68
	Zr-O	5.6 ± 0.6	2.21 ± 0.02	0.105 ± 0.011			
	Zr-Zr	2.0 ± 0.3	3.28 ± 0.03	0.110 ± 0.017			
Hf L _{III} -edge	Hf-O	4.2 ± 0.4	2.00 ± 0.02	0.067 ± 0.007	1.106	2.98 - 14.02	30.48
	Hf-O	2.4 ± 0.2	2.19 ± 0.02	0.077 ± 0.008			
	Hf-Hf	1.8 ± 0.2	3.47 ± 0.03	0.110 ± 0.017			

^a absorber (A) - backscatterers (Bs), ^b coordination number N, ^c interatomic distance r, ^d Debye-Waller factor σ with its calculated deviation and ^e Fermi energy E_F.

Due to the low absorption jump at the Zr K-edge owing to the high extinction in the sample, the signal to noise ratio was not good in the measured spectrum and the EXAFS spectrum could be evaluated only till a k -range of 10 \AA^{-1} . In the analysis of the EXAFS function, a three shell model could be fitted for both the cases. The structural parameters obtained for the Hf L_{III} -edge evaluation are in very good agreement with those reported for **CH3**, indicating that the presence of zirconium does not influence the structural evolution of the hafnium components in the mixture. In both the cases, the presence of Zr-O-Si, Hf-O-Si or Zr-O-Hf mixed bonds could not be evidenced by EXAFS analysis. In addition, as the sample was predominantly amorphous, it was not possible to match the EXAFS determined values with any of the well-known crystalline polymorphs of zirconia or hafnia.

The comparison of the XANES region of **CZH1**, measured at the Zr K-edge is shown in Figure 5.3.21, along with tetragonal and monoclinic modifications of ZrO_2 , which were used as references.

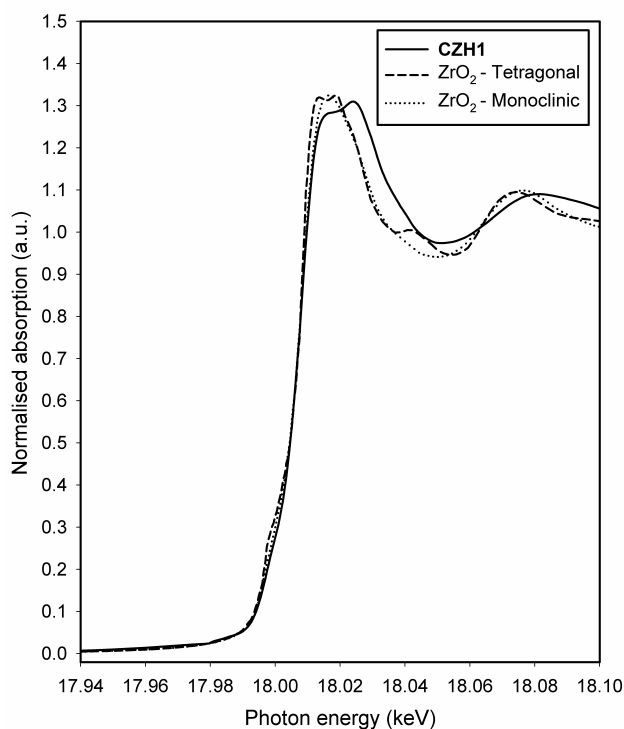


Figure 5.3.21. XANES region of **CZH1** and ZrO_2 polymorphs measured at Zr K-edge.

It could be observed that the **CZH1** was similar to that of the tetragonal polymorph, characterized by the presence of a twin peak over the absorption edge. Based on this evidence, the tendency towards the formation of tetragonal zirconia could be inferred. This information is further strengthened by the XRD investigations on the sample

calcined at 1000°C, which indicate the presence of tetragonal zirconia [5.3.16]. The XANES region at the Hf L_{III}-edge did not show any remarkable features.

5.3.5. Conclusion

The EXAFS studies on the hybrid materials containing zirconium and hafnium oxo clusters reveal that the clusters lose their structural integrity upon incorporation in the polysiloxane matrices, irrespective of the nature of the polysiloxane and the ratio between the polysiloxane and the cluster. The investigations on the mixed metal oxides formed by the calcination of the hybrid materials indicate that silicon to metal composition has strong influences on the local structure of the obtained oxides. In all the cases, the presence of Zr-O-Si, Hf-O-Si or Zr-O-Hf mixed bonds could not be evidenced. Even though, the obtained structural parameters could not be matched with any of the well known crystalline polymorphs of the respective oxides, the XANES studies reveal the tendency towards the formation of tetragonal zirconia in the calcined samples.

5.4. Mechanistic studies on nucleation of ZnS nanoparticles

5.4.1. Introduction

Metal sulphide nanoparticles are intensively investigated particularly due to their interesting physico-chemical properties attributable to quantum confinement effects [5.4.1]. Synthetic routes for the preparation of sulphide nanoparticles are of fundamental importance for the study of the properties at the nanoscale level. The recent advances in the preparation of many metal sulphide based isolated semiconductor nanoparticles have been described in literature, which reviewed the different synthetic approaches ranging from colloidal routes to synthesis in confined matrices to metal-organic routes [5.4.2]. Among metal sulphides, zinc sulphide nanocrystals have been extensively studied due to their outstanding physical properties [5.4.3, 5.4.4].

In this work, a novel method is employed for the synthesis of ZnS nanoparticles, which avoids the use of toxic sulphur sources and can be performed by a simple procedure in a short time. In this process, a stable suspension of small particles is obtained by using a suitable combination of precursors and solvents that favours nucleation over particle growth and prevents coagulation. The molecular level understanding of the kinetics and mechanisms controlling the stepwise evolution (nucleation and growth) of the precursors to give the final materials, can be utilised to improve the synthetic pathways used for the preparation of these systems and to achieve a better control on the particle size. In the present study, the reactions leading to the formation of zinc sulphide nanoparticles were investigated by means of time resolved *in situ* XAFS measurements. Solutions of thioacetic acid and zinc salt (acetate or oxide) dissolved in a solvent (acetic acid or acetone) were investigated and compared with the corresponding zinc precursor and crystalline zinc sulphide to obtain information about the evolution of the structural environment around the zinc atoms in solution. The influence of the precursor and the solvent medium on the nucleation of zinc sulphide nanoparticles was also studied. The XAFS measurements of the samples were performed at the Zn K-edge at 9659 eV at the XAS beamline at ANKA, Karlsruhe. Energy calibration was monitored using a zinc metal foil. All experiments were carried out in transmission mode using Si(111) double crystal monochromator at ambient conditions. In the fitting procedure, coordination numbers, interatomic distances, Debye-Waller factor and Fermi energy value were determined by iterations.

5.4.2. Reactions with zinc acetate

Thioacetic acid and zinc acetate dissolved in acetic acid

In the EXAFS studies, zinc acetate was first analysed in solid state and a single shell with about 5.4 oxygen backscatters could be fitted at about 2.03 Å distance. Later, zinc acetate was dissolved in acetic acid and to this solution, thioacetic acid was added and the mixture was stirred. The experimentally determined and the theoretically calculated EXAFS functions in k -space and their Fourier transforms in real space for the mixture of thioacetic acid and zinc acetate dissolved in acetic acid measured at different time intervals are shown in Figure 5.4.1 along with zinc acetate and zinc sulphide, which were used as references. The obtained structural parameters are given in Table 5.4.1.

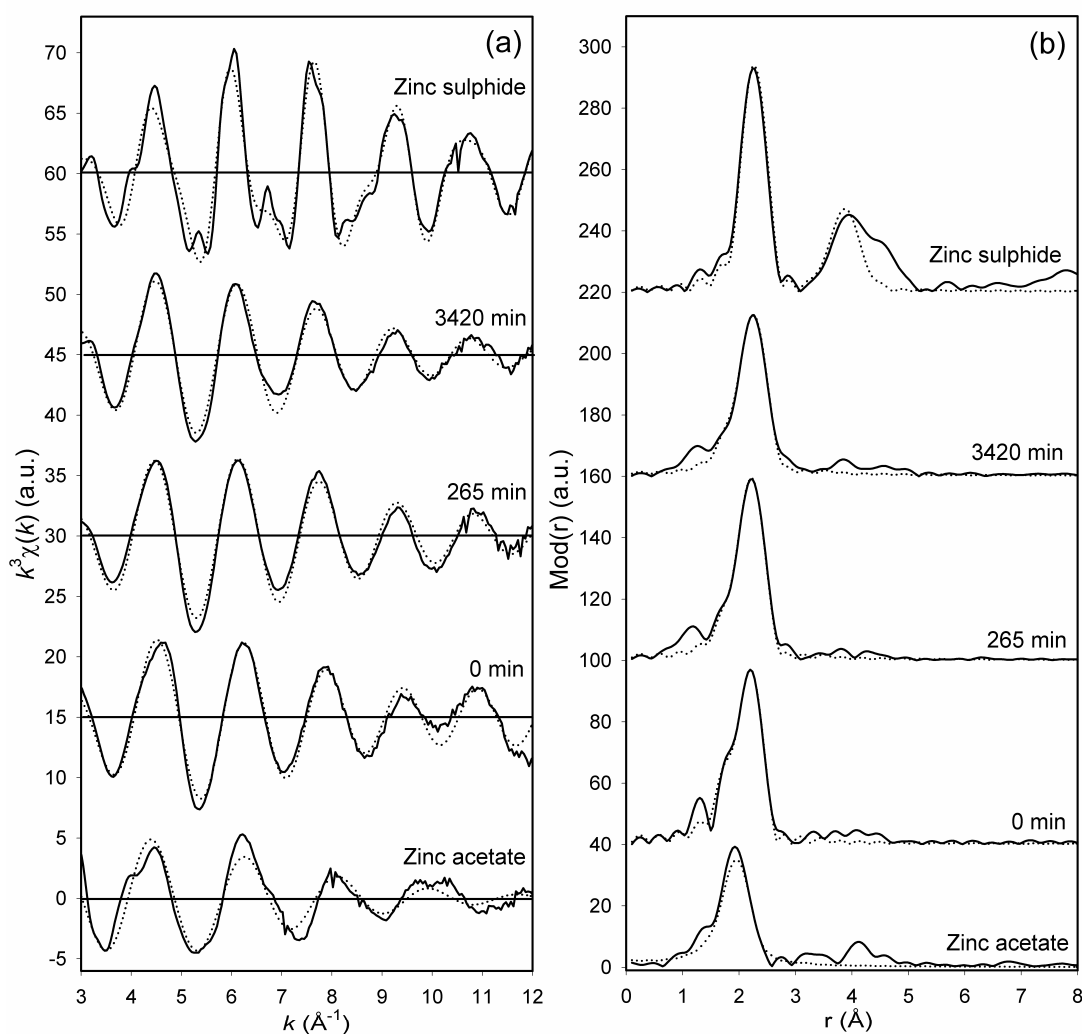


Figure 5.4.1. Experimental (solid line) and calculated (dotted line) EXAFS functions (a) and their Fourier transforms (b) for the mixture of thioacetic acid and zinc acetate dissolved in acetic acid measured at different time intervals, along with the references.

Table 5.4.1. EXAFS obtained structural parameters for the reaction of thioacetic acid and zinc acetate dissolved in acetic acid, measured at different time intervals

Sample/ Time	A-Bs ^a	N ^b	r ^c [Å]	σ ^d [Å]	E_F ^e [eV]	k-range [Å ⁻¹]	R-factor
Zinc acetate	Zn-O	5.4 ± 0.5	2.03 ± 0.02	0.110 ± 0.011	5.238	2.97 - 12.01	38.97
0 min	Zn-O Zn-S	3.6 ± 0.4 1.7 ± 0.3	2.00 ± 0.02 2.29 ± 0.02	0.095 ± 0.009 0.050 ± 0.008	2.316	2.98 - 12.02	21.03
15 min	Zn-O Zn-S	3.8 ± 0.4 2.0 ± 0.3	2.01 ± 0.02 2.29 ± 0.02	0.110 ± 0.011 0.063 ± 0.009	2.342	2.98 - 12.03	19.56
30 min	Zn-O Zn-S	3.7 ± 0.4 2.2 ± 0.3	2.02 ± 0.02 2.30 ± 0.02	0.102 ± 0.010 0.074 ± 0.011	0.938	3.00 - 12.01	23.42
65 min	Zn-O Zn-S	3.8 ± 0.4 2.1 ± 0.3	2.02 ± 0.02 2.30 ± 0.02	0.105 ± 0.011 0.074 ± 0.009	0.860	2.99 - 12.01	27.15
100 min	Zn-O Zn-S	3.8 ± 0.4 2.1 ± 0.3	2.03 ± 0.02 2.31 ± 0.02	0.102 ± 0.010 0.074 ± 0.011	0.812	2.99 - 12.01	23.08
135 min	Zn-O Zn-S	3.8 ± 0.4 2.1 ± 0.3	2.04 ± 0.02 2.31 ± 0.02	0.102 ± 0.011 0.071 ± 0.009	-0.052	2.99 - 12.00	22.71
170 min	Zn-O Zn-S	3.8 ± 0.4 2.1 ± 0.3	2.04 ± 0.02 2.31 ± 0.02	0.102 ± 0.011 0.071 ± 0.009	-0.231	2.98 - 12.00	21.41
265 min	Zn-O Zn-S	2.9 ± 0.3 3.1 ± 0.4	2.04 ± 0.02 2.31 ± 0.02	0.112 ± 0.011 0.081 ± 0.012	0.388	2.97 - 12.01	20.29
910 min	Zn-O Zn-S	2.9 ± 0.3 3.0 ± 0.4	2.03 ± 0.02 2.32 ± 0.02	0.107 ± 0.011 0.081 ± 0.012	-0.359	2.98 - 12.00	17.52
3420 min	Zn-O Zn-S	1.6 ± 0.2 4.1 ± 0.6	2.01 ± 0.02 2.33 ± 0.02	0.102 ± 0.010 0.095 ± 0.014	0.841	2.99 - 12.01	20.03
Zinc sulphide	Zn-S Zn-Zn	4.1 ± 0.4 11.6 ± 2.3	2.33 ± 0.02 3.80 ± 0.04	0.074 ± 0.007 0.122 ± 0.024	-1.772	2.97 - 12.00	25.71

^a absorber (A) - backscatterers (Bs), ^b coordination number N, ^c interatomic distance r, ^d Debye-Waller factor σ with its calculated deviation and ^e Fermi energy E_F .

The analysis indicates a decrease in the coordination number of the oxygen backscatterers as a function of time and the origin of new backscatterers at a distance of 2.29 Å, which could be unambiguously assigned to sulphur atoms. The obtained value is in agreement with the Zn-S distance in bithiourea-zinc acetate [5.4.5]. These findings indicate that the coordination of the metal by sulphur occurs instantaneously as the mixture is prepared, which could probably be attributed to the immediate formation of a

hydrated zinc thioacetate complex as a transition species. Additional measurements were performed at subsequent time intervals up to 3420 min. During the reaction, the structural parameters remained nearly unaltered until 170 min. But the measurements performed after 265 min indicate changes in the obtained structural parameters leading to a decrease in the coordination number of oxygen backscatterers and to an increase in the coordination number of sulphur backscatterers, indicating a gradual increase in the formation of Zn-S species. This supposition was confirmed by the measurements performed after 3420 min where a further increase in the coordination number of sulphur atoms and a decrease in the coordination number of oxygen atoms were observed. It could be evidenced that upon passage of time the quantity of Zn-S species increases and Zn-O species decreases. Comparison of the obtained structural parameters with those of crystalline ZnS reveals that complete formation of zinc sulphide does not occur even after 3420 min. A possible explanation for this observation could be the co-existence of unreacted zinc-oxygen species in the solution along with the freshly formed zinc-sulphur species. Another possibility is that there are still some water molecules coordinated to the metal atom.

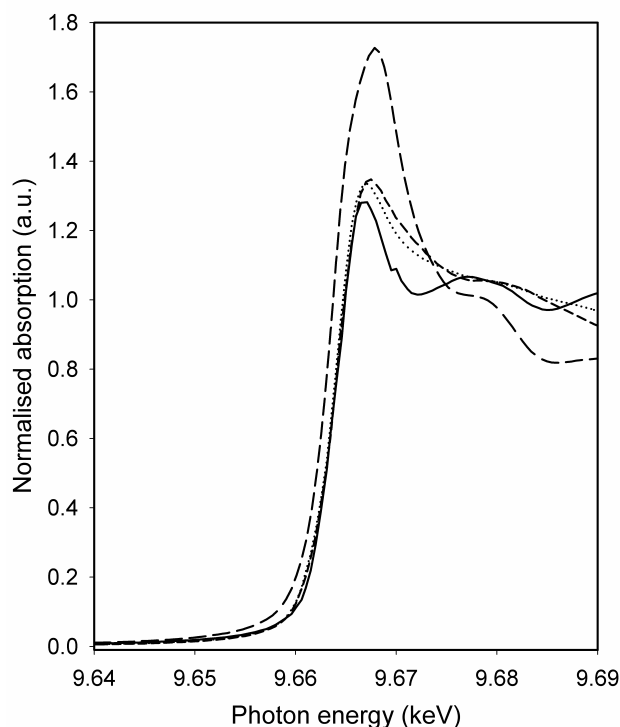


Figure 5.4.2. Zn K-edge XANES spectra recorded during the course of the reaction of thioacetic acid and zinc acetate dissolved in acetic acid. [Zinc acetate (long dashed line), 0 min (short dashed line), 265 min (dotted line) and zinc sulphide (solid line)].

The XANES spectra measured at the Zn K-edge during the course of the reaction of thioacetic acid and zinc acetate dissolved in acetic acid is shown in Figure 5.4.2. For the sake of clarity, only few representative spectra are shown. Although there are changes in the XANES region during the reaction when going from an oxygen to sulphur neighbours, it is difficult to conclude the nature of the growing particle, since both the unreacted zinc-oxygen species and the resulting zinc-sulphur species contribute to the XANES data. Nevertheless, it was possible to monitor the extent of the reaction employing the time-resolved XANES measurements. It is evident that there is a gradual change in the white line (the peak of the absorption edge) intensity with time, approaching that of the sulphide form, in agreement with a similar study reported recently [5.4.6]. The decrease in the white line intensity as a function of time suggests that the reaction results in the formation of zinc-sulphide species.

Thioacetic acid and zinc acetate dissolved in acetone

The experimentally determined and the theoretically calculated EXAFS functions in k -space and their Fourier transforms in real space for the mixture of thioacetic acid and zinc acetate dissolved in acetone measured at different time intervals are shown in Figure 5.4.3 and the obtained structural parameters are given in Table 5.4.2. The time dependent structural evolution of the mixture of thioacetic acid and zinc acetate dissolved in acetone is similar to the observations made with the same precursor used earlier with acetic acid. In this case as well, the coordination of sulphur to zinc occurs immediately when the reaction mixture is prepared. However, contrary to the reaction made in acetic acid, the spectra show no changes even after 260 min of reaction time. In all the cases, a two shell model could be fitted, having about four oxygen backscatterers at about 2.02 Å distance and about two sulphur backscatterers at about 2.29 Å distance. Nevertheless, the spectrum acquired after 2260 min of reaction time indicates a gradual increase in the formation of zinc-sulphur species, which could be observed from the increase in the coordination number of the sulphur atoms and the decrease in the coordination number of the oxygen atoms. Similar to the observations made in the case of acetic acid solution, the complete formation of zinc sulphide could not be evidenced even after 2260 min, which could be attributed to the same reasons mentioned earlier. It could be observed that upon passage of time the quantity of Zn-S species increases and Zn-O species decreases.

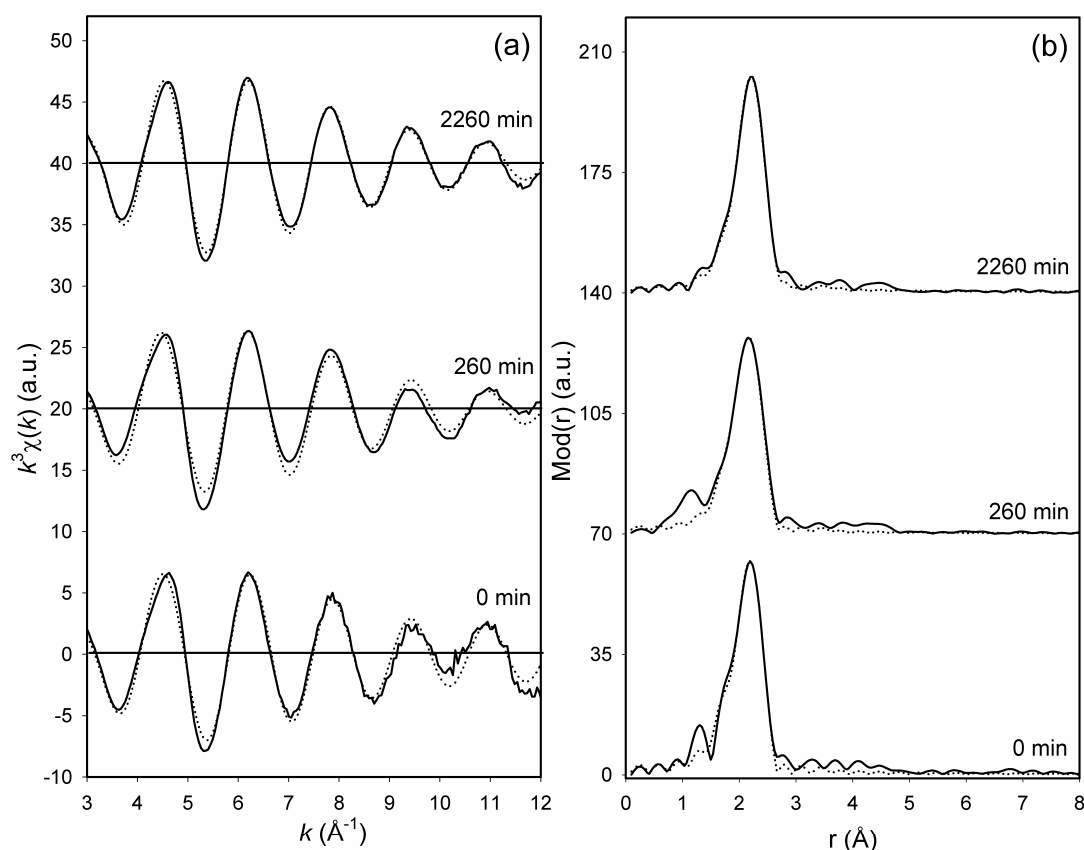


Figure 5.4.3. Experimental (solid line) and calculated (dotted line) EXAFS functions (a) and their Fourier transforms (b) for the mixture of thioacetic acid and zinc acetate dissolved in acetone measured at different time intervals.

Table 5.4.2. EXAFS obtained structural parameters for the reaction of thioacetic acid and zinc acetate dissolved in acetone, measured at different time intervals

Time	A-Bs ^a	N ^b	r ^c [\AA]	σ ^d [\AA]	E_F ^e [eV]	k -range [\AA^{-1}]	R-factor
0 min	Zn-O Zn-S	3.8 ± 0.4 2.1 ± 0.2	2.01 ± 0.02 2.29 ± 0.02	0.105 ± 0.011 0.059 ± 0.009	1.980	2.97 - 12.03	20.19
10 min	Zn-O Zn-S	4.0 ± 0.4 2.1 ± 0.2	2.01 ± 0.02 2.29 ± 0.02	0.092 ± 0.009 0.059 ± 0.009	1.610	2.99 - 12.02	14.46
35 min	Zn-O Zn-S	3.7 ± 0.4 2.2 ± 0.2	2.03 ± 0.02 2.29 ± 0.02	0.102 ± 0.010 0.071 ± 0.011	1.457	2.98 - 12.02	23.33
260 min	Zn-O Zn-S	3.6 ± 0.4 2.2 ± 0.2	2.03 ± 0.02 2.30 ± 0.02	0.100 ± 0.010 0.074 ± 0.011	0.572	2.98 - 12.01	23.98
2260 min	Zn-O Zn-S	2.0 ± 0.2 4.0 ± 0.4	2.00 ± 0.02 2.29 ± 0.02	0.107 ± 0.011 0.089 ± 0.013	2.898	2.97 - 12.04	11.02

^a absorber (A) - backscatters (Bs), ^b coordination number N, ^c interatomic distance r, ^d Debye-Waller factor σ with its calculated deviation and ^e Fermi energy E_F .

The XANES spectra recorded at the Zn K-edge during the course of the reaction of thioacetic acid and zinc acetate dissolved in acetone is shown in Figure 5.4.4. A gradual decrease in the white line intensity as a function of time, suggesting the formation of zinc-sulphide species could be noticed in this case as well.

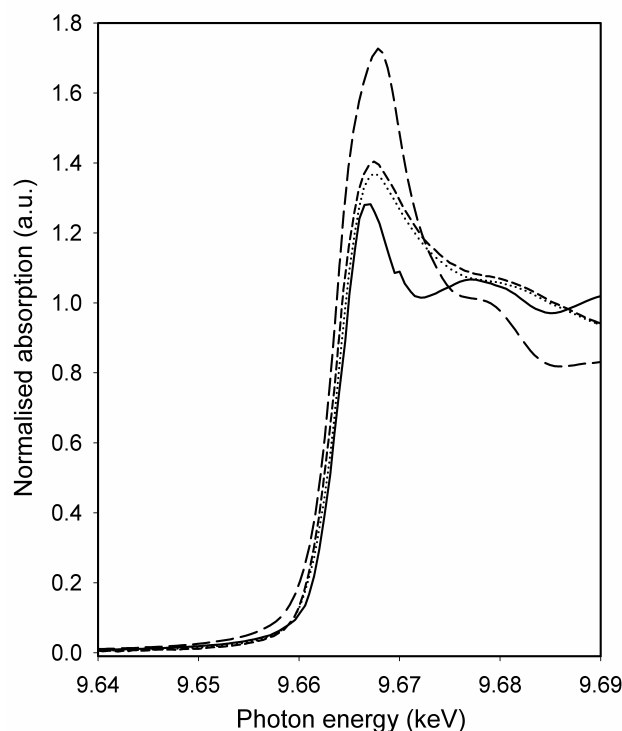


Figure 5.4.4. Zn K-edge XANES spectra measured during the course of the reaction of thioacetic acid and zinc acetate dissolved in acetone. [Zinc acetate (long dashed), 0 min (short dashed), 260 min (dotted) and zinc sulphide (solid line)].

5.4.3. Reactions with zinc oxide

Thioacetic acid and zinc oxide dissolved in acetic acid

In this case, EXAFS and XANES investigations could not be carried out on the reaction mixture, as the addition of thioacetic acid to zinc oxide dissolved in acetic acid instantaneously yielded a rough white precipitate and a colourless solution.

Thioacetic acid and zinc oxide dissolved in acetone

The EXAFS investigations on thioacetic acid and zinc oxide dissolved in acetone indicates the immediate coordination of the sulphur atoms to the metal, similar to the observations made in the earlier cases with zinc acetate precursor. The experimentally determined and the theoretically calculated EXAFS functions in k -space and their Fourier transforms in real space for the mixture of thioacetic acid and zinc oxide

dissolved in acetone measured at different time intervals are shown in Figure 5.4.5, along with zinc oxide, which was used as reference. The determined structural parameters are summarised in Table 5.4.3.

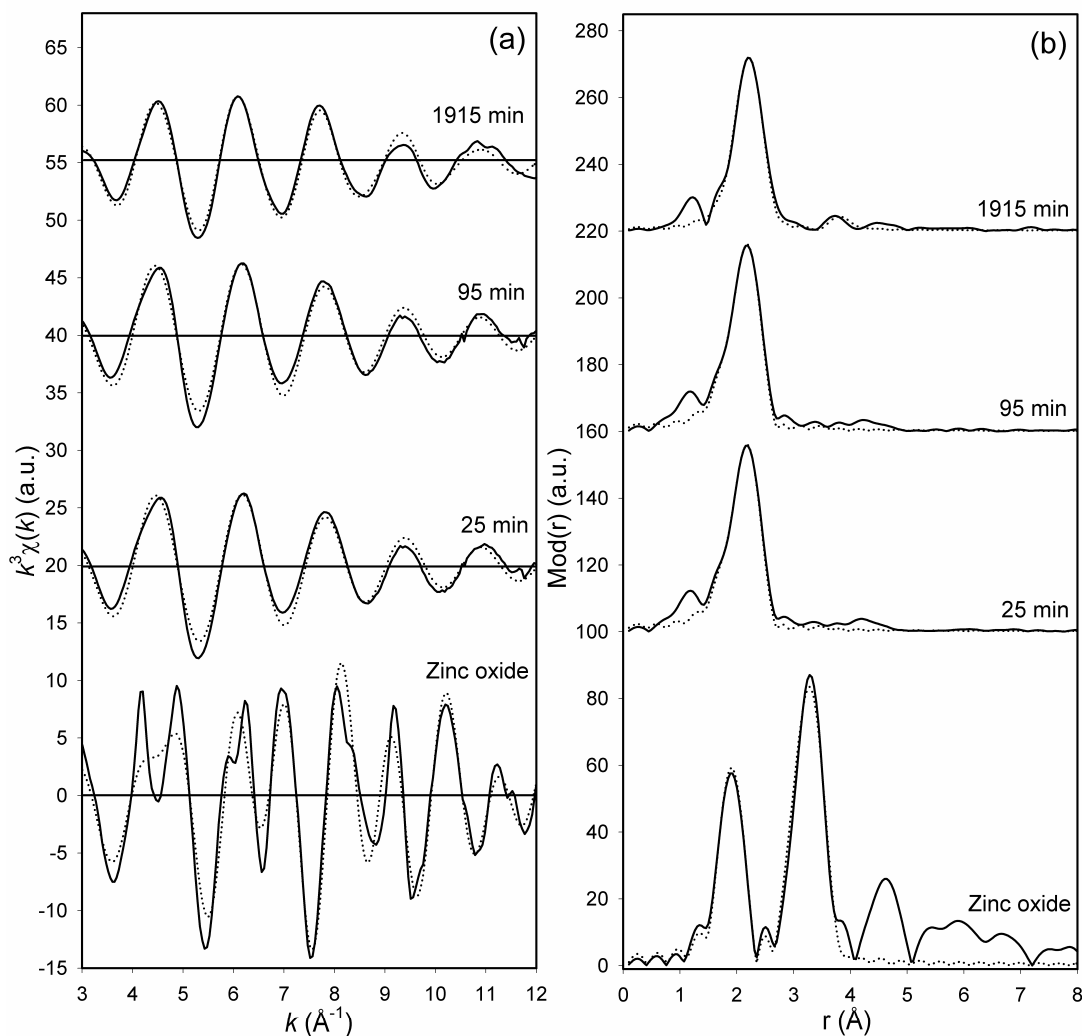


Figure 5.4.5. Experimental (solid line) and calculated (dotted line) EXAFS functions (a) and their Fourier transforms (b) for the mixture of thioacetic acid and zinc oxide dissolved in acetone measured at different time intervals, along with zinc oxide.

In the EXAFS analysis, a two shell model could be fitted, with about four oxygen backscatterers at a distance of about 2.04 \AA and about two sulphur backscatterers at about 2.30 \AA distance. The spectra remain almost the same even after 95 min reaction time, whereas the spectrum measured after 1915 min reaction time indicates significant increase in the formation of zinc-sulphur species in the mixture, as suggested by an increase in the coordination number from two to four for the sulphur atoms. In addition, a zinc backscatterer could also be determined at about 3.79 \AA distance, in agreement

with the Zn-Zn distance in zinc sulphide [5.4.7]. It could be observed that upon passage of time the quantity of Zn-S species increases and Zn-O species decreases.

Table 5.4.3. EXAFS obtained structural parameters for the reaction of thioacetic acid and zinc oxide dissolved in acetone, measured at different time intervals

Sample/Time	A-Bs ^a	N ^b	r ^c [Å]	σ ^d [Å]	E_F ^e [eV]	k-range [Å ⁻¹]	R-factor
Zinc oxide	Zn-O	4.3 ± 0.4	1.96 ± 0.02	0.063 ± 0.006	1.178	2.97 - 12.02	36.21
	Zn-Zn	12.6 ± 2.5	3.21 ± 0.03	0.097 ± 0.019			
25 min	Zn-O	3.7 ± 0.4	2.04 ± 0.02	0.105 ± 0.011	0.224	3.00 - 12.01	22.46
	Zn-S	2.2 ± 0.2	2.30 ± 0.02	0.071 ± 0.011			
60 min	Zn-O	3.6 ± 0.4	2.04 ± 0.02	0.102 ± 0.010	0.592	2.98 - 12.01	23.27
	Zn-S	2.2 ± 0.2	2.30 ± 0.02	0.071 ± 0.011			
95 min	Zn-O	3.7 ± 0.4	2.04 ± 0.02	0.105 ± 0.011	-0.161	2.99 - 12.00	22.44
	Zn-S	2.2 ± 0.2	2.31 ± 0.02	0.071 ± 0.011			
1915 min	Zn-O	1.5 ± 0.1	2.04 ± 0.02	0.105 ± 0.011	1.110	3.00 - 12.02	19.33
	Zn-S	3.8 ± 0.6	2.31 ± 0.02	0.095 ± 0.014			
	Zn-Zn	1.0 ± 0.2	3.79 ± 0.04	0.107 ± 0.021			

^a absorber (A) - backscatters (Bs), ^b coordination number N, ^c interatomic distance r, ^d Debye-Waller factor σ with its calculated deviation and ^e Fermi energy E_F .

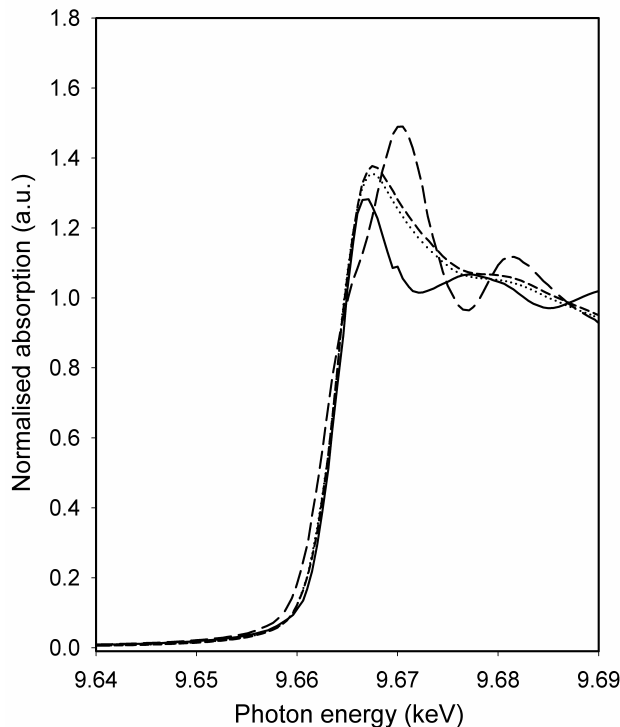


Figure 5.4.6. Zn K-edge XANES spectra measured during the course of the reaction of thioacetic acid and zinc oxide dissolved in acetone. [Zinc oxide (long dashed), 25 min (short dashed), 95 min (dotted) and zinc sulphide (solid line)].

The XANES spectra recorded at the Zn K-edge during the course of the reaction of thioacetic acid and zinc oxide dissolved in acetone is shown in Figure 5.4.6. As noticed in the earlier cases, the XANES region shows a decrease in the white line intensity indicating the formation of zinc-sulphide species in this reaction mixture as well.

5.4.4. Conclusion

The EXAFS and XANES investigations on the reaction of thioacetic acid and zinc precursors dissolved in acetic acid or acetone reveals that the coordination of sulphur atoms takes places immediately when the mixture is prepared and zinc-sulphur species gradually evolves during the course of the reaction. In the case of zinc acetate precursor, even after 3420 min reaction time in the mixture with acetic acid and 2260 min reaction time in the mixture with acetone, the complete formation of ZnS could not be evidenced, which could possibly be attributed either to the presence of unreacted zinc-oxygen species in the mixture or to the coordination of water molecules on to the metal atom. However, in the case of zinc oxide in acetone a relatively higher quantity of zinc sulphide formation could be evidenced even after 1915 min reaction time. The obtained results indicate that zinc oxide reacts comparatively faster with thioacetic acid than zinc acetate. The choice of the reaction medium plays a crucial role in determining the dissolution of the precursors in the solvents, but does not have strong influences on the mechanism of the reaction.

5.5. Time resolved *in situ* studies on key steps of sol-gel process

5.5.1. Introduction

The sol-gel process is a very powerful method for the preparation of nanostructured ceramics, glasses, coatings, fibres and new mixed organic-inorganic materials of technical importance [5.5.1-5.5.2]. In this process, a molecularly homogeneous solution is converted to a sol, a dispersion of colloidal particles in a liquid. The sol reacts further to form a gel, which is an elastic interconnected network with pores of sub-micrometric dimensions and polymeric chains whose average length is larger than a micrometer. Upon drying and thermal treatment, the gel is converted to the final nanostructured material [5.5.1]. The main advantages of the sol-gel process compared to the conventional synthesis routes are the lower sintering temperature, better control of the composition and high homogeneity of the product. An overview of the sol-gel process is pictorially depicted in Figure 5.5.1.

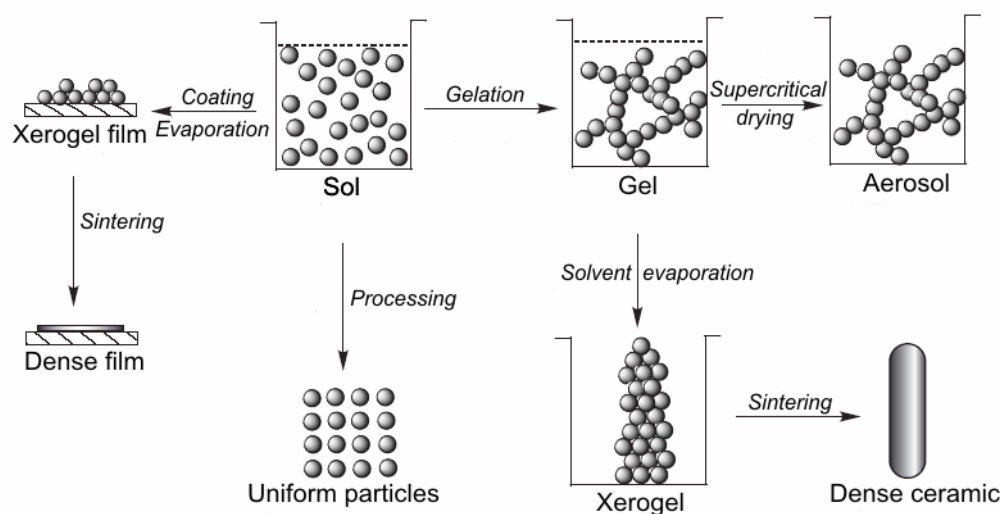
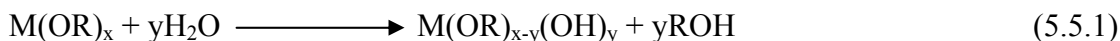


Figure 5.5.1. Overview of the sol-gel process, adapted from literature [5.5.1].

The main requirements for suitable sol-gel precursors are solubility in the reaction media and reactivity towards the hydrolysis process giving monomers or oligomers. They should be easily converted into the corresponding gel by chemical reactions and to the nanosystem by subsequent physical treatments. Furthermore, they should not yield by-products which may affect the purity and the homogeneity of the gel. Molecular precursors which combine all these properties are alkoxides having general formula $M(OR)_x$, where M refers to a metal or metalloid and R refers to the alkyl group [5.5.3]. Metal alkoxides (henceforth also refers to metalloid alkoxides) are generally very

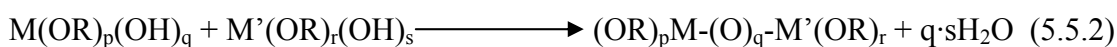
reactive due to the presence of electronegative alkoxy groups making the metal atoms highly prone to nucleophilic attack [5.5.4]. Therefore, metal alkoxides are highly susceptible to hydrolysis and condensation. The main feature of the sol-gel process is the formation of a network by hydrolysis and condensation reactions. The basic steps involved in these two reactions are mentioned below.

Hydrolysis reaction:



M = metal or metalloid; R = alkyl group; x, y = number of moieties involved

Condensation reaction:



M, M' = metal or metalloid; R = alkyl group; p,q,r,s = number of moieties involved

If M = M', then homocondensation and if M ≠ M', then heterocondensation

The chemical reactivity of metal alkoxides depends on the positive charge of the metal atom and on the ability of the metal to increase its coordination number. By controlling the kinetics of the hydrolysis and condensation reactions, it is possible to alter the polymeric structure of the gels. The effect of these structural variations at the molecular level is maintained in the product derived from the gels, thus allowing property modifications in the final materials [5.5.5]. The property and morphology of the materials depend on various factors, such as, type and structure of the metal alkoxide precursors, solvent, acidity, temperature and chemical modification by complexing agents [5.5.6].

The primary aim of the work was to investigate the key steps of the sol-gel process in order to study the structural evolution of the system from the metal alkoxide stage to the polycondensate stage. Time resolved *in situ* XAFS and Raman spectroscopic measurements were performed on germanium, hafnium and tantalum alkoxides to investigate the hydrolysis and condensation reactions in pure state and as a mixture with pre-hydrolysed silicon alkoxide. In addition, complexation of the bidentate ligand, acetylacetonate and the influence of this chemical modification on the kinetics of the hydrolysis and condensation reactions were also studied.

5.5.2. Structure of pure alkoxides

The commercially available alkoxides - Ge(OMe)₄, Ge(OEt)₄, Ge(OⁱPr)₄, Ge(OⁿBu)₄, Hf(OⁿBu)₄ and Ta(OEt)₅ were purchased from ABCR GmbH, Karlsruhe,

Germany and were measured as solutions in anhydrous ethanol. Due to the high moisture sensitivity of metal alkoxides, all procedures involved in preparation and structural characterisation were carried out under dry argon atmosphere. The transmission mode XAFS measurements of the samples were performed at Ge K-edge at 11103 eV, Hf L_{III}-edge at 9561 eV and Ta L_{III}-edge at 9881 eV at the XAS beamline at ANKA, Karlsruhe using Si(111) double crystal monochromator at ambient conditions. Energy calibration was monitored using a platinum metal foil (having L_{III}-edge at 11564 eV) for the Ge K-edge measurements, hafnium metal foil for the Hf L_{III}-edge measurements and tungsten metal foil (having L_{III}-edge at 10207 eV) for the Ta L_{III}-edge measurements.

The structural investigations were initially performed on four different germanium alkoxides – Ge(OMe)₄, Ge(OEt)₄, Ge(OⁱPr)₄ and Ge(OⁿBu)₄ in order to determine whether there exists any structural variations when going up on the homologous series. The experimentally determined and the theoretically calculated EXAFS functions in *k*-space and their Fourier transforms in real space for the four different germanium alkoxides, measured at the Ge K-edge, are shown in Figure 5.5.2 and the corresponding structural parameters are tabulated in Table 5.5.1.

Table 5.5.1. EXAFS obtained structural parameters for the different germanium alkoxides

Sample	A-Bs ^a	N ^b	r ^c [Å]	σ ^d [Å]	E _F ^e [eV]	<i>k</i> -range [Å ⁻¹]	R-factor
Ge(OMe) ₄	Ge-O	5.9 ± 0.6	1.74 ± 0.02	0.055 ± 0.006	2.388	2.98 - 15.04	21.42
	Ge-C	6.3 ± 0.9	2.79 ± 0.03	0.087 ± 0.013			
Ge(OEt) ₄	Ge-O	5.7 ± 0.6	1.75 ± 0.02	0.055 ± 0.006	1.486	2.98 - 15.03	16.71
	Ge-C	6.0 ± 0.9	2.79 ± 0.03	0.087 ± 0.013			
Ge(O ⁱ Pr) ₄	Ge-O	5.7 ± 0.6	1.75 ± 0.02	0.055 ± 0.006	1.386	2.97 - 15.03	24.46
	Ge-C	6.1 ± 0.9	2.80 ± 0.03	0.087 ± 0.013			
Ge(O ⁿ Bu) ₄	Ge-O	5.8 ± 0.6	1.75 ± 0.02	0.055 ± 0.006	0.968	2.99 - 15.03	16.16
	Ge-C	6.2 ± 0.9	2.79 ± 0.03	0.087 ± 0.013			

^a absorber (A) - backscatterers (Bs), ^b coordination number N, ^c interatomic distance r, ^d Debye-Waller factor σ with its calculated deviation and ^e Fermi energy E_F.

The EXAFS spectra obtained for the different germanium alkoxides were identical. In all the cases, two distinct shells could be fitted, one with about six oxygen backscatterers at 1.75 Å distance and the other with about six carbon backscatterers at 2.79 Å distance. These backscatterers correspond to the four terminal alkoxy groups and

the two coordinated alcohol molecules. Furthermore, no near-neighbour germanium backscatterer could be evidenced from the EXAFS measurements on the pure alkoxides, which indicates that all the four investigated germanium alkoxides are monomeric in nature irrespective of the chain length and branching of alkoxy groups, which is in agreement with the data already reported in the literature [5.5.4]. Based on the EXAFS investigations the molecular structure proposed for $\text{Ge}(\text{OR})_4$ is depicted in Figure 5.5.3.

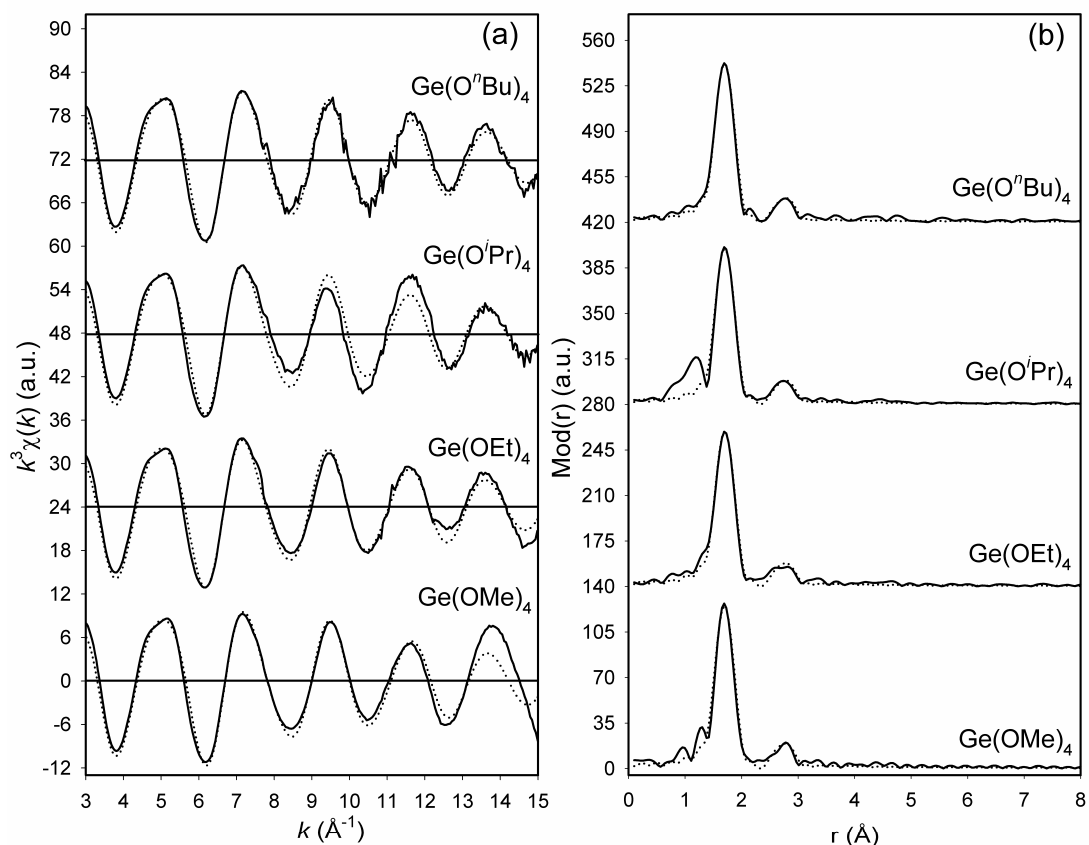
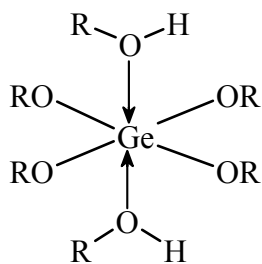


Figure 5.5.2. Experimental (solid line) and calculated (dotted line) EXAFS functions (a) and their Fourier transforms (b) for the germanium alkoxides measured at the Ge K-edge.



R = Alkyl group

Figure 5.5.3. Proposed molecular structure of $\text{Ge}(\text{OR})_4$.

In literature, a dimeric structure was determined for zirconium alkoxides [5.5.7]. However, due to the chemical similarity of hafnium and zirconium, and of their compounds an analogous structure could be expected. The experimentally determined and theoretically calculated EXAFS functions in k -space and their Fourier transformations in real space for $\text{Hf}(\text{O}^n\text{Bu})_4$, measured at the Hf L_{III} -edge, are shown in Figure 5.5.4. The corresponding structural parameters are tabulated in Table 5.5.2.

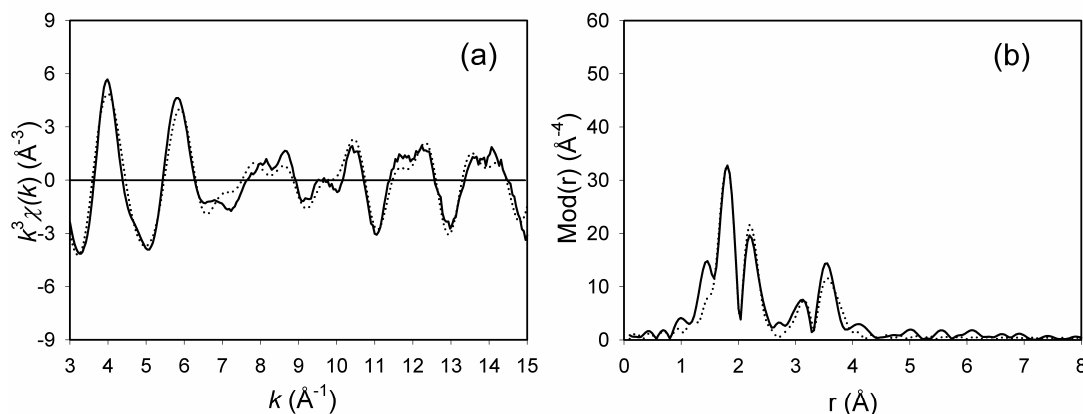


Figure 5.5.4. Experimental (solid line) and calculated (dotted line) EXAFS functions (a) and their Fourier transforms (b) for $\text{Hf}(\text{O}^n\text{Bu})_4$ measured at the Hf L_{III} -edge.

Table 5.5.2. EXAFS obtained structural parameters for $\text{Hf}(\text{O}^n\text{Bu})_4$

Sample	A-Bs ^a	N ^b	r ^c [Å]	σ ^d [Å]	E _F ^e [eV]	k-range [Å ⁻¹]	R-factor
$\text{Hf}(\text{O}^n\text{Bu})_4$	Hf-O	2.4 ± 0.2	1.95 ± 0.02	0.050 ± 0.005	0.738	2.96 - 15.01	30.05
	Hf-O	4.6 ± 0.5	2.14 ± 0.02	0.087 ± 0.009			
	Hf-C	2.3 ± 0.4	3.12 ± 0.03	0.092 ± 0.014			
	Hf-Hf	1.1 ± 0.2	3.42 ± 0.04	0.071 ± 0.014			

^a absorber (A) - backscatterers (Bs), ^b coordination number N, ^c interatomic distance r, ^d Debye-Waller factor σ with its calculated deviation and ^e Fermi energy E_F.

In the analysis of the EXAFS function, a four shell model was applied. The first shell with about two oxygen backscatterers at 1.95 Å, the second shell with about four oxygen backscatterers at 2.14 Å, the third shell with about two carbon backscatterers at 3.12 Å and the fourth shell with a single hafnium backscatterer at 3.42 Å distance could be fitted. The obtained structural parameters are in good agreement with the single crystal data on $\text{Hf}(\text{O}^i\text{Pr})_4$ [5.5.8], which revealed a dimeric structure for the alkoxide, wherein each hafnium atom is coordinated by three terminal and two bridging alkoxy groups as well as one terminal alcoholic group. The results indicate that $\text{Hf}(\text{O}^n\text{Bu})_4$ has a dimeric structure with a six-fold coordination around each hafnium atom. Based on EXAFS studies molecular structure proposed for $\text{Hf}(\text{O}^n\text{Bu})_4$ is shown in Figure 5.5.5.

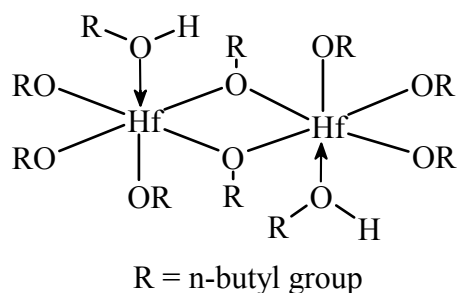


Figure 5.5.5. Proposed molecular structure of $\text{Hf}(\text{O}^n\text{Bu})_4$.

The studies performed on Ta(V) alkoxides by Bradley et al. revealed a dimeric structure for these compounds and the degree of oligomerisation is lowered when they are dissolved in alcohols [5.5.9]. The molecular structure of $\text{Ta}(\text{OEt})_5$ in solution studied by means of ^1H NMR investigations revealed that there is a dynamic equilibrium between monomeric and dimeric species [5.5.10]. The investigations on the electrochemical synthesis of tantalum alkoxides indicated that tantalum pentaalkoxides prefer an octahedral coordination, which is either obtained by dimerisation or by coordination of a solvate atom, such as an alcohol [5.5.11].

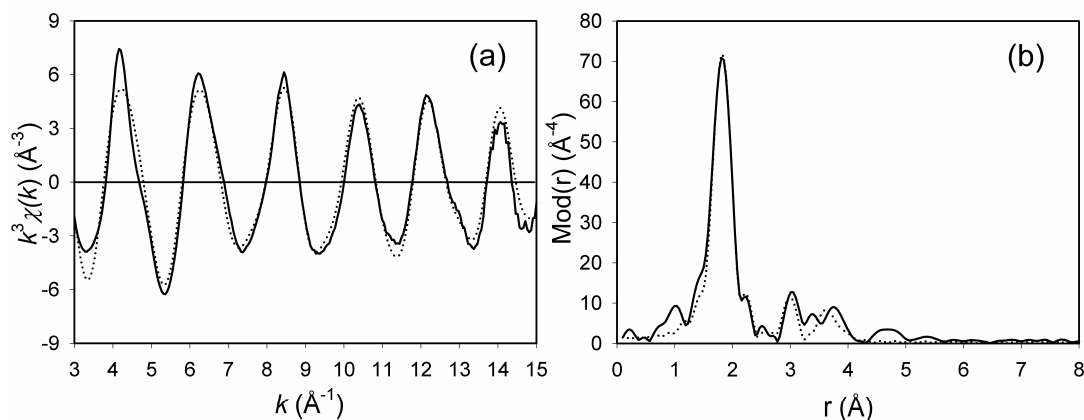


Figure 5.5.6. Experimental (solid line) and calculated (dotted line) EXAFS functions (a) and their Fourier transforms (b) for $\text{Ta}(\text{OEt})_5$ measured at the Ta L_{III} -edge.

Table 5.5.3. EXAFS obtained structural parameters for $\text{Ta}(\text{OEt})_5$

Sample	A-Bs ^a	N ^b	r ^c [Å]	σ ^d [Å]	E _F ^e [eV]	k-range [Å ⁻¹]	R-factor
Ta(OEt) ₅	Ta-O	4.5 ± 0.5	1.91 ± 0.02	0.050 ± 0.005	-1.496	3.00 - 15.01	20.17
	Ta-O	2.6 ± 0.3	2.12 ± 0.02	0.077 ± 0.009			
	Ta-C	3.4 ± 0.5	3.07 ± 0.03	0.071 ± 0.011			
	Ta-Ta	0.8 ± 0.2	3.49 ± 0.04	0.071 ± 0.014			

^a absorber (A) - backscatterers (Bs), ^b coordination number N, ^c interatomic distance r, ^d Debye-Waller factor σ with its calculated deviation and ^e Fermi energy E_F.

The experimentally determined and theoretically calculated EXAFS functions in k -space and their Fourier transformations in real space for $\text{Ta}(\text{OEt})_5$, measured at the Ta L_{III} -edge, are shown in Figure 5.5.6 and the structural parameters are given in Table 5.5.3. The analysis of the EXAFS function was performed using a four shell model in this case as well. The first two coordination shells consist of oxygen atoms, having four backscatterers at 1.91 Å and two backscatterers at 2.12 Å distance. The third shell comprises of three carbon backscatterers at 3.07 Å and the fourth shell has a single tantalum backscatterer at 3.49 Å distance. The obtained structural parameters confirm the dimeric structure of $\text{Ta}(\text{OEt})_5$ with a six-fold coordination around each tantalum atom. The results are in good agreement with those reported in the literature [5.5.12, 5.5.13]. Based on the EXAFS investigations the molecular structure proposed for $\text{Ta}(\text{OEt})_5$ is depicted in Figure 5.5.7.

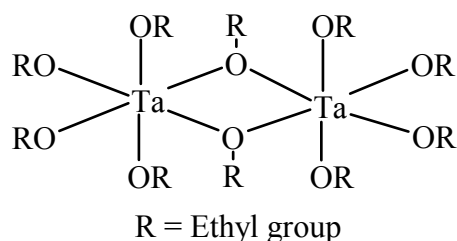


Figure 5.5.7. Proposed molecular structure of $\text{Ta}(\text{OEt})_5$.

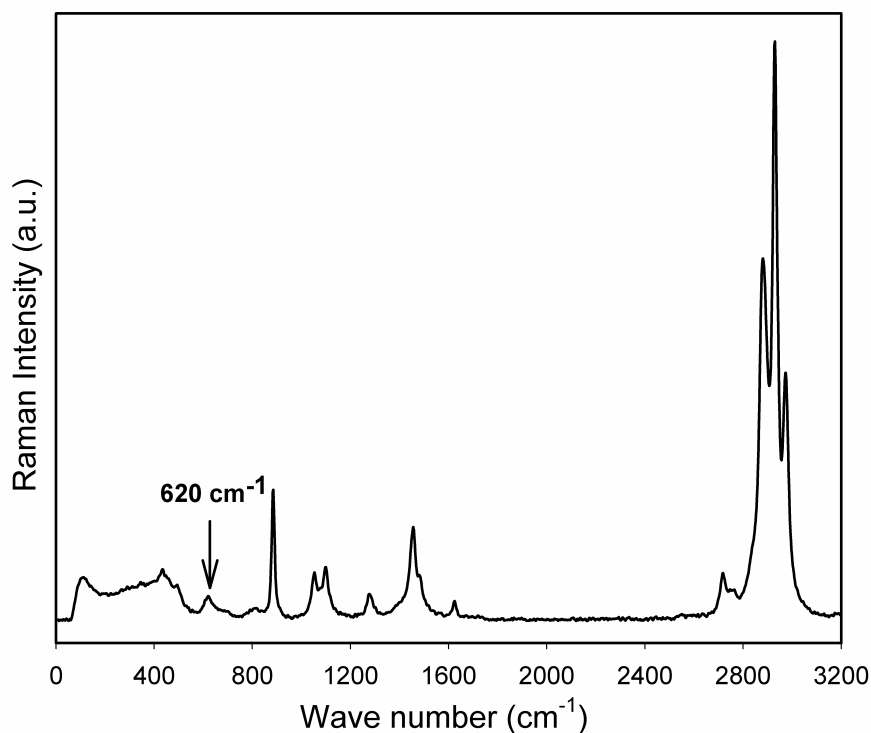


Figure 5.5.8. Raman spectrum of $\text{Ge}(\text{OEt})_4$.

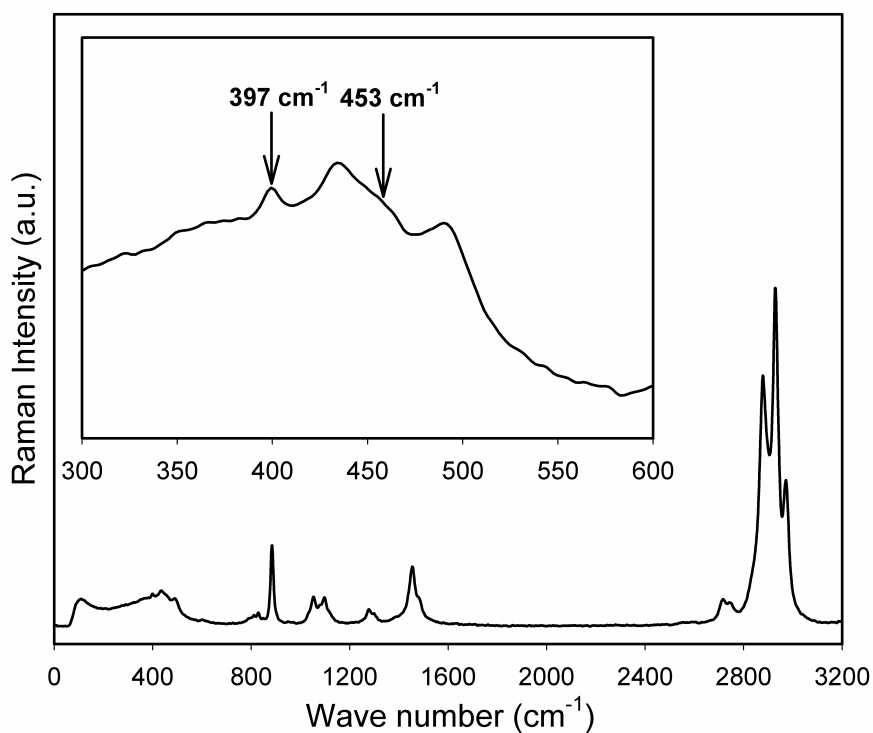


Figure 5.5.9. Raman spectrum of $\text{Hf}(\text{O}^m\text{Bu})_4$.

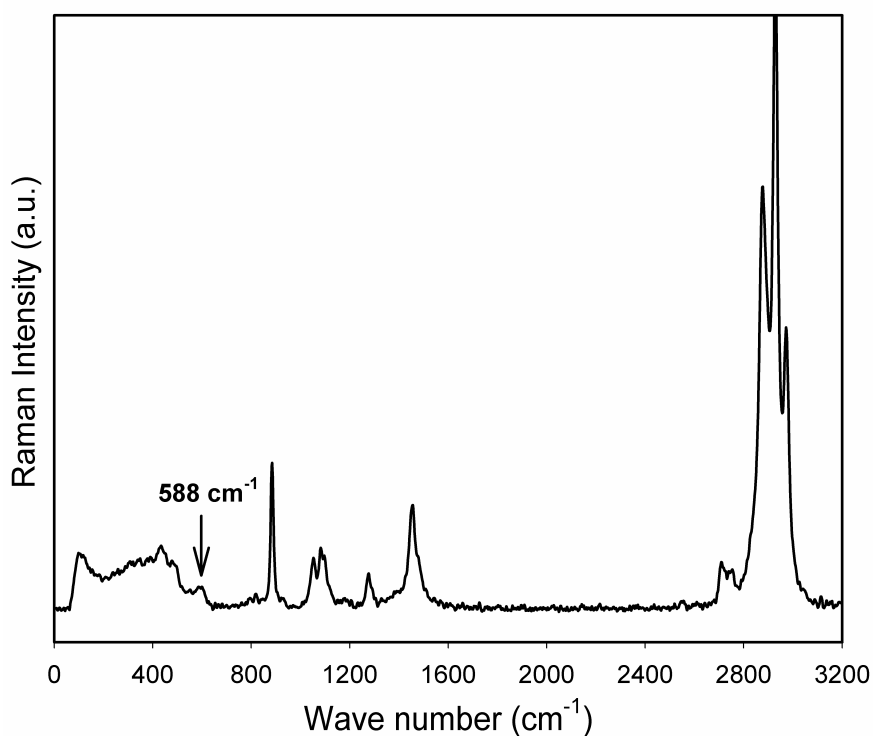


Figure 5.5.10. Raman spectrum of $\text{Ta}(\text{OEt})_5$.

The Raman spectroscopic measurements on the samples were performed at a laser power level of 1250 mW using a quartz cuvette and for an average spectrum, 1024 scans were accumulated. The Raman spectra of $\text{Ge}(\text{OEt})_4$, $\text{Hf}(\text{O}^m\text{Bu})_4$ and $\text{Ta}(\text{OEt})_5$ are

shown in Figures 5.5.8, 5.5.9 and 5.5.10, respectively. In the spectrum of $\text{Ge}(\text{OEt})_4$, the peak at 620 cm^{-1} could be assigned to Ge-O vibrations and the band around 875 cm^{-1} could be assigned to C-O vibrations [5.5.14]. In the spectrum of $\text{Hf}(\text{O}^n\text{Bu})_4$, the peak at 397 cm^{-1} and the shoulder at 453 cm^{-1} could be assigned to Hf-O vibrations [5.5.15] and the bands around 1030 and 1080 cm^{-1} are attributed to the Hf(-O-C) stretching vibrations [5.5.16]. In the spectrum of $\text{Ta}(\text{OEt})_5$, the peak at 588 cm^{-1} could be assigned to Ta-O vibrations [5.5.17] and the bands around 1080 cm^{-1} are attributed to the Ta(-O-C) stretching vibrations [5.5.16]. In all the spectra, the peak at 1050 cm^{-1} is attributed to C-C vibrations and the peaks between 2800 and 2950 cm^{-1} are ascribed to the C-H vibrations of the alkyl groups [5.5.14].

5.5.3. Hydrolysis and condensation of pure alkoxides

The hydrolysis and condensation reactions were studied by adding to the ethanol solutions of metal alkoxides a stoichiometric amount of acidified deionised water (using 37% HCl as catalyst). The solutions were stirred for about 5 min before measurements. Typical molar ratios in solutions were $\text{M}(\text{OR})_x$: EtOH: H_2O : HCl = 1:20:2:0.01. Soon after the addition of water, the formation of a turbid solution could be visually observed, ascribable to the fast hydrolysis and condensation reactions in all the three alkoxides. EXAFS measurements were performed on the solution immediately after mixing and subsequent measurements were carried out at different time intervals.

The experimentally determined and the theoretically calculated EXAFS functions in k -space and their Fourier transforms in real space for $\text{Ge}(\text{O}^n\text{Bu})_4$ and water mixture measured at different time intervals are shown in Figure 5.5.11. For clarity reasons only representative spectra at three different time intervals are shown. The obtained structural parameters are tabulated in Table 5.5.4. The results show that $\text{Ge}(\text{O}^n\text{Bu})_4$ immediately undergoes hydrolysis and condensation reactions, as indicated by the formation of a new Ge backscatterer at 3.16 \AA , a distance typical of Ge-O-Ge. Moreover, a slight variation in the coordination number of oxygen and carbon shell could be noted, in comparison to the pure $\text{Ge}(\text{O}^n\text{Bu})_4$, which could possibly be attributed to the formation of the condensation product. The spectra collected at different time intervals did not show any variations in the structural parameters in comparison with those obtained immediately after mixing.

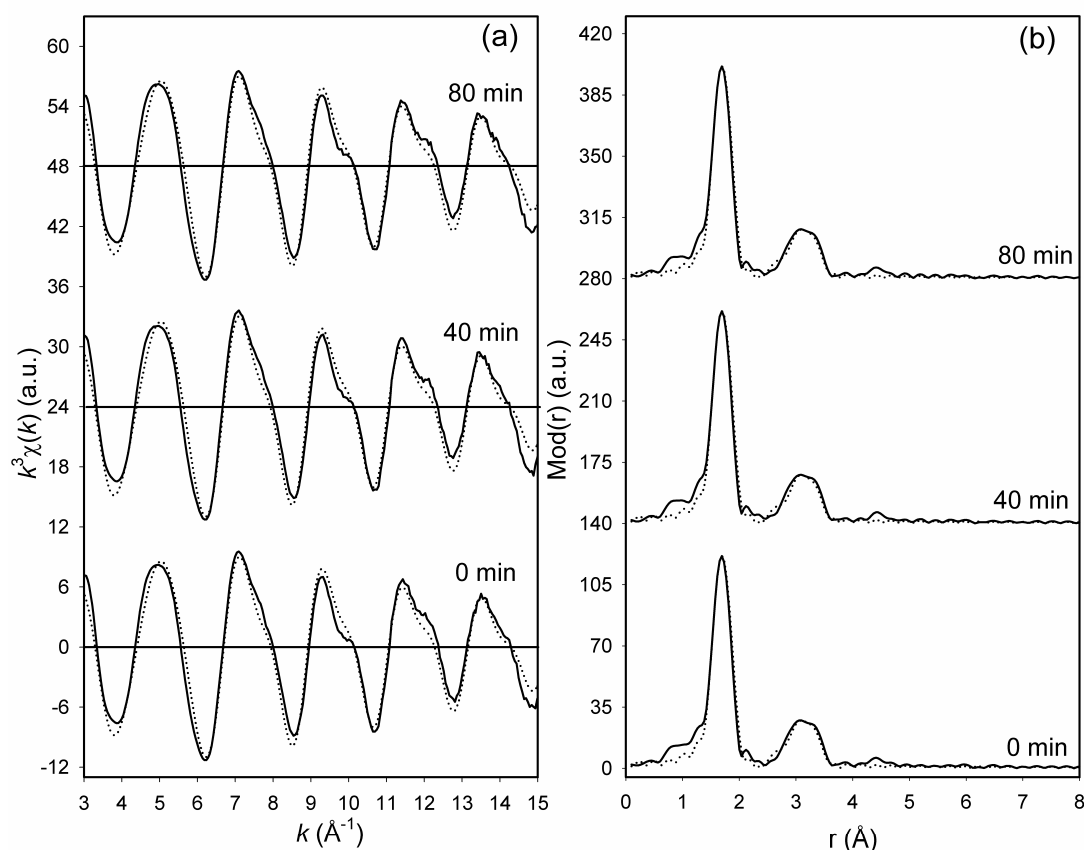


Figure 5.5.11. Experimental (solid line) and calculated (dotted line) EXAFS functions (a) and their Fourier transforms (b) for $\text{Ge}(\text{O}^n\text{Bu})_4$ and water mixture measured at different time intervals, at the Ge K-edge.

Table 5.5.4. EXAFS obtained structural parameters for $\text{Ge}(\text{O}^n\text{Bu})_4$ and water mixture measured at different time intervals

Time	A-Bs ^a	N ^b	r ^c [\AA]	σ ^d [\AA]	E_F ^e [eV]	k -range [\AA^{-1}]	R-factor
0 min	Ge-O Ge-C Ge-Ge	5.3 ± 0.5 4.9 ± 0.7 1.1 ± 0.2	1.74 ± 0.02 2.82 ± 0.03 3.16 ± 0.04	0.050 ± 0.005 0.097 ± 0.015 0.050 ± 0.010	1.673	2.95 - 15.04	20.36
40 min	Ge-O Ge-C Ge-Ge	5.3 ± 0.5 5.4 ± 0.8 1.0 ± 0.2	1.74 ± 0.02 2.82 ± 0.03 3.16 ± 0.04	0.050 ± 0.005 0.102 ± 0.015 0.050 ± 0.010	1.836	2.95 - 15.04	20.97
60 min	Ge-O Ge-C Ge-Ge	5.2 ± 0.5 5.0 ± 0.8 1.1 ± 0.2	1.74 ± 0.02 2.82 ± 0.03 3.16 ± 0.04	0.050 ± 0.005 0.097 ± 0.015 0.050 ± 0.010	1.541	2.94 - 15.03	19.31
80 min	Ge-O Ge-C Ge-Ge	5.3 ± 0.5 4.9 ± 0.7 1.1 ± 0.2	1.74 ± 0.02 2.82 ± 0.03 3.16 ± 0.04	0.050 ± 0.005 0.095 ± 0.014 0.050 ± 0.010	1.558	2.94 - 15.03	20.14

^a absorber (A) - backscatterers (Bs), ^b coordination number N, ^c interatomic distance r , ^d Debye-Waller factor σ with its calculated deviation and ^e Fermi energy E_F .

The experimentally determined and the theoretically calculated EXAFS functions in k -space and their Fourier transforms in real space for $\text{Hf}(\text{O}^n\text{Bu})_4$ and water mixture measured at Hf L_{III} -edge are shown in Figure 5.5.12 and the structural parameters are summarised in Table 5.5.5. The results show that $\text{Hf}(\text{O}^n\text{Bu})_4$ instantaneously undergoes hydrolysis and condensation reactions, as indicated by the change in the coordination number of hafnium and carbon backscatterers. Moreover, the oxygen shells are no longer separated but occur as a single shell at 2.12 Å distance and an increase in Hf-C distance from 3.12 Å to 3.21 Å could also be noticed, in comparison to the pure $\text{Hf}(\text{O}^n\text{Bu})_4$. The signal to noise ratio is not good for the EXAFS spectra obtained immediately after the addition of water, owing to the inhomogeneities caused in the solution during the initial stages of gelation. Furthermore, the spectra acquired at different time intervals did not show any remarkable variations in the structural parameters in comparison with those obtained immediately after mixing.

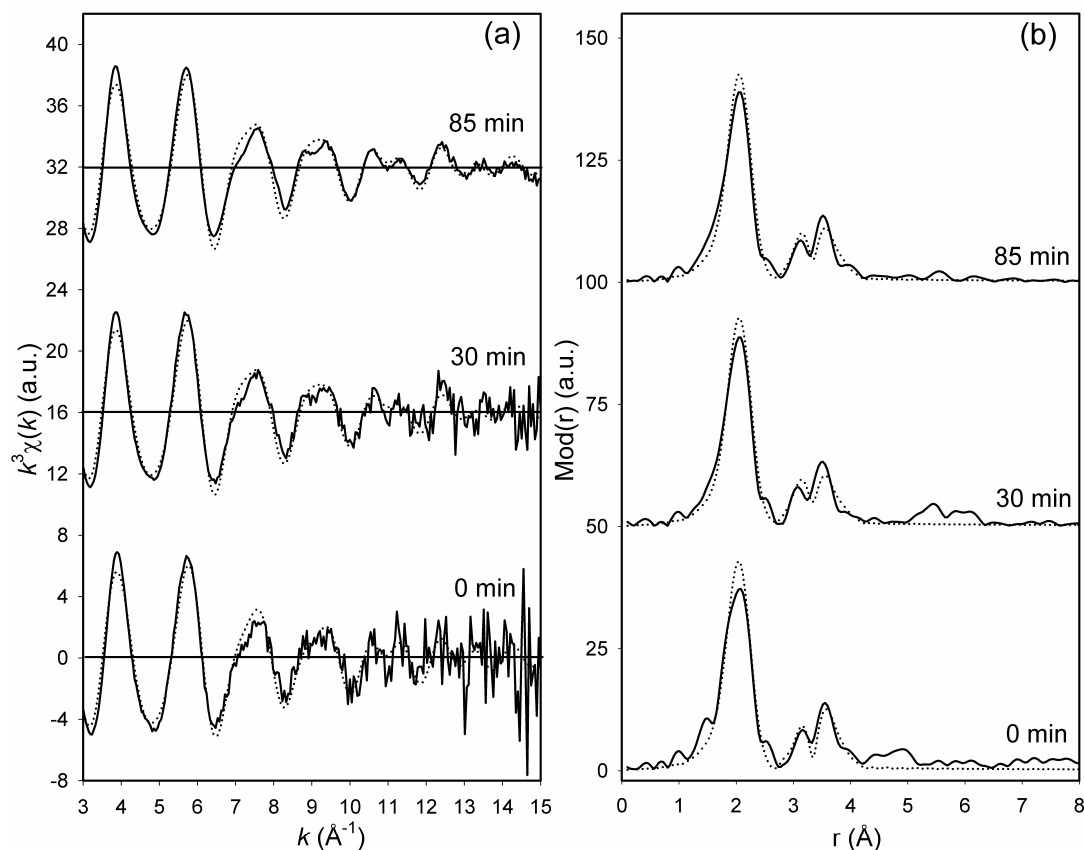


Figure 5.5.12. Experimental (solid line) and calculated (dotted line) EXAFS functions (a) and their Fourier transforms (b) for $\text{Hf}(\text{O}^n\text{Bu})_4$ and water mixture measured at different time intervals, at the Hf L_{III} -edge.

Table 5.5.5. EXAFS obtained structural parameters for $\text{Hf}(\text{O}^i\text{Bu})_4$ and water mixture measured at different time intervals

Time	A-Bs ^a	N ^b	r ^c [Å]	σ ^d [Å]	E_F ^e [eV]	k-range [Å ⁻¹]	R-factor
0 min	Hf-O	6.7 ± 0.7	2.12 ± 0.02	0.095 ± 0.010	-0.591	2.99 - 15.00	40.02
	Hf-C	5.1 ± 0.8	3.17 ± 0.03	0.122 ± 0.018			
	Hf-Hf	2.2 ± 0.4	3.44 ± 0.04	0.089 ± 0.018			
30 min	Hf-O	6.5 ± 0.7	2.13 ± 0.02	0.092 ± 0.009	-0.651	2.98 - 15.00	32.41
	Hf-C	5.4 ± 0.8	3.21 ± 0.03	0.122 ± 0.018			
	Hf-Hf	2.2 ± 0.4	3.44 ± 0.04	0.095 ± 0.019			
85 min	Hf-O	6.5 ± 0.7	2.13 ± 0.02	0.095 ± 0.010	-0.859	2.97 - 15.00	24.37
	Hf-C	5.7 ± 0.8	3.21 ± 0.03	0.122 ± 0.018			
	Hf-Hf	2.1 ± 0.4	3.44 ± 0.04	0.092 ± 0.018			

^a absorber (A) - backscatterers (Bs), ^b coordination number N, ^c interatomic distance r, ^d Debye-Waller factor σ with its calculated deviation and ^e Fermi energy E_F .

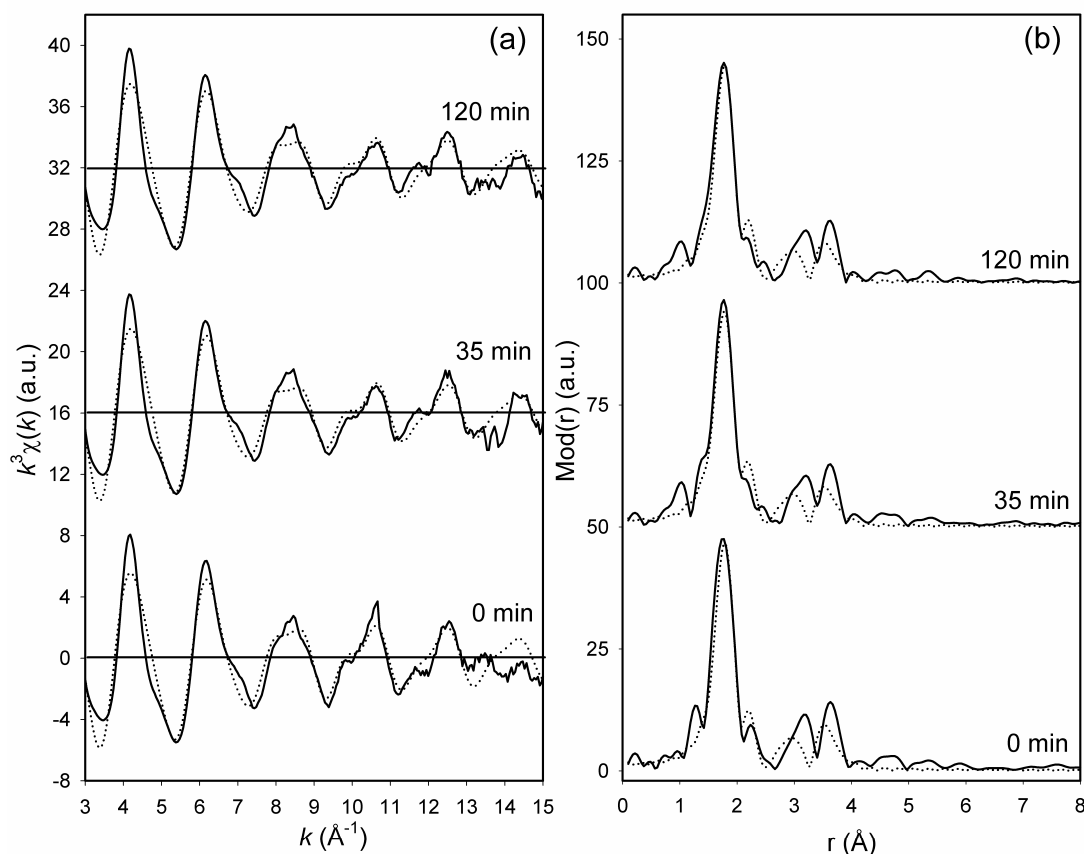


Figure 5.5.13. Experimental (solid line) and calculated (dotted line) EXAFS functions (a) and their Fourier transforms (b) for $\text{Ta}(\text{OEt})_5$ and water mixture measured at different time intervals, at the Ta L_{III} -edge.

Table 5.5.6. EXAFS obtained structural parameters for Ta(OEt)₅ and water mixture measured at different time intervals

Time	A-Bs ^a	N ^b	r ^c [Å]	σ ^d [Å]	E _F ^e [eV]	k-range [Å ⁻¹]	R-factor
0 min	Ta-O	4.4 ± 0.5	1.91 ± 0.02	0.071 ± 0.007	-0.790	2.99 - 15.01	37.73
	Ta-O	2.6 ± 0.3	2.09 ± 0.02	0.071 ± 0.007			
	Ta-C	4.6 ± 0.7	3.02 ± 0.03	0.097 ± 0.015			
	Ta-Ta	1.8 ± 0.3	3.37 ± 0.04	0.092 ± 0.018			
35 min	Ta-O	4.3 ± 0.5	1.91 ± 0.02	0.071 ± 0.007	-0.242	2.98 - 15.02	33.73
	Ta-O	2.7 ± 0.3	2.08 ± 0.02	0.071 ± 0.007			
	Ta-C	4.3 ± 0.7	3.02 ± 0.03	0.097 ± 0.015			
	Ta-Ta	1.6 ± 0.3	3.36 ± 0.04	0.092 ± 0.018			
120 min	Ta-O	4.3 ± 0.5	1.91 ± 0.02	0.071 ± 0.007	-0.447	2.97 - 15.02	33.68
	Ta-O	2.6 ± 0.3	2.09 ± 0.02	0.071 ± 0.007			
	Ta-C	4.3 ± 0.7	3.02 ± 0.03	0.097 ± 0.015			
	Ta-Ta	1.6 ± 0.3	3.36 ± 0.04	0.092 ± 0.018			

^a absorber (A) - backscatterers (Bs), ^b coordination number N, ^c interatomic distance r, ^d Debye-Waller factor σ with its calculated deviation and ^e Fermi energy E_F.

The experimentally determined and the theoretically calculated EXAFS functions in *k*-space and their Fourier transforms in real space for Ta(OEt)₅ and water mixture measured at Ta L_{III}-edge are shown in Figure 5.5.13 and the obtained structural parameters are tabulated in Table 5.5.6. The results show that Ta(OEt)₅ instantaneously undergoes hydrolysis and condensation reactions, as indicated by the change in the coordination number of tantalum and carbon backscatterers in comparison to pure Ta(OEt)₅. Furthermore, a remarkable shortening of the Ta-Ta distance could also be noticed as a result of the condensation process. The EXAFS spectra acquired at different time intervals did not show any remarkable variations in the structural parameters in comparison with those obtained immediately after the addition of water, thus confirming that hydrolysis and condensation reactions occur immediately after mixing.

Raman spectroscopic investigations were performed in order to obtain deeper insights into the hydrolysis and condensation mechanisms of the metal alkoxides. Studies were performed on M(OR)_x and water in the same molar ratio (1:2) as used for the EXAFS investigations. The spectra of Ge(OEt)₄ and water measured immediately and 24 h after mixing are shown in Figure 5.5.14 along with the spectrum of pure Ge(OEt)₄. The intensity of the Ge-O peak at 620 cm⁻¹ in pure Ge(OEt)₄ gets reduced in the mixture with water, which could be attributed to the decrease in the concentration of germanium species in the solution owing to condensation and subsequent precipitation.

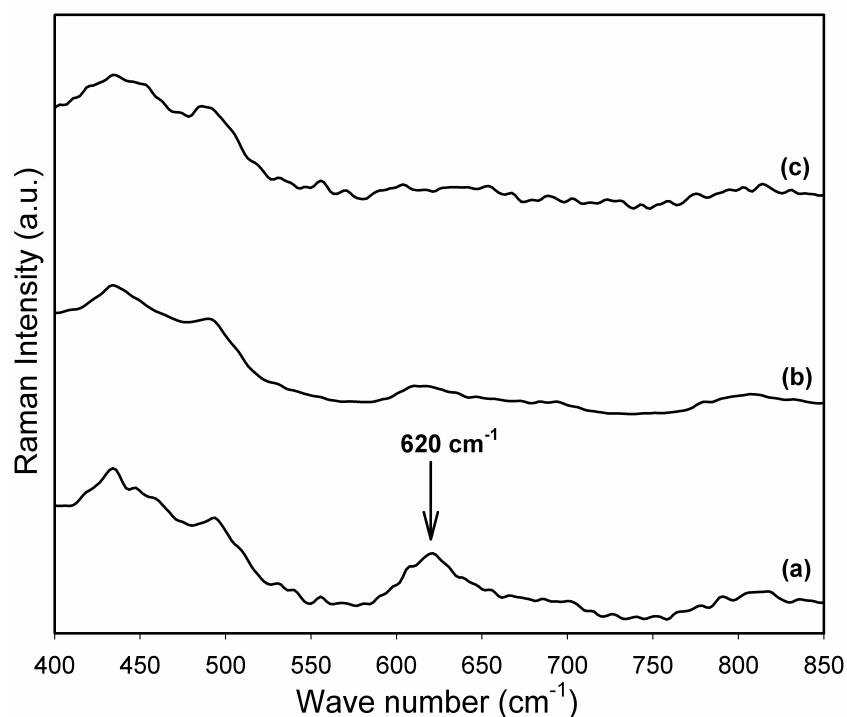


Figure 5.5.14. Raman spectra of $\text{Ge}(\text{OEt})_4$ and water measured at different time intervals along with pure $\text{Ge}(\text{OEt})_4$. [(a) $\text{Ge}(\text{OEt})_4$, (b) $\text{Ge}(\text{OEt})_4 + \text{H}_2\text{O}$ (0 h) and (c) $\text{Ge}(\text{OEt})_4 + \text{H}_2\text{O}$ (24 h)].

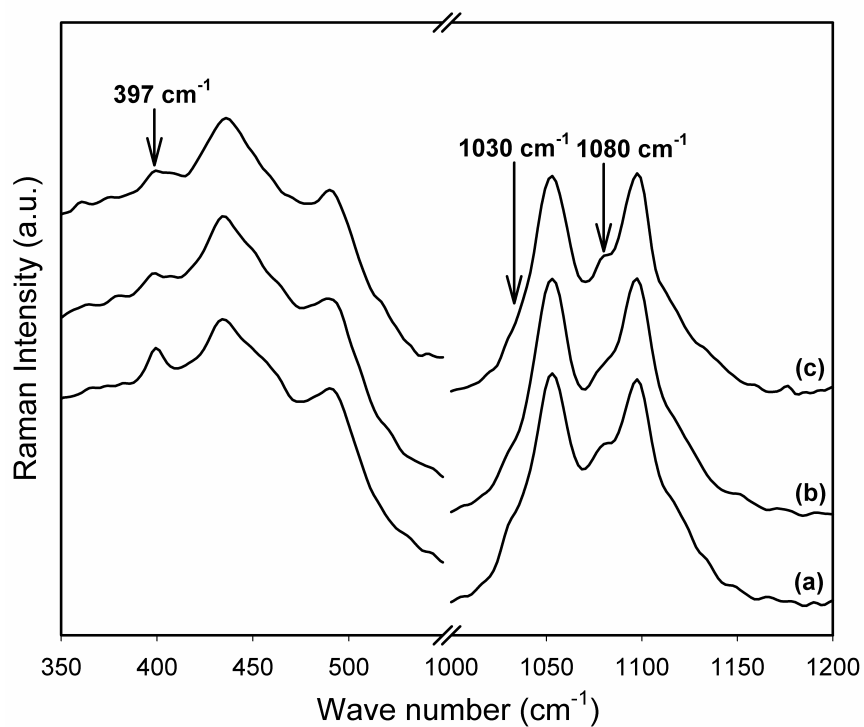


Figure 5.5.15. Raman spectra of $\text{Hf}(\text{O}^n\text{Bu})_4$ and water mixture measured at different time intervals along with $\text{Hf}(\text{O}^n\text{Bu})_4$. [(a) $\text{Hf}(\text{O}^n\text{Bu})_4$, (b) $\text{Hf}(\text{O}^n\text{Bu})_4 + \text{H}_2\text{O}$ (0 h) and (c) $\text{Hf}(\text{O}^n\text{Bu})_4 + \text{H}_2\text{O}$ (48 h)].

Raman spectra of $\text{Hf}(\text{O}^i\text{Bu})_4$ and water measured immediately and 48 h after mixing are shown in Figure 5.5.15 along with the spectrum of pure $\text{Hf}(\text{O}^i\text{Bu})_4$. The peak at 397 cm^{-1} , corresponding to Hf-O vibrations, could be observed in both the spectra indicating the presence of hafnium species in the solution [5.5.15]. It is interesting to note the decrease in the intensity of the Hf(-O-C) bands ascribable to the alkoxy groups at 1030 and 1080 cm^{-1} , owing to the formation of the condensation product upon the addition of water. A similar behaviour was also observed in the infrared spectroscopic studies on the hydrolysis and condensation behaviour of titanium alkoxides [5.5.18].

Raman spectra of $\text{Ta}(\text{OEt})_5$ and water measured immediately and 48 h after mixing are shown in Figure 5.5.16 along with the spectrum of pure $\text{Ta}(\text{OEt})_5$. The intensity of the Ta-O peak 588 cm^{-1} in pure $\text{Ta}(\text{OEt})_5$ gets reduced in the mixture with water, which could be attributed to the decrease of tantalum species in the solution owing to condensation and subsequent precipitation. Furthermore, decrease in the intensity of Ta(-O-C) bands ascribable to the alkoxy groups at 1080 cm^{-1} could be observed in this case as well.

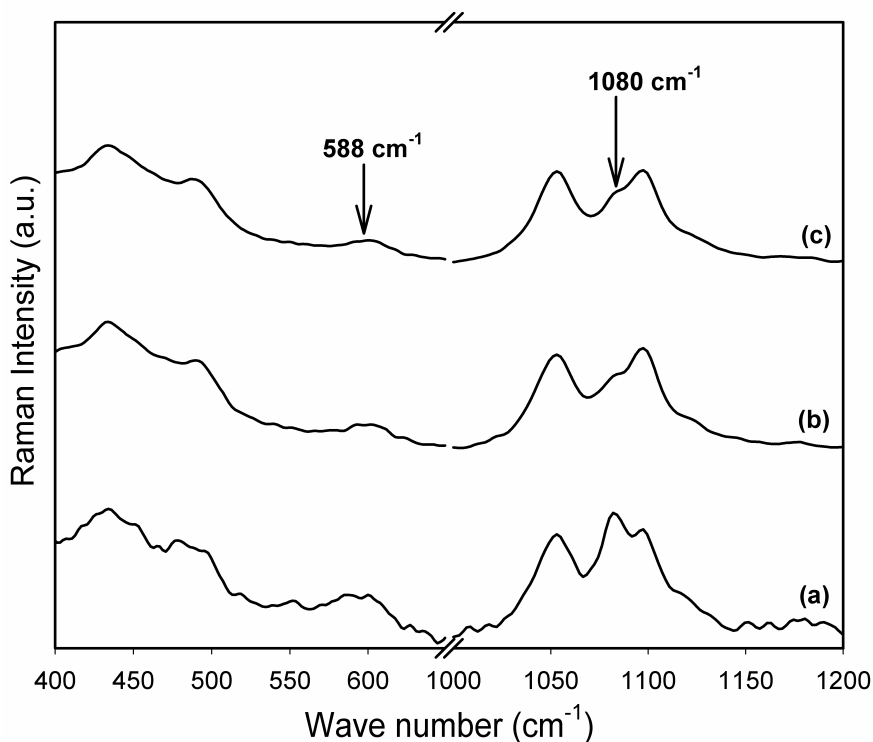


Figure 5.5.16. Raman spectra of $\text{Ta}(\text{OEt})_5$ and water mixture measured at different time intervals along with $\text{Ta}(\text{OEt})_5$. [(a) $\text{Ta}(\text{OEt})_5$, (b) $\text{Ta}(\text{OEt})_5 + \text{H}_2\text{O}$ (0 h) and (c) $\text{Ta}(\text{OEt})_5 + \text{H}_2\text{O}$ (48 h)].

In all the cases, the spectrum measured 24/48 h after mixing is similar to the spectrum acquired immediately after mixing, indicating that the hydrolysis and condensation reactions occur immediately after the addition of water, in agreement with the EXAFS results.

5.5.4. Influence of chemical modification by acetylacetonone

The alkoxide precursors are very reactive, and complexation of the metal by a ligand is frequently used to reduce the reactivity and to enable the control of the polycondensation process [5.5.19]. The complexing ability depends both on the nature of the ligand and of the metal. Metal alkoxides easily react with organic acids or β -diketones with the substitution of one or more alkoxy groups and form metal chelates or chelate-like compounds [5.5.4,5.5.20]. The bidentate ligand acetylacetonone (*acac*, 2,4-pentadione) is predominantly employed as chemical modifier, which coordinates to the metal and thereby reducing the reactivity of the metal alkoxide [5.5.21]. In order to investigate the influence of chemical modification, *acac* was added to alkoxide in a molar ratio alkoxide:*acac* = 1:2.

The experimentally determined and the theoretically calculated EXAFS functions in *k*-space and their Fourier transforms in real space for $\text{Ge}(\text{O}^n\text{Bu})_4$ -*acac* mixture measured at different time intervals are shown in Figure 5.5.17 and the obtained structural parameters are tabulated in Table 5.5.7.

Table 5.5.7. EXAFS obtained structural parameters for $\text{Ge}(\text{O}^n\text{Bu})_4$ -*acac* mixture measured at different time intervals

Time	A-Bs ^a	N ^b	r ^c [Å]	σ ^d [Å]	E_F ^e [eV]	<i>k</i> -range [Å ⁻¹]	R-factor
0 min	Ge-O Ge-C	5.9 ± 0.6 6.3 ± 1.0	1.74 ± 0.02 2.79 ± 0.03	0.050 ± 0.005 0.081 ± 0.012	0.694	2.98 - 15.03	25.54
210 min	Ge-O Ge-C	5.6 ± 0.6 6.4 ± 1.0	1.75 ± 0.02 2.78 ± 0.03	0.063 ± 0.006 0.095 ± 0.014	3.848	2.97 - 15.01	32.28
825 min	Ge-O Ge-C	5.6 ± 0.6 6.3 ± 1.0	1.75 ± 0.02 2.78 ± 0.03	0.059 ± 0.006 0.087 ± 0.013	2.824	2.96 - 15.00	24.78

^a absorber (A) - backscatterers (Bs), ^b coordination number N, ^c interatomic distance r, ^d Debye-Waller factor σ with its calculated deviation and ^e Fermi energy E_F .

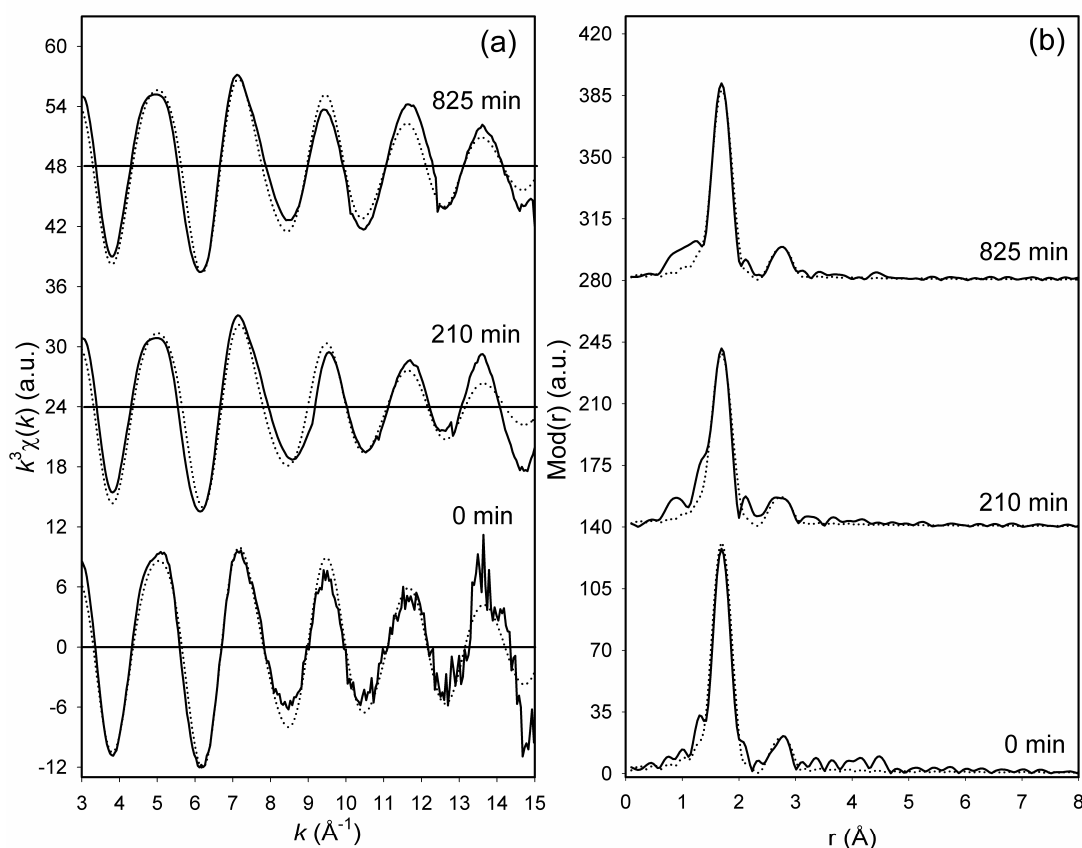


Figure 5.5.17. Experimental (solid line) and calculated (dotted line) EXAFS functions (a) and their Fourier transforms (b) for $\text{Ge}(\text{O}^n\text{Bu})_4$ -*acac* mixture measured at different time intervals, at the Ge K-edge.

The EXAFS analysis yielded same results for the measurements performed at different time intervals and the obtained structural parameters resemble those of the pure $\text{Ge}(\text{O}^n\text{Bu})_4$. The coordination of the ligand with the metal could not be evidenced even 825 min after mixing, indicating that $\text{Ge}(\text{O}^n\text{Bu})_4$ does not undergo chemical modification by *acac*.

The experimentally determined and theoretically calculated EXAFS functions in k -space and their Fourier transforms in real space for $\text{Hf}(\text{O}^n\text{Bu})_4$ -*acac* mixture measured at different time intervals, at Hf L_{III} -edge are shown in Figure 5.5.18 and the obtained structural parameters are given in Table 5.5.8. The EXAFS results indicate that the chemical modification with *acac* takes place immediately after mixing causing an increase in the coordination number of the oxygen and carbon shells. In addition, a substantial increase in Hf-C and Hf-Hf distances could also be observed (in comparison with $\text{Hf}(\text{O}^n\text{Bu})_4$) as a consequence of chemical modification. Subsequent measurements

performed at 35 and 120 min does not show any significant changes in the structural parameters in comparison with those obtained immediately after mixing.

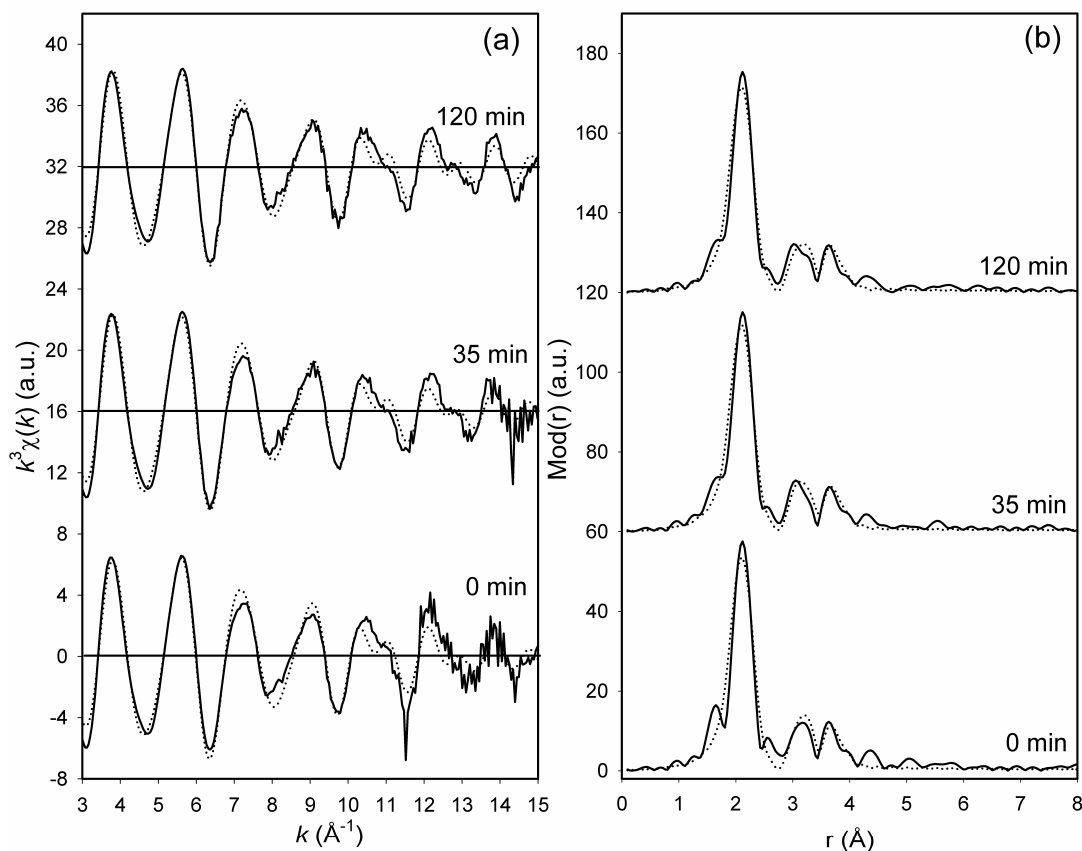


Figure 5.5.18. Experimental (solid line) and calculated (dotted line) EXAFS functions (a) and their Fourier transforms (b) for $\text{Hf}(\text{O}^n\text{Bu})_4\text{-acac}$ mixture measured at different time intervals, at the Hf L_{III} -edge.

Table 5.5.8. EXAFS obtained structural parameters for $\text{Hf}(\text{O}^n\text{Bu})_4\text{-acac}$ mixture measured at different time intervals

Time	A-Bs ^a	N ^b	r ^c [Å]	σ ^d [Å]	E _F ^e [eV]	k-range [Å ⁻¹]	R-factor
0 min	Hf-O	7.6 ± 0.8	2.17 ± 0.02	0.087 ± 0.009	-1.393	2.99 - 15.04	27.87
	Hf-C	4.8 ± 0.7	3.21 ± 0.03	0.063 ± 0.010			
	Hf-Hf	1.1 ± 0.2	3.54 ± 0.04	0.071 ± 0.014			
35 min	Hf-O	7.7 ± 0.8	2.17 ± 0.02	0.089 ± 0.009	-1.940	2.97 - 15.04	24.18
	Hf-C	4.7 ± 0.7	3.20 ± 0.03	0.067 ± 0.010			
	Hf-Hf	1.1 ± 0.2	3.54 ± 0.04	0.071 ± 0.014			
120 min	Hf-O	7.7 ± 0.8	2.17 ± 0.02	0.089 ± 0.009	-1.097	2.96 - 15.04	22.17
	Hf-C	4.9 ± 0.7	3.20 ± 0.03	0.071 ± 0.011			
	Hf-Hf	1.0 ± 0.2	3.53 ± 0.04	0.067 ± 0.013			

^aabsorber (A) - backscatterers (Bs), ^bcoordination number N, ^cinteratomic distance r, ^dDebye-Waller factor σ with its calculated deviation and ^eFermi energy E_F.

The experimentally determined and theoretically calculated EXAFS functions in k -space and their Fourier transforms in real space for Ta(OEt)₅-*acac* mixture measured at different time intervals, at Ta L_{III}-edge are shown in Figure 5.5.19. For clarity reasons, representative spectra measured at three different time intervals are shown. The EXAFS determined structural parameters are given in Table 5.5.9. The EXAFS results indicate that the chemical modification with *acac* occurs immediately (within 15 min) causing an increase in the coordination number of the first shell oxygen atoms, in comparison with the parameters obtained for pure Ta(OEt)₅. As a consequence of chemical modification, the cleavage of the dimeric structure to a monomeric structure can be evidenced as the tantalum shell at 3.49 Å could no longer be fitted. Subsequent measurements performed at 50, 85 and 950 min did not show any significant changes in the structural parameters in comparison with those obtained immediately after mixing.

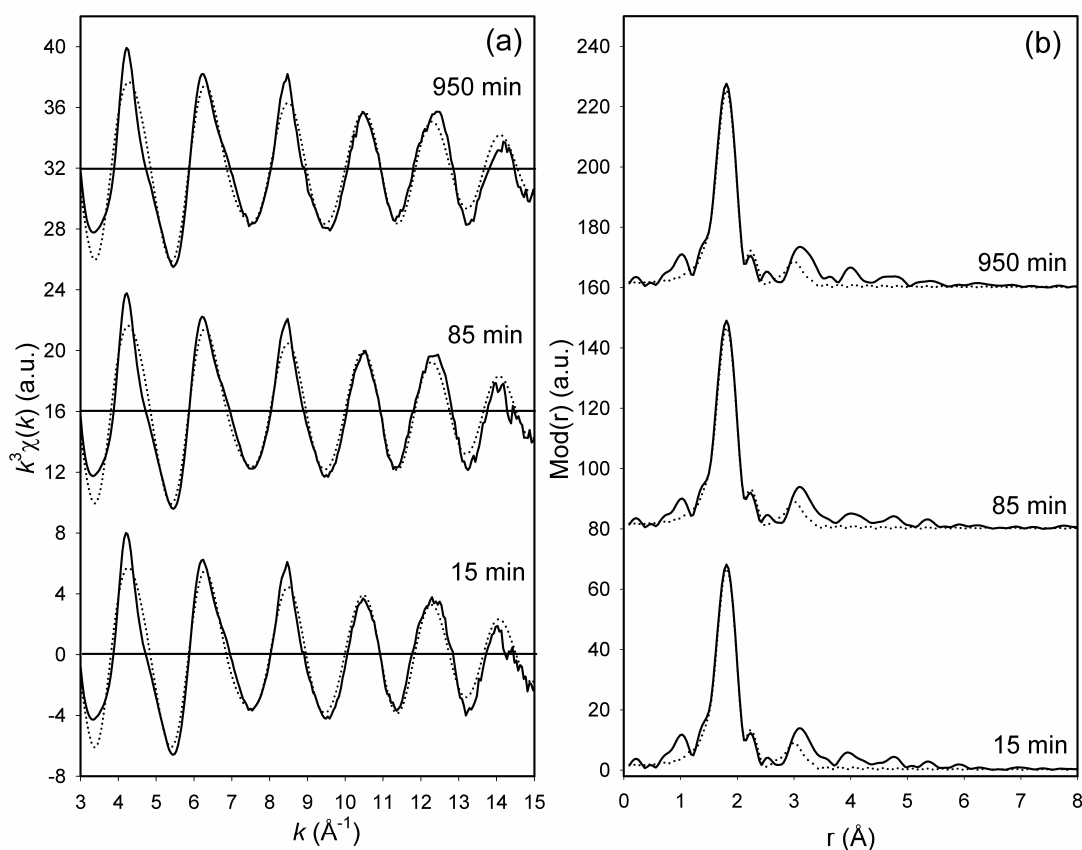


Figure 5.5.19. Experimental (solid line) and calculated (dotted line) EXAFS functions (a) and their Fourier transforms (b) for Ta(OEt)₅-*acac* mixture measured at different time intervals, at the Ta L_{III}-edge.

Table 5.5.9. EXAFS obtained structural parameters for Ta(OEt)₅-*acac* mixture measured at different time intervals

Time	A-Bs ^a	N ^b	r ^c [Å]	σ ^d [Å]	E _F ^e [eV]	k-range [Å ⁻¹]	R-factor
15 min	Ta-O	5.9 ± 0.6	1.91 ± 0.02	0.071 ± 0.007	-0.285	2.97 - 15.02	25.25
	Ta-O	2.0 ± 0.2	2.14 ± 0.02	0.050 ± 0.005			
	Ta-C	4.5 ± 0.7	3.06 ± 0.03	0.097 ± 0.015			
	Ta-Ta	0.0 ± 0.0	-	-			
50 min	Ta-O	5.9 ± 0.6	1.91 ± 0.02	0.071 ± 0.007	-0.125	2.98 - 15.02	24.20
	Ta-O	1.9 ± 0.2	2.14 ± 0.02	0.050 ± 0.005			
	Ta-C	4.3 ± 0.7	3.07 ± 0.03	0.095 ± 0.014			
85 min	Ta-O	5.9 ± 0.6	1.91 ± 0.02	0.071 ± 0.007	-0.585	2.97 - 15.03	24.08
	Ta-O	2.0 ± 0.2	2.14 ± 0.02	0.050 ± 0.005			
	Ta-C	4.4 ± 0.7	3.07 ± 0.03	0.097 ± 0.015			
950 min	Ta-O	5.8 ± 0.6	1.91 ± 0.02	0.071 ± 0.007	0.362	3.00 - 15.02	25.97
	Ta-O	1.9 ± 0.2	2.13 ± 0.02	0.055 ± 0.006			
	Ta-C	4.3 ± 0.7	3.06 ± 0.03	0.097 ± 0.015			

^a absorber (A) - backscatterers (Bs), ^b coordination number N, ^c interatomic distance r, ^d Debye-Waller factor σ with its calculated deviation and ^e Fermi energy E_F.

The XANES region of Hf(OⁿBu)₄ and Ta(OEt)₅ before and after the addition of *acac* are presented in Figures 5.5.20 and 5.5.21, respectively.

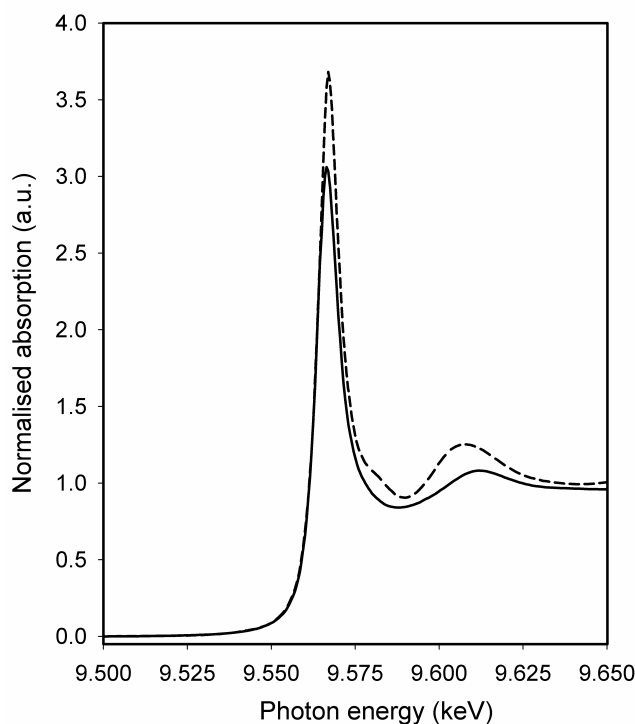


Figure 5.5.20. Comparison of the XANES regions of pure Hf(OⁿBu)₄ (solid line) and *acac* modified Hf(OⁿBu)₄ (dashed line).

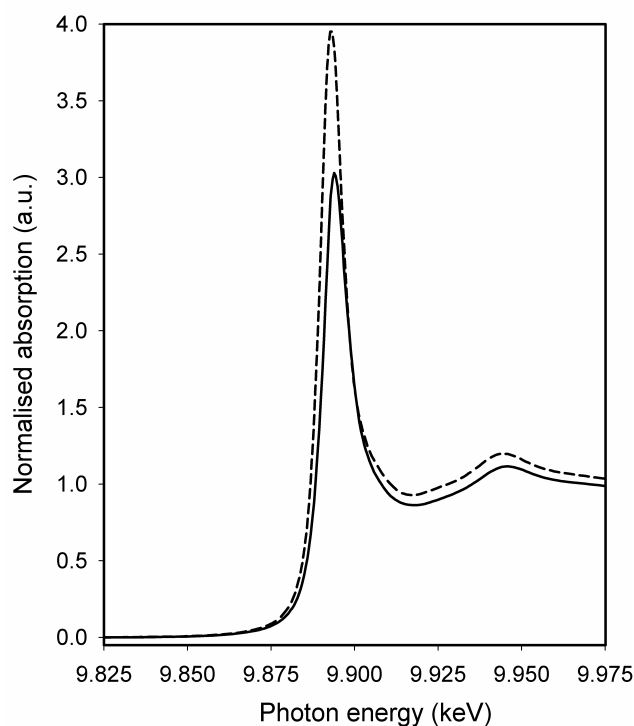


Figure 5.5.21. Comparison of the XANES regions of pure $\text{Ta}(\text{OEt})_5$ (solid line) and *acac* modified $\text{Ta}(\text{OEt})_5$ (dashed line).

In both the cases, a significant increase in the intensity of the white line (the peak of the absorption edge) could be observed upon the addition of *acac*, which could be attributed to a change in the coordination geometry around the hafnium/tantalum atom from a 6-fold to an 8-fold coordination. This result is in agreement with an earlier investigation on the chemical modification of zirconium alkoxides by the same ligand [5.5.22].

Raman spectroscopic measurements were performed on alkoxide-*acac* mixture in the same molar ratio as used for EXAFS measurements, to further investigate the results observed from EXAFS analysis. The Raman spectra of alkoxide-*acac* mixture measured at different time intervals are shown along with the spectrum of the corresponding pure alkoxide in Figures 5.5.22, 5.5.23 and 5.5.24 for $\text{Ge}(\text{OEt})_4$, $\text{Hf}(\text{O}^i\text{Bu})_4$ and $\text{Ta}(\text{OEt})_5$, respectively.

In $\text{Ge}(\text{OEt})_4$ -*acac* mixture, the spectra are characterised by the presence of the peak at 1605 cm^{-1} corresponding to the C-O stretching modes of the free enol form of *acac* [5.5.18]. This peak should disappear upon the coordination of *acac* to the metal atom. However, the presence of this peak was pointed out in all the spectra, thus indicating that no coordination took place. In agreement with the EXAFS investigations, no

remarkable changes could be observed in the Raman spectra measured at different time intervals. Furthermore, the Raman studies indicate that the coordination of *acac* does not occur even 48 h after mixing.

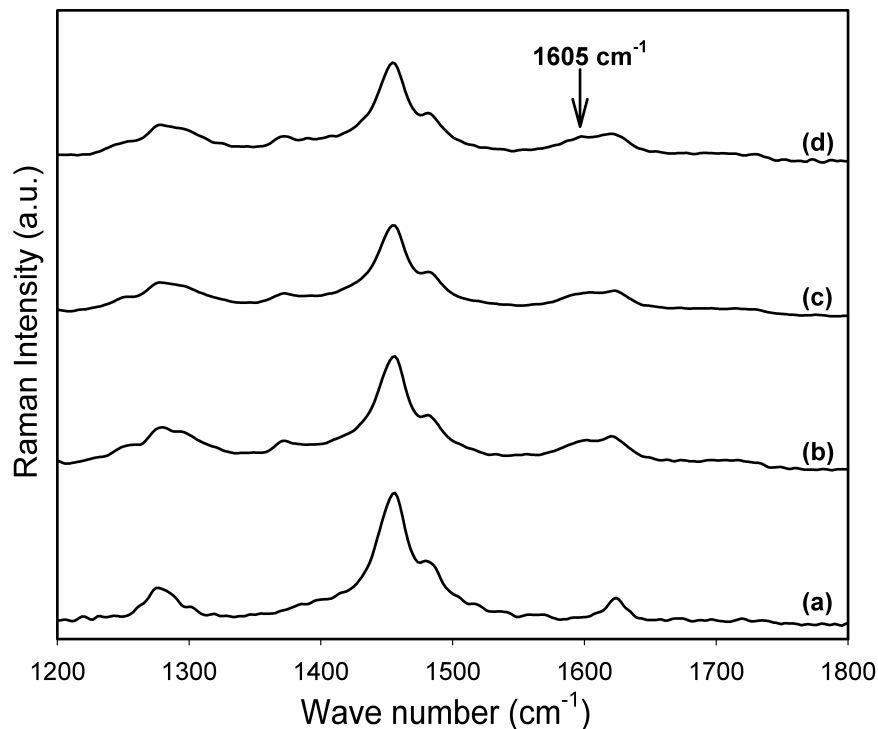


Figure 5.5.22. Raman spectra of $\text{Ge}(\text{OEt})_4$ -*acac* mixture measured at different time intervals along with pure $\text{Ge}(\text{OEt})_4$. [(a) $\text{Ge}(\text{OEt})_4$, (b) $\text{Ge}(\text{OEt})_4 + \textit{acac}$ (0 h), (c) $\text{Ge}(\text{OEt})_4 + \textit{acac}$ (24 h) and (d) $\text{Ge}(\text{OEt})_4 + \textit{acac}$ (48 h)].

In the Raman spectra of $\text{Hf}(\text{O}^i\text{Bu})_4$ -*acac* mixture and $\text{Ta}(\text{OEt})_5$ -*acac* mixture, the instantaneous coordination of *acac* to the metal could be evidenced. As a result of the coordination of *acac*, a substantial increase in the Raman intensity was also observed for the peaks at 1290 and 1370 cm^{-1} , which correspond to the symmetric C–C stretching modes and the symmetric methyl deformation, respectively [5.5.23]. The ligand can be attached to one central atom through one coordinating atom (monodentate), or through two coordinating atoms (chelating bidentate) [5.5.20, 5.5.21]. Generally the latter form of coordination is energetically more favoured than the monodentate. Another possibility of coordination of β -diketones is that the ligand forms a bridge between two different central metal atoms (bridging bidentate). In literature it is reported that a distinction between monodentate and bidentate can be successfully performed, but in the case of the existence of bidentate no clear distinction between a chelating or bridging attachment of the ligand is possible [5.5.18, 5.5.21, 5.5.23].

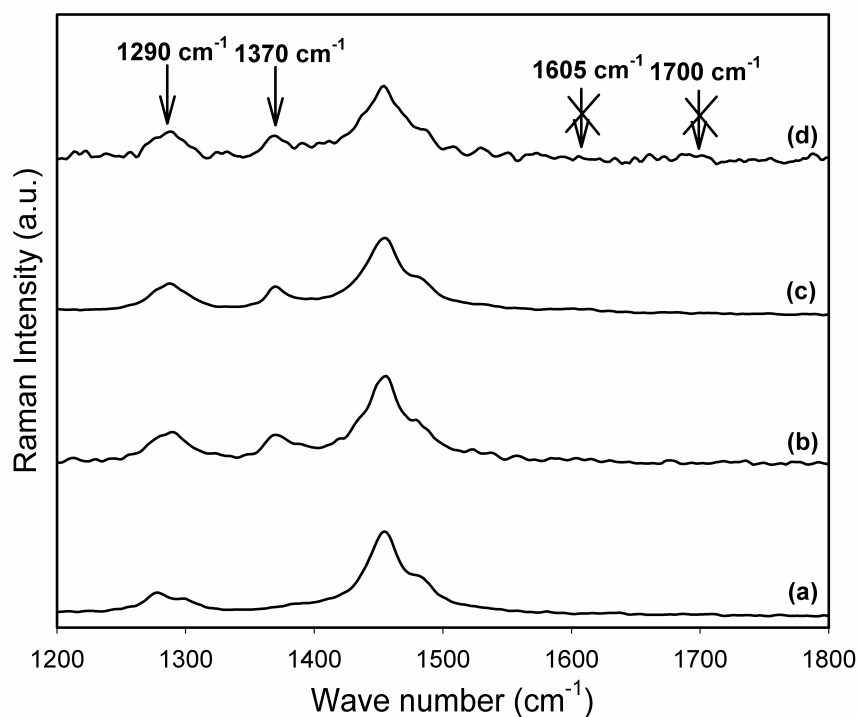


Figure 5.5.23. Raman spectra of $\text{Hf}(\text{O}^n\text{Bu})_4$ -acac mixture measured at different time intervals along with $\text{Hf}(\text{O}^n\text{Bu})_4$. [(a) $\text{Hf}(\text{O}^n\text{Bu})_4$, (b) $\text{Hf}(\text{O}^n\text{Bu})_4 + \text{acac}$ (0 h), (c) $\text{Hf}(\text{O}^n\text{Bu})_4 + \text{acac}$ (24 h) and (d) $\text{Hf}(\text{O}^n\text{Bu})_4 + \text{acac}$ (48 h)].

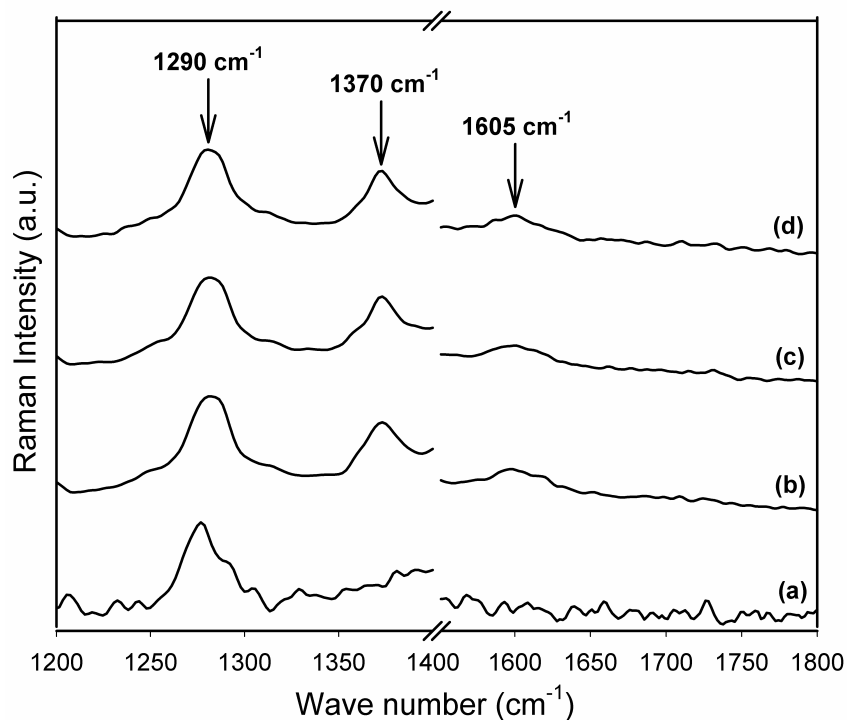


Figure 5.5.24. Raman spectra of $\text{Ta}(\text{OEt})_5$ -acac mixture measured at different time intervals along with $\text{Ta}(\text{OEt})_5$. [(a) $\text{Ta}(\text{OEt})_5$, (b) $\text{Ta}(\text{OEt})_5 + \text{acac}$ (0 h), (c) $\text{Ta}(\text{OEt})_5 + \text{acac}$ (24 h) and (d) $\text{Ta}(\text{OEt})_5 + \text{acac}$ (48 h)].

In $\text{Hf}(\text{O}^n\text{Bu})_4$ -*acac* mixture, the peak at 1605 cm^{-1} corresponding to the C-O stretching modes of the free enol form of *acac* and the bands around 1700 cm^{-1} corresponding to the C=O stretching vibrations of the free keto form of *acac*, could not be evidenced. These results indicate that all the carbonyl groups are coordinated, which was also observed in the studies reported on *acac* modification on titanium alkoxides [5.5.18]. Furthermore, the complete disappearance of the bands around 1700 cm^{-1} , in comparison to pure *acac*, indicates that a bidentate coordination has occurred. Moreover, the spectra acquired at 24 and 48 h after mixing do not show any variations compared to the spectrum collected immediately after mixing, indicating that the coordination of *acac* is stable even 48 h after mixing.

In $\text{Ta}(\text{OEt})_5$ -*acac* mixture, the peak at 1605 cm^{-1} corresponding to the C-O stretching modes of the free enol form of *acac* can be evidenced indicating the presence of some uncoordinated *acac* moieties. It can be hypothesised that out of the two *acac* molecules per tantalum atom, only one is coordinated, which is in agreement with the infrared spectroscopic investigations performed on the same mixture [5.5.24]. Due to this reason, it could not be unequivocally clarified whether a monodentate or a bidentate coordination has occurred. Furthermore, the spectra acquired at 24 and 48 h after mixing did not show any variations compared to the spectrum collected immediately after mixing, indicating that the coordination of *acac* is stable even 48 h after mixing and the persistence of the peak at 1605 cm^{-1} shows that further coordination of the ligand did not occur during this time period.

5.5.5. Hydrolysis and condensation of chemically modified alkoxides

Investigations on the hydrolysis and condensation reactions of metal alkoxides in the presence of *acac* were performed in order to verify whether the addition of the ligand had induced any changes in the condensation behaviour. The solution for the measurements was prepared by mixing metal alkoxide, *acac* and water in a 1:2:2 molar ratio. In the case of germanium alkoxide, water was added to a 3 h aged $\text{Ge}(\text{OR})_4$ -*acac* mixture, whereas in the case of hafnium and tantalum alkoxides, water was added to the freshly prepared alkoxide-*acac* mixture. The experimentally determined and the theoretically calculated EXAFS functions in *k*-space and their Fourier transforms in real space for $\text{Ge}(\text{O}^n\text{Bu})_4$, *acac* and water mixture measured at different time intervals are shown in Figure 5.5.25. The obtained structural parameters are listed in Table 5.5.10.

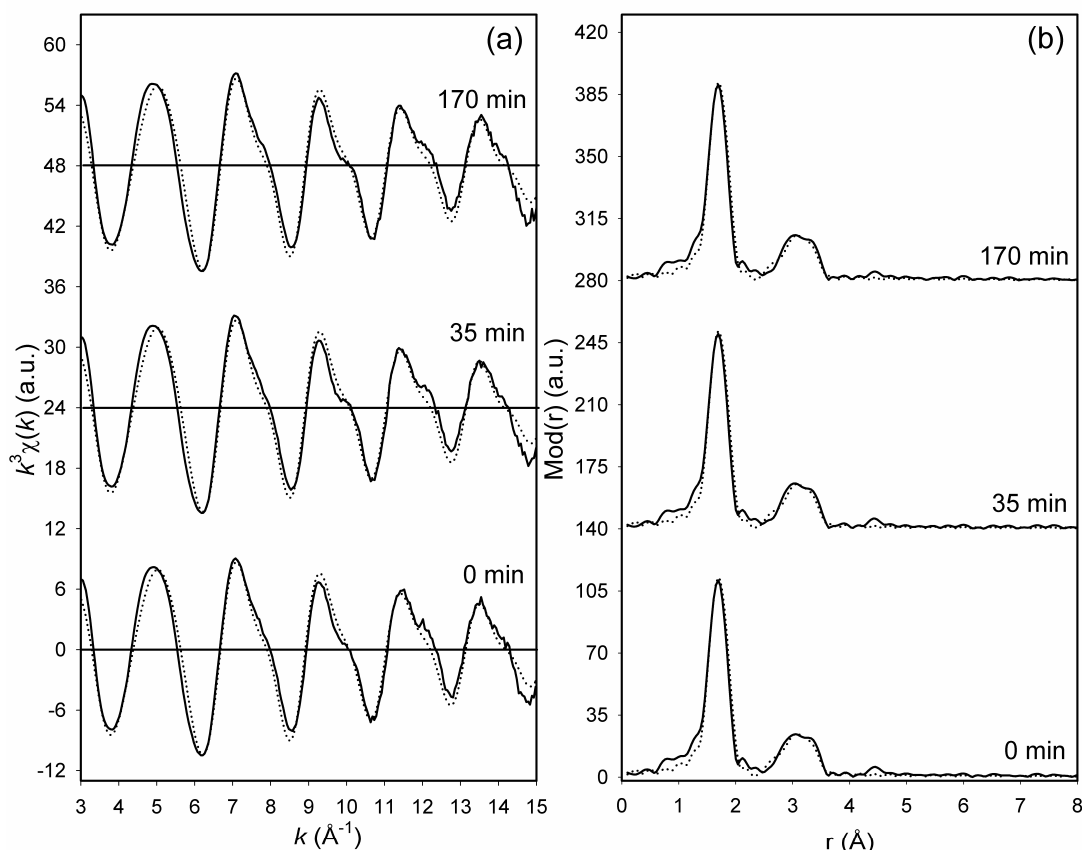


Figure 5.5.25. Experimental (solid line) and calculated (dotted line) EXAFS functions (a) and their Fourier transforms (b) for $\text{Ge}(\text{O}^n\text{Bu})_4$, *acac* and water mixture measured at different time intervals, at the Ge K-edge.

Table 5.5.10. EXAFS obtained structural parameters for $\text{Ge}(\text{O}^n\text{Bu})_4$, *acac* and water mixture measured at different time intervals

Time	A-Bs ^a	N ^b	r ^c [Å]	σ^d [Å]	E_F^e [eV]	k-range [Å ⁻¹]	R-factor
0 min	Ge-O	5.1 ± 0.5	1.75 ± 0.02	0.050 ± 0.005	0.706	2.98 - 15.03	19.92
	Ge-C	5.0 ± 0.8	2.82 ± 0.03	0.092 ± 0.014			
	Ge-Ge	1.0 ± 0.2	3.16 ± 0.04	0.055 ± 0.011			
35 min	Ge-O	5.1 ± 0.5	1.75 ± 0.02	0.050 ± 0.005	1.200	3.00 - 15.03	20.78
	Ge-C	5.1 ± 0.8	2.82 ± 0.03	0.097 ± 0.015			
	Ge-Ge	1.0 ± 0.2	3.16 ± 0.04	0.055 ± 0.011			
70 min	Ge-O	5.1 ± 0.5	1.75 ± 0.02	0.050 ± 0.005	0.919	2.95 - 15.03	20.55
	Ge-C	5.2 ± 0.8	2.82 ± 0.03	0.095 ± 0.015			
	Ge-Ge	1.0 ± 0.2	3.16 ± 0.04	0.055 ± 0.011			
170 min	Ge-O	5.0 ± 0.5	1.75 ± 0.02	0.050 ± 0.005	0.939	2.99 - 15.03	20.99
	Ge-C	5.0 ± 0.8	2.82 ± 0.03	0.095 ± 0.015			
	Ge-Ge	1.0 ± 0.2	3.16 ± 0.04	0.055 ± 0.011			

^a absorber (A) - backscatterers (Bs), ^b coordination number N, ^c interatomic distance r, ^d Debye-Waller factor σ with its calculated deviation and ^e Fermi energy E_F .

The EXAFS analysis shows that the hydrolysis and condensation reactions occur instantaneously upon the addition of water in the presence of *acac* as well, which could also be visually observed by the development of turbidity in the solution. The fast hydrolysis and condensation could be attributed to the non-coordination of the ligand to the germanium atom. The obtained structural parameters are in agreement with those measured in the analogous solution prepared without *acac*. Subsequent measurements performed at different time intervals also indicate no changes in the structural parameters in comparison with the measurements performed immediately after mixing.

The experimentally determined and theoretically calculated EXAFS functions in k -space and their Fourier transforms in real space for $\text{Hf}(\text{O}^n\text{Bu})_4$, *acac* and water mixture measured at Hf L_{III} -edge are shown in Figure 5.5.26. For clarity reasons, representative spectra measured at three different time intervals are shown. The structural parameters are summarised in Table 5.5.11.

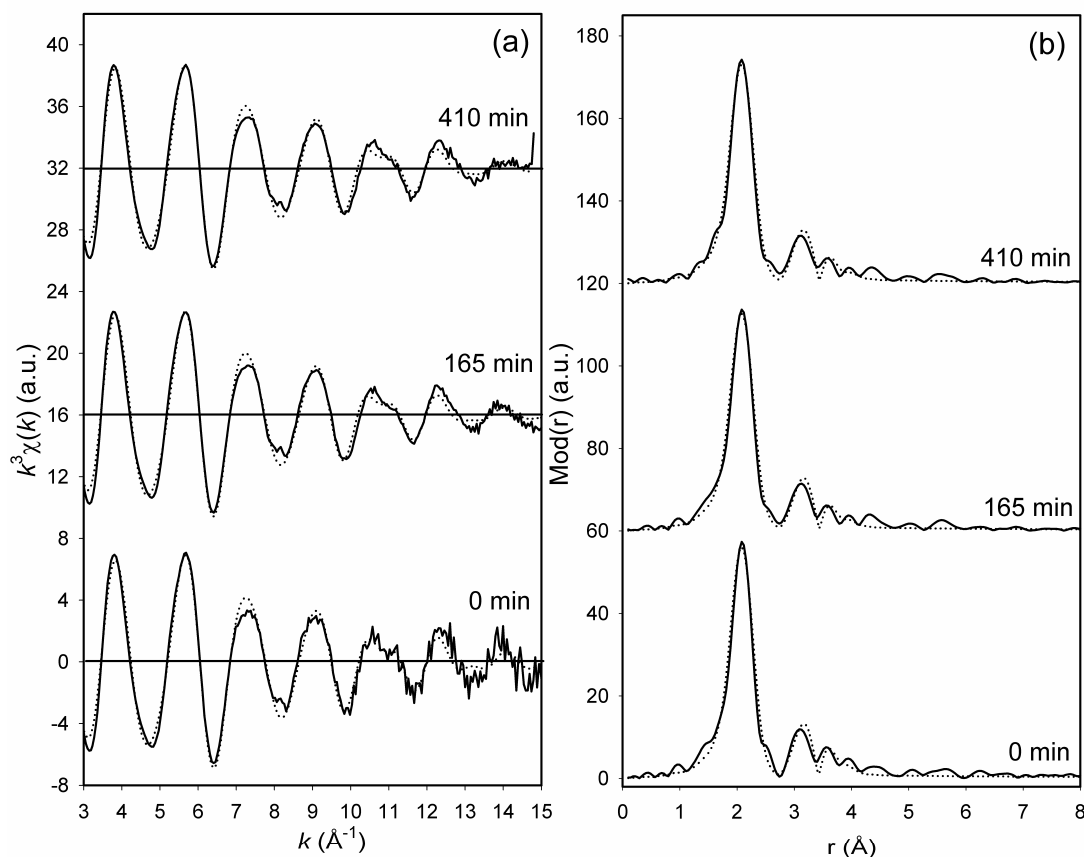


Figure 5.5.26. Experimental (solid line) and calculated (dotted line) EXAFS functions (a) and their Fourier transforms (b) for $\text{Hf}(\text{O}^n\text{Bu})_4$, *acac* and water mixture measured at different time intervals, at the Hf L_{III} -edge.

Table 5.5.11. EXAFS obtained structural parameters for Hf(OⁿBu)₄, *acac* and water mixture measured at different time intervals

Time	A-Bs ^a	N ^b	r ^c [Å]	σ ^d [Å]	E _F ^e [eV]	k-range [Å ⁻¹]	R-factor
0 min	Hf-O	8.0 ± 0.8	2.15 ± 0.02	0.089 ± 0.009	-1.792	2.98 - 15.04	21.06
	Hf-C	5.0 ± 0.8	3.20 ± 0.03	0.081 ± 0.012			
	Hf-Hf	1.3 ± 0.3	3.48 ± 0.04	0.092 ± 0.018			
15 min	Hf-O	8.0 ± 0.8	2.15 ± 0.02	0.089 ± 0.009	-1.737	2.98 - 15.04	24.36
	Hf-C	5.2 ± 0.8	3.20 ± 0.03	0.087 ± 0.013			
	Hf-Hf	1.1 ± 0.3	3.48 ± 0.04	0.087 ± 0.017			
30 min	Hf-O	8.0 ± 0.8	2.15 ± 0.02	0.089 ± 0.009	-1.187	3.00 - 15.04	24.82
	Hf-C	5.0 ± 0.8	3.19 ± 0.03	0.077 ± 0.012			
	Hf-Hf	1.4 ± 0.3	3.51 ± 0.04	0.092 ± 0.018			
85 min	Hf-O	8.0 ± 0.8	2.15 ± 0.02	0.092 ± 0.009	-1.543	2.99 - 15.04	17.02
	Hf-C	5.0 ± 0.8	3.21 ± 0.03	0.081 ± 0.012			
	Hf-Hf	1.3 ± 0.3	3.50 ± 0.04	0.097 ± 0.019			
165 min	Hf-O	8.0 ± 0.8	2.15 ± 0.02	0.092 ± 0.009	-1.539	2.99 - 15.04	16.74
	Hf-C	4.9 ± 0.8	3.21 ± 0.03	0.081 ± 0.012			
	Hf-Hf	1.4 ± 0.3	3.50 ± 0.04	0.097 ± 0.019			
240 min	Hf-O	8.0 ± 0.8	2.15 ± 0.02	0.092 ± 0.009	-1.502	2.99 - 15.04	16.51
	Hf-C	4.9 ± 0.8	3.20 ± 0.03	0.077 ± 0.012			
	Hf-Hf	1.5 ± 0.3	3.51 ± 0.04	0.100 ± 0.020			
410 min	Hf-O	8.0 ± 0.8	2.15 ± 0.02	0.092 ± 0.009	-1.057	2.97 - 14.79	16.38
	Hf-C	5.1 ± 0.8	3.20 ± 0.03	0.081 ± 0.012			
	Hf-Hf	1.5 ± 0.3	3.51 ± 0.04	0.097 ± 0.019			

^a absorber (A) - backscatterers (Bs), ^b coordination number N, ^c interatomic distance r, ^d Debye-Waller factor σ with its calculated deviation and ^e Fermi energy E_F.

The EXAFS results show that the condensation reaction has not occurred in the chemically modified hafnium alkoxide even 410 min after the addition of water and the solution remained clear. This is evidenced by the similarity in the obtained structural parameters in comparison with the parameters obtained before the addition of water. The coordination of the ligand to the hafnium atom has hindered the condensation reaction.

The experimentally determined and theoretically calculated EXAFS functions in *k*-space and their Fourier transforms in real space for Ta(OEt)₅, *acac* and water mixture measured at Ta L_{III}-edge are shown in Figure 5.5.27. For clarity reasons, representative spectra measured at three different time intervals are shown. The EXAFS obtained structural parameters are given in Table 5.5.12.

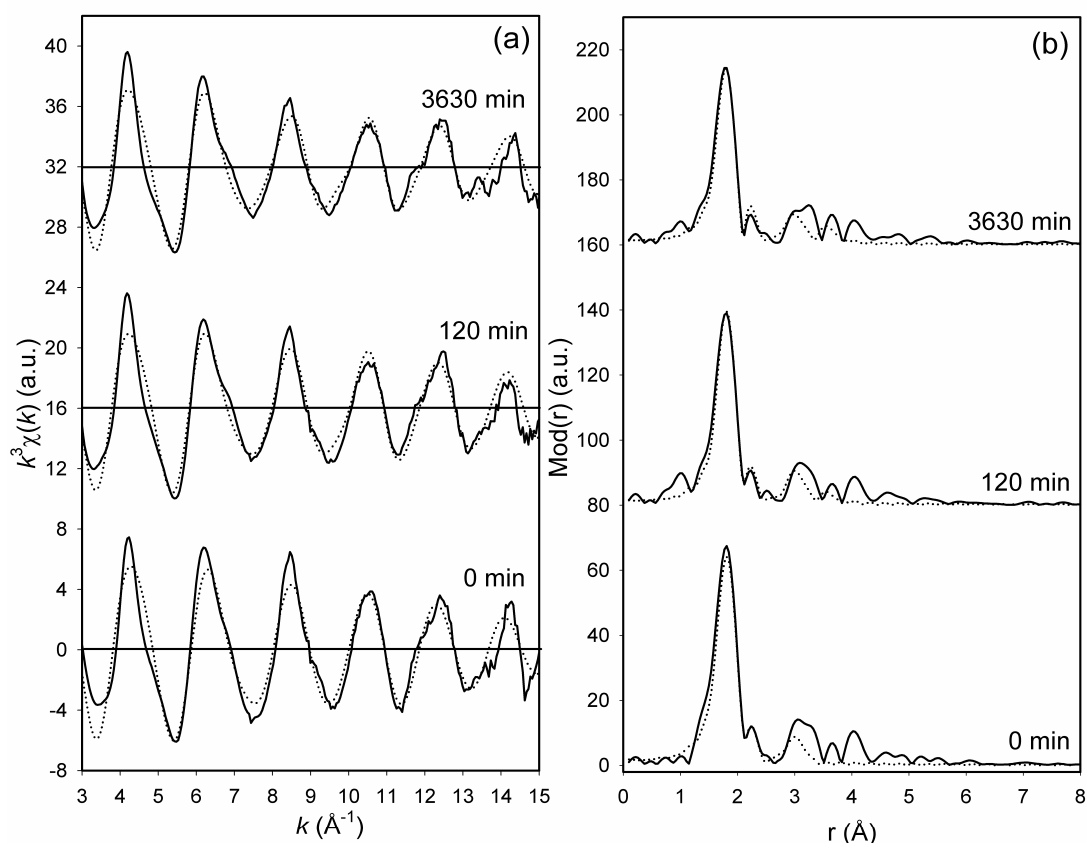


Figure 5.5.27. Experimental (solid line) and calculated (dotted line) EXAFS functions (a) and their Fourier transforms (b) for Ta(OEt)₅, acac and water mixture measured at different time intervals, at the Ta L_{III}-edge.

Table 5.5.12. EXAFS obtained structural parameters for Ta(OEt)₅, acac and water mixture measured at different time intervals

Time	A-Bs ^a	N ^b	r ^c [Å]	σ ^d [Å]	E _F ^e [eV]	k-range [Å ⁻¹]	R-factor
0 min	Ta-O	5.8 ± 0.6	1.91 ± 0.02	0.071 ± 0.007	-0.572	3.00 - 15.02	31.46
	Ta-O	1.8 ± 0.2	2.14 ± 0.02	0.055 ± 0.006			
	Ta-C	4.1 ± 0.6	3.06 ± 0.03	0.095 ± 0.014			
	Ta-Ta	0.0 ± 0.0	-	-			
35 min	Ta-O	4.7 ± 0.5	1.91 ± 0.02	0.059 ± 0.006	-0.479	3.00 - 15.02	27.96
	Ta-O	2.3 ± 0.2	2.12 ± 0.02	0.067 ± 0.007			
	Ta-C	3.7 ± 0.5	3.08 ± 0.03	0.071 ± 0.011			
	Ta-Ta	0.4 ± 0.1	3.42 ± 0.04	0.067 ± 0.013			
120 min	Ta-O	4.6 ± 0.5	1.91 ± 0.02	0.063 ± 0.006	-0.803	2.99 - 15.01	28.86
	Ta-O	2.2 ± 0.2	2.12 ± 0.02	0.067 ± 0.007			
	Ta-C	3.9 ± 0.6	3.07 ± 0.03	0.077 ± 0.012			
	Ta-Ta	0.4 ± 0.1	3.41 ± 0.04	0.077 ± 0.015			
3630 min	Ta-O	4.7 ± 0.5	1.91 ± 0.02	0.067 ± 0.006	-0.349	2.97 - 15.02	30.28
	Ta-O	2.3 ± 0.2	2.11 ± 0.02	0.067 ± 0.007			
	Ta-C	4.1 ± 0.6	3.06 ± 0.03	0.084 ± 0.013			
	Ta-Ta	0.6 ± 0.1	3.40 ± 0.04	0.077 ± 0.015			

^aabsorber (A) - backscatterers (Bs), ^bcoordination number N, ^cinteratomic distance r, ^dDebye-Waller factor σ with its calculated deviation and ^eFermi energy E_F.

The EXAFS results show that the condensation reaction has slowed down in the chemically modified tantalum alkoxide. The condensation starts in the time interval between 0 and 35 min after the addition of water to the *acac* modified tantalum alkoxide, evidenced by the appearance of the tantalum backscatterer at 3.42 Å distance. However it proceeds very slowly and even after 3630 min a substantial increase in the coordination number of tantalum backscatterers cannot be evidenced.

Raman spectroscopic measurements were performed on solutions with the same molar ratio as used for the EXAFS measurements. Raman spectra recorded immediately and after subsequent time intervals following the addition of water to the alkoxide-*acac* mixture are shown along with the spectrum of corresponding alkoxide-*acac* mixture in Figures 5.5.28, 5.5.29 and 5.5.30 for $\text{Ge}(\text{OEt})_4$, $\text{Hf}(\text{O}^i\text{Bu})_4$ and $\text{Ta}(\text{OEt})_5$, respectively.

In the Raman spectra of $\text{Ge}(\text{OEt})_4$ -*acac*-water solution, the peak due to Ge-O vibrations at 620 cm^{-1} , decreases in intensity owing to condensation and precipitation, similar to the previous investigations performed without *acac*. Moreover, the peak due to the free enol form of *acac* at 1605 cm^{-1} could also be evidenced in all the measured spectra.

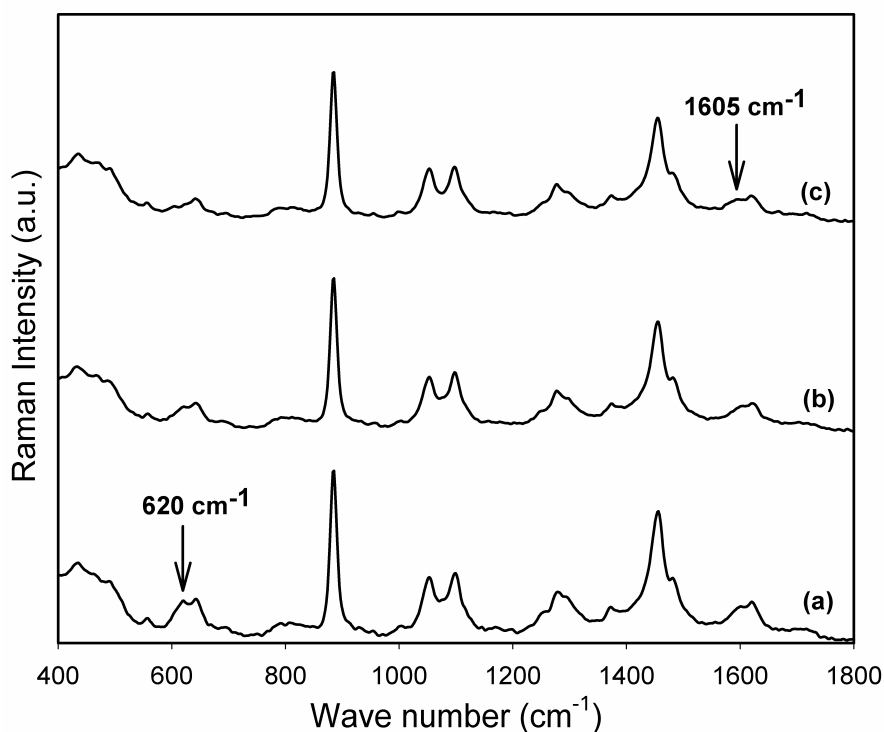


Figure 5.5.28. Raman spectra of $\text{Ge}(\text{OEt})_4$ -*acac*-water solution measured at different time intervals along with $\text{Ge}(\text{OEt})_4$ -*acac* mixture. [(a) $\text{Ge}(\text{OEt})_4 + \text{acac}$ (0 h), (b) $\text{Ge}(\text{OEt})_4 + \text{acac} + \text{H}_2\text{O}$ (0 h) and (c) $\text{Ge}(\text{OEt})_4 + \text{acac} + \text{H}_2\text{O}$ (24 h)].

In the Raman spectra of $\text{Hf}(\text{O}^n\text{Bu})_4$ -*acac*-water solution, the peak at 397 cm^{-1} , corresponding to Hf-O vibrations, could be observed in all the spectra indicating the presence of hafnium species in the solution. Furthermore, the spectra acquired before and after the addition of water to the $\text{Hf}(\text{O}^n\text{Bu})_4$ -*acac* mixture look alike, clearly indicating that the solution is stable even 96 h after preparation. Thus, from the Raman studies, it can be deduced that the chemical modification of $\text{Hf}(\text{O}^n\text{Bu})_4$ by *acac* has hindered the hydrolysis and condensation reaction in agreement with the EXAFS results.

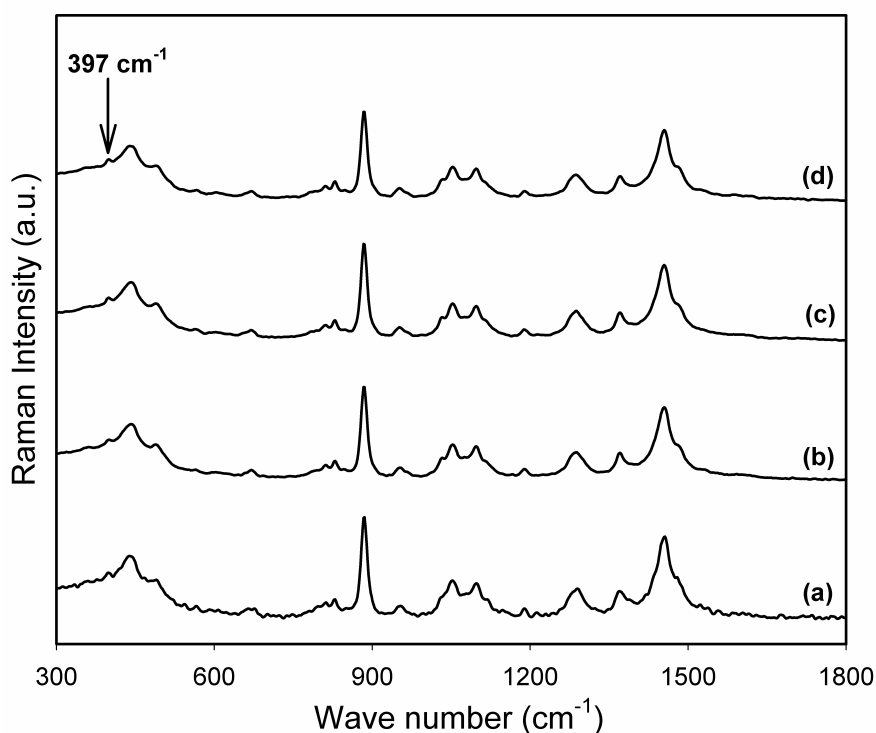


Figure 5.5.29. Raman spectra of $\text{Hf}(\text{O}^n\text{Bu})_4$ -*acac*-water solution measured at different time intervals along with $\text{Hf}(\text{O}^n\text{Bu})_4$ -*acac* mixture. [(a) $\text{Hf}(\text{O}^n\text{Bu})_4 + \text{acac}$ (0 h), (b) $\text{Hf}(\text{O}^n\text{Bu})_4 + \text{acac} + \text{H}_2\text{O}$ (0 h), (c) $\text{Hf}(\text{O}^n\text{Bu})_4 + \text{acac} + \text{H}_2\text{O}$ (24 h) and (d) $\text{Hf}(\text{O}^n\text{Bu})_4 + \text{acac} + \text{H}_2\text{O}$ (96 h)].

In the Raman spectra of $\text{Ta}(\text{OEt})_5$ -*acac*-water solution, even though the decrease in the intensity of the Ta-O peak at 588 cm^{-1} could not be clearly observed, it is interesting to note the time dependent decrease in the intensity of Ta(-O-C) peak at 1080 cm^{-1} owing to condensation reaction. Thus, from the Raman studies, it can be inferred that the chemical modification of $\text{Ta}(\text{OEt})_5$ by *acac* has slowed down the hydrolysis and condensation reaction in agreement with the EXAFS results.

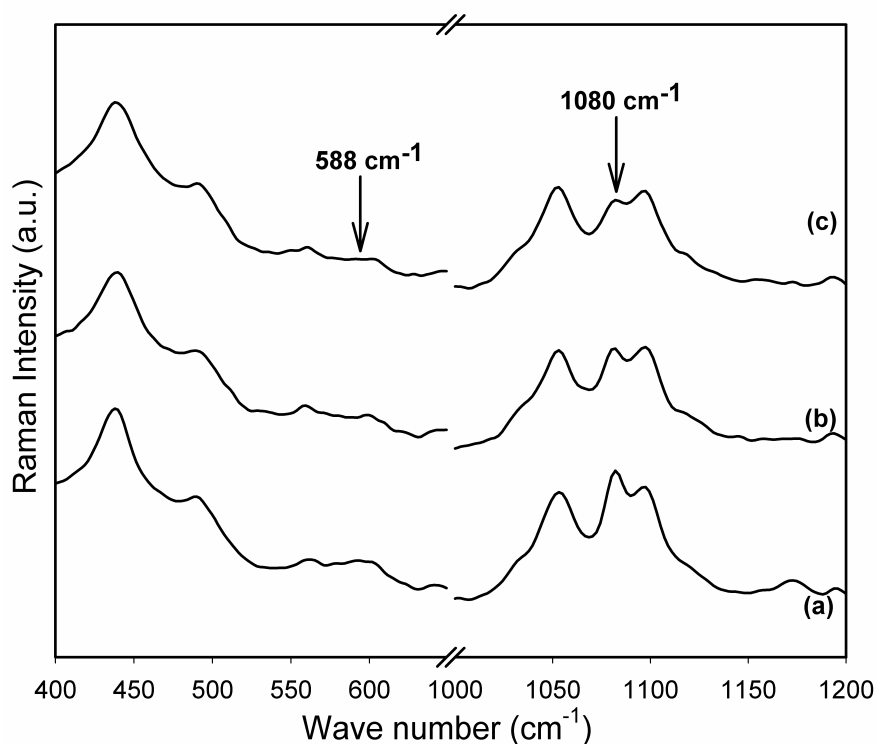


Figure 5.5.30. Raman spectra of $\text{Ta}(\text{OEt})_5\text{-acac}$ -water solution measured at different time intervals along with $\text{Ta}(\text{OEt})_5\text{-acac}$ mixture. [(a) $\text{Ta}(\text{OEt})_5 + \text{acac}$ (0 h), (b) $\text{Ta}(\text{OEt})_5 + \text{acac} + \text{H}_2\text{O}$ (0 h) and (c) $\text{Ta}(\text{OEt})_5 + \text{acac} + \text{H}_2\text{O}$ (24 h)].

5.5.6. Structure of mixture of alkoxides

Structural investigations on the mixture of metal alkoxide with pre-hydrolysed $\text{Si}(\text{OEt})_4$ were carried out by means of EXAFS and Raman spectroscopy in order to determine whether the addition of another alkoxide alters the structure of metal alkoxide thereby building a mixed Si-O-M (M = Ge, Hf, Ta) bond. The investigations were performed on metal alkoxide mixed with pre-hydrolysed $\text{Si}(\text{OEt})_4$ in molar ratio 1:1.

The experimentally determined and the theoretically calculated EXAFS functions in k -space and their Fourier transforms in real space for metal alkoxides mixed with pre-hydrolysed $\text{Si}(\text{OEt})_4$, measured at different time intervals are shown in Figures 5.5.31, 5.5.32 and 5.5.33. For reasons of clarity, only representative spectra measured at three different time intervals are presented. The obtained structural parameters are listed in Tables 5.5.13, 5.5.14 and 5.5.15 for $\text{Ge}(\text{O}^n\text{Bu})_4$, $\text{Hf}(\text{O}^n\text{Bu})_4$ and $\text{Ta}(\text{OEt})_5$, respectively.

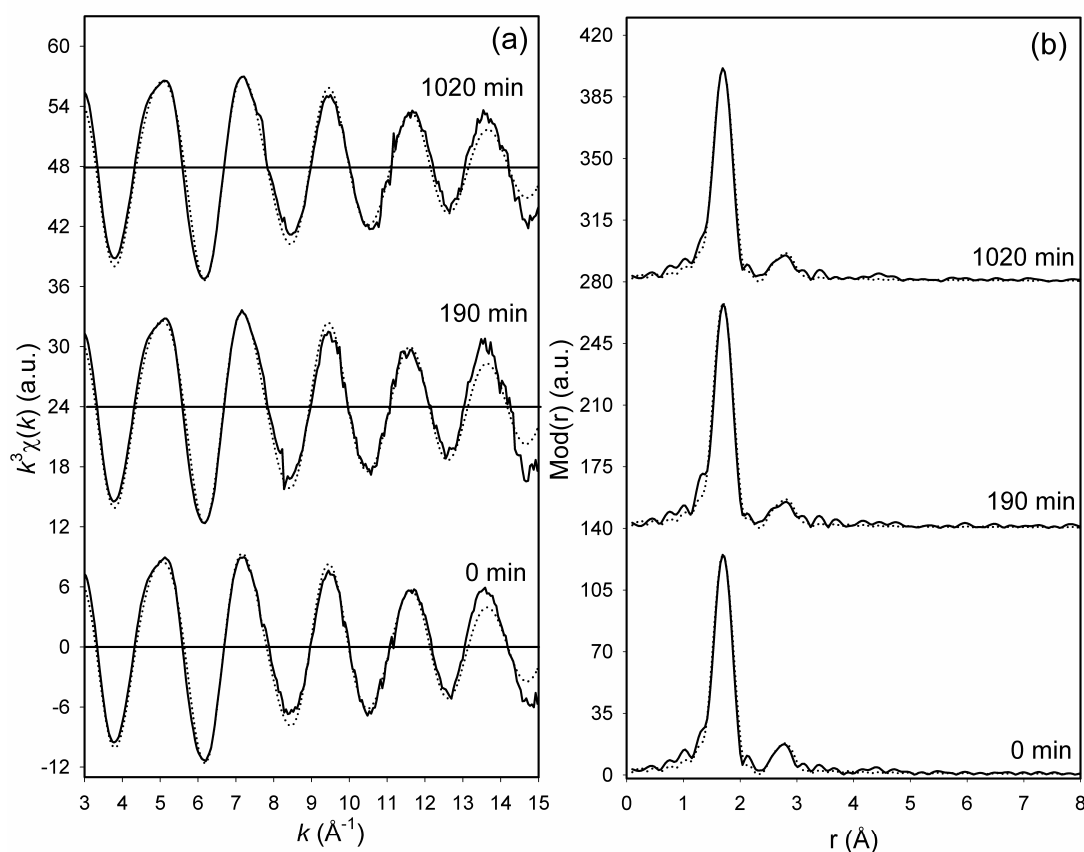


Figure 5.5.31. Experimental (solid line) and calculated (dotted line) EXAFS functions (a) and their Fourier transforms (b) for $\text{Ge}(\text{O}^n\text{Bu})_4$ mixed with pre-hydrolysed $\text{Si}(\text{OEt})_4$ measured at different time intervals, at the Ge K-edge.

Table 5.5.13. EXAFS obtained structural parameters for $\text{Ge}(\text{O}^n\text{Bu})_4$ mixed with pre-hydrolysed $\text{Si}(\text{OEt})_4$ measured at different time intervals

Time	A-Bs ^a	N ^b	r ^c [\AA]	σ ^d [\AA]	E_F ^e [eV]	k -range [\AA^{-1}]	R-factor
0 min	Ge-O	5.8 ± 0.6	1.75 ± 0.02	0.055 ± 0.006	0.259	2.96 - 15.02	15.94
	Ge-C	6.2 ± 0.9	2.80 ± 0.03	0.089 ± 0.013			
35 min	Ge-O	6.4 ± 0.6	1.73 ± 0.02	0.050 ± 0.005	2.662	2.99 - 15.00	38.92
	Ge-C	5.6 ± 0.8	2.76 ± 0.03	0.084 ± 0.013			
190 min	Ge-O	5.8 ± 0.6	1.75 ± 0.02	0.050 ± 0.005	0.001	2.99 - 15.02	17.79
	Ge-C	6.8 ± 1.0	2.81 ± 0.03	0.097 ± 0.015			
370 min	Ge-O	5.8 ± 0.6	1.75 ± 0.02	0.055 ± 0.006	-0.018	2.99 - 15.02	15.74
	Ge-C	6.7 ± 1.0	2.81 ± 0.03	0.097 ± 0.015			
1020 min	Ge-O	5.8 ± 0.6	1.75 ± 0.02	0.055 ± 0.006	0.474	2.97 - 15.03	16.66
	Ge-C	6.6 ± 1.0	2.80 ± 0.03	0.097 ± 0.015			

^aabsorber (A) - backscatterers (Bs), ^b coordination number N, ^c interatomic distance r , ^d Debye-Waller factor σ with its calculated deviation and ^e Fermi energy E_F .

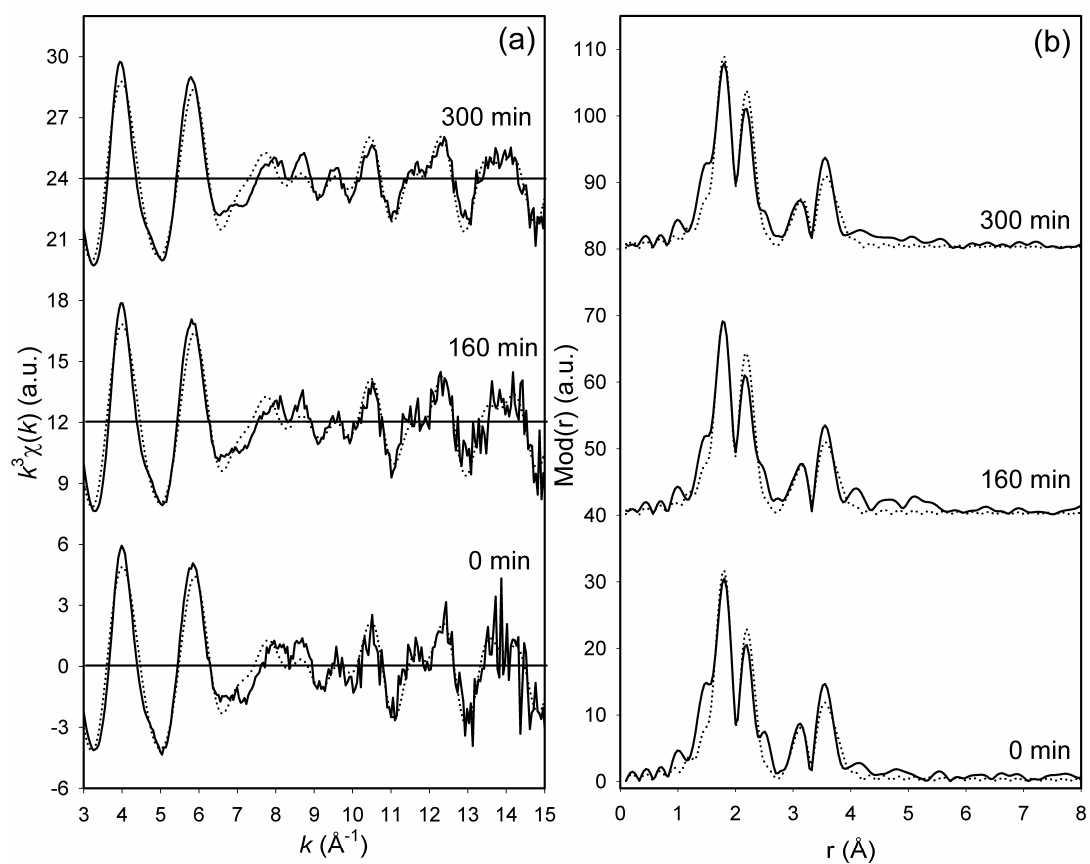


Figure 5.5.32. Experimental (solid line) and calculated (dotted line) EXAFS functions (a) and their Fourier transforms (b) for $\text{Hf}(\text{O}^m\text{Bu})_4$ mixed with pre-hydrolysed $\text{Si}(\text{OEt})_4$ measured at different time intervals, at the Hf L_{III} -edge.

Table 5.5.14. EXAFS obtained structural parameters for $\text{Hf}(\text{O}^m\text{Bu})_4$ mixed with pre-hydrolysed $\text{Si}(\text{OEt})_4$ measured at different time intervals

Time	A-Bs ^a	N ^b	r ^c [\AA]	σ ^d [\AA]	E_F ^e [eV]	k -range [\AA^{-1}]	R-factor
0 min	Hf-O	2.3 ± 0.2	1.95 ± 0.02	0.050 ± 0.005	0.866	2.97 - 15.01	37.10
	Hf-O	4.5 ± 0.5	2.13 ± 0.02	0.081 ± 0.008			
	Hf-C	1.7 ± 0.3	3.13 ± 0.03	0.067 ± 0.010			
	Hf-Hf	1.2 ± 0.2	3.41 ± 0.04	0.071 ± 0.014			
160 min	Hf-O	2.2 ± 0.2	1.95 ± 0.02	0.050 ± 0.005	1.560	3.00 - 15.02	36.97
	Hf-O	4.4 ± 0.5	2.13 ± 0.02	0.077 ± 0.008			
	Hf-C	2.2 ± 0.3	3.13 ± 0.03	0.084 ± 0.013			
	Hf-Hf	1.1 ± 0.2	3.42 ± 0.04	0.074 ± 0.015			
300 min	Hf-O	2.2 ± 0.2	1.96 ± 0.02	0.050 ± 0.005	0.782	2.97 - 15.01	31.23
	Hf-O	4.3 ± 0.5	2.14 ± 0.02	0.077 ± 0.008			
	Hf-C	2.2 ± 0.3	3.13 ± 0.03	0.077 ± 0.012			
	Hf-Hf	1.1 ± 0.2	3.43 ± 0.04	0.074 ± 0.014			

^a absorber (A) - backscatterers (Bs), ^b coordination number N, ^c interatomic distance r, ^d Debye-Waller factor σ with its calculated deviation and ^e Fermi energy E_F .

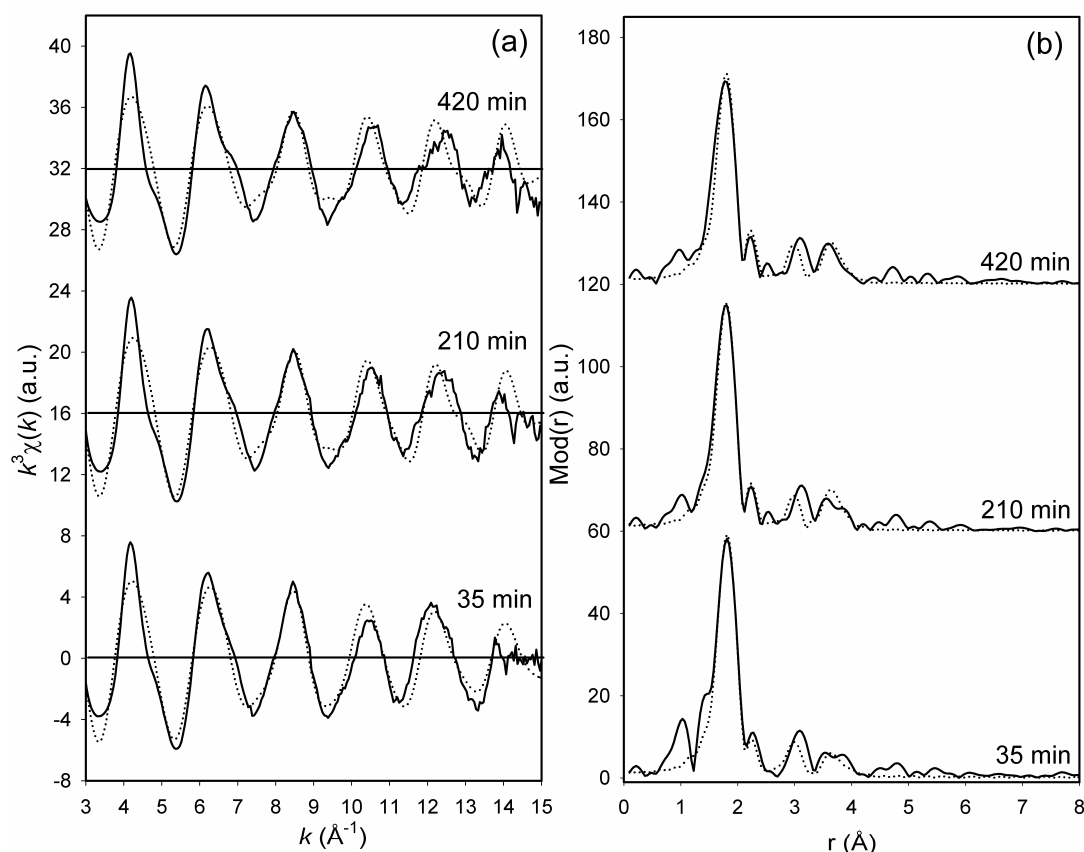


Figure 5.5.33. Experimental (solid line) and calculated (dotted line) EXAFS functions (a) and their Fourier transforms (b) for $\text{Ta}(\text{OEt})_5$ mixed with pre-hydrolysed $\text{Si}(\text{OEt})_4$ measured at different time intervals, at the Ta L_{III} -edge.

Table 5.5.15. EXAFS obtained structural parameters for $\text{Ta}(\text{OEt})_5$ mixed with pre-hydrolysed $\text{Si}(\text{OEt})_4$ measured at different time intervals

Time	A-Bs ^a	N ^b	r ^c [\AA]	σ ^d [\AA]	E_F ^e [eV]	k -range [\AA^{-1}]	R-factor
35 min	Ta-O	4.6 ± 0.5	1.91 ± 0.02	0.063 ± 0.006	-1.007	2.98 - 15.01	33.36
	Ta-O	2.7 ± 0.3	2.13 ± 0.02	0.084 ± 0.008			
	Ta-C	3.9 ± 0.6	3.07 ± 0.03	0.089 ± 0.013			
	Ta-Ta	1.0 ± 0.2	3.50 ± 0.04	0.087 ± 0.017			
210 min	Ta-O	4.7 ± 0.5	1.91 ± 0.02	0.063 ± 0.006	-0.341	2.97 - 15.02	36.39
	Ta-O	2.4 ± 0.3	2.12 ± 0.02	0.071 ± 0.007			
	Ta-C	3.7 ± 0.5	3.07 ± 0.03	0.087 ± 0.013			
	Ta-Ta	1.0 ± 0.2	3.49 ± 0.04	0.071 ± 0.014			
420 min	Ta-O	4.4 ± 0.4	1.91 ± 0.02	0.063 ± 0.006	-2.473	3.00 - 15.00	43.47
	Ta-O	2.6 ± 0.3	2.12 ± 0.02	0.071 ± 0.007			
	Ta-C	3.9 ± 0.6	3.08 ± 0.03	0.081 ± 0.012			
	Ta-Ta	1.0 ± 0.2	3.49 ± 0.04	0.071 ± 0.014			

^a absorber (A) - backscatterers (Bs), ^b coordination number N, ^c interatomic distance r, ^d Debye-Waller factor σ with its calculated deviation and ^e Fermi energy E_F .

For all the three cases, the EXAFS analysis reveals that the structural parameters for the mixture of alkoxides at different time intervals were similar to each other and in agreement with those of the corresponding pure alkoxides. The results indicate that the addition of pre-hydrolysed $\text{Si}(\text{OEt})_4$ does not change the structure around the metal atoms. Even after aging the two alkoxides remain as separate entities in the solution. Furthermore, M-O-Si (M = Ge, Hf, Ta) mixed bonds could not be evidenced from the EXAFS studies.

The Raman spectra recorded for metal alkoxide mixed with pre-hydrolysed $\text{Si}(\text{OEt})_4$ at different time intervals are shown along with the spectrum of the corresponding pure alkoxide and $\text{Si}(\text{OEt})_4$ in Figures 5.5.34, 5.5.35 and 5.5.36 for $\text{Ge}(\text{OEt})_4$, $\text{Hf}(\text{O}^n\text{Bu})_4$ and $\text{Ta}(\text{OEt})_5$, respectively. In all the three cases, the peak at 658 cm^{-1} characteristic of Si-O vibrations in $\text{Si}(\text{OEt})_4$ could be observed along with the corresponding M-O peak from the metal alkoxide (620 cm^{-1} in $\text{Ge}(\text{OEt})_4$, 397 cm^{-1} in $\text{Hf}(\text{O}^n\text{Bu})_4$ and 588 cm^{-1} in $\text{Ta}(\text{OEt})_5$). The spectra acquired at different time intervals does not show any remarkable changes in comparison to the spectrum obtained immediately after mixing.

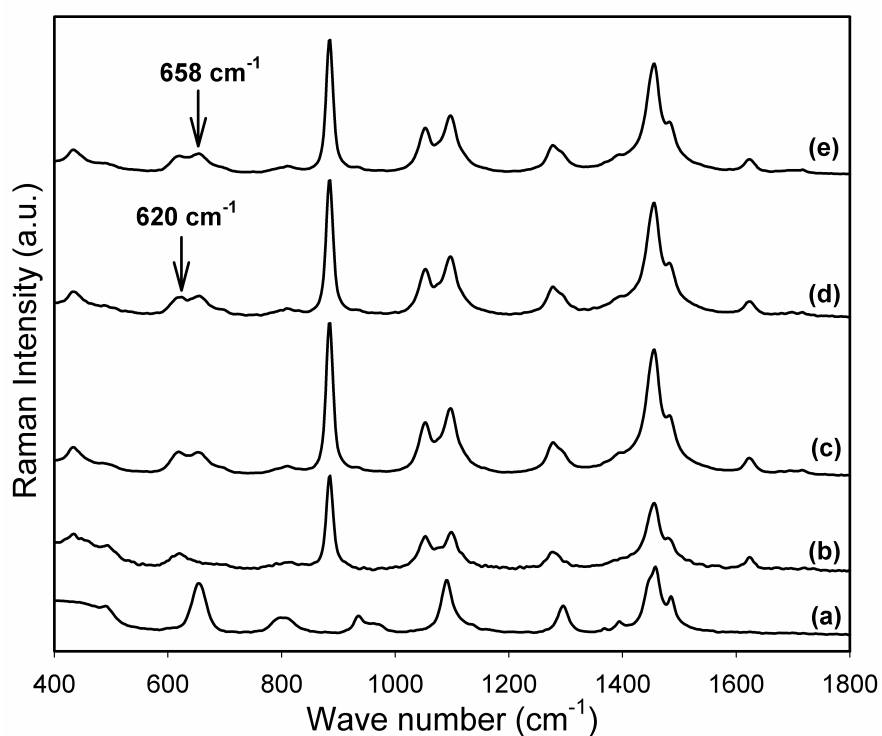


Figure 5.5.34. Raman spectra of $\text{Ge}(\text{OEt})_4$ mixed with pre-hydrolysed $\text{Si}(\text{OEt})_4$ measured at different time intervals along with pure $\text{Ge}(\text{OEt})_4$ and $\text{Si}(\text{OEt})_4$. [(a) $\text{Si}(\text{OEt})_4$, (b) $\text{Ge}(\text{OEt})_4$, (c) $\text{Si}(\text{OEt})_4 + \text{Ge}(\text{OEt})_4$ (0h), (d) $\text{Si}(\text{OEt})_4 + \text{Ge}(\text{OEt})_4$ (24h) and (e) $\text{Si}(\text{OEt})_4 + \text{Ge}(\text{OEt})_4$ (48 h)].

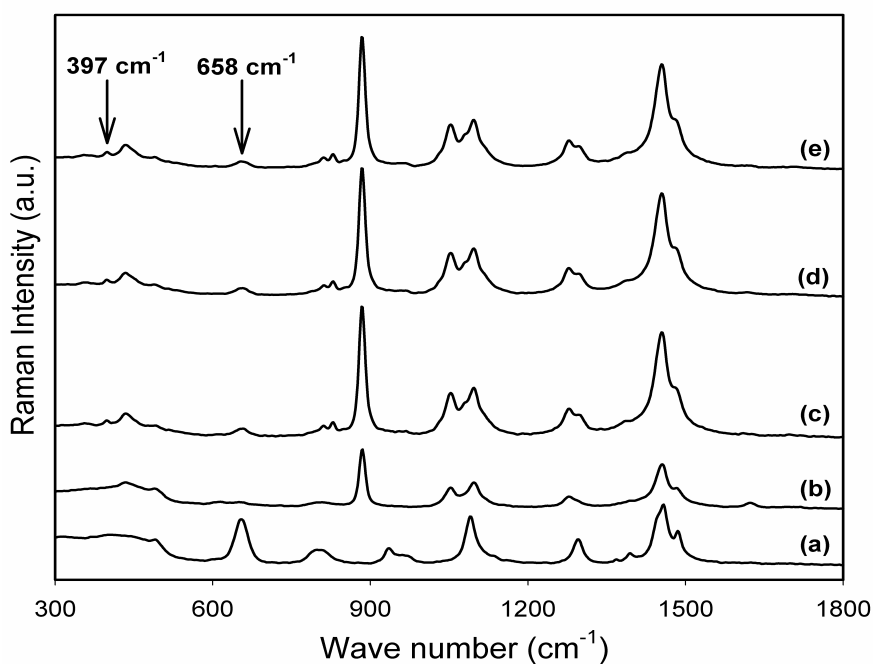


Figure 5.5.35. Raman spectra of $\text{Hf}(\text{O}^n\text{Bu})_4$ mixed with pre-hydrolysed $\text{Si}(\text{OEt})_4$ measured at different time intervals along with pure $\text{Hf}(\text{O}^n\text{Bu})_4$ and $\text{Si}(\text{OEt})_4$. [(a) $\text{Si}(\text{OEt})_4$, (b) $\text{Hf}(\text{O}^n\text{Bu})_4$, (c) $\text{Si}(\text{OEt})_4 + \text{Hf}(\text{O}^n\text{Bu})_4$ (0 h), (d) $\text{Si}(\text{OEt})_4 + \text{Hf}(\text{O}^n\text{Bu})_4$ (24 h) and (e) $\text{Si}(\text{OEt})_4 + \text{Hf}(\text{O}^n\text{Bu})_4$ (48 h)].

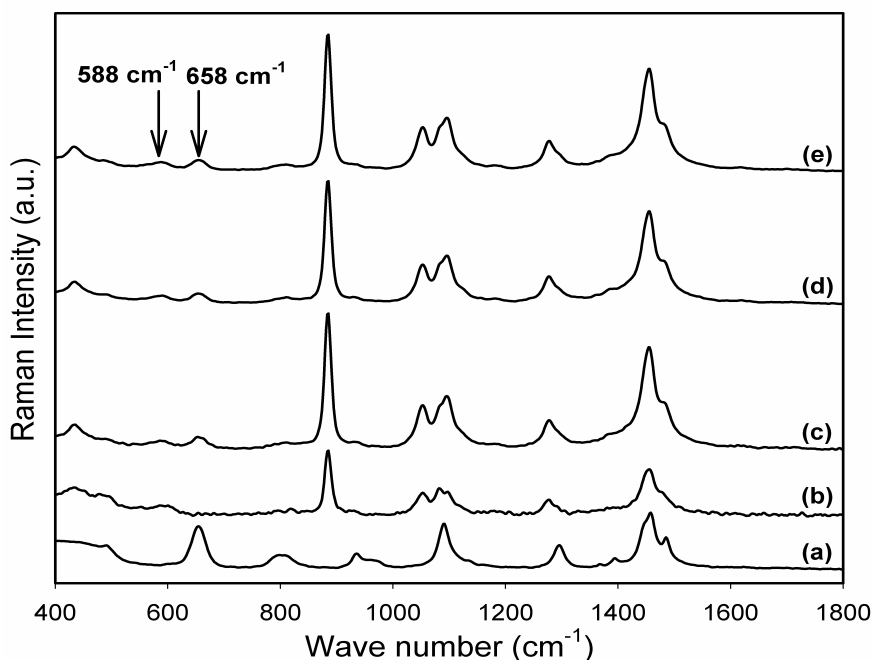


Figure 5.5.36. Raman spectra of $\text{Ta}(\text{OEt})_5$ mixed with pre-hydrolysed $\text{Si}(\text{OEt})_4$ measured at different time intervals along with pure $\text{Ta}(\text{OEt})_5$ and $\text{Si}(\text{OEt})_4$. [(a) $\text{Si}(\text{OEt})_4$, (b) $\text{Ta}(\text{OEt})_5$, (c) $\text{Si}(\text{OEt})_4 + \text{Ta}(\text{OEt})_5$ (0 h), (d) $\text{Si}(\text{OEt})_4 + \text{Ta}(\text{OEt})_5$ (24 h) and (e) $\text{Si}(\text{OEt})_4 + \text{Ta}(\text{OEt})_5$ (48 h)].

In all the cases, the peaks corresponding to M-O-Si vibrations could not be evidenced, indicating that the alkoxides retain their structural integrity in the mixture, which is in agreement with the results obtained from the EXAFS analysis.

5.5.7. Hydrolysis and condensation of mixture of alkoxides

Hydrolysis and condensation behaviour of metal alkoxide mixed with pre-hydrolysed $\text{Si}(\text{OEt})_4$ was investigated in order to study the influence of the addition of pre-hydrolysed $\text{Si}(\text{OEt})_4$ on the formation of the condensation product, especially to investigate whether in the formed gel, homo- or hetero- condensation species are present. The sample for the measurements was prepared by mixing metal alkoxide, pre-hydrolysed $\text{Si}(\text{OEt})_4$ and water in 1:2:2 molar ratio. The experimentally determined and the theoretically calculated EXAFS functions in k -space and their Fourier transforms in real space for metal alkoxides, pre-hydrolysed $\text{Si}(\text{OEt})_4$ and water mixture measured at different time intervals are shown in Figures 5.5.37, 5.5.38 and 5.5.39 and the obtained structural parameters are summarised in Tables 5.5.16, 5.5.17 and 5.5.18 for $\text{Ge}(\text{O}^n\text{Bu})_4$, $\text{Hf}(\text{O}^n\text{Bu})_4$ and $\text{Ta}(\text{OEt})_5$, respectively. For clarity reasons, three representative spectra are shown in each case and only the corresponding structural parameters are listed.

The evaluation of the EXAFS spectra indicates that the hydrolysis and condensation reactions occur instantaneously upon the addition of water to the mixture of alkoxides, as confirmed by the immediate formation of a turbid solution, in all the three cases. It is interesting to note that the obtained structural parameters are in agreement with those obtained when water was added to corresponding pure alkoxide in the same molar ratio. In particular, a higher backscatterer at a distance of 3.16 Å could be determined in the case of $\text{Ge}(\text{O}^n\text{Bu})_4$ -pre-hydrolysed $\text{Si}(\text{OEt})_4$ -water mixture, which could be unequivocally assigned to germanium, thus proving the formation of Ge-O-Ge species, whereas in the case of $\text{Hf}(\text{O}^n\text{Bu})_4$ -pre-hydrolysed $\text{Si}(\text{OEt})_4$ -water mixture and $\text{Ta}(\text{OEt})_5$ -pre-hydrolysed $\text{Si}(\text{OEt})_4$ -water mixture, an increase in the coordination number of hafnium/tantalum backscatterers at the distance of about 3.44 Å/3.36 Å could be observed, indicating the development of a homocondensation species. Moreover, the subsequent measurements performed at different time intervals revealed no remarkable changes in the structural parameter in comparison with the measurements performed immediately after mixing. Furthermore, in all the cases, M-O-Si mixed bonds attributable to the formation of a heterocondensation product could not be evidenced,

which could be due to the differences in the reactivities of corresponding metal alkoxides and $\text{Si}(\text{OEt})_4$ with respect to their condensation behaviour.

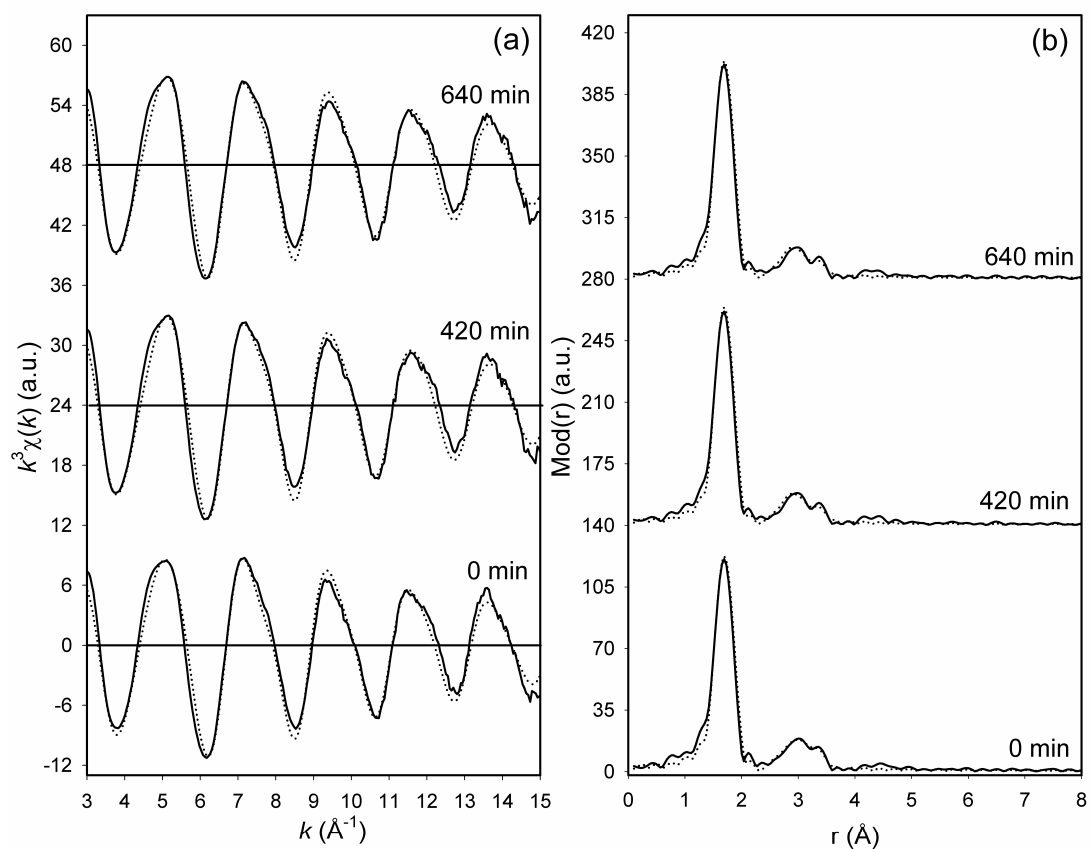


Figure 5.5.37. Experimental (solid line) and calculated (dotted line) EXAFS functions (a) and their Fourier transforms (b) for $\text{Ge}(\text{O}^n\text{Bu})_4$, pre-hydrolysed $\text{Si}(\text{OEt})_4$ and water mixture measured at different time intervals, at the Ge K-edge.

Table 5.5.16. EXAFS obtained structural parameters for $\text{Ge}(\text{O}^n\text{Bu})_4$, pre-hydrolysed $\text{Si}(\text{OEt})_4$ and water mixture measured at different time intervals

Time	A-Bs ^a	N ^b	r ^c [\AA]	σ ^d [\AA]	E_F ^e [eV]	k -range [\AA^{-1}]	R-factor
0 min	Ge-O Ge-C Ge-Ge	5.3 ± 0.5 5.9 ± 0.9 0.9 ± 0.2	1.74 ± 0.02 2.83 ± 0.03 3.17 ± 0.04	0.050 ± 0.005 0.102 ± 0.015 0.067 ± 0.013	0.696	2.98 - 15.03	16.79
420 min	Ge-O Ge-C Ge-Ge	5.4 ± 0.5 6.6 ± 1.0 0.8 ± 0.2	1.74 ± 0.02 2.84 ± 0.03 3.17 ± 0.04	0.050 ± 0.005 0.100 ± 0.015 0.071 ± 0.014	0.009	2.95 - 15.02	16.22
640 min	Ge-O Ge-C Ge-Ge	5.3 ± 0.5 6.6 ± 1.0 0.8 ± 0.2	1.74 ± 0.02 2.85 ± 0.03 3.17 ± 0.04	0.050 ± 0.005 0.102 ± 0.015 0.074 ± 0.015	0.001	2.95 - 15.02	16.29

^a absorber (A) - backscatterers (Bs), ^b coordination number N, ^c interatomic distance r , ^d Debye-Waller factor σ with its calculated deviation and ^e Fermi energy E_F .

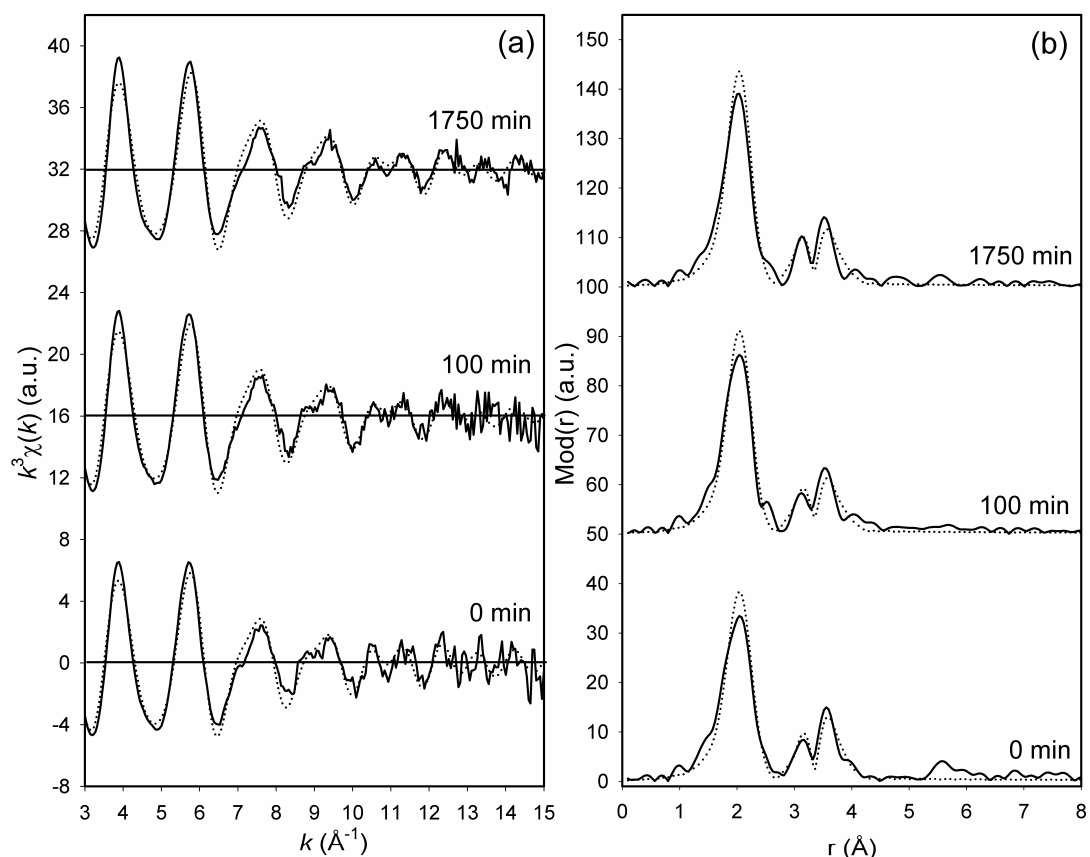


Figure 5.5.38. Experimental (solid line) and calculated (dotted line) EXAFS functions (a) and their Fourier transforms (b) for $\text{Hf}(\text{O}^n\text{Bu})_4$, pre-hydrolysed $\text{Si}(\text{OEt})_4$ and water mixture measured at different time intervals, at the Hf L_{III} -edge.

Table 5.5.17. EXAFS obtained structural parameters for $\text{Hf}(\text{O}^n\text{Bu})_4$, pre-hydrolysed $\text{Si}(\text{OEt})_4$ and water mixture measured at different time intervals

Time	A-Bs ^a	N ^b	r ^c [Å]	σ ^d [Å]	E_F ^e [eV]	k-range [Å ⁻¹]	R-factor
0 min	Hf-O	6.7 ± 0.7	2.12 ± 0.02	0.100 ± 0.010	-0.680	2.98 - 15.05	32.96
	Hf-C	5.3 ± 0.8	3.19 ± 0.03	0.120 ± 0.018			
	Hf-Hf	2.1 ± 0.4	3.45 ± 0.04	0.087 ± 0.017			
100 min	Hf-O	6.6 ± 0.7	2.12 ± 0.02	0.097 ± 0.010	-0.463	2.99 - 15.05	32.40
	Hf-C	5.4 ± 0.8	3.18 ± 0.03	0.120 ± 0.018			
	Hf-Hf	2.3 ± 0.4	3.45 ± 0.04	0.095 ± 0.019			
1750 min	Hf-O	6.7 ± 0.7	2.11 ± 0.02	0.097 ± 0.010	-0.465	2.99 - 15.05	30.23
	Hf-C	5.3 ± 0.8	3.17 ± 0.03	0.114 ± 0.017			
	Hf-Hf	2.2 ± 0.4	3.44 ± 0.04	0.092 ± 0.018			

^a absorber (A) - backscatterers (Bs), ^b coordination number N, ^c interatomic distance r, ^d Debye-Waller factor σ with its calculated deviation and ^e Fermi energy E_F .

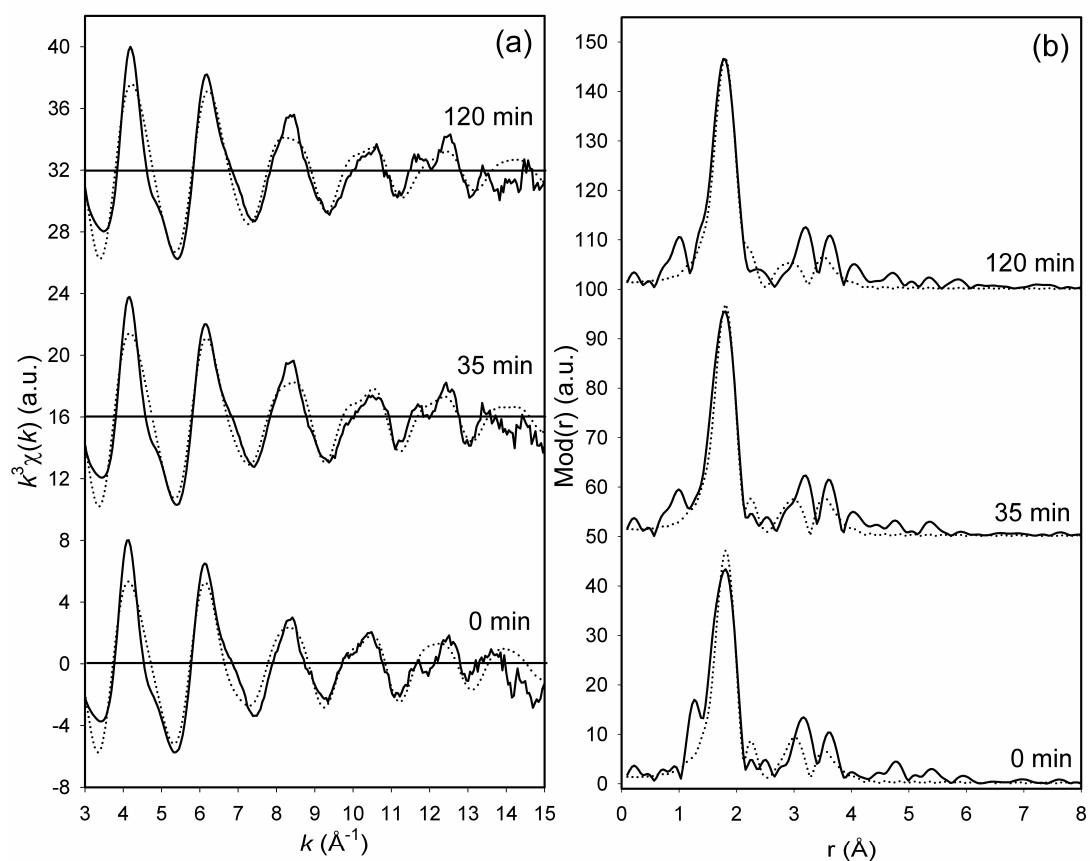


Figure 5.5.39. Experimental (solid line) and calculated (dotted line) EXAFS functions (a) and their Fourier transforms (b) for $\text{Ta}(\text{OEt})_5$, pre-hydrolysed $\text{Si}(\text{OEt})_4$ and water mixture measured at different time intervals, at the Ta L_{III} -edge.

Table 5.5.18. EXAFS obtained structural parameters for $\text{Ta}(\text{OEt})_5$, pre-hydrolysed $\text{Si}(\text{OEt})_4$ and water mixture measured at different time intervals

Time	A-Bs ^a	N ^b	r ^c [\AA]	σ ^d [\AA]	E_F ^e [eV]	k -range [\AA^{-1}]	R-factor
0 min	Ta-O	4.5 ± 0.5	1.93 ± 0.02	0.071 ± 0.007	-3.480	2.99 – 14.99	42.20
	Ta-O	2.8 ± 0.3	2.11 ± 0.02	0.087 ± 0.009			
	Ta-C	4.9 ± 0.7	3.06 ± 0.03	0.095 ± 0.014			
	Ta-Ta	1.6 ± 0.3	3.37 ± 0.04	0.097 ± 0.019			
35 min	Ta-O	4.8 ± 0.5	1.92 ± 0.02	0.074 ± 0.007	-1.461	3.00 – 15.01	36.97
	Ta-O	2.5 ± 0.3	2.11 ± 0.02	0.087 ± 0.009			
	Ta-C	4.5 ± 0.7	3.04 ± 0.03	0.097 ± 0.015			
	Ta-Ta	1.6 ± 0.3	3.37 ± 0.04	0.095 ± 0.019			
120 min	Ta-O	4.4 ± 0.4	1.91 ± 0.02	0.074 ± 0.007	-0.751	2.99 – 15.01	37.16
	Ta-O	2.4 ± 0.2	2.08 ± 0.02	0.084 ± 0.008			
	Ta-C	4.9 ± 0.7	3.00 ± 0.03	0.114 ± 0.017			
	Ta-Ta	1.6 ± 0.3	3.36 ± 0.04	0.100 ± 0.020			

^a absorber (A) - backscatterers (Bs), ^b coordination number N, ^c interatomic distance r, ^d Debye-Waller factor σ with its calculated deviation and ^e Fermi energy E_F .

The results were further verified by Raman spectroscopic investigations performed under similar reaction conditions. The Raman spectra measured for metal alkoxide, pre-hydrolysed $\text{Si}(\text{OEt})_4$ and water at different time intervals are shown along with the spectrum of the corresponding pure alkoxide -pre-hydrolysed $\text{Si}(\text{OEt})_4$ mixture in Figures 5.5.40, 5.5.41 and 5.5.42 for $\text{Ge}(\text{OEt})_4$, $\text{Hf}(\text{O}^i\text{Bu})_4$ and $\text{Ta}(\text{OEt})_5$, respectively.

In the Raman spectra of the metal alkoxide, pre-hydrolysed $\text{Si}(\text{OEt})_4$ and water mixture, the characteristic peaks belonging to M-O and Si-O vibrations could be noticed. In the spectra of $\text{Ge}(\text{OEt})_4$, pre-hydrolysed $\text{Si}(\text{OEt})_4$ and water mixture, the intensity of the peak at 620 cm^{-1} has decreased due to the decrease in the concentration of the germanium species in the solution as a result of gelation and precipitation. In the spectra of $\text{Hf}(\text{O}^i\text{Bu})_4$, pre-hydrolysed $\text{Si}(\text{OEt})_4$ and water mixture, the decrease in the intensity of Hf-O peak at 397 cm^{-1} and Hf(-O-C) bands at 1030 and 1080 cm^{-1} could be evidenced owing to the formation of the condensation product. In the spectra of $\text{Ta}(\text{OEt})_5$, pre-hydrolysed $\text{Si}(\text{OEt})_4$ and water mixture, the decrease in the intensity Ta-O peak at 588 cm^{-1} and Ta(-O-C) band at 1080 cm^{-1} could be observed, which indicates the decrease of tantalum species in the solution owing to condensation.

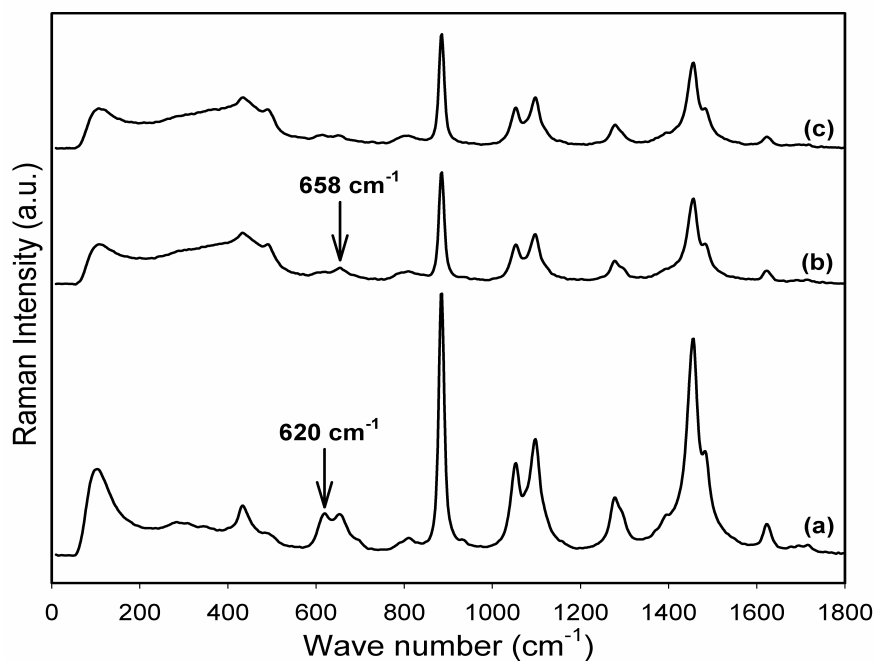


Figure 5.5.40. Raman spectra of $\text{Ge}(\text{OEt})_4$, pre-hydrolysed $\text{Si}(\text{OEt})_4$ and water mixture measured at different time intervals along with $\text{Ge}(\text{OEt})_4$ mixed with pre-hydrolysed $\text{Si}(\text{OEt})_4$. [(a) $\text{Si}(\text{OEt})_4 + \text{Ge}(\text{OEt})_4$ (0 h), (b) $\text{Si}(\text{OEt})_4 + \text{Ge}(\text{OEt})_4 + \text{H}_2\text{O}$ (0 h) and (c) $\text{Si}(\text{OEt})_4 + \text{Ge}(\text{OEt})_4 + \text{H}_2\text{O}$ (24 h)].

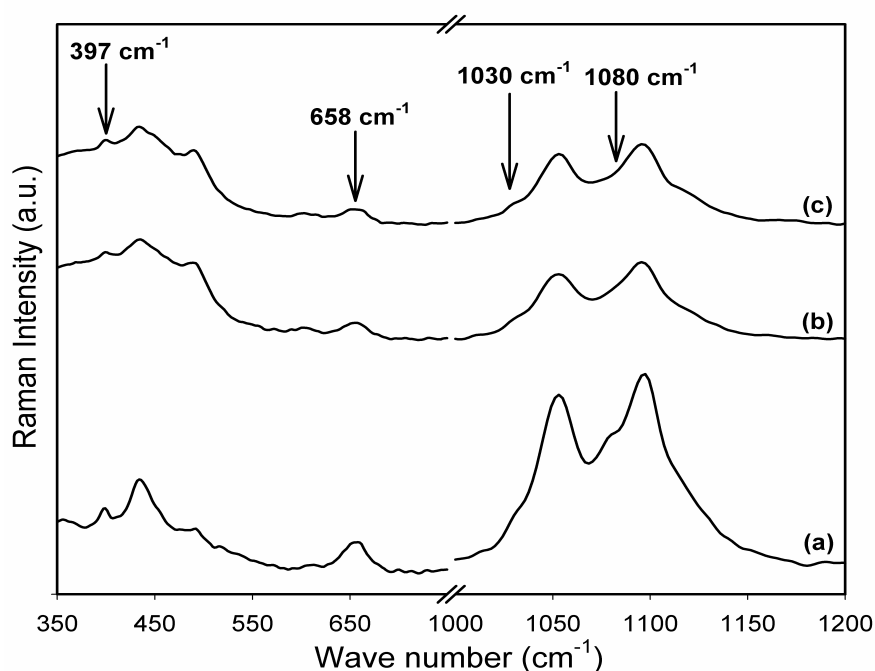


Figure 5.5.41. Raman spectra of $\text{Hf}(\text{O}^n\text{Bu})_4$, pre-hydrolysed $\text{Si}(\text{OEt})_4$ and water mixture measured at different time intervals along with $\text{Hf}(\text{O}^n\text{Bu})_4$ -pre-hydrolysed $\text{Si}(\text{OEt})_4$ mixture. [(a) $\text{Si}(\text{OEt})_4 + \text{Hf}(\text{O}^n\text{Bu})_4$ (0 h), (b) $\text{Si}(\text{OEt})_4 + \text{Hf}(\text{O}^n\text{Bu})_4 + \text{H}_2\text{O}$ (0 h) and (c) $\text{Si}(\text{OEt})_4 + \text{Hf}(\text{O}^n\text{Bu})_4 + \text{H}_2\text{O}$ (24 h)].

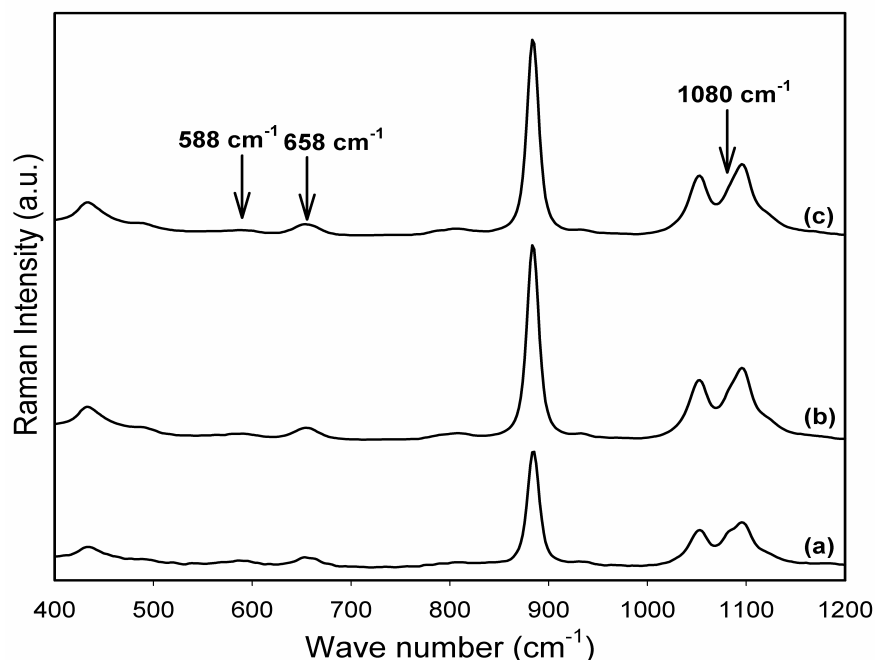


Figure 5.5.42. Raman spectra of $\text{Ta}(\text{OEt})_5$, pre-hydrolysed $\text{Si}(\text{OEt})_4$ and water mixture measured at different time intervals along with $\text{Ta}(\text{OEt})_5$ -pre-hydrolysed $\text{Si}(\text{OEt})_4$ mixture. [(a) $\text{Si}(\text{OEt})_4 + \text{Ta}(\text{OEt})_5$ (0 h), (b) $\text{Si}(\text{OEt})_4 + \text{Ta}(\text{OEt})_5 + \text{H}_2\text{O}$ (0 h) and (c) $\text{Si}(\text{OEt})_4 + \text{Ta}(\text{OEt})_5 + \text{H}_2\text{O}$ (24 h)].

In all the three cases, the spectrum measured 24 h after mixing does not show any significant variations in comparison to the spectrum acquired immediately after mixing. Furthermore, in all the cases, mixed M-O-Si vibrations could not be observed.

5.5.8. Conclusion

The EXAFS and Raman spectroscopic investigations on germanium alkoxides revealed that $\text{Ge}(\text{OMe})_4$, $\text{Ge}(\text{OEt})_4$, $\text{Ge}(\text{O}^i\text{Pr})_4$ and $\text{Ge}(\text{O}^n\text{Bu})_4$ are monomeric in nature and have similar structures, indicating that the alkoxy group does not influence the general structure of the germanium alkoxides. The studies on $\text{Hf}(\text{O}^n\text{Bu})_4$ and $\text{Ta}(\text{OEt})_5$ reveals that they have a dimeric structure. The results show that all the three metal alkoxides instantaneously undergo hydrolysis and condensation upon the addition of water and no remarkable structural changes take place at subsequent time intervals. The chemical modification of germanium alkoxide by *acac* does not occur even 48 h after mixing, as the coordination of the ligand on to the metal could not be observed, while the coordination occurs immediately in case of $\text{Hf}(\text{O}^n\text{Bu})_4$ and $\text{Ta}(\text{OEt})_5$ causing a change in the coordination geometry around the metal atom from a 6-fold to an 8-fold coordination. The Raman spectroscopic investigations on $\text{Hf}(\text{O}^n\text{Bu})_4$ reveals that there exists no free carbonyl groups and a bidentate coordination has occurred, whereas the studies on $\text{Ta}(\text{OEt})_5$ reveal that not all the carbonyl groups of the added *acac* were involved in the coordination process. The hydrolysis and condensation reactions occur immediately upon the addition of water to the germanium alkoxide-*acac* mixture, owing to the absence of coordination of the ligand, but the reactions have been hindered in the *acac* modified $\text{Hf}(\text{O}^n\text{Bu})_4$ and $\text{Ta}(\text{OEt})_5$ solutions. In addition, the structure of the metal alkoxides is not altered by the addition of pre-hydrolysed $\text{Si}(\text{OEt})_4$ and even after 48 h the alkoxides remain as individual entities in the solution. The investigations on the hydrolysis and condensation reactions of this mixture of alkoxides reveal the formation of a homocondensation product in all the three cases, which could be attributed to the differences in the reactivities of the different alkoxides.

Chapter 6 Summary and outlook

The research work deals with the structural investigations on organometallic complexes and nanomaterials, having active metal centers. An insight into the structure of these materials is of vital concern as the functional properties are strongly dependent on the chemical structure. X-ray absorption fine structure (XAFS) and Raman spectroscopy are powerful techniques to characterise disordered systems regardless of the state of the samples and can yield complementary information about the structure.

In the present work, XAFS measurements were performed in transmission and fluorescence modes at the beamlines X1, E4 and A1 at HASYLAB, Hamburg and at the XAS beamline at ANKA, Karlsruhe. The samples in solid state were embedded in polymer matrices and pressed into pellets, before measurements. In the case of liquid samples, the required quantity of sample was filled into the specially designed liquid sample cell comprising of Kapton[®] foil windows. In all cases, the measurements were performed at ambient conditions. The program WINXAS was used for normalisation, AUTOBK was used for the removal of background and EXCURV92/98 was used for the evaluation of the EXAFS function. The Raman measurements were performed on Bruker RFS 100/S FT Raman spectrometer and the infrared measurements were carried out on Bruker IFS 66v/S FT-IR spectrometer. The Raman and FT-IR spectra were analysed using the finger-print method.

In this framework, optically active metallophthalocyanines were studied by means of EXAFS spectroscopy for the local structure around the metal center. The investigations revealed that, in the case of dimeric gallium and ruthenium phthalocyanines, the metal–metal distances were found to be 2.46 Å and 2.43 Å respectively, and the metal centers were located about 0.5 Å out of plane from the macrocycle, projecting inwards. The results obtained from the gallium- and indium μ -oxo-bridged phthalocyanine dimers were in agreement with the general structure of the phthalocyanine complexes. In addition, the studies on peripherally fluorinated ruthenium phthalocyanines with tetrahydrofuran or pyridine ligands indicated six-fold coordination geometry around the ruthenium atom, where the substituted ligands were located axially in an octahedral arrangement on both sides of the phthalocyanine macrocycle. In all the cases, the influence of the phthalocyanine macrocycle in the spectra was evident from the EXAFS data analysis.

The EXAFS studies performed on catalytically active ruthenium(II) complexes indicated that the complexes retain their structural integrity when they are embedded or supported on polysiloxane matrices to form stationary phase materials. The variations in the catalytic activity of the complexes with different ligands can be correlated to the differences observed in the electronic structure around the active ruthenium center, probed by means of AXAFS studies. Furthermore, the investigations revealed that the co-catalyst (^tBuOK) plays a crucial role not only in enhancing the catalytic activity but also in influencing the structure of the intermediate species. It is significant to note that out of the two chlorine atoms bonded to the ruthenium metal center, only one is abstracted during the reaction of the complex with the co-catalyst.

The EXAFS investigations on bio-active ruthenium(III) complexes revealed an octahedral structure for both the ligand I and ligand II complexes. However, the exact geometry of the coordinated ligands could not be verified by means of EXAFS. The effect of various parameters involved in the multiple scattering calculations has been elucidated and the studies indicated that a minimum set of values are already sufficient to yield a reasonable fit. Additionally, AXAFS spectroscopy has been utilised as a tool to probe the influence of the different substituent atoms on the electronic properties of the central ruthenium atom. Furthermore, theoretical calculations on the electronic structure of these complexes, using density functional theory is proposed as a future work. Hence, a comparison could be performed between the AXAFS investigations and theoretical calculations.

The time resolved XAFS measurements were performed on the hydrogenation reaction of catalytically active PCP pincer ligand iridium complexes in *in operando* conditions. The obtained results suggested several vague possibilities concerning the existence of the theoretically postulated Ir(V) intermediate species and an unequivocal conclusion could not be reached. Many questions such as, the time window of the reaction, the directional shift in the equilibrium of the reaction, the activity of the complexes, the optimal hydrogen pressure, the quantity of the Ir(V) intermediate species and its life time, remain unanswered. It is proposed as a future work, to investigate this hydrogenation reaction with optimised reaction parameters. Furthermore, QXAFS measurements performed in combination with UV-Vis spectroscopy is also expected to provide deeper insights into the reaction mechanism.

The structural investigations on $\text{Cd}(\text{O-}^i\text{PrXan})_2$ and $\text{Zn}(\text{O-}^i\text{PrXan})_2$ by means of EXAFS revealed that the compounds have metal–sulphur distances and coordination numbers similar to those of the corresponding metal sulphides, suggesting their suitability as single-source CVD precursors. Moreover, Raman and FT-IR spectroscopic techniques provided additional structural information about these compounds.

The structural studies were performed on nanostructured mixed oxide materials by means of XAFS and Raman spectroscopy. The EXAFS investigations on the nanophasic undoped and calcium doped LaCoO_3 powders indicated that the perovskite network was not formed in the xerogels and the effects of calcium doping on the local structure could not be unequivocally inferred. The undoped LaCoO_3 powders evolved towards a nanocrystalline structure during thermal treatment but no significant local structural changes ascribable to the annealing temperatures could be evidenced for the samples annealed between 700 and 1000°C. Conversely, calcium doping had a substantial influence on the local structure, which was dependent on the annealing temperatures. These changes could be attributed to the formation of cobalt and calcium oxide-based compounds, the distortion of the perovskite structure and the substitution of some of the La(III) species by Ca(II) ions. The expected change in the oxidation states of cobalt between the xerogels and the annealed samples could also be evidenced from the edge energy shift in the XANES region. The studies on the La–Sr–Co–Fe–O nanocomposites revealed the formation of $\text{La}_{0.6}\text{Sr}_{0.4}\text{Co}_{0.9}\text{Fe}_{0.1}\text{O}_3$ along with Co_3O_4 and perhaps La_2CoO_4 in La–Sr–Co–Fe–O mixed oxide (support). The influence of Fe_2O_3 doping on La–Sr–Co–Fe–O mixed oxide is significant and changes in the local structure can be observed at all the different measured edges. Apart from the distortion in the perovskite structure, the formation of other oxide-based compounds such as CoO and Fe_2O_3 could be evidenced as a result of Fe_2O_3 doping. The studies on mixed Fe–Ti–O nanocomposites reveal that the structure of the supported and bulk mixed oxides prepared by wet impregnation and co-precipitation methods are similar to each other and resemble that of rutile TiO_2 . Furthermore, the iron doping does not significantly alter the local structure around the titanium atoms. The studies on mixed W–Ce–O nanocomposites showed that the structure of the different WO_3/CeO_2 samples is similar to that of crystalline CeO_2 and, WO_3 doping does not modify the local environment around the cerium atoms. Similarly the studies on mixed Ce–Y–Zr–O nanocomposites revealed that yttria stabilised zirconia retains its structural integrity even after doping with CeO_2 .

The EXAFS and XANES investigations on ferrite based magnetic nanomaterials revealed that CuFe_2O_4 nanoparticles have a structure analogous to that of the bulk material. The studies further indicated that all the copper ions occupy the octahedral sites and the iron ions are distributed between the tetrahedral and octahedral sites. The investigations on $\text{CuFe}_2\text{O}_4\text{-SnO}_2$ and $\text{CuFe}_2\text{O}_4\text{-CeO}_2$ nanocomposites showed that the incorporation of the tetravalent metal oxides does not alter the local structure of CuFe_2O_4 nanoparticles. However, the studies on $\text{CuFe}_2\text{O}_4\text{-NiO}$ nanocomposites revealed the formation of NiFe_2O_4 and CuO in addition to the existence of CuFe_2O_4 nanoparticles. Furthermore, a partial substitution of the copper ions by nickel could also be evidenced.

The EXAFS studies on the inorganic-organic hybrid materials containing zirconium and hafnium oxo clusters revealed that the clusters lose their structural integrity upon incorporation in the polysiloxane matrices, irrespective of the nature of the silane and the ratio between the silane and the cluster. The investigations on the mixed metal oxides formed by the calcination of the hybrid materials indicated that silicon to metal composition has strong influences on the local structure of the obtained oxides. In all the cases, the presence of Zr-O-Si, Hf-O-Si or Zr-O-Hf mixed bonds could not be evidenced. Even though, the obtained structural parameters could not be matched with any of the well known crystalline polymorphs of the respective oxides, the XANES studies revealed the tendency towards the formation of tetragonal zirconia in the calcined samples.

The EXAFS and XANES studies on the nucleation of zinc sulphide nanoparticles by the reaction of thioacetic acid and zinc precursors dissolved in acetic acid or acetone revealed that the coordination of sulphur atoms takes places immediately when the mixture is prepared and zinc-sulphur species gradually evolves during the course of the reaction. In the case of zinc acetate precursor, even after 3420 min reaction time in the mixture with acetic acid and 2260 min reaction time in the mixture with acetone, the complete formation of ZnS could not be evidenced, which could possibly be attributed either to the presence of unreacted zinc-oxygen species in the mixture or to the coordination of water molecules on to the metal atom. However, in the case of zinc oxide in acetone a relatively higher quantity of zinc sulphide formation could be evidenced even after 1915 min reaction time. The obtained results indicated that zinc oxide reacts comparatively faster with thioacetic acid than zinc acetate. The choice of

the reaction medium plays a crucial role in determining the dissolution of the precursors in the solvents, but does not have strong influences on the mechanism of the reaction.

Time resolved *in situ* studies were performed on the key steps of sol-gel process. The EXAFS and Raman spectroscopic investigations on germanium alkoxides revealed that $\text{Ge}(\text{OMe})_4$, $\text{Ge}(\text{OEt})_4$, $\text{Ge}(\text{O}^i\text{Pr})_4$ and $\text{Ge}(\text{O}^n\text{Bu})_4$ are monomeric in nature and have similar structures, indicating that the alkoxy group does not influence the general structure of the germanium alkoxides. The studies on $\text{Hf}(\text{O}^n\text{Bu})_4$ and $\text{Ta}(\text{OEt})_5$ showed that they have a dimeric structure. The results indicated that all the three metal alkoxides instantaneously undergo hydrolysis and condensation reactions upon the addition of water and no remarkable structural changes take place at subsequent time intervals. The chemical modification of germanium alkoxide by acetylacetonone does not occur even 48 h after mixing, as the coordination of the ligand on to the metal could not be observed. However, the coordination occurs immediately in case of $\text{Hf}(\text{O}^n\text{Bu})_4$ and $\text{Ta}(\text{OEt})_5$ causing a change in the coordination geometry around the metal atom from a 6-fold to an 8-fold coordination. Additionally, the Raman spectroscopic investigations on $\text{Hf}(\text{O}^n\text{Bu})_4$ revealed that there exists no free carbonyl groups and a bidentate coordination has occurred, whereas the studies on $\text{Ta}(\text{OEt})_5$ indicated that not all the carbonyl groups of the added acetylacetonone were involved in the coordination process. The hydrolysis and condensation reactions occur immediately upon the addition of water to the germanium alkoxide-acetylacetonone mixture, owing to the absence of coordination of the ligand, while the reactions have been hindered in the acetylacetonone modified $\text{Hf}(\text{O}^n\text{Bu})_4$ and $\text{Ta}(\text{OEt})_5$ solutions. In addition, the structure of the metal alkoxides is not altered by the addition of pre-hydrolysed $\text{Si}(\text{OEt})_4$ and even after 48 h the alkoxides remain as individual entities in the solution. The investigations on the hydrolysis and condensation reactions of this mixture of alkoxides revealed the formation of a homocondensation product in all the three cases, which could be attributed to the differences in the reactivities of the different alkoxides. In most cases, the time-resolved *in situ* studies on the key steps of sol-gel process revealed that the reactions proceed much faster than the conventional time scales (min) used in the present measurements. Hence, observing these reactions using ultrafast spectroscopic methods would provide further understanding of the fundamental steps in detail, and is proposed as a future work. These information are vital for the preparation of tailor made materials with tunable properties suitable for specific applications.

Zusammenfassung und Ausblick

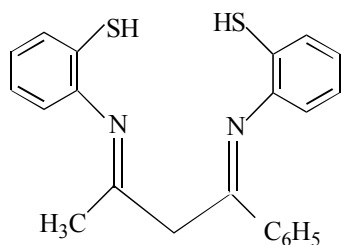
Die vorliegende Arbeit beschäftigt sich mit der Untersuchung der Struktur organometallischer Komplexe und Nanomaterialien mit aktiven Metallzentren. Da die Eigenschaften dieser Verbindungen sehr stark von ihrer Struktur abhängen, ist die Kenntnis ihrer Struktur von fundamentaler Bedeutung. Die Röntgenabsorptionsfeinstruktur spektroskopie (XAFS - X-ray absorption fine structure spectroscopy) und Ramanspektroskopie bieten sich als aussagekräftige Techniken an, um ungeordnete Systeme, unabhängig von ihrem Aggregatzustand, zu charakterisieren.

Die hier vorgestellten XAFS Untersuchungen wurden als Transmissions- und Fluoreszenzmessungen an den Meßplätzen X1, E4 und A1 des Hamburger Synchrotronstrahlungslabors (HASYLAB) und an dem XAS (X-ray absorption spectroscopy) Meßplatz des Karlsruher Speicherrings ANKA durchgeführt. Die Feststoffe wurden mit Polymeren vermengt und zu Tabletten gepreßt. Flüssigkeiten wurden in einer speziell angefertigten Zelle mit Kaptonfolie als Fenstermaterial untersucht. Zur Datenauswertung wurden die Programme WINXAS (Normierung), AUTOBK (Eliminierung der Untergrundstreuung) und EXCURV92/98 (Ermittlung der EXAFS-Funktion – extended X-ray absorption fine structure) verwendet. Die Raman-Messungen wurden an einem Bruker RFS 100/S FT Raman- und die IR-Messungen an einem Bruker IFS 66v/S FT-IR-Spektrometer vorgenommen und über die „fingerprint“-Methode analysiert.

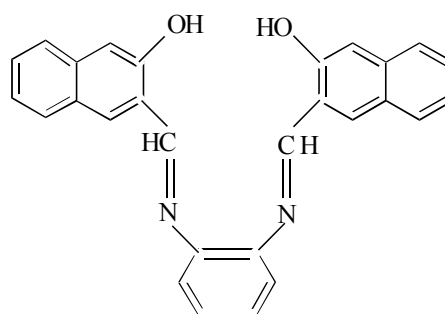
Die lokale Umgebung der Metallzentren von optisch aktiven Metallphtalocyaninen wurde mit Hilfe der EXAFS Spektroskopie untersucht. Dabei zeigte sich, daß im Falle der dimeren Gallium- und Ruthenium-Phtalocyanine die Metall-Metallabstände bei 2.46 und 2.43 Å liegen und die Metallzentren etwa 0.5 Å aus der Ebene der Makrozyklen, jeweils nach innen gerichtet, herausragen. Die Ergebnisse der Untersuchungen der Gallium- und Indium- μ -Oxo-verbrückten Phtalocyanindimeren sind in Übereinstimmung mit der allgemein bekannten Struktur der Phtalocyaninkomplexen. Ergänzende Untersuchungen an peripherfluorierten Ruthenium Phtalocyaninen mit Tetrahydrofuran oder Pyridin als weiteren Liganden zeigten eine sechsfache Koordination des Ruthenium-Atoms, wobei die Lösungsmittelmoleküle in der oktaederischen Anordnung die axialen Positionen einnehmen. Der Einfluß des Phtalocyaninmakrozyklus auf die Struktur war in allen Fällen aus der EXAFS Analyse ersichtlich.

Die EXAFS Untersuchungen von katalytisch aktiven Ruthenium(II) Komplexe ergaben, daß die Komplexe ihre Struktur beibehalten, wenn sie in Polysiloxanmatrizen eingebettet oder solche als Träger verwendet werden. Die Unterschiede in der katalytischen Aktivität der Komplexe in Abhängigkeit von den Liganden kann so die Ergebnisse der AXAFS (atomic XAFS) Studien mit Unterschieden in der elektronischen Struktur um das aktive Zentrum des Ruthenium korreliert werden. Des weiteren zeigen die Untersuchungen, daß der Co-Katalysator (^tBuOK) eine entscheidende Rolle spielt, und zwar nicht nur, weil er die katalytische Aktivität erhöht, sondern auch weil er die Struktur der intermediär gebildeten Spezies beeinflusst. Bemerkenswert ist, daß von den zwei Chlor-Atomen die an das Ruthenium gebunden sind, während der Reaktion mit dem Co-Katalysator nur eines abstrahiert wird.

Bio-aktive Ruthenium(III) Komplexe wurden ebenfalls mit Hilfe der Röntgenabsorptionsspektroskopie untersucht. Dabei konnte eine oktaedrische Struktur sowohl bei Ligand I (Schiff'sche Base als Ligand, mit Stickstoff und Schwefel eines Chromophors als Koordinationsstellen) als auch bei Ligand II (Schiff'sche Base als Ligand mit Stickstoff und Sauerstoff eines Chromophors als Koordinationsstellen) festgestellt werden.



Ligand I



Ligand II

Die exakte Geometrie konnte jedoch nicht ermittelt werden. Der Einfluß der zahlreichen Parametern die hier in die Berechnung der Mehrfachstreuung eingehen, wurde eingehend untersucht, und es zeigte sich, daß ein sehr kleiner Satz von Parametern ausreicht, um eine vernünftige Anpassung an die experimentellen Daten zu erhalten. Schließlich wurden zusätzliche AXAFS Experimente durchgeführt, um Näheres über den Substituenteneinfluß auf die elektronischen Eigenschaften des zentralen Ruthenium Atoms zu erfahren. Hier sind jedoch theoretische Rechnungen, z.B. Dichtefunktionalrechnungen nötig, um durch einen Vergleich mit den AXAFS Daten plausible Aussagen treffen zu können.

Die Hydrierung von katalytisch aktiven PCP (Phosphor-Kohlenstoff-Phosphor-Verbindungen)-Iridium Komplexen wurde mit zeitaufgelösten XAFS Messungen *in operando* verfolgt. Die Ergebnisse geben einen vagen Anhaltspunkt dafür, daß die Reaktion über eine theoretisch bereits postulierte Ir(V) Zwischenstufe verläuft. Ein eindeutiger Beweis konnte dafür jedoch nicht erbracht werden. Der Einfluß vieler Faktoren, wie z. B. das Zeitfenster für die Beobachtung der Reaktion, die Verschiebung des Gleichgewichtes der Reaktion, die Aktivität der Komplexe, der optimale Wasserstoffdruck, die Menge der gebildeten Ir(V) Zwischenstufe und deren Lebensdauer, bleibt unbekannt. Es würde sich anbieten, diese Hydrierungsreaktion mit optimierten Parametern erneut zu untersuchen. Des weiteren würden QXAFS (Quick XAFS) Messungen in Kombination mit UV-Vis Spektren sicherlich einen tieferen Einblick in den Mechanismus der Reaktion erlauben.

Strukturuntersuchungen von $\text{Cd}(\text{O}^i\text{PrXan})_2$ und $\text{Zn}(\text{O}^i\text{PrXan})_2$ mit Hilfe der EXAFS-Spektroskopie ergaben, daß die Metall-Schwefel-Abstände und Koordinationszahlen denen der Metallsulfidverbindungen entsprechen. Diese Verbindungen würden sich somit wahrscheinlich zur Anwendung als CVD-Precursoren eignen. Auch im Falle dieser Materialien rundeten Raman- und FT-IR-Untersuchungen das strukturelle Bild aus den Röntgenmessungen ab.

Nanostrukturierte Mischoxide wurden mit Hilfe der XAFS- und Raman-Spektroskopie untersucht. Aus EXAFS Messungen von nichtdotiertem und Calciumdotierten LaCoO_3 Pulvern konnte abgeleitet werden, daß die Xerogele keine Perowskit-Struktur ausbilden. Der Einfluß der Calcium Ionen auf die lokale Struktur in den Xerogelen konnte nicht eindeutig bestimmt werden. Nach einer thermischer Behandlung im Bereich von 700 bis 1000°C zeigte reines LaCoO_3 eine Tendenz hin zu einer nanokristallinen Struktur, allerdings konnten keine signifikanten Änderungen in der lokalen Umgebung der betrachteten Metallatome festgestellt werden. Andererseits zeigten die mit Calcium dotierten Proben eine deutliche Abhängigkeit der Struktur von der Temperatur. Diese Strukturänderungen beruhen auf der Bildung von Cobalt- und Calciumoxiden, der Verzerrung der vorliegenden Perowskit-Struktur und teilweise auf der Substitution einiger La(III) Ionen durch Ca(II) Ionen in der ursprünglichen Verbindung. Beim Übergang von den Xerogelen zu den getemperten Proben konnte die erwartete Änderung in der Oxidationsstufe des Cobalts mit der Energieverschiebung der Kantenlage in der XANES-Region belegt werden. Die Untersuchungen der La-Sr-Co-

Fe-O Nanokompositen zeigten, daß $\text{La}_{0.6}\text{Sr}_{0.4}\text{Co}_{0.9}\text{Fe}_{0.1}\text{O}_3$, zusammen mit Co_3O_4 und eventuell La_2CoO_4 , in einer La-Sr-Co-Fe-O Mischoxidmatrix gebildet werden. Der Einfluß der Dotierung der La-Sr-Co-Fe-O-Mischoxide mit Fe_2O_3 ist signifikant, und Veränderungen in der lokalen Umgebung konnten durch Röntgenexperimente an verschiedenen Absorptionskanten beobachtet werden. Abgesehen von einer Verzerrung der Perowskit-Struktur durch die Einlagerung des Eisenoxides, konnte die Entstehung weiterer oxidischer Komponenten, wie CoO , nachgewiesen werden. Die Untersuchungen der gemischten Fe-Ti-O-Nanokompositen zeigten, daß die Mischoxide unabhängig von ihrer Darstellungsmethode eine Rutil ähnliche Struktur aufweisen. Die Eisendotierung scheint die lokale Umgebung der Titanatome hier nicht zu beeinflussen. Im Falle der W-Ce-O Mischoxide zeigte sich, daß die Struktur der verschiedenen Proben ähnlich der des Ceroxides ist und die Dotierung mit Wolframoxid die lokale Umgebung der Ceratome nicht ändert. Analoge Ergebnisse erhält man aus der Untersuchung von Ce-Y-Zr-O-Nanokompositen. Hier behält das Yttrium stabilisierte Zirkonoxid im wesentlichen seine Struktur bei, unabhängig vom Gehalt an CeO_2 .

Die EXAFS und XANES Untersuchungen der magnetischen Nanomaterialien auf Ferritbasis zeigten, daß die CuFe_2O_4 Nanopartikel die Struktur des Bulkmaterials beibehalten. Alle Kupferatome besetzen in der Ferritstruktur oktaedrische Lücken, während die Eisenatome auf Tetraeder- und Oktaederlücken verteilt sind. Die Ergebnisse der Untersuchungen von $\text{CuFe}_2\text{O}_4\text{-SnO}_2$ und $\text{CuFe}_2\text{O}_4\text{-CeO}_2$ Nanokompositen ergaben, daß die Dotierung mit den vierwertigen Metalloxiden die Struktur nicht beeinflußt. Hingegen bilden sich im System $\text{CuFe}_2\text{O}_4\text{-NiO}$ zusätzlich die Oxide NiFe_2O_4 und CuO aus. Auch eine partielle Substitution von Kupfer durch Nickel in der ursprünglichen Verbindung kann nicht ausgeschlossen werden.

Die EXAFS Untersuchungen der anorganisch-organischen Hybridmaterialien mit Zirkonium- und Hafnium-Oxo-Cluster beweisen, daß die Cluster durch Einbettung in die Polysiloxan-Matrix, unabhängig von der Art des Silans und des Stoffmengenverhältnisses Silan/Cluster, ihre ursprüngliche Struktur verlieren. Die Hybridmaterialien wurden calciniert. Die Untersuchungen der entstandenen Mischoxide sind ein Beleg dafür, daß das Silicium-Metall-Verhältnis die Struktur der Oxide stark beeinflußt. In allen Fällen konnte das Vorliegen von gemischten Bindungen des Typs Zr-O-Si, Hf-O-Si oder Zr-O-Hf nicht nachgewiesen werden. Die angepaßten Parameter konnten mit keiner der bekannten kristallinen Strukturen in Einklang gebracht werden,

jedoch zeigten die XANES Experimente an den calcinierten Proben eine Tendenz hin zur Ausbildung einer tetragonalen Zirkonoxidstruktur.

Die Entstehung von Zinksulfid-Nanopartikel durch Reaktion von Thioessigsäure mit Zinkprecursoren in Essigsäure oder Aceton wurde mittels EXAFS und XANES untersucht. Dabei konnte festgestellt werden, daß der Schwefel sofort zweifach koordiniert wird, das Zinksulfid aber erst nach und nach ausfällt. Wird Zinkacetat als Precursor verwendet, so ist nach einer Reaktionszeit in Essigsäure von 3420 Minuten und nach 2260 Minuten in Aceton das Zinksulfid noch nicht quantitativ ausgefallen. Die Gründe dafür könnten entweder in der Anwesenheit von nicht reaktiven Zink-Sauerstoff-Spezies oder in der Koordination von Wassermolekülen zu finden sein. Für das System Zinkoxid in Aceton konnte ein höherer Umsatz bereits nach 1915 Minuten registriert werden. Zinkoxid reagiert mit Thioessigsäure schneller als Zinkacetat. Die Wahl des Reaktionsmediums spielt hier also eine entscheidende Rolle, ohne jedoch den Mechanismus der Reaktion zu beeinflussen.

Ausgewählte Schritte des Sol-Gel-Prozesses wurden mittels zeitaufgelösten *in-situ* Experimenten untersucht. Die EXAFS- und Raman-Studien der Germaniumalkoxide zeigten, daß $\text{Ge}(\text{OMe})_4$, $\text{Ge}(\text{OEt})_4$, $\text{Ge}(\text{O}^i\text{Pr})_4$, und $\text{Ge}(\text{O}^n\text{Bu})_4$ monomerer Natur sind und ähnliche Struktur haben. Damit wird deutlich, daß die Alkoxidgruppen die Struktur der Germaniumalkoxide nicht beeinflussen. $\text{Hf}(\text{O}^n\text{Bu})_4$ und $\text{Ta}(\text{OEt})_5$ liegen hingegen in dimerer Form vor. Die Untersuchungen zeigten, daß alle drei Metallalkoxide bei Wasserzugabe sofort hydrolysiert werden und Kondensationsreaktionen eingehen, wobei jedoch keine wesentlichen strukturellen Veränderungen zu vermerken sind. Eine chemische Modifizierung der Germaniumalkoxide durch Zugabe von Acetylaceton findet selbst nach 48 Stunden nicht statt. Im Falle von $\text{Hf}(\text{O}^n\text{Bu})_4$ und $\text{Ta}(\text{OEt})_5$ ändert sich die Koordinationszahl augenblicklich von sechs nach acht, sobald Acetylaceton zugegeben wird. Ergänzende Raman-Messungen belegen, daß im Falle von $\text{Hf}(\text{O}^n\text{Bu})_4$ nach Zugabe von Acetylaceton keine freien Carbonyl-Gruppen vorliegen, während bei $\text{Ta}(\text{OEt})_5$ nicht alle Carbonyl-Gruppen an der Koordination beteiligt sind. Wird zu einer Germanium-Alkoxid-Acetylaceton-Mischung Wasser zugegeben, so setzen die Hydrolyse und die Kondensationsreaktionen sofort ein. Im Gegensatz dazu, reagieren die analogen Acetylaceton- $\text{Hf}(\text{O}^n\text{Bu})_4$ und Acetylaceton- $\text{Ta}(\text{OEt})_5$ Mischungen bei Zugabe von Wasser überhaupt nicht. Die Struktur der Alkoxide bleibt mindestens 48 Stunden unverändert, selbst wenn partiell hydrolysiertes $\text{Si}(\text{OEt})_4$ zugegeben wird. Die

Untersuchung des Hydrolyse- und Kondensationsverhaltens einer Mischung dieser Alkoxide ergab in allen drei Fällen, daß eine Homokondensation vorliegt, die auf die unterschiedliche Reaktivität der jeweiligen Alkoxide zurückgeführt werden kann. Die Hydrolyse- und Kondensationsreaktionen dieser Alkoxidmischungen erfolgen auf einer sehr kurzen Zeitskala, was ihre Beobachtung mit Hilfe konventioneller spektroskopischer Methoden erschwert. Um Materialien mit maßgeschneiderten Eigenschaften darzustellen, sind Messungen mit Ultrakurzzeitmethoden unbedingt erforderlich.

References

Chapter 1.1.

- [1.1.1] B. K. Teo, EXAFS: Basic Principles and Data Analysis, Springer, Berlin, 1986.
- [1.1.2] H. Bertagnolli, T. S. Ertel, *Angew. Chem. Int. Ed.* 33 (1994) 45.
- [1.1.3] D. C. Koningsberger, R. Prins, Ed., X-ray Absorption: Principles, Applications, Techniques of EXAFS, SEXAFS and XANES, Wiley, New York, 1988.
- [1.1.4] F. Wong, F. W. Lytle, R. P. Messmer, D. H. Maylotte, *Phys. Rev. B* 1984, 30, 5596.
- [1.1.5] I. N. Levine, *Physical Chemistry*, 5th Edition, McGraw-Hill, Boston, 2002.

Chapter 2.1.

- [2.1.1] J. J. Rehr, R. C. Albers, *Rev. Mod. Phys.* 72 (2000) 621.
- [2.1.2] B. K. Teo, P. A. Lee, *J. Am. Chem. Soc.* 101 (1979) 2815.
- [2.1.3] B. K. Teo, D. C. Joy, Ed., EXAFS spectroscopy: Techniques and Applications, Plenum Press, New York, 1981.
- [2.1.4] B. M. Kincaid, P. M. Eisenberger, *Chem. Phys. Lett.* 34 (1975) 1361.
- [2.1.5] A. Bianconi, EXAFS and Near Edge Structures III, Springer Verlag, Berlin, 1984.
- [2.1.6] D. E. Sayers, E. A. Stern, F. W. Lytle, *Phys. Rev. Lett.* 27 (1971) 1204.
- [2.1.7] F. W. Lytle, D. E. Sayers, E. A. Stern, *Phys. Rev. B* 11 (1975) 4825.
- [2.1.8] E. A. Stern, D. E. Sayers, F. W. Lytle, *Phys. Rev. B* 11 (1975) 4835.
- [2.1.9] J. Stoehr, NEXAFS Spectroscopy, Springer Verlag, Berlin, 1996.
- [2.1.10] J. J. Boland, S. E. Crane, J. D. Baldenschwieler, *J. Chem. Phys.* 77 (1982) 142.
- [2.1.11] P. A. Lee, J. B. Pendry, *Phys. Rev. B* 11 (1975) 2795.
- [2.1.12] J. Mustre, Y. Yacoby, E. A. Stern, J. J. Rehr, *Phys. Rev. B* 42 (1990) 10843.
- [2.1.13] B. W. Holland, J. B. Pendry, R. F. Pettifer, J. Bordas, *J. Phys. C* 11 (1978) 633.
- [2.1.14] J. J. Rehr, C. H. Booth, F. Bridges, S. I. Zabinsky, *Phys. Rev. B* 49 (1994) 12347.
- [2.1.15] H. Wende, C. Litwinski, A. Scherz, T. Gleitsmann, Z. Li, C. Sorg, K. Baberschke, A. Ankudinov, J. J. Rehr, C. Jung, *J. Phys.: Condens. Matter* 15 (2003) 5197.
- [2.1.16] W. E. O'Grady, X. Qian, D. E. Ramaker, *J. Phys. Chem. B* 101 (1997) 5624.

- [2.1.17] D. E. Ramaker, B. L. Mojet, D. C. Koningsberger, W. E. O'Grady, *J. Phys.: Condens. Matter* 10 (1998) 8753.

Chapter 2.2.

- [2.2.1] J. Weidlein, U. Mueller, K. Dehnicke, *Schwingungsspektroskopie*, 2nd Edition, Georg Thieme Verlag, Stuttgart, 1988.
- [2.2.2] C. N. Banwell, E. M. McCash, *Fundamentals of Molecular Spectroscopy*, 15th Reprint, Tata McGraw-Hill, New Delhi, 2003.
- [2.2.3] D. A. Long, *Raman Spectroscopy*, McGraw-Hill, London, 1977.
- [2.2.4] B. Schrader, Ed., *Infrared and Raman Spectroscopy*, VCH, Weinheim, 1995.
- [2.2.5] H. A. Szymanski, Ed., *Raman Spectroscopy – Theory and Practice*, Vol. 1 and 2, Plenum, New York, 1967.
- [2.2.6] R. L. McCreery, *Raman Spectroscopy for Chemical Analysis*, Wiley-Interscience, New York, 2000.

Chapter 3.1.

- [3.1.1] P. W. Atkins, J. de Paula, *Physical Chemistry*, 8th Edition, Oxford University Press, Oxford, 2006.
- [3.1.2] G. H. Stout, L. H. Jensen, *X-ray Structure Determination*, Wiley, New York, 1989.
- [3.1.3] R. Frahm, *Physica B* 158 (1989) 342.
- [3.1.4] M. Hagelstein, S. Cunis, R. Frahm, W. Niemann, P. Rabe, *Physica B* 158 (1989) 324.
- [3.1.5] A. Fontaine, E. Dartyge, J. P. Itie, A. Fucha, A. Polain, H. Tolentino, G. Tourillon, *Top. Curr. Chem.* 151 (1989) 179.
- [3.1.6] U. Eberhardinger, Ph.D. Thesis, University of Stuttgart, Stuttgart, 2002.
- [3.1.7] T. S. Ertel, Ph.D. Thesis, University of Wuerzburg, Wuerzburg, 1991.

Chapter 3.2.

- [3.2.1] T. Ressler, *J. de Phys. IV* 7 (1997) C2.
- [3.2.2] T. Ressler, *J. Synch. Rad.* 5 (1998) 118.
- [3.2.3] J. A. Victoreen, *J. Appl. Phys.* 18 (1948) 855.

- [3.2.4] J. A. Victoreen, *J. Appl. Phys.* 14 (1943) 95.
- [3.2.5] J. A. Victoreen, *J. Appl. Phys.* 20 (1949) 1141.
- [3.2.6] M. Newville, Tutorial notes on XAFS, 2004.
- [3.2.7] T. S. Ertel, H. Bertagnolli, S. Hueckmann, U. Kolb, D. Peter, *Appl. Spectrosc.* 46 (1992) 690.
- [3.2.8] J. J. Boland, F. G. Halaka, J. D. Baldeschwieler, *Phys. Rev. B* 28 (1983) 2921.
- [3.2.9] M. Newville, P. Livins, Y. Yacoby, J. J. Rehr, E. A. Stern, *Phys. Rev. B* 47 (1993) 14126.
- [3.2.10] C. de Boor, *A Practical Guide to Splines*, Springer Verlag, New York, 1978.
- [3.2.11] W. H. Press, B. P. Flannery, S. A. Teukolsky, W. T. Vetterling, *Numerical Recipes*, Cambridge University Press, Cambridge, 1989.
- [3.2.12] D. E. Sayers, B. A. Bunker, *Chem. Anal.* 92 (1988) 211.
- [3.2.13] S. J. Gurman, N. Binsted, I. Ross, *J. Phys. C* 19 (1986) 1845.
- [3.2.14] P. A. Lee, J. B. Pendry, *Phys. Rev. B* 11 (1975) 2795.
- [3.2.15] A. G. McKale, G. S. Knapp, S. K. Chan, *Phys. Rev. B* 33 (1986) 841.
- [3.2.16] A. G. McKale, B. W. Veal, A. P. Paulikas, S. K. Chan, G. S. Knapp, *J. Am. Chem. Soc.* 110 (1988) 3763.
- [3.2.17] G. E. van Dorssen, D. C. Koningsberger, D. E. Ramaker, *J. Phys. Condens. Matter* 14 (2002) 13529.

Chapter 4.1.

- [4.1.1] N. B. Mckeown, *Phthalocyanine Materials: Synthesis, Structure and Function*, Eds. B. Dunn, J. W. Goodby, A. R. West, Cambridge University Press, 1998.
- [4.1.2] C. G. Claessens, W. J. Blau, M. Cook, M. Hanack, R. J. M. Nolte, T. Torres, D. Torres, *Monat. Chem.* 132 (2001) 3.
- [4.1.3] D. Dini, M. Barthel, M. Hanack, *Eur. J. Org. Chem.* 20 (2001) 3759.
- [4.1.4] M. Hanack, D. Dini, M. Barthel, S. Vagin, *Chem. Record* 2 (2002) 129.
- [4.1.5] J. S. Shirk, R. G. S. Pong, S. R. Flom, H. Heckmann, M. Hanack, *J. Phys. Chem. A* 104 (2000) 1438.
- [4.1.6] M. Hanack, T. Schneider, M. Barthel, J. S. Shrink, S. R. Flom, R. G. S. Pong, *Coord. Chem. Rev.* 219-221 (2001) 235.

References

- [4.1.7] J. W. Perry, K. Mansour, I. Y. S. Lee, X. L. Wu, P. V. Bedworth, C. T. Chen, D. Ng, S. R. Marder, P. Miles, T. Wada, M. Tian, H. Sasabe, *Science* 273 (1996) 1533.
- [4.1.8] Y. Chen, L. R. Subramanian, M. Barthel, M. Hanack, *Eur. J. Inorg. Chem.* (2002) 1032.
- [4.1.9] M. Barthel, D. Dini, S. Vagin, M. Hanack, *Eur. J. Org. Chem.* (2002) 3756.
- [4.1.10] G. Rojo, G. Martin, F. Agullo-Lopez, T. Torres, H. Heckmann, M. Hanack, *J. Phys. Chem. B* 104 (2000) 7066.
- [4.1.11] H. Bertagnolli, W. J. Blau, Y. Chen, D. Dini, M. P. Feth, S. M. O'Flaherty, M. Hanack, V. Krishnan, *J. Mater. Chem.* 15 (2005) 683.
- [4.1.12] W. Uhl, T. Spies, R. Koch, *J. Chem. Soc., Dalton Trans.* (1999) 2385.
- [4.1.13] P. Wei, X. W. Li, G. H. Robinson, *Chem. Commun.* (1999) 1287.
- [4.1.14] K. S. Klimek, C. Cui, H. W. Roesky, M. Noltemeyer, H. G. Schmidt, *Organometallics* 19 (2000) 3085.
- [4.1.15] W. Uhl, T. Spies, *Z. Anorg. Allg. Chem.* 626 (2000) 1059.
- [4.1.16] D. R. Tackley, G. Dent, W. E. Smith, *Phys. Chem. Chem. Phys.* 3 (2001) 1419.
- [4.1.17] K. J. Wynne, *Inorg. Chem.* 23 (1984) 4658.
- [4.1.18] L. H. Vogt Jr., A. Zalkin, D. H. Templeton, *Inorg. Chem.* 6 (1967) 1725.
- [4.1.19] C. Fietzek, M. Seiler, B. Goerlach, P. Schuetz, U. Weimar, M. Hanack, C. Ziegler, H. Bertagnolli, *J. Mater. Chem.* 12 (2002) 2305.
- [4.1.20] K. J. Wynne, *Inorg. Chem.* 24 (1985) 1339.
- [4.1.21] V. Krishnan, T. E. Youssef, M. Hanack, H. Bertagnolli, manuscript submitted.
- [4.1.22] A. Capobianchi, A. M. Paletti, G. Pennesi, G. Rossi, R. Caminiti, C. Ercolani, *Inorg. Chem.* 33 (1994) 4635.
- [4.1.23] J. P. Collman, C. E. Barnes, P. N. Swepston, J. A. Ibers, *J. Am. Chem. Soc.* 106 (1984) 3500.
- [4.1.24] L. F. Warren, V. L. Goedken, *J. Chem. Soc.* (1978) 909.
- [4.1.25] A. Weber, T. S. Ertel, U. Reinoehl, H. Bertagnolli, M. Leuze, M. Hees, M. Hanack, *Eur. J. Inorg. Chem.* (2000) 2289.
- [4.1.26] H. Bertagnolli, A. Weber, W. Hoerner, T. S. Ertel, U. Reinoehl, M. Hanack, M. Hees, R. Polley, *Inorg. Chem.* 36 (1997) 6397.
- [4.1.27] A. Weber, T. S. Ertel, U. Reinoehl, M. Feth, H. Bertagnolli, M. Leuze, M. Hanack, *Eur. J. Inorg. Chem.* (2001) 679.

- [4.1.28] M. K. Engel, Report Kawamura Inst. Chem. Res. (1997) 11.
- [4.1.29] A. R. Hollmann, E. Wiberg, Lehrbuch der Anorganische Chemie, Walter de Griyter, Berlin, 101 (1995) 832.
- [4.1.30] Y. Chen, L. R. Subramanian, M. Fujitsuka, O. Ito, S. O'Flaherty, W. J. Blau, T. Schneider, D. Dini, M. Hanack, Chem. Eur. J. 8 (2002) 4248.
- [4.1.31] V. Krishnan, M. P. Feth, E. Wendel, Y. Chen, M. Hanack, H. Bertagnolli, Z. Phys. Chem. 218 (2004) 1.
- [4.1.32] Y. Chen, M. Barthel, M. Seiler, L. R. Subramanian, H. Bertagnolli, M. Hanack, Angew. Chem. Int. Ed. 114 (2002) 3373.
- [4.1.33] S. S. Hasnain, in X-ray Absorption Fine Structure: International Workshop on Standards and Criteria in XAFS, Ellis Horwood, New York (1991) 751-770.
- [4.1.34] R. W. Joyner, K. J. Martin, P. Meethan, J. Phys. C 20 (1987) 4005.

Chapter 4.2.

- [4.2.1] B. Cornils, W. A. Hermann, Ed., Applied Homogeneous Catalysis with Organometallic Compounds, Wiley VCH, Weinheim, 1996.
- [4.2.2] E. Lindner, T. Schneller, F. Auer, H. A. Mayer, Angew. Chem. Int. Ed. 38 (1999) 2154.
- [4.2.3] E. Lindner, S. Al-Gharabli, I. Warad, H. A. Mayer, S. Steinbrecher, E. Plies, M. Seiler, H. Bertagnolli, Z. Anorg. Allg. Chem. 629 (2003) 161.
- [4.2.4] E. Lindner, T. Salesch, S. Brugger, S. Steinbrecher, E. Plies, M. Seiler, H. Bertagnolli, H. A. Mayer, Eur. J. Inorg. Chem. (2002) 1998.
- [4.2.5] E. Lindner, S. Al-Gharabli, H. A. Mayer, Inorg. Chim. Acta 334 (2002) 113.
- [4.2.6] E. Lindner, A. Ghanem, I. Warad, K. Eichele, H. A. Mayer, V. Schurig, Tetrahedron: Asymmetry 14 (2003) 1045.
- [4.2.7] T. Ohkuma, H. Ooka, S. Hashiguchi, T. Ikariya, R. Noyori, J. Am. Chem. Soc. 117 (1995) 2675.
- [4.2.8] T. Ohkuma, H. Ooka, T. Ikariya, R. Noyori, J. Am. Chem. Soc. 117 (1995) 10417.
- [4.2.9] R. Noyori, T. Ohkuma, Angew. Chem. Int. Ed. 40 (2001) 40.
- [4.2.10] M. Yamakawa, H. Ito, R. Noyori, J. Am. Chem. Soc. 122 (2000) 1466.
- [4.2.11] T. Ohkuma, H. Takeno, Y. Honda, R. Noyori, Adv. Synth. Catal. 343 (2001) 369.

- [4.2.12] R. Noyori, M. Yamakawa, S. Hashiguchi, *J. Org. Chem.* 66 (2001) 7931.
- [4.2.13] E. Lindner, I. Warad, K. Eichele, H. A. Mayer, *Inorg. Chim. Acta* 350 (2003) 49.
- [4.2.14] E. Lindner, H. A. Mayer, I. Warad, K. Eichele, *J. Organomet. Chem.* 665 (2003) 176.
- [4.2.15] D. -Y. Wu, E. Lindner, H. A. Mayer, Z. -J. Jiang, V. Krishnan, H. Bertagnolli, *Chem. Mater.* 17 (2005) 3951.
- [4.2.16] A. M. J. van der Eerden, T. Visser, T. A. Nijhuis, Y. Ikeda, M. Lepage, D. C. Koningsberger, B. M. Weckhuysen, *J. Am. Chem. Soc.* 127 (2005) 3272.
- [4.2.17] M. Tromp, M. Q. Slagt, R. J. M. K. Gebbink, G. van Koten, D. E. Ramaker, D. C. Koningsberger, *Phys. Chem. Chem. Phys.* 6 (2004) 4397.
- [4.2.18] K. R. Hartmann, P. Chen, *Angew. Chem. Int. Ed.* 40 (2001) 3581.

Chapter 4.3.

- [4.3.1] A. D. Garnovskii, A. L. Nivorozhkin, V. I. Minkin, *Coord. Chem Rev.* 126 (1993) 1.
- [4.3.2] B. J. Holliday, C. A. Mirkin, *Angew. Chem. Int. Ed. Engl.* 40 (2001) 2023.
- [4.3.3] C. Piguet, G. Bernardinelli, G. Hopfgartner, *Chem. Rev.* 97 (1997) 2005 and the references therein.
- [4.3.4] P. J. McCarthy, R. J. Hovey, K. Ueno, A. E. Martell, *J. Am. Chem. Soc.* 77 (1995) 5820.
- [4.3.5] J. D. Charrier, D. Deniand, A. Reliquet, J. C. Meslin, *J. Chem. Soc., Dalton Trans.* (2001) 1212.
- [4.3.6] E. B. Tjaden, D. C. Swenson, J. L. Petersen, R. F. Jordan, *Organometallics* 14 (1995) 371.
- [4.3.7] E. N. Jacobsen, W. Zhang, M. L. Guler, *J. Am. Chem. Soc.* 113 (1991) 6703.
- [4.3.8] J. E. Kovacic, *Spectrochim. Acta* 23A (1982) 183.
- [4.3.9] R. Atkins, G. Brewer, *Inorg. Chem.* 24 (1985) 128.
- [4.3.10] L. Rousso, N. Friedman, M. Sheves, O. Ottolenghi, *Biochemistry* 34 (1995) 12059.
- [4.3.11] R. Campo, J. J. Criado, E. Garcia, M. R. Hermosa, A. J. Sanchez, J. L. Manzano, E. Montc, E. R. Fernandez, F. Sanz, *J. Inorg. Biochem.* 89 (2002) 74.

- [4.3.12] J. Z. Wu, L. Zuan, *J. Inorg. Biochem.* 98 (2004) 41.
- [4.3.13] R. Karvembu, K. Natarajan, *Polyhedron* 21 (2002) 1721.
- [4.3.14] J. Reedijk, *Curr. Opin. Chem. Biol.* 3 (1999) 236.
- [4.3.15] R. Gagliardi, G. Sava, S. Pacor, G. Mestroni, E. Alessio, *Clin. Exp. Metastasis* 12 (1994) 93.
- [4.3.16] C. S. Allardyce, P. J. Dyson, D. J. Ellis, S. L. Heath, *Chem. Commun.* (2001) 1396.
- [4.3.17] R. Prabhakaran, A. Geetha, M. Thilagavathi, R. Karvembu, V. Krishnan, H. Bertagnolli, K. Natarajan, *J. Inorg. Biochem.* 98 (2004) 2131.
- [4.3.18] P. Neubold, B. S. P. C. D. Vedova, K. Wieghardt, B. Nuber, J. Weiss, *Inorg. Chem.* 29 (1990) 3355.
- [4.3.19] E. Lindner, I. Warad, K. Eichele, H. A. Mayer, *Inorg. Chim. Acta* 350 (2003) 49.
- [4.3.20] J. F. Bickley, A. A. La Pensee, S. J. Higgins, C. A. Stuart, *J. Chem. Soc., Dalton Trans.* (2003) 4663.
- [4.3.21] N. J. Holmes, A. R. J. Genge, W. Levason, M. Webster, *J. Chem. Soc., Dalton Trans.* (1997) 2331.
- [4.3.22] P. M. T. Piggot, L. A. Hall, A. J. P. White, D. J. Williams, *Inorg. Chim. Acta* 357 (2004) 207.
- [4.3.23] P. M. T. Piggot, L. A. Hall, A. J. P. White, D. J. Williams, *Inorg. Chim. Acta* 357 (2004) 250.
- [4.3.24] R. Prabhakaran, V. Krishnan, A. Geetha, H. Bertagnolli, K. Natarajan, *Inorg. Chim. Acta* 359 (2006) 1114.
- [4.3.25] W. -L. Man, T. -M. Tang, T. -W. Wong, T. -C. Lau, S. -M. Peng, W. -T. Wong, *J. Am. Chem. Soc.* 126 (2004) 478.
- [4.3.26] M. Tromp, J. A. van Bokhoven, M. Q. Slagt, R. J. M. K. Gebbink, G. van Koten, D. E. Ramaker, D. C. Koningsberger, *J. Am. Chem. Soc.* 126 (2004) 4090.

Chapter 4.4.

- [4.4.1] B. R. James, Ed., *Catalysis by Metal Complexes*, Kluwer Academic Publishers, Dordrecht, 2000.
- [4.4.2] J. A. Johnson, D. Sames, *J. Am. Chem. Soc.* 122 (2000) 6321.

- [4.4.3] M. J. Burk, R. H. Crabtree, *J. Am. Chem. Soc.* 109 (1987) 8025.
- [4.4.4] B. A. Arndtsen, R. G. Bergman, *Science* 270 (1995) 1970.
- [4.4.5] I. Bach, R. Goddard, C. Kopiske, K. Seevogel, K. Porschke, *Organometallics* 18 (1999) 10.
- [4.4.6] C. M. Jensen, *Chem. Commun.* (1999) 2443.
- [4.4.7] M. Kanzelberger, B. Singh, M. Czerw, K. Krogh-Jespersen, A. S. Goldman, *J. Am. Chem. Soc.* 122 (2000) 11017.
- [4.4.8] F. C. Liu, A. S. Goldman, *Chem. Commun.* (1999) 655.
- [4.4.9] S. Niu, M. B. Hall, *J. Am. Chem. Soc.* 121 (1999) 3992.
- [4.4.10] P. Brandt, C. Hedberg, P. G. Andersson, *Chem. Eur. J.* 9 (2003) 339.
- [4.4.11] S. R. Klei, T. D. Tilley, R. G. Bergman, *J. Am. Chem. Soc.* 122 (2000) 1816.
- [4.4.12] H. A. Y. Mohammad, J. C. Grimm, K. Eichele, H. -G. Mack, B. Speiser, F. Novak, M. G. Quintanilla, W. C. Kaska, H. A. Mayer, *Organometallics* 21 (2002) 5775.
- [4.4.13] W. Leis, H. A. Mayer, personal communication.

Chapter 4.5.

- [4.5.1] D. Barreca, A. Gasparotto, C. Maragno, R. Seraglia, E. Tondello, A. Venzo, V. Krishnan, H. Bertagnolli, *Appl. Organomet. Chem.* 19 (2005) 59.
- [4.5.2] D. Barreca, A. Gasparotto, C. Maragno, R. Seraglia, E. Tondello, A. Venzo, V. Krishnan, H. Bertagnolli, *Appl. Organomet. Chem.* 19 (2005) 1002.
- [4.5.3] F. Maury, *Chem. Vap. Depos.* 2 (1996) 113.
- [4.5.4] A. N. Gleizes, *Chem. Vap. Depos.* 6 (2000) 155.
- [4.5.5] D. Barreca, E. Tondello, D. Lydon, T. R. Spalding, M. Fabrizio, *Chem. Vap. Depos.* 9 (2003) 93.
- [4.5.6] D. Rodic, V. Spasojevic, A. Bajorek, P. Oennerud, *J. Magnet. Magnet. Mater.* 152 (1996) 159.
- [4.5.7] N. B. Colthup, L. P. Powell, *Spectrochim. Acta* 43 (1987) 317.
- [4.5.8] J. Weidlein, U. Mueller, K. Dehnicke, *Schwingungsspektroskopie*, 2nd Edition, Georg Thieme Verlag, Stuttgart, 1988.
- [4.5.9] O. Siiman, D. D. Titus, C. D. Cowman, J. Fresco, H. B. Gray, *J. Am. Chem. Soc.* 96 (1974) 2353.
- [4.5.10] L. H. Little, G. W. Poling, J. Leja, *Can. J. Chem.* 39 (1961) 745.

- [4.5.11] R. Mattes, G. Pauleickhoff, *Spectrochim. Acta* 30 (1974) 379.
- [4.5.12] M. R. Hunt, G. A. Kruger, L. Smith, G. Winter, *Aust. J. Chem.* 24 (1971) 53.
- [4.5.13] W. Goepel, H. D. Wiemhoefer, *Statistische Thermodynamik*, Spektrum Akademische Verlag, Berlin, 2000.
- [4.5.14] E. H. Kisi, M. M. Elcombe, *Acta Crystallogr., Sect. C: Cryst. Struct. Commun.* 45 (1989) 1867.

Chapter 5.1.

- [5.1.1] U. Schubert, N. Huesing, *Synthesis of Inorganic Materials*, Wiley, Weinheim, 2005.
- [5.1.2] A. Glisenti, *J. Mol. Catal. A: Chemical* 153 (2000) 169.
- [5.1.3] N. R. Singh, S. K. Tiwari, S. P. Singh, N. K. Singh, G. Poillerat, P. Chartier, *J. Chem. Soc., Faraday Trans.* 92 (1996) 2593.
- [5.1.4] K. R. Kendall, C. Navas, J. K. Thomas, H. C. zur Loye, *Chem. Mater.* 8 (1996) 642.
- [5.1.5] S. Kaliaguine, A. van Neste, V. Syabo, J. E. Gallot, M. Basir, R. Muzychuk, *Appl. Catal. A* 209 (2001) 345.
- [5.1.6] M. A. Pena, J. L. G. Fierro, *Chem. Rev.* 101 (2001) 1981.
- [5.1.7] N. Q. Minh, T. Takahashi, *Science and Technology of Ceramic Fuel Cells*, Elsevier, Amsterdam, 1995.
- [5.1.8] J. Larmine, A. Dicks, *Fuel Systems Explained*, Wiley, Weinheim, 2000.
- [5.1.9] A. Trovarelli, *Catal. Rev. Sci. Eng.* 38 (1996) 439.
- [5.1.10] K. Klaubunde, in *Nanoscale Materials in Chemistry*, Wiley, New York, 2001.
- [5.1.11] Z. Qi, C. Shi, Y. Wei, Z. Wang, T. Liu, T. Hu, Z. Zhao, F. Li, *J. Phys.: Condens. Matter* 13 (2001) 11503.
- [5.1.12] R. D. Monte, J. Kaspar, *J. Mater. Chem.* 15 (2005) 633.
- [5.1.13] V. Krishnan, G. Bottaro, S. Gross, L. Armelao, E. Tondello, H. Bertagnolli, *J. Mater. Chem.* 15 (2005) 2020.
- [5.1.14] G. Thornton, B. C. Tofield, A. W. Hewat, *J. Solid State Chem.* 61 (1986) 301.
- [5.1.15] W. L. Roth, *J. Phys. Chem. Solids* 25 (1964) 1.
- [5.1.16] L. Armelao, D. Barreca, G. Bottaro, A. Caneschi, C. Sangregorio, A. Gasparotto, S. Gialanella, C. Maragno, E. Tondello, *Mater. Res. Soc. Symp. Proc.* 848 (2005) FF 9.5.1.

- [5.1.17] A. Glisenti, personal communication.
- [5.1.18] R. Sonntag, S. Neov, V. Kozhukarov, D. Neov, J. E. ten Elshof, *Physik (Berlin)* 241 (1998) 393.
- [5.1.19] V. G. Sathe, S. K. Paranjpe, V. Siruguri, A. V. Pimpale, *J. Phys.: Condens. Matter* 10 (1998) 4045.
- [5.1.20] F. Prado, T. Armstrong, A. caneiro, A. Manthiram, *J. Electrochem. Soc.* 148 (2001) 7.
- [5.1.21] U. Lehmann, H. Mueller-Buschbaum, *Z. Anorg. Allg. Chem.* 470 (1980) 59.
- [5.1.22] G. Shirane, S. J. Pickart, R. Nathans, Y. Ishikawa, *J. Phys. Chem. Solids* 10 (1959) 35.
- [5.1.23] V. Krishnan, S. Heislbetz, M. M. Natile, A. Glisenti, H. Bertagnolli, *Mater. Chem. Phys.* 92 (2005) 394.
- [5.1.24] B. Pourmellec, J. F. Marucco, B. Touzelin, *Phys. Rev. B* 35 (1987) 2284.
- [5.1.25] U. Gesenhues, T. Rentschler, *J. Solid State Chem.* 143 (1999) 210.
- [5.1.26] G. A. Samara, P. S. Peercy, *Phys. Rev. B* 7 (1973) 1131.
- [5.1.27] P. Merle, J. Pascual, J. Camassel, H. Mathieu, *Phys. Rev. B* 21 (1980) 1617.
- [5.1.28] S. P. S. Porto, P. A. Fleury, T. C. Damen, *Phys. Rev.* 154 (1967) 522.
- [5.1.29] W. F. Zhang, Y. L. He, M. S. Zhang, Z. Yin, Q. Chen, *J. Phys. D: Appl. Phys.* 33 (2000) 912.
- [5.1.30] A. Glisenti, personal communication.
- [5.1.31] E. A. Kuemmerle, G. Heger, *J. Solid State Chem.* 147 (1999) 485.
- [5.1.32] A. B. Hungria, A. Martinez-Arias, M. Fernandez-Garcia, A. Iglesias-Juez, A. Guerrero-Ruiz, J. J. Calvino, J. C. Conesa, J. Soria, *Chem. Mater.* 15 (2003) 4309.
- [5.1.33] B. M. Reddy, A. Khan, Y. Yamada, T. Kobayashi, S. Loidant, J. -C. Volta, *Langmuir* 19 (2003) 3025.
- [5.1.34] J. E. Spanier, R. D. Robinson, F. Zhang, S. W. Chan, I. P. Herman, *Phys. Rev. B* 64 (2001) 245407.
- [5.1.35] J. R. Mc Bride, K. C. Hass, B. D. Poindexter, W. H. Weber, *J. Appl. Phys.* 76 (1994) 2435.
- [5.1.36] V. G. Keramida, W. B. White, *J. Chem. Phys.* 59 (1973) 1561.
- [5.1.37] A. Glisenti, personal communication.
- [5.1.38] P. Li, I. -W. Chen, J. E. Penner-Hahn, *Phys. Rev. B* 48 (1993)10063.

- [5.1.39] P. Li, I. -W. Chen, J. E. Penner-Hahn, *Phys. Rev. B* 48 (1993)10074.
- [5.1.40] P. Li, I. -W. Chen, J. E. Penner-Hahn, *Phys. Rev. B* 48 (1993)10082.
- [5.1.41] G. E. Rush, A. V. Chadwick, I. Kosacki, H. U. Anderson, *J. Phys. Chem. B* 104 (2000) 9597.
- [5.1.42] Z. Qi, C. Shi, Y. Wei, Z. Wang, T. Liu, T. Hu, Z. Zhao, F. Li, *J. Phys.: Condens. Matter* 13 (2001) 11503.
- [5.1.43] J. Cai, C. Raptis, Y. S. Raptis, E. Anastassakis, *Phys. Rev. B* 51 (1995) 201.
- [5.1.44] C. G. Kontoyannis, M. Orkoula, *J. Mater. Sci.* 29 (1994) 5316.
- [5.1.45] A. Sekulic, K. Furic, *J. Mater. Sci. Lett.* 16 (1997) 260.
- [5.1.46] C. Perry, D. Liu, R. Ingel, *J. Amer. Ceram. Soc.* 68 (1985) C-184.
- [5.1.47] A. Feinberg, C. H. Perry, *J. Phys. Chem. Solids* 42 (1981) 3.
- [5.1.48] D. W. Liu, N. Lacher, X. M. Xu, *High Temp. Sci.* 30 (1990) 1.

Chapter 5.2.

- [5.2.1] R. C. O’Handley, *Modern Magnetic Materials – Principles and Applications*, John Wiley and Sons, New York, 2000.
- [5.2.2] U. Haefeli, W. Schuett, J. Teller, M. Zborowski, *Scientific and Clinical Applications of Magnetic Carriers*, Plenum Press, New York, 1997.
- [5.2.3] R. K. Selvan, C. O. Augustin, L. J. Berchmans, R. Saraswathi, *Mater. Res. Bull.* 38 (2003) 41.
- [5.2.4] J. B. Goodenough, A. L. Loeb, *Phys. Rev.* 98 (1955) 391.
- [5.2.5] E. F. Bertaut, *J. Phys. Radium* 12 (1951) 252.
- [5.2.6] D. S. McClure, *J. Phys. Chem. Solids* 3 (1957) 318.
- [5.2.7] J. D. Dunitz, L. E. Orgel, *J. Phys. Chem. Solids* 3 (1957) 20.
- [5.2.8] B. Jayadevan, K. Tohji, K. Nakatsuka, A. Narayanasamy, *J. Magn. Magn. Mater.* 217 (2000) 99.
- [5.2.9] V. G. Harris, N. C. Koon, C. M. Williams, Q. Zhang, M. Abe, J. P. Kirkland, D. A. McKeown, *IEEE Trans. Magnetics* 31 (1995) 3473.
- [5.2.10] E. Prince, R. G. Treuting, *Acta Crystallogr.* 9 (1956) 1025.
- [5.2.11] V. G. Harris, N. C. Koon, C. M. Williams, Q. Zhang, M. Abe, J. P. Kirkland, *Appl. Phys. Lett.* 68 (1996) 2082.
- [5.2.12] G. M. Bhongale, V. B. Sapre, D. K. Kulkarni, *Bull. Mater. Sci.* 16 (1993) 243.
- [5.2.13] H. Ohnishi, T. Teranishi, *J. Phys. Soc. Jpn.* 16 (1961) 35.

- [5.2.14] N. Nanba, *J. Appl. Phys.* 49 (1978) 2950.
- [5.2.15] J. M. Tranquada, S. M. Heald, A. R. Moodenbaugh, *Phys. Rev. B* 36 (1987) 5263.
- [5.2.16] G. A. Waychunas, M. J. Apte, G. E. Brown Jr., *Phys. Chem. Miner.* 10 (1983) 1.
- [5.2.17] R. K. Selvan, C. O. Augustin, personal communication.
- [5.2.18] R. K. Selvan, C. O. Augustin, personal communication.
- [5.2.19] A. Soldatov, T. S. Ivanchenko, S. Della-Longa, A. Kotani, Y. Iwamoto, A. Bianconi, *Phys. Rev. B* 50 (1994) 5074.
- [5.2.20] A. Bianconi, A. Marcelli, H. Dexpert, R. Karnatak, A. Kotani, T. Jo, J. Petiau, *Phys. Rev. B* 35 (1987) 806.
- [5.2.21] S. Chkoundali, S. Ammar, N. Jouini, F. Fievet, P. Molinie, M. Danot, F. Villain, J. -M. Greneche, *J. Phys.: Condens. Matter* 16 (2004) 4357.
- [5.2.22] S. Asbrink, L. J. Norrby, *Acta Crystallogr.* 26 (1970) 8.
- [5.2.23] R. W. Cairns, E. Ott, *J. Am. Chem. Soc.* 55 (1933) 527.
- [5.2.24] K. N. Subramanyam, *J. Phys. C* 4 (1971) 2266.
- [5.2.25] R. K. Selvan, C. O. Augustin, personal communication.

Chapter 5.3.

- [5.3.1] U. Schubert, N. Huesing, *Synthesis of Inorganic Materials*, Wiley VCH, Weinheim, 2000.
- [5.3.2] G. Kickelbick, M. P. Feth, H. Bertagnolli, B. Moraru, G. Trimmel, U. Schubert, *Monatsh. Chem.* 133 (2002) 919.
- [5.3.3] U. Schubert, *Chem. Mater.* 13 (2001) 3487.
- [5.3.4] U. Schubert, T. Voelkel, N. Moszner, *Chem. Mater.* 13 (2001) 3811.
- [5.3.5] S. Gross, V. D. Noto, G. Kickelbick, U. Schubert, *Mater. Res. Soc. Symp. Proc.* 726 (2002) 47.
- [5.3.6] L. Armelao, H. Bertagnolli, S. Gross, V. Krishnan, U. Lavrencic-Stangar, K. Mueller, B. Orel, G. Srinivasan, E. Tondello, A. Zattin, *J. Mater. Chem.* 15 (2005) 1954.
- [5.3.7] G. Kickelbick, M. P. Feth, H. Bertagnolli, M. Puchberger, D. Holzinger, S. Gross, *J. Chem. Soc., Dalton Trans.* (2002) 3892.
- [5.3.8] S. Doeuff, Y. Dromzee, F. Taulelle, C. Sanchez, *Inorg. Chem.* 28 (1989) 4439.

- [5.3.9] U. Schubert, E. Arpac, W. Glaubitt, A. Helmerich, C. Chau, *Chem. Mater.* 4 (1992) 291.
- [5.3.10] G. Kickelbick, U. Schubert, *Eur. J. Inorg. Chem.* (1998) 159.
- [5.3.11] G. Trimmel, S. Gross, G. Kickelbick, U. Schubert, *Appl. Organomet. Chem.* 15 (2001) 401.
- [5.3.12] B. Moraru, G. Kickelbick, M. Battistella, U. Schubert, *J. Organomet. Chem.* 636 (2001) 172.
- [5.3.13] F. Meneghetti, Diploma Thesis, University of Padua, Padua, 2006.
- [5.3.14] S. Gross, G. Kickelbick, M. Puchberger, U. Schubert, *Monatsh. Chem.* 134 (2003) 1053.
- [5.3.15] M. P. Feth, G. Kickelbick, S. Gross, M. Bauer, V. Krishnan, E. Wendel, U. Schubert, H. Bertagnolli, *HASYLAB Annual report* (2003) 291.
- [5.3.16] L. Armelao, H. Bertagnolli, D. Bleiner, M. Groenewolt, S. Gross, V. Krishnan, C. Sada, U. Schubert, E. Tondello, A. Zattin, manuscript in preparation.

Chapter 5.4.

- [5.4.1] N. N. Greenwood, A. Earnshaw, *Chemistry of the Elements*, Butterworth-Heinemann, Oxford, 1995.
- [5.4.2] M. Green, P. O'Brien, *Chem. Commun.* (1999) 2235.
- [5.4.3] R. Rossetti, R. Hull, J. M. Gibson, L. E. Brus, *J. Phys. Chem.* 82 (1985) 552.
- [5.4.4] M. K. Koranjai, D. D. Gupta, *Thin Solid Films* 155 (1987) 309.
- [5.4.5] L. Cavalca, G. F. Gasparri, G. D. Andretti, P. Domiano, *Acta Crystallogr.* 22 (1967) 90.
- [5.4.6] F. Meneau, G. Sankar, N. Morgante, R. Winter, C. R. A. Catlow, G. N. Greaves, J. M. Thomas, *Faraday Discuss.* 122 (2002) 203.
- [5.4.7] E. H. Kisi, M. M. Elcombe, *Acta Crystallogr., Sect. C: Cryst. Struct. Commun.* 45 (1989) 1867.

Chapter 5.5.

- [5.5.1] C. J. Brinker, G. W. Scherer, *Sol-Gel Science – The Physics and Chemistry of Sol-Gel Processing*, Academic Press, San Diego, 1990.

- [5.5.2] L. C. Klein, Ed., *Sol-Gel Technology for Thin Films, Fibres, Preforms, Electronics and Specialty Shapes*, Noyes Publications, Park Ridge N. J., 1988.
- [5.5.3] M. Guglielmi, G. Carturan, *J. Non-Cryst. Solids* 100 (1988) 16.
- [5.5.4] D. C. Bradley, R. C. Mehrotra, D. P. Gaur, *Metal Alkoxides*, Academic Press, London, 1978.
- [5.5.5] G. Orcel, L. L. Hench, *J. Non-Cryst. Solids* 79 (1986) 177.
- [5.5.6] S. Doeuff, M. Henry, C. Sanchez, J. Livage, *J. Non-Cryst. Solids* 89 (1987) 206.
- [5.5.7] D. Peter, T. S. Ertel, H. Bertagnolli, *J. Sol-Gel. Sci. Technol.* 3 (1994) 91.
- [5.5.8] M. Veith, S. Mathur, C. Mathur, V. Huch, *J. Chem. Soc., Dalton Trans.* (1997) 2101.
- [5.5.9] D. C. Bradley, B. N. Chakravarti, W. Wardlaw, *J. Chem. Soc.* (1956) 2381.
- [5.5.10] L. G. Hubert-Pfalzgraf, J. G. Riess, *Bull. Chem. Soc. France* 11 (1968) 4348.
- [5.5.11] N. Y. Turova, A. V. Korolev, D. E. Tchebukov, A. I. Belokon, A. I. Yanovsky, Y. T. Struchkov, *Polyhedron* 15 (1996) 3869.
- [5.5.12] D. C. Bradley, H. Holloway, *Can. J. Chem.* 29 (1961) 1818.
- [5.5.13] D. C. Bradley, H. Holloway, *Can. J. Chem.* 40 (1962) 62.
- [5.5.14] J. Weidlein, U. Mueller, K. Dehnicke, *Schwingungsspektroskopie*, Thieme Verlag, Stuttgart, 1982.
- [5.5.15] S. X. Lao, R. M. Martin, J. P. Chang, *J. Vac. Sci. Technol. A* 23 (2005) 488.
- [5.5.16] F. R. Dollish, W. G. Fateley, F. F. Bentley, *Characteristic Raman Frequencies of Organic Compounds*, Verlag Chemie, New York, 1974.
- [5.5.17] N. Kaliwoh, J. Zhang, I. W. Boyd, *Appl. Surf. Sci.* 168 (2000) 13.
- [5.5.18] A. Leautic, F. Babonneau, J. Livage, *Chem. Mater.* 1 (1989) 248.
- [5.5.19] H. Cattet, P. Audebert, C. Sanchez, P. Hapiot, *J. Phys. Chem. B* 102 (1998) 1193 and the references therein.
- [5.5.20] R. C. Mehrotra, R. Bohara, *Metal Carboxylates*, Academic Press, London, 1993.
- [5.5.21] R. C. Mehrotra, R. Bohra, D. P. Gaur, *Metal β -diketonates and Allied Derivatives*, Academic Press, London, 1978.
- [5.5.22] D. Peter, T. S. Ertel, H. Bertagnolli, *J. Sol-Gel Sci. Technol.* 5 (1995) 5.
- [5.5.23] R. C. Fay, T. J. Pinnavaia, *Inorg. Chem.* 7 (1968) 508.
- [5.5.24] S. Mueller, Diploma Thesis, University of Stuttgart, Stuttgart, 2005.

Appendix

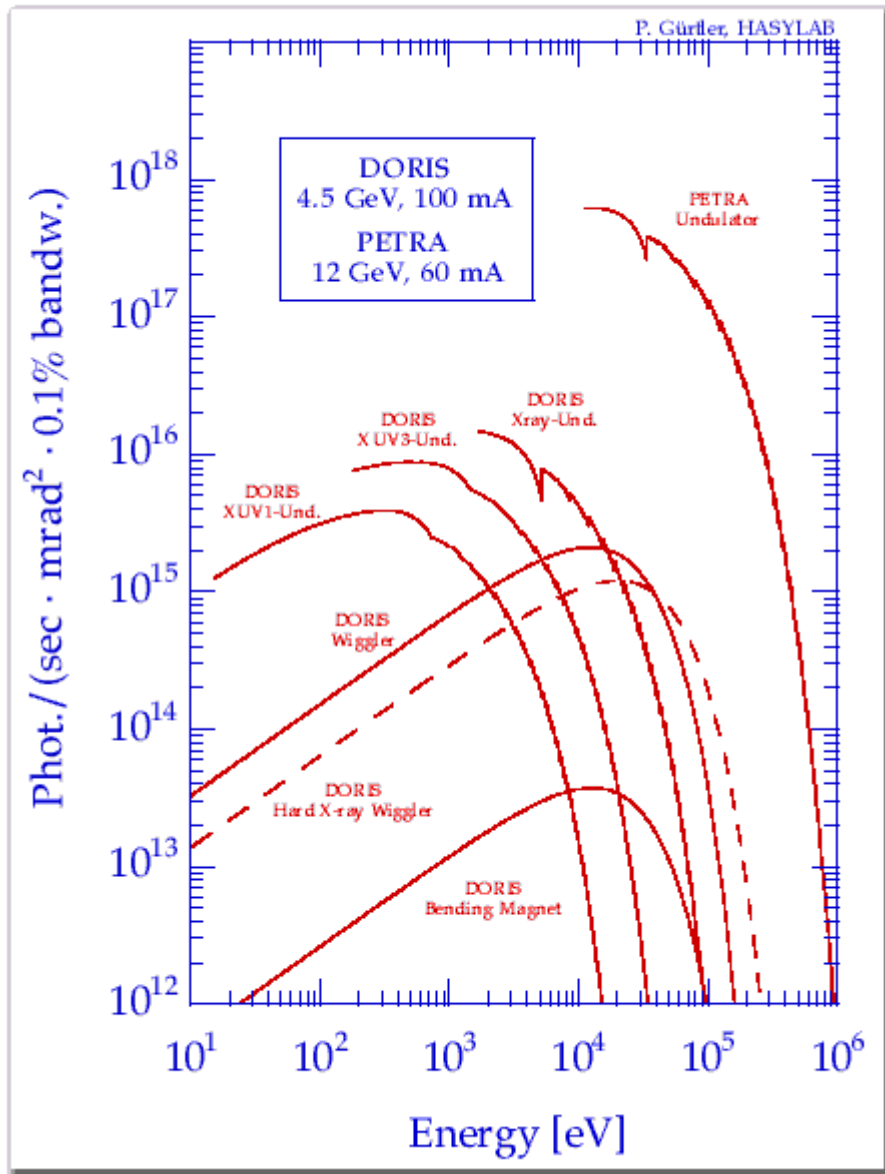
A1. Main parameters of Doris III at HASYLAB

(Adapted from <http://www-hasylab.desy.de/>)

Positron energy	4.45 GeV
Initial positron beam current (5 bunches)	120 mA
Circumference	289.2 m
Number of buckets	482
Number of bunches	1 (for tests), 2 and 5
Bunch separation (minimum)	964 ns (for tests), 480 ns and 192 ns
Horizontal positron beam emittance	404 pi nrad
Coupling factor	3%
Vertical positron beam emittance	12 pi nrad
Positron beam energy spread (rms)	0.11%
Curvature radius of bending magnets	12.1849 m
Magnetic field of bending magnets	1.2182 T
Critical photon energy from bending magnets	16.04 keV

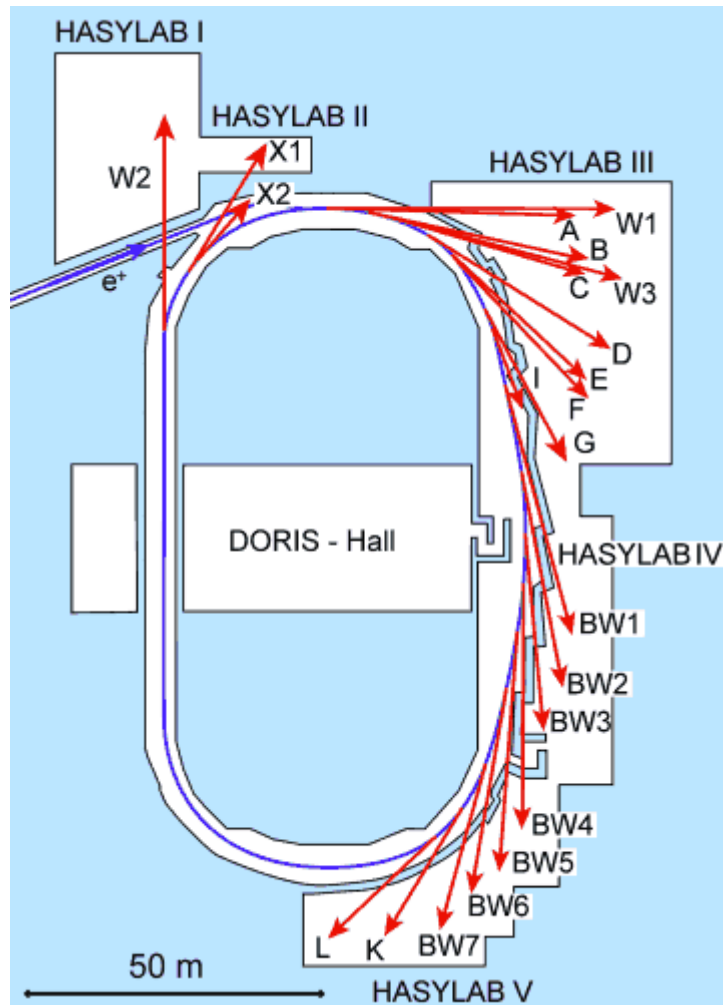
A2. Photon flux at HASYLAB

(Adapted from <http://www-hasylab.desy.de/>)



A3. Overview of the experimental stations at HASYLAB

(Adapted from <http://www-hasylab.desy.de/>)



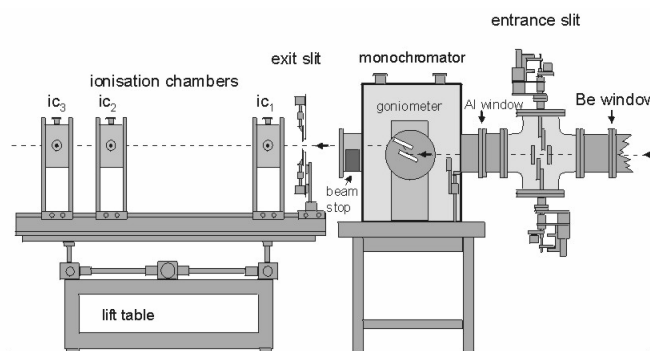
A4. Instrument specification for beamline X1 at HASYLAB

(Adapted from <http://www-hasylab.desy.de/>)

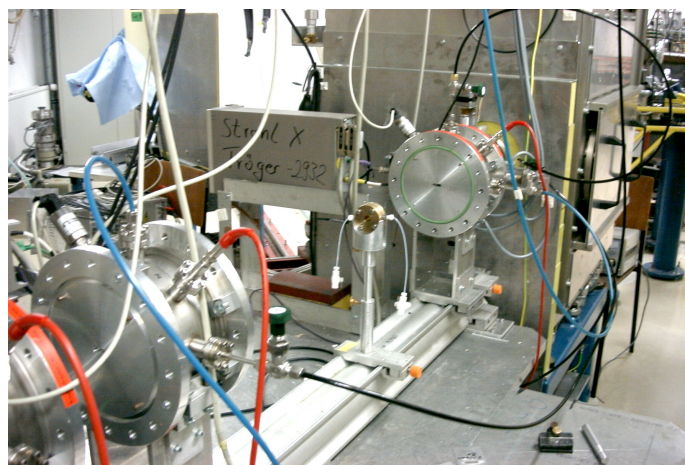
Parameters

Monochromator crystals	Si(111), Si(311) and Si(511) Crystals can be remotely exchanged within 1 min. All relevant parameters are changed accordingly so that no subsequent realignment of the beamline is necessary. Energy calibration of the beam line is preserved within better than 2 eV.
Mirrors	Not available
Energy range	~6 keV to 80 keV
Beam size	20 mm horiz. x 10 mm vert.
Flux at sample	2×10^9 ph mm ⁻² s ⁻¹ per 100mA at 9 keV 7×10^8 ph mm ⁻² s ⁻¹ per 100mA at 19 keV
Detectors for transmission measurements	Ionisation chambers filled with inert gases
Detectors for fluorescence measurements	Five-element high-countrate Ge detector
Energy resolution for Si(311)	1 eV around 10 keV 5 eV around 18 keV 20 eV around 35 keV

Scheme



Picture



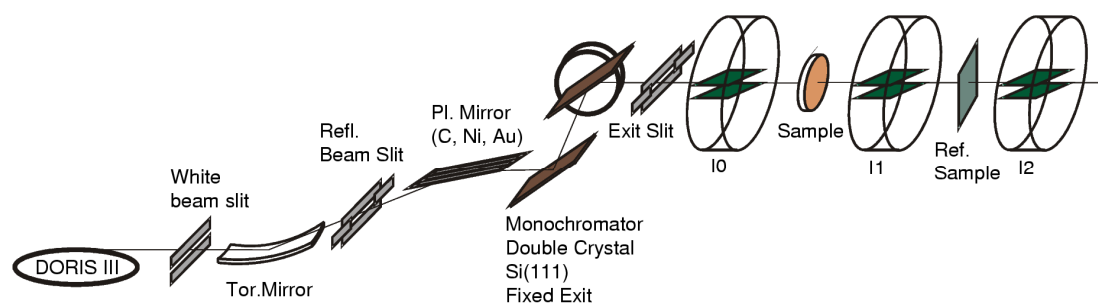
A5. Instrument specification for beamline E4 at HASYLAB

(Adapted from <http://www-hasylab.desy.de/>)

Parameters

Monochromator crystals	Si(111) Water cooling on first crystal
Mirrors	(1) Toroidal mirror with Au-coating (2) Plane mirror with C-, Ni- or Au-coating (7 mrad incidence/exit angle for both mirrors)
Energy range	2.8 – 5.0 keV (C-mirror) 4.5 - 8.5 keV (Ni-mirror) 8.0 - 11.0 keV (Au-mirror)
Beam size	2 x 6 mm
Flux at sample	1×10^{10} ph mm ⁻² s ⁻¹ per 100mA
Detectors for transmission measurements	Ionisation chambers filled with inert gases
Detectors for fluorescence measurements	Five-element high-countrate Ge detector
Energy resolution for Si(111)	0.8 eV at 3.2 keV

Scheme



Picture



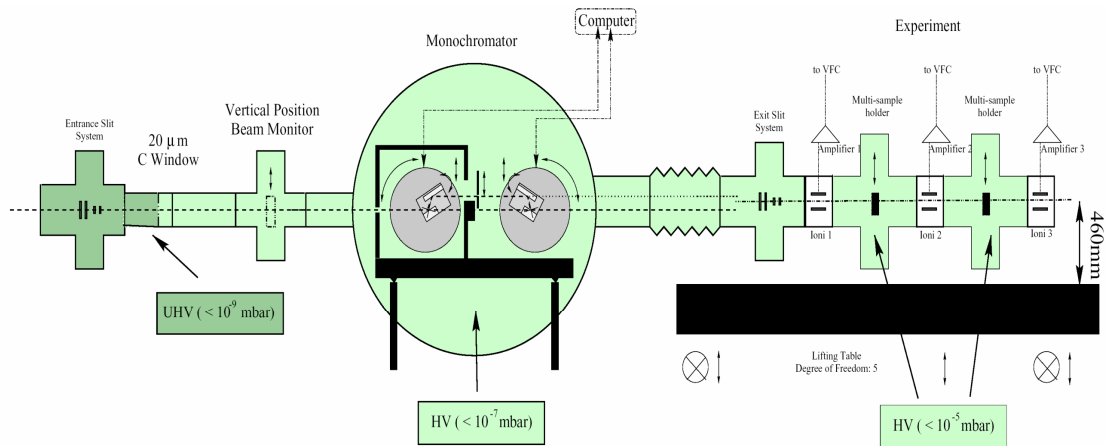
A6. Instrument specification for beamline A1 at HASYLAB

(Adapted from <http://www-hasylab.desy.de/>)

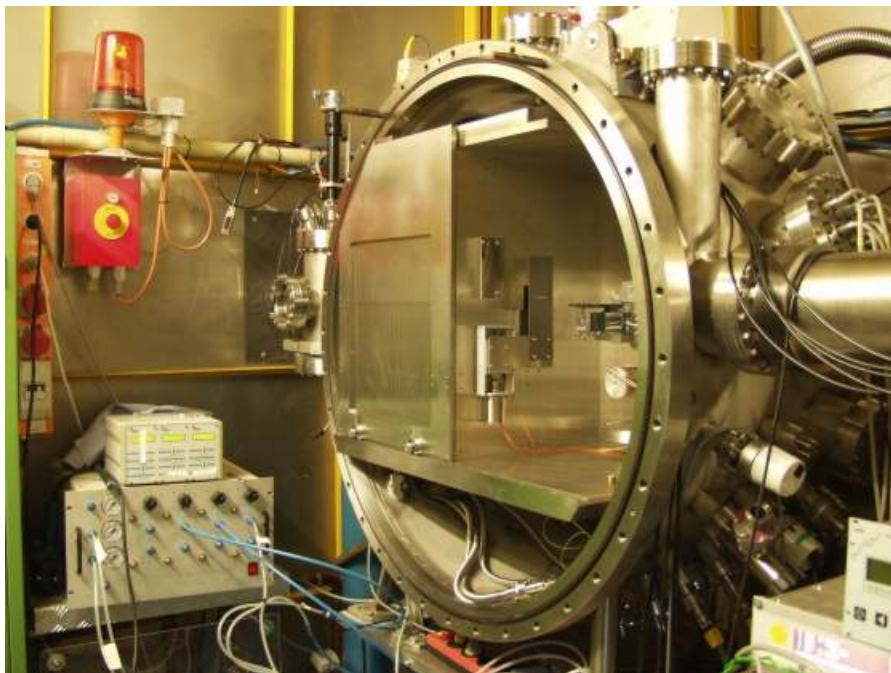
Parameters

Monochromator crystals	Si(111) and Si(311) - Both channel cut
Mirrors	Not available
Energy range	2.4 - 17.0 keV (with Si(111)) 11.0 - 32.0 keV (with Si(311))
Beam size	1 x 8 mm
Flux at sample	$1 \times 10^9 \text{ ph mm}^{-2} \text{ s}^{-1}$ per 100mA at 9 keV
Detectors for transmission measurements	Ionisation chambers filled with inert gases
Detectors for fluorescence measurements	7 pixel SiLi and 5 pixel HPGe-detector

Scheme



Picture

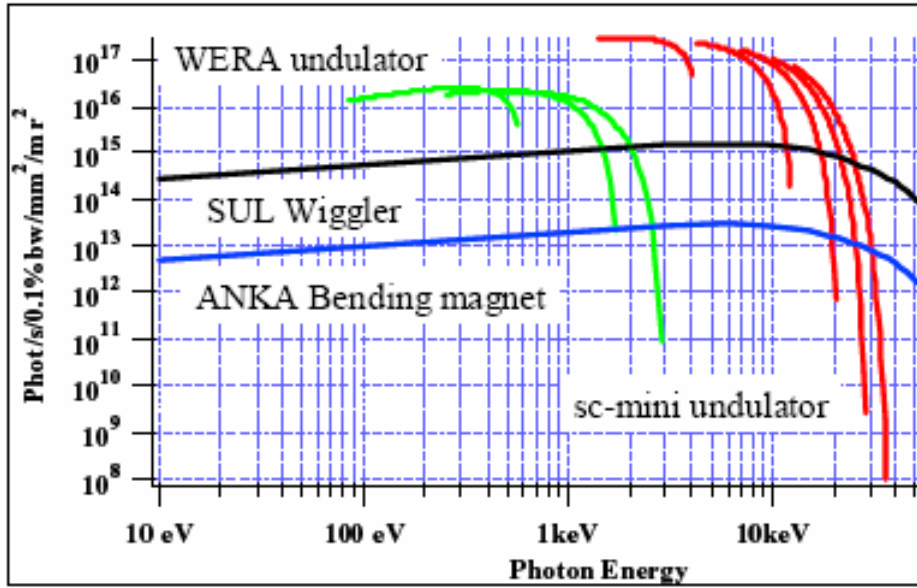


A7. Main parameters of synchrotron ring at ANKA(Adapted from <http://ankaweb.fzk.de/>)

Electron energy	2.5 GeV
Initial electron beam current	200 mA
Circumference	110.4 m
RF-Frequency	500 MHz
Horizontal beam emittance	100 nmrad
Horizontal beta-function	0.9 – 20.9 m
Vertical beam emittance	2.72 nmrad
Vertical beta-fuction	1.8 – 19.7 m
Curvature radius of dipole magnets	5.5593 m
Magnetic field of dipole magnets	1.5 T
Number of dipole magnets	16

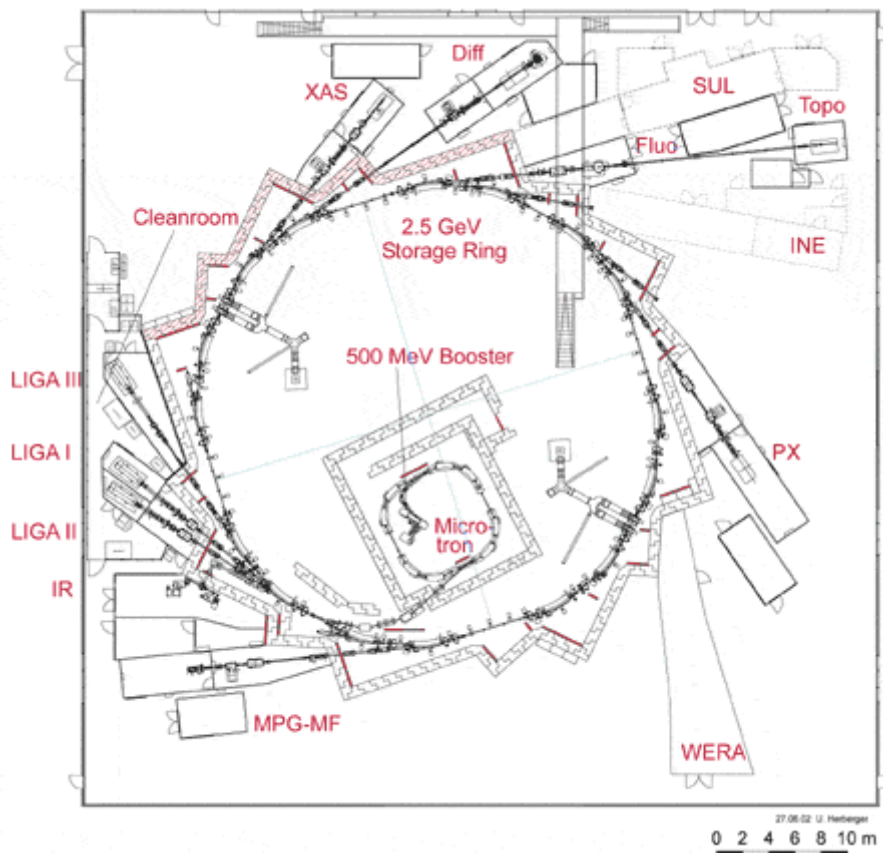
A8. Photon flux at ANKA

(Adapted from <http://ankaweb.fzk.de/>)



A9. Overview of the experimental stations at ANKA

(Adapted from <http://ankaweb.fzk.de/>)



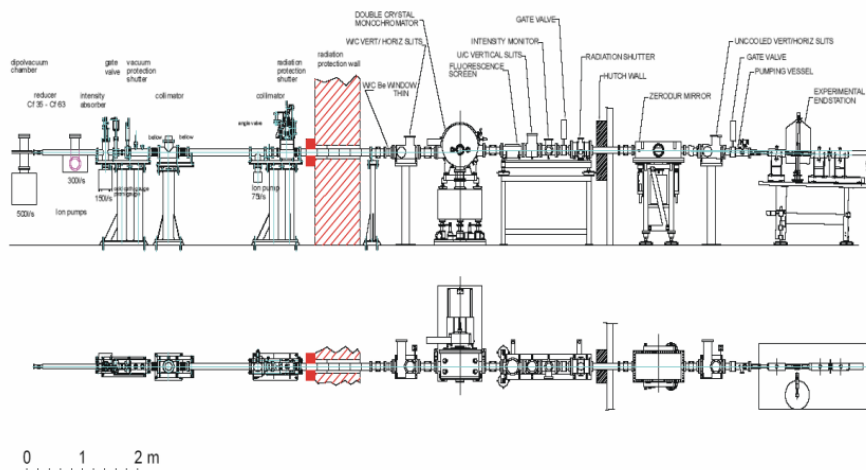
A10. Instrument specification for XAS beamline at ANKA

(Adapted from <http://ankaweb.fzk.de/>)

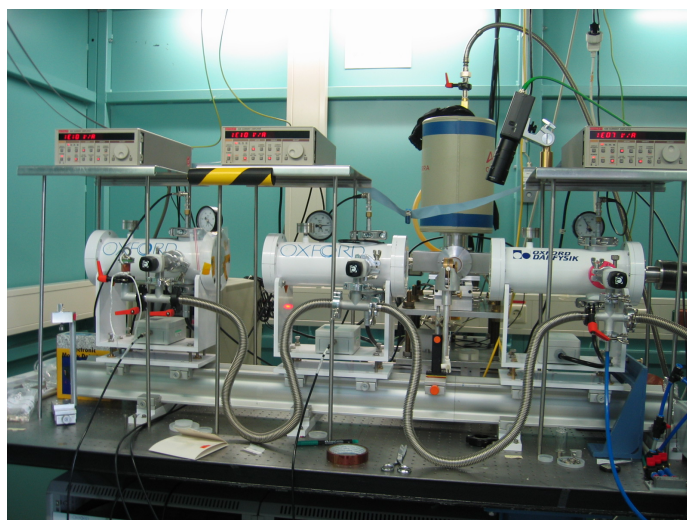
Parameters

Monochromator crystals	Si(111) and Si(311) Crystals can be remotely exchanged within 30 min.
Mirrors	Planar zerodur mirror to suppress higher harmonics at low energies
Energy range	2.4 keV to 25 keV
Beam size	20 mm horiz. x 2 mm vert.
Flux at sample	1×10^{10} ph mm ⁻² s ⁻¹ per 140mA at 9 keV
Detectors for transmission measurements	Ionisation chambers filled with inert gases
Detectors for fluorescence measurements	Five-element high-countrate Ge detector
Energy resolution ($\Delta E/E$)	Si(111): 2×10^{-4} Si(311): 1×10^{-4}

Scheme

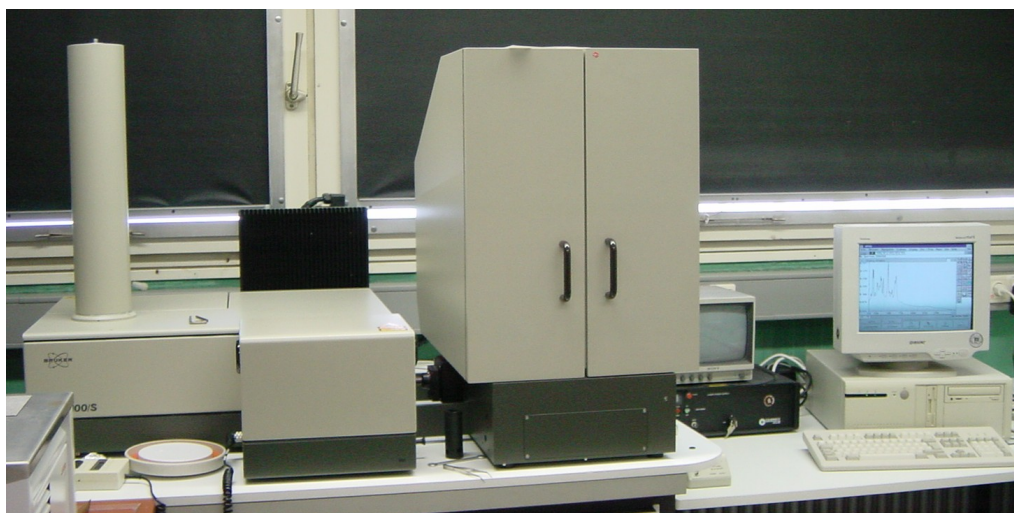


Picture



A11. Instrument specification for Raman spectrometer**Parameters**

Spectrometer system	Fourier transform Raman spectrometer
Manufacturer	Bruker
Model	RFS 100/S
Light source	Nd:YAG Laser
Wavelength	1064 nm
Maximum power level	1.5 W
Detector	Germanium detector (D 418-S) - cooled with liquid nitrogen
Filter system	Rayleigh interference filter
Measurement geometry	180° - reflection
Measurement range	10 - 4000 cm ⁻¹
Resolution	4 cm ⁻¹
Sample holder for solids	Metal holders
Sample holder for liquids	Quartz cuvette
Computer system	OS/2-PC
Software	OPUS 3.0

Picture

A12. Instrument specification for infrared spectrometer

Parameters

Spectrometer system	Fourier transform infrared spectrometer
Manufacturer	Bruker
Model	IFS 66/S
Light source	Globar
Detector	DLATGS and MCT detectors
Beam splitter	KBr splitter
Measurement geometry	Transmission
Measurement range	400 - 4000 cm^{-1}
Resolution	2 cm^{-1}
Sample preparation	KBr pellet
Computer system	Windows 2000
Software	OPUS 4.0

Picture



Curriculum Vitae

Venkata Krishnan

Born on Sep 25, 1979 in Gobichetipalayam T.N., India



School education

- 1985-1990 Primary school education at Vidya Vikashini in Coimbatore, Tamil Nadu, India
- 1990-1995 Secondary school education at Chinmaya Vidyalaya in Coimbatore, Tamil Nadu, India
- May 1995 Passed the Matriculation examination in First class
- 1995-1997 Higher secondary school education at Chinmaya Vidyalaya in Coimbatore, Tamil Nadu, India
- May 1997 Passed the Higher secondary examination in First class

College education

- 1997-2000 Studied B.Sc. in Applied Sciences at PSG College of Technology (formerly affiliated to Bharathiar University), Coimbatore, Tamil Nadu, India
- Nov 1999- Apr 2000 Dissertation on “*Synthesis and characterization of phosphorus containing polyester*” with Dr. S. C. Murugavel
- Apr 2000 Passed B.Sc. degree examination in First class.
- 2000-2002 Studied M.Sc. in Materials Science at PSG College of Technology (formerly affiliated to Bharathiar University), Coimbatore, Tamil Nadu, India
- Nov 2001- Apr 2002 Dissertation on “*Preparation and investigation of the properties of diphasic ferroelectric ceramic-polymer composites*” with Prof. Dr. M. S. Vijaya
- Apr 2002 Passed M.Sc. degree examination in First class

Doctoral work

- 2002-2006 Doctoral work at the Institute of Physical Chemistry, University of Stuttgart, Stuttgart, Germany
- Jul 2002- Jun 2006 Dissertation on “*Structural investigations on organometallic complexes and nanomaterials by X-ray absorption fine structure and Raman spectroscopy*” with Prof. Dr. H. Bertagnolli

